SCHOLARLY PUBLICATIONS

A CURRENT AWARENESS BULLETIN
OF RESEARCH OUTPUT

@DTU

(16th Edition)

APRIL 2014

BY: CENTRAL LIBRARY

DELHI TECHNOLOGICAL UNIVERSITY
(FORMERLY *DELHI COLLEGE OF ENGINEERING)*
GOVT. OF N.C.T. OF DELHI
SHAHBAD DAULATPUR, MAIN BAWANA ROAD
DELHI 110042

PREFACE

This is the Sixteenth Issue of Current Awareness Bulletin started by Delhi Technological University, Central Library. The aim of the bulletin is to compile, preserve and disseminate information published by the faculty, students and alumni for mutual benefits. The bulletin also aims to propagate the intellectual contribution of Delhi Technological University (DTU) as a whole to the academia.

The bulletin contains information resources available in the internet in the form of articles, reports, presentations published in international journals, websites, etc. by the faculty and students of DTU. The publications of faculty and student which are not covered in this bulletin may be because of the reason that the full text either was not accessible or could not be searched by the search engine used by the library for this purpose.

The learned faculty and students are requested to provide their uncovered publications to the library either through email or in CD, etc to make the bulletin more comprehensive.

This issue contains the information published during April 2014. The arrangement of the contents is alphabetical. The full text of the article which is either subscribed by the university or available in the web is provided in this bulletin.

Central Library

CONTENTS

1. A Generic Membrane Computing-based Sudoku Solver Dipti Deodhare, Shailesh Sonone and ***Anubha Gupta***, Delhi College of Engineering

2. A Novel DFAL based Frequency Divider, Himanshu Puri, Kshitij Ghai, Kirti Gupta and ***Neeta Pandey,*** Electronics and Communication

3. A SECURITY BASED ARCHITECTURE FOR MANET, Ekata Gupta and ***Dr.S.K.Saxena***, CSE Department

4. A study and comparison of Uninterruptible Power Supply topologies, ***$Arnav Gupta***

5. Action-based trust computation algorithm for Online Social Network Mohit Gambhir, ***~Dr. Moinuddin,***

6. An Analysis of Telecommunication Fraud using Outlier Detection Model based on Similar Coefficient Sum, ***Daya Gupta***, Payal Pahwa, ***@Rajiv Arora***, Computer Engineering

7. Assessment of Renewable Energy in India, ***£Rijul Dhingra, £Abhinav Jain, £Abhishek Pandey, and £Srishti Mahajan,*** environmental engineering

8. Availability Analysis with Opportunistic Maintenance of a Two Component Deteriorating System, ***Joel P. Varghese*** and ***Girish Kumar***

9. Biosensors for pathogen detection: A smart approach towards clinical diagnosis, Renu Singh, Maumita Das Mukherjee, Gajjala Sumana, Rajinder K. Gupta, Seema Sood and ***B.D. Malhotra***, Department of Biotechnology

10. Blending of Ethanol in Gasoline:Impact on SI Engine Performance and Emissions ***Amit Pal***, Deptt of Mechanical Engineering

11. CALCULATION OF POTENTIAL ENERGY TERM IN VARIABLE MOMENT OF INERTIA NUCLEAR SOFTNESS (MINS) MODEL Hardik P. Trivedi, Pallavi Bhatt, Anil Kumar, Lalit Kumar Gupta, Jai Prakash Gupta, Krishna Chandra and ***Than Singh Saini**, Department of Physics

12. Chaotic Map Based Steganography of Gray Scale Images in Wavelet Domain, ***Shalu Garg** and ***Monika Mathur**, Department of Electronics and Communication

13. Comparative analysis of statistical and machine learning methods for predicting faulty modules, ***Ruchika Malhotra**, Department of Software Engineering

14. Computer Simulation of Trombe Wall for Porous and Non-Porous Strutcures, ***Vishav Kamal** and ***R. S. Mishra**, Department of Mechanical Engineering

15. Consolidation of clayey gouge amid permeating rock masses, Tanmay Banik, Tanay Sukumar, Amit Kumar, ***Naresh Akshay Jain** and***Ashutosh Trivedi**, Civil Engineering

16. CORPORATE GOVERNANCE IN INSURANCE SECTOR, ***Priyanka Chaudhary**, Delhi School of Management, Delhi Technological University

17. Critical Assessment of River Water Quality and Wastewater Treatment Plant (WWTP), **@Allaa M. Aenab**, PhD Student, Environmental Engineering & ***S. K. Singh**, Professor, Dean & Head of Environmental Engineering

18. Design and Assemble of Low Cost Prepaid Smart Card Energy Meter – A Novel Design, ***Sudarshan K. Valluru**, Department of Electrical Engineering

19. Design of Stacked Miniaturized Slotted Antenna with Enhanced Bandwidth for WiMAX Application, Jimmy Gautam,***N. Jayanthi**, ECE Department

20. Efficient Resolution Of Mixed Pixels Using BioInspired Heuristics, ***Tanu Varshney**, ***Lavika Goel**, ***Daya Gupta**, HOD,COE Department and V.K.Panchal

21. Energy and Exergy Analysis of A Wet Ethanol Based HCCI Engine Combined Cycle **#Dr. Shailesh Kumar Trivedi, ~Dr. Ahmad Faizan Sherwani** and Dr. Abid Haleem

22. Experimental and Numerical Analysis of Negative Spring Back in V-Bending of if Steel, ***Rohit Shukla***, Automobile Engineering, ***Vijay Gautam***, Mechanical Engineering

23. Experimental Investigation on Hydrodynamic Journal Bearing using SAE 10W30 Multi Grade Oil, ***Paras Kumar***, and ***Ashish Kumar Gupta***, Mechanical Engineering

24. Generalized neural network and wavelet transform based approachfor fault location estimation of a transmission line, Majid Jamila, Abul Kalama, A.Q. Ansaria, ***M. Rizwan***, Department of Electrical Engineering

25. In-flight gas phase growth of metal/multi layer graphene core shell nanoparticles with controllable sizes, Saurabh K. Sengar, B. R. Mehta, Rakesh Kumar & ***Vinod Singh***, Applied Physics

26. Intelligent Video Target Tracking using an Evolutionary Particle Filter based upon Improved Cuckoo Search, Gurjit Singh Walia, ***Rajiv Kapoor***, Electronics and Communication

27. Thermodynamic performance evaluation of multievaporators single compressor and single expansion valve and liquid vapour heat exchanger in vapour compression refrigeration systems using thirteen eco friendly refrigerants for reducing global warming and ozone depletion, ***Prof. R.S Mishra,*** Mechanical Engineering

28. Linde and Claude System Second Law Comparison for Liquefaction of Air, ***Devender Kumar*** and ***R.S Mishra***, Department Of Mechanical Engineering

29. Low Power D-latch design using MCML Tri-state Buffers, ***Radhika***, ***Neeta Pandey, *Kirti Gupta,*** Electronics and Communication and Maneesha Gupta

30. Methods for Improving First and Second Law Efficiencies of Vapour Compression Refrigeration Systems Using Flash-Intercooler with Ecofriendly Refrigerants, ***Kapil Chopra, V. Sahni, R. S. Mishra,*** Mechanical Engineering

31. MRDMS-Mobile Replicated Database Management Synchronization ***Divyashikha Sethia, *Swati Mehta, *Anant Chowdhary, *Kartikeya Bhatt,*** and ***Siddharth Bhatnagar***, Department of Computer Engineering

32. Multiferroic properties of BiFeO3/BaTiO3 multilayeredthin films, Savita Sharma, MonikaTomar, AshokKumar, ***NitinK.Puri*** and ***Vinay Gupta**, Applied Physics

33. NO2 Sensing Properties of WO3 Thin Films Deposited by Rf-Magnetron Sputtering, ***Savita Sharma***, Monika Tomar, ***Nitin K. Puri*** and Vinay Gupta, Department of Applied Physics,

34. Optimization of Process Parameters for Gas Tungsten Arc Welding of AA1100 Aluminium Alloy, ***Vijay Gautam,*** Department of Mechanical Engineering

35. Performance Analysis of PID and Fuzzy PD+I Controller on Nonlinear Systems, ***Bharat Bhushan, *Nupur Jha, *Sangeeta Devra*** and ***Sarath S. Pillai***, Department of Electrical Engineering

36. Performance Analysis of Three-phase Four-wire Shunt Active Power Filter, Harsha Vanjani, ***#U. K. Choudhury*** (M.Tech)

37. Physico-Chemical Characterization of Cathode Material, Li1+x(Mn0.4Ni0.4Fe0.2)1-xO2 (x=0.2) for Lithium Ion Batteries, ***$Rishibrind K. Upadhyay*** and ***Amrish K. Panwar***, applied physics

38. Portfolio Optimization: Indifference Curve Approach, Nand Kumar, Archana Singh, ***Ranganath M S*** and ***Amandeep Kaur***, Department of Mechanical Engineering

39. Recommendation System for Highly Sparse Datasets: A Hybrid Approach, Himanshu Chadha, ***Ankita Jain, *Aditi Singh*** and ***Ankur Ahuja***

40. Reptiles Inspired Biomimetic Materials and Their Novel Applications, Kishor Kalauni, K. M. Gupta and !Isha Bharti, Teaching-cum-Research Fellow, Applied Physics

41. Simple toughening of epoxy thermosets by preformed thermoplastics, Saurabh Chaudhary, Surekha Parthasarathy, Chitra Rajagopal, Prasun Roy and Devendra Kumar, Department of Applied Chemistry and Polymer Technology

42. SRF based Modeling and Control of Cascaded Multilevel Active Rectifier with Uniform DC-Buses, ***Amritesh Kumar, *Dhruv Kumar*** and ***Daya Ram Meena,*** Electrical Engineering

43. Stochastic Comparisons of Residual Entropy of Order Statistics and Some Characterization Results, *Ramesh C. Gupta, *H.C. Taneja and *Richa Thapliya, Department of Applied Mathematics

44. Study of Aluminum Oxide Abrasive on Tempered Glass in Abrasive Jet Machining Using Taguchi Method, ***Punit Grover,** ***Sanjay Kumar** and ***Qasim Murtaza**, Department of Mechanical Engineering

45. Study on Naive Bayesian Classifier and its relation to Information Gain, ***Anjana Kumari***

46. Thermodynamic Analysis and Comparison for "COP" In Solid Adsorption Refrigeration Systems (BaCl2-NH3 & SrCl2-NH3, Jitendra Kumar, Vikas Verma, Pradhuman Dobhal and ***Naushad.A.Ansari,** Department of Mechanical Engineering

47. Thermodynamic Comparison of Linde and Claude Systems for Liquefaction of Gases ***Devender Kumar** and ***R. S. Mishra**, Department Of Mechanical Engineering

48. Two Zone Combustion Model for SI Engines to Study the Variations in Cylinder Pressures and Temperatures between Adiabatic Combustion and Eichelberg's Correlation, ***Rajkumar Singh,** **£***Vikram Singh,* **£***Sarthak Piplani* and **£***Aditya Tyagi,* Department of ME

***Faculty** **@Research Scholar** **$PG Scholar #Alumni**
£Undergraduate Student **~ Ex Faculty** **<Ex Research Scholar**
! Teaching-cum-Research Fellow

A Generic Membrane Computing-based Sudoku Solver

Dipti Deodhare, Shailesh Sonone
Centre for Artificial Intelligence and Robotics (DRDO)
Bangalore, India.
dipti@cair.drdo.in , ssonone@cair.drdo.in

Anubha Gupta
Delhi College of Engineering, New Delhi, India.
(She worked as a Trainee in Centre for Artificial Intelligence and Robotics, DRDO, Bangalore under the guidance of first and second author)

***Abstract*- Sudoku is a logic-based, combinatorial number placement puzzle, with the objective of filling an $n^2 \times n^2$ grid of cells with digits so that each column, row and $n \times n$ sub-grid (box) that compose the grid contain all the digits from *1* to n^2. In this paper we study the problem of implementing the Sudoku solving algorithm through the membrane computing paradigm. The devices of this paradigm are called *P systems*. The solution is obtained by first finding a unique candidate in rows, columns and boxes using the constraints, and then applying various Sudoku solving strategies. Finally, if every strategy fails, the solution is searched through a brute force method. If the solution is obtainable, the P system returns the object YES to the environment. If the Sudoku is unsolvable, the P system returns the object NO to the environment and the system eventually halts. The main contribution of this paper is that the basic P System model defined in [1] has been extended further with additional powerful strategies based on the deductive logic popular with human solvers. The objectives of this effort are twofold (*i*) to study the very expressive, compact & elegant representation system membrane computing offers (*ii*) to study the resilience & flexibility offered by the representation to permit addition of new strategies; this being an important requirement in real life applications. The results are presented and discussed for some of the most difficult Sudoku problems available in open source literature. The model will find a solution if it exists. In this sense the model is a generic Sudoku solver.**

Keywords— Membrane Computing, Sudoku solver

I. INTRODUCTION

An important objective of Computer Science in general and Artificial Intelligence in particular is to handle combinatorial search efficiently. Another equally important requirement is to establish resilient knowledge representation mechanisms that are both expressive as well as afford the ease of introduction of new strategies/rules/mechanisms without the need of bringing down the complex application program/system the solution is a part of. Traditionally, combinatorial search algorithms are discussed in the context of evaluating moves in games characterized by the need of exploring large spaces for the solution. The advantage being that the problem definition is easy to articulate since it is common knowledge and the complexity offered is prototypical in nature. Sudoku is a puzzle game defined for a single player, hugely popular across the globe. It consists of partially completed row-column grid of cells [5]. The objective is to fill in each cell a prescribed set of n^2 distinct numbers, typically $\{1, ..., n^2\}$, so that each row, column and the sub-grid (box) contain all the numbers 1 through n^2, exactly once. Although the 9×9 grid with 3×3 sub-grids is by far the most common, many variants exist. The general problem of solving Sudoku puzzles on $n^2 \times n^2$ grids of $n \times n$ boxes is known to be NP-complete [9]. Researchers have devised algorithms using backtracking/ CSP (Constraints Satisfaction Problems) techniques and using domain specific strategies to solve Sudoku problems [6].

In this paper we have studied the paradigm of membrane computing for the specific problem of solving Sudoku and compared the performance results with the conventional brute force algorithm. We have extended the *P System* model defined in [1] with additional powerful strategies which provide the solution to the hardest problems fast. The P System defined in [1] works on an assumption that in any configuration of a partial solution to the Sudoku problem, there exists at least one unfilled cell *(i, j)* with a unique candidate (possible assignment). But this is often not true and hence the model does not always return the solution even if a valid solution exists. We have improvised the rules in [1] and augmented them with powerful strategies, based on deductive logic typically used by human solvers. These strategies prune the number of probable candidates for the unfilled cells and increase the probability of finding unique candidates for them, thus being able to solve hard Sudoku fast. After the strategies have pruned the solution space and are unable to remove anymore candidate options, the model checks for availability of unique candidates in as yet unfilled cells. On success it proceeds again with a check-reset cycle described in detail in Section V and VI. In the event that no unique candidates are found for any unfilled cell the model goes to the brute force method from the last configuration (partial solution with the pruned candidate sets for unfilled cells) obtained so far. It is pertinent to note that starting from a valid Sudoku the strategies ensure that the evolution of the solution subsequent to their application does not compromise the validity of the Sudoku and the strategies significantly speed up the brute force method. Moreover, the brute force method used in this model does further on-the-fly pruning during run time which helps in improving the performance. Our solution also solves under constrained Sudoku problems. The model will find a

978-1-4799-2900-9/14/$31.00 ©2014 IEEE

solution if it exists. In this sense the model is a generic Sudoku solver. Ten strategies from open source literature have been translated and inserted in the P System model defined in [1]. As can be seen in the detailed presentation in subsequent sections, the expression is compact. Also, extending an existing model was facilitated by the P System representation. As such, we demonstrate the elegance of representation and ease of extension offered by the Membrane Computing paradigm.

Membrane Computing (MC) is a branch of natural computing which builds new non-deterministic computational models from the study of biological cells, particularly of the cellular membranes, their structure, functioning and interactions in tissues or higher-order biological structures [2]. In [2], MC was introduced by Gheorghe Paun who first conceived the model in 1998 with an assumption that the processes taking place in the cellular membranes of the living cells can be interpreted as computations. The devices of this model are known as P systems. A P system consists of a membrane structure, which can be a hierarchical arrangement of membranes, as in a cell, a tissue or a neural net. MC models are distributed and parallel computing models, possessing multi-sets of symbol objects encapsulated into compartments defined by membranes (with evolution rules and evolving objects communicating between the compartments and the environment). A membrane can be considered as a barrier between two regions, ensuring a selective communication between the two regions. According to Gheorghe Paun, the Euclidean space gets divided into a finite "inside" and an infinite "outside". Chemicals in a biological membrane are modeled as objects to be computed by the P system. Objects are specified by multi-sets of unique symbols, or alternatively strings of symbols. The region defined by a membrane contains whole numbers of identical copies of each object and/or another membrane, so that a P system has exactly one outermost membrane, also called the skin membrane.

We use the family of P systems $\{\Pi(n) : n \in N\}$ reported in [1] such that the problem instance for a Sudoku puzzle is encoded as a multi-set, which is used as an input to the P system. A solution is obtained by applying the production rules which encode various strategies to find a unique candidate for a square (an unfilled cell) in a grid thus finding out the partial valid solution. The P system comes to a halting configuration with an output to the skin membrane when a complete and valid solution is arrived at. Although the rules can be applied randomly (*i.e.* in a *non-deterministic* manner), we have imposed priorities so that the rules are applied in a particular order to solve the Sudoku problem.

II. Overview of P System Model

A *transition P system* (of degree $m \geq 1$) [2] is a construct of the form

$$\Pi = (O, C, \mu, w_1, w_2, \ldots, w_m, R_1, R_2, \ldots, R_m, i_o),$$

such that

1. O is a set of (finite and non-empty) alphabet of objects,

2. $C \subset O$ is a set of catalysts,

3. μ is a membrane structure which consists of m membranes, labeled $1,2,\ldots,m$; the number of membranes define the degree m.

4. $w_1, w_2, \ldots, w_m$ are strings over O representing the multi-sets of objects present in the membranes $1,2,\ldots,m$ of μ.

5. $R_1, R_2, \ldots, R_m$ are finite sets of evolution rules associated with the membranes $1,2,\ldots,m$ of μ. Note that *inter se* priorities between rules can be defined, in which case, the rules are applied as per the given priority.

6. i_o is either one of the labels $1,2,\ldots,m$, and the respective membrane is the output region of the system,

The rules are of the form $u \rightarrow v$ or $u \rightarrow v\delta$, with $u \in O^+$ and $v \in (O \times Move)^*$, where $Move = \{here, in, out\}$. δ denotes the action of *membrane dissolving*. The rules can be *catalytic*, *i.e.* of the form $ca \rightarrow cv$ or $ca \rightarrow cv\delta$, with $a \in O - C$, $c \in C$, $v \in ((O-C) \times Move)^*$; the catalysts help the other objects to evolve but they themselves never evolve or change the region or membrane. The rules are typically of the following types:

- *Object evolution rule:* $[\neg in\ u\ cat \rightarrow v]_e$. The multi-set u evolves to the multi-set v in the membrane with label e. The objects from the set *cat* (catalysts) should be present and none of the objects from the set *in* (inhibitors) should be present in order to apply the rule. It is to be noted that *cat* and *in* act as *catalysts* and remain unchanged after applying the rule.
- *Dissolution rules:* $[u]_e \rightarrow O$. The multi-set u dissolves membrane e and evolves to object O. The skin membrane is never dissolved.
- *Send-out or send-in communication rules:* $[a]_e \rightarrow [\ ]_e a$. The object a is sent out of the membrane labeled e to the membrane immediately outside. Similarly there can be a *send-in* rule.

The P System is a synchronous device with a global clock; the configuration of the system changes at every time step by applying rules to each membrane in a non-deterministic and maximally parallel manner. A sequence of transitions constitutes a computation. A computation is successful if the system halts, it reaches a configuration where no rule can be applied to the existing objects and the output region i_0 still exists in the halting configuration.

III. Basic Rules to Solve Sudoku

A Sudoku grid of order n consists of n^4 entries with n^2 copies of each number $\{1, \ldots, n^2\}$ to be placed into $n^2 \times n^2$ grid, arranged in a pattern of $n \times n$ sub-grids (also called as boxes). A Sudoku grid adheres to the property that in each row, column and box no two entries are the same. The problem consists of partially completed grid of rows and columns with the objective to complete the assignment, satisfying the basic property of Sudoku. The basic constraints on the assignment of numbers to a cell can be written as: (*i*) A cell has one and only one number, (*ii*) a number appears at most once in each row, (*iii*) a number appears at most once in each column, (*iv*) a number appears at most once in each box. Following these four constraints, the assignment of a number to a cell follows the basic property of Sudoku.

Some of the Sudoku puzzles can only be solved using logic that is too complex for human solvers. A compilation of the latest hardest Sudoku puzzles (order 3) according to a number of openly accessible solver programs is given in [6], [10] and [13]. We present the performance statistics of our membrane computing model in Section X on these hardest Sudoku problems. We also run our solution on Sudoku provided by a Finnish mathematician who claims to have penned the hardest Sudoku [10]. Apart from this, we also run our solution on higher order Sudoku i.e order 4 to 7 and prove that it works with performance improvement over pure brute-force method.

IV. BRUTE FORCE ALGORITHM

A brute force algorithm visits the empty cells in some order, filling in digits sequentially from the available choices, or backtracking (removing failed choices) when stymied. For the purposes of this exposition, a naive iteration order of left to right, top to bottom is assumed. The iteration could, however, visit the empty cells in any order. The order can even be randomized for each solution attempt with no harm to the algorithm. Randomized algorithms are less vulnerable to worst case inputs, but don't have consistent running times when solving the same problem repeatedly.

V. MEMBRANE COMPUTING BASED SUDOKU SOLVER

In this section we study the membrane computing model (P system model) $\{\Pi(n): n \in N\}$ so as to solve the Sudoku problem of order n. The initial partial solution of the problem is provided to the MC model as its input. The P system applies rules, evolving and dissolving required objects and producing the output objects. The various strategic rules are applied to eliminate more and more number of probable candidates for a particular cell, thus striving to obtain a unique candidate for the cell. If after applying all the strategies, not a single square with a unique candidate is found, then it applies the brute force method to solve the Sudoku. When a complete solution is obtained, the P system sends out an object YES to the environment along with the solution encoded as a multi-set in the skin membrane of the halting configuration. If the inputs to the model are such that the P system cannot solve the Sudoku completely, then it returns the object NO to the environment along with the latest partial solution encoded in the skin membrane of the halting configuration.

VI. APPROACH: THE MODEL

Similar to the model presented in [1], and adapting the same notation, the P system of order n which solves the Sudoku is a construct $\Pi(n) = <\Gamma, H, \mu, w_e, w_s, i_0, R_1, R_2, R_3,..., R_{25}>$ with priorities $R_1 > R_2 > .... > R_{25}$.

- The object $\Gamma = \{ s_{ijx}, z_{ijx}, box_{ijx}, sq_{ij}, f_{ix}, c_{jx}, b_{kx}, a_{ij}, r_{ij} : i,j,k,x \in \{1,...,n^2\}\} \cup \{k_0, k_1, k_2, w, p, d\}$
- The set of labels $H = \{e,s\}$.
- The membrane structure $\mu = [\,[\,]_e\,]_s$.
- The initial multi-sets $w_e = \{k_1\} \cup \{ box_{ijx}, sq_{ij}, f_{ix}, c_{jx}, b_{kx}, r_{ij}{}^{n^2} : i,j,k,x \in \{1,...,n^2\}\}$ and $w_s = \emptyset$
- $i_0 = e$, *i.e.* the input membrane is e.

The P system $\Pi(n)$ depends only on the order n of Sudoku and it does not increase the number of membranes along the computation. These rules are applied according to the following principles:

- All the rules are applied in parallel and in a maximal manner. In one step, one object of a membrane can be used by only one rule (chosen in a nondeterministic way), but any object which can evolve by one rule of any form, must do it.
- If a membrane is dissolved, its contents (multi-set and internal membranes) are left free in the surrounding region.
- If there are objects in this membrane which evolve by means of evolution rules and a membrane e is dissolved at the same time, then we suppose that first the evolution rules are used and then the dissolution is produced. Of course, this process takes only one step.
- Rules have been prioritized.

The input for a Sudoku puzzle is encoded as a multi-set z_{ijx} to provide the initial inputs to the P system, where x represents the number placed at the square *(i,j)*. The initial configuration also contains information about the box_{ijk}, where k denotes the box number of the cell *(i,j)* with $i,j \in \{1,...,n^2\}$. The other objects present in the initial configuration are f_{ix}, c_{jx}, b_{kx} and sq_{ij}. f_{ix} represents the possibility of placement of the number x in the row i, *i.e.* x is not placed in i^{th} row yet, and can be placed in future configurations. Analogously, c_{jx} and b_{kx} represent the possibility of placement of the number x in the column j and box k. Finally, sq_{ij} are witnesses of the existence of the corresponding square *(i,j)*.

The model is based on the sequence of the following stages: (1) Checking for unique candidates in each row, column and box. If unique candidates are found, they are placed in their corresponding squares. (2) If no unique candidates are found in the first step, various Sudoku solving strategies are applied to prune the candidate set of cells. Consequent to this, if unique candidates are found in the changed configuration, they are placed in the squares. (3) After placing the unique candidates found in the above steps, the system resets itself and follows the steps again. This Checking – Reset stage stops either when the Sudoku is solved, or the Sudoku is found to be unsolvable.

VII. GENERALIZED PRODUCTION RULES FOR SOLVING SUDOKU OF ORDER N

In this section, we reproduce the basic rules stated in paper [1]. In the next section, we discuss the improvements to these rules using different Sudoku solving strategies.

Rule 1: $R_1 \equiv [z_{ijx} \rightarrow s_{ijx}\, p]_e$ *for* $i,j,x \in \{1,...,n^2\}$

Each input object z_{ijx} produces the output object s_{ijx} and one copy of object p. In any configuration, the copies of object p represent the number of candidates placed on the Sudoku that are in their right positions.

Rule 2: $R_2 \equiv [f_{ix}\ s_{ijx} \rightarrow \varepsilon\ ]_e$ *for* $i,j,x \in \{1,...,n^2\}$, f_{ix} *dissolves and* s_{ijx} *acts as a catalyst.*

$[c_{jx}\ s_{ijx} \rightarrow \varepsilon\ ]_e$ *for* $i,j,x \in \{1,...,n^2\}$, c_{jx} *dissolves and* s_{ijx} *acts as a catalyst.*

$[b_{kx}\ s_{ijx}\ box_{ijk} \rightarrow \varepsilon\ ]_e$ *for* $i,j,x \in \{1,...,n^2\}$, b_{kx} *dissolves and* s_{ijx}, box_{ijk} *act as catalyst.*

The output object s_{ijx} represents that the number x is placed in the square *(i,j)*. Therefore, the objects f_{ix}, c_{jx} and b_{kx} must get dissolved. ‚ε' represents that all the non-catalytic objects mentioned in the left side of a rule get dissolved.

Rule 3: $R_3 \equiv [\neg d\ \neg r_{ij}\ sq_{ij}\ k_1 \rightarrow r_{ij}^{n^2}\ d]_e$ *for* $i,j \in \{1,...,n^2\}$, sq_{ij}, k_1 *act as a catalyst. One copy of object d is produced.*

We add n^2 copies of each object r_{ij} to the membrane *e*. Object r_{ij} is used to denote the number of possible assignments from $\{1,...,n^2\}$ to a cell *(i,j)* at a given configuration.

Rule 4: $R_4 \equiv [k_1 \rightarrow k_0]_e$

The reset stage ends with the evolution of object k_1, used as catalyst in previous sets of operations, to the object k_0.

Rule 5: $R_5 \equiv [\neg s_{ijx}\ \neg m_{ijx}\ r_{ij}\ f_{ix}\ c_{jx}\ b_{kx}\ box_{ijk} \rightarrow m_{ijx}\ a_{ij}]_e$ *for* $i,j,x \in \{1,...,n^2\}$, *and* f_{ix}, c_{jx}, b_{kx}, box_{ijk} *act as catalysts,* $\neg s_{ijx}$ *act as a condition for this rule, one copy of* r_{ij} *dissolves.*

The checking stage starts with rule R_5. If f_{ix}, c_{jx} and b_{kx} are present in the membrane *e*, then *x* is the probable candidate that can be placed at square *(i,j)*. This probable candidate is denoted by m_{ijx}. The question is to determine if *x* is the unique candidate. This is checked by rules from set R_6 using r_{ij} and a_{ij}. Before applying this rule (R_5), we have checked that for all squares *(i, j),* we have n^2 copies of r_{ij} in membrane *e* and zero copies of a_{ij}. If f_{ix}, c_{jx} and b_{kx} are present in the membrane (they act as catalysts), then the corresponding rule is applied. The application of the rule removes one copy of r_{ij} and produces one copy of a_{ij}. The occurrence of m_{ijx} ensures that the rule is applied only once. Having found the probable candidates for each cell, it is also checked whether the candidate *x* is a unique candidate for the box of *(i,j)* by next rule R_6.

Rule 6: $R_6 \equiv [\neg s_{ijq}\ r_{ij}^{n^2-1}\ a_{ij}\ f_{ix}\ c_{jx}\ b_{kx}\ box_{ijk} \rightarrow s_{ijx}\ p\ w]_e$ *for* $i,j,x,q \in \{1,...,n^2\}$, box_{ijk} *acts as a catalyst.*

If there exists only one copy of a_{ij} and n^2-*1* copies of r_{ij}, then this represents that the square *(i,j)* has a unique candidate *x,* where the square *(i,j)* lies inside the box *k*. The rules delete the objects f_{ix}, c_{jx} and b_{kx} and introduce the objects s_{ijx}, *p* and *w*. When the copies of *p* reach n^4, the cycle reset-checking stops and *w* is a witness of the application of the rule.

Rule 7 & 8: $R_7 \equiv [w\ k_0 \rightarrow k_2]_e$
$R_8 \equiv [w \rightarrow \varepsilon]_e \quad [k_0]_e \rightarrow NO$

The production of object *w* implies that at least one unique candidate was present in the grid and it has been placed. The reset-checking cycle must repeat to find out any new occurrences of unique candidates due to the placement of new numbers in the grid. In this case, the objects *w* and k_0 are consumed by rule R_7, producing k_2. If no *w* is present in the membrane *e*, this means that no new numbers are placed on the Sudoku grid and the present configuration is just the same as the previous one. Therefore, to terminate the Sudoku, k_0 dissolves the membrane *e* and returns an object NO to the skin membrane.

Rule 9: $R_9 \equiv [p^{n^4}]_e \rightarrow YES$

The copies of *p* denote the number of correctly filled squares in the Sudoku grid. When the copies reach a value n^4, this means every cell in the Sudoku grid is filled with a true solution *x i.e.* the Sudoku is completely solved. Then membrane *e* is dissolved and the P system returns an object YES to the skin membrane.

Rule-10: $R_{10} \equiv [d\ a_{ij} \rightarrow \varepsilon]_e\ \ [d\ r_{ij} \rightarrow \varepsilon]_e$
$[d\ m_{ijx} \rightarrow \varepsilon]_e$ *for* $i,j,k \in \{1,...,n^2\}$, $x \in \{1,...,n\}$, *d acts as a condition.*

This set of rules marks the end of the checking stage. Before starting with the next round of checking stage, we ensure all the markers m_{ijx} and the counters a_{ij} and r_{ij} are set to zero.

Rule 11: $R_{11} \equiv [d \rightarrow \varepsilon]_e\ \ [k_2 \rightarrow k_1]_e$

The inhibitor *d* is removed and the catalyst k_1 is produced, so that the rules from the set R_2 can be applied marking the start of the reset stage.

Rule 12 & 13: $R_{12} \equiv [YES]_s \rightarrow [\ ]_s\ YES \quad [NO]_s \rightarrow [\ ]_s\ NO$
$R_{13} \equiv [p \rightarrow \varepsilon]_s\ \ [m_{ijx} \rightarrow \varepsilon]_s\ [a_{ij} \rightarrow \varepsilon]_s\ [f_{ix} \rightarrow \varepsilon]_s$
$[c_{jx} \rightarrow \varepsilon]_s\ \ [b_{kx} \rightarrow \varepsilon]_s\ [r_{ij} \rightarrow \varepsilon]_s\ [d \rightarrow \varepsilon]_s$
$[box_{ijk} \rightarrow \varepsilon]_s\ [sq_{ij} \rightarrow \varepsilon]_s$

When the membrane *e* is dissolved, then the P system returns either YES or NO to the skin membrane. In the last step of the configuration, the object YES or NO is sent out to the environment and all auxiliary objects are removed from the membrane *s*.

The above stated rules are based on the property that in all partial solutions of the Sudoku, there exists at least one square *(i, j)* with a unique candidate. It does not apply any candidate elimination strategy to generate unique candidates further. Thus, apart from solving Sudoku of order 2 and very easy Sudoku of order 3, the above stated rules fail to produce the output for harder Sudoku problems as also pointed out by the authors in [1].

VIII. RULES FOR STRATEGIES

In an attempt to solve hard Sudoku puzzles, as an improvisation to the above rules, the following rules are stated. When the above model finds that no more unique candidates can be found out in R_6, the P system moves on to Sudoku solving strategies. These strategies prune possible candidates for a square (candidate set) following some logic creating a possibility of generating unique candidates further so as to solve hard Sudoku of order *n*. If all the strategies also fail, then the rules go for a *brute-force* method from the last partial solution to generate a valid solution.

The following rules are added after R_7. When the model detects that no unique candidate can be found for any of the unfilled cells *(i,j)* after R_7, the model applies Sudoku solving strategies as shown below resulting in pruning the candidate sets further in a hope to identifying unique candidates. When all the strategies also fail, the model goes to a brute-force method from the last partial solution configuration onwards, eventually finding out the solution to the problem.

Strategy 1: Pruning using *Naked Pairs* (NP)
$R_{7.1} \equiv [\neg w\ k_0 \rightarrow Strategies]_e$

$\boldsymbol{R_{7.2}} \equiv [Strategies\ r_{ij}{}^{n^2-2}\ \ r_{kj}{}^{n^2-2}\ m_{ijx}\ m_{ijq}\ m_{kjx}\ m_{kjq} \rightarrow NPr_{jx}\ NPr_{jq}]_e$ *for i,j,k,x c {1,...,n^2}. //Indicates presence of NP in column j for (x,q).*
$[NPr_{jx}\ m_{ljx}\ a_{lj} \rightarrow r_{lj}]_e$ *for l,j,x c {1,...,n^2} and l≠i,k. // removes values of Naked Pair (x,q) from the corresponding column j.*

$[Strategies\ r_{ij}{}^{n^2-2}\ r_{ik}{}^{n^2-2} m_{ijx}\ m_{ijq}\ m_{ikx}\ m_{ikq} \rightarrow NPc_{ix}\ NPc_{iq}]_e$ *for i,j,k,x c {1,...,n^2}. //Indicates presence of NP in row i for (x,q).*
$[NPc_{ix}\ m_{ilx}\ a_{il} \rightarrow r_{il}]_e$ *for i,l,x c {1,...,n^2} and l≠j,k. // removes values of Naked Pair (x,q) from the corresponding row i.*

$[Strategies\ r_{ij}{}^{n^2-2} r_{kl}{}^{n^2-2}\ m_{ijx}\ m_{ijq}\ m_{klx}\ m_{klq}\ box_{ijp}\ box_{klp} \rightarrow NPb_{px}\ NPb_{pq}]_e$ *for i,j,k,l,x c {1,...,n^2} and p represents the box number of cell (i,j) and (k,l). // Indicates presence of NP in the box p for (x,q).*

$[NPb_{px}\ m_{qvx}\ a_{qv}\ box_{qvp}\ box_{ijp}\ box_{klp} \rightarrow r_{qv}]_e$ *for q,v,x c {1,...,n^2} and q≠i,k v≠j,l. //p represents box number of (i,j) and (k,l) where x is one of the candidates of Naked Pair. Prunes (x,q) from other cells of box p.*
Note: All *box* objects (*e.g* box_{ijk}) act as catalyst in the above rules. An inhibitor *Strategies* must be present in all the strategies (1 to 10) being discussed here, though it is not explicitly mentioned from Strategy 2 onwards.

These set of rules will search the grid for *Naked Pairs* [7] in rows, columns and boxes. When a Naked Pair is found in any row (column/box), the rules dissolve one copy of a_{ij} to produce one copy of r_{ij} corresponding to that particular value of x (for which the naked pair is formed) in the cell (i,j) along the corresponding row (column/box) and then removes the candidate from that cell. For *e.g.* in the figure below, naked pairs are formed by two candidates (1 and 6) in row 1 and other two candidates (6 and 7) in row 3. This indicates that the candidates 1 and 6 necessarily need to be assigned to cells *(A,2)* and *(A,3)* only in any order. Therefore, the candidates (1 and 6) must be deleted from cell *(A,4)*, *(A,5)* and *(A,6)* along row 1, similarly, the candidates (6 and 7) must be deleted from cell *(C,1)* and *(C,5)* along row 3. The pruning can be done in a similar way if a naked pair is found along a column or in a box.

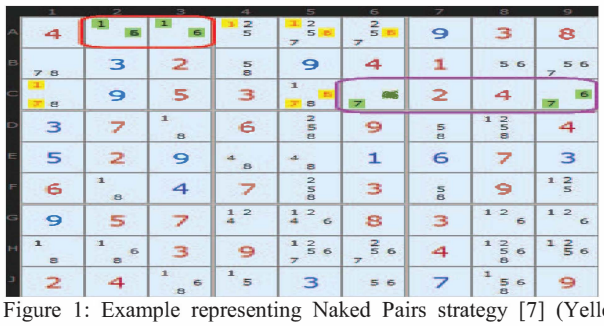


Figure 1: Example representing Naked Pairs strategy [7] (Yellow colored numbers are deleted by the naked pairs shown in green).

Strategy 2: Pruning using *Naked Triplets* (NT)
$\boldsymbol{R_{7.3}} \equiv [m_{ijx}\ m_{ijq}\ m_{iju}\ r_{ij}{}^{n^2-3}\ m_{kjx}\ m_{kjq}\ m_{kju}\ r_{kj}{}^{n^2-3} m_{ljx}\ m_{ljq}\ m_{lju}\ r_{lj}{}^{n^2-3} \rightarrow NTr_{jx}\ NTr_{jq}\ NTr_{ju}\ ]_e$ *for i,j,k,l,x,q,u c {1,...,n^2}. //Indicate presence of NT in column j for (x,q,u).*
$[NTr_{jx}\ m_{qjx}\ a_{qj} \rightarrow r_{qj}]_e$ *for l,j,q,x c {1,...,n^2} and q≠i,k,l.// removes values of Naked Triplets (x,q,u) from the corresponding column j.*

$[m_{ijx}\ m_{ijq}\ m_{iju}\ r_{ij}{}^{n^2-3}\ m_{ikx}\ m_{ikq}\ m_{iku}\ r_{ik}{}^{n^2-3} m_{ilx}\ m_{ilq}\ m_{ilu}\ r_{il}{}^{n^2-3} \rightarrow NTc_{ix}\ NTc_{iq}\ NTc_{iu}\ ]_e$ *for i,j,k,l,x,q,u c {1,...,n^2}. //Indicate presence of NT in row i for (x,q,u)*

$[NTc_{ix}\ m_{iqx}\ a_{iq} \rightarrow r_{iq}]_e$ *for i,l,q,x c {1,...,n^2} and q≠j,k,l. // removes values of Naked Triplets (x,q,u) from the corresponding row i.*

$[m_{ijx}\ m_{ijq}\ m_{iju}\ r_{ij}{}^{n^2-3}\ m_{klx}\ m_{klq}\ m_{klu}\ r_{kl}{}^{n^2-3}\ m_{vyx}\ m_{vyq}\ m_{vyu}\ r_{vy}{}^{n^2-3} box_{ijp}\ box_{klp}\ box_{vyp} \rightarrow NTb_{px}\ NTb_{pq}\ NTb_{pu}\ ]_e$ *for i,j,k,l,v,y,x,q,u c {1,...,n^2} and p represents the box number of cell (i,j),(k,l),(v,y). //Indicate presence of NT in box p for (x,q,u).*

$[NTb_{px}\ m_{ghx}\ a_{gh}\ box_{ghp}\ box_{ijp}\ box_{klp}\ box_{vyp} \rightarrow r_{gh}]_e$ *for g,h,x c {1,...,n^2} and g≠i,k,v, h≠j,l,y and p represents box number of cell (i,j) , (k,l) , (v,y) and (g,h). // Prunes (x,q,u) from other cells of box p.*
Note: All *box* objects (*e.g* box_{ijk}) act as catalyst in above rules.

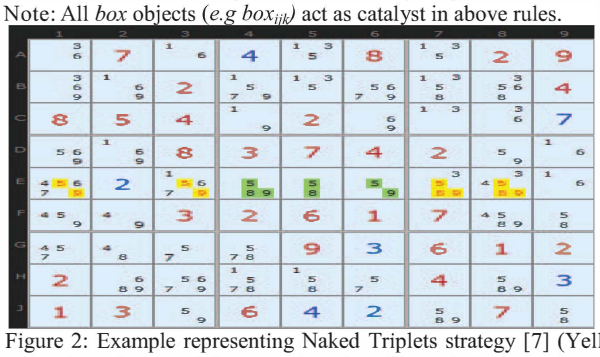


Figure 2: Example representing Naked Triplets strategy [7] (Yellow colored numbers are deleted by the naked triplets in green).

These set of rules will search the grid for *Naked Triplets* [7] in rows, columns and boxes. When a Naked Triplet is found in any row (column/box), the rules dissolve one copy of a_{ij} to produce one copy of r_{ij} corresponding to that particular value of x (for which the naked triplet is formed) in the cell (i, j) along the corresponding row (column/box) and then removes the candidate from that cell. For *e.g.* in the figure above, a naked triplet is formed by (5, 8 and 9) in row 5 (*i.e. cell (E,4), (E,5) and (E,6)*), therefore, the candidates (5,8 and 9) are deleted from cell *(E,1)*, *(E,3)*, *(E,7)* and *(E,8)* along row 5. The pruning can be done in a similar way if a naked triplet is found along a column or in a box.

Strategy 3: Pruning using *Pointing Pairs* (PP)
$\boldsymbol{R_{7.4}} \equiv [m_{ijx}\ m_{kjx}\ \neg m_{lyx}\ box_{ijp}\ box_{kjp}\ box_{lyp} \rightarrow PPr_{jx}]_e$ *for i,j,k,l,y,x c {1,...,n^2} y≠j and cells (i,j), (k,j) and (l,y) lie in the same box p. //Indicates presence of PP along column j.*

$[PPr_{jx}\ m_{ljx}\ a_{lj} \rightarrow r_{lj}]_e$ *for l,j,x c {1,...,n^2} and l≠i,k. // removes PP value x from the corresponding column j.*

$[m_{ijx}\ m_{ikx}\ \neg m_{lyx}\ box_{ijp}\ box_{ikp}\ box_{lyp} \rightarrow PPc_{ix}]_e$ *for i,j,k,l,y,x c {1,...,n^2} l≠i and the cells (i,j), (i,k) and (l,y) lies in the same box. //Indicates presence of PP along row i.*

$[PPc_{ix}\ m_{ilx}\ a_{il} \rightarrow r_{il}]_e$ *for i,l,x c {1,...,n^2} and l≠j,k. // removes PP value x from the corresponding row i.*
Note: All *box* objects (*e.g.* box_{ijk}) act as catalyst in above rules.

Pointing pairs [7] are the two cells containing a probable candidate x, such that the two cells are aligned either along a row or a column lying in the same box with the constraint that the probability of placing that candidate x is limited to that

particular row or column inside the box only. If such a pair is found then all the occurrences of that particular candidate x can be dissolved for any other cell along the row or column outside that box. For example in the figure below, pointing pairs are candidate 3 in row 2 and box 3, therefore, candidate 2 is deleted from cell *(G,2)* along row 7 outside box 8, similarly, candidate 3 is deleted from cell *(B,1)*, cell *(B,2)* and cell *(B,3)* along row 2 outside box 3.

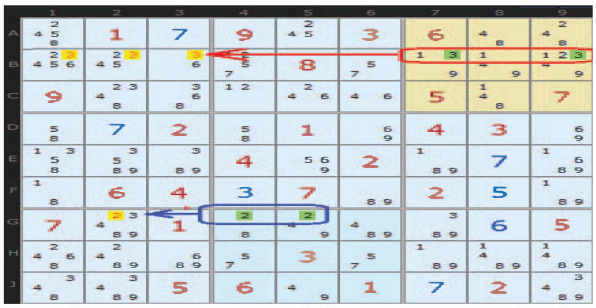


Figure 3: Example representing Pointing Pairs strategy [7] (Yellow colored numbers are deleted by the pointing pair in green).

Strategy 4: Pruning using *Box-line Reduction* (BL)

$\boldsymbol{R}_{7.5} \equiv [m_{ijx}\, m_{ilx}\, \neg m_{iyx}\, box_{ijk}\, box_{ilk} \rightarrow BL_{ikx}]_e$ *for i,j,l,x c {1,...,n^2} and k is the box number of cells (i,j) and (i,l) and y≠j,l. //Indicate presence of box-line value x in box k and row i.*

$[BL_{ikx}\, m_{ljx}\, a_{lj}\, box_{ljk} \rightarrow r_{lj}]_e$ *for i,j,l,x c {1,...,n^2} and l≠i and k is also the box number of cell (l,j). // removes box-line value x from all rows l s.t. l≠i within box k.*

$[m_{ijx}\, m_{ljx}\, \neg m_{yjx}\, box_{ijk}\, box_{ljk} \rightarrow BL_{jkx}]_e$ *for i,j,l,x c {1,...,n^2} and k is the box number of cells (i,j) and (l,j) and v≠i,l. //Indicate presence of box-line value x in box k and column j.*

$[BL_{jkx}\, m_{ilx}\, a_{il}\, box_{ilk} \rightarrow r_{il}]_e$ *for i,j,l,x c {1,...,n^2} and l≠j and k is also the box number of cell (i,l). // removes box-line value x from all columns l s.t l≠j within box k.*

Note: All *box* objects (*e.g* box_{ijk}) act as catalyst in above rules.

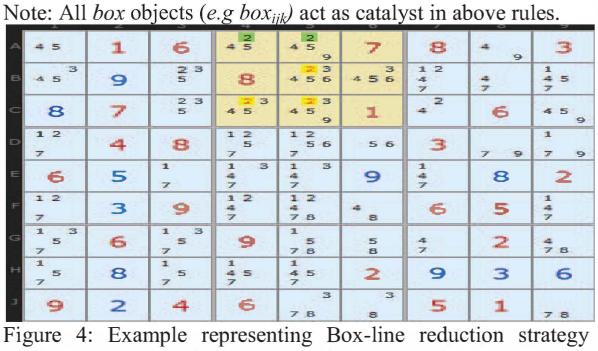


Figure 4: Example representing Box-line reduction strategy [7] (Yellow colored numbers are deleted by the numbers in green).

In *Box-line reduction* strategy [7], if along a row (column), a possible candidate x appears only in two cells such that both these cells appear in the same box, then the probable candidate x can be dissolved from any other cell in the box. For *e.g.* in the figure above, candidate 2 is a box-line candidate for row 1 formed by two cells *(A,4)* and *(A,5)* in box 2. It means that 2 can be assigned to either cell *(A,4)* or *(A,5)*, hence its occurrence from other cells in the box must disappear. Therefore, any other occurrence of 2 in a box 2 can be dissolved. Hence, candidate 2 is removed from cells *(B,5)*, *(C,4)* and *(C,5)*.

Strategy 5: Pruning using *X-wing* (XW)

$\boldsymbol{R}_{7.6} \equiv [m_{ijx}\, m_{ikx}\, m_{ljx}\, m_{lkx}\, \neg m_{ivx}\, \neg m_{lyx} \rightarrow XW_{jx}\, XW_{kx}]_e$ *for i,j,k,l,v,y,x c {1,...,n^2} and v,y≠j, v,y≠k. //indicates that XW pruning can be done for column j and k for value x.*

$[XW_{jx}\, m_{vjx}\, a_{vj} \rightarrow r_{vj}]_e$ *for j,v,x c {1,..,n^2} and v≠i, v≠l.//removes value x from the cells of column j.*

$[m_{ijx}\, m_{ikx}\, m_{ljx}\, m_{lkx}\, \neg m_{yjx}\, \neg m_{ykx} \rightarrow XW_{ix}\, XW_{lx}]_e$ *for i,j,k,l,v,y,x c {1,...,n^2} and v,y≠i, v,y≠l. //indicates that XW pruning can be done for row i and l for value x.*

$[XW_{ix}\, m_{ivx}\, a_{iv} \rightarrow r_{iv}]_e$ *for i,v,x c {1,...,n^2} and v≠j, v≠k. //removes value x from the cells of row i.*

In X-Wing strategy [7], if along two rows (columns), a probable candidate x is present in only two columns (rows) such that the columns (rows) in the two rows (columns) also match, then an X is formed in the grid. This X dissolves the probable candidate x from the cells along the columns (rows) of X grid. For *e.g.* as shown in the figure below, 7 forms an X in the grid *i.e.* cell *(B,4)*, *(B,8)*, *(F,4)* and *(F,8)* such that 7 appears only in these cells along row 2 and row 6. Due to X in the grid, 7 must appear in both columns i.e. column 4 and 8, but it has to be either *(B,4)* and *(F,8)* OR (B,8) and (F,4). Therefore, 7 must be deleted from cell *(A,4)*, *(E,4)*, *(H,4)*, *(J,4)* along column 4 and cell *(H,6)*, *(J,6)* along column 8.

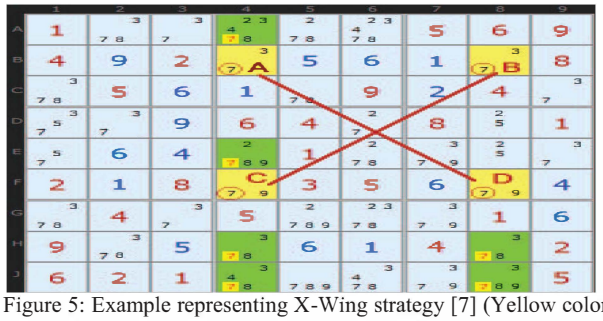


Figure 5: Example representing X-Wing strategy [7] (Yellow colored numbers are deleted by the number forming X).

Strategy 6: Pruning using *Sword-Fish* (SF)

$\boldsymbol{R}_{7.7} \equiv [m_{ijx}\, m_{ikx}\, m_{ilx}\, m_{i_2jx}\, m_{i_2kx}\, m_{i_2lx}\, m_{i_3jx}\, m_{i_3kx}\, m_{i_3lx}\, \neg m_{ivx}\, \neg m_{i_2yx}\, \neg m_{i_3qx} \rightarrow SF_{jx}\, SF_{kx}\, SF_{lx}]_e$ *for i,i$_2$,i$_3$,j,k,l,v,y,q,x c {1,...,n^2} and v,y,q≠j, v,y,q≠k, v,y,q≠l. //Indicates SF for columns j,k and l for value x. All objects on LHS act as catalysts and inhibitors.*

$[SF_{jx}\, m_{vjx}\, a_{vj} \rightarrow r_{vj}]_e$ *for j,v,x c {1,...,n^2} and v≠i,v≠i$_2$,v≠i$_3$.*

$[m_{ijx}\, m_{kjx}\, m_{ljx}\, m_{ij_2x}\, m_{kj_2x}\, m_{lj_2x}\, m_{ij_3x}\, m_{kj_3x}\, m_{lj_3x}\, \neg m_{vjx}\, \neg m_{qj_2x}\, \neg m_{yj_3x} \rightarrow SF_{ix}\, SF_{kx}\, SF_{lx}]_e$ *for i,j,j$_2$,j$_3$,k,l,v,y,q,x c {1,...,n^2} and v,y,q≠i, v,y,q≠l, v,y,q≠k. //Indicates SF for rows i,i and k for value x. All objects on LHS act as catalysts and inhibitors.*

$[SF_{ix}\, m_{ivx}\, a_{iv} \rightarrow r_{iv}]_e$ *for i,v,x c {1,...,n^2} and v≠j,v≠j$_2$,v≠j$_3$.*

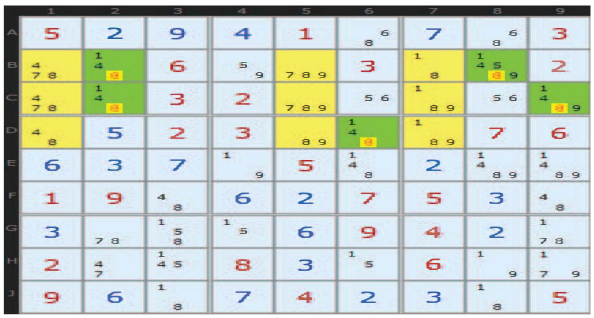


Figure 6: Example representing Sword-Fish strategy [7] (Yellow colored numbers are deleted by the number forming sword fish).

These rules formulate *Sword-Fish* strategy [7]. If along three rows (columns), a probable candidate *x* is present in only three columns (rows) such that the columns (rows) in the three rows (columns) also match, then applying the sword-fish strategy, the probable candidate *x* can be dissolved from any other cells from these rows (columns). For *e.g.* in the figure above, sword fish is formed by the candidate 8 in cells *(B,1), (B,5), (B,7); (C,1), (C,5), (C,7); (D,1), (D,5), (D,7)* along columns *1*, *5* and *7*. It can also be noted that candidate *8* is not appearing in any other cells in column *1*, *5* and *7* except the Sword-fish cells. This indicates that *8* must appear in column *1*, *5* and *8* along the rows *2*, *3* and *4* respectively in any order. Therefore any other occurrence of *8* in rows *2*, *6*, *4* must get deleted. Hence, we remove *8* from cell *(B,2), (B,8), (C,2), (C,9)* and *(D,6)*.

Strategy 7: Pruning using *Jelly-Fish* (JF)

$\boldsymbol{R}_{7.8} \equiv [m_{i_1 jx}\ m_{i_1 kx}\ m_{i_1 lx}\ m_{i_1 nx}\ \ m_{i_2 jx}\ m_{i_2 kx}\ m_{i_2 lx}\ m_{i_2 nx}\ m_{i_3 jx}\ m_{i_3 kx}\ m_{i_3 lx}\ m_{i_3 nx}\ \ m_{i_4 jx}\ m_{i_4 kx}\ m_{i_4 lx}\ m_{i_4 nx}\ \neg m_{i_1 vx}\ \neg m_{i_2 yx}\ \neg m_{i_3 qx}\ \neg m_{i_4 tx} \rightarrow JF_{jx}\ JF_{kx}\ JF_{lx}\ JF_{nx}]_e$ *for* i_1,i_2,i_3,i_4, *j,k,l,n,v,y,q,t,x c {1,...,n²} and v,y,q,t≠j, v,y,q,t≠k, v,y,q,t≠l , v,y,q,t≠n. //Indicates JF for columns j,k,l,n for value x. All objects on LHS act as catalysts and inhibitors.*

$[JF_{jx}\ m_{vjx}\ a_{vj} \rightarrow r_{vj}]_e$ *for j,v,x c {1,...,n²} and v≠*i_1,*v≠*i_2,*v≠*i_3, *v≠*i_4 *//Rule for pruning*

$[m_{ij_1x}\ m_{kj_1x}\ m_{lj_1x}\ m_{nj_1x}\ m_{ij_2x}\ m_{kj_2x}\ m_{lj_2x}\ m_{nj_2x}\ m_{ij_3x}\ m_{kj_3x}\ m_{lj_3x}\ m_{nj_3x}\ m_{ij_4x}\ m_{kj_4x}\ m_{lj_4x}\ m_{nj_4x}\ \neg m_{vj_1x}\ \neg m_{qj_2x}\ \neg m_{yj_3x}\ \neg m_{tj_4x} \rightarrow JF_{ix}\ JF_{kx}\ JF_{lx}\ JF_{nx}]_e$ *for* i,j_1,j_2,j_3,j_4*,k,l,n,v,y,q,t,x c {1,...,n²} and v,y,q,t≠i, v,y,q,t≠l, v,y,q,t≠k , v,y,q,t≠n. //Indicates JF for rows i,i and k for value x. All objects on LHS act as catalysts and inhibitors.*

$[JF_{ix}\ m_{ivx}\ a_{iv} \rightarrow r_{iv}]_e$ *for i,v,x c {1,...,n²} and v≠*j_1,*v≠*j_2,*v≠*j_3, *v≠*j_4 *//Rule for pruning*

The Jelly-Fish (Stuart 2012) strategy is an extension of Sword-Fish. In this, one more row and column is added which makes 4 X 4 cells. The pruning of candidate values in cells take place in the same way as explained in Figure 6. The only difference is that it is for 4 X 4 rectangles as opposed to 3 X 3 rectangles in Sword-Fish.

Strategy 8: Pruning using *XYZ-Wing*

$\boldsymbol{R}_{7.9} \equiv$

$[m_{ijx}m_{ijy}m_{ijz}r_{ij}^{n^2-3}\ \ m_{lkx}m_{lkz}r_{lk}^{n^2-2}\ \ m_{ipy}m_{ipz}r_{ip}^{n^2-2}\ \ box_{ijb}\ box_{lkb} \rightarrow XYZ_{rsz}]_e$ *for i,j,k,l,x c {1,....,n²} and p≠j,*box_{ijb}=box_{rsb},*r=i, r≠j. //On the left-hand side all elements act as catalysts. XYZ-wing found for cell (r,s) with above conditions where the candidate z can be removed* ***XYZ and YZ are row aligned***

$[XYZ_{rsz}\ m_{rsz}\ a_{rs} \rightarrow r_{rs}]_e$ *for r,s,z c {1,....,n²}, and* box_{ijb}= box_{rsb},*r=i , r≠j // Pruning takes place along the row XYZ and YZ cells*

$[m_{ijx}m_{ijy}m_{ijz}r_{ij}^{n^2-3}\ m_{lkx}m_{lkz}r_{lk}^{n^2-2}\ m_{pjy}\ m_{pjz}r_{pj}^{n^2-2}\ \ box_{ijb}box_{lkb} \rightarrow XYZ_{rsz}]_e$ *for i,j,k,l,v,y,x c {1,....,n²} and p≠i,* box_{ijb}=box_{rsb},*r≠i,r=j. //On the left-hand side all elements act as catalysts. XYZ-wing found for cell (r,s) with above conditions where the candidate z can be removed.* ***XYZ and YZ are column aligned****.*

$[XYZ_{rsz}\ m_{rsz}\ a_{rs} \rightarrow r_{rs}]_e$ *for r,s,z c {1,....,n²}, and* box_{ijb}=box_{rsb}, *r≠i, r=j // Pruning takes place along the column XYZ and YZ cells*

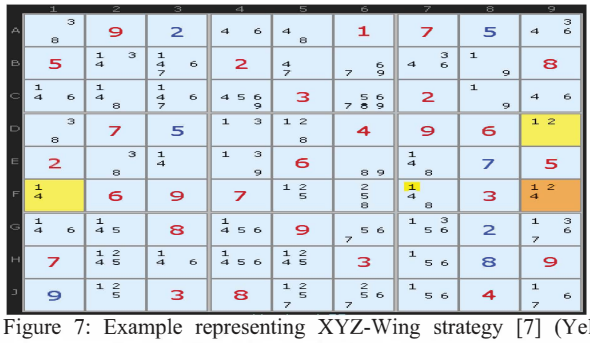


Figure 7: Example representing XYZ-Wing strategy [7] (Yellow colored numbers are deleted due to XYZ-wing).

This is an extension of Y-Wing or (XY-Wing). In this, three cells contain only 3 different numbers between them, but fall outside the confines of one row/column/box, with one of the cells (the 'apex' or 'hinge') being able to see the other two; those other two having only one number in common; and the apex having all three numbers as candidates.

In this example the candidate number is 1 and *(F, 9)* is the Hinge. It can be noticed that candidates 1 & 2 in *(D, 9)* and candidates 1 & 4 in *(F, 1)*. If *(D, 9)* contains a 2 then (F, 1) and (F, 9) become a naked pair of 1 & 4 and the naked pair rule applies. Same with *(F, 1) i.e.* if *(F, 1)* takes 4 then *(D, 9)* and *(F, 9)* become a naked pair of 1 & 2 each. If any of the three are 1 then 1 is still part of the formation. In all possible assignment of values to these three cells, it is evident that *(F, 7)* cannot have value 1.

Strategy 9: Pruning using Finned X-Wing

$\boldsymbol{R}_{7.10} \equiv [m_{ijx}\ m_{ikx}\ m_{ljx}\ \ m_{lkx}\ \neg m_{lyx}\ \ m_{iyx} \rightarrow FXWr_{ix}]_e$ *for i, j, l, k, l, x, q c {1,...,n²} & y≠j & y ≠k*

//Finned X wing found on the i^{th} *row with extra 'x' candidates.*

$[FXWr_{ix}\ \ m_{pqx}\ a_{pq}\ box_{iyb}\ box_{pqb} \rightarrow r_{pq}]_e$ *for i, x, y c {1,...,n²} & y≠j & y≠k &* $box_{iyb} \neq box_{pqb}$

//i.e. x candidate in cell (p, q) is in the same box, where candidate x is also found in cell (i, y) from above rule as fin cells.

Note: box_{iyb}, box_{pqb} *act as catalysts*

$[m_{ijx}\ m_{ilx}\ m_{ljx}\ m_{lkx}\ m_{ykx}\ m_{yjx} \rightarrow FXWc_{jx}]_e$ *for i, j, l, k, l, x, q ϵ {1,.....,n^2} & y≠i & y ≠l*
//Finned X wing found on the j^{th} column with extra 'x' candidates.

$[FXWc_{jx}\ m_{pqx}\ a_{pq}\ box_{yjb}\ box_{pqb} \rightarrow r_{pq}]_e$ *for i, x, y c {1,...,n^2} & y≠j & y≠k & box_{yjb}=box_{pqb} //i.e. X candidate in cell (p, q) is in the same box, where candidate x is also found in cell (y, j) from above rule as fin cell.*



Figure 8: Example representing Finned X-Wing strategy [7] (Yellow colored numbers are deleted due to Finned X-Wing).

This is an extension of X-Wing strategy in which the X-Wing is identified (in figure 8, *(C, 6), (C, 9), (G, 6) and (G, 9)*), but the extra candidates doesn't make it X-Wing (*e.g.* candidate 7 in *(G, 7)* and *(G, 8)* doesn't allow it to be X-Wing). These extra candidates are called as Finn. This causes removal of candidate value 7 from *(H, 9)* because in all possible combination, *(H, 9)* cannot have value 7.

Strategy 10: Pruning using Y-Wing

$\boldsymbol{R_{7.11}}\equiv$

Type1:- *Candidates {A,B} and {B,C} are in same box and {A,C} is in different box aligned to {A,B} in a row/column*

Case-1:- *AB and AC are row aligned*

$[m_{ija}\ m_{ijb}\ r_{ij}^{n^2-2}\ m_{klb}\ m_{klc}\ r_{kl}^{n^2-2} m_{ij_1a}\ m_{ij_1c}\ r_{ij_1}^{n^2-2} box_{ij_1b_2} box_{klb_1} box_{ijb_1} \rightarrow YWing1r_{b_1 i\, b_2 kc}]_e$ *for i, j, k, l, j_1, j_2, b_1, b_2 C{1,...,n^2} i≠k ,j≠l //AB and BC are in same box b_1 and AC is different box b_2 , row aligned with AB. Indicates that Y-wing of type-1 exist for box b_1 for row i and box b_2 for row k for candidate c, hence must be pruned.*

$[YWing1r_{b_1 i\, b_2 kc}\ m_{ij2c}\ m_{kj3c}\ a_{ij2}\ a_{kj3}\ box_{ij_2b_1}\ box_{kj_3b_2} \rightarrow r_{ij2}\ r_{kj3}]_e$ *// box_{ijb_1}=$box_{ij_2b_1}$ and $box_{kj_3b_2}$=$box_{ij_1b_2}$. Pruning of candidate c from cell (i, j_2) and cell(k,j_3) for i,k, j_2,j_3 C {1,...,n^2} j_2≠j, j_3≠ j_1 .*

Case-2:- *AB and AC are column aligned*

$[m_{ija}\ m_{ijb}\ r_{ij}^{n^2-2} m_{klb} m_{klc} r_{kj}^{n^2-2}\ m_{i_1ja} m_{i_1jc}\ r_{i_1j}^{n^2-2}\ box_{ijb_1}\ box_{klb_1}\ box_{i_1jb_2} \rightarrow YWing1c_{b_1jb_2lc}]_e$ *for i, j,k, l, i_1, b_1, b_2 C{1,...,n^2} i≠k, j≠l //AB and BC are in same box b_1, AC is in different box b_2 , column aligned with A.B Y-Wing exist for box b_1 for column j and box b_2 for column l for candidate c, hence must be pruned.*

$[YWing1c_{b_1jb_2lc}\ m_{i_2jc}\ m_{i_3lc}\ a_{i_2j}\ a_{i_3l}\ box_{i_2jb_1} box_{i_3lb_2} \rightarrow r_{i_2j}\ r_{i_3l}]_e$ *for i_2, j, l_3, l, b_1, b_2, c C{1,...,n^2} i_2=i, i_3= i_1 //box_{ijb_1} = $box_{i_2jb_1}$ & $box_{i_1jb_2}$ = $box_{i_3lb_2}$. All objects except box objects dissolve indicating pruning of c.*

Type 2:- *Candidates {A,B}, {B,C} and {A,C} are in different boxes with {B,C} and {A,C} in line of view with {A,B}*

$[m_{ija} m_{ijb}\ r_{ij}^{n^2-2}\ m_{kjb} m_{kjc}\ r_{kj}^{n^2-2}\ m_{ila} m_{ilc} r_{il}^{n^2-2}\ box_{ijb_1} box_{kjb_2} box_{ilb_3} \rightarrow YWing2_{klc}]_e$

for i, j,k, l, b_1, b_2, b_3, a,b,c C{1,...,n^2} //i=k & j=l i.e. YWing exist for cell(k,l) for candidate c and must be pruned.

$[YWing2_{klc}\ m_{klc} \rightarrow \#]_e$ *for k, l, c C{1,...,n^2} //candidate c is pruned from cell (k ,l).*

Note: All box objects act as catalysts.

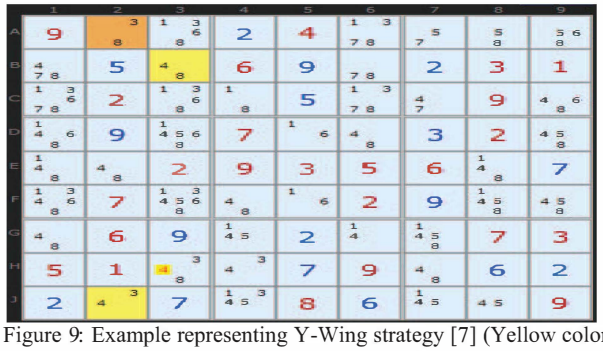


Figure 9: Example representing Y-Wing strategy [7] (Yellow colored numbers are deleted due to Y-Wing).

In this, cell *(A, 2)* and *(B, 3)* are in the same box and cell *(J, 2)* is aligned to *(A, 2)* but in different box. All these cells have three distinct values i.e. 3,8 and 4. It can be seen that cell *(A, 2)* is the hinge representing AB and cell *(B, 3)* and *(J, 2)* represent corners i.e BC and AC respectively. In all possible combinations, it is found that cell *(H, 3)* cannot be 4 since either *(B, 3)* or *(J, 2)* will be 4 in all possible combinations. Similarly cell *(B, 2)* and *(C, 2)* can never have value 4 if it is a candidate in any possible combinations.

Rule for placing value *x* in *(i,j)*:

$\boldsymbol{R_{7.12}} \equiv [\neg s_{ijq}\ r_{ij}^{n^2-1}\ a_{ij}\ f_{ix}\ c_{jx}\ b_{kx}\ m_{ijx} \rightarrow s_{ijx}\ p\ w]_e$ *for i,j,x,q c {1,...,n^2}.*

This rule is similar to the R_6 of placing unique candidates in particular squares, only with the minute variation that this rule takes place in the presence of the marker m_{ijx} indicating the unique candidate *x* for the square *(i,j)*. The rule deletes the objects f_{ix}, c_{jx} and b_{kx} and introduces the objects s_{ijx}, *p* and *w*.

If the Sudoku is hard enough that none of the above strategies are able to find any unique candidate for any cell, then the production rules follow a brute force method of solving the Sudoku from the last configuration (*i.e.* last partial solution with pruned candidate sets for unfilled cells).

After applying all the strategies and placing the unique candidates the same rules from R_8 onwards are applied, marking the end of the checking stage and entering the reset stage if required.

IX. RESULTS

We have tested the membrane computing model in MATLAB© and compared the performance with the conventional brute-force method. The computer used was an Intel Core2, Windows XP with 4 GB RAM. We have observed that the MC model performs better than the conventional brute-force method and it is also able to solve the

most difficult Sudoku problems available in the open literature.

We have observed that if more number of strategies is implemented, the performance improves significantly. To prove this, we have evaluated performance of puzzles for order =3,4,5,6 and 7 against MC version1(with six strategies only) and MC version 2(with six plus additional four strategies). We have observed improvement in the performance for higher order puzzles with more number of strategies since more pruning of search space is ensured thus guiding towards solution fast. We have shown the performance statistics for some of the hard puzzles available from open literature in Section 10. We also have included some of the higher order puzzles from open literature. In order to test the model in a MATLAB© environment, the rules have been coded sequentially in reset-check cycle mode. If the rules are encoded and run in a P System simulator (*e.g. P Lingua* [3]), the environment will try to use *non-determinism and maximal parallelism* which will improve the performance further and also it will be able to solve higher order *n* puzzles fast. At present, all the rules could not be tested in the P-Lingua simulator simultaneously (for $n > 2$) since the available versions of P-Lingua are unable to handle vast number of objects and a large number of rules due to the generation of large xml output files that cause memory overruns. However, a proof of concept using MATLAB© convincingly demonstrates the elegance of representation provided by P systems and the correctness of our implementation.

X. PERFORMANCE STATISTICS

The following are the results for some of the latest hardest problems from the available literature.

AI Escorgate Puzzle 1 (Top 10 puzzles from [10])

```
1  .  .  |  .  .  7  |  .  9  .
.  3  .  |  .  2  .  |  .  .  8
.  .  9  |  6  .  .  |  5  .  .
--------+-----------+----------
.  .  5  |  3  .  .  |  9  .  .
.  1  .  |  .  8  .  |  .  .  2
6  .  .  |  .  .  4  |  .  .  .
--------+-----------+----------
3  .  .  |  .  .  .  |  .  1  .
.  4  .  |  .  .  .  |  .  .  7
.  .  7  |  .  .  .  |  3  .  .
```

Output:

```
1  6  2  8  5  7  4  9  3
5  3  4  1  2  9  6  7  8
7  8  9  6  4  3  5  2  1
4  7  5  3  1  2  9  8  6
9  1  3  5  8  6  7  4  2
6  2  8  7  9  4  1  3  5
3  5  6  4  7  8  2  1  9
2  4  1  9  3  5  8  6  7
8  9  7  2  6  1  3  5  4
With membrane computing (6 strategies): Total time->5.343 s
With membrane computing (10 strategies): Total time->4.007 s
With brute force:        Total time->42.418 s
```

TABLE I: PERFORMANCE COMPARISON OF MC WITH STRATEGIES *VS* CONVENTIONAL BRUTE-FORCE METHOD.

Puzzle	Pure Brute-force	MC paradigm (6 Strategies + Brute-force)	MC paradigm (10 Strategies + Brute-force)
AI Escorgate Puzzle-1 (Order=3) [10]	42.418 s	5.343s	4.007s
AI Killer Application Puzzle-2 (Order=3) [10]	47.677 s	10.089s	9.079s
AI Lucky Diamond Puzzle -3 (Order=3) [10]	49.000 s	4.471s	4.440s
AI Worm Hole Puzzle-4 (Order=3) [10]	86.405 s	15.852s	14.548s
AI labyrinth Puzzle -5 (Order=3) [10]	74.732 s	4.242s	4.211s
AI Circles Puzzle -6 (Order=3) [10]	14.010 s	4.135s	3.998s
AI squadron Puzzle -7 (Order=3) [10]	144.240 s	18.241s	17.845s
AI honeypot Puzzle-8 (Order=3) [10]	60.353 s	10.761s	10.347s
AI tweezers Puzzle -9 (Order=3) [10]	46.544 s	4.934s	4.123s
AI broken brick Puzzle -10 (Order=3) [10]	11.065 s	4.616s	4.316s
HardestSudokusThread-02085;Discrepancy (Order=3) [6] [13]	97.073 s	20.471s	19.871s
HardestSudokusThread-01418;coloin (Order=3) [6] [13]	3495.115 s (Approx 1 hour)	224.951s	200.765s
golden nugget (Order=3) [6] [13]	38.917 s	7.533s	6.956s
HardestSudokusThread-00245;Red_Dwarf (Order=3) [6] [13]	185.602 s	18.079s	17.045s
Hardest Puzzle from [11]	101.561s	4.254s (Note: it did not use brute-force option at all)	3.762s (Note: it did not use brute-force option at all)
Puzzle number: 15362 (Order=4) [12]	Did not converge even after 3600 s	287.202s (Note: it did not use brute-force option at all)	200.103s (Note: it did not use brute-force option at all)
Puzzle number: 32137 (Order=4) [12]	Did not converge even after 3600 s	1324.243s	1120.211s
Puzzle number: 20132 (Order=4) [12]	Did not converge even after 3600 s	0.405s (Note: it did not use brute-force option at all)	0.403s (Note: it did not use brute-force option at all)
Puzzle number: 5251 (Order=4) [12]	Did not converge even after 3600 s	2756s	2433s
Puzzle number: 19329 (Order=4) [12]	Did not converge even after 3600 s	2700s	2345s

Puzzle number: 1010 (Order=4) [12]	Did not converge even after 3600 s	525s	446s
Puzzle number: 4902 (Order=4) [12]	Did not converge even after 3600 s	532s	431s
Puzzle number: 21802 (Order=4) [12]	Did not converge even after 3600 s	2452s	411s
Puzzle number: 420 (Order=5) [12]	Did not converge even after 24 hrs	49245s	37131s
Puzzle number: 219 (Order=5) [12]	Did not converge even after 24 hrs	47245s	38131s
Puzzle number: 262 (Order=5) [12]	Did not converge even after 24 hrs	43198s	34821s
Puzzle number: 402 (Order=5) [12]	Did not converge even after 24 hrs	41562s	35423s
Puzzle number: 1731 (Order=6) [12]	Did not converge even after 24 hrs	67341s	43546s
Puzzle number: 1549 (Order=6) [12]	Did not converge even after 24 hrs	73146s	46731s
Puzzle number: 775 (Order=6) [12]	Did not converge even after 24 hrs	70432s	48721s
Puzzle number: 1523 (Order=6) [12]	Did not converge even after 24 hrs	78211s	48342s
Puzzle number: 1365 (Order=7) [12]	Did not converge even after 24 hrs	82314s	52108s
Puzzle number: 1308 (Order=7) [12]	Did not converge even after 24 hrs	83518s	56712s
Puzzle number: 1306 (Order=7) [12]	Did not converge even after 30 hrs	86514s	57613s
Puzzle number: 1306 (Order=7) [12]	Did not converge even after 30 hrs	85134s	53421s
Puzzle number: 2384 (Order=7) [12]	Did not converge even after 30 hrs	98560s	70731s

XI. CONCLUSION

In this paper we have implemented ten strategies to solve Sudoku problems. These include some basic and some tough strategies used by human solvers based on deductive logic. Importantly, an existing P system model [1] was extended to incorporate these new strategies. As mentioned earlier a proof of concept using MATLAB© has been established. As expected these strategies have achieved efficiency by reducing the effective size of the search space. The results in Table 1 summarize the improvement in the performance of the algorithm. Any valid Sudoku of order *n* can be solved. We have also tested the algorithm on Sudoku instances of higher order 4 to 7. Since the search is combinatory in nature the search space for Sudoku of higher order can be expected to be significantly larger than that of lower order. As a consequence, pruning strategies demonstrate more dramatic impact on the performance of the algorithm for the Sudoku of higher order as seen in Table 1.

For our study, more importantly, was the ease with which these ten strategies could be compactly translated and incorporated in an existing P system framework. There are more strategies available [7]. It would not be difficult to incrementally add these new strategies as new rules in the P system. Keeping this in mind, it is not difficult to motivate the conjecture that a complex enterprise level application incorporating P systems based solutions could be better evolved and maintained in response to dynamic, real-life situations.

The model can be tested in a P-Lingua simulator where the notion of *non-determinism and maximal parallelism* can be studied [8]. As of now, with the available P-Lingua simulator, we have only been able to test for Sudoku of order 2 forcing us to program the rules in MATLAB©. Beyond order 2, the simulator suffers from out-of-memory problems. The MATLAB© based solution of course does not permit the study of the impact of maximal parallelism on the performance of the system. Nevertheless, representational efficiency and extensibility have been convincingly demonstrated. Further, even without parallelism, the model is more efficient indicating the correctness of the articulation of the pruning strategies. With the stable P-Lingua simulator, the drastic performance improvement can be seen due to *maximal parallelism*. But that need to be tested and verified which will be future area of work. Although, we have included results only for a few Sudoku, we have run the model over several Sudoku and the results are consistent. Establishing high performance, scalable simulators for membrane computing is an important focus area for future efforts in this domain.

REFERENCES

[1] Diaz-Pernil, Daniel, Carlos M. Fernandez-Marquez Carlos M, Garcia-Quismondo Manuel, Guti errez-Naranjo Miguel A., Martınez-del-Amor Miguel A., 2010. Solving Sudoku with Membrane Computing, In *IEEE Fifth International Conf. on Bio-inspired Computing: Theories and Applications BIS-TA, 09/2010, Vol 1, Changsha, China.*

[2] Paun, Gheorghe, 2000. Computing with membranes In *Journal of Computer and System Sciences,* 61, 1, pp. 108-143.

[3] Ignacio Pérez Hurtado, 2011. Introduction to P-Lingua, September 5, 2011. Osuna, Sevilla, Spain.

[4] Wikipedia Membrane Computing, 2012. *http://en.wikipedia.org/wiki/membrane_computing.*

[5] Wikipedia Sudoku, 2012. http://en.wikipedia.org/wiki/Sudoku.

[6] Wikipedia Sudoku Algorithms, 2012. *http://en.wikipedia.org/wiki/Sudoku_algorithms.* (Accessed between Sept to Dec 2012)
[7] Stuart, 2012. *http://www.sudokuwiki.org/strategy_families.*
[8] Research Group on Natural Computing, 2012. *http://www.p-lingua.org/.*
[9] T. Yato and T. Seta. 2003. Complexity and Completeness of Finding Another Solution and Its Application to Puzzles. *IEICE Trans. Fundamentals, E86-A (5) 1052-1060.*
[10] Inkala, 2006. *http://www.aisudoku.com/index_en.html* (accessed between Sept to Dec 2012)
[11] USA Today, 2006. *http://www.usatoday.com/news/offbeat/2006-11-06- sudoku_x.htm* (accessed between Sept to Dec 2012)
[12] Hanssen, n.d. *http://www.menneske.no/sudoku/eng/.*
[13] *http://forum.enjoysudoku.com/the-hardest-sudokus-new-thread-t6539.html* (accessed between Sept to Dec 2012)

2014 International Conference on Signal Processing and Integrated Networks (SPIN)

A Novel DFAL based Frequency Divider

Himanshu Puri, Kshitij Ghai, Kirti Gupta
Department of Electronics and Communication
Bharati Vidyapeeth's College of Engineering
Paschim Vihar, New Delhi
h.puri18@gmail.com, xityzghai@gmail.com,
kirtigupta22@gmail.com

Neeta Pandey
Electronics and Communication Department
Delhi Technological University,
Bawana Road, New Delhi
n66pandey@rediffmail.com

***Abstract*—With the increased interest in low power digital devices operating at low frequencies, the demand for high performance adiabatic logic circuits is on the rise. A frequency divider is extensively used for frequency synthesis in transceivers, and Phase Locked Loops (PLL) circuits. This paper proposes a novel diode free adiabatic logic (DFAL) based frequency divider for low power applications. The proposed circuit eliminates the use of diodes in charging and discharging paths to lower the power consumption and amplitude degradation. The functionality of the proposed circuit is verified and compared with the two-phase clocked adiabatic static CMOS logic (2PASCL) based and conventional CMOS frequency divider. All the simulations are performed in Tanner EDA using 180nm CMOS technology parameters. The simulation result shows that the proposed DFAL frequency divider outperforms the 2PASCL divider.**

Keywords—adiabatic, digital circuit, DFAL, frequency divider, low power.

I. INTRODUCTION

With the advances in VLSI technology, there is a great demand of portable devices that perform high speed computing and support multimedia applications. However, the increased functionality and high speed operation result in high power dissipation which eventually creates a need for low power design solutions. Different solutions both at the architectural and structural levels have been suggested. One possible approach is to adopt adiabatic logic style over conventional CMOS logic style for circuit design. Adiabatic logic style is more energy efficient than the conventional CMOS logic style [1]. A number of families based on adiabatic logic style have been proposed in literature [2-8].

The common adiabatic logic families that are frequently used are 2PADCL [2], ECRL [3], ADL [4], QSERL [5] and GFCAL [6]. The mentioned logic families however suffer from the drawbacks of amplitude degradation, large time delays and circuit complexity. In this paper a DFAL based frequency divider is proposed.

The paper first briefly describes the operation of the DFAL style in section II. Thereafter, the circuit of the frequency divider based on the DFAL style is proposed in section III. The proposed frequency divider design is functionally verified and its performance is compared with the conventional CMOS logic and 2PASCL style in section IV. All the simulations are carried using 0.18 µm technology parameters. Finally, the conclusions are drawn in the last section.

II. DIODE FREE ADIABATIC LOGIC STYLE (DFAL)

The common adiabatic logic families suffer from amplitude degradation, large time delays and circuit complexity. These drawbacks can be eliminated by using DFAL style. The DFAL style removes the diode from the charging and discharging path to overcome the above disadvantages.

The basic structure of a DFAL inverter is shown in Fig. 1a. The transistors M1, M2 implement the inverter. The transistor M3 is added in series with the transistor M2 for discharging and recycling of the output node charge. Its usage reduces the power dissipation significantly because it acts as a low value resistance, as compared to other adiabatic logic families which use diodes in the discharging path [2, 7]. The DFAL inverter employs spilt level sinusoidal power clock, as given in Fig.1b. This clock, in comparison to ramp or sinusoidal waveform, abates power dissipation, delay and degradation in output amplitude swing [5]. In spilt level sinusoidal power clock, two clocks named V_{SC} and V_{SCBAR} are used respectively. They are composed of DC and sinusoidal components as given below:

$$V_{SC} = \frac{V_{DD}}{4} \sin(\omega t + \Phi) + \frac{3}{4} V_{DD} \quad (1)$$

$$V_{SCBAR} = \frac{V_{DD}}{4} \sin(\omega t + \Phi) + \frac{1}{4} V_{DD} \quad (2)$$

where V_{DD} is the DC power supply, Φ is the phase difference which is usually taken as 180°. It can be observed that the voltage levels of V_{SC} and V_{SCBAR} differ by $V_{DD}/2$ which helps in improving the performance of the logic family [8].

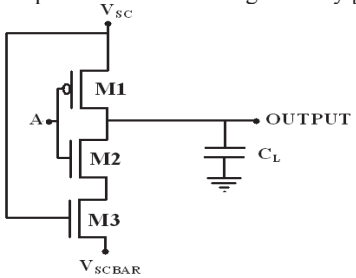


Fig. 1(a).- DFAL inverter circuit

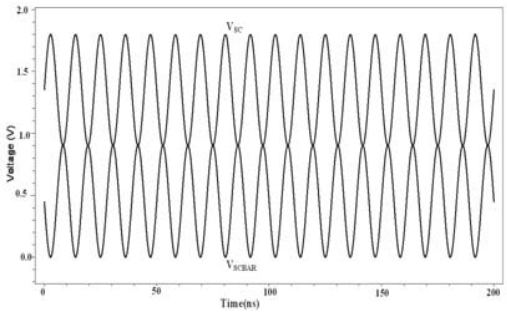


Fig.1(b). Split level sinusoidal power clock

The operation of the DFAL inverter can be divided into two phases namely evaluation phase and hold phase, depending upon the supply clock phases. In the evaluation phase, the V_{SC} makes a positive transition while V_{SCBAR} makes a negative transition. Conversely, in the hold phase, the clocks V_{SC} and V_{SCBAR} makes negative and positive transitions respectively.

In the evaluation phase, for a LOW value of the input A the transistor M1 is turned ON. If the output node Q is at the LOW value then the load capacitance C_L is charged via M2 resulting in the HIGH output state. Conversely, if the input A is HIGH the transistor M2 is turned ON and if at the same time output node Q is HIGH, then the discharging and recycling of output node charges to the power clock (V_{SCBAR}) takes place ,via M2 and M3, causing the output to be LOW.

In the hold phase no transition at the voltage level at the output node occurs. Therefore, the output node remains in the LOW state even if the nMOS network is ON. Similarly, the output continues to be in the HIGH state when the pMOS network is ON. Therefore, in the hold phase, as the switching activity at the output node is reduced, the power dissipation is significantly lowered.

III. FREQUENCY DIVIDER

A frequency divider, also referred to as a clock divider, produces an output signal whose frequency is a fraction of the input frequency. It is commonly implemented as a cascade of divide-by-two stages. A general block diagram of the frequency divider obtained by cascading T-flip flops is shown in Fig. 2. The circuit switches after every two pulses of the applied input signal, hence, dividing input's frequency by two. In real cases, a T- flip flop is implemented by using two cross-coupled feedback D-latches driven by opposite clock signals as illustrated in Fig. 3.

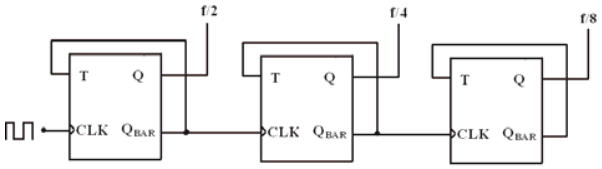


Fig. 2: General block diagram of frequency divider using T flip-flops.

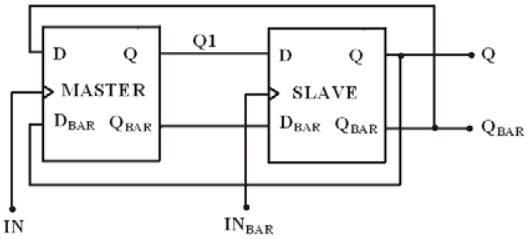


Fig. 3: Divide-by-2 frequency divider using master-slave D-latch

The MOS level implementation of the proposed DFAL based frequency divider is shown in Fig. 4. As illustrated in Fig. 3, the proposed divider consists of two DFAL based D-latch in master-slave configuration. The inputs IN and INBAR are applied at the clock inputs of the master and slave D-latch respectively. Considering that the initial output of the divider Q is HIGH. In the first evaluation phase, when IN is at HIGH level the master D-latch is enabled and it makes intermediate output Q1 LOW. However, the slave D-latch remains isolated during this period. After this in the second evaluation phase when the IN goes LOW, the slave D-latch gets enabled and transfers the intermediate node value Q1 to the output. Thus,

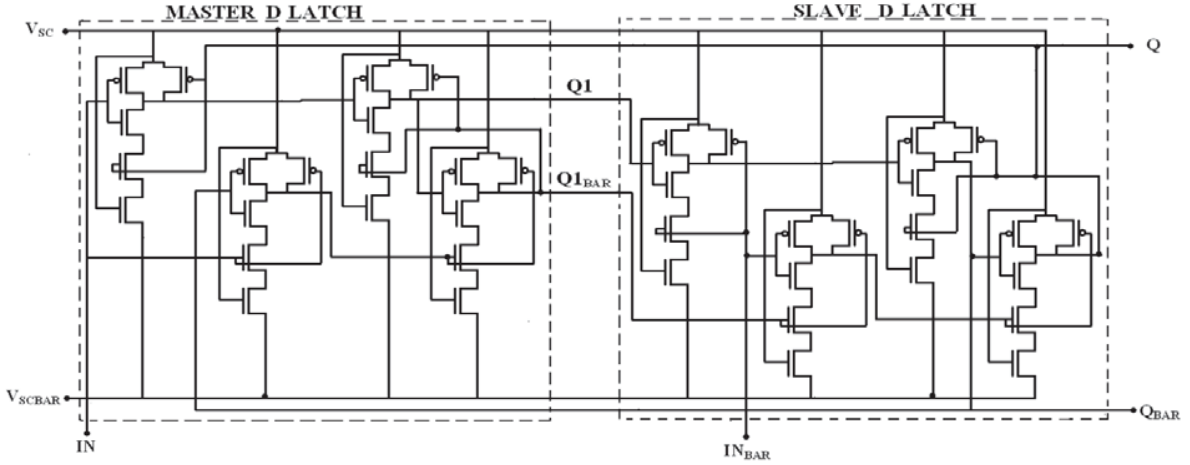


Fig. 4: Proposed DFAL based Frequency Divider

at the end of the second evaluation phase, the output Q produces a LOW value. In the similar manner, when the output Q is LOW and IN is HIGH the master makes the intermediate output Q1 HIGH during the evaluation phase. Correspondingly, Q becomes HIGH at the hold phase.

IV. SIMULATION RESULTS

In this section, the functionality of the proposed DFAL based frequency divider is verified. Thereafter, the performance of the DFAL frequency divider is compared with the CMOS and the 2PASCL frequency dividers. The comparison has been made in terms of power dissipation and delay for different values of the load capacitance and frequency of the input. All the simulations are performed in Tanner EDA by using 0.18 µm CMOS technology parameters and with a supply voltage of 1.8 V.

A. Proposed DFAL based frequency divider

The functionality of the proposed DFAL based frequency divider (Fig. 4) is verified for the specifications shown in Table I. The waveforms of the power supply V_{SC}, input IN, intermediate node Q1 and the output node Q is shown in Fig 5. It can be observed that it conforms to the functionality.

B. Performance comparison

In this subsection, the performance of the proposed DFAL frequency divider is compared with the CMOS and 2PASCL frequency divider. The MOS diagram of the 2PASCL frequency divider is shown in Fig. 6. The frequency dividers are compared in terms of the power dissipation, delay and power delay product (PDP) for various values of the load capacitance and input frequency. The results have been listed in Table II and III and have also been compared graphically in Fig. 7 and Fig. 8. It has been found that the proposed DFAL shows a maximum PDP reduction of about 66.05% in comparison to other families for various values of load capacitance and a maximum PDP reduction of about 76.76% for various operating frequencies. In terms of delay, the proposed divider is faster than the CMOS frequency divider but has higher delay values than the 2PASCL as plotted in Fig.7 .When compared on the basis of PDP, it can be seen that proposed frequency divider exhibits much lower PDP values than the CMOS and 2PASCL frequency divider. Similar results are obtained when the frequency dividers are simulated at different frequencies. This confirms that the proposed DFAL frequency divider is much more efficient in comparison to CMOS and 2PASCL based frequency dividers.

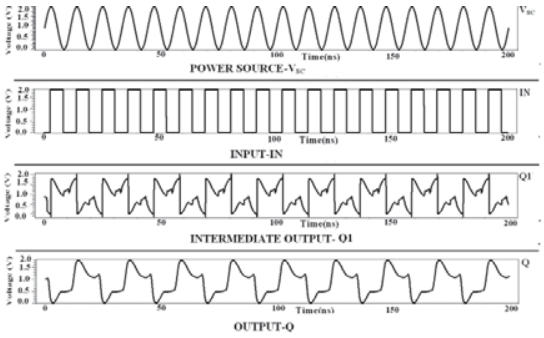


Fig. 5.-Simulation waveform of DFAL frequency divider

Table I: Simulation Parameters

Parameter	Value
MOS dimensions	0.6 µm/ 0.18 µm
Power supply (V_{SC}) frequency	50 MHz
Load capacitor	100 fF
Input (IN) frequency	50 MHz

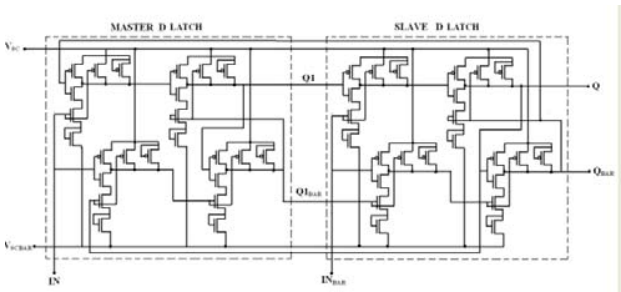


Fig. 6: 2PASCL based frequency divider

Table II: Performance comparison w.r.t to the load capacitance frequency of the input (IN)

Capacitance / Logic Family	20fF	40fF	60fF	80fF	100fF	120fF	150fF
Power dissipation (µW)							
CMOS	9.2	13.13	17.13	21.11	25.14	29.46	35.27
2PASCL	7.1	8.66	9.93	11.08	12.01	12.89	14.00
DFAL	4.6	5.51	6.70	7.56	8.70	10.00	12.37
Delay (ns)							
CMOS	4.92	4.86	4.81	4.76	4.71	4.66	4.58
2PASCL	4.41	4.20	4.03	3.84	3.84	3.98	4.22
DFAL	4.76	4.71	4.66	4.63	4.60	4.57	4.53
Power delay product (PDP)							
CMOS	45.26	63.81	82.39	100.48	118.41	137.28	161.54
2PASCL	31.31	36.37	40.02	42.55	46.12	51.30	59.08
DFAL	21.89	25.95	31.22	35.01	40.02	45.7	56.04

Table III: Power dissipation (µW) comparison w.r.t to the frequency of the input (IN)

Frequency / Logic Family	10MHz	20MHz	30MHz	40MHz	50MHz	60MHz	70MHz	80MHz	90MHz
	Power dissipation (µW)								
CMOS	7.696	12.060	16.443	20.780	25.142	29.502	33.870	38.221	42.601
2PASCL	3.004	5.975	7.975	10.439	12.009	14.011	15.520	16.835	18.185
DFAL	1.788	3.283	4.995	6.809	8.698	10.148	13.301	15.886	18.577
	Delay (ns)								
CMOS	24.714	12.214	8.044	5.964	4.713	3.884	3.286	2.838	2.488
2PASCL	22.235	10.582	6.726	4.822	3.836	3.377	3.038	2.739	2.588
DFAL	23.886	11.794	7.783	5.794	4.6015	3.183	3.243	2.819	2.486
	Power delay product (PDP)								
CMOS	190.19	147.3	132.27	123.93	118.49	114.59	111.297	108.47	105.99
2PASCL	66.79	63.23	53.64	50.34	46.06	47.32	47.15	46.11	47.06
DFAL	42.71	38.72	38.88	39.45	40.03	32.3	43.135	44.78	46.18

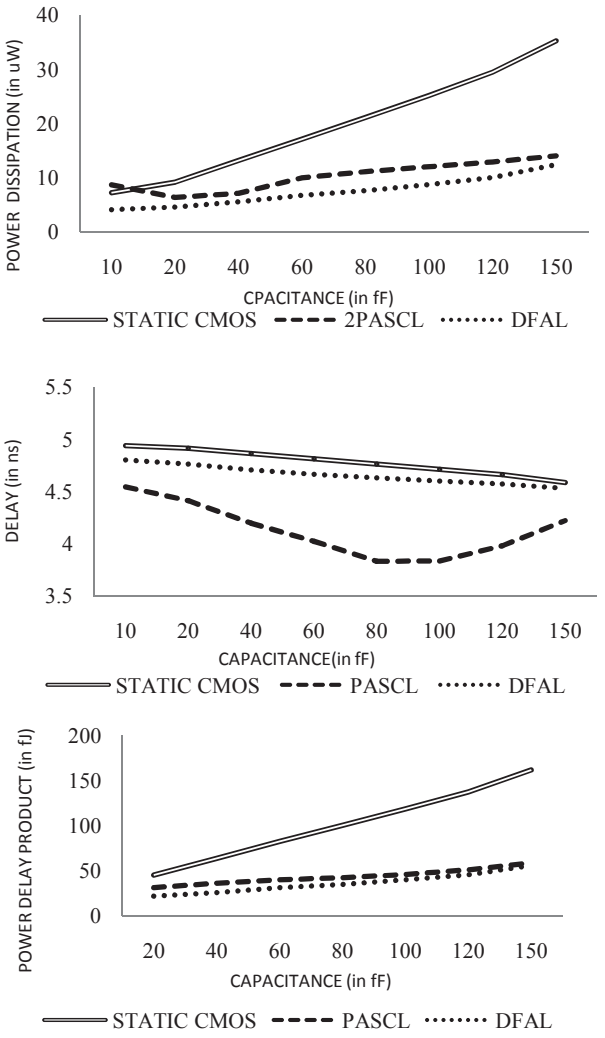


Fig. 7: Power dissipation, delay and PDP of frequency dividers with capacitance

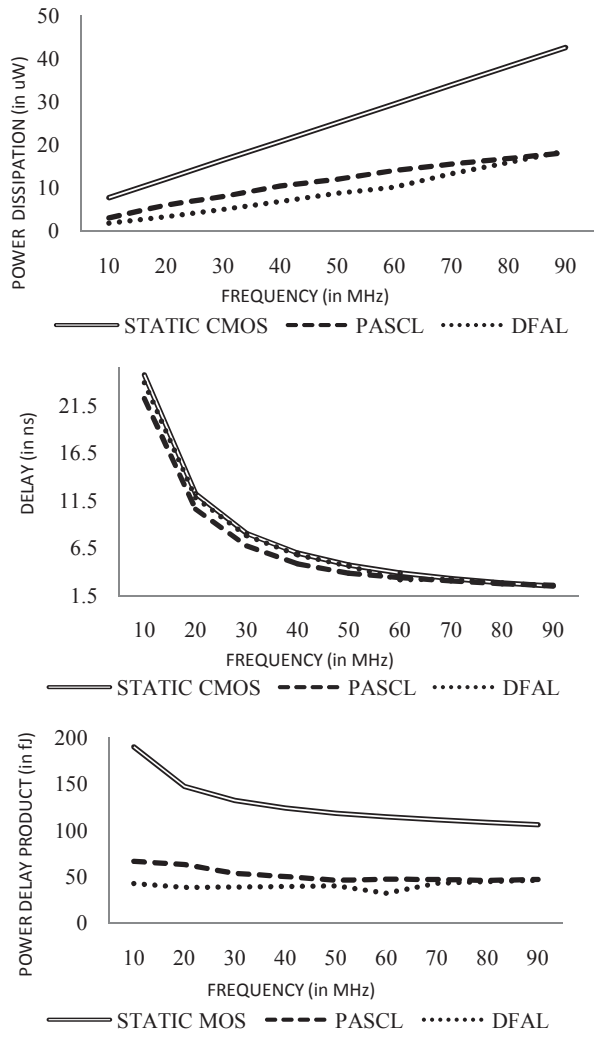


Fig. 8: Power dissipation, delay and PDP of frequency dividers with frequency

V. CONCLUSION:

In this paper, a novel diode free adiabatic logic(DFAL) frequency divider for low power applications is proposed. The proposed circuit avoids the diodes in charging and discharging paths in comparison to the existing ones. The functionality of the proposed circuit is verified and compared with the existing two-phase clocked adiabatic static CMOS logic (2PASCL) based and conventional CMOS frequency divider. All the simulations are carried out in Tanner EDA using 180nm CMOS technology parameters. It is found that the proposed frequency divider is power efficient than the existing ones.

References

[1] Hamid Mahmoodi-Meimand, Ali Afzali-Kusha and Mehrdad Nourani," Efficiency of Adiabatic Logic for Low-Power, Low-Noise VLSI" Circuits and Systems, 2000. Proceedings of the 43rd IEEE Midwest Symposium Volume:1

[2] Y. Takahashi, Y. Fukuta, T. Sekine, and M. Yokoyama, "2PADCL: Two phase drive adiabatic dynamic CMOS logic," in Proc. IEEE APCCAS, Dec., 2006, pp. 1486-1489.

[3] Y. Moon and D.K. Jeong, "An efficient charge recovery logic circuit," Solid-States Circuits., IEEE Journal, Vol.31, Issue4, Apr., 1996, pp.514-522.

[4] A.G. Dickinson and J.S. Denker, "Adiabatic dynamic logic," Solid-States Circuits, IEEE Journal, Vol.30, Issue3, Mar., 1995, pp.311-315

[5] Y. Ye, and K. Roy, "QSERL: Quasi-static energy recovery logic," Solid-States Circuits., IEEE Journal, Vol.36, Issue 2, Feb., 2001, pp. 239-248

[6] N. S. S. Reddy, M. Satyam, and K. L. Kishore, "Cascadable adiabatic logic circuits for low-power applications," IET Circuits, Devices and Systems, vol. 2, no. 6, pp. 518–526, 2008.

[7] Nazrul Anuar, Yasuhiro Takahashi, and Toshikazu Sekine, "Two Phase Clocked Adiabatic Static CMOS Logic and its Logic Family", Journal of Semiconductor Technology and Science, VOL.10, NO.1, MARCH, 2010

[8] Shipra Upadhyay, R. A.Mishra, R. K. Nagaria, and S. P. Singh, "DFAL: Diode-Free Adiabatic Logic Circuits", Hindawi Publishing Corporation ISRN Electronics, Volume 2013, Article ID 673601, 12 pages

[9] Changhua Cao and Kenneth K. O, "A Power Efficient 26-GHz 32:1 Static Frequency Divider in 130-nm Bulk CMOS", IEEE Microwave and Wireless components letters VOL. 15, NO. 11, NOVEMBER 2005

A SECURITY BASED ARCHITECTURE FOR MANET

Ekata Gupta [1], Dr.S.K.Saxena [2]

[1] MCA Department, GNIM, New Delhi and Research Scholar, Mewar University
[2] CSE Department, Delhi Technological University (Formerly Delhi College of Engineering)
[1] ekata_2000@yahoo.com, [2] saxena58@gmail.com

Abstract

A Mobile ad Hoc network is a kind of mobile network that is dynamically changing and they have a fully decentralized topology. The security of Mobile Ad hoc Network (MANET) is more rigorous than that of traditional network. Therefore security remains a major challenge for these networks due to their feature. Moreover in the absence of central monitoring points there is a lack of defense mechanism. An intermediate node which takes part in packet forwarding may behave differently and drop packets instead of forwarding them. This malicious node falsely advertises itself as a trustworthy node; such behavior is called black hole attack. In this paper security architecture for detecting a cooperative black hole attack is presented.

Keywords: MANET, AODV, security, cooperative Black hole.

I. Introduction

In the recent years, wireless technology has a tremendous rise in popularity and usage, thus opening new fields of applications in the domain of networking. One of the most important of these fields concerns mobile ad hoc networks (MANET), where the participating nodes do not rely on any existing network infrastructure. At any time and any place, the MANET can interlink many mobile terminals in limited region .Therefore; the interconnections between nodes are capable of changing on continual and arbitrary basis. Nodes within each other's radio range communicate directly via wireless links, while those that are further apart use other nodes as relays. Security in mobile ad hoc networks is a hard to achieve due to dynamically changing and fully decentralized topology as well as

the vulnerabilities and limitations of wireless data transmissions. These include passive eavesdropping, active interfering, and denial- of service.One of the most critical problems in MANETs is the security vulnerabilities of the routing protocols.

Our approach detects the packet forwarding Misbehavior detection and detection of routing misbehavior using AODV protocol.

AODV is vulnerable to the well-known black – hole attack although there has been lot of research on detection and prevention of an attack in MANET, most of the schemes have low detection rate, high complexity of detection algorithms, security vulnerabilities in the schemes themselves or high rate of false positives.

In this paper a mechanism is proposed to identify cooperative black hole with the help of security architecture design.

II. Security analysis of MANET

MANET is different from the fixed IP network as well as the general wireless network, which poses new challenges to guarantee its security The security threats confronted by MANET is the extension and expansion of that be confronted by wired network in the wireless field, which mainly comes from wireless channels and networks. The threats can be divided into two categories of passive attack and active attack.

1) Passive attack

Passive attack is essentially to listen or surveillance the message transmission process to obtain some secret

2) Active attack

Comparing with passive attack, the passive attack usually does not change the transmission data, while active attack will tamper data stream or create false data stream. The active attack includes four kinds of message replay, Fraud Counterfeiting, Message tampering and Denial of Service

III. Cooperative black hole attack

A malicious node that incorrectly sends, the RREP that is has the latest route with minimum hop count to destination and then it drops all the receiving packets, this is called black hole attack. Black hole attack in AODV can be performed in 2 ways

1. Using Route Reply(RREP)
2. Using Route Request(RREQ)

If multiple malicious node gather together to work cooperatively the attack effect is more This is known as cooperative black hole attack.

The black hole attack works in two phases. In the first phase the malicious node advertises itself of having a valid route to the destination even though the route is spurious. In the second phase the attacker node drops the intercepted packet without forwarding them. There is more subtle form of attack when the attacker suppresses or modifies the packets.

Now when these malicious nodes work in groups it becomes even more subtle.

IV. Cooperative Manet security architecture design

A. Objective of MANET Security

The objective of MANET security are in accordance with that of traditional network ,including data availability, confidentiality , integrity , security authentication and non- repudiation . Availability indicates that even in the face of various attacks normal services required are available.

Confidentiality means that unauthorized entities cannot access the information.

Integrity means that the information cannot be modified or destroyed Security authentication indicate that both the ends are authenticated to send and receive message

Non-repudiation means sender cannot deny that message it has sent and similarly the receiver cannot deny that message has been received.

B. Security architecture of MANET

Security should develop together with the network as an integral part but not a remedial measure. Even though OSI layers provide us with the advantage of modularity, flexibility and standardization the security should be considered from layer to layer.

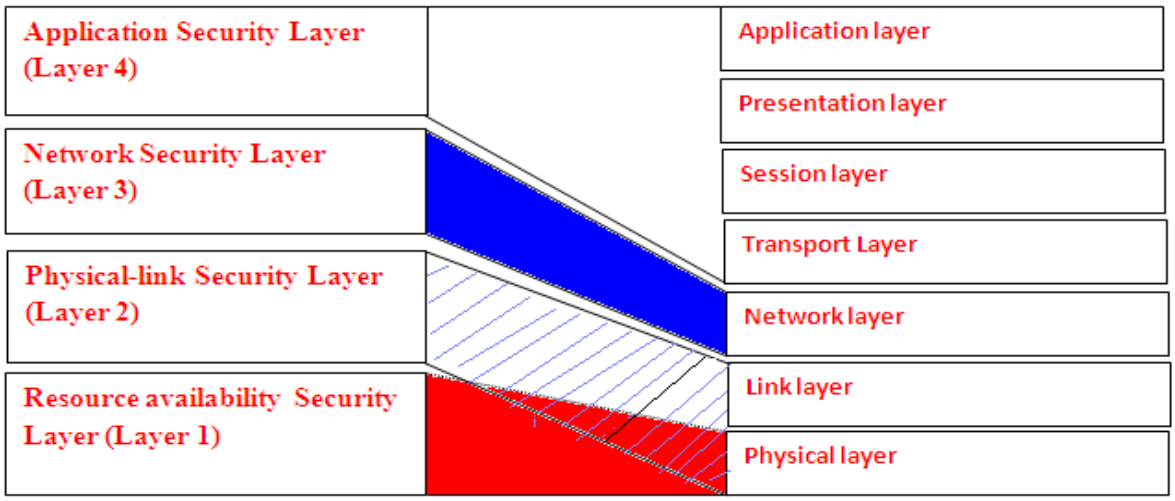


Fig 1: Cooperative Manet security architecture

According to the hierarchy idea of OSI model, the cooperative Manet security architecture is being designed.

1. Layer1 Resource availability security layer

This layer forms the foundation or the base of all the layers. The functions designed at this layer would be used by the upper layers. Manet is an infrastructure less and distributed network so the security required for Manet should be of distributed kind .so with the help of this layer a security relationship can be established between the nodes.

2. Layer 2 Physical-link security layer

When we look at the wired or wireless network there is some kind of protection mechanism through firewall or through access control but in Manets the channel can be attacked from any direction and on any node. The main task of this layer is to protect the data from tampering or destroying.

3. Layer 3 network security layer

In Manet a node must play two roles (I) communication with other nodes (ii) routing of packets .In addition a host may be required to forward a meant packet. The former requires mutual cooperation and sharing correct routing information among the nodes to maintain the network connection in correct.

Routing is most important in Manet for it relates to the topology of the whole network this mechanism modifies the AODV protocol by introducing data routing information (DRI) table which each node maintains. Two additional bits are being sent along the RREQ message. This first bit indicates routing information from the node and the second bit indicates routing information through the node.
When a node as N1 generates a packet for node N2 the following task are performed

i. The ids of both the nodes are recorded.
ii. A record to keep track of number of receiving and forwarding packets to and from node N2.
iii. The entire record is signed by node N1 using its private key.

Each node also maintains a self table (ST) and a Recorded table (RT)

A. ARCHITECTURE:

In this architecture of cooperative security agents we pass DRI and ST-RT table as an input to Cooperative
Security Agents. Monitor processing takes charge of monitoring all one-hop neighbors' activities and filtering and encoding them. In the Memory Library, the behavior patterns of attack nodes are kept to represent various known attack methods.

Mode 1: Rec (N1, M), Delete (N1, M). Node N1 receives the message M and then deletes it, not transmitting it in accordance with the routing table. It is Interrupt Attack.

Mode 2: Rec (N1, M), Modify(S N1, M), Send (N1, M). Node N1 receives the message M, and then transmitting it to next hop node after modifying packet content. Next hop node will receive the wrong packet information. It is the Error Message Attack.

Mode 3: Rec (N1, M), Reply (M, N), Send (N1, N). Node N1 receives message M, and then sends the reply message to make wrong routing direction. It is the Black Hole Attack.

Mode 4: Make (N1, M), Broadcast (N1, M). Node N1 generates and broadcasts a large number of messages in a short period of time, leading to normal nodes not working properly. It is DoS Attack.

If one behavior matches the previous defined attack patterns, it is likely to be attack node the role of the decision-making module is to identify attacks, position the invaders, and send out an instruction to its neighbor nodes to arouse the Counterattack Agents.

In addition to this the black hole detecting component is used to collect the network node ID of these nodes and to analyze them.

Thus it would reduce the time required for black hole detection about a particular node and improve the system performance.

In Alert, Responses and cooperative agent module is used to identify the alert level of the node.

1 Serious : Drop the node Id and alert all the neighboring nodes
2 Moderate : Dynamic decision is taken whether to drop the node or not
3 Slight: do not care condition.

The cooperative and communication agent is used to receive alert messages from other security agents. After receiving these alerts the agent makes a judgment is larger than 0.5 and then adds a new rule to its table

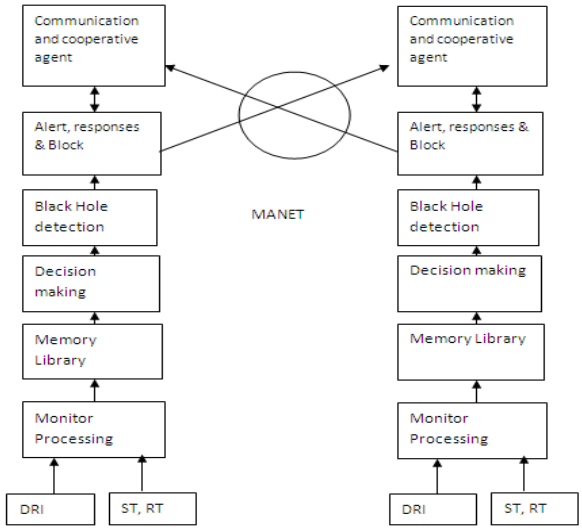


Fig 2: Architecture of Cooperative Security Agents

4 Layer 4 Application security layer

The application security layer refers to the security of
End-system, such as security protocols of Secure Socket Layer (SSL), Secure Shell (SSH), Secure Electronic Transaction (SET) and others. The protocols are independent of the underlying network security layer, which encrypt the data before it enter into the network layer to ensure data security. In the layer, the security protocol being used is determined by the application programs running in the system, such as SSL is the protocol to enhance security Web transmission; the SSH is the protocol to enhance security Telnet/FTP transmission.

The application security layer is corresponding to four layers from the transport layer to the application layer of OSI model, which defines secure mechanisms related to application programs in the end systems, such as SET protocol, so it is separated from the underlying layers.

V. Conclusion

Owing to characteristics of open medium, dynamic topology and distribution, the security of Mobile Ad hoc Network (MANET) is more rigorous than that of traditional network. Referring to the hierarchy idea of OSI reference model, the paper divided the security architecture into four layers of Layer1 Resource availability security layer, Layer 2 Physical-link security layer, Layer 3 network security layer, Layer 4 Application security layer.

The functions of each layer ware also described in detail. Thus, the security mechanism of the whole network is considered from the aspect of system architecture, which provides framework for secure network design.

A security method has been proposed to detect black hole and cooperative black hole nodes in a MANET and thereby identify a secure routing path from a source node to a destination node by avoiding the black hole nodes.

This mechanism can effectively detect malicious nodes and mitigate the negative impact caused by the Black hole and cooperative black hole attack.

VI. References

[1] Sen, J.; Koilakonda, S.; Ukil, A., "A Mechanism for Detecting of Cooperative Black hole Attack in Mobile Ad Hoc Networks", Second International Conference on Intelligent Systems, Modelling and Simulation (ISMS), pp.338-343, Jan. 2011.

[2] Latha Tamilselvan, V. Sankaranarayanan, “Prevention of Co-operative Black hole Attack in MANET”, Journal of Networks, Vol 3, No 5, 13-20, May 2008.
[3] Abderrahmane Baadache, Ali Belmehdi, “Avoiding Black hole and Cooperative Black hole Attacks in Wireless Ad hoc Networks”,
(IJCSIS) International Journal of Computer Science and Information Security, Vol. 7, No. 1, 2010.
[4] Li Shi-Chang, Yang Hao-Lan, Zhu Qing-Sheng “Research on MANET Security Architecture Design” , 2010 International Conference on Signal Acquisition and Processing
[5] Vaishali Mohite, Lata Ragha “Cooperative Security agents for Manet” , 2012 World Congress on Information and Communication Technologies
[6] Mishra A., Nadkarni K. and Patcha A., “Intrusion Detection in Wireless Ad hoc Networks,” IEEE Wireless Communications, vol.11, 2004, pp. 275-283.
[7] Xia Ye, Junshan Li,” A Security Architecture Based on Immune Agents for MANET” ICWCSC 2010X
[8] Y. Zhang and W. Lee, “Intrusion Detection in Wireless Ad-Hoc Networks,” Proceedings of the 6th Annual International Conference on
Mobile Computing and Networking, MobiCom’ 2000, pp. 275-283.
[9] Azer, M.A., et al., A Survey on Trust and reputation Schemes in Ad Hoc Networks, 3rd Intl. Conf. on Availability, Reliability and Security (ARES), 2008.
[10] Omar, M., Challal, Y., and Bouabdallah, A., Reliable and Fully Distributed Trust Model for Mobile Ad Hoc Networks. Computers & Security, 2009.Vol. 28 No.(3-4): p. 199-214.

A study and comparison of Uninterruptible Power Supply topologies

Arnav Gupta

DTU/2K12/EL/020

Delhi Technological University

Introduction

An uninterruptible power source is an electromechanical/electrochemical system that provides backup or emergency power to a load when the power supply from the input becomes absent (or becomes unusable due to fluctuations in voltage signal).

The main difference of an UPS from a Auxiliary Power Supply system like generators is that it provides instantaneous or near-instantaneous protection from input power interruptions. In many cases an UPS provides intermediate power while Primary Power is switched to Auxilliary power.

Power is stored in an UPS in batteries or flywheels, with flywheels being very uncommon and mostly used for extremely specific purposes.

UPS systems are mostly used where an unexpected power disruption could cause injuries, fatalities, serious business disruption or data loss. Data Centres, Workstations, Servers, Space systems all heavily depend on UPS systems.

Uninterruptible Power Systems can broadly classified into two categories based on the method of power supply switching it uses: -

1. On-Line UPS
2. Off-Line UPS

There are multiple varieties of both, including line-interactive designs which tries to get implement the best of both worlds. The topology in which the components are arranged and the method of power supply switching has far and wide implications on the scope of applications of UPS systems.

Basic Components

A battery based UPS system consists of three main components: -

1. Rectifier
2. Battery (storage)
3. Inverter

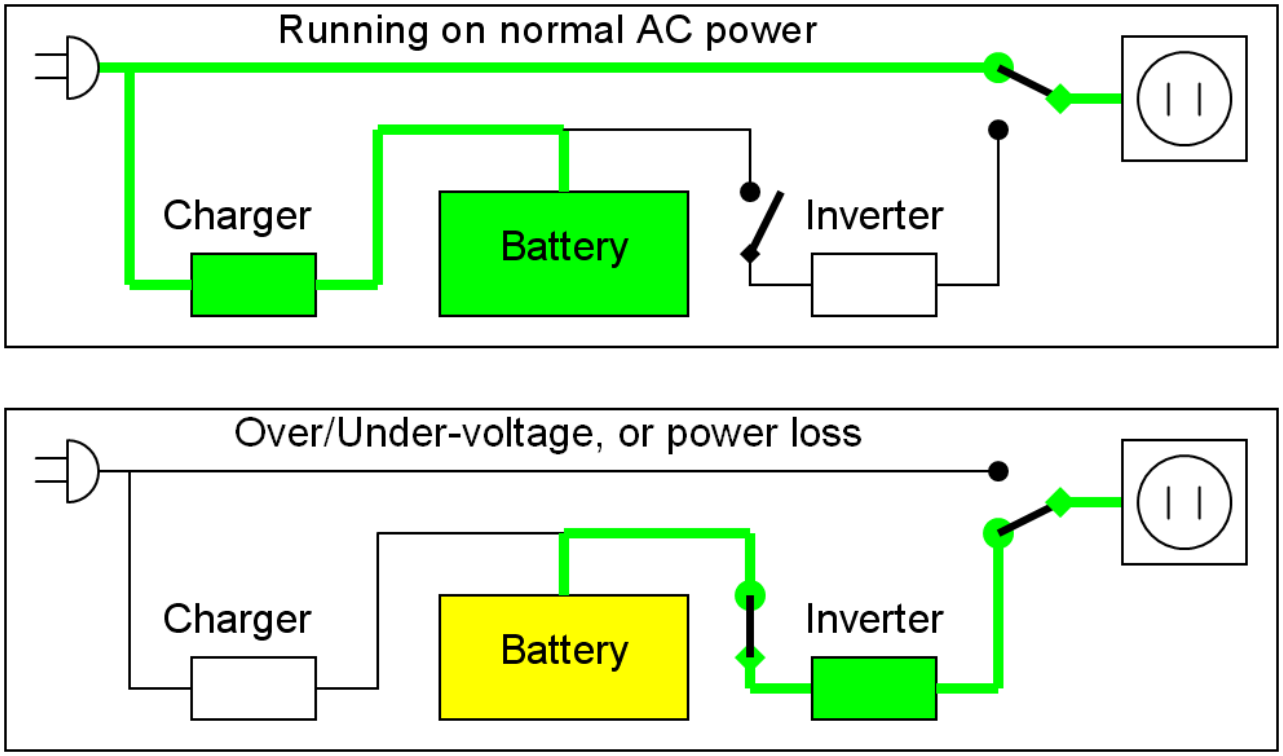
These components are connected in various topologies, along with transformers, to cater to different application needs.

Rectifier is placed between the supply mains and the battery to convert AC to DC.

Battery is used to store electrical energy. Various types of cells can be used depending on the form-factor needed.

Inverter is placed between the battery and the load so that DC can be converted back to AC. In some internal UPS systems used by computers, Inverted may not be needed as the load operated on DC.

Transformers are needed to step down voltage from supply to charging voltage and from battery output voltage to load supply voltage.



Simple block diagram showing the components and their operations while running on AC power, and while running on battery power.

Objectives

While initially conceived to provide emergency power during loss of supply, the scope of problems that an UPS system aims to solve can include any or all of the following

1. Blackouts
2. Brownouts
3. Swells
4. Spikes
5. Frequency Drifts

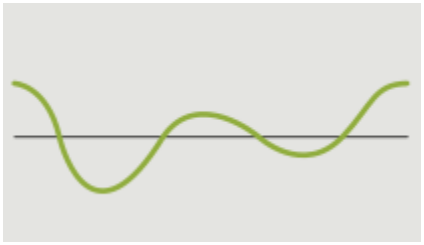
Blackout

A blackout means that there is no power supply at all. It can be due to an excessive demand of electrical energy, storms, ice on the power lines, road accidents, excavations, earthquakes, etc.



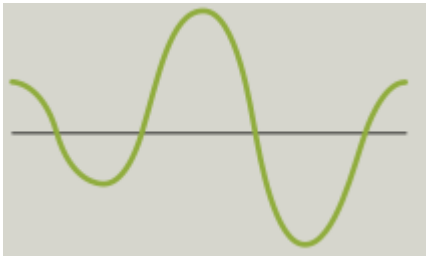
Brownout

Brief drop in voltage levels. This is the most common disturbance (even 87%) due to the power supply and is caused by the activation of electric devices such as motors, compressors, lifts and freight lifts.



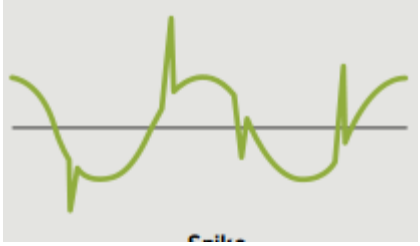
Swell

This is a short voltage increase, typically lasting 1/120 of a second. Overvoltage may be caused by very powerful electric motors, such as air-conditioning systems. When these turn off, the excess voltage is dissipated on the electric line.



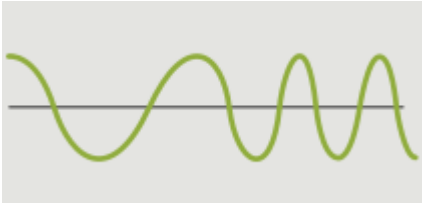
Spike

A spike, or voltage transient, is a sudden surge in voltage. Spikes are generally caused by lightning and can also occur then the mains supply is restored after a power failure.



Frequency Drift

They generally occur in the energy produced by power-supply units. These variations cause errors in the execution of calculations, interpretation issues related to magnetic supports (discs, tapes, etc.), various kinds of problems associated with electromechanical applications.



Specifications

The following factors relating to the intended application should be taken into account when specifying a UPS.

- **Hold up time** is the length of time that the power supply used in an application can still provide a viable output without an input supply. This is possible because the energy stored in capacitive and inductive elements in the power supply can continue to supply the load for a short period. For example, in switch mode power supplies, typically used in computer equipment, the hold up time can range from 10-30 ms.
- **Transfer time** is the time taken by the UPS to switch from mains to the battery back up in case of mains failure or from battery power to mains power when normal power is restored. This time should be significantly less than the application hold up time to allow for a safety margin.

  For computer applications a transfer time of less than 5 ms is advisable, however, it should be noted that an oversensitive unit may make unnecessary power transfers.

- **Power handling** is the normal power consumption of the application which the UPS must be able to supply during emergency periods.
- **Inrush current** is the momentary peak input current required by electrical equipment when it is initially switched on due to charging up inductive and capacitive loads. This can be many times it's normal operating current but is usually of very short duration. It can effect the sizing of UPS and the setting and timing of protection circuits.
- **Back up time** is the time period for which the UPS is required to support the load in case of mains failure. The required back up time depends on the user's system design and objectives. It may only need to be long enough to provide power to permit the orderly shut down of the application or it could be required to power the application for the full duration of any expected power outage. Alternatively the UPS may only be needed long enough to permit the connection and start up of alternative power from a high power rotary generator. The capacity of the UPS storage battery is determined by the current drawn by the load and the required back up time.
- **Power conditioning or line conditioning** is the provision of a regulated voltage and frequency power line with a pure sine wave free from electrical noise and ripple.
- **Isolation** is the complete electrical separation of the output of the UPS from the input power line. Power is coupled from the line input to the UPS output through separate windings in a transformer. Because there is no physical connection from input to output, the effect of transient interference from the mains supply is minimised and the safety of the application is improved.
- **Orderly shutdown** is the process of sequentially closing down hardware and/or software processes in the application so that no corruption of data occurs and/or no safety hazards are created. The back up time should be long enough to permit orderly shut down of the application.
- **Load shedding** is the ability to selectively shut off power to less critical loads during an extended power failure while maintaining power to the more critical loads thus extending the effective back up time of the UPS.
- **Load sequencing** is the ability to selectively turn on or off specific loads in a pre-set pattern during start up and/or shutdown. This may be for safety reasons or to minimise the initial inrush current.
- **Recharge time** is the length of time UPS takes to recharge the batteries after a discharge.

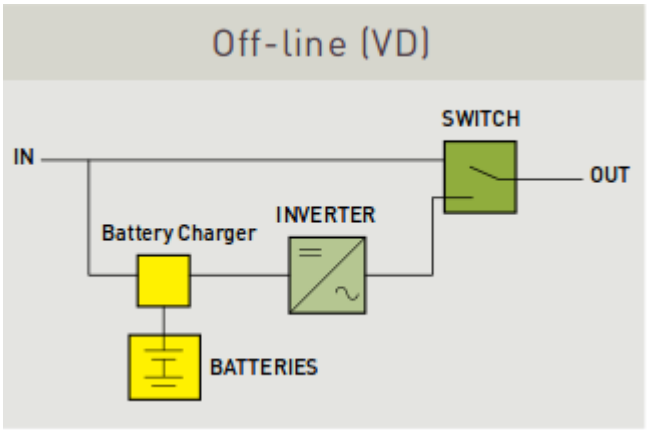
- **Hot swapping** is changing equipment while power is being supplied and used. This may be necessary for changing over battery packs.

Basic UPS Topologies

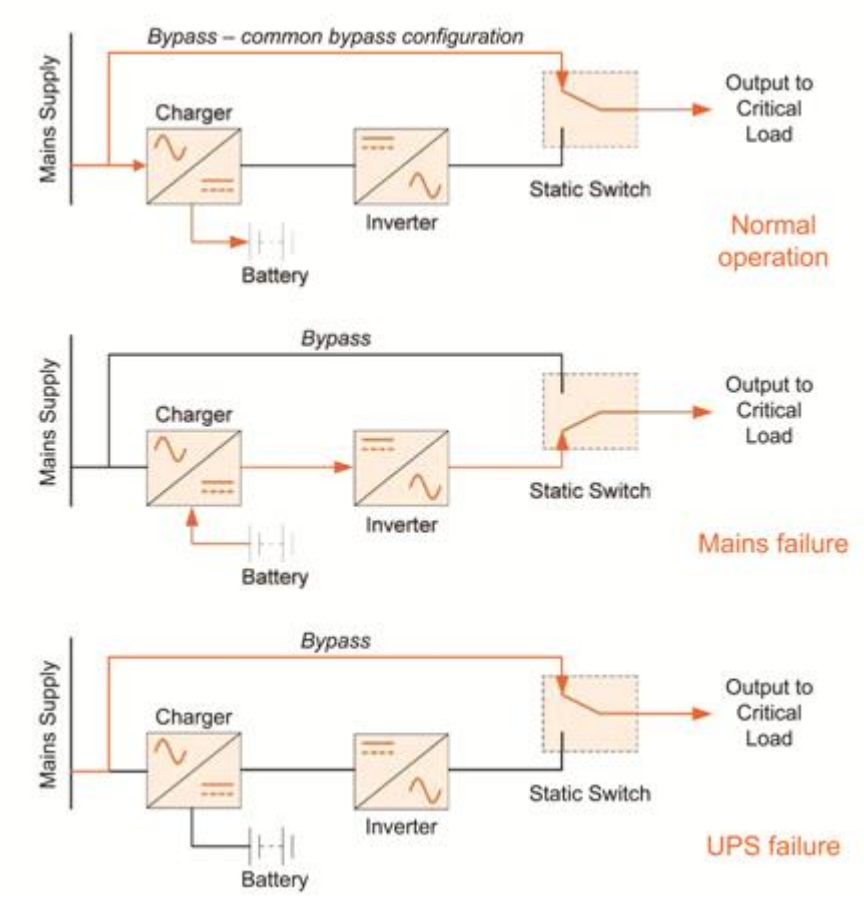
Off-Line UPS

In an offline configuration, when mains power supply is present, it is directly fed to the load. Parallely if the batteries are not fully charged, they are charged from mains too.

When there is interruption in the supply, a transfer switch shift supply from mains to battery output.



Simple block diagram of offline configuration



Modes of operation of offline UPS

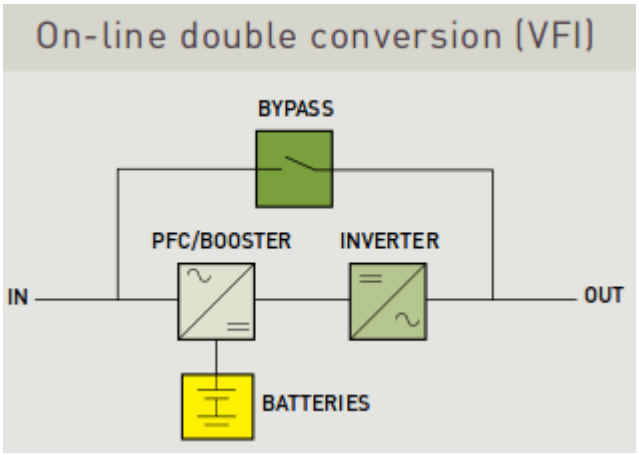
An off line UPS, during normal operation, feeds raw mains to the critical load through a bypass line and static switch. The load is therefore exposed to poor voltage regulation and possibly noise and transients from the mains. If the mains transgresses preset limits, the static switch transfers the load to the UPS's inverter and battery – a changeover break that can last from 2 ms to 10 ms. Many operators of data centres and other sensitive equipment consider off line UPS systems to be unsuitable for their applications because of these power quality and changeover break factors.

Another disadvantage of a basic off line system is that, unlike an on line design, it cannot compensate for mains supply voltage limit transgressions. Instead it must respond immediately by switching between bypass and the inverter for every transgression event. This can happen frequently if the mains supply is unstable or the critical load has a tight voltage tolerance. Apart from subjecting the load to frequent supply interruptions, the battery may have its life reduced or be insufficiently charged as a result.

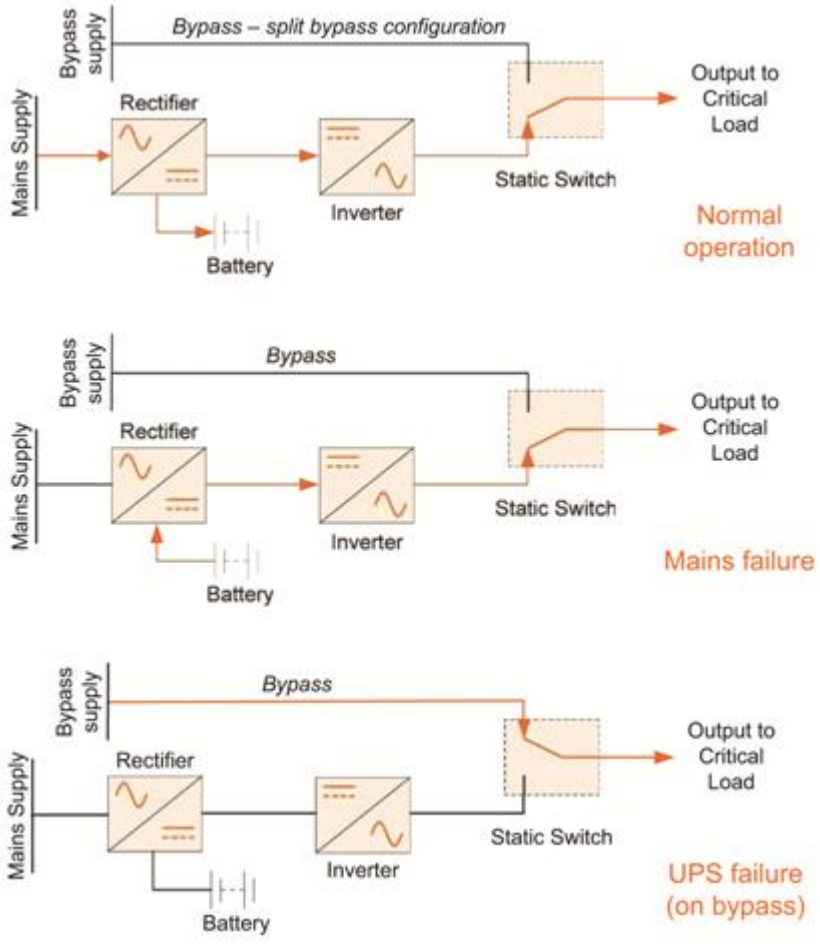
However applications which can tolerate these disadvantages enjoy two key cost benefits from using off line topology. Firstly, an off line UPS reduces capital costs compared with an on line equivalent through using lower-rated components and dispensing with a power rectifier. Secondly, running costs are lower because the charger and inverter, with their inevitable inefficiencies, are not on line during normal operation.

On-Line UPS

In this configuration, the load is always fed from the backup source, and never fed directly supply power. There is no transfer switch involved and hence it has no transient characteristics. This is needed in high precision loads where the spikes or disturbances associated with the transfer switching can result in disruptions.



Block diagram of online UPS



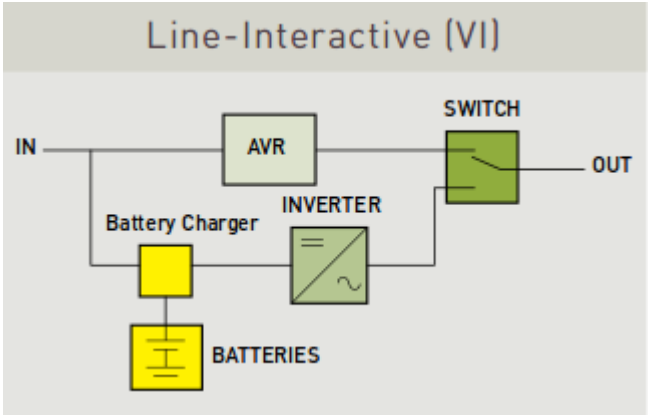
operation modes of online UPS

An on line UPS performs has a series of power blocks between the mains supply and the critical load. The first of these is a rectifier/charger which float charges the battery while the mains is present. It also supplies a stable DC voltage to the second block - an inverter which feeds the critical load. During a mains failure the floating battery seamlessly takes over the task of supplying DC to the inverter, to which it is permanently connected. Therefore, the event remains truly invisible to the critical load unless the battery becomes discharged. This seamless power continuity is a key attraction for critical applications that may not be capable of riding out a switching delay.

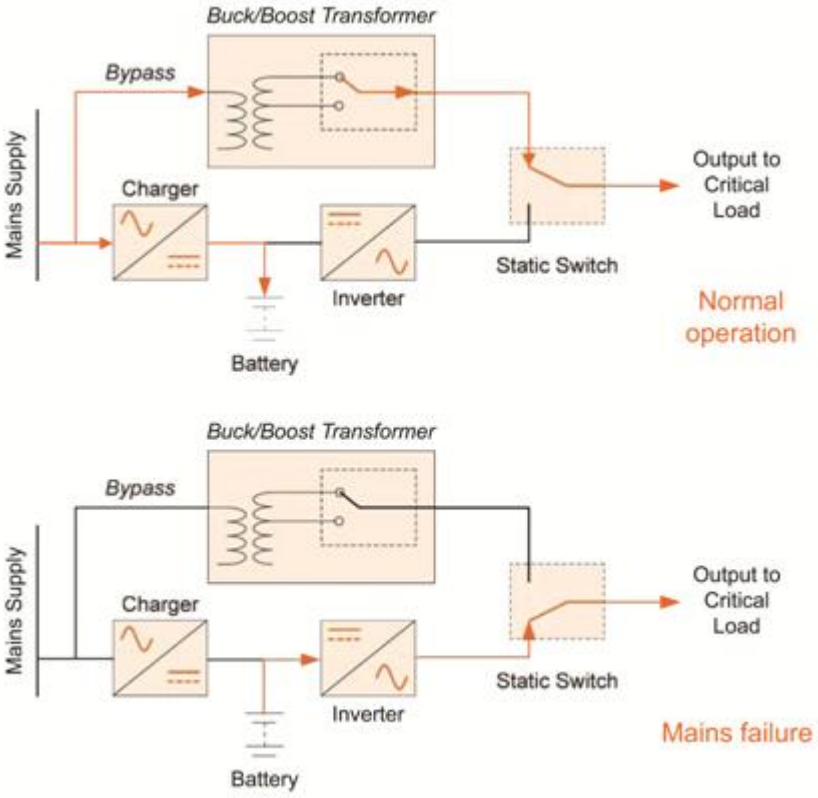
Another major advantage arises from the on line UPS's dual conversion topology. The input rectifier removes all the incoming mains spikes, transients and noise by converting it into DC. The inverter then feeds the load with a clean new AC waveform which is tightly regulated by the UPS. The rectifier also provides power factor correction, which reduces high frequency harmonics and the current drawn from the mains. The on line UPS acts as a true power firewall, protecting sensitive instrumentation and ICT equipment from mains-borne problems while improving the load presented to the mains.

Line Interactive UPS

Technically line-interactive UPS is a variant of offline UPS since it also does not use battery as a source when mains supply is present, but the mains supply passes through an Automatic Voltage Regulator, so the mains signal is not directly passed on the load, but a signal form corrected against disruptions is fed to the load.



Block diagram of line interactive UPS



operation modes of line interactive UPS

Some UPS manufacturers also offer line-interactive UPS systems. These use off line topology, but address the voltage transgression problems of off line systems mentioned earlier. They do so by providing voltage regulation in the raw mains line which supplies the load during normal operation. This voltage regulation, by reducing the number of 'out of limit' voltage events reaching the load, lowers the frequency of mains – battery transfers. Apart from subjecting the load to fewer power

interruptions, this design offers slightly better running cost efficiency and less battery ‘wear’ than off line systems.

Line-interactive systems are usually implemented with buck/boost transformers or ferroresonant transformers. Buck/boost transformers will maintain their load voltage over an input voltage range of +20% to -30%, however their switching involves tap changes which impose step voltage changes on the load. Line interactive implementations based on ferroresonant transformers can typically supply a load voltage within 3% of nominal over a raw supply range of +20% to -40%. They also provide power conditioning and protection from disturbances such as electrical line noise. However, their key advantage is that they store enough electrical energy to support most PC loads while the UPS inverter switches on, effectively creating an on line UPS solution.

With today’s rising energy prices, pressure to improve energy efficiency and data centre PUE has renewed interest in eco mode operation of on line UPSs. This mode allows users to route raw mains directly to their critical load during normal operation to save the energy that would otherwise be lost through the UPS’s inefficiencies. However, in exchange for this energy gain of perhaps 3%, the critical load is being exposed to mains disturbances and transfer events, as with an off line UPS. Some users will accept this trade-off, especially as they can choose to operate the UPS in on line rather than Eco mode during periods of increased utility grid disturbances.

Standardisation of topologies

Mis-leading terminologies

The standardisation bodies observed that the term "on-line", which taken literally means "on utility power", does not represent the true situation in this topology. The load is supplied by the inverter and not directly by the AC mains. The term was nonetheless fairly rapidly construed to mean a UPS supplying a load continuously via an inverter connected in series with the AC mains.

Again, the standardisation bodies observed that the term "off-line", which taken literally means "not on utility power", does not represent the true situation in this topology. The load is primarily supplied directly with AC-input power supplied from the utility and the inverter action is demanded only sporadically, in the event of a problem with the utility power.

The term "line interactive" is used for UPS implementing reversible inverters. However, the uncertainty created by the many versions of topologies exposed consumers to abusive tactics. For example, some UPS were termed "in-line" and in some cases, the term "on-line" was utilised in a very misleading manner.

New standards

An IEC (International Electrotechnical Commission) working group undertook to draft a standard on the types of UPS and the methods utilised to measure their performance. Cenelec (European standardisation committee) adopted the contents of the IEC standard.

These efforts produced **IEC 62040-3** standard and its European equivalent **ENV 50091-3** (which would be **EN 50091** once finalised), which clearly define the standardised types of UPS and the methods used to measure their performance.

Three standard types of UPS are defined by their topology and their operating principle. The three types of UPS have the following topologies:

1. **passive standby** (formerly called off-line)
2. **line-interactive**
3. **double conversion** (formerly called on-line).

The standards define the following terms for input power

primary power : power normally continuously available which is usually supplied by an electrical utility company but sometimes by the user's own generation plant

standby power : power intended to replace primary power in the event of primary power failure.

Practically speaking, a UPS has one or two inputs:

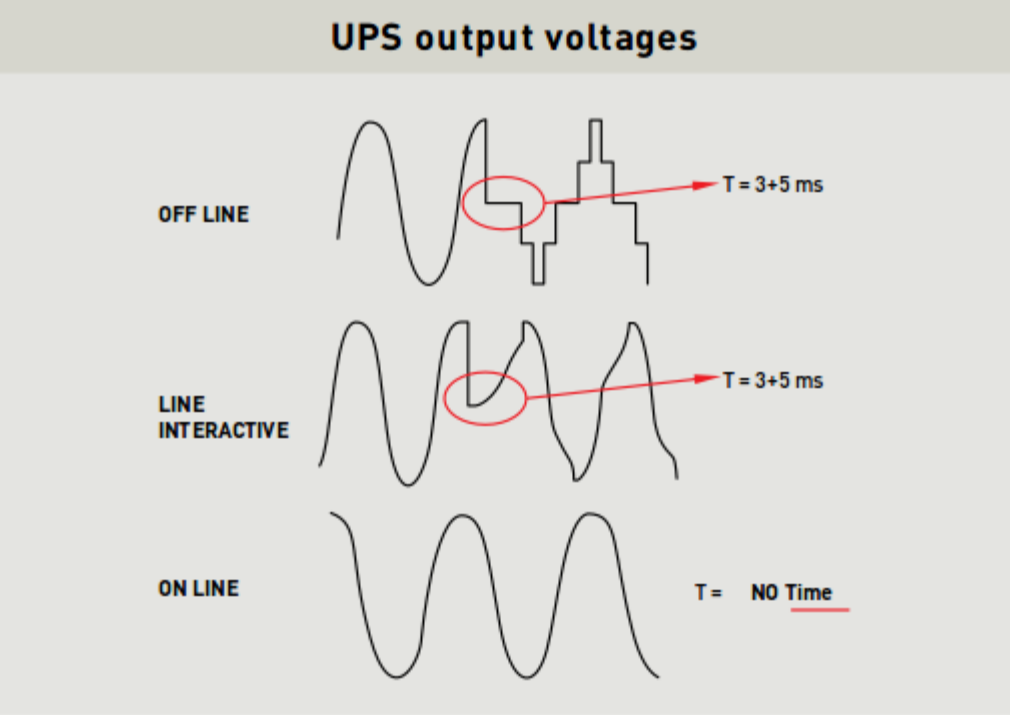
the **normal AC input** (sometimes called Mains 1) is supplied with primary power.

the **bypass AC input** (sometimes called Mains 2), when it exists, may also be supplied with primary power or, where possible, with back up power (for instance a separate cable from the same main

low-voltage switchboard).

Comparison of UPS Topologies

Transfer-time signal characteristics



As can be seen from the figure, both online and line-interactive UPS has a transient of ~8ms (common home UPS) due to the transfer switching.

On the other hand online has zero transient.

It is important to note here that most common appliances, even computers, have a ride through time of 10ms or more. Thus a transient response spanning less than 10ms does not generally cause a large problem, and can be in most cases neglected.

Voltage and Frequency dependence

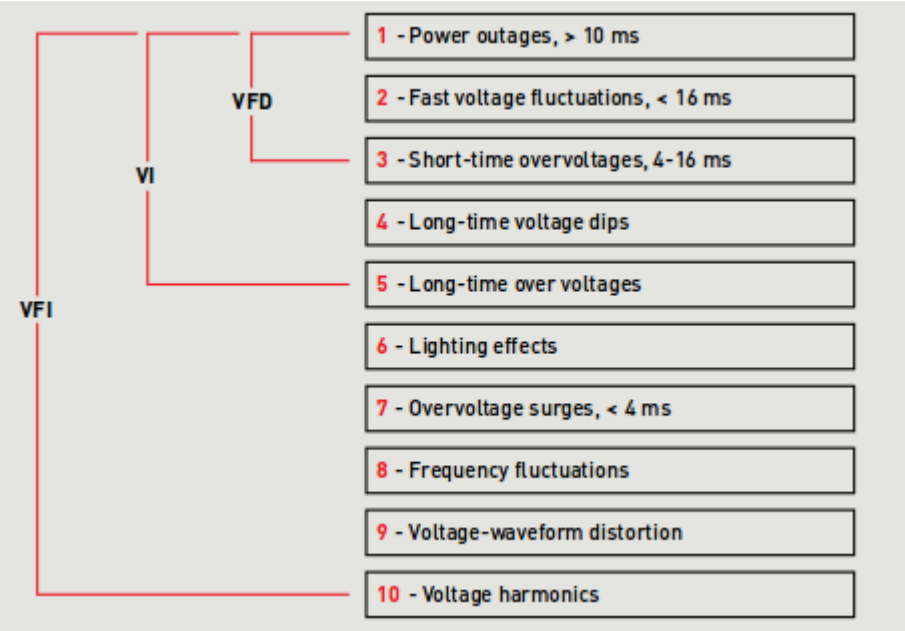
Online UPS is also known as **VFI** (Voltage and Frequency Independent) UPS because output waveform has no dependence on input waveform.

Offline UPS is also known as **VFD** (Voltage and Frequency Dependent) UPS because output waveform can get affected by disruptions in both Voltage as well as frequency.

Line-interactive UPS is known as **VI** (Voltage Independent) UPS because output waveform is shielded against Voltage fluctuations by the AVR but it still is not independent of input waveform's frequency.

Scope of operation

Following is a list of input waveform interruptions that an UPS can protect the load against



VFD - Offline UPS
VI - Line interactive UPS
VFI - Online UPS

Energy Efficiency

Another factor to consider is the additional energy needed to operate a double-conversion on-line UPS over time. A double-conversion on-line UPS continuously operates with efficiency between 85% and 92%, depending on the particular design, compared to 96% to 98% for a line-interactive UPS. A 90% efficient 1000W UPS for example, fully loaded, will consume 100W of power continuously. This translates into roughly $100 per year in additional utility costs (on average). In addition to the utility costs, this 100W of heat must be removed from the environment, incurring additional cooling costs that will vary depending on the particular cooling system's efficiency. This may not seem like a lot, but when considering the sum of all losses over many UPSs across an enterprise, or even the total lifetime energy consumption of a single UPS, it becomes a significant factor in the UPS total cost of ownership. In comparison, a similarly loaded line-interactive UPS will incur less than a third as much energy cost per load power.

Conclusion

Current Technologies

Overall, operators responsible for data centres and other critical or sensitive loads prefer the processed, 'no break' power that only on line UPSs can provide. However to make the most of the topology and its potential for protection, the UPSs should be installed as part of a power scheme that caters for all eventualities. For example, suppose the UPS rectifier and bypass line are fed from a common power source, which at some time suffers a power failure period exceeding the autonomy of the UPS battery. The UPS has no further options, so power to the critical load is lost. In some applications this may be acceptable, because the UPS battery autonomy provides enough time for the critical load to be shut down systematically and safely. In others, this will not be enough; any loss of service is unacceptable.

One solution is to use a configuration known as a split bypass system, in which the bypass line and UPS rectifier are connected to different mains supplies. This means that if the UPS's supply fails and its battery becomes exhausted, the UPS can switch to the still-healthy bypass line to deliver continued – although unprotected - power to the load.

Another widely used solution is to connect a standby generator as an alternative feed to the UPS. If the UPS detects a mains failure which is more than a transient problem, it can send a startup signal to the generator. This can then run up to speed and stabilise within the UPS battery autonomy, so the load enjoys continued clean power without interruption.

As well as protecting the load from power supply problems, the UPS must also manage problems caused by the load itself. The UPS's response to an overload may be to transfer it to bypass – but if the bypass supply is not available, this will simply deprive the load of power. A better alternative can be to allow the UPS to supply the overload for a set period; enough for automatic disconnection by a protection fuse or circuit breaker. During this period, the UPS itself can be protected by being operated in current-limited, reduced voltage mode, which is preferable to a total loss of power.

TOPOLOGY	Reliability	Total Cost of Ownership	Input	Output	Size / weight
Line-interactive	+ Fewer parts Lower operating temperature	+ Lower initial cost (fewer parts) Lower operating cost (less electricity)	– No PFC Extreme voltage distortion can require frequent battery usage	+ / – Output frequency varies within a configurable range	– Typically larger/heavier
Double-conversion On-line	– Many parts Higher operating temperature	– Higher initial cost (more parts) Higher operating cost (electricity and cooling)	+ Has PFC Accepts extreme voltage distortion without going to battery	+ Output fixed to a configurable frequency	+ Typically smaller/lighter, especially at higher power levels

In summary we can say that for critical applications or those involving sensitive equipment, on line UPS topology is the only real solution, due to its delivery of conditioned power and seamless transfer to battery. For less critical applications, off line topology may be suitable, and is attractive due to its reduced capital and operating costs. Line interactive systems offer an improvement on off line topology, with better power conditioning and regulation, and reduced battery wear. Ferroresonant transformer line interactive solutions also offer seamless load transfer. Pressure to reduce PUE has increased interest in Eco mode operation, but this shares most of the characteristics and disadvantages of off line topology. The best possible power quality and availability results come from on line UPS systems designed into an overall power protection strategy.

New Technologies and Future scope

Modular UPS

Modular UPS architecture (or topology) is a method designed to reduce cost and give UPS users flexibility in system configuration and use. Modular UPS systems consists of fixed control and power switching modules. The battery storage element is modularized. Typical systems are designed to fit into one rack. Larger UPS system designed for large IT installations span multiple racks and consists of dozens to hundreds of modules. Battery storage “modules” are configured from one to as many as ten modules in typical medium size UPS system. Each battery “module” gives a fixed power storage capacity.

Hybrid topology / double conversion on demand

These hybrid designs do not have official designations, although one name used by HP and Eaton is "double conversion on demand". This style of UPS is targeted towards high-efficiency applications while still maintaining the features and protection level offered by double conversion.

A hybrid (double conversion on demand) UPS operates as an off-line/standby UPS when power conditions are within a certain preset window. This allows the UPS to achieve very high efficiency ratings. When the power conditions fluctuate outside of the predefined windows, the UPS switches to online/double-conversion operation. In double-conversion mode the UPS can adjust for voltage variations without having to use battery power, can filter out line noise and control frequency.

Fast Rotary Tiny Wheel UPS (FRTW)

A newer implementation of flywheel UPS has seen faster wheels rotating at higher speeds. These cannot store large amounts of energy as MI of wheel is small, but they are used to provide power for very short spans of time (ranging in seconds) while power is switched.

A flywheel, in essence is always online so has no transient distortions of waveform.

References

1. A **Guide to Chose your UPS**; Legrand Power Systems Intl. Pvt. Ltd.
2. **UPS Topologies** - an Introduction & Comparison; http://upspower.co.uk
3. **UPS Topologies and Standards**; THE **MERLIN GERIN** KNOW-HOW; J.P. BEAUDET - J.N. FIORINA - O. PINON
4. **Technical Comparison of On-line vs. Line-interactive UPS designs**; APC; Jeffrey Samstad, Michael Hoff
5. Sato, E.K.; Kinoshita, M.; Yamamoto, Y.; Amboh, T., "**Redundant, High Density, High Efficiency Double Conversion Uninterruptible Power System**," *Industry Applications Society Annual Meeting, 2009. IAS 2009.* ***IEEE*** , vol., no., pp.1,8, 4-8 Oct. 2009
6. Linard, F. M A; Henn, G. A L; Cruz, C. M T; Bascope, R. P T; Oliveira, D.S., "**Double conversion uninterrupted power system with integration of the rectifier and the inverter**," *Power Electronics Conference, 2009. COBEP '09. Brazilian* ***IEEE***, vol., no., pp.551,557, Sept. 27 2009-Oct. 1 2009

Action-based trust computation algorithm for Online Social Network

Mohit Gambhir
Department of Computer Engg.
Jamia Millia Islamia,
New Delhi, India.
email:mohitgambhir@gmail.com

Dr. M. N Doja
Department of Computer Engg.
Jamia Millia Islamia,
New Delhi, India.

Dr. Moinuddin
Pro-VC,
Delhi Technological University,
Delhi, India

Abstract— Online Social Network (OSN) is a growing platform that enables people to get hold of news, communicate with family and old friends with whom they have lost contact, to promote a business, to invite friends to an event and to get people to collaborate. Researchers have been finding out ways to stop the negative activities over the social media by imposing the privacy settings in the leading OSNs. The privacy settings let the user to control who can access what information in his/her profile. None of these have given the entity of trust enough thought. In this research, An algorithm is proposed to evaluate and compute the Trust Factor for a user which measures the credibility of a user in the OSN world. The Trust factor considers the actions performed by the user in the OSN and the type of content being posted on the OSN, thereby; the user is responsible for his/her reputation in the OSN world. This will enable the users to decide which content is reliable and which user is credible.

Keywords- social media; Online Social Network (OSN); trust factor; credibility; trustworthiness

I. INTRODUCTION

Online Social Networks (OSNs) [1] [2] [3] are gathering of Internet users in such a webspace which provides them a sense of equality and belongingness. OSNs are the platform where users showcase their talent, share their views and opinions about a topic or news, share videos, photos and blog entries. Facebook, Twitter, Google+, Pinterest, MySpace are the frontrunners of OSNs in today's internet world. Evolution of OSNs over the last two decades has presented with many issues like quality of posted contents, privacy issues, cyber-bullying, trust issues etc. As OSNs mature, issues that centre on proper use of such networks are also growing and making headlines like Privacy [4], Access to Information, Potential for Misuse, Risk for Child Safety [5], Trolling [6], Online Bullying [7], Interpersonal Communication and Credibility of Content and Trustworthiness of User. Authors feel that the area of trust management for OSNs is of utmost importance, especially given the exponential growth of online communities. Trust, has been heavily studied by researchers in psychology, philosophy and sociology; research in these fields show that trust is a subjective view that varies greatly among people, situations and environment. However, this very subjectivity of trust has been overlooked in OSNs. At the moment, trust in OSNs is expressed by using simple access control methods that use a one-size-fits-all approach for all users. Trust cannot be expressed subjectively, nor can it be personalised. There is a strong need of a trust model that enables users to make annotations of trust freely and confidently. Much research has been carried out in the field of computer science in relation to trust management, various algorithms, systems and models have been produced, such as Pretty Good Privacy (PGP) [8], REFEREE [9], SULTAN [10], Friend Of A Friend (FOAF) [11], TRELLIS [12], Jøsang's trust model [13], Marsh's trust model [14] and many more.

Primarily, the work done till date in trust management is based on access control and don't compute the Trust Factor quantitatively. Access control doesn't necessarily give the exact idea about the credibility of a user in OSN. The already existing models nowhere considers the users' actions as major factor in computing Trust or credibility. Thereby, a model is needed that considers the type of message being posted and the actions performed by the user.

This paper emphasizes on finding the Credibility/Trust of a user in the OSNs, which is based on the actions performed by the user after logging into the OSN. The proposed trust model based on the content type and the actions performed by the user may lead to users being more careful in posting sensitive content on such a public platform as OSNs. The user is responsible for his universal reputation which is measured by the trust factor. This will lead to enabling a user to decide whether to interact with and post what kind of contents. Also, the users will be able to know the credibility of the content being posted by another user before taking action based on the content.

Organization of the paper is as follows: section 2 discusses the term TRUST, importance of trust management in OSN, current methodology used in trust management, current issues and advancement associated with it. A Novel algorithm is proposed to compute the trust of a user in OSN in section 3. Section 4 shows the snapshots of implementation of proposed algorithm and result analysis. Section 5 gives idea of contribution of proposed work. Last section concludes the paper.

II. WHAT IS TRUST?

The term "Trust" stands for a diversity of concepts depending on the person you ask. To some, trust is predictability, where evidence of one's reputation suggests a most-likely outcome; to others, trust is dependability, where one truly believes in another and accepts not understanding some things; yet, to many, trust is letting others make

978-1-4799-4910-6/14 $31.00 © 2014 IEEE
DOI 10.1109/ACCT.2014.89

decisions for you and knowing that they would act in your best interest.

Dasgupta [15] defines trust as "the expectation of one person about the actions of others that affects the first person's choice, when an action must be taken before the actions of others are known".

Trust is the root of almost any personal or economic interaction. Keser [16] states "trust as the expectation of other person's goodwill and benign intent, implying that in certain situations those persons will place the interests of others before their own".

A. Importance of Trust Management in OSNs

In OSN, people may communicate with their friends whom they know personally and other members of the network who are the friends of their friends and may be friends of their friend's network. They share their experiences and opinions within the social network about an item. The user faces the problem of evaluating trustworthiness of a user in the OSNs. Opinions, reputations and recommendations and actions that a user performs in the OSNs influence his trustworthiness. Thus, trust is a critical issue as it highly impacts person's decision to go on-line, what to do on-line and interact with which persons.

Trust information can help a user make decisions, sort and filter information, receive recommendations, and develop a context within a community with respect to whom to trust and why. Trust needs to be facilitated into online social networking websites, in order to provide users with the necessary tools and much desired freedom to express their subjective views of trust just like in the offline world.

In summary, trust cannot be defined by a single consensus, there is a wide and varied range of synonyms for trust, and the answer to "what is trust" cannot be easily provided.

B. Advancements in Trust Management

The issue of trust has been gaining an increasing amount of attention in a number of research communities including online service provision. There are many different views of how to measure and use trust. As trust is a social phenomenon, the model of trust for the artificial world like Internet should be based on how trust works between people in society.

Current work in the area of trust management ("web of trust") can be classified into two classes. Approaches of the first class infer trustworthiness by propagating trustworthiness from a participant to another. Approaches of the second class infer trustworthiness by machine learning from prior interactions of a user and are called predictive. In "web of trust", each user expresses the degree of its trustworthiness in others. By doing so, a user helps the other in deciding which users are to trust or to distrust, without prior interaction. This falls in the category of predictive and a user is not responsible for his trustworthiness.

Computing trust requires some parameters such as information about the reputation of a given user. Reputation means the level of trust assigned by the online community (or part of the community) to the user. This can be expressed according to the rating process used in several sites such as eBay, or a statement of trust.

Stephen Marsh [14] in his PhD thesis describes a model which is based on social and psychological factors. He defines trust in three categories; namely the basic trust, general trust and situational trust. These trust values are used to help a user to decide if it is worth it or not to interact with another user. But, there is no mention of the actions performed by a user.

Abdul-Rahman et al. [17] have proposed that the trust concept can be divided into direct and recommended trust. Recommended trust can be derived from word-of-mouth recommendations, which they consider as reputation. Schillo et al [18] have proposed a trust model for scenarios where interaction result is Boolean, either good or bad, between two users. Pujol [7] has proposed a method for calculating the reputation of a given user in a social network by making use of PageRank™ algorithm. O' Donovan et al [19] have described trust as the reliability of a partner profile to deliver accurate recommendations in the past. They described two models of trust which they called profile-level trust and item-level trust.

An interesting project related to secure OSN is Safebook [20] that leverages the trust relationships that are part of the social network application itself. Safebook is a decentralized privacy preserving OSN that is governed by the aim of avoiding centralized control over the user data. The decentralization is provided by the use of peer-to-peer technology.

L.H. Vu et al [21] describe a new application of threshold-based secret sharing in OSN. They select the most reliable users based on an effective trust measure. Relationships between the involved users are used to estimate the trustworthiness of a user.

Some algorithms include Advogato, Appleseed, Sunny, and Moleseed. Advogato's Trust Metric [22] evaluates a set of peer certificates, resulting in a set of accounts accepted. These certificates are represented as a graph, with each account as a node, and each certificate as a directed edge. The goal of the trust metric is to accept as many valid accounts as possible, while also reducing the impact of attackers. Advogato performs certification to three different levels: Apprentice, Journeyer, and Master. This is actually done by running the basic trust metric three times, using the "level" value in the certificate as a threshold. Thus, certification of Apprentices is computed using all certificates, while Master is computed using Master certificates only.

C. Current Methodology Used in Trust Management

Current Trust Mechanisms used in OSNs are limited to simple privacy settings where users can control who can view their profile and interact with them or can include them in some community. In Facebook, a user can control the sections that can be viewed in three different levels of association, viz, friend, friend of a friend, outsider who has no ties with the user. They can also select who can send them a friend request.

In OSN, different friendship intensities have different levels of default trust, which should be reflected in the privacy settings. The typical user does not change their privacy settings that often. Therefore, the default setting should be appropriate in order to actually preserve privacy. Since users normally don't do it themselves, it would be nice to have an automated way of finding out about the intensity of the friendship and derive the privacy settings from the intensity value. Users do not only change the privacy settings often enough, but also the OSNs have not provided a distinction between the types of friendships, as every relation is a friend, regardless of how intense the relation is.

OSN users are unable to control these privacy vulnerabilities because: 1) Not enough privacy control settings are provided by OSNs, 2) The users do not know they have these settings, 3) The privacy controls are difficult to use, 4) Friendship is the only type of relationship provided by most OSNs to establish a connection between individuals, and 5) Individuals are unable to identify potential privacy leakage connections because their social networks consist of unreliable friends.

D. Current Issues in Trust Management

As discussed in previous section, current methodology being used in trust management in OSNs basically considers access control and privacy mechanisms. This doesn't address the issue of trust management in OSNs quite satisfactorily. Some issues with the current methodology are as follows:

- *One-size-fits-all Approach:* For majority of the OSNs, access control seems to be the only way through which trust can be expressed and maintained. If a user limits access to his profile, that means he/she doesn't trust you. Many friends of a single user in Facebook are not necessarily friends; they are just connected to each other because they don't dislike each other [1]. In certain situations we want private information to be known only by a small group of people and not by random strangers. The other way around, we are willing to reveal personal information to anonymous strangers, but not to those who know us better. The inflexible, one-size-fits-all approach cannot provide users the freedom to express their various levels of trust in a given network, therefore, fail to provide a tailored trust model for users in OSNs.
- *Single-faceted approach:* Currently, trust in OSNs is modeled as granting various levels of access controls to specified groups of users, there is no other option given. This single-faceted approach takes a simplified view on trust and fails to provide a variety of definitions for trust as we have found in the state of the art studies.

In any of the approach, the trustworthiness is mere an access control mechanism which covers all the users in the OSNs. And every user has different trustworthiness in different OSN but there is not universal trustworthiness of a user who is identified through Open ID.

OpenID is decentralized **S**ingle **S**ign **O**n (SSO) system for the web. OpenID is like a universal identifier for a user in OSNs platforms over the internet [23]. Like, universal ID to identify the user, it becomes less cumbersome to compute the universal trustworthiness of a particular user, whose actions are responsible for the trustworthiness to increase or dip, depending upon what actions he/she performs.

III. PROPOSED WORK

All the early trust models compute Trust factor or trustworthiness either by probability or the prediction of Trust factors predicted. In this paper an algorithm is proposed to calculate Trust factor on the basis of the actions performed by the user while being logged in on a online social networking site. Actions can be: liking a post, commenting on a post, sharing a post, tagging on an image, posting a text as a status message, posting an image, posting a link, posting a video. Other parameters are also taken into consideration while computing the Trust Factor. There values have been assumed for the simulating the algorithm in different test case scenarios as follows:

- Weight for Action (Wa): Every action on the OSN site has a weightage. The weight depends upon the time being taken to accomplish an action. Share and Comment have higher weight than like, dislike, tag. This is because sharing and commenting on a post needs more time and effort as compared to liking or tagging.

Share= .008, like= .006, comment= .007, dislike = .006, tagging =.005, Post= .008

- Weight for Post (Wp): A post may be a video, photos, links or message. In many OSNs, Photo is given more weightage as compared to a video or a link. Also, a text message and photo get more reach than any link or video on the OSN.

Photo=.003, Video=.002, Link=.001, Message=.003

- Weight for Category (Wc): The category of the content is also very important factor in computing the Trust Factor. Sensitive content, like a pornographic video or an abusive text message or an image related to violence will decrease the Trust Factor of a user. Whereas non-sensitive content, like, a beautiful nature image, inspirational quote or a video tutorial about technology will increase the Trust Factor.

Sensitive category= -.009, Non-sensitive category= .001

- Post Credibility (Pc): When a message is being posted by the user, Trust Factor is evaluated according to the messages they have posted on the OSN sites. Messages posted by the user are checked and categorized using the proposed **Message evaluation algorithm**. If the message is okay according to user, Message is posted and trust factor increases otherwise the message is gone through a manual evaluation phase and the trust factor is decreased.

The user logs into the OSN using username – password pair. The user performs some actions; the weight of the action is calculated as Wa. If the action is post, the

Matching_Process algorithm is called which evaluates the category of the message. If the message is sensitive, then Post Credibility decreases, otherwise, it increases. Fig. 1 describes the data flow for the proposed Trust Computation Algorithm.

Here, P_c determines whether the message which is to be posted is of right commitment or not. In other words, Post Credibility is the measure of the kind of message which is to be posted. It is used in the calculation of Trust factor only when the action performed is Post (If (Type(Wa)==POST)). It is incremented by a factor of .001 if the message being posted is categorized in a non-sensitive category (e.g., academics, music, etc.); and gets decremented by a factor of .009 if the message is categorized in a sensitive category (alcohol, violence, etc.)

E_s is Edge Score. It defines the variation in Trust Factor. Whether a message has been posted or any other action has been performed by the user, Edge Score is calculated using Weights specified. Fig. 2 explains how the Trust Factor is calculated. Fig. 3 is used to evaluate the category of the message being posted onto the social networking site. First, all the keywords in the message are found out. These keywords are then passed through some Information Retrieval Techniques like, Lemmatization, Stemming, Stop Word Removal to get the appropriate keywords to be processed.

After that, the keywords are matched with their synonyms in the synonym database. All the synonyms are mapped with category database, which find out whether the keywords belong to sensitive category, or not. If the message belongs to the non-sensitive category, the flag is assigned a zero and the message gets posted. If the message belongs to the sensitive category the flag is assigned a one and the message goes for manual evaluation. Fig.4 describes the matching process.

A. Example of Proposed Work

There are three users: User A, User B, User C. Table 1 describes the actions being performed by the three users. According to the table, User A is performing both actions on both sensitive and non-sensitive contents, which classifies as the average test case. User B is performing actions on only non-sensitive content; thus, the case is the best case. User C is performing actions on only sensitive content; the case here becomes the worst case.

Before computing the Trust Factor, some seed values of T_f and P_c have been assumed.

The seed value for T_f:

$A(T_f) = B(T_f) = C(T_f) = 2.000$

Seed value for P_c:

$A(P_c) = B(P_c) = C(P_c) = 0.001$

It can be seen from the table that whenever the user posts some sensitive information, the T_f should decrease. Also, T_f should decrease when the user interacts with the sensitive content, viz. like, tag, share, etc.

Similarly, when the user interacts with the non-sensitive content, T_f should increase. Another point worth mentioning is that the Trust Factor is computed after every action. This is because the Trust Factor is dependent on every action that the user performs in the OSN environment.

Also, the seed values are assumed to be in decimals up to three points. The reason behind this is when a user logs into an OSN; he/she performs lots of actions in quick successions. If the seed value is assumed to be integer, the range of the Trust Factor will get very large which will be very difficult to analyze.

IV. IMPLEMENTATION AND RESULT ANALYSIS

The Proposed Trust computation algorithm is implemented using PHP (Hypertext Preprocessor), which is the widely used platform for developing Online Social Networks and web applications.

Login to Social Circle using the username-password after logging in, a page similar to a newsfeed in an OSN gets opened where the user performs the action. In the newsfeed page, the user has options of performing as many actions as he/she wants as long as he/she is logged in. The actions that the user can perform are: posting a message, posting a photo, posting a video, posting a link, liking a post, disliking a post, sharing a post, tagging a post, commenting on a post. A user posts a message in the text area. Also, there is an option to select the category the message belongs to. When the message is written in the text area, the matching algorithm comes into action to calculate the category of the message. If the category of the message selected matches with the category calculated, Trust Factor will increase otherwise decreases as shown in Fig. 5 and Fig. 6

The user has an option of posting a photo. While posting the photo, the user is asked the whether the photo being posted is of sensitive category or not. If the user selects that the photo being posted is sensitive, the Trust Factor decreases, otherwise it increases as shown in Fig. 7 and Fig.8. The user has an option of posting a video. While posting the video, the user is asked the whether the video being posted is of sensitive category or not. If the user selects that the video being posted is sensitive, the Trust Factor decreases, otherwise it increases as shown in Fig. 9 and 10. In this case, the video is uploaded from the resident machine. No option of sharing a video URL is given.

The user can share a link. While posting the URL, the user is asked the whether the URL being posted is of sensitive category or not. If the user selects it to be sensitive, the Trust Factor decreases, otherwise it increases. A user can like a photo posted by other users in the OSN. The photo can be either a non-sensitive photo or a sensitive photo. Depending upon the type of photo being liked, the Trust Factor either increases or decreases. A user can tag a photo either posted by self or by other users in the OSN. The photo can be either a sensitive photo or a non-sensitive photo.

Depending upon the type of photo being tagged, the Trust Factor either increases or decreases.

A user can like a video posted by other users in the OSN. The video can belong to either non-sensitive or a sensitive category. Depending upon the type of video being liked, the Trust Factor either increases or decreases

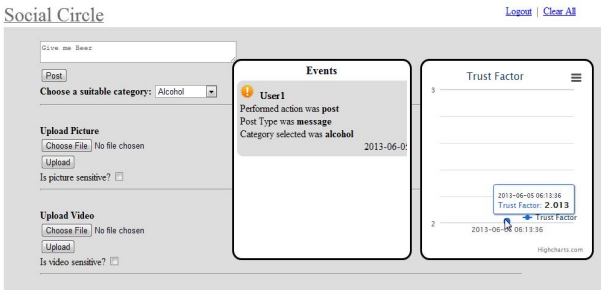


Fig.5: Posting a message

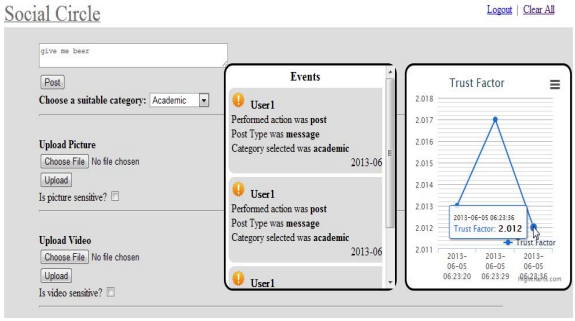


Fig.6: Posting a message

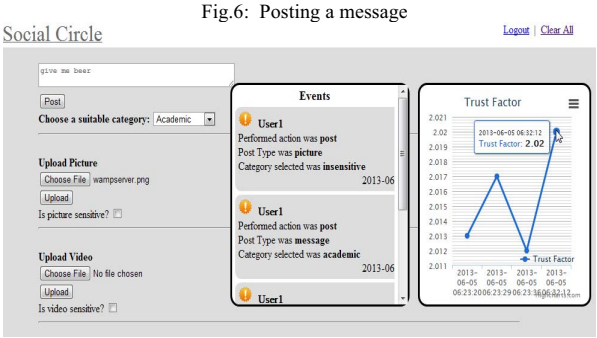


Fig.7: Posting a non-sensitive photo

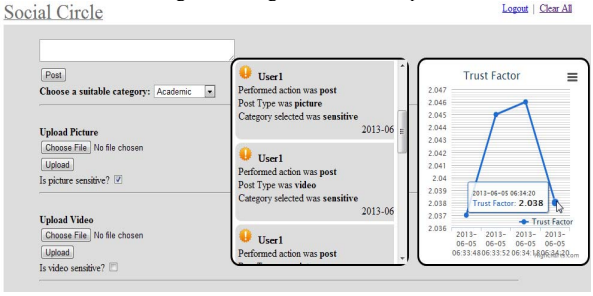


Fig.8: Posting a sensitive photo

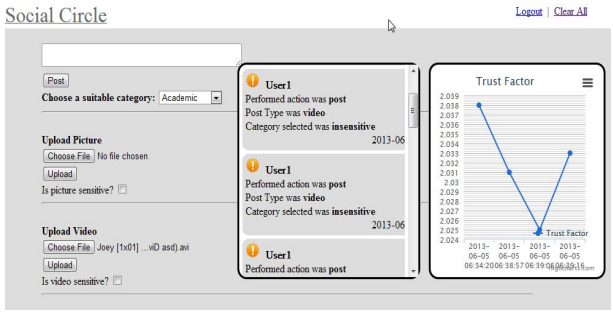


Fig.9: Posting a non-sensitive video

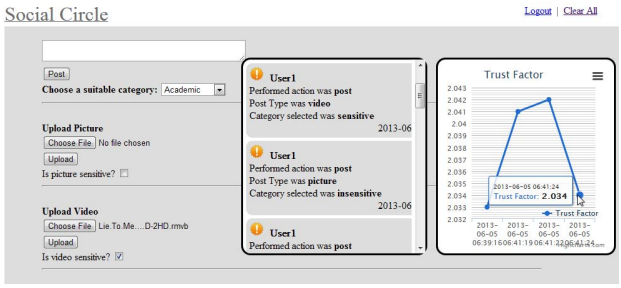


Fig.10: Posting a sensitive video

As per the example in the previous section, the following trust factor can be found for the three users, User 1, User 2 and User 3. Each user performs four actions viz. 1) Uploading a video, 2) Tagging a photo, 3) Posting a message, and 4) Liking a photo. User 1 interacts with both sensitive and non-sensitive category which is the average case scenario. User 2 interacts with only non-sensitive category, which is the best case scenario. User 3 interacts with only sensitive category, which is the worst case scenario. The variation in Trust Factor after every action has been presented in the graph of Fig. 25.

TABLE I TRUST FACTOR OF EVERY USER AFTER ACTION PERFORMED

	User 1 (T_f)	User 2 (T_f)	User 3 (T_f)
Action 1	**2.002**	**2.020**	**2.002**
Action 2	**2.011**	**2.029**	**2.001**
Action 3	**2.005**	**2.051**	**1.995**
Action 4	**2.014**	**2.060**	**1.994**

The Action-based Trust Computation Algorithm accurately calculates the Trust Factor of a user based on the action he/she performs in the OSN. This trust factor is the measure of the credibility of the user and is the real life equivalent of reputation over the OSN universe. Also, this Trust Factor is of universal nature, depending solely on the action performed and the type of content.

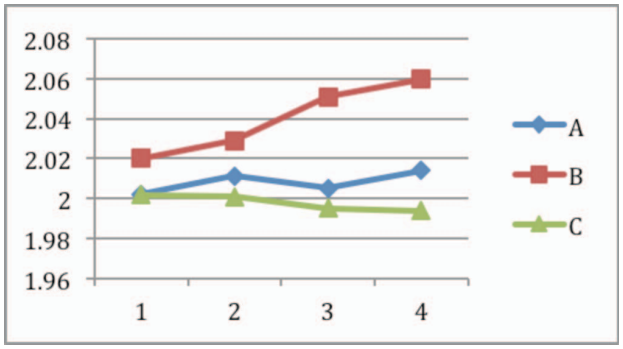


Fig.25: Graph Representation of Trust Factors of the three users

V. Contribution Of The Proposed Work

Proposing the new trust model based on the content type and the actions performed by the user may lead to users being more careful in posting sensitive content on such a public platform as OSNs. The standard and the credibility of content type to be posted on the OSN shall be maintained. Since, the reputation of the user is in one's own hands, the actions now performed and interactions with sensitive content shall see a downfall.

Cyber bullying, anxiety, depression and other adverse affects of OSN in teenagers shall be easier to curb. It shall become easier to watch that the new generation doesn't indulge in any malicious activities. For instance, if a user's Trust Factor is seeing a constant dip over successive days; that means the user's account is involved in malicious activities.

VI. Conclusion

The Trust Factor for the user is the measure of credibility of the user in OSN. This is the real world equivalent of reputation. The contribution of this paper is to initiate in development of a practical model of trust computation based on the action and the type of content being posted by the user. The trust factor computation will enable the user to make a good decision on whether to interact with a particular user or not and the content posted by that user is reliable or not. A standard on what kind of content is posted on the OSNs can be maintained. This shall make the OSN universe cleaner from malicious users and other negative elements in the OSN.

References

[1] Bo Fu, *"Trust Management in Online Social Networks"*, M.Sc. Dissertation, Department of Computer Science, University of Dublin, Trinity College, pp. 5-12, 2007

[2] http://www.webmasterview.com/2011/08/social-networking-history/

[3] Nicole B Ellison, "*Social network sites: Definition, history, and scholarship* "Journal of Computer-Mediated Communication, Vol. 13(1), pp. 210-230, 2007.

[4] Laura Garton, Caroline Haythornthwaite, and Barry Wellman. *"Studying Online Social Networks."* Journal of Computer-Mediated Communication, Vol. 3.1, pp. 0-0, 2006.

[5] Andreas M. Kaplan, and Michael Haenlein. *"Users of the world, unite! The challenges and opportunities of Social Media,"* Business horizons, Vol. 53(1), pp. 59-68, 2010.

[6] Susan Herring, Kirk Job-Sluder, Rebecca Scheckler, and Sasha Barab. *"Searching for safety online: Managing" trolling" in a feminist forum."* The Information Society, Vol 18(5), pp. 371-384, 2002.

[7] J. M. Pujol, R. Sanguesa, J. Delgado. *"Extracting reputation in multi-agent system by means of social network topology"*, in proceedings of the First International Joint Conference on Autonomous Agents and Multi-Agent Systems, Italy, pp. 467-474, 2002.

[8] P. R. Zimmerman , "The Official PGP Users Guide", MIT Press, Cambridge, MA, USA, 1995.

[9] Y. Chu, J. Feigenbaum, B. LaMacchia, P. Resnick and Ma. Strauss, "*REFEREE: Trust Management for Web Applications.*", The World Wide Web Journal, Vol. 2(3), pp. 127-139, 1997.

[10] T.Grandison, M. Sloman, "*SULTAN - A Language for Trust Specification and Analysis*", in proceedings of the 8th Annual Workshop HP Open View University Association (HP-OVUA), Berlin, Germany, June 24-27, 2001. http://link.springer.com/chapter/10.1007/3-540-44875-6_7

[11] E. Dumbill, and X. M. L. Watch. "*Finding friends with XML and RDF*," June 2002. IBM's XML Watch, June 2002

[12] Yolanda Gil, and Varun Ratnakar. *"Trusting Information Sources One Citizen at a Time."* In proceedings of the First International Semantic Web Conference—ISWC 2002, Springer Berlin Heidelberg, Sardinia, Italy, pp. 162-176, 2002.

[13] A. Jøsang, "*The Right Type of Trust for Distributed Systems*", in proceedings of The Workshop on New Security Paradigms. Lake Arrowhead, California, United States, ACM Press, pp. 119-131, 1996

[14] S. Marsh, "*Formalising Trust as a Computational Concept*", Ph.D. thesis, Department of Mathematics and Computer Science, University of Stirling, 1994.

[15] P. R. Z P. Dasgupta, Trust as a Commodity. In *Trust: Making and Breaking Cooperative Relations*, D. Gambetta (ed.). Oxford, Basil Blackwell, 1990.

[16] C. Keser, "*Experimental games for the design of reputation management systems*," IBM Systems Journal, vol.42, no.3, pp.498-506, 2003.

[17] Abdul-Rahman and S. Hailes, "*Supporting Trust in Virtual Communities*", in proceedings of the Hawaii International Conference on System Sciences, USA, 2004

[18] M. Schillo, P. Funk, and M. Rovatsos, *"Using Trust for Detecting Deceitful Agents in Aritficial Societies"*. Applied Artificial Intelligence, 2000.

[19] J. O'Donovan and B. Smyth. *"Trust in Recommender Systems"*. IUI'05, USA, 2005

[20] L. A. Cutillo, R. Molva, and T. Strufe, *"Privacy preserving social networking through decentralization"* In Wireless On Demand Network Systems and Services, 2009.

[21] L. H. Vu, K. Aberer, S. Buchegger and A. Datta *"Enabling Secure Secret Sharing in Distributed Online Social Networks,"* in proceedings of the 2009 Annual Computer Security Applications Conference ACSAC '09, IEEE Computer Society, pp. 419-428, Washington D.C., 2009.

[22] http://www.advogato.org/trust-metric.html

[23] http://en.wikipedia.org/wiki/Openid

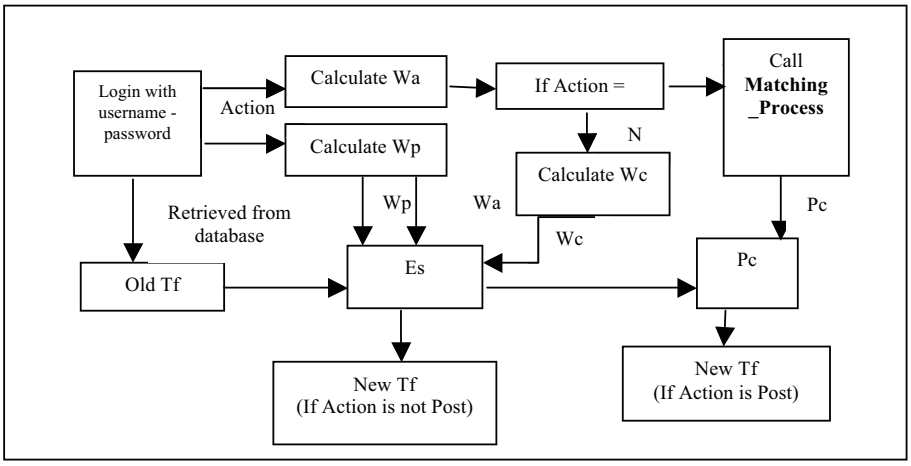


Fig.1 Flow of Data in the Proposed Framework

Algorithm CAL_TRUST_FACTOR (username, password, action, post)
Input: username, password, action, post
Output: Trust Factor of user.

```
Login from openid.
While (true)
{
    Calculate Weight for Action (Wa).
    Calculate Weight for post (Wp).
    If (Type(Wa)==POST) then
    {
      Wc=0
      Call Matching_Process (Input, CAT_SEL)
       If (Flag==0)
          Calculate Pc = old (Pc)+.009 ///Every right commitment
       Else
          Pc = old (Pc)-.009    //Every wrong commitment
     }
     Else
       Calculate Weight for category (Wc)
        Calculate Es = Wp + Wc +Wa
        If (Type(Wa)==POST) then
           Calculate  Trust factor (Tf )= old (Tf) + Pc + Es
        Else
           Calculate  Trust factor (Tf )= old (Tf) + Es
}
```

Fig. 2: Algorithm of Computation of Trust Factor

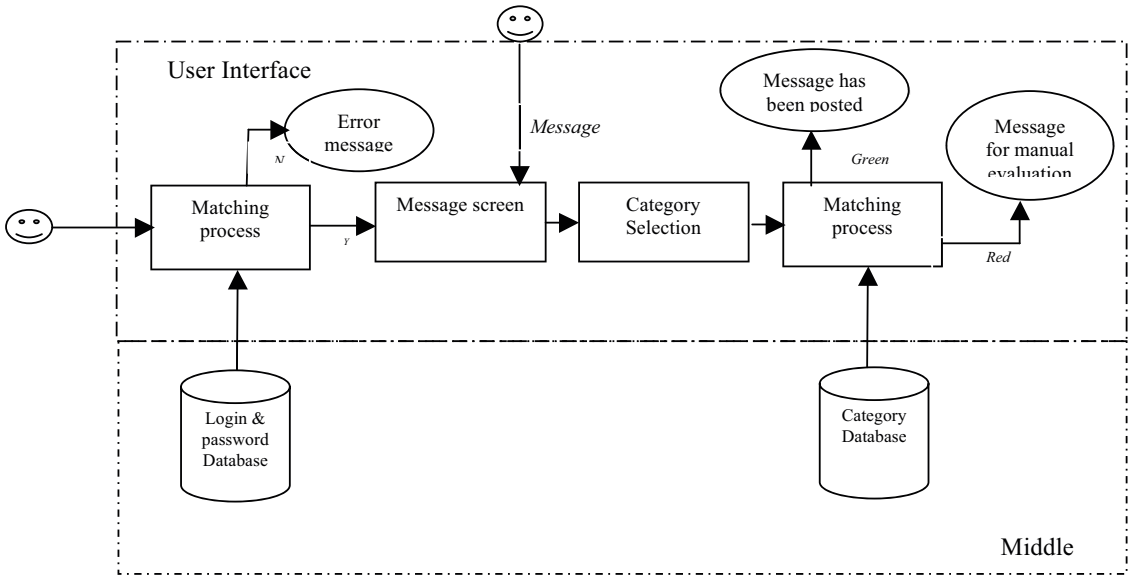


Fig. 3 Flow of Data in the Message Evaluation Algorithm

Algorithm MATCHING_PROCESS (INPUT, CAT_SEL)
INPUT: Message to be posted
CAT_SEL: Category selected by user
For each message to be posted ( )
{
Find out keywords in the message.
For each keyword ( )
Find out all possible synonyms (SYN[ ]).
For each synonym ()
{
If (SYN==CAT_DATABASE)
{
If (CAT_DATABASE==CAT_SEL)
{
Message has been Posted.
Flag=0;
}
Else
{
Message for Manual Evaluation
Flag=1;
}
}
}

Fig. 4: Algorithm of Message Evaluation Algorithm

International Journal of Soft Computing and Engineering (IJSCE)
ISSN: 2231-2307, Volume-4, Issue-ICCIN-2K14, March 2014

An Analysis of Telecommunication Fraud using Outlier Detection Model based on Similar Coefficient Sum

Daya Gupta, Payal Pahwa, Rajiv Arora

Abstract— In modern day, new technologies have a great impact on people's life. This has resulted in the increase of frauds in today's technological environment. Service providing companies such as telecommunication companies, banking companies etc. suffer from financial losses due to the customers' fraudulent behaviors. Telecommunication fraud not only financially effects the company but also effects the individual customers as well. So detection of fraud is very important in today's life. In this paper, we have identified the customer's fraudulent behaviour using outlier detection model based on similar coefficient sum. In this approach, frauds are detected by computing coefficient sum of every two objects. This method has also been implemented in Mat Lab R2010a and the obtained results show the feasibility and validity of the method.

Keywords—Data Mining; Fraud Detection; Similar Coefficient Sum; Outlier.

I. INTRODUCTION

Fraud can be referred to as the particular actions of employment of any services without being charged intention as in [1]. A deception made intentionally for selfish gains or to damage other individuals is also called a fraud as in [2]. This definition of fraud may vary according the legal jurisdiction it lies in. It is a violation of the civil law and is a criminal offence. Common purposes of fraud include the defrauding people of their valuables and money but some fraud to gain prestige and respect rather than any monetary gain like in some science fields.

The scale in which frauds are happening have risen over the years to about 5% of the annual revenue in a typical organization averaging the median loss to $160,000 [3]. The frauds done by the owners and executives are most costly than the employee frauds by around 9 times. These frauds usually occur in the following industries: banking, manufacturing, government and telecommunications.

One of the major impact of frauds is on the telecommunications industry. It suffers losses annually amounting to billion of US dollars because of the fraud in the networks as in [4] [5] [6] [7] [8] [9]. Not only financially, a fraud result in loss of services, distress and reduces the confidence in customers [9]. Frauds have also considerably effected the revenues of the network operators by making losses of about 2 to 6 percent of its total revenue. It is also pointed out by [10] that it is difficult to provide the exact estimates because some frauds can never be detected and the network operators don't wish to release the figures on fraud losses publically.

Manuscript received May 2014

Daya Gupta, Computer Engineering Department Delhi Technological University, New Delhi, India

Payal Pahwa, Computer Engineering Department, BPIT, Guru Gobind Singh Indraprastha University New Delhi, India

Rajiv Arora, Research Scholar, Computer Engineering Department, Delhi Technological University New Delhi, India

The increasing competition in the telecommunication industry and the rise in the losses [6] has resulted in the fraud has escalated from being a problem that the network operators could bear to one that is dominates trade and general press majorly as in [7].

Hence, our concern is to deal with the frauds in telecommunication industry.

Various researchers have proposed various techniques like classification techniques based on user profiling [11], rule based methods [12] [13], using expert knowledge based on some threshold [14] etc. for detection of frauds. Outlier mining is a well known technique used for pattern recognition in data mining. A pattern which doesn't behave normally is defined as an outlier as in [15]. Defining a region representing normal behavior and declaring any observation in the data that is not belonging in the region as an outlier is a straight forward approach to detect outliers. Outlier mining has the following advantages over the mining methods based on statistics: First, this method can effectively find outliers**,** unknown to the distribution of data set. Second it overcomes the shortcoming that outlier mining doesn't require prior knowledge of the distribution of laws for constructing of probabilistic model based.

This paper investigates the technique of outlier mining for finding the frauds in telecommunication. Since outlier mining discards the irrelevant transactions and hence efficiently detect fraudulent behavior. We show the results on a data set of telecommunication. Thereby outlier mining increases the success rate by 90%.

The structure of paper is as follows:

A brief introduction of literature review is given in section II. Similar Coefficient Sum approach is discussed in Section III. The implementation details and results are discussed in section IV. Section V is the concluding section.

II. RELATED WORK

Although the research on fraud and its detection has been carried out for many years and telecommunication companies have spent relatively more money on this than the research community, still their efforts do not reach beyond the limit of the companies and have not been made accessible by the public research community.

The various faces of digital transmission of wireless communication have been discussed in [17].

Tumbling is the vulnerability of wireless communication to a wireless fraud. [17] Keeping in mind that the fraud could allow the fraudsters to access and steal telephone services and digital technology. This work has also mentioned about clone frauds and attempts to stop cloners.

Increase in the incidents of phone frauds with corporation and telecommunication companies are reported in [11]. It has talked about the alliance formed to stop phone frauds,

Published By:
Blue Eyes Intelligence Engineering
& Sciences Publication Pvt. Ltd.

preventive measures being taken by the customers and telephone companies to fight fraud and the foil the cloning of the cell phone.

The use of knowledge-based approach to examine the call records obtained from cellular switches in real time is considered in [14]. They affirm the use of uniform thresholds to all of a carrier's subscribers effectively forces comparison against an imaginary subscriber. However, they decided to model every subscriber individually and let the subscribers' profile to be adaptive in time. They also use knowledge about the usual fundamental behavior, for example, doubtful destination numbers. The analysis component present in them finds out if the alarm, taken together, is good enough to be reviewed by a human analyst. Hence the system is credited with the ability to detect frauds swiftly and helps to analysts to concentrate on the most dangerous and most likely to be frauds. The authors have reported their first attempt to detect frauds in a database of stimulated calls as in [18]. A supervised feed-forward neural network is used to detect any anomalous use. There are six unique user types simulated stochastically according to the users' calling patterns. Two set of features are derived from this data, the first one shows the recent use and the other one shows the long term behavior. They both are accumulated statistics of call data over time windows of unique lengths. The input to the neural network is this data. Classifier's performance is estimated to be 92.5% on the test data, which has limited value in view of the simulated data and a need to give the class specific estimates on accuracy arises. This has been reported in [19]

Rule-based methods of detecting frauds are presented in [12] [13]. Adaptive rule sets are used by the authors to uncover the indicators of fraudulent behavior from a database of cellular calls. Profiles are made using these indicators, which are then used as the features to a system combining the evidence from multiple profilers to generate alarms. Rule selection is also used to choose a set of rules that cover larger sets of fraudulent cases. These rules further constitute monitors, which are in turn pruned by a feature selection methodology. Output of these monitors is weighted together by a learning, linear threshold unit. The results are then examined with a cost model in which misclassification cost is proportional to the time.

User profiling and classification techniques for the detection of frauds in mobile communication networks are presented in [20]. The identification of relevant user groups on the basis of call data is reported by the author: each user assigned to the relevant group. Neural networks and the probabilistic models are used by him to learn the usage patterns from the call data. There is an attempt by the author to promote the dynamic modeling of the behavioral pattern for detecting frauds.

All the research papers as identified above do not use the technique of outlier mining on the available data. As already discussed if this technique is used we can easily found the outliers without prior knowledge about the data sets. Hence, this distinctively differentiates our work from already existing ones and clearly defines the central focus of this paper.

III. FRAUD DETECTION BASED ON OUTLIER MINING

The problem of finding patterns in data that deviate from normal behavior is called Outlier Detection in [21]. According to the application domains, these patterns are named e.g. Outliers, anomalies, exceptions, discordant observations, novelties or noise. The fact that the results can lead to critical information on the basis of which we can take an action makes the process of outlier detection important. Similar Coefficient Sum is an example of an outlier mining technique.

A. Similar Coefficient Sum

The concept of similar coefficient sum is initiated by Jiang Lingmin [22]. This method judges whether it is outlier or not according to the similar coefficient sum-based outlier detection algorithm and it is described as follows [22]:

Let X = [x1, x2, x3… xn} be a set of objects to be checked, every object with m indexes, that is, xi = [xi1, xi2, xi3… xim}

Using Data Matrix will be presented as follows:

$$X = \begin{bmatrix} x_{11} & x_{12} & \cdots & x_{1m} \\ x_{21} & x_{22} & \cdots & x_{2m} \\ \vdots & \vdots & \ddots & \vdots \\ x_{n1} & x_{n2} & \cdots & x_{nm} \end{bmatrix}$$

Now, outlier sets of n objects are required. Before estimating the dispersion degree of objects among X, similar coefficient rij between every object is computed first, and then the similar coefficient matrix, that is

$$R = \begin{bmatrix} r_{11} & r_{12} & \cdots & r_{1n} \\ r_{21} & r_{22} & \cdots & r_{2n} \\ \vdots & \vdots & \ddots & \vdots \\ r_{n1} & r_{n2} & \cdots & r_{nn} \end{bmatrix}$$

$$r_{ij} = 1 - \sqrt{\frac{1}{n}\sum_{k=1}^{m}\left(x_{ik} - x_{jk}\right)^2}$$

$$p_i = \sum_{j=1}^{n} r_{ij}$$

pi is the sum of the ith line in similar coefficient matrix, the smallest, the furthest between object i and other objects. That means object i is candidate item of outlier set.

$$\lambda_i = \frac{p_{max} - p_i}{p_{max}} \times 100\%$$

λ is the threshold, and all object which have λi>= λ are considered as outlier set.

It means if value of particular object is greater than the threshold value then that object is considered as an outlier and is a fraud. Also when the value of object less than threshold then is not considered to be a fraud. Design process of our process is discussed in next sub section.

B. Design Process of Our Appraoch

The design process of our approach of finding the outlier based on similar coefficient sum is as follows:

First we clean the raw call detail records (CDR) on the basis of name using data cleansing algorithm as discussed in [23] so that we find the duplicity in data set and then we apply the outlier mining approach similar coefficient sum on individual customer records and the performance is evaluated using some performance indicators as discussed in [24]. True Positive (TP) represents the positive tuples (tuples of main class of interest) that are correctly detected as fraud, whereas False Positive (FP) represents the negative tuples (tuples of class of non interest) that are incorrectly detected as fraud. True Negative (TN) represents the negative tuples that are correctly detected as fraud whereas False Negative (FN) represents the positive tuples that are incorrectly detected as fraud. True positive rate represents the proportion of positive tuples that are

Published By:
Blue Eyes Intelligence Engineering
& Sciences Publication Pvt. Ltd.

International Journal of Soft Computing and Engineering (IJSCE)
ISSN: 2231-2307, Volume-4, Issue-ICCIN-2K14, March 2014

correctly identified. False positive represents the proportion of positive tuples that are incorrectly identified. The accuracy or the success rate represents the number of correct instances divided by the total number of instances. The process is shown in Fig.1 below:

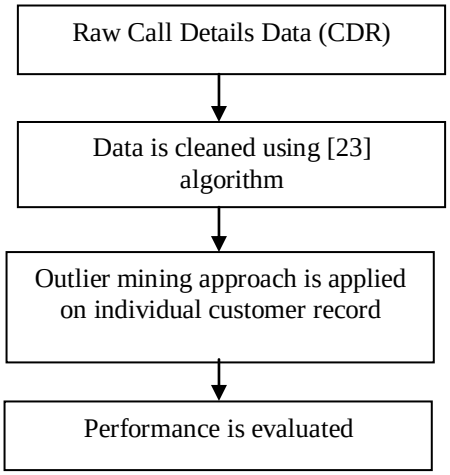


Fig.1 Design Process of our Approach

IV. EXPERIMNET AND RESULT ANALYSIS

We have implemented the described approach using MatLab R2010. The telecommunication companies do not, in general, agree to share the data sets of their customers with researchers, therefore we have taken the datasets available on the internet. But this data doesn't contain the fraudulent entries. So we introduce some fraudulent data with the help of experts of the private sector telecommunication industry. We have cleaned the data on the basis of name using cleansing algorithm which is described in [23].

We divide the datasets customer wise by using IF-then-Else classifiers and this is shown in fig.2. We have taken 50 entries of 20 customers for evaluating our approach. We have shown few entries and few attributes in the screen starts due to space limitation. After data cleansing, we apply the outlier mining technique similar coefficient sum on individual customers. If we look at Fig.2, we see that third tuple detect as outliers. We evaluate our approach using some performance indicators as discussed above.

TABLE I
CUSTOMER WISE DATSET

Name	Called Number	Calling Number	Duration
N1	10612899	68373748102	2
N1	612283725	68373748102	43
N1	613069656	68373748102	675
N1	613481951	68373748102	33

The values of TP, TN, FP and FN are graphically fig. 3. The TP Rate, FP Rate and Success Rate are shown in fig. 4. For better efficiency, TP Rate should be high and FP Rate must be low. For TP Rate high, TP Must be high and TN & FP must be low.

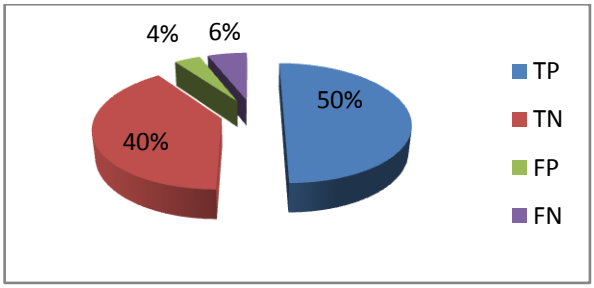
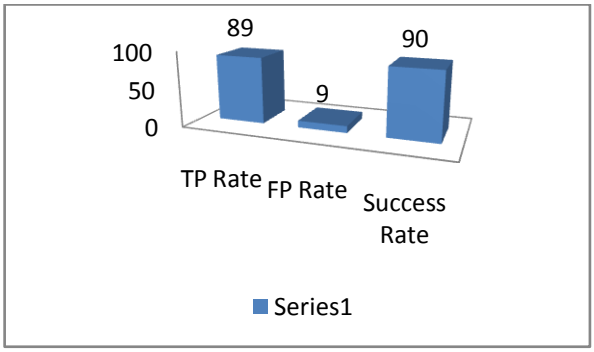


Fig.3 TP, TN, FP, FN of above Data Sets



V. CONCLUSIONS

We have proposed an outlier mining approach based on similar coefficient sum for finding frauds in telecommunication industry. Outlier mining effectively finds outliers**,** unknown to the distribution of data set. This technique detect the abnormal behavior of individual customer on the basis of their past call details in an efficient manner. The manual intervention in the proposed algorithm is highly negligible resulting in high degree of automation and accuracy. We have implemented this technique in Mat Lab R2010a.

REFERENCES

[1]. Investigating Fraudulent Acts, University Of Houston System Administrative Memorandum", http://www.uhsa.uh.edu/samiAM/01C04.htm, 2000.
[2]. http://www.princeton.edu/~achaney/tmve/wiki100k/docs/Fraud.html
[3]. L.Cortesão, F.Martins, A.Rosa, P. Carvalho," Fraud Management Systems in Telecommunications: a practical approach" ICT, 2005.
[4]. Davis, A. B. and S. K. Goyal (1993). Management of cellular fraud: Knowledge-based detection, classification and prevention. In *Proceedings of the 13th International Conference on Artificial Intelligence, Expert Systems and Natural Language, Avignon, France*, Volume 2,pp. 155–164.
[5]. Johnson, M. (1996). Cause and effect of telecoms fraud. *Telecommunication (International Edition) 30* (12), 80–84.
[6]. Parker, T. (1996). The twists and turns of fraud. *Telephony 231* (supplement issue), 18– 21.
[7]. O'Shea, D. (1997). Beating the bugs: Telecom fraud. *Telephony 232*(3), 24.
[8]. Pequeno, K. A. (1997). Real-time fraud detection: Telecom's next big step. *Telecommunications (Americas Edition) 3 1*(5), 59–60.
[9]. Hoath, P. (1998). Telecoms fraud, the gory details. *Computer Fraud & Security 20* (1), 10–14.
[10]. Barson, P., S. Field, N. Davey, G. McAskie, and R. Frank (1996).The detection of fraud in mobile phone networks. *Neural Network World 6*(4), 477–484.
[11]. Phone fraud: The battle rages on. Communication News, 33(8):8, 1996.
[12]. T. Fawcett and F. Provost. Combining data mining and machine learning for effective user profiling. In E. Simoudis, J. Han, and U. Fayyad, editors, Proceedings of the 13th International Conference on Machine Learning, pages 8–13, 1996.
[13]. T. Fawcett and F. Provost. Adaptive fraud detection. Journal of Data mining and Knowledge Discovery, 1(3):291–316, 1997.

Published By:
Blue Eyes Intelligence Engineering
& Sciences Publication Pvt. Ltd.

[14]. A.B. Davis and S. K. Goyal. Management of cellular fraud: Knowledge based detection, classification and prevention. In Proceedings of the 13th International Conference on Artificial Intelligence, Expert Systems and Natural Language, Vol. 2, pages 155–164, Avignon, France, 1993.

[15]. Ben-Gal I., Outlier detection, In: Maimon O. and Rockach L. (Eds.) Data Mining and Knowledge Discovery Handbook: A Complete Guide for Practitioners and Researchers," Kluwer Academic Publishers, 2005, ISBN 0-387-24435-2.

[16]. H. Kvarnstrom, E. Lundin, and E. Jonsson. Combining fraud and intrusion detection – meeting new requirements –. In Proceedings of the 5th Nordic Workshop on Secure IT systems (NordSec2000), Reykjavik, Iceland, October 2000.

[17]. R. A. Shaffer. Good guys, bad guys and digital. Forbes, 154(4):122, 1994.

[18]. P. Barson, S. Field, N. Davey, G. McAskie, and R. Frank. The detection of fraud in mobile phone networks. Neural Network World, 6(4):477–484, 1996.

[19]. S. Field and P. Hobson. Techniques for telecommunications fraud management. In J. Alspector, R. Goodman, and T. X. Brown, editors, Proceedings of International Workshop on Applications of Neural Networks to Telecommunications, Vol. 3, pages 107–115, New Jersey, USA, 1997. Lawrence Erlbaum.

[20]. J. Hollmen. User Profiling and Classification for Fraud Detection in Mobile Communication Networks. PhD thesis, Helsinki University of Technology, Department of Cognitive and Computer Science and Engineering, 2000. Espoo, Finland.

[21]. Victoria J. Hodge and Jim Austin," A Survey of Outlier Detection Methodologies", *Kluwer Academic Publishers, 2004.*

[22]. Jiang Lingmin. Clustering Algorithm to Check Outlier Based on Similar Coefficient Sum. Computer Engineering. Vol.29, Nov, 2003, pp.183-185.

[23]. Arora R, Pahwa P., Bansal S.," Alliance Rules for Data Warehouse Cleansing", International Conference on Signal Processing Systems IEEE, pages 743-747, 2009.

[24]. *Han J., Kamber M.," Data Mining: Concepts and Techniques", 2nd ed. ISBN 1-55860-901-6 Morgan Kaufmann Publishers, March 2006.*

Published By:
Blue Eyes Intelligence Engineering
& Sciences Publication Pvt. Ltd.

Assessment of Renewable Energy in India

Rijul Dhingra, Abhinav Jain, Abhishek Pandey, and Srishti Mahajan

***Abstract*—Most of the power generation in India is carried out by conventional energy sources, coal and mineral oil-based power plants which contribute heavily to greenhouse gases emission. This focuses the solution of the energy crisis on judicious utilization of abundant renewable energy resources. This paper reviews the renewable energy scenario of India. It begins by describing the importance of renewable energy and its advantages over fossil fuels. It gives an overview of the renewable energies in India while evaluating the current status and the deployment of each of these technologies to date in India. It also reviews the multi-criteria assessment of different renewable energy and draws out vital conclusions. It is based on the secondary information collected from various mass media including internet, various reports and other International Institutions.**

***Index Terms*—Conventional energy sources, greenhouse gases, renewable energy.**

I. Introduction

In this competitive world, every country wants to be in the league of developed countries by rapid growth and employment generation. The pernicious effect and ecological disequilibrium caused by rapid industrialisation and increasing population can't be unheeded. This can directly be linked with immense amount of carbon emission and this process seems to be augmentative and ageless. Seeing vagaries in climate, an international joint action is captious in steering an effectual, impartial and economical response to this challenge. For a vast country like India which stands sixth in the world in terms of energy consumptions, the dependency on a single resource or technology to carry out all energy requirement while tackling issues related to environmental impacts and fuel supplies is impractical and undoable [1]. Therefore incorporating non-carbon emitting resources have become an integral part to attain sustainability and cut down burden on fossil fuel reserves. Seeing India's domestic market and large number of investors, country is ideally placed to take benefit from what renewable energy sources can offer. The variations in climatic zones provides ample amount of wind, sunlight, water flow rate which have enormous potential to undergo growth to energy sector and can be an alternative to fossil fuels. If given full support by the government, India can establish itself as world leader in judiciously using its resources of business and private investors for expanding renewable energy. Focusing on clean energy and seeing its enormous potential, renewable energy is likely to become the foundation of India's energy sector.

The key drivers for renewable energy are [2]:

1) Large unexplored potential
2) Gap between demand and supply with increase in population
3) Environmental concerns
4) Beef up India's energy security
5) Pressure from shareholders on high emission industry sectors
6) A practical solution for rural electrification

In present scenario, India is one of the largest consumers of fossil fuel such as crude oil, coal etc. This uncontrollable increase in use of Non-renewable energies such as fossil fuel, oil, natural gas has led to fluctuation of demand & supply. This leads us to the uncertainty of the future of Non-renewable energies. Having a negative Energy Balance for decades, India is forced to purchase energy from other countries to fulfill the needs of the entire country. The advancement of renewable energy resources will accelerate the development of the energy sector in the country so that it can meet its growth aspirations.

II. Why Are Renewable Sources Better Than Oil Resources?

A broad comparison between renewable sources of energy and oil resources based on some factors is given below, see Table I. It indicates that renewable resources are the future for the country in the energy sector and there is a need to completely unleash the potential of these resources.

TABLE I: Difference between Renewable Energy and Oil Resources

	Renewable sources of energy	Oil Reserves
1. Availability	They are abundant in nature	Oil reserves are limited in nature
2. Regeneration	Can be Regenerated; Inexhaustible resource	Ore is drained , can't be regenerated
3. Emission	Zero emission	releases greenhouse gases
4. Environmental effect of use	There is no adverse effect on Environment. The whole system is pollution free and environment friendly.	Harmful to the environment
5. Transportation	Used where it is available or transported where needed	Has to be transported from its source site for further processing, exposing the environment to pollution from accidents
6. Distribution	Evenly distributed in world.	Uneven distribution which leads to flow gap and price fluctuations.

Manuscript received October 10, 2013; revised March 3, 2014.

Rijul Dhingra, Abhinav Jain, Abhishek Pandey, and Srishti Mahajan are with Delhi Technological University, Delhi, India, 110042 (e-mail: Rijuldhingra93@gmail.com, abhinavjain93@gmail.com, abhishekp131@gmail.com, srishtimahajan.94@gmail.com).

DOI: 10.7763/IJESD.2014.V5.527

7. Development	Leads to more sustainable development. i.e. more jobs opportunities	Lesser sustainable development
8. Storage	Need storage between production and consumption.	Portable form of energy. Easy to store
9. Climate Change	Depends on altercation of climate	Do not depend on weather modifications
10. Area	Large amount of land is required	Not large geographical area is required
11. Geo-political implications	Reduces our reliance on oil, Safe guarding national security. Allows for self-sufficiency [3]	Over-reliance on oil as a resource can undermine a country's energy security. [3]
12. Cost	High Capital and Maintenance cost.[4]	Cost of producing is low since they are naturally available. Furthermore they are cheap to transform from one form of energy to another. [4]
13. Energy Supply	Once generated, they produce high amount of energy.	limited supply only

III. Renewable Energy Scenario in India

Hydro - Falling rainfall can be a very good indicator for people to judge those areas where water can be readily available to be used to produce energy from it. This kind of energy produced from water is known as hydroelectric energy. These hydroelectric power plants can then be implemented in such regions of heavy rainfall. There are 12 major such plants in India- 3 in Bihar, 2 in Andhra Pradesh and one in Punjab, Uttaranchal, Karnataka, Uttar Pradesh, Sikkim, Jammu and Kashmir and Gujarat each.

Biomass - One third contributor of energy to India is biomass with a potential of 22,536MW – [5] which comprises of solid biomass, which is an organic, non-fossil material of biological origins. Biogas which is principally methane and carbon dioxide is produced by anaerobic digestion of biomass and combusted to produce heat. Currently, India has 3697MW [6] installed capacity. Following is a list of some States with most potential for biomass reduction: Andhra Pradesh (200 MW), Bihar (200 MW), Gujarat (200 MW), Karnataka (300 MW), Maharashtra (1,000 MW), Punjab (150 MW), Tamil Nadu (350 MW), Uttar Pradesh (1,000 MW) [7].

Solar - India being situated between the tropic of cancer and the equator , has an average temperature of 25℃ – 27.5℃ [7] and receives 260-300 clear sunny days per year making it the best solar resource in the world. India has an installed power capacity of 1686 MW, making it sixth largest consumer in the world. Major plants are located in Gujarat, Rajasthan, Jodhpur, Tamil Nadu and Orissa.

Wind - Electrical energy and mechanical energy can also be produced by wind energy. India has 19051 MWof installed capacity and ranks 5th and has a potential of utilization up to 102772MW. Some of the major wind energy plants are located in Tamil Nadu (7160MW), Gujarat (3093MW) and Maharashtra (2976MW).

Geothermal - One energy sources that has not been exploited at all, is the geothermal energy, which is an enormous, underused heat and power resource that is clean, reliable and home grown. [8]With growing dependence on coal and with increasing environmental problems, India will soon have to start exploiting this source of energy which has a potential of about 10000 MW [9]. Chhattisgarh government has decided to establish the first Geothermal Power Plant of the country in Tattapani area of the Balrampur district with the help of NTPC.

Nuclear - Nuclear power stands fourth in electricity generation in India after thermal, hydro and wind. India stands ninth in the world in terms of number of operational nuclear power reactors and has 20 nuclear reactors in operation in six nuclear power plants, generating 5,780 MW, also seven nuclear reactors are under construction. India's electricity generation is expected to reach 20,000 MW by 2020. The Biggest Nuclear plant in India is located in Tarapur, Maharashtra, 1400MW, followed by Rawatbhata in Kota Rajasthan, 1180 MW and KaigaKarnataka, 880 MW. Kudankulam, Tamil Nadu of 2000MW, India's biggest power plant is under construction.

Ocean - There is a huge potential of tidal and marine energy in India which can be produced from ocean. For the tidal energy potential- locations are the Gulf of Cambay and the Gulf of Kachchh on the west coast with max tidal range- 8m to 11m and average range- 5m to 7m .The Ganges Delta, Sunder bans West Bengal too has good locations for small scale tidal power development. The tidal power potential in India is 8000-9000 MW- 7000 MW [10] in the Gulf of Cambay, 1200 MW in the Gulf of Kachchh and less than 100 MW in Sunder bans. And for the marine energy potential- along the 6000 Km of coast is about 40,000 MW. A British tidal energy company, Atlantis Resources, is expected to set up a tidal power plant with the capacity to generate over 50 MW inthe Gulf of Kutch with construction already started in early 2012.

IV. Multi-Criteria Assessment of Renewable Energy

An assessment of different types of renewable energies is carried out, see Table II.

TABLE II: Difference between Wind, Hydro, Biomass, Solar, Geothermal, Ocean, Nuclear Energy

Criteria	**Wind**	**Hydro**	**Biomass**
1. Efficiency (%)	30[10]	80[10]	1[10]
2. Land requirement	High	Very high	Extremely high
3. Approx. Potential For India (MW)	102772	84000	22536

4. Electricity cost (c/kWh)	7	8	14
5. Installed capacity (MW)	19051	38748	3697
7. Carbon dioxide ($kgCO_2$/KWh)	0.02	0.04	1.18
6. Work qualifications	Low	Moderate	Low
8. Independence of electricity generation	Very High	High	High
9. Turnkey cost	Low	Very high	Low
10. Social And individual risks	Low	High	Low
11. Construction time	Low	Very high	Moderate
12. Wastes Generated	No waste	No waste	Some wastes
13. Energy Source	Inexhaustible	Inexhaustible	Developed By Keeping in mind the availability of biomass
14. Operation & management costs	Very low	Low	Very low
15. Necessity of participative decision-making processes	Low	Very High	Low

Criteria	**Solar**	**Geothermal**	**Ocean**	**Nuclear**
1. Efficiency (%)	15	8	3	33
2. Land requirement	High	Low	Very low	Very low
Criteria	**Solar**	**Geothermal**	**Ocean**	**Nuclear**
3. Approx. Potential For India (MW)	-	10000	40000	-
4. Electricity cost (c/kWh)	17	8	25	4
5. Installed capacity (MW)	1686	0	1	5780
7. Carbon dioxide ($kgCO_2$/KWh)	0.1	0.06	0.02	0.025
6. Work qualifications	Low	Moderate	High	Very High
8. Independence of electricity generation	Very High	High	High	Low
9. Turnkey cost	Low	High	High	Very high
10. Social And individual risks	Low	Low	Low	Very High
11. Construction time	Low	High	High	High
12. Wastes Generated	No waste	No waste	No waste	Highly toxic Wastes generated
13. Energy Source	Inexhaustible	Limited sites but Inexhaustible	Variable but Inexhaustible	Exhaustible
14. Operation & management costs	Very low	Low	Moderate	High
15. Necessity of participative decision-making processes	Low	Low	Low	Very high

V. Analysis and Findings

The efficiency of the conversion processes involved is highest in hydro at about 80% and least for biomass and ocean.

Land requirement for biomass energy is higher in comparison to others as it needs significant amount of land for the biomass. Hydro power also require large amount of land in creating the reservoirs.

Carbon dioxide generated is only high for the biomass energy, all other renewable energy involve negligible or very low CO_2 emissions.

Work qualifications consider average years of education for workforce which considers the technicality of the processes involved. It is very high for Nuclear Energy as compared to others with solar, wind requires very low work qualifications.

Turnkey cost is very high for Nuclear and Hydropower since plants or projects of these require high capital input than others.

Social and individual risk includes subjective health fears due to normal operation as well as Health effects from accidents. In case of Nuclear energy risks involved are high as also witnessed over the time and recently in Fukushima reactor incident in Japan. Wind, solar, geothermal etc. does not involve such high risks.

Wastes generated are nearly negligible except for Nuclear power where highly radioactive wastes are produced and require proper waste management.

Autonomy of electricity generation is very high for wind, solar, biomass, etc. but is questionable in case nuclear energy because fuel sometimes comes from other countries and hydro where projects on rivers flowing through more than one nation have certain risks.

Energy source for wind, solar, geothermal and ocean are inexhaustible whereas for biomass and nuclear power, it is exhaustible.

Necessity of participative decision-making processes is pretty high in cases of nuclear and hydro power as risks for the stakeholders involved are high. It's pretty low in case of other sources.

Operation & management costs are high for nuclear power whereas nearly all other have comparatively low O&M costs.

VI. Conclusion

Looking at the present scenario, a sustainable energy system in country like India is essential/the need of the hour for sustainable development. Because of the Inequality in energy distribution, renewable energy has the possibility of becoming the foundation for the country's future energy requirements. An analysis on the demand for new renewable technologies clearly shows a shift in preference towards these technologies as a source of energy- wind, biomass, and geothermal, tidal and marine, hydropower, solar photovoltaic. The popularity of renewable technologies can be noted by continued rapid growth, despite economic breakdown and financial crisis. Introduction and use of renewable energy on a large scale will help in tackling issues like energy scarcity, variations in fuel prices and help India to be self-sustainable. India is already facing energy crisis as many parts still survive without electricity, hence renewable energy can act as panacea to its problems. [11] But availability of capital is inhibiting the growth of renewable energy. Future growth in renewable energy will require new technology, favourable policies backed by innovative financing. This report calls upon all the stakeholders to take charge and discuss the conditions that favour renewable energy deployment and find creative solutions. The Indian government should realize the long term benefits of renewable power generation and mark it top priority during their economic growth plans. They should increase their financial support for renewable energy in a variety of ways which includes funds for demonstration projects and loan guarantees. These measures will help in shifting the similar investment schemes of energy sector away for typically undervalued investment costs of fossil fuels. This report is meant only as an overview in hopes that it will encourage even more rapid and extensive development of the renewable energy resources on the Indian subcontinent.

References

[1] D. S. Arora, S. Busche, S. Cowlin, T. Engelmeier, H. Jaritz, A. Milbrandt, and S. Wang, "Indian renewable energy status report," *NREL*, October 2010.

[2] *New Renewable Energy in India: Harnessing the Potential*, Export-Import Bank of India, pp. 116-118, January 2011.

[3] V. Verneker, "Distributed Renewable Energy Generation in India," M.Sc. thesis, Dept. of Sustainable Energy & Environment, Cardiff University, Cardiff, United Kingdom, Sept. 2008.

[4] S. Guru, "Renewable energy sources in India, is it viable?" *Working Papers Series*, Julian Simon Centre for Policy Research, October 2002.

[5] State-wise potential of various renewable energy technologies. (July 2013). [Online]. p. 1. Available: http://data.gov.in/sites/default/files/Statewise_Potential_of_Various_Renewable_Energy_Technologies_1.xls

[6] Report to the people. (2013). [Online]. pp. 37-38. Available: http://pmindia.gov.in/report_to_people/2012-2013/report_PMO_English.pdf

[7] P. Meisen and E. Quéneudec. (October 2006). Overview of sustainable renewable energy potential of India. [Online]. Available: http://www.geni.org/globalenergy/research/renewable-energy-potential-of-india/Renewable%20Energy%20Potential%20for%20India.pdf

[8] R. K. Gera, H. M. Rai, Y. Parvej, and H. Soni, "Renewable energy scenario in India: Opportunities and challenges," *Indian Journal of Electrical and Biomedical Engineering*, vol. 1, no. 1, pp. 10-16, 1 January-June 2013.

[9] Delhi International Energy Conference 2010. [Online]. Available: http://www.direc2010.gov.in/geothermal.html.

[10] N. H. Afgan and M. G. Carvalho, "Multi-criteria assessment of new and renewable energy power plants," *Energy*, vol. 27, pp. 739–755, 2002.

[11] A. Ringwald, "India renewable energy trends," *Centre for Social Markets*, July 2008.



Rijul Dhingra was born on August 23, 1993 in Delhi. He is currently pursuing B. Tech in environmental engineering from Delhi Technological University, Delhi.

He has completed 6 weeks internship at Central Pollution Control Board (CPCB), Delhi. A review paper on the millennium development goals is accepted at the Clute Institute, Orlando. His current interests are future development of India in the environmental industry, quality control/assurance of air, water supply.



Abhinav Jain was born on September 29, 1993 in Delhi. He is currently pursuing B. Tech in environmental engineering from Delhi Technological University, Delhi.

He has completed 6 weeks internship at Central Pollution Control Board (CPCB), Delhi. His current interests are renewable energy, water supply and wastewater treatment.



Abhishek Pandey was born on January 31, 1993 in Delhi. He is currently pursuing B. Tech in environmental engineering from Delhi Technological University, Delhi.

He has completed 6 weeks internship at Central Pollution Control Board (CPCB), Delhi. His current interests are noise monitoring system and renewable energy.



Srishti Mahajan was born on March 19, 1993 in Delhi. She is currently pursuing B. Tech in environmental engineering from Delhi Technological University, Delhi.

A review paper on the millennium development goals is accepted at the Clute Institute, Orlando. Her current interests are renewable energy and waste water treatment, remote sensing.

Availability Analysis with Opportunistic Maintenance of a Two Component Deteriorating System

Joel P. Varghese and Girish Kumar

***Abstract*—This paper describes the opportunistic maintenance model for availability analysis of two component series system using the Markov and the Monte Carlo Simulation methods. The system model is developed incorporating four states for each component considering their level of degradation. Separate models are developed for three cases of corrective repair such perfect, imperfect, and minimal repair with and without condition based opportunistic maintenance. These models are solved using analytical Markov approach. The solutions are validated by the Monte Carlo Simulation. Since the Markov approach is limited to exponential failure and repair rates, the Monte Carlo Simulation based codes can be further extended to accommodate systems which follow non-exponential failure and repair rates.**

***Index Terms*—Availability, markov, monte carlo simulation, opportunistic maintenance.**

I. Introduction

Maintenance has been defined as a combination of technical and associated administrative actions intended to retain an item or system in, or restore it to, a state in which it can perform its required function [1]. The nascence of modern high technology components has resulted in an increase in complexity and cost of industrial components and systems. This makes it important to maximize the utilization of these components and systems throughout its lifetime. In recent times, the total maintenance cost is largely becoming a substantial portion of the total operating cost of the system or component. Thus the development of a judicious and effective maintenance policy is a major concern for industrial and manufacturing engineers.

Conventional maintenance policies encompass simple corrective and preventive maintenance for components. Corrective maintenance is effectively illustrated by the philosophy "if it isn't broken, don't fix it" [2]. Preventive maintenance, on the other hand, consists of certain scheduled activities that are performed while the system is still functioning. The underlying aim behind preventive maintenance is to reduce the number of unplanned system downtime due to system or component failure.

In the current industrial scenario of increased demand and surfeit global competition, such primitive maintenance policies will not suffice and provide an advantageous edge over competitors. From the maintenance point of view, this advantageous edge can be facilitated by increasing system or component availability which means reducing downtime without compromising on the system reliability. This has resulted in the adoption of much more efficient maintenance policies such as condition based maintenance and opportunistic maintenance. Opportunistic maintenance can be visualized as a fruitful combination of corrective and preventive maintenance. Opportunistic maintenance makes maximum utilization of the time to perform corrective maintenance on a component or system by using this time to carry out preventive maintenance on components which may require maintenance in the near future. Opportunistic maintenance is not a maintenance policy for a single component, but for a collection of components in a production line or plant [3].

The work in the field of opportunistic maintenance first began by [4]. The authors implemented the opportunistic policy for unmonitored components/systems. Reference [5] shows how this policy was investigated for two components in series, but no mathematical treatment for availability measure was proposed. An imperfect maintenance concept in this context was applied by [6]. Since then, many extensions of opportunistic maintenance have been introduced and studied in the literature. The Markov and Semi-Markov approaches have been used in literature to analyze various maintenance policies. Reference [7] shows how a Markov renewal process was used to construct a maintenance cost model for a simple multi-unit system. A continuous time Markov chain was used by [8] to describe the degradation of a component. A cost model was developed including the presence of resource constraints. Dynamic programming was used by [9] to analyze a condition based and opportunistic model for a two unit deteriorating system involving a cost model. The transient behavior of a multi-unit system was studied by [10] using renewal theory. The instantaneous availability for a fixed time was calculated and a methodology was developed to find times to preventive and opportunistic maintenance such that cost is minimized. His components had binary levels of degradation, i.e. operating or failed.

In the existing literature, the Markov model has been used to analyze systems undergoing various corrective and preventive repairs. The application of Markov for systems undergoing opportunistic maintenance has not been explored so far. Also, the existing literature doesn't take into account multi-state degradation of components and considers components with binary states. The existing literature has resorted to a cost model to analyze and compare various maintenance policies without giving much significance in quantifying the gains of opportunistic maintenance.

This paper overcomes these limitations by firstly developing a system model considering multi-state

Manuscript received November 2, 2013; revised February 15, 2014.

The authors are with Delhi Technological University, Shahbad Daulatpur, Main Bawana Road, Delhi-110042, India (e-mail: joelprince25@gmail.com, girish_kumar_ar@yahoo.com).

degradation and providing an analytical method based on Markov to analyze the availability. Opportunistic maintenance policies for different types of corrective repairs such as perfect, imperfect, and minimal repairs have been considered. Acknowledging the limitation of the Markov method to be useful for components having exponential failure and repair rates, a Monte Carlo Simulation method is also presented which has been correctly validated by the Markov model to extend this availability analysis to systems having non-exponential failure and repair distributions. The gains of an opportunistic maintenance policy has been quantified in terms of availability of system and this provides us with a suitable decision making tool to choose the best maintenance policy and also compare different combinations of components in terms of availability for a particular maintenance policy.

Software such as RAPTOR (ARNIC, Annapolis, MD), BlockSim (Reliasoft, Tucson, AZ), *et al.*, are widely used for availability analysis of repairable systems. These software programs do not yet have a module for opportunistic maintenance. The proposed methodology can be used as an extension for these software programs.

The remaining paper is organized as follows. Section II will enumerate the approaches used. Section III will describe the system modeling to incorporate multi-level degradation and corrective repair i.e. perfect, imperfect, and minimal, with and without opportunistic maintenance. The solutions of the models based on Markov and Monte Carlo Simulation will be described in Section IV. Section V will use an example to illustrate the methodology, and discuss the results. Finally, Section VI concludes the work.

II. Approaches

A. Overview of Markov Method

Markov models are frequently used in reliability and maintainability work where events, such as the failure or repair of the module, can occur at any point in time. The Markov method evaluates the probability of jumping from one known state into the next logical state. This continues until the system being considered has reached the final or totally failed state or until a particular mission time is achieved**.** The basic assumption of a Markov Process is that the behavior of the system in each state is memory less [11]. For any given system, a Markov model consists of a list of the possible states of that system, the possible transition paths between those states, and the rate parameters of those transitions. Let the symbol λ denotes the rate parameter of the transition from State 1 to State 2 and be $y_i(t)$ the probability of the system being in State *i* at time *t*. Fig. 1 shows the Markov model for a simple component with binary states.

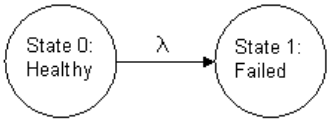


Fig. 1. Markov model for a simple component.

The set of differential equations for this simple model are given by (1), (2) and (3).

$$\frac{dy_0}{dt} = -\lambda y_0 \tag{1}$$

$$\frac{dy_1}{dt} = \lambda y_1 \tag{2}$$

$$y_0 + y_1 = 1 \tag{3}$$

B. Overview of Monte Carlo Simulation

The Monte Carlo Simulation is a powerful and versatile tool based on random sampling which has a wide range of applications in various fields. One underlying principle of Monte Carlo Simulation is the law of large numbers, which states that the larger the sample, the more likely the sample mean will be a good estimate of the population mean [12]. The Monte Carlo Simulation can be used to model the availability of systems. It makes use of the failure and repair statistical distributions of components or systems to analyze the system behavior over time [13].

Initially, the simulation time to failure and repair time of the component or system are generated. Random numbers are created using an uniform distribution (*U*) in the interval (0, 1), and a suitable conversion method is used to convert these random numbers into the times for failure and repair. The frequently used conversion methods include the inverse transform method, composition method and acceptance–rejection method. We shall use the inverse transform method in this article due to its simplicity. However, its use is limited to when the repair and failure distributions can be inverted analytically. For an exponential distribution, with parameter λ, the expression for the random variable *T* which can be the time to failure or time to repair using an inverse transform method is given by (4).

$$T = -\frac{1}{\lambda}\ln(1-U) \tag{4}$$

Also, since the (1-*U*) is distributed in the same way as *U*, *T* can be given by (5).

$$T = -\frac{1}{\lambda}\ln U \tag{5}$$

Similarly, for a Weibull distribution with parameters 'θ' and 'β' the expression is (6).

$$T = -\theta\left(\ln U\right)\frac{1}{\beta} \tag{6}$$

After the generation of the failure and repair times of all components or systems according to the appropriate distribution, the sequence of failures and repairs for the system are simulated for a specific mission time. This process is repeated for a large number of simulations. The system availability for a given mission time is calculated as the ratio of the total up time of the system for the total number of simulations to the total of mission time of all of the simulations.

III. System Modeling

The system studied in this research is a two component series multi-unit system shown in Fig. 2. The term "unit" could be a component, a set of components, or even a subsystem which can be part of a greater robust or intricate industrial system.

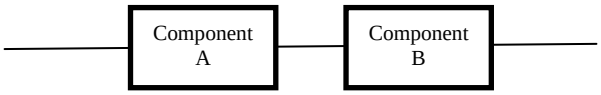


Fig. 2. System model.

A. Modeling Multi-Level Degradation

Practically any component/unit which is part of an industrial system undergoes multiple levels of degradation before reaching the failed state. Multi-level degradation, therefore, implies that the component will not have a constant failure rate up to the failed state, but the failure rate will vary as the component reaches the failed state. Each component is assumed to have four levels of degradation with are given by, State 1(Initial State / Good as new), State 2 (Middle State), State 3(Better than worst), and State 4(Failed State).

B. Repair Action

Since a series system is considered, once a component fails the system will shut down. Corrective repair must be performed on the failed component. The corrective maintenance can be of three types namely perfect, imperfect, or minimal repair. Perfect repair implies that the component is repaired from the 'failed state' to the 'good as new state' (State 1). Imperfect repair implies that the component is repaired from the failed state to the middle state (State 2). Imperfect repair implies a repair of lesser intensity as compared to perfect repair but of a quicker duration. Minimal repair implies that the component is repaired from the failed state to the better than worst state (State 3). Minimal repair is of least intensity and quickest duration. This downtime during the corrective repair process provides an opportunity to perform preventive maintenance on the non-failed component.

C. Model Development

The proposed model of two component series system incorporating multi-level degradation can be developed considering the above mentioned multi-level degradation and repair action.

The system contains two components each having a possibility of being in one of the four states at a particular instant of time. Their series combination gives a total of sixteen possible states the entire system can exist throughout its lifetime. This is inclusive of the system state in which both components are in a failed state. In a series system, this state can occur only if both the components fail simultaneously. The probability of this event is considered to be negligible and can be neglected. The generalized assumptions made for the model are as follows.

1) The opportunistic maintenance activity is assumed to be completed before the failed component gets repaired.
2) The component can function perfectly in all states except the failed state.

IV. Solution to the System Model

A. Analytical Markov Approach

Solution of the system model with the analytical Markov approach involves the following steps.

Step 1: Construct a state diagram of the system representing all possible states of the system. The transition from one state to another is specified by an arrow whose direction indicates the direction of transition. Transition rates from one state to another can also be specified in the state diagram by overlaying it with the arrow.

Step 2: Model the differential equation for a particular system corresponding to each state in the similar lines as (1), (2) and (3).

Step 3: Solve the differential equations simultaneously with suitable initial condition and the required mission time. The availability of the system at the specified mission time is calculated by summing the probabilities of the non-failed system states at a particular mission time.

B. Monte Carlo Simulation

The Monte Carlo Simulation codes which simulate the functioning of the system throughout its mission time are developed, and availability is computed for a large number of trails. The Monte Carlo Simulation codes are based on the following algorithm.

Step 1: Generate random numbers with uniform distribution corresponding to each possible transition of component A and B (failure and repair).

Step 2: Convert these numbers into a value of operating time using the inverse transform method based on the exponential distribution or a non- exponential distribution based on the required condition.

Step 3: At each state compare the times of the possible transition and proceed to the state with the minimum transition time while reducing this time from the transition time of the state not chosen.

Step 4: When a failed state is reached, add the repair time to the system downtime and reset the transition times and the repair time for the failed component.

Step 5: Repeat the steps 1-4 till the cumulative time of the sequence is equal to or more than mission time.

Step 6: Add the downtime for this trail to the total downtime.

Step 7: Repeat steps 5-6 for the required number of trails.

Step 8: Calculate the system availability by dividing the total downtime upon the total mission times after all the trails.

V. Illustration

A power system consisting of a power transformer (Component A) and a protection and control subsystem for power transformer (Component B) in series was selected for the case study to demonstrate the methodology for availability assessment. The exponential failure and repair distribution is assumed for each subsystem and the data for failure rate and repair rate is taken from the literature [14]. Table I shows the literature values for failure and repair rates of both the components.

To incorporate multi- level degradation in the example, the

assumption is made that the failure rates of each of the component increases as it deteriorates. This assumption is based on the discussions with experts from the industry who are working in the field of maintenance. The failure and repair rates for different degrading states are obtained by dividing the binary state data available from the literature in consultation with the industry experts. Failure rates (λ) are in failures per hour and repair rate (μ) are in repairs per hour. The superscript and subscript represent the components and the state transition respectively. The respective calculated values are ${}^{A}\lambda_{12}$ = 1.142 x 10^{-4}, ${}^{A}\lambda_{23}$= 1.713 x 10^{-4}, ${}^{A}\lambda_{34}$ = 3.43 x 10^{-4}, ${}^{B}\lambda_{12}$ = 1.712 x 10^{-4}, ${}^{B}\lambda_{34}$ =5.136x10^{-4}, ${}^{A}\mu_{41}$ =8.621x10^{-3} , ${}^{A}\mu_{42}$ = 17.24 x 10^{-3}, ${}^{A}\mu_{43}$ = 34.48 x 10^{-3}, ${}^{B}\mu_{41}$ = 6.76 x 10^{-2}, ${}^{B}\mu_{42}$ = 13.51 x 10^{-2}, ${}^{B}\mu_{43}$ = 27.03x 10^{-2}.

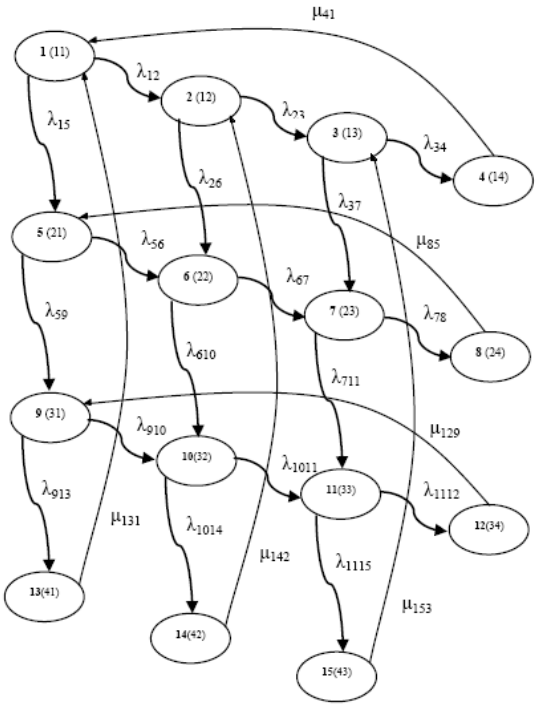


Fig. 3. Corrective Maintenance (Perfect Repair).

Once the transition parameters of failure and repair have been defined the state diagram is drawn. The state diagram for perfect repair is shown in Fig. 3. Fig. 4 shows the state diagram for perfect repair with opportunistic maintenance. Due to space considerations the state diagrams for imperfect and minimal repair with and without opportunistic maintenance are not shown but can be developed along the similar lines. The failure rates and repair rates can also be expressed in terms of system state as λ_{ij} or μ_{ij} where "*i*" represent the state of the system before transition and "*j*" represents the state after transition. From Fig. 3 and Fig. 4 it is noticeable that ${}^{A}\lambda_{12} = \lambda_{15} = \lambda_{26} = \lambda_{37}$. If y_i represents the probability of the system being at the state *i* at the time *t*, then as specified in Section II-A, the set of differential equations are derived for the models shown in Fig. 3 and Fig. 4. The set of equations for Fig. 3 are listed in Appendix I and for Fig. 4 in Appendix II.

TABLE I: LITERATURE VALUES FOR THE COMPONENTS

Component	Temporary Failure Rate	Sustained Failure Rate	Average Failure Rate	Mean Repair Time
Power Transformers (33-110 kV)	0.4 / (100 transformers, year)	0.6 / (100 transformers, year)	0.5/ (100 transformers, year)	116 hours
Protection and control for power transformers (33-110 kV)	0.9 / (100 transformers, year)	0.6 / (100 transformers, year)	0.75 / (100 transformers, year)	14.8 hours

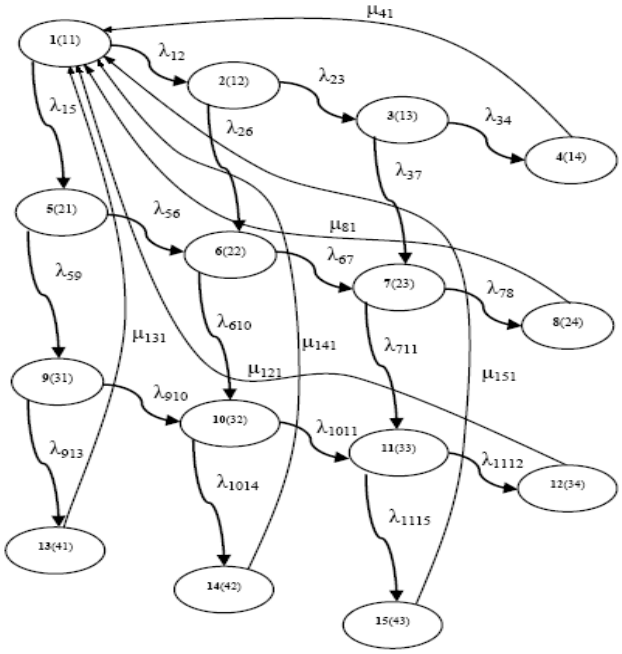


Fig. 4. Corrective maintenance (perfect repair) with opportunistic maintenance.

TABLE II: SYSTEM AVAILABILITY

Repair Action	Availability without Opportunistic Maintenance using Markov	Availability without Opportunistic Maintenance using Monte Carlo Simulation	Availability with Opportunistic Maintenance using Markov	Availability with Opportunistic Maintenance using Monte Carlo Simulation
Perfect Repair	0.99217	0.99219	0.99483	0.99483
Imperfect Repair	0.99216	0.99216	0.9964	0.9964
Minimal Repair	0.98829	0.98889	0.99615	0.99552

Similarly the set of differential equations can be developed for the cases of imperfect and minimal repairs with and without opportunistic maintenance. The sets of differential equations for each model are solved using MATLAB (Matlab 7.7 2008) with initial conditions as $y_1(0)=1$, $y_2(0)=0$, $y_3(0)=0$, $y_4(0)=0$, $y_5(0)=0$, $y_6(0)=0$, $y_7(0)=0$, $y_8(0)=0$, $y_9(0)=0$, $y_{10}(0)=0$, $y_{11}(0)=0$, $y_{12}(0)=0$, $y_{13}(0)=0$, $y_{14}(0)=0$, $y_{15}(0)=0$ and for larger values mission time to get the steady state results. The system availability is obtained by summing the probabilities of

operating states. The availability results based on Markov are shown in Table II.

The solution of the model is also obtained using Monte Carlo Simulation Methods. The codes are developed based on the algorithm in section IV-B. The system availability results based on the Monte Carlo Simulation are shown in Table II.

The results clearly show that when the system undergoes opportunistic maintenance there is an increase in the system availability for perfect, imperfect, and minimal repair. This implies that for the given system an opportunistic maintenance policy would increase the availability irrespective of the maintenance action. The Markov and Monte Carlo Simulation give us matching values of system availability. Thus the Monte Carlo Simulation code has been validated and can be further extended to components having a non-exponential failure and repair rates, such as Weibull or Lognormal. Quantifying the gains of opportunistic maintenance using an availability measure helps to identify the maintenance policy resulting in maximum availability. The above results for the illustrative example clearly show that if the system follows an opportunistic maintenance policy with imperfect repair, the system availability will be maximized. This is valid for the current set of data but depending upon the failure and repair rates, the policy may change. This doesn't imply that it is the optimal maintenance policy. The trade-offs in each case should be considered in terms of cost, effect on component life (as an imperfect or minimal repair results in more frequent system failure) and the opportunistic maintenance policy selected must be such that the economic gain due to the increase in system availability must compensate for the cost acquired by performing opportunistic maintenance.

VI. Conclusion

In this article an analytical Markov model is applied to find the system availability of a two component series system with opportunistic maintenance. Separate models are developed for different corrective actions namely perfect, imperfect, and minimal repairs with and without opportunistic maintenance. The results of system availability in all cases are validated using the Monte Carlo Simulation. The Monte Carlo simulation approach can be further extended for components having non-exponential distributions such as Weibull and lognormal distributions. This approach can be used as an extension for the existing software which does not have the opportunistic maintenance module. The suggested approach provides a realistic assessment of availability values of the repairable system due to the incorporation of multi-state degradation. This work can be further extended to more complex systems with more components in various configurations having more levels of degradation. A cost function can also be developed to analyze the economic pros and cons of carrying out opportunistic maintenance. There is a scope for development of a model for an optimal maintenance policy based cost and availability under the limited maintenance resources.

Appendix I

$$\frac{dy_1}{dt} = -(\lambda_{12}+\lambda_{15})y_1 + \mu_{41}y_4 + \mu_{131}y_{13}$$
$$\frac{dy_2}{dt} = -(\lambda_{23}+\lambda_{26})y_2 + \lambda_{12}y_1 + \mu_{41}y_4$$
$$\frac{dy_3}{dt} = -(\lambda_{34}+\lambda_{37})y_3 + \lambda_{23}y_2 + \mu_{153}y_{15}$$
$$\frac{dy_4}{dt} = \lambda_{34}y_3 - \mu_{41}y_4$$
$$\frac{dy_5}{dt} = -(\lambda_{56}+\lambda_{59})y_5 + \lambda_{15}y_1 + \mu_{85}y_8$$
$$\frac{dy_6}{dt} = -(\lambda_{67}+\lambda_{610})y_6 + \lambda_{26}y_2 + \lambda_{56}y_5$$
$$\frac{dy_7}{dt} = -(\lambda_{711}+\lambda_{78})y_7 + \lambda_{67}y_6 + \lambda_{37}y_3$$
$$\frac{dy_8}{dt} = \lambda_{78}y_7 - \mu_{85}y_8$$
$$\frac{dy_9}{dt} = -(\lambda_{910}+\lambda_{913})y_9 + \lambda_{59}y_5 + \mu_{129}y_{12}$$
$$\frac{dy_{10}}{dt} = -(\lambda_{1011}+\lambda_{1014})y_{10} + \lambda_{910}y_9 + \lambda_{610}y_6$$
$$\frac{dy_{11}}{dt} = -(\lambda_{1112}+\lambda_{1115})y_{11} + \lambda_{711}y_7 + \lambda_{1011}y_{10}$$
$$\frac{dy_{12}}{dt} = \lambda_{1112}y_{11} - \mu_{129}y_{12}$$
$$\frac{dy_{13}}{dt} = \lambda_{913}y_9 - \mu_{131}y_{13}$$
$$\frac{dy_{14}}{dt} = \lambda_{1014}y_{10} - \mu_{142}y_{14}$$
$$\frac{dy_{15}}{dt} = \lambda_{1115}y_{11} - \mu_{153}y_{15}$$

Appendix II

$$\frac{dy_1}{dt} = -(\lambda_{12}+\lambda_{15})y_1 + \mu_{41}y_4 + \mu_{131}y_{13} + \mu_{81}y_8 + \mu_{121}y_{12} + \mu_{141}y_{14} + \mu_{151}y_{15}$$
$$\frac{dy_2}{dt} = -(\lambda_{23}+\lambda_{26})y_2 + \lambda_{12}y_1$$
$$\frac{dy_3}{dt} = -(\lambda_{34}+\lambda_{37})y_3 + \lambda_{23}y_2$$
$$\frac{dy_4}{dt} = \lambda_{34}y_3 - \mu_{41}y_4$$
$$\frac{dy_5}{dt} = -(\lambda_{56}+\lambda_{59})y_5 + \lambda_{15}y_1$$
$$\frac{dy_6}{dt} = -(\lambda_{67}+\lambda_{610})y_6 + \lambda_{26}y_2 + \lambda_{56}y_5$$
$$\frac{dy_7}{dt} = -(\lambda_{711}+\lambda_{78})y_7 + \lambda_{67}y_6 + \lambda_{37}y_3$$
$$\frac{dy_9}{dt} = -(\lambda_{910}+\lambda_{913})y_9 + \lambda_{59}y_5$$

$$\frac{dy_{10}}{dt} = -\left(\lambda_{1011}+\lambda_{1014}\right)y_{10} + \lambda_{910}y_9 + \lambda_{610}y_6$$

$$\frac{dy_{11}}{dt} = -\left(\lambda_{1112}+\lambda_{1115}\right)y_{11} + \lambda_{711}y_7 + \lambda_{1011}y_{10}$$

$$\frac{dy_{12}}{dt} = \lambda_{1112}y_{11} - \mu_{121}y_{12}$$

$$\frac{dy_{13}}{dt} = \lambda_{913}y_9 - \mu_{131}y_{13}$$

$$\frac{dy_{14}}{dt} = \lambda_{1014}y_{10} - \mu_{141}y_{14}$$

$$\frac{dy_{15}}{dt} = \lambda_{1115}y_{11} - \mu_{151}y_{15}$$

REFERENCES

[1] *Collection and exchange of reliability and maintenance data for equipment*, ISO 14224, 2004.

[2] J. Huang, "Preventive maintenance program development for multi-unit system with economic dependency- stochastic modeling and simulation study," Ph.D. Dissertation, Dept. of Industrial and Management Systems, University of South Florida, University of South Florida, Tampa, 1993.

[3] R. P. Nicolai and R. Dekker, "Optimal maintenance of multi-component systems: A review," K. A. H. Kobbacy and D. N. P. Murthy, eds, London, 2008.

[4] R. Radner and D. W. Jorgenson, "Opportunistic replacement of a single part in the presence of several monitored parts," *Management Science*, vol. 10, issue 1, pp. 70–84, 1963.

[5] F. A. V. D. D. Schouten and S. G. Vanneste, "Analysis and computation of (n, N)strategies for maintenance of a two component system," *European Journal of Operational Research*, vol. 48, issue 2, pp. 260–274, 1990.

[6] H. Wang, H. Pham, and A. E. Izundu, "Optimal preparedness maintenance of multi-unit systems with imperfect maintenance and economic dependence," *Recent advances in reliability and quality engineering*. New Jersey: World Scientific, pp. 75–92, 2001.

[7] B. Castanier, A Grall, and C. Berenguer, "A condition-based maintenance policy with non-periodic inspections for a two-unit series system," *Reliability Engineering and System Safety*, vol. 87, pp. 109-120, January 2005.

[8] S. Ambani, L. Li, and J. Ni, "Condition-Based maintenance decision-making for multiple machine systems," *Journal of Manufacturing Science and Engineering*, vol. 131, pp. 0310091-0310099, 2009.

[9] Z. Zhang, S. Wu, and B. Li, "A condition-based and opportunistic maintenance model," in *Proc. International Conference on Quality, Reliability, Risk, Maintenance, and Safety Engineering*, pp. 590 – 595, Xi'an, 2011.

[10] S. Jain, "Opportunistic maintenance policy of a multi-unit system under transient state," M.S. Thesis, Dept. of Industrial and Management Systems, University of South Florida, Tampa, Florida, 2005.

[11] Relex Software Technical Brief. Markov Analysis Accurately Models Dynamic Behaviors. [Online]. Available: www.relexsoftware.com/reliability/brief/markov_brief1.asp

[12] MIL-HDBK-338B, *Military Handbook, Electronic Reliability Design Handbook*, Washington, DC, USA: United States Department of Defense, 1998.

[13] A. Dennis, "Application of Monte Carlo simulation system reliability analysis," presented at the 20th International Pump Users Symposium, Houston, Texas, March 17–20, 2003.

[14] F. Roos and S. Lindahl, "Distribution system component failure rates and repair times - an overview," presented at the Nordic Distribution and Asset Management Conference, Espoo, Finland, August 23-24, 2004.



Joel P. Varghese is a third year engineering student. He is pursuing his bachelor of technology degree in mechanical engineering at Delhi Technological University, Delhi, India.



Girish Kumar is presently an assistant professor in Mechanical Engineering Department at Delhi Technological University, Delhi, India. He is also pursuing his doctoral degree from the Indian Institute of Technology, Delhi, India. His current research interest is in the RAM modeling and analysis of repairable mechanical systems.

Sensors and Actuators B 197 (2014) 385–404

Contents lists available at ScienceDirect

Sensors and Actuators B: Chemical

journal homepage: www.elsevier.com/locate/snb

Review

Biosensors for pathogen detection: A smart approach towards clinical diagnosis

Renu Singh[a,b,f], Maumita Das Mukherjee[d], Gajjala Sumana[a], Rajinder K. Gupta[b], Seema Sood[e], B.D. Malhotra[c,*]

[a] Department of Science & Technology Centre on Biomolecular Electronics, Biomedical Instrumentation Section, National Physical Laboratory (Council of Scientific & Industrial Research), Dr. K.S. Krishnan Marg, New Delhi 110012, India
[b] School of Biotechnology, Guru Gobind Singh Indraprastha University, Sector -16 C, Dwarka, Delhi 110075, India
[c] Department of Biotechnology, Delhi Technological University, Shahbad Daulatpur, Main Bawana Road, Delhi 110042, India
[d] Amity Institute of Applied Sciences, Amity University, Sector 125, Noida, UP, India
[e] Department of Microbiology, All India Institute of Medical Sciences, New Delhi 110002, India
[f] Sensors & Aerosols Laboratory, School of Mechanical and Nuclear Engineering, Ulsan National Institute of Science and Technology, UNIST-gil 50, Eonyang-eup, Ulju-gun, Ulsan 689-798, South Korea

ARTICLE INFO

Article history:
Received 17 July 2013
Received in revised form 10 February 2014
Accepted 2 March 2014
Available online 12 March 2014

Keywords:
Nucleic acid sensor
Human pathogen
Diseases
Bacteria
Virus
Electrochemical

ABSTRACT

The present review concerns the recent developments of nucleic acid biosensors for detection of the human pathogens as infectious diseases management at an early stage is currently of prime interest so as to circumvent the delay in diagnosis, side effects of drugs and unnecessary health hazards. The advantages of biosensors over existing detection methodologies and the role of various immobilization matrices used for fabrication of nucleic acid sensors are discussed. Besides this, efforts have been made to discuss the various techniques used for biosensor construction, the analytical performance of these biodevices for the bacterial and viral pathogens for their applications to medical diagnosis.

© 2014 Elsevier B.V. All rights reserved.

Contents

1. Introduction 386
2. Conventional techniques for detection of pathogens 386
3. Electrochemical biosensors 387
   3.1. Electrochemical nucleic acid sensors for pathogen detection 389
      3.1.1. Electrochemical nucleic acid sensors for bacterial pathogens detection 389
      3.1.2. Electrochemical nucleic acid sensors for viral pathogens detection 394
4. Optical nucleic acid sensors for bacterial and viral pathogens detection 397
5. Other nucleic acid sensors for bacterial and viral pathogens detection 397
6. Challenges and future prospects 400
7. Conclusions 401
   Acknowledgements 402
   Appendix A. Supplementary data 402
   References 402
   Biographies 404

* Corresponding author. Tel.: +91 11 27294668; fax: +91 11 27871023.
E-mail addresses: bansi.malhotra@gmail.com, bansi.malhotra@dce.ac.in (B.D. Malhotra).

http://dx.doi.org/10.1016/j.snb.2014.03.005
0925-4005/© 2014 Elsevier B.V. All rights reserved.

1. Introduction

Recent years have seen continued growth of the interdisciplinary field of biosensors due to an increased interest between basic and applied sciences researchers for development of novel electronic devices that can be utilized for a variety of applications including human health care and environmental monitoring [1]. A biosensor is an integrated miniaturized analytical device that integrates biological sensing elements like enzymes [2], antibodies [3], nucleic acids [4], cells etc. with transducer equipped with an electronic amplifier [5]. Biosensors offer interesting features such as real-time, on-site, simultaneous detection of multiple pathogenic agents utilizing selectivity of the biomolecules and the processing power of modern nano-electronics [6,7]. They are known to provide fast and accurate results arising due to interaction of an analyte with a given biomolecule and have been found to have applications in various fields including clinical diagnostics [8], environmental monitoring [9], bioprocess monitoring [10], food, water [11] and agricultural product processing [12], etc. According to IUPAC, a biosensor is a self-contained integral device which is capable of providing specific quantitative or semi-quantitative analytical information using a biological element.

There is an increased interest towards the development of nucleic acid biosensors for clinical monitoring [13]. Voltammetry of nucleic acids after the discovery of anodic peak specific for guanine is an important milestone for monitoring of double-stranded and denatured single-stranded DNA. Monitoring change in the DNA redox properties (oxidation of guanine) provides a unique opportunity to detect the hybridization process [14]. Though, the electrochemical detection using guanine oxidation is known to cause irreversible damage to DNA; however, redox indicator-based indirect electrochemistry has been shown to be an important alternative for development of nucleic acid hybridization biosensors. The electrochemical DNA biosensors with redox indicators like methylene blue (MB) [15,16], daunomycin [17], metal complexes such as ruthenium (Ru) complex [18], cobalt complex [19] etc. have been found to be advantageous due to re-usability of the electrode. Besides this, electrochemical biosensors do not require additional labelling step and can be easily integrated with electronics for fabrication of miniaturized devices for diagnosis of infectious diseases and the detection of pathogenic biological species of environmental and clinical interest. Thus, DNA hybridization biosensor technology is at the vanguard of clinical diagnosis which commonly relies on measuring techniques like electrochemical [20], optical [21] and mass-sensitive [22] to recognize the complementary target DNA strand.

For the fabrication of a high performance biosensor, the role of an immobilization matrix is very crucial. Among the various matrices, nanomaterials are being explored due to their exceptional optical and electrical properties owing to electron and phonon confinement, high surface-to-volume ratio, modified surface work function, high surface reaction activity, high catalytic efficiency and strong adsorption ability. In particular, nanomaterials with engineered morphology, size, functionality, adsorption capability and high biomolecule loading capacity have been found to provide enhanced electron transport between a biomolecule and the electrode. The microenvironment provided by a nanomaterial may help a biomolecule to retain its conformation with maximum biological activity, resulting in enhanced signal transduction and biosensor stability. These unique properties of nanomaterials can perhaps be utilized for interfacing biological recognition events with electronic signal transduction and for designing a new generation of bioelectronics devices that may exhibit novel functions.

Infectious diseases, especially those resulting from life-threatening pathogens, have significantly increased over the past few decades, and deaths may occur primarily because of delay in diagnosis, side effects of drugs and commodities necessary for rapid detection, prevention or cure [23]. Pathogens are microbes that are capable of causing illness, remain the world's greatest killer of children and young adults, accounting approximately 13 million deaths a year. Pathogen detection is currently of utmost importance, due to health and safety concern [24–35]. The most common pathogens are bacteria, viruses, fungi and parasites (SI). The increased viral outbreaks e.g., H1N1 flu, H5N1 flu, and SARS etc., recently boost the alarm and raised significant worries as the viruses could rapidly spread and turn into a pandemic. In spite of developments in the diagnostic fields for pathogen detection, there is an urgent need for availability of rapid, portable and accurate diagnostic technique that can be used to control the epidemics and may perhaps have a significant impact on clinical management. This manuscript deals with the recent development of electrochemical, optical biosensing techniques based on nucleic acids for pathogens detection that have implications towards the clinical diagnosis of bacterial and viral infections.

2. Conventional techniques for detection of pathogens

The traditional methods for pathogen detection include microscopy, culture and serology. Microscopy is simple, easy to use and a versatile technique. Culture is the gold standard for diagnosis of many microorganisms, e.g., *Mycobacterium tuberculosis* and serology forms the mainstay of diagnosis in some of the diseases, e.g., syphilis. The traditional methods of detection are inexpensive but protracted methods. Microscopy has limited sensitivity in many settings and the interpretation may be subjective. On the other hand, culture runs the risk of contamination with commensal flora and the possibility of reduced viability during transportation. In addition, choice of culture media and interpretation of culture results requires technical skill. The main disadvantage of serology is the requirement of convalescent sera and the occurrence of false-positive results due to cross-reaction with other organisms. The last two decades have seen a switch to molecular methods that offer a growth independent strategy. It is particularly sited for unculturable organisms, e.g., *Treponema pallidum*; difficult to grow organisms, e.g., HIV, HBV, *Bordetella pertussis*; slow growing organism, e.g., *Mycobacterium tuberculosis*; and dangerous to culture organisms, e.g., *Coxiella burnetii*. Molecular methods include the non-amplification methods, e.g., hybridization using probes as well as amplification based methods. The nucleic acid amplification techniques (NAATs) have taken an irreversible position in diagnostics. These include polymerase chain reaction-PCR, transcription based amplification (target amplification), ligase chain reaction-LCR (probe amplification), branch DNA technology (signal amplification) and loop-mediated isothermal amplification-LAMP (isothermal amplification). These methods are known to be sensitive and yield both qualitative and quantitative information of the tested microorganisms. However, these techniques are expensive and require long assay time (Fig. 1).

Among nucleic acid amplification tests, PCR which is most commonly used, can detect a single copy of a target DNA sequence, and thus, can be used to detect a single pathogenic bacterium. It is promising because it detects the organism by amplifying the target rather than the signal, and is therefore less prone to producing false-positives. Thus, PCR detection of pathogens has distinct advantages over culture and other standard as it offers the advantages of specificity, sensitivity, rapidity, accuracy and capacity to detect small amounts of target nucleic acid in a sample [36–41].

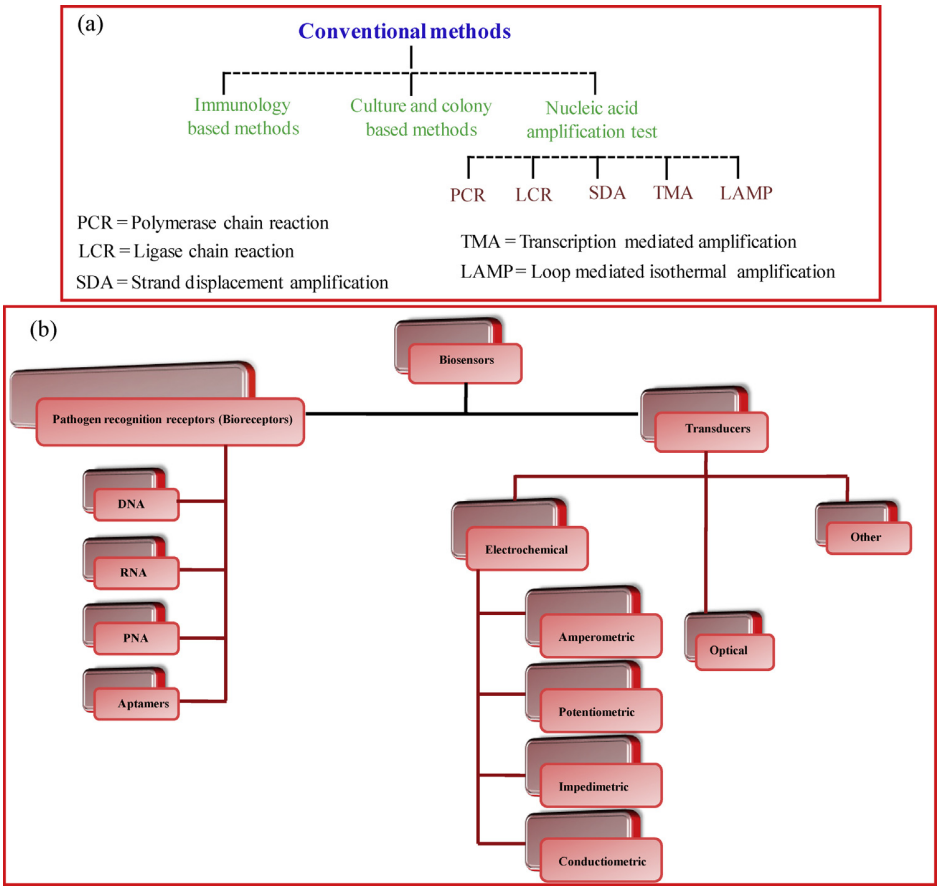


Fig. 1. (a) Different existing conventional methods employed for human pathogen detection. (b) Classification of biosensors.

3. Electrochemical biosensors

A biosensor is a bioanalytical device incorporating a molecular recognition entity associated with or integrated with a physicochemical transducer [5] (Fig. 2). It consists of two main components: a bioreceptor or biorecognition element, which recognizes the target analyte and a transducer, for converting the recognition event into a measurable electrical signal. A bioreceptor

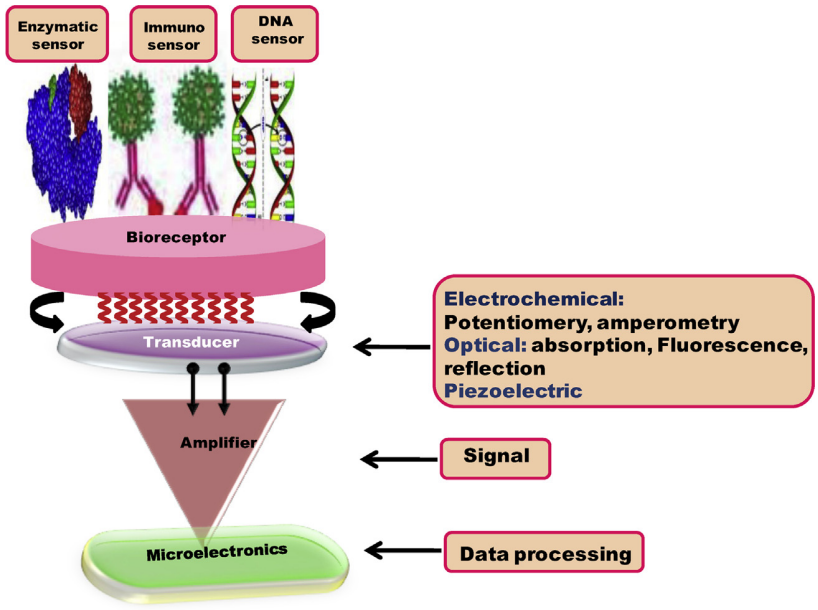


Fig. 2. Biosensors act to convert biological information to an electrical signal through a molecular recognition reaction on a physical transducer.

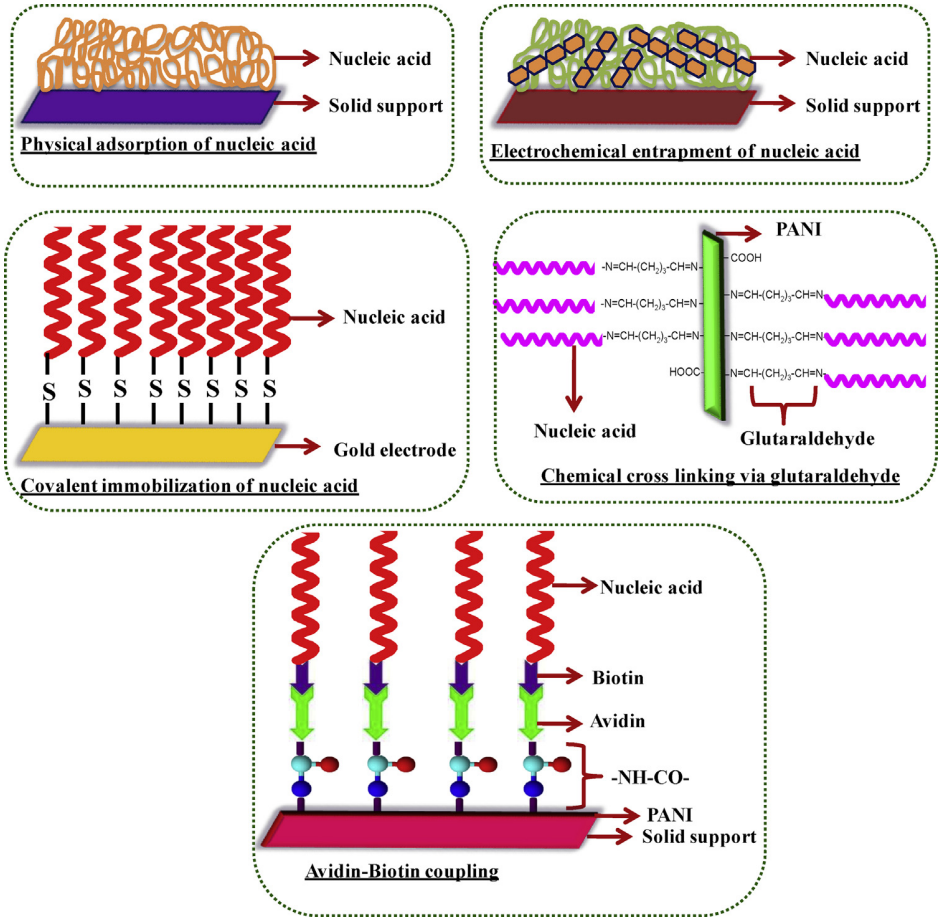


Fig. 3. Schematic showing the immobilization of DNA onto solid support via different immobilization methods.

can be a nucleic acid (DNA, PNA, RNA and aptamer etc.) (Supplementary Figs. 1–4), enzyme, antibody, cell and microorganism etc. [42–45] and the transduction may be electrochemical, optical and piezoelectric. The immobilization of a nucleic acid molecule onto a matrix (Fig. 3) requires complete retention of their biological recognition properties in the active state (Fig. 4a). The desired probes are attached at one terminus onto the surface (Fig. 4b). This allows for the highest degree of thermodynamic freedom that significantly speeds up the hybridization rate. Binding should not occur at the nucleotide bases, since these sites are the target capture sites.

The bioreceptor recognizes the target analyte and the corresponding biological response in turn are converted into equivalent electrical signal by the transducer. The amplifier in the biosensor responds to the small input signal from the transducer and delivers a large output signal that contains the essential features of an input signal. The amplified signal is then processed by the signal processor wherein it can be stored, displayed and analyzed. Biosensors can be classified as point-of-care devices which can bring the capability of analyzing clinical samples at home or at the doctor's office. In order to develop appropriate biosensor technologies, specific markers need to be identified to ensure specificity of the given devices. Biosensors provide advanced platforms for biomarker analysis with the advantages of being easy to use, are inexpensive, rapid and robust and offer multi-analyte testing capability. Biosensors have been widely applied to a variety of analytical problems in medicine, the environment, food, process industries, security and defense [46,47].

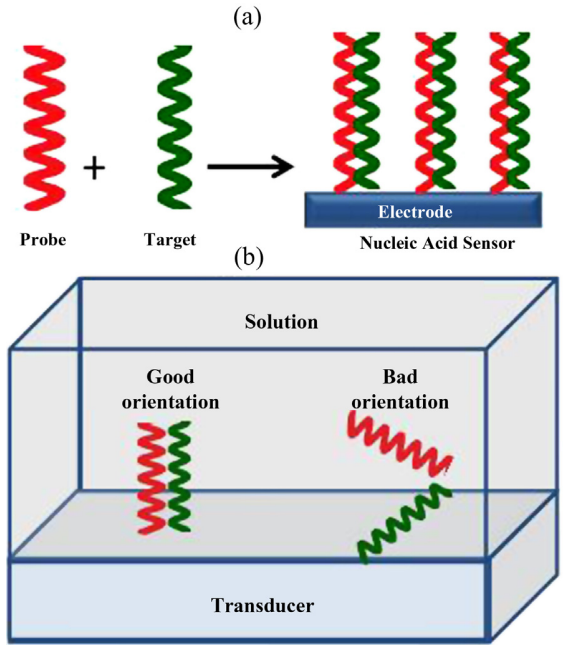


Fig. 4. (a) Schematic showing working principle of a nucleic acid sensor. (b) Illustration of good vs. bad orientation of probes.

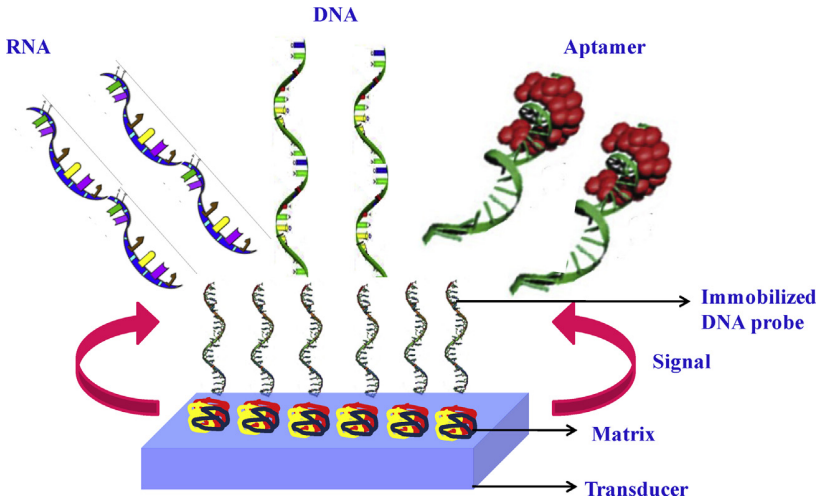


Fig. 5. Schematic exhibits the interaction of different nucleic acid based analytes with the immobilized probe.

Biosensors have broadly been classified into two categories depending on the biorecognition element (bioreceptor) and the method of detection i.e. transducer (Fig. 1b). The biorecognition elements, mainly used in nucleic acid sensors, can be further divided as (i) *DNA*, (ii) *RNA*, (iii) *PNA* and (iv) *Aptamer* [48,49]. Biorecognition elements DNA/RNA/PNA/aptamers nucleic acid fragments rely on either complementary base-pairing between the sensor's nucleic acid sequence and the analyte of interest, or generating nucleic acid structures [50] (Fig. 5).

On the basis of transducing element, biosensors can be categorized as electrochemical, optical, piezoelectric, and thermal sensors. Among the various biosensors, electrochemical biosensors have gained considerable interest as bioanalytical devices and have played an important role in the detection of desired pathogens [51]. They allow high sensitivity, lower detection limits, automation, reduced costs of testing, and development of disposable devices and methodologies capable of working with very small sample volumes. Further, unlike spectroscopy-based techniques, electrochemical sensors are not affected by sample turbidity, quenching, or interference from absorbing and fluorescing compounds, and they require relatively simple instrumentation that is low-power and can be easily miniaturized. Use of electrochemical techniques, over optical and other transduction techniques, exhibits excellent sensitivity and a large linear detection range in a wide range of solvents, electrolytes, temperatures, etc.

3.1. Electrochemical nucleic acid sensors for pathogen detection

Majority of the biosensors used for detection of pathogens are electrochemical in nature. The advantages of electrochemical biosensors include high sensitivity, suitability for microfabrication, and simple instrumentation. Electrochemical detection is commonly employed as a means of investigating the recognition between DNA–DNA, DNA–PNA, DNA–RNA and DNA–aptamers for nucleic acid pathogen detection [52–54]. The electrochemical sensors are based on measurement of changes in current, potential and impedance induced due to biochemical reactions. Electrochemical transducers have been considered as a simple and sensitive method of DNA hybridization detection using affinity of single-stranded DNA for complementary strands for both indirect and direct measurement methods [55–58]. Indirect approaches are based on detection of an electroactive label that may intercalate or associate with a double-stranded DNA. On the other hand, direct methods are label-free and rely mostly on the intrinsic electroactivity of nucleobases. Use of electrochemical impedance spectroscopy [EIS, 59,60] by monitoring both resistance and reactance in a biosensor is becoming more common. Considering the suitability and ease of handling and easy detection, researchers are focusing on electrochemical biosensors for pathogen detection.

3.1.1. Electrochemical nucleic acid sensors for bacterial pathogens detection

Researchers are continuously evaluating several new engineered materials for the fabrication of bioelectrode for bacterial pathogen detection [61,62]. Among them, the thin films of polymers like polyaniline (PANI), nanostructured metal oxides like ZrO_2, self assembled monolayers (SAM) of silanes, carbon nanostructures like carbon nanotubes, fullerene etc. are some of the widely used materials in the present age. Since the biotin–strept(avidin) system has high binding capacity for nucleic acids immobilization due to the high affinity constant ($Ka = 10^{15}\ M^{-1}$) between avidin and biotin, it is also widely used to immobilize nucleic acids on solid support interface to construct biosensors for bacterial detection. Arora et al. have made a significant contribution for the development of voltammetric biosensors utilizing avidin-modified polyaniline (PANI) electrochemically deposited onto a platinum (Pt) disc electrode for direct detection of *E. coli* by immobilizing a 5′-biotin-labelled *E. coli* probe, in the presence of methylene blue as a DNA hybridization indicator (Fig. 6). Depending on the target sample and the sonication time, this biotin immobilized avidin PANI bioelectrode can be utilized to electrochemically detect a complementary target probe (0.009 ng/μL), *E. coli* genomic DNA (0.01 ng/μL) and 11 *E. coli* cells/mL in 60 s to 14 min without using PCR and can be used 5–7 times at temperatures of 30–45 °C. [63]. Shiraishi et al. have observed that the incorporation of fullerene into this polymeric structure dramatically improves the surface coverage of the immobilized probe specific to *E. coli* extracted from 16S rDNA [64]. SAM is considered an ideal method to immobilize the nucleic acid in the construction of biosensors for bacterial detection which provides a convenient and flexible route to generate ultrathin and ordered biological monomolecular films on a variety of substrates by organic molecules (both aliphatic and aromatic) containing free anchor groups such as thiols, disulphides, amines, silanes, or acids. Loaiza et al. have worked on a new approach of the fabrication of SAM of 3,3′-dithiodipropionic acid di(N-succinimidyl ester) (DTSP), which usually used as a spacer, onto gold (Au) disc and immobilized 25-base single-stranded probe specific to *E. coli* lac Z gene. [65]. Pandey

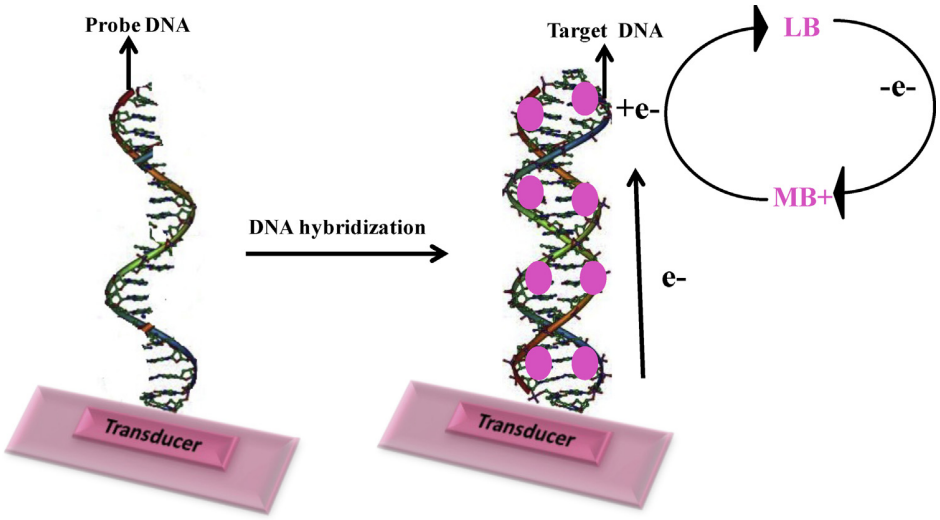


Fig. 6. MB interaction in the DNA hybridization event.

et al. have utilized the SAM platform for the detection of *E. coli* using 1-fluoro-2-nitro-4-azidobenzene modified octadecanethiol SAM and have observed that the fabricated sensor exhibits high sensitivity (0.5×10^{-18} M) and linearity as 0.5×10^{-18}–1×10^{-6} M [66]. However, the SAM immobilization method still suffers from some drawbacks, such as electric field induced and thermal desorption of monolayer and nonspecific adsorption due to high surface energy. Solanki et al. have exploited sol–gel derived nano zirconia (ZrO_2) platform for the detection of *E. coli*. They have immobilized 17-base single stranded (ss) DNA identified from the 16S rRNA coding region of *E. coli*, and utilized this bioelectrode for sensing of *E. coli*. This sensor has shown high selectivity and sensitivity towards hybridization with detection limits of 10^{-6}–10^{6} pM of complementary DNA which may be due to the nanostructured ZrO_2 which provided more surface area [67]. Wu et al. have fabricated a simple signal-off DNA sensor that employs an Exonuclease III-aided target recycling strategy for sequence specific DNA detection with excellent discrimination ability for single-nucleotide polymorphism. A redox mediator, $Ru(NH_3)_6^{3+}$ (RuHex) is electrostatically adsorbed onto signalling probe and provides detection limit as low as 20 fM. [68]. Majid et al. have exploited o-nitro phenol, released from o-nitrophenyl-D-galactopyranose as catalyzed by -galactosidase, a tetramer of *E. coli*, for the detection of *E. coli* contamination in foodstuffs, using a boron doped diamond electrode poised at 0.93 V, without any surface modification. The enzyme is effectively induced by isopropyl-D-thiogalacto-pyranoside with the maximum enzyme activity observed with sodium dodecyl sulfate at 50 °C. A biphasic calibration plot is observed as 4×10^4 to 2×10^5 cells/mL and 2×10^5 to 6×10^6 cells/mL for the first and second region, respectively. The detection limit is 4×10^4 cells/mL with a total analysis time of 1.5 h [69]. The electrochemical impedance studies (EIS) for the monitoring of DNA hybridization have also attracted much attention. This interesting technique allows analysis of interfacial changes originating from biorecognition events at electrode surfaces. Besides this, it offers several advantages such as simplicity, label-free detection, low cost, easy operation and can be miniaturized. Wang et al. have demonstrated a novel biosensor based on ssDNA probe functionalized aluminium anodized oxide (AAO) nanopore membranes for *E. coli* O157:H7 DNA detection via impedimentary. An original and dynamic polymerase-extending DNA hybridization procedure has also been proposed, wherein hybridization occurs in the presence of Taq DNA polymerase and deoxynucleotide triphosphates under controlled reaction temperature [70]. Pandey et al. have reported micro dendritic structural cystine (Cys) modified DNA electrode for detection of *E. coli* that exhibits linear response in the concentration range of 10^{-6} to 10^{-14} M with response time of 30 min [71]. In spite of its convenience, this method has however found limited applications due to low stability and the random orientation of the bio-recognition elements immobilizing on electrodes, resulted in the decrease of the binding. In spite of these interesting developments, these biosensing devices suffer from some drawbacks such as EIS signals resulting from nucleic acid-based impedimetric biosensors are remarkably affected by repulsions between the negatively charged phosphate backbone and redox anions such as $[Fe(CN)_6]^{3-/4-}$ that make the quantification of DNA hybridization reactions rather difficult.

The detection of life threatening, food borne bacterial pathogens, biosensor has been considered as an important tool and presently holds great promise for the diagnosis of diseases. Hence, the researchers are using conducting polymers as a platform due to their unique properties. Food-borne bacterial pathogen *Salmonella Enteritidis* has been detected electrochemically by Zhang et al. who fabricated streptavidin modified nanoporous silicon based biosensor for the detection of biotin modified DNA. The observed results show that the DNA probe is specific to the target DNA, and the porous silicon-based biosensor provides more active surface area and higher sensitivity ($1\ ng\ mL^{-1}$) than the planar silicon based biosensor [72]. Though the biotin–strept(avidin) system is an effective method to immobilize the bio-recognition elements on the surface of solid supports, this method has disadvantages such as the high cost of the reagents involved and the need for a suitable linker layer attached to the electrode. Nandakumar et al. have detected *Salmonella typhimurium* using EIS concentrations in the order of 500 CFU/mL which is lower than infectious pathogen levels [73]. The efforts should be directed for delineating the mechanism of the surface modified semiconductor electrode, especially modified with DNA sequences. At the same time, decreasing the random error during sensor fabrication to confirm the stability of the signal is a key issue.

Foodborne pathogen *Bacillus cereus* has been detected using a conducting polymer as a platform via cyclic voltammetry by Velusamy et al. [74]. The fabricated sensor shows 10^3 CFU/mL detection limit, allowing rapid detection of this bacterial pathogen [75]. This group has electrochemically polymerized a conducting pyrrole with $MgCl_2$ as a doping electrolyte for the specific detection of *B. cereus*. This DNA hybridization biosensor has been found

to have improved selectivity, sensitivity and reproducibility of hybridization events. This method does not require special chemical modification of the DNA and hence can be easily used. The major limitation relates to the physical adsorption of DNA which is weaker than the covalent binding resulting in lower sensitivity [76] An emerging food borne pathogen *Aeromonas hydrophila* has been detected via chronocoulometry and square wave voltammetry (SWV) by Tichoniuk et al. using SAM of thiolated (th) DNA [77].

Sheng et al. have reported PANI based ultrasensitive biosensor for detection of the amplified target syphilis DNA. The current response of PANI is linearly related to target DNA concentration between 1.0 pM and 1.0 nM with a correlation coefficient of 0.998. The detection limit is determined to be as 0.5 pM with the signal-to-noise ratio of 3 [78].

Wang et al. have utilized reduced graphene oxide platform for the fabrication of a highly sensitive and selective nucleic acid sensor for the detection of methicillin-resistant *S. aureus* and observed that the sensor can be used to detect up to 100 fM of target concentration [79]. Castro et al. have developed an electrochemical method, different from the real time-PCR approach, for semi-quantitative evaluation of *L. pneumophila*. A PCR assay targeting the 16S-rRNA gene of *L. pneumophila* giving rise to a 95-mer amplicon has been established. Amplicons have been hybridized with a biotin-labelled reporter sequence and then to a thiolated stem-loop structure immobilized onto gold electrode as a reporter molecule with 1-naphthyl phosphate as a substrate. After 40 cycles of PCR amplification, this methodology has limit of detection (LOD) of 10 genomes, allowing reliable detection of 10^2 genomes of *L. pneumophila* as well as distinguishing 10^3 and 10^4 genomes of the pathogen [80]. Damrow et al. have developed anthrax DNA biosensor for detection of *Bacillus anthracis* using the principle of DNA displacement via amperommetry. They have used "Signal On" transduction method that leads to larger current when hybridization occurs between test sample and the captured probe [81] (Supplementary Fig. 5).

For the detection of life threatening, food borne bacterial pathogens, biosensor has been considered as an important tool and presently holds great promise for the diagnosis of diseases. The researchers have been focusing on conducting polymers as a platform due its unique properties. Prabhakar et al. have reported fabrication of conducting polymer based DNA and PNA based hybridization biosensor for detection of *M. tuberculosis*. The authors have also investigated the effect of various redox indicators on the hybridization events. Compared to Ru complex, MB has been found to have better redox behaviour to capture DNA hybridization. PNA immobilized polypyrrole (PPY) polyvinylsulphonate electrode can be used to detect complementary sequence in heat-shocked genomic DNA and in serum samples, containing genomic *M. tuberculosis* DNA up to 2.5 pg/μl within about 60 s at 30 °C and can be used 8–9 times [82]. The specific interaction between guanines and MB is confirmed by observed linear relationship between the number of guanine bases in the oligonucleotide used to modify the electrode and the amount of charge passed. In another approach, the same group has utilized twenty-base long NH_2-modified DNA and PNA probes specific to *M. tuberculosis*, covalently immobilized onto PANI/Au electrode to detect nucleic acid hybridization. They have shown that PNA-PANI/Au electrode exhibits improved specificity (1000 times) and detection limit of 0.125×10^{-18} M as compared to that of DNA-PANI/Au electrode (2.5×10^{-18} M) [83]. Covalent binding of DNA onto electrode allows enough freedom of motion of the immobilized DNA molecule and enables the control of orientation and hybridization capacity. Though the conducting polymer based sensors exhibit good characteristics. However, there is a greater scope to improve the characteristics of nucleic acid based DNA biosensors for *M. tuberculosis* detection based on nano-structured metal oxides, quantum dots, carbon nanotubes (CNT), graphene etc. In view of the recent revelations and potential applications of CNT-DNA nanobiohybrid, the core–shell structural biowire comprising of CNT and DNA has been fabricated via electrophoretic deposition technique by Das et al. (Supplementary Fig. 6). They have postulated the wrapping mechanism in the light of co-ordination chemistry and have revealed that peripheral wrapping of DNA along the length of CNT in nanoscale may act as a single nanowire enhancing the electron transport capability. These Mg^{2+} ions assisted core (CNT)–shell (DNA) complexes have implications towards the fabrication of novel nano-biochips and ultrasensitive biomolecular electronic systems that are likely to revolutionize the emerging field of genotronics [84].

The nanostructured metal oxides and their composites are of utmost research interest. In recent years emphasis has been given to the synthesis of nanostructured metal oxides and carbon nanostructures composite to enhance the surface coverage, electrical and mechanical properties which can be used in fields like medical diagnosis. Considering the synergy between biocompatible ZrO_2 and electrochemically superior CNT, ZrO_2 grafted CNTs (crystallite size of ZrO_2 ~28.63 nm), obtained via isothermal hydrolysis of zirconium oxychloride in presence of CNT, have been electrophoretically deposited onto indium tin oxide (ITO) substrate and used for the immobilization of ssDNA specific to *M. Tuberculosis* [85] (Supplementary Fig. 7) by Das et al. EIS studies indicate ~3.5 fold enhancement in charge transfer behaviour of NanoZrO_2-CNT/ITO electrode compared to that of NanoZrO_2/ITO electrode and bioelectrode is able to detect 1×10^{-8} mM of target DNA concentration.

Sexually transmitted diseases (STD) currently represent a major public health problem in the world and the advent of human immunodeficiency virus infection during the last decade has highlighted the importance of its rapid, easy, cost-effective way of detection. Singh et al. have fabricated STD (Gonorrhoea) sensor based on nucleic acid probe (from *Opa*, a multi-copy gene of *N. gonorrhoeae*) functionalized using avidin–biotin as cross-linking agent onto PANI matrix. This DNA functionalized electrode can be used to specifically detect up to 0.5×10^{-15} M of complementary target within 60 s of hybridization time at 25 °C by DPV using MB [86]. In order to amplify the detection signal and achieve lower detection limits, the main interaction signal may be enhanced by the incorporation of multi walled carbon nanotubes (MWCNT) that provide conducting channels facilitating faster charge transfer via electrons from one polymer chain to the other and finally to the electrode surface. Singh et al. incorporated MWCNT into PANI matrix and utilized it as a platform for the immobilization of 5′ amino-labelled probe specific to *N. gonorrhoeae*. The DPV studies have revealed that this sensor can selectively detect complementary DNA concentration up to a lower detection limit of 1.2×10^{-17} M [4].

Singh et al. have recently utilized chitosan (CH)–iron oxide (Fe_3O_4) nanobiocomposite for the detection of *N. gonorrhoeae* (Supplementary Fig. 8). It has been found that the presence of Fe_3O_4 nanoparticles (~18 nm) increases the electro-active surface area of the nanobiocomposite that provides desirable environment for loading of DNA with better conformation leading to increased electron transfer kinetics between the medium and electrode. This STD biosensor has been found to have a detection limit (1×10^{-15} M) and a wide dynamic range (from 1×10^{-16} M to 1×10^{-6} M) using the complementary target DNA. In addition, the sensing system has been utilized to accurately discriminate complementary sequence from mis-match sequences [87]. Another species of *Neisseria* has been detected via biosensor by Patel et al. They have fabricated an electrochemical biosensor by immobilizing thiolated ssDNA onto Au coated glass electrode and have shown that it can detect the complementary DNA in the range of 7–42 ng/μl revealing sensitivity as 115.8 μA/ng [88]. This sensor can be used to detect genomic

Table 1
Electrochemical nucleic acid sensors for bacterial pathogen detection.

Matrix	Microorganism detected	Method of immobilization	Measurement conditions	Redox indicator	Detection limit	Detection range	Correlation coefficient	Detection time	Reusability	Technique used	[Reference] (year)
PANI electrochemically deposited onto a Pt disc electrode	*E. coli*	Avidin–biotin coupling	20 μM MB pretreatment in phosphate buffer, 0.05 M, pH 7.0, at 0.1 V pulse height of 50 mV, and pulse width of 70 ms for 10 s, 30–45 °C	MB	Artificial DNA (0.009 ng/μL), *E. coli* genomic DNA (0.01 ng/μL) and *E. coli* cells (11 cells/mL)	0.0064–2.3 ng/μL	–	8–14 min, 60–360 s, 60 s	5–7 times	DPV	[63] (2007)
Fullerene into poly(methyl methacrylate)	*E. coli*	Physical adsorption	0.02 M Tris–HCl buffer, pH 7.0, room temperature (RT)	$(Co(phen)_3)^{3+}$	–	–	–	–	–	DPV	[64] (2007)
DTSP-SAM	*E. coli*	Covalent binding	−0.50 to +0.10 V with amplitude of 30 mV and a step potential of 5 mV at 100 Hz,50 mM Tris–HCl, 20 mM NaCl, pH 7.2, 25 ± 0.5 °C	MB	45 nM	3.1–50.0 ng	0.999	–	10 times	SWV	[65] (2007)
Sol–gel derived Nano ZrO_2	*E. coli*	Electrostatic interaction	PBS, 50 mM, pH 7.0 and 0.7% NaCl, 20 μM MB	MB	10^{-6} pM	10^{-6}–10^{6} pM	0.993	–	–	DPV	[67] (2009)
Au electrode	Sequence-specific DNA	Au–SH bond	10 mM Tris–HCl, 5 M RuHex, pH 7.0, 22–25 °C	$Ru(NH_3)_6^{3+}$	20 fM	20 fM to 50 pM	0.8974	–	–	SWV	[68] (2011)
1-Fluoro-2-nitro-4-azidobenzene modified octadecanethiol SAM	*E. coli*	Covalent binding	PBS 0.05 M, pH 7.0, after pre-incubation in 20 μM MB at +0.1 V for 10 s, 25 °C	MB	0.5×10^{-18} M	0.5×10^{-18} to 1×10^{-6} M	0.99	60 s	10 times	DPV	[66] (2011a)
Boron doped diamond electrode	*E. coli*	Physical adsorption	10 mL, 50 mM phosphate, pH 7, or 50 mM Britton–Robinson, pH 4, buffer, 20 and 50 °C	$[Fe(CN)_6]^{3-/4-}$	4×10^4 cells/mL	4×10^4 and 2×10^5 cells/mL	0.9919	<1.5 h	–	CV	[69] (2008)
AAO nanopore membranes	*E. coli*	Covalent binding	10 mM $[Fe(CN)_6]^{3-/4-}$ in PBS, pH 7.0, 20 V vs. Ag/AgClo by applying 5 mV AC voltage	$[Fe(CN)_6]^{3-/4-}$	0.5 nM	–	–	–	–	CV, EIS	[70] (2009)
Micro dendritic structural cys modified electrode	*E. coli*	Covalent binding	PBS, 50 mM, pH 7.0, 0.9% NaCl containing 1 mM $[Fe(CN)_6]^{3-/4-}$	$[Fe(CN)_6]^{3-/4-}$	10^{-14} M	10^{-6} to 10^{-14} M	0.9916	30 min	4 times	EIS	[71] (2011b)
Nanoporous silicon	*Salmonella Enteritidis*	Physical adsorption	−1.2 V to 1.5 V at a scan rate of 50 mV/s, 5 mM $K_4Fe(CN)_6$ solution with 1 M KCl, 59 °C	$[Fe(CN)_6]^{3-/4-}$	1 ng mL^{-1}	–	–	60 min	–	CV	[72] (2008)
Polypyrrole onto Au electrode	*Bacillus cereus*	Physical adsorption	0.0–0.7 V at a scanning rate of 50 mV/s	–	10^3 CFU/mL	–	–	5 min	–	CV	[74–76] (2010, 2009)
SAM of mercaptoethanol or mercaptohexanol or mercaptononanol	*Aeromonas hydrophila*	Electrostatic interaction	Pulse amplitude of 40 mV, potential step of 1 mV, frequency of 100 Hz	MB	2.5 μg cm^{-3}	1–10 μM	0.99	15 min	–	SWV	[77] (2010)
PANI	*Treponema pallidum*	Au–SH bond	5.0 mM $K_3Fe(CN)_6/K_4Fe(CN)_6$ (1:1), 0.2 M KCl at a bias potential of +195 mV (vs. SCE), frequency range of 10^5 to 10^{-2} Hz	$K_3Fe(CN)_6/K_4Fe(CN)_6$	0.5 pM	1.0 pM and 1.0 nM	0.998	–	–	SWV, EIS	[78] (2010)

Table 1 (*Continued*)

Matrix	Microorganism detected	Method of immobilization	Measurement conditions	Redox indicator	Detection limit	Detection range	Correlation coefficient	Detection time	Reusability	Technique used	[Reference] (year)
Reduced graphene oxide	Methicillin-resistant *S. aureus*	Electrostatic interaction	0.1 Hz to 100,000 Hz in the pH 7.4 phosphate buffer with 5 mV amplitude, RT	$[Fe(CN)_6]^{3-/4-}$	10^{-13} fM	10^{-6} to 10^{-14} M	–	30 min	–	EIS	[79] (2011)
Polycrystalline gold	*Legionella pneumophila*	Physical adsorption	0.5 M Tris–HCl, pH 9.8, 1 mM $MgCl_2$, 20 °C	–	20 nM, 10^2 genomes	2×10^{-10} to 2×10^{-8} M	0.996	2 h	–	DPV	[80] (2009)
PNA as a capture probe onto Au electrode	*Bacillus anthracis*	Au–SH bond	MB, 37 °C	MB	20 nM	0–20 nm		5 h	–	DPV	[81] (2009)
PNA-PPy-PVS/ITO electrode	*Mycobacterium tuberculosis*	Covalent binding	MB at scan rate of 50 mV/s; and Ruthenium complex pretreatment at pulse height: 60 mV, frequency: 150 Hz; in phosphate buffer 0.05 M, pH 7.0, 30 °C	Ru complex, MB	0.1 fmole, 0.1 attomole and 1.0 pmole, 2.5 pg/μl, 1.0 ng/μl	110–0.1 fmole, 12–0.1 attomole, 1 μmole to 0.01 pmole, 200–2.5 pg/μl, 5–0.1 ng/μl	0.99, 0.60, 0.84	30 s, 60 min	8–9 times	CV, SWV	[82] (2008a)
DNA, PNA-PANI/Au electrode	*Mycobacterium tuberculosis*	Covalent binding	MB pretreatment in phosphate buffer 0.05 M, pH 7.0 at Pulse height: 60 mV, frequency: 150 Hz	MB	2.5×10^{-18} mol, 0.125×10^{-18} mole, 5 pg/μl	2.5×10^{-18} to 15.0×10^{-18} mole, 0.125×10^{-18} to 10.0×10^{-18} mole	–	30 s, 60 s	6–7 and 13–15 times	CV, SWV	[83] (2008b)
CNT–DNA core–shell	*Mycobacterium tuberculosis*	Covalent binding	PBS; 0.05 M, pH 7.0, 10 mL 20 μM MB, 30 °C	MB	0.1 nM	0.2 mM to 0.1 nM	0.994	–	–	DPV	[84] (2012)
NanoZrO_2-CNT/ITO electrode	*Mycobacterium tuberculosis*	Electrostatic interaction	$[Fe(CN)_6]^{3-/4-}$ in PBS pH 7.0	$[Fe(CN)_6]^{3-/4-}$	1×10^{-8} mM	1×10^{-2} to 1×10^{-8} mM	0.995	20 min	–	EIS	[85] (2011)
PANI/ITO	*Neisseria gonorrhoeae*	Avidin–biotin coupling	Methylene blue at pulse height of 50 mV, pulse width of 70 ms in 0.05 M phosphate buffer of pH 7.0 containing 0.153 M NaCl, 25 °C	MB	0.5×10^{-15} M	1×10^{-16} to 1×10^{-6} M	0.9974	60 s	10 times	DPV	[86] (2009)
PANI-MWCNT nanocomposite onto ITO electrode	*Neisseria gonorrhoeae*	Covalent binding	Methylene blue at pulse height of 50 mV, pulse width of 70 ms in 0.05 M phosphate buffer of pH 7.0 containing 0.153 M NaCl, 25 °C	MB	1.2×10^{-17} M	1×10^{-17} to 1×10^{-6} M	–	60 s	10 times	DPV	[4] (2010)
CH-Fe_3O_4 nanocomposite onto ITO electrode	*Neisseria gonorrhoeae*	Avidin–biotin coupling	Methylene blue at pulse height of 50 mV, pulse width of 70 ms in 0.05 M phosphate buffer of pH 7.0 containing 0.153 M NaCl, 25 °C	MB	1×10^{-15} M	1×10^{-16} to 1×10^{-6} M	0.99	–	15 times	DPV	[87] (2011)
Thiolated ssDNA onto Au coated glass electrode	*Neisseria meningitis*	Au–SH bond	PBS containing 40 μM MB	MB	–	10–60 ng/μl	0.990	60 s, 5 min		CV	[88] (2010)
Thiolated ssDNA onto Au coated glass electrode	*Neisseria meningitis*	Au–SH bond	50 mM PB, pH 7.0 containing 40 μM MB	MB	–	7–42 ng/μl	0.917	60 s		CV	[89] (2009)

DNA and PCR amplicon up to 10–60 ng/μl revealing sensitivities as 0.0115 μA/ng cm^{-2} and 0.0056 μA/ng cm^{-2}, respectively [89] (Table 1).

3.1.2. Electrochemical nucleic acid sensors for viral pathogens detection

Rapid identification of viruses has important implications for medical healthcare. The presently available methods of detection are mainly based on rapid immunoassay techniques that require trained manpower and are time consuming and expensive. However a biosensor facilitates a doctor to identify the specific virus quickly and prescribe an appropriate course of treatment. Viruses can be advantageously used for the development of a real-time sensor to rapidly and selectively detect target in a variety of harsh conditions, such as under acidic or basic pH ranges.

Hepatitis B is an infectious illness of the liver caused by the hepatitis B virus (HBV) that affects hominoidea, including humans. Originally known as "serum hepatitis", the disease has caused epidemics in parts of Asia and Africa, and it is endemic in China. About a third of the world population has been infected at one point in their lives including 350 million who are chronic carriers. Hence it is important to diagnose HBV in its early stages. In this context, Ariksoysal et al. have developed a novel assay for voltammetric detection of DNA sequences related to the hepatitis B virus (HBV) genotype on the development of lamivudine resistance by monitoring the oxidation signal of guanine (G). Under optimum conditions, biosensor can be used to detect 457 fmol/mL of target DNA [90]. Kara et al. have developed direct label free electrochemical genosensor with an aim to optimize the effect of probe sequence relative position in an amplicon related to HBV. Hybridization occurs after surface coverage with denatured amplicons followed by identification by using the differences between the responses of G oxidation signals [91]. Li et al. have utilized a novel hybridization indicator, bis(benzimidazole)cadmium(II) dinitrate [Cd(bzim)$_2$(NO$_3$)$_2$], to develop an electrochemical DNA biosensor for detection of a short DNA sequence related to the HBV with the detection range 1.49×10^{-7} M to 1.06×10^{-6} M and detection limit of 8.4×10^{-8} M. The novelty of this sensor lies in the selection of the redox indicator but this DNA biosensor suffers from the narrow detection range [92]. Li et al. have used [Cu(dmp)(H$_2$O)Cl$_2$] (dmp = 2,9-dimethyl-1,10-phenanthroline) as a redox indicator to improve the detection limit (7.0×10^{-8} M) for the HBV detection. [93]. Ding et al. have exploited 2,9-dimethyl-1,10-phenantroline cobalt [Co(dmp)(H$_2$O)(NO$_3$)$_2$] as redox indicator and studied its interaction with DNA. Under the optimum conditions, the electrical signal exhibits a linear relationship with the concentration of target DNA ranging from 3.96×10^{-7} to 1.32×10^{-6} M, and the detection limit is 1.94×10^{-8} M [94]. Niu et al. have detected HBV virus following the same DNA hybridization principle but with different redox indicator such as rutin–Cu complex. It has been revealed that the target DNA for coliform virus gene can be quantified and ranges from 1.62×10^{-8} mol L^{-1} to 8.10×10^{-7} mol L^{-1} with a good linearity and a detection limit of 2.3×10^{-9} mol L^{-1} [95]. Zhang et al. have utilized the complex diaquabis[N-(2-pyridinylmethyl) benzamide-k^2 N,O]-cadmium(II) dinitrate {[CdL$_2$(H$_2$O)$_2$](NO$_3$)$_2$, wherein L = N-(2-pyridinylmethyl) benzamide}, as a electroactive indicator for voltammetric detection of HBV. They have observed that the target HBV DNA can selectively detect HBV from 1.01×10^{-8} to 1.62×10^{-6} mol L^{-1} with good linearity with detection limit of 7.19×10^{-9} mol L^{-1} [96].

Hepatitis C is an infectious disease affecting primarily the liver, caused by the hepatitis C virus (HCV). The infection is often asymptomatic, but chronic infection can lead to scarring of the liver and ultimately to cirrhosis, which is generally apparent after many years. In some cases, those with cirrhosis likely to result in liver failure, liver cancer or life-threatening esophageal and gastric varices. Riccardi et al. have demonstrated an electrochemical transduction scheme for the detection of HCV. However, this sensor takes much longer time (10 min) for the hybridization to occur [97]. Pournaghi-Azar et al. have detected the HCV virus using DPV monitoring of G signal revealing 6.5 nM detection limit [98].

Liu et al. have developed a new electrochemical approach for qualitative and quantitative detection of HCV based on the site-specific DNA cleavage of BamHI endonuclease. The difference in the peak current varies linearly with the concentration of target DNA ranging from 0.1 to 2.5 μM. [99]. Hejazi et al. have developed Au electrode modified with a SAM composed of PNA probe and 6-mercaptohexanol (MCH) for detection of short sequences of HCV and found the detection limit as 5.7×10^{-11} M [100].

Human immunodeficiency virus (HIV) is known to be an important virus that is known to affect humans. HIV is a lentivirus that causes the acquired immunodeficiency syndrome which is a condition in humans in which progressive failure of the immune system allows life-threatening opportunistic infections and cancers to thrive. The early detection of HIV is very important to manage the disease and prevent the spreading of the disease effectively. In this context, nanomaterials and their composites have been found to provide interesting platform for the fabrication of nucleic acid based biosensors for HIV detection. An ultra-trace voltammetric method has been developed by Wang et al. for the detection of HIV-1. CNT loaded with silver nanoparticles, placed on a gold microelectrode, have been used as a matrix for immobilization of 21-mer ssDNA. The detection range varies from 1.0 to 100 pM with the detection limit of 0.5 pM [101]. Haseen et al. have fabricated streptavidin modified magnetic nanoparticles based DNA biosensor for detection of HBV. A layer of functionalized nanoparticles is directly immobilized onto bare Au electrode using a magnet. Non-faradic impedance spectroscopy technique can be used to detect 50 pmol of HBV DNA and 160 pmol of HIV DNA on sample of 20 μL [102]. Tran et al. have fabricated CH/Fe_3O_4 nanobiocomposite-based platform for electrochemical HIV-1 detection. Suitable microenvironment provided by Fe_3O_4 nanoparticles contributes to higher electron transfer and enhanced sensitivity. This electrode has a low detection limit (50 pM), acceptable stability and good reproducibility [41]. MWCNT have been used as a platform by Tam et al. for the detection of another pathogenic virus known as influenza virus. The results show that the DNA sensor can detect as low as 0.5 nM of the target DNA samples. This method has a longer response time of ~4 min [103]. Chen et al. have demonstrated an ultrasensitive electrochemical biosensor for the detection of influenza A virus based on glucose oxidase (GOx)-catalyzed deposition of copper hexacyanoferrate (CuHCF) nanoparticles. The detection limit of 1.0 fM has been assigned to the high sensitivity of DPV technique, high catalytic activity of GOx, and the cumulative nature of the formation of the CuHCF nanoparticles catalyzed by GOx attached to the hybridized DNA. This sensor has linearity of 1.0 fM to 10 pM and a detection limit of 1.0 fM [104]. Fan et al. have developed a facile ethanolamine/glucose mixed solution route for the controllable synthesis of cadmium selenide (CdSe) hollow nanostructures and consequently used it for the fabrication of electrochemical DNA sensor for Avian Influenza Virus (AIV) detection [105]. AIV can be detected using MWCNT–cobalt phthalocyanine (CoPc) nanocomposite and poly (amidoamine) (PAMAM) dendrimer as a platform onto glassy carbon electrode (GCE). This nucleic acid sensor is based on oxidation signals of guanine without any external labels and can be used to detect from 0.01 to 500 ng mL^{-1} with a detection limit of 1.0 pg/mL [106].

Zari et al. have fabricated thssDNA immobilized screen printed electrode (SPE) for the detection of short DNA fragments specific to the human papilloma virus (HPV) followed by hybridization. They have utilized guanine oxidation signal to detect the hybridization phenomena by treating DNA with 0.5 M chloridric acid and

Table 2
Electrochemical nucleic acid sensors for viral pathogen detection.

Matrix	Method of immobilization	Measurement conditions	Microorganism detected	Redox indicator	Detection limit	Detection range	Correlation coefficient	Detection time	Technique used	[Reference] (year)
Pencil graphite electrode (PGE)	Physical adsorption	+0.75 and 1.40 V in ABS with 20 mmol L^{-1} NaCl, 25 ± 0.5 °C	Hepatitis B virus	–	457 fmol/mL	–	–	15 min	DPV	[90] (2005)
Amino linked inosine modified capture probes immobilized onto PGE	Electrostatic interaction, covalent binding	2× SSC buffer with amplitude of 10 mV at 20 mV/s scan rate, 25 °C	Hepatitis B virus	–	–	–	–	–	DPV	[91] (2007)
GCE	Covalent binding	CV, −0.40 V to −1.20 V, 60 mV/s DPV, −1.20 V to −0.40 V; pulse pH 50 mV for 60 ms, step height 2 mV, and step time 0.1 s, 40 °C	Hepatitis B virus	bis(benzimidazole) cadmium(II) dinitrate $[Cd(bzim)_2(NO_3)_2]$	8.4×10^{-8} M	1.49×10^{-7} M to 1.06×10^{-6} M	0.9973	15 min	CV, DPV	[92] (2007a)
GCE	Covalent binding	0.2 M BR buffer, pH 7.0, 0.1 mM $[Cu(dmp)(H_2O)Cl_2]$ at 60 mV/s, 25 °C	Hepatitis B virus	$[Cu(dmp)(H_2O)Cl_2]$ (dmp = 2,9-dimethyl-1,10-phenanthroline)	7.0×10^{-8} M	8.82×10^{-8} to 8.82×10^{-7}M	0.9937	–	DPV	[93] (2007b)
GCE	Covalent binding	CV, −0.20 V to −0.40 V, 0.10 V s^{-1} DPV, −0.20 V to 0.40 V, amplitude 0.05 V, 25 °C	Hepatitis B virus	2,9-Dimethyl-1,10-phenantroline cobalt $[Co(dmp)(H_2O)(NO_3)_2]$	1.94×10^{-8} M	3.96×10^{-7} to 1.32×10^{-6} M	0.9951	–	CV, DPV	[94] (2008)
GCE	Covalent binding	0.2 mol L^{-1} B-R buffer solution, pH 4.0; potential scan from 0.2 V to −0.4 V at the scan rate of 0.1 V s^{-1}	Hepatitis B virus	Rutin–Cu complex	2.3×10^{-9} mol L^{-1}	1.62×10^{-8} mol L^{-1} to 8.10×10^{-7} mol L^{-1}	0.9989	5 min	DPV	[95] (2009)
GCE	Covalent binding	50 mmol L^{-1} PBS, pH 7.4; 0.2 mol L^{-1} NaAc-HAc media, pH 7.02, $[CdL_2]^{2+}$, −0.4 to −1.1 V	Hepatitis B virus	Diaquabis[N-(2-pyridinylmethyl) benzamide-k^2 N,O]-cadmium(II) dinitrate $\{[CdL_2(H_2O)_2](NO_3)_2$, wherein L = N-(2-pyridinylmethyl) benzamide$\}$	7.19×10^{-9} mol L^{-1}	1.01×10^{-8} to 1.62×10^{-6} mol L^{-1}	0.9962	–	DPV	[96] (2007)
PPy film deposited at microelectrodes	Electrostatic interaction	0.1 mol L^{-1} Tris–HCl buffer pH 7.2	Hepatitis C virus	$[Cu(dmp)(H_2O)Cl_2]$ (dmp = 2,9-dimethyl-1,10-phenanthroline)	1.0×10^{-15} mol L^{-1}	–	–	10 min	CV	[97] (2006)
20-mer DNA containing 2 guanine and 11 cytosine bases as probe onto PGE	Covalent binding	20 mM Tris–HCl buffer, pH 7.00; potential 0.50 to 1.2 V at a pulse amplitude of 25 mV	Hepatitis C virus	2,9-Dimethyl-1,10-phenantroline cobalt $[Co(dmp)(H_2O)(NO_3)_2]$	6.5 nM	0.05–0.75 μM	0.999	15 min	DPV	[98] (2009)
Thionine-labelled probe DNA self-assembled onto Au electrode	Au–SH bond	0.1 M acetate buffer, pH 5 at 50 mV/s	Hepatitis C virus	Thionine	0.1 μM	0.1–2.5 μM	0.999	–	CV	[99] (2009)
PNA SAM and 6-MCH onto Au electrode	Covalent binding	20 mM Tris–HCl buffer, pH 7.0, 20 mM NaCl and potential 0.10 to −0.50 V at a pulse amplitude of 25 mV, 85–90 °C	Hepatitis C virus	MB	5.7×10^{-11} M	1–50 nM	0.999	2 min	DPV	[100] (2010)

Table 2 (*Continued*)

Matrix	Method of immobilization	Measurement conditions	Microorganism detected	Redox indicator	Detection limit	Detection range	Correlation coefficient	Detection time	Technique used	[Reference] (year)
CNT loaded with silver nanoparticles	Au–SH bond	0.10 M PBS, pH 7.4, pulse amplitude, 20 mV; pulse width, 60 ms; scan rate, 20 mV/s, RT	HIV-1	–	0.5 pM	1.0×10^{-12} to 1.0×10^{-10} M	0.9956	60 min	DPV	[101] (2011)
Streptavidin modified magnetic nanoparticles onto Au electrode	Streptavidin–biotin coupling	PBS buffer pH 7; frequency range between 100 mHz and 100 kHz under a potential value of −300 mV, RT	HIV	$[Fe(CN)_6]^{4-/3-}$	50 pmol of HBV DNA and 160 pmol of HIV DNA	2.53 nmol/mL to 50.6 nmol/mL	–	–	EIS	[102] (2008)
CH/Fe_3O_4 nanobio-composite onto SPE	Covalent binding	CV: scan rate: 50 mV/s; potential range: −0.5 V ∓ 0.2 V vs. SCE. SWV: frequency: 12.5 Hz; start potential: −0.6 V; end potential: +0.4 V; step: 8 mV; amplitude: 25 mV EIS: frequency range from 200 kHz to 10 mHz using 5 mV	HIV-1	MB	50 pM	50–300 pM	–	–	EIS, SWV	[41] (2011)
MWCNT onto SiO_2 grown Si wafer	Covalent binding	PBS, pH 7.5	HIV	–	0.5 nM	1 and 10 nM	–	4 min	EIS	[103] (2009)
CuHCF nanoparticles onto Au electrode	Avidin–biotin coupling	Potential, 4 mV–1.0 V; step potential, 4 mV; amplitude, 50 mV; pulse, 0.05 s; and pulse period, 0.2 s; electrolyte solution, 0.10 M KNO_3, RT	HIV	–	1.0 fM	1.0 fM to 10 pM	0.98	2 h	DPV	[104] (2010)
CdSe hollow nanostructures onto GCE	Physical adsorption	B–R buffer, pH 7.0, containing 2.0×10^{-5} mol L^{-1} MB with 0.02 mol L^{-1} NaCl, Scan rate 50 mV/s, 40 °C	AIV	MB	1.0×10^{-12} mol L^{-1}	–	–	60 min	DPV	[105] (2010)
(MWNTs–CoPc) and PAMAM	Covalent binding	TBS (20 mM Tris–HCl buffer solution), pH 7.0, 20 mM NaCl +0.30 to +1.20 V pulse amplitude 0.1 V, pulse width 0.05 s, and pulse period 0.2 s	AIV	–	1.0 pg/mL	0.01–500 ng mL^{-1}	0.998	20 min	DPV	[106] (2009)
ThssDNA immobilized SPE Au electrode	Au–SH bond	0.25 M acetate buffer pH5.8, potential 0.6 V, frequency 25 Hz, amplitude 40 mV, and step potential 5 mV, RT	Human papilloma virus (HPV)	–	2 pg mL^{-1}	0.5–5 ng. mL^{-1}	0.998	5 min	SWV	[107] (2009)
ThssDNA immobilized SPE Au electrode	Au–SH bond	PBS pH 7.4, 2 steps at 0 V for 1 ms and −0.2 V for 0.5 s, RT	HPV	TMB	10 nM	0.1–50 nM	0.999	1 h	Steps and sweeps technique	[108] (2010)
AuNPs and two-component oligonucleotide-modified MBs	Covalent binding		HTLV-I, HTLV-II	–	1.71×10^{-12} M for T_1-DNA and 1.55×10^{-12} M for T_2-DNA	4.4×10^{-11} to 2.0×10^{-9} M	0.9955 and 0.9975	–	DPV	[109] (2009)

the acid-released purine bases can be detected using SWV. Under optimal conditions, this sensor has a good calibration range of target DNA sequence with detection limit of 2 pg mL^{-1}, but suffers from its reusability. As guanine oxidation is monitored, the electrode can be used only once [107]. Civit et al. reported in 2010, a proof-of-concept of an electrochemical genosensor array for the simultaneous detection of two HPV types, HPV16E7p and HPV45E6 sequences. The detection limit obtained is in the pM range that is sufficient for majority of real RNA/DNA samples obtained from PCR amplification [108]. Zhang et al. have developed a sensitive label-free bio-barcode assay for quantitative detection, based on the redox activity of G and adenine (A) nucleobases, of two nucleic acid targets Human T-lymphotropic virus (HTLV-I and HTLV-II) simultaneously This DNA biosensor based on two-component oligonucleotide-modified Au nanoparticles (NPs) and two-component oligonucleotide-modified magnetic beads (MBs). On release of the adsorbed thiolated barcode DNA strands (poly A and poly G) from the AuNPs surface with dithiothreitol and acidic dipurinization, the electrochemical measurements can be directly performed. It has been observed that the sensor can detect target sequences in the range from 4.4×10^{-11} to 2.0×10^{-9} M, and the detection limit is estimated 1.71×10^{-12} M for T_1-DNA and 1.55×10^{-12} M for T_2-DNA [109] (Table 2).

4. Optical nucleic acid sensors for bacterial and viral pathogens detection

Optical transducers are particularly attractive for application to direct (label-free) detection of bacteria [110]. Among these, surface plasmon resonance (SPR) sensors based on reflectance spectroscopy are in the advent of current science. In SPR measurements resonance angle is very sensitive to the change in refractive index and hence it can be exploited for sensor application. The SPR shift in millidegrees, due to the change in refractive index, is used as the response to quantify the binding of the macromolecules at the sensor surface. These types of sensors can be used to detect minute changes in the refractive index where biomolecules bind with the receptors immobilized on the optical transducer surface.

Prabhakar et al. have reported cysteine modified NH_2-end PNA and 5′-thiol end labelled DNA based for detection of *Mycobacterium tuberculosis* using SPR technique (Fig. 7). The PNA/Au bioelectrode shows improved detection limit (1.0 ng mL^{-1}) over the DNA-Au bioelectrode (3.0 ng mL^{-1}). The values of the association (*k*a) and dissociation rate constant (*k*d) for the complementary sequence in case of the PNA/Au bioelectrode have been estimated to be as 8.5×10^4 m^{-1} s^{-1} and 3.6×10^{-3} s^{-1}, respectively [111]. Cheong et al. have reported a microfluidic chip using the longitudinal resonance of Au nanorods that transforms near infrared energy into thermal energy. The resulting heat causes pathogen lysis. Consequently, the DNA can be extracted out of the cell body and transferred to the PCR system. Two different Au rods AR 3 and AR 15 exhibit efficient lysis of *E. coli* cells and quick pathogen detection by real-time PCR using SYBR Green I without any optical hindrance (Ct values, 21.60 and 22.07 respectively). When a different Taq polymerase is used without hot start, they have obtained better Ct values (17.31 and 18.67 for AR 3 and 15 respectively) with the Au nanorods, suggesting that Au nanorods are also compatible with different Taq polymerases. This has led to successful demonstration of a one step real-time PCR system for pathogen detection without removal or changing of reagents [112]. Bai et al. have demonstrated an SPR biosensor using biotinylated aptamers immobilized on the gold surface coated with streptavidin via streptavidin–biotin binding. They observed an increase in the refraction index when immobilized aptamers captured AIV H5N1 in a sample solution and it was linearly related ($R^2 = 0.99$) to the concentration of AIV in the range of 0.128 to 1.28 HAU. Negligible signal (<4% of H5N1) has been observed from six non-target AIV subtypes. The AIV H5N1 in poultry swab samples with concentrations of 0.128 to 12.8 HAU could be detected using this aptasensor in 1.5 h [113].

Drinking water is usually contaminated with pathogens and their toxins; hence biosensors aimed at detecting these pathogens would be highly expedient. Baeumner et al., have developed a highly sensitive and specific RNA biosensor for the rapid detection of viable *E. coli* as an indicator organism in water that can detect as few as 40 viable *E. coli* in water [114]. The same group has developed quantitative and highly sensitive, yet simple and rapid, biosensor system for the detection of nucleic acid sequences [115]. Wang et al. have proposed a method that allows for the simultaneous, real-time discrimination of *S. aureus*, *P. aeruginosa*, *C. tetani* and *C. perfringens* in mixed bacterial infections. Moreover, this method has a specificity equivalent to bacterial culture based methods and allows for the semi-quantitative assessment of multiple bacteria, which is helpful for the clinical diagnosis and follow-up treatment [116]. Zuo et al. used a simple strategy to integrate the aptamer-functionalized GO biosensor in the microfluidic biochip through the novel use of the porous chromatography paper as a simple 3D storage substrate for the aptamer-functionalized GO nano-biosensor in microwells. This approach detects pathogen microorganisms directly, without cumbersome sample preparation procedures, making it feasible for field detection [117] (Table 3).

5. Other nucleic acid sensors for bacterial and viral pathogens detection

Many other techniques have been reported for pathogen detection. In this context, Chua et al. have fabricated the glass fibre-based lateral flow DNA biosensor that uses capture reagents coupled to carrier beads and detector reagent bioconjugated to AuNps, for the detection of foodborne pathogen, *Vibrio cholerae*. The DNA biosensor contains a test line that captures the target PCR amplicons, an internal amplification control (IC) line which captures IC amplicons and a control line that acts as membrane control to validate the functionality of this device. The test line captures biotin labelled DNA, while the IC line captures digoxigenin labelled DNA. The detector reagent recognizes the fluorescein haptens of the amplified DNA and produces visual red lines. This DNA biosensor has LOD of 5 ng of target DNA. A clinical evaluation was carried out with 174 strains of *V. cholerae* and non *V. cholerae* bacteria and the DNA biosensor recorded 100% for both sensitivity and specificity. It is thus a viable alternative to agarose gel analysis and is easy-to-use, disposable [118]. Hao et al. have developed a quartz crystal microbalance (QCM) biosensor to detect *B. anthracis* based on the recognition of its specific DNA sequences, i.e., the 168 bp fragment of the Ba813 gene in chromosomes and the 340 bp fragment of the PAG gene in plasmid pXO1 via thssDNA immobilization onto Au QCM electrode to hybridize with the target ssDNA sequence obtained by asymmetric PCR (Fig. 8). To amplify the signal, a thiol-DNA fragment complementary to the other end of the target DNA was functionalized with AuNPs. The LOD reached 3.5×10^2 CFU/mL of *B. anthracis* vegetative cells just after asymmetric PCR amplification, but without culture enrichment [119]. Shen et al. have increased the binding of bacteria to their carbohydrate receptor through bacterial surface binding lectins that significantly enhanced specificity and sensitivity of QCM biosensors [120]. Fletcher et al. have demonstrated a modular biosensor that can rapidly identify sequences associated with the Dengue virus genome. Disruption of the aptamer releases the restriction endonuclease EcoRI from aptamer-mediated inhibition. Active

Table 3
Optical nucleic acid sensors biosensors for bacterial and viral pathogens detection.

Matrix	Microorganism detected	Method of immobilization	Measurement conditions	Type of biosensor	Detection limit	Detection range	Detection time	Correlation coefficient	Reusability	Technique used	[Reference] (year)
PNA/Au bioelectrode DNA-Au bioelectrode	*Mycobacterium tuberculosis*	Au–SH bond	800 s (association phase or nucleic acid hybridization), 25 °C	PNA, DNA biosensor	1.0 ng mL^{-1}, 3.0 ng mL^{-1}	5–50 ng mL^{-1}	600 s	–	8–9 times	SPR	[111] (2008c)
Au nanoparticle	*E. coli*	–	PBS buffer	Optothermal biosensor	10,000 cells μl^{-1}	–	30 s	–	–	Real-time PCR	[112] (2008)
Au surface	AIV H5N1	Avidin–biotin coupling	PBS buffer	Aptasensor	0.128 HAU	0.128–1.28 HAU	1.5 h	0.99	5–7 times	SPR	[113] (2012)
Biotinylated aptamers immobilized on the gold surface	*E. coli*	Physical adsorption	Wavelength 560 nm, potassium phosphate buffer, pH 7.5, RT	RNA biosensor	5 fmol per sample, 40 *E. coli* CFU/mL	5 fmol to 5 pmol, 0 and 1,000,000 CFU/mL	15–20 min	0.9631	-	Reflectometry	[114] (2003)
Liposomes entrapping sulforhodamine B coated with streptavidin, and polyethersulfone membranes with anti-fluorescein antibodies	*E. coli*, *C. parvum* and *B. anthracis*	Avidin–biotin coupling	Wavelength 560 nm, Tris buffer, 42 °C	RNA, DNA biosensor	50 fmol, 10 fmol, 10 fmol	0.1–100,000 fmol	20–30 min	–	–	Fluorescence	[115] (2004)
SPR Au chip	*Pseudomonas aeruginosa*, *Staphylococcus aureus*, *Clostridium tetani* and *Clostridium perfringens*	Au–SH bonding	System buffer, ±0.1 °C at 25–60 °C	SPR based DNA sensor	0.03 nM, 0.02 nM, 0.01 nM, 0.02 nM	0.1–100 nM	15 min	>0.99	>100 times	SPR	[116] (2011)
A PDMS/paper/glass hybrid microfluidic biochip	*Lactobacillus acidophilus*, *Staphylococcus aureus* and *Salmonella enterica*	Covalent binding	Fluorescence intensities, Cy3 optical filters (Ex = 550 nm; Em = 570 nm). 37 °C	Aptamer microfluidic sensor	11.0 CFU/mL, 61 CFU/mL, 800 CFU/mL	9.4–150.0 CFU/mL, –10^4–10^6 CFU/mL, 42.2–675.0 CFU/mL		99.7, 99.5, 99.3	–	Fluorescence	[117] (2013)

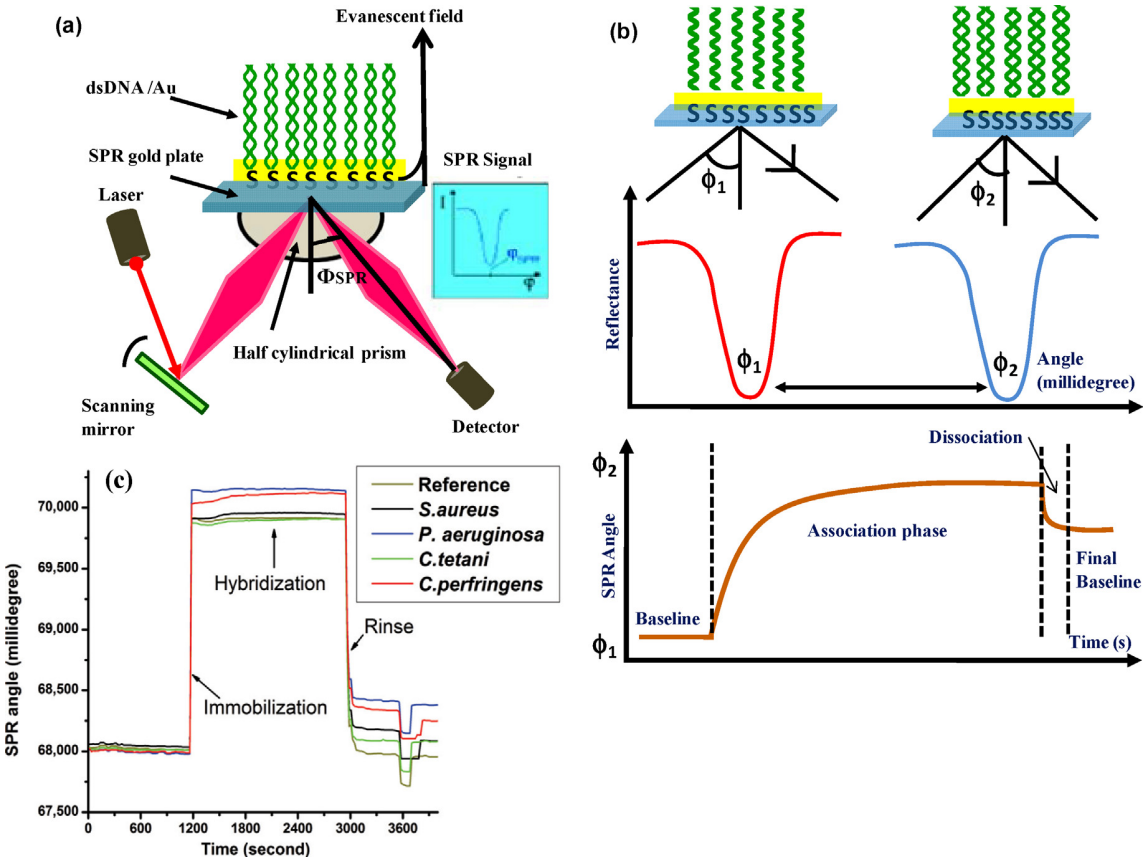


Fig. 7. (a) Principle of surface plasmon resonance measurement and (b) Schematic of change in resonance angle due to binding of target DNA with ssDNA via hybridization. (c) Real-time detection of four bacteria by SPR biosensor [39].

EcoRI can rapidly cleave multiple signalling molecules to generate a detectable signal [121]. Zhang et al. have presented an innovative silicon nanowire (SiNW) based sensor for highly sensitive and rapid detection of RT-PCR product of Dengue serotype 2 (DEN-2). A specific PNA is covalently attached onto the SiNW surface. A complementary fragment of DEN-2 (69 bp) is obtained through one-step RT-PCR amplification, and is applied to the PNA-functionalized SiNW. The hybridization event can be verified by measuring the resistance change of the SiNW before and after binding of the RT-PCR product of DEN-2 to the PNA sequence. It has been found that the SiNW sensor can detect below 10 fM concentration of the amplicons within 30 min [122]. Lin et al. have demonstrated functionalized poly-crystalline silicon nanowire field-effect transistor (FET) based sensor for detection of high pathogenic strain virus (H5 and H7) DNA of AIV. Specific electric changes are observed for AI virus DNA sensing when nanowire surface of poly-SiNW FET is modified with complementary captured DNA probe and target DNA (H5) at fM to pM range could be distinguished [123]. Wu et al. have developed a circulating-flow system for real-time detection of *E. coli* O157:H7 gene eaeA. Synthetic oligonucleotide targets (30 and 104-mer) and PCR-amplified DNA fragments from the *E. coli* O157:H7 eaeA gene (104 bp) have been

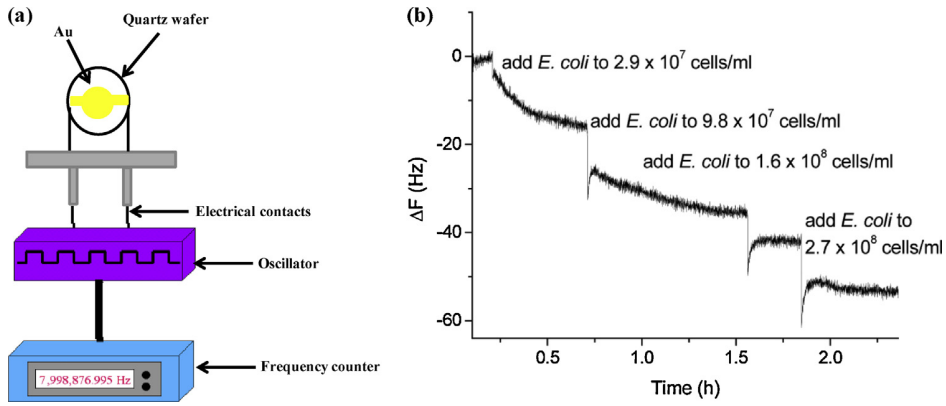


Fig. 8. (a) Schematic of QCM setup. (b) Frequency change vs. time curve when the mannose-QCM electrode was exposed to different concentrations of *E. coli* W1485 [120].

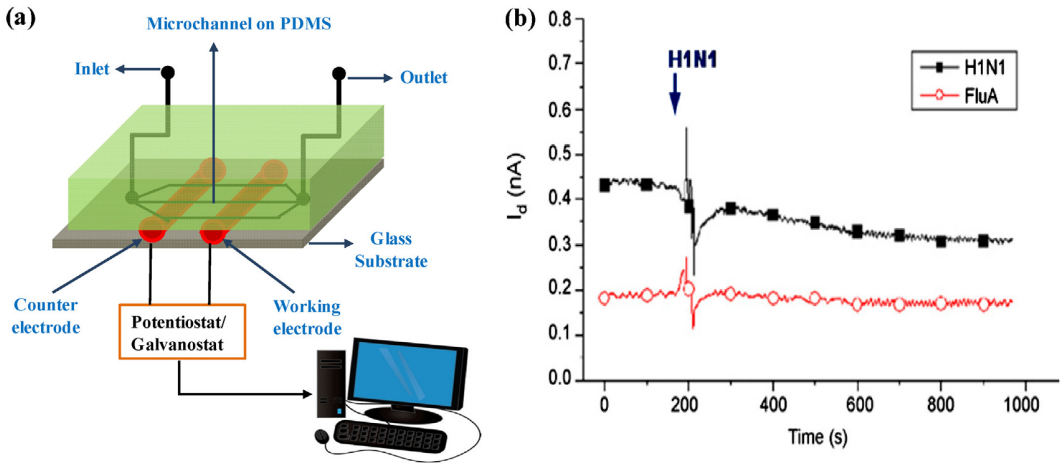


Fig. 9. (a) Schematic of a microfluidic module. (b) Results of the differential measurement from the SiNW biosensor [132].

used for immobilization and hybridization. The addition of 12-dT to the probes as a spacer, significantly enhanced ($P < 0.05$) 1.4- and 2-fold hybridization efficiency when the probes hybridized with 30- and 104-mer targets, respectively [124]. Liu et al. have demonstrated the feasibility of detecting 250 zM *E. coli* O157:H7 *eae*A target DNA by using a magnetic bead-based DNA detection assay with designed labelling strategy within 40–60 min [125]. Schrumpf et al. have developed a new method for the detection of nucleic acid hybridization, based on a simple latex agglutination test that can be evaluated by the unaided eye. In artificially contaminated chicken samples, 3 colony-forming units (CFU)/25 g can be detected in one of three replicates, and 30 CFU/25 g were detected in both replicates when samples for PCR are taken directly from primary enrichment [126].

A microfluidic biosensor [127] comprising of a network of microchannels fabricated in polydimethylsiloxane (PDMS) substrate and super paramagnetic beads are incorporated into the system as a mobile solid support and can be operated under continuous solution flow of up to 80 $\mu L\,min^{-1}$. This assay reduced time up to only 15 min including sample incubation time [128–130].

Roh et al. have developed RNA biosensor for HCV NS3 protein detection. They have previously shown that quantum dots-conjugated RNA oligonucleotide can recognize the HCV NS3 protein specifically and sensitively. At a concentration of 0.01 $\mu g\,mL^{-1}$, 7,8,4′-trihydroxyisoflavone and 6,7,4′-trihydroxyisoflavone showed more than a 30% inhibition activity of a nanoparticle-based RNA oligonucleotide biochip system [131].

A subtype of influenza virus H1N1, has been reported by Kao et al. They have fabricated a silicon based microfluidic device for H1N1 2009 strain vs. the seasonal influenza A strain (Fig. 9). The proposed system includes two functional modules: a multiplexed PCR module for amplification of nucleic acid target and a multiplexed SiNW module for sequence determination. The PCR module consists of a microfluidic PCR chamber and an electrical controller to perform a multiplexed protocol that can simultaneously detect enriched specific segment of both H1N1 and FluA strains, with 10^4–10^5 amplification efficiency. The system has a sensitivity of 20–30 fg/μl for H1N1 and seasonal FluA nucleic acids in a 10 μl sample [132] (Table 4).

6. Challenges and future prospects

The management of pathogen detection using a simple, rapid and cost-effective method presents a major challenge to the biological safety of the world. The field of pathogen detection is nascent and therefore, faces a dynamic set of challenges as the field evolves. One of the major challenges in pathogen detection using electrochemical nucleic acid sensor design is to immobilize biomolecules onto an electrode substrate for effective signal transduction. Detecting pathogens using biosensors is a relatively new concept and many of the techniques discussed, are still in their infancy. Existing pathogen detection methods are time consuming and expensive, and consequently, demand for accurate pathogenic biosensors for rapid detection is increasing. The electrochemical techniques will probably become more popular as microelectronics and microfluidics also progress. Some techniques are restricted due to unsuitability in-field and requirement of highly trained personnel. Many of these methods currently have limitations involving sensor surface formation, reproducibility, renewability and necessary sample preparation. The immense efforts are needed to develop this comprehensive library of core techniques into practical diagnostic applications. The general basis of methods to detect binding pathogenic analytes to specific bioreceptors are available but require refinement and in some cases further miniaturization. With the increasing use of novel nanomaterials, like nano-structured metal oxides, CNTs, grapheme, quantum dots, nano-structured conducting polymers etc., the problem of immobilization of biomolecules to obtain proper signal transduction has been minimized to a greater extent.

The commercial biosensors for pathogen detection are tips of the iceberg compared to the vast literature on academic research. The intrinsic disadvantages (slow response, low sensitivity, and poor selectivity) using bacteria and virus as the biosensing element limit the widespread interest of biosensors for pathogen detection on the market. Fortunately, with the amalgamation of biotechnology, nano-technology, physics, chemistry, electronics, bioengineering and novel immobilization strategy in the past years, biosensors for pathogen detection are becoming more powerful in the field of analytical biochemistry.

The new bioreceptor designs are being evolved to increase both the sensitivity, selectivity and signal amplification of pathogenic sensors. The sensors will become smaller and portable and the resulting costs will reduce, as fewer or new materials are utilized. This will hopefully lead to the production of sensitive, cheap, reliable and rapid detection systems for use in the clinical environment for diagnosis of pathogenic infections. A fruitful fusion between biological sciences and other disciplines will help to realize the full potential of this technology in the future.

Table 4
Other nucleic acid sensors biosensors for bacterial and viral pathogens detection.

Matrix	Microorganism detected	Method of immobilization	Measurement conditions	Type of biosensor	Detection limit	Detection range	Detection time	Technique used	[Reference] (year)
AuNps	*Vibrio cholerae*	Covalent binding	50 μl 10 mM PBS, pH 7.4 with 0.5% Tween-20, 24 °C	Disposable lateral flow-based DNA biosensor	5 ng	1–100 ng	10 min	Glass fibre membrane carrier bead system	[118] (2011)
AuNPs coated QCM electrode	*B. anthracis*	Au–SH bond	0.3 M NaCl, 10 mM PB with pH 7.4, 200 μl/min of buffer, 30 °C	DNA biosensor	3.5×10^2 CFU/mL	3.5×10^2 to 3.5×10^7 CFU/mL	30 min	QCM	[119] (2011)
Au-Mannose SAM	*E. coli*	Au–SH bond	1.0 mL of PBS buffer (pH 7.2) with 1 mM Mn^{2+} and 1 mM Ca^{2+}	Cell based biosensor	Few hundred bacterial cells	7.5×10^2 to 7.5×10^7 cells/mL	–	QCM	[120] (2007)
Dengue serotype target-induced biosensor assay	Dengue virus genome	–	Buffered solution containing the aptamer/EcoRI complex and MBL, 30 °C	Novel modular biosensor	6 pmol	–	20 min	Fluorescence	[121] (2010)
SiNW	Dengue serotype 2	Covalent binding	10 μm PNA in citrate buffer (15 mM sodium citrate, 150 mM NaCl, pH 7.4), RT	PNA biosensor	10 fM	100 fM to 1 fM	30 min	Electrical detection	[122] (2010)
Poly-SiNW-FET	AIV	Cross linking	Bias voltage (VG from 5.0 to 9.0 V with a step of 1.0 V) while sweeping the VD from 0 to 3.0 V in PBS (10 mM, pH 7.0), RT	FET DNA biosensor	1 fM	100 pM to 100 fM	3 min	Electrical detection	[123] (2009)
Au QCM electrode	*E. coli*	Au–SH bond	0.1 Hz, sampling period: 1 s, frequency range: 2–16 MHz, temperature range: 4–60 °C and voltage: 110 V, 50–60 Hz	DNA biosensor	0.5 μM	0–1 μM	30 min	Circulating-flow QCM	[124] (2007)
Magnetic bead with multi-layers quantum dots labelling	*E. coli*	–	20 mM Tris–HCl, pH 7.5, 1.0 M LiCl, 2 mM EDTA, RT	Fluorescence based assay	250 zM	500 zM to 250 zM	40–60 min	QCM	[125] (2008)
Polystyrene beads with PCR DNA product	*Salmonella* spp.	–	10 mM Tris–HCl, pH 8	Multiplex assays	3 CFU/25 g, 30 CFU/25 g	–	7 min		[126] (2007)
PDMS – superparam-agnetic beads	*Bacillus anthracis*, *Cryptosporidium parvum*, *E. coli*, *Dengue viru*	Avidin–biotin coupling	540/25 nm band pass exciter; 620/60 nm band pass emitter, and 100 W mercury illumination source, 10 mM Tris–HCl, 1 mM EDTA, 2 M NaCl, pH 7.5, RT	Microfluidic RNA biosensor	–	–	–	Fluorescence	[128] (2005)
Carboxyl-terminated QDs605	HCV	Covalent binding	Phosphate buffer pH 7.2, RT	Inhibitor screening on a biochip	0.01 $\mu g\,mL^{-1}$	0.1–0.5 $\mu g\,mL^{-1}$	–	Emission wavelength as the optical imaging probe	[131] (2012)
SiNW based microfluidic	Influenza virus H1N1	–	–	DNA based microfluidic system	20–30 fg/μl	50 pg to 2 μg	15–20 min	Electrical detection	[132] (2011)

7. Conclusions

In summary, recent developments in nucleic acid biosensors for pathogen detection have been reviewed. The conventional pathogen detection methods are sensitive but still lag behind the analytical methods due to long response time and decreasing in the response time is a needle in a haystack problem. Electrochemical techniques offer a sensitive approach for direct or multi step measurement for pathogen detection. These methods provide the possibility of simultaneous measurement of various analytes in short time. Besides this, recent developments in nanotechnology and materials science can be advantageously used to obtain engineered and customized nanomaterials that could provide novel platforms for immobilization of biorecognition component that may lead to the development of useful and reliable biosensor devices. And the use of microarray for simultaneous measurement with integrated microfluidic system, molecularly imprinted may provide solution for reliable pathogen detection and in fabrication of smart low cost point-of-care devices. Efforts should be directed towards the synthesis of novel nanomaterials for the fabrication

of electrochemical and other biosensors on a large scale so as to benefit the mankind. With exposure of the commercial market the applications of the biosensor technology can be greatly enhanced and with time, miniaturized biosensor for pathogen detection may become available that could be used near a patient's bedside, a doctor's clinic or even home use.

Acknowledgements

Renu Singh is thankful to Council of Scientific and Industrial Research (CSIR), India for the award of Senior Research Fellowship. We acknowledge the financial support received from Department of Science & Technology (DST) [DST/TSG/ME/2008/18 and GAP-070932], in-house project (OLP-070632D), Department of Biotechnology, Govt. of India (DBT/GAP070832), and Indian Council of Medical Research, India (Grant No. ICMR/5/3/8/91/GM/2010-RHN).

Appendix A. Supplementary data

Supplementary data associated with this article can be found, in the online version, at http://dx.doi.org/10.1016/j.snb.2014.03.005.

References

[1] A.K. Wanekaya, W. Chen, A. Mulchandani, Recent biosensing developments in environmental security, J. Environ. Monit. 10 (2008) 703–712.
[2] M.I. Prodromidis, M.I. Karayannis, Enzyme based amperometric biosensors for food analysis, Electroanalysis 14 (2002) 241–261.
[3] P.J. Conroy, S. Hearty, P. Leonard, R.J. O'Kennedy, Antibody production, design and use for biosensor-based applications, Semin. Cell Dev. Biol. 1 (2009) 10–26.
[4] R. Singh, C. Dhand, G. Sumana, R. Verma, S. Sood, R.K. Gupta, B.D. Malhotra, Polyaniline/carbon nanotubes platform for sexually transmitted disease detection, J. Mol. Recognit. 23 (2010) 472–479.
[5] B.D. Malhotra, A. Chaubey, S.P. Singh, Prospects of conducting polymers in biosensors, Anal. Chim. Acta 18 (2006) 59–74.
[6] J.J. Gooding, Biosensor technology for detecting biological warfare agents: recent progress and future trends, Anal. Chim. Acta 559 (2006) 137–151.
[7] R. Syam, K.J. Davis, M.D. Pratheesh, B.S. Joseph, Biosensors: a novel approach for pathogen detection, VETSCAN 7 (2012).
[8] M.S. Belluzo, M.E. Ribone, C.M. Lagier, Assembling amperometric biosensors for clinical diagnostics, Sensors 8 (2008) 1366–1399.
[9] S. Rodriguez-Mozaza, M.J. López de Aldaa, M.P. Marcob, D. Barceló, Biosensors for environmental monitoring. A global perspective, Talanta 65 (2005) 291–297.
[10] A. Mulchandani, A.S. Bassi, Principles and applications of biosensors for bioprocess monitoring and control, Crit. Rev. Biotechnol. 15 (1995) 105–124.
[11] P. Leonard, St. Hearty, J. Brennan, L. Dunne, J. Quinn, T. Chakraborty, R. O'Kennedy, Advances in biosensors for detection of pathogens in food and water, Enzyme Microb. Technol. 32 (2003) 3–13.
[12] Li. Suiqiong, A. Simonian, B.A. Chin, Sensors for Agriculture and the Food Industry, The Electrochemical Society Interface Winter, 2010.
[13] G. Leegsma-Vogt, M.M. Rhemrev-Boom, R.G. Tiessen, K. Venema, J. Korf, M. Jeffrey, W.G. Halliday, K.C. Taylor, The potential of biosensor technology in clinical monitoring and experimental research, Biomed. Mater. Eng. 14 (2004) 455–464.
[14] S. Cagnin, M. Caraballo, C. Guiducci, P. Martini, M. Ross, M. SantaAna, D. Danley, T. West, G. Lanfranchi, Overview of electrochemical DNA biosensors: new approaches to detect the expression of life, Sensors 9 (2009) 3122–3148.
[15] R. Singh, R. Verma, G. Sumana, A.K. Srivastava, S. Sood, R.K. Gupta, B.D. Malhotra, Nanobiocomposite platform based on polyaniline-iron oxide-carbon nanotubes for bacterial detection, Bioelectrochemistry 86 (2012) 30–37.
[16] R. Singh, Z. Matharu, A.K. Srivastava, S. Sood, R.K. Gupta, B.D. Malhotra, Nanostructured platform for the detection of *Neisseria gonorrhoeae* using electrochemical impedance spectroscopy and differential pulse voltammetry, Microchim. Acta 177 (2012) 201–210.
[17] P.N. Chandra, H.B. Noha, M.S. Wonb, Y.B. Shim, Bioelectrochemistry fundamentals, experimental techniques and applications, Biosens. Bioelectron. 26 (2011) 4442–4449.
[18] S.B. Pieper, S.P. Mestas, K.L. Lear, Z. Zhong, K.F. Reardon, Phosphorescence characteristics of ruthenium complex as an optical transducer for biosensors, Appl. Phys. Lett. 92 (2008) 081915.
[19] Li. Guangjiu, N. Liu, S. Liu, S. Zhang, Electrochemical biosensor based on the interaction between copper (II) complex with 4,5-diazafluorene-9-one and bromine ligands and deoxyribonucleic acid, Electrochim. Acta 53 (2008) 2870–2876.
[20] D. Grieshaber, R. MacKenzie, J. Vörös, E. Reimhu, Electrochemical biosensors – sensor principles and architectures, Sensors 8 (2008) 1400–1458.
[21] H. Fan, P. Ju, S. Ai, Controllable synthesis of CdSe nanostructures with tunable morphology and their application in DNA biosensor of Avian Influenza, Sens. Actuators B 149 (2010) 98–104.
[22] G. García-Martinez, E.A. Bustabad, H. Perrot, C. Gabrielli, B. Bucur, M. Lazerges, D. Rose, Development of a mass sensitive quartz crystal microbalance (QCM)-based DNA biosensor using a 50 MHz electronic oscillator circuit, Sensors 11 (2011) 7656–7664.
[23] P. Tallury, A.L. Malhotra, M. Byrne, S. Santra, Nanobioimaging and sensing of infectious diseases, Adv. Drug Deliv. Rev. 62 (2010) 424–437.
[24] L. Su, W. Jia, C. Hou, Y. Lei, Microbial biosensors: a review, Biosens. Bioelectron. 26 (2011) 1788–1799.
[25] A.M. AbdEl-Malek, S.F.H. Ali, R.H. Moemen, A. Mohamed, K.I. Elsayh, Occurrence of Listeria species in meat, chicken products and human stools in Assiut city, Egypt with PCR use for rapid identification of *Listeria monocytogenes*, Vet. World 3 (2010) 353–359.
[26] E. De Boer, R.R. Beumer, Methodology for detection and typing of foodborne microorganisms, Int. J. Food Microbiol. 50 (1999) 119–130.
[27] Anon, Directorate-General (1999).
[28] K. Silbernagel, R. Jechorek, W.M. Barbour, P. Mrozinski, W. Alejo, V. Aleo, V. Andeloro, F. Beacorn, J. Benzinger, S. Bogar, C. Brayman, J. Broom, M. Carson, C. Carver, C. Cheng, B. Centrella, J. Clayborn, C. Collins, C. Deibel, M. Divine, S.J. Eliasberg, D. Farmer, S. Frye, T. Gatesy, E. Goodstein, C. Halker, G.V. Hall, P. Hanson, G. Hartman, K. Heddaeus, J. Hembree, J. Hutchins, P. Istafanos, J. Jenkins, K. Kerdahi, S. Kremer, A. Lal, S. Leighton, D. Lester, J.H. Lewis, J. Lin, J. Martin, M. Maselli, P. McCarthy, B. McGovern, M. Mills, F. Mohnke, B. Moon, D. Moss, M. Plaza, S. Robeson, H. Romero, D. Rubalcaba, M. Schultz, J. Seehusen, C. Shaw, K. Siem, E. Sloan, J. Stanerson, N. Stepanova, K. Van, K. Enkenvoort, M. Vialpando, W. Warren, K. Watts, K. Wilson, T. Woodruff, Evaluation of the BAX system for detection of *Listeria monocytogenes*, J. AOAC Int. 87 (2004) 395–410.
[29] M.W. Sanderson, G.M. Gay, D.D. Hancock, C.C. Gay, L.K. Fox, T.E. Bess, Sensitivity of bacteriologic culture for detection of *Escherichia coli* O157:H7 in bovine feces, J. Clin. Microbiol. 33 (1995) 2616–2619.
[30] H. Takahashi, B. Kimura, Y. Tanaka, J. Shinozaki, T. Suda, T. Fujii, Real-time PCR and enrichment culture for sensitive detection and enumeration of *Escherichia coli*, J. Microbiol. Methods 79 (2009) 124–127.
[31] S.D. Saroj, R. Shashidhar, M. Karani, J.R. Bandekar, Distribution of *Salmonella* pathogenicity island (SPI)-8 and SPI-10 among different serotypes of *Salmonella*, J. Med. Microbiol. 57 (2008) 424–427.
[32] B.P. Upadhyay, F. Utrarachkij, J. Thongshoob, Y. Mahakunkijcharoen, N. Wongchinda, USDA, Hudson Foods Recalls Beef Burgers Nationwide for *E. coli* O157:H7 (1997) http;//www.fsis.usda.gov/OA/recalls/prelease/pro015-97.html.
[33] M. Magliulo, P. Simoni, M. Guardigli, E. Michelini, M. Luciani, R. Lelli, A rapid multiplexed chemiluminescent immunoassay for the detection of *Escherichia coli* O157:H7, *Yersinia enterocolitica*, *Salmonella typhimurium*, and *Listeria monocytogenes* pathogen bacteria, J. Agric. Food Chem. 55 (2007) 4933–4939.
[34] R.P. Jechorek, R.L. Johnson, Evaluation of the VIDAS staph enterotoxin II (SET 2) immunoassay method for the detection of staphylococcal enterotoxins in selected foods: collaborative study, J. AOAC Int. 91 (2008) 164–173.
[35] I. Hochel, J. Skvor, Characterization of rabbit antibodies for immunochemical detection of *Yersinia enterocolitica*, Folia Microbiol. (Praha) 52 (2007) 511–518.
[36] G. Panicker, M.L. Myers, A.K. Bej, Rapid detection of *Vibrio vulnificus* in shellfish and Gulf of Mexico water by real-time PCR, Appl. Environ. Microbiol. 70 (2004) 498–507.
[37] S.W. Polson, J.L. Higgins, C.M. Woodley, PCR-based assay for the detection of four coral pathogens, in: Proc. of the 11th International Coral Reef Symposium, Ft. Lauderdale, Florida, 8, 2008.
[38] M. Palka-Santini, B.E. Cleven, L. Eichinger, M. Krönke, O. Krut, Large scale multiplex PCR improves pathogen detection by DNA microarrays, BMC Microbiol. 9 (2009).
[39] R. Wang, C. Xue, M. Gao, H. Qi, C. Zhang, Biosensors for environmental monitoring. A global perspective, Microchim. Acta 172 (2011) 291–297.
[40] A.M. Caliendo, Multiplex PCR and emerging technologies for the detection of respiratory pathogens, Clin. Infect. Dis. 52 (2011) S326–S330.
[41] L.D. Tran, B.H. Nguyen, N.V. Hieu, H.V. Tran, H.L. Nguyen, P.X. Nguyen, Electrochemical detection of short HIV sequences on chitosan/Fe_3O_4 nanoparticle based screen printed electrodes, Mater. Sci. Eng. C 31 (2011) 477–485.
[42] J. Wang, PNA biosensors for nucleic acid detection, Curr. Issues Mol. Biol. 2 (1999) 117–122.
[43] J. Wang, DNA biosensors based on peptide nucleic acid (PNA) recognition layers. A review, Biosens. Bioelectron. 13 (1998) 757–762.
[44] K. Kerman, M. Kobayashi, E. Tamiya, Recent trends in electrochemical DNA biosensor technology, Meas. Sci. Technol. 15 (2004) R1.
[45] R.E. Wang, Y. Zhang, J. Cai, W. Cai, T. Gao, Aptamer-based fluorescent biosensors, Curr. Med. Chem. 27 (2011) 4175–4184.
[46] M.I. Pividori, S. Alegret, Electrochemical biosensors for food safety, Contrib. Sci. 2 (2010) 1575–6343.
[47] K. Arora, S. Chand, B.D. Malhotra, Recent developments in bio-molecular electronics technique for food pathogens, Anal. Chim. Acta 568 (2006) 259–274.
[48] S. Song, L. Wang, J. Li, J. Zhao, C. Fan, Aptamer-based biosensors, Trend. Anal. Chem. 27 (2008).

[49] K.M. Song, S. Lee, C. Ban, Aptamers and their biological applications, Sensors 12 (2012) 612–631.
[50] A. Sassolas, B.D. Leca-Bouvier, L.J. Blum, DNA biosensors and microarrays, Chem. Rev. 108 (2008) 109–139.
[51] M. Nayak, A. Kotian, S. Marathe, D. Chakravortty, Detection of microorganisms using biosensors—a smarter way towards detection techniques, Biosens. Bioelectron. 25 (2009) 661–667.
[52] T.G. Drummond, M.G. hill, J.K. barton, Electrochemical DNA sensors, Nat. Biotechnol. 21 (2003) 1192–1199.
[53] E.A. Mothershed, A.M. Whitney, Nucleic acid-based methods for the detection of bacterial pathogens: present and future considerations for the clinical laboratory, Clin. Chim. Acta 363 (2006) 206–220.
[54] S. Girousi, S. Karastogianni, C. Serpi, Innovative configurations of electrochemical DNA biosensors (a review), Sens. Electroanal. 6 (2011) 65–87.
[55] M. Mascini, F. Lucarelli, I. Paichetti, G. Marrazza, Y. Zhou, S. Xu, Electrochemical application of DNA biosensors, Int. Conf. Sens. Technol. 4414 (2001) 0277–786.
[56] J.J. Gooding, Electrochemical DNA hybridization biosensors, Electroanalysis 14 (2002) 1149–1156.
[57] F. Lucarelli, S. Tombelli, M. Minunni, G. Marrazza, M. Mascini, Electrochemical and piezoelectric DNA biosensors for hybridisation detection, Anal. Chim. Acta 609 (2008) 139–159.
[58] P. He, Y. Xu, Y. Fang, A review: electrochemical DNA biosensors for sequence recognition, Anal. Lett. 38 (2005) 2597–2623.
[59] Y. Wang, Z. Ye, Y. Ying, New trends in impedimetric biosensors for the detection of foodborne pathogenic bacteria, Sensors 12 (2012) 3449–3471.
[60] L. Yang, R. Bashir, Electrical/electrochemical impedance for rapid detection of foodborne pathogenic bacteria, Biotechnol. Adv. 26 (2008) 135–150.
[61] D.H. Yu, B. Blankert, J.C. Vire, J.M. Kauffmann, Biosensors in drug discovery and drug analysis, Anal. Lett. 38 (2005) 1687–1701.
[62] J.C. Liao, M. Mastali, Y. Li, V. Gau, M.A. Suchard, J. Babbitt, J. Gornbein, E.M. Landaw, E.R. McCabe, B.M. Churchill, D.A. Haake, Development of an advanced electrochemical DNA biosensor for bacterial pathogen detection, J. Mol. Diagn. 9 (2007) 158–168.
[63] K. Arora, N. Prabhakar, S. Chand, B.D. Malhotra, *Escherichia coli* genosensor based on polyaniline, Anal. Chem. 79 (2007) 6152–6158.
[64] H. Shiraishi, T. Itoh, H. Hayashi, K. Takagi, M. Sakane, T. Mori, J. Wang, Electrochemical detection of *E. coli* 16S rDNA sequence using air-plasma-activated fullerene-impregnated screen printed electrodes, Bioelectrochemistry 70 (2007) 481–487.
[65] Ó.A. Loaiza, S. Campuzano, M. Pedrero, J.M. Pingarrón, DNA sensor based on an *Escherichia coli* lac Z gene probe immobilization at self-assembled monolayers-modified gold electrodes, Talanta 73 (2007) 838–844.
[66] C.M. Pandey, R. Singh, G. Sumana, M.K. Pandey, B.D. Malhotra, Electrochemical genosensor based on modified octadecanethiol self-assembled monolayer for *Escherichia coli* detection, Sens. Actuators B 151 (2011) 333–340.
[67] P.R. Solanki, A. Kaushik, P.M. Chavhan, S.N. Maheshwari, B.D. Malhotra, Nanostructured zirconium oxide based genosensor for *Escherichia coli* detection, Electrochem. Commun. 11 (2009) 2272–2277.
[68] D. Wu, B.C. Yin, B.C. Ye, A label-free electrochemical DNA sensor based on exonuclease III-aided target recycling strategy for sequence-specific detection of femtomolar DNA, Biosens. Bioelectron. 28 (2011) 232–238.
[69] E. Majid, K.B. Male, J.H.T. Luong, Boron doped diamond biosensor for detection of *Escherichia coli*, J. Agric. Food Chem. 56 (2008) 7691–7695.
[70] L. Wang, Q. Liu, Z. Hu, Y. Zhang, C. Wu, M. Yang, P. Wang, A novel electrochemical biosensor based on dynamic polymerase-extending hybridization for *E. coli* O157:H7 DNA detection, Talanta 78 (2009) 647–652.
[71] C.M. Pandey, G. Sumana, B.D. Malhotra, Microstructured cystine dendrites based impedimetric sensor for nucleic acid detection, Biomacromolecules 8 (2011) 2925–2932.
[72] D. Zhang, E.C. Alocilja, Characterization of nanoporous silicon-based DNA biosensor for the detection of *Salmonella Enteritidis*, IEEE Sens. J. 8 (2008).
[73] V. Nandakumar, J.T. La Belle, J. Reed, M. Shah, D. Cochran, L. Joshi, T.L. Alford, A methodology for rapid detection of *Salmonella typhimurium* using label-free electrochemical impedance spectroscopy, Biosens. Bioelectron. 24 (2008) 1039–1042.
[74] V. Velusamy, K. Arshak, O. Korostynska, K. Oliwa, C. Adley, An overview of foodborne pathogen detection: in the perspective of biosensors, Biotechnol. Adv. 28 (2010) 232–254.
[75] V. Velusamy, K. Arshak, O. Korostynska, K. Oliw, C. Adley, Design of a real time biorecognition system to detect foodborne pathogens-DNA biosensor, in: SAS – IEEE Sensors Applications Symposium New Orleans, LA, USA, 2009, pp. 17–19.
[76] V. Velusamy, K. Arshak, C. Yang, L. Yu, O. Korostynska, K. Oliwa-Stasiak, C. Adley, IEEE Sensors Applications Symposium, SAS 5439420, 2010, pp. 135–138.
[77] M. Tichoniuk, D. Gwiazdowska, M. Ligaj, M. Filipiak, Electrochemical detection of foodborne pathogen *Aeromonas hydrophila* by DNA hybridization biosensor, Biosens. Bioelectron. 26 (2010) 1618–1623.
[78] Q. Sheng, J. Wang, J. Zheng, Z. Xu, H. Zhang, Ultrasensitive electrical biosensing of syphilis DNA using target-guided formation of polyaniline based on enzyme-catalyzed polymerization, Biosens. Bioelectron. 25 (2010) 2071–2077.
[79] Z. Wang, J. Zhang, P. Chen, X. Zhou, Y. Yang, S. Wu, L. Niu, Y. Han, L. Wang, P. Chen, F. Boey, Q. Zhang, B. Liedberg, H. Zhang, Label-free, electrochemical detection of methicillin-resistant *Staphylococcus aureus* DNA with reduced graphene oxide-modified electrodes, Biosens. Bioelectron. 26 (2011) 3881–3886.
[80] R. Miranda-Castro, N. de-los-Santos-Álvarez, M.J. Lobo-Castã nón, A.J. Miranda-Ordieres, P. Tũ nón-Blanco, PCR-coupled electrochemical sensing of *Legionella pneumophila*, Biosens. Bioelectron. 24 (2009) 2390–2396.
[81] T. Damrow, B. Hagemeyer, H. Ismail, R. Oldham, Electronic Anthrax DNA Biosensor Review, 2009.
[82] N. Prabhakar, H. Singh, B.D. Malhotra, Nucleic acid immobilized polypyrrole-polyvinylsulphonate film for *Mycobacterium tuberculosis* detection, Electrochem. Commun. 10 (2008) 821–826.
[83] N. Prabhakar, K. Arora, H. Singh, B.D. Malhotra, Polyaniline based nucleic acid sensor, J. Phys. Chem. B 112 (2008) 4808–4816.
[84] M. Das, C. Dhand, G. Sumana, A.K. Srivastava, R. Nagarajan, B.D. Malhotra, Electrophoretically fabricated core–shell CNT-DNA biowires for biosensing, J. Mater. Chem. 22 (2012) 2727–2732.
[85] M. Das, C. Dhand, G. Sumana, A.K. Srivastava, N. Vijayan, R. Nagarajan, B.D. Malhotra, Zirconia grafted carbon nanotubes based biosensor for *M. Tuberculosis* detection, Appl. Phys. Lett. 99 (2011) 143702–143703.
[86] R. Singh, R. Prasad, G. Sumana, K. Arora, S. Sood, R.K. Gupta, B.D. Malhotra, STD sensor based on nucleic acid functionalized nanostructured polyaniline, Biosens. Bioelectron. 24 (2009) 2232–2238.
[87] R. Singh, R. Verma, A. Kaushik, G. Sumana, S. Sood, R.K. Gupta, B.D. Malhotra, Chitosan-iron oxide nano-composite platform for mismatch-discriminating DNA hybridization for detection of *Neisseria gonorrhoeae* causing sexually transmitted disease, Biosens. Bioelectron. 26 (2011) 2967–2974.
[88] M.K. Patel, P.K. Solanki, A. Kumar, S. Khare, S. Gupta, B.D. Malhotra, Electrochemical DNA sensor for *Neisseria meningitidis* detection, Biosens. Bioelectron. 25 (2010) 2586–2591.
[89] M.K. Patel, P.K. Solanki, S. Seth, S. Gupta, S. Khare, A. Kumar, B.D. Malhotra, CtrA gene based electrochemical DNA sensor for detection of meningitis, Electrochem. Commun. 11 (2009) 969–973.
[90] D.O. Ariksoysal, H. Karadeniz, A. Erdem, A. Sengonul, A.A. Sayiner, M. Ozsoz, Label-free electrochemical hybridization genosensor for the detection of hepatitis B virus genotype on the development of lamivudine resistance, Anal. Chem. 77 (2005) 4908–4917.
[91] P. Kara, S. Cavdar, B. Meric, S. Erensoy, M. Ozsoz, Electrochemical probe DNA design in PCR amplicon sequence for the optimum detection of microbiological diseases, Bioelectrochemistry 71 (2007) 204–210.
[92] X.M. Li, H.Q. Ju, Li.P. Du, S.S. Zhang, A nucleic acid biosensor for the detection of a short sequence related to the hepatitis B virus using bis benzimidazole cadmium II dinitrate as an electrochemical indicator, J. Inorg. Chem. 101 (2007) 1165–1171.
[93] X.M. Li, H.Q. Ju, C.F. Ding, S.S. Zhang, Nucleic acid biosensor for detection of hepatitis B virus using 2, 9-dimethyl-1,10-phenanthroline copper complex as electrochemical indicator, Anal. Chim. Acta 582 (2007) 158–163.
[94] C. Ding, F. Zhao, M. Zhang, S. Zhang, Hybridization biosensor using 2, 9-dimethyl-1,10-phenantroline cobalt as electrochemical indicator for detection of hepatitis B virus DNA, Bioelectrochemistry 72 (2008) 28–33.
[95] S.Y. Niu, M.L. Wu, L.Z. Hu, Z.H. Mei, S.H. Liu, Nucleic acid biosensor for DNA hybridization detection using rutin–Cu as an electrochemical indicator, Electrochim. Acta 54 (2009) 1564–1569.
[96] S. Zhang, Q. Tan, F. Li, X. Zhang, Hybridization biosensor using diaquabis[N-2-pyridinylmethyl benzamide-k2 N,O]-cadmium II dinitrate as a new electroactive indicator for detection of human hepatitis B virus DNA, Sens. Actuators B 124 (2007) 290–296.
[97] C.S. Riccardi, J. Kowalik, M. Josowicz, H. Yamanaka, B. Mizaikoff, C. Kranz, Label-free DNA detection of hepatitis C virus HCV-1, in: ECS 210th Meeting 2091, 2006.
[98] M.H. Pournaghi-Azar, F. Ahour, M.S. Hejazi, Differential pulse voltammetric detection of hepatitis C virus 1a oligonucleotide chain by a label-free electrochemical DNA hybridization biosensor using consensus sequence of hepatitis C virus 1a probe on the pencil graphite electrode, Electroanalysis 21 (2009) 1822–1828.
[99] S. Liu, Y. Hu, J. Jin, H. Zhang, C. Cai, Electrochemical detection of hepatitis C virus based on site-specific DNA cleavage of BamHI endonuclease, Chem. Commun. (2009) 1635–1637.
[100] M.S. Hejazi, M.H. Pournaghi-Azar, F. Ahour, Electrochemical detection of short sequences of hepatitis C 3a virus using a peptide nucleic acid-assembled gold electrode, Anal. Biochem. 399 (2010) 118–124.
[101] R. Wang, C. Xue, M. Gao, H. Qi, C. Zhang, Ultratrace voltammetric method for the detection of DNA sequence related to human immunodeficiency virus type 1, Microchim. Acta 172 (2011) 291–297.
[102] W.M. Hassen, C. Chaix, A. Abdelghani, F. Bessueille, D. Leonard, N. Jaffrezic-Renault, An impedimetric DNA sensor based on functionalized magnetic nanoparticles for HIV and HBV detection, Sens. Actuators B 134 (2008) 755–760.
[103] P.D. Tam, N.V. Hieu, N.D. Chien, A.T. Le, A.T. Tuan, DNA sensor development based on multi-wall carbon nanotubes for label-free influenza virus type A detection, J. Immunol. Methods 350 (2009) 118–124.
[104] X. Chen, H. Xie, Z.Y. Seow, Z. Gao, An ultrasensitive DNA biosensor based on enzyme-catalyzed deposition of cupric hexacyanoferrate nanoparticles, Biosens. Bioelectron. 25 (2010) 1420–1426.

[105] H. Fan, P. Ju, S. Ai, Controllable synthesis of CdSe nanostructures with tunable morphology and their application in DNA biosensor of Avian Influenza Virus, Sens. Actuators B 149 (2010) 98–104.
[106] X. Zhu, S. Ai, Q. Chen, H. Yin, J. Xu, Label-free electrochemical detection of Avian Influenza Virus genotype utilizing multi-walled carbon nanotubes–cobalt phthalocyanine–PAMAM nanocomposite modified glassy carbon electrode, Electrochem. Commun. 11 (2009) 1543–1546.
[107] N. Zari, A. Amine, M.M. Ennaji, Label-free DNA biosensor for electrochemical detection of short DNA sequences related to human papilloma virus, Anal. Lett. 42 (2009) 519–535.
[108] L. Civit, A. Fragoso, C.K. O'Sullivan, Electrochemical biosensor for the multiplexed detection of human papillomavirus genes, Biosens. Bioelectron. 26 (2010) 1684–1687.
[109] X. Zhang, H. Su, S. Bi, S. Li, S. Zhang, DNA-based amplified electrical biobarcode assay for one-pot detection of two target DNAs, Biosens. Bioelectron. 24 (2009) 2730–2734.
[110] H.I. Peng, B.L. Miller, Recent advancements in optical DNA biosensors: exploiting the plasmonic effects of metal nanoparticles, Analyst 136 (2011) 436–447.
[111] N. Prabhakar, K. Arora, S.K. Arya, P.R. Solanki, M. Iwamoto, H. Singh, B.D. Malhotra, Nucleic acid sensor for *M. tuberculosis* detection based on surface plasmon resonance, Analyst 133 (2008) 1587–1592.
[112] K.H. Cheong, D.K. Yi, J.G. Lee, J.M. Park, M.J. Kim, J.B. Edel, C. Koa, Gold nanoparticles for one step DNA extraction and real-time PCR of pathogens in a single chamber, Lab Chip 8 (2008) 810–813.
[113] H. Bai, R. Wang, B. Hargis, H. Lu, Y. Li, A SPR aptasensor for detection of avian influenza virus H5N1, Sensors 12 (2012) 12506–12518.
[114] A.J. Baeumner, R.N. Cohen, V.M. Junhong Min, RNA biosensor for the rapid detection of viable *Escherichia coli* in drinking water, Biosens. Bioelectron. 18 (2003) 405–413.
[115] A.J. Baeumner, C.J. Ching, Y.W. Andrew Price, A generic sandwich-type biosensor with nanomolar detection limits, Anal. Bioanal. Chem. 378 (2004) 1587–1593.
[116] J. Wang, Y. Luo, B. Zhang, M. Chen, J. Huang, K. Zhang, W. Gao, W. Fu, T. Jiang, P. Liao, Rapid label-free identification of mixed bacterial infections by surface plasmon resonance, J. Trans. Med. 85 (2011).
[117] P. Zuo, X. Li, D. Dominguez, B.C. Ye, A PDMS/paper/glass hybrid microfluidic biochip integrated with aptamer-functionalized graphene oxide nanobiosensors for one-step multiplexed pathogen detection, Lab Chip 13 (13) (2013) 3828–3921.
[118] A.L. Chua, C.Y. Yean, M. Ravichandran, B.H. Lim, P. Lalitha, A rapid DNA biosensor for the molecular diagnosis of infectious disease, Biosens. Bioelectron. 26 (2011) 3825–3831.
[119] R.Z. Hao, H.B. Song, G.M. Zuo, R.F. Yang, H.P. Wei, D.B. Wang, Z.Q. Cui, Z.P. Zhang, Z.X. Cheng, X.A. Zhang, DNA probe functionalized QCM biosensor based on gold nanoparticle amplification for *Bacillus anthracis* detection, Biosens. Bioelectron. 26 (2011) 3398–3404.
[120] Z. Shen, M. Huang, C. Xiao, Y. Zhang, X. Zeng, P.G. Wang, Non-labeled QCM biosensor for bacterial detection using carbohydrate and lectin recognitions, Anal. Chem. 79 (2007) 2312–2319.
[121] S.J. Fletcher, L.W. Phillips, A.S. Milligan, S.J. Rodd, Toward specific detection of Dengue virus serotypes using a novel modular biosensor, Biosens. Bioelectron. 26 (2010) 1696–1700.
[122] G.J. Zhang, L. Zhang, M.J. Huang, Z.H.H. Luo, G.K.I. Tay, E.J.A. Lim, T.G. Kang, Y. Chen, Silicon nanowire biosensor for highly sensitive and rapid detection of Dengue virus, Sens. Actuators B 146 (2010) 138–144.
[123] C.H. Lin, C.H. Hung, C.Y. Hsiao, H.C. Lin, F.H. Ko, Y.S. Yang, Poly-silicon nanowire field-effect transistor for ultrasensitive and label-free detection of pathogenic avian influenza, Biosens. Bioelectron. 24 (2009) 3019–3024.
[124] V.C.H. Wu, S.H. Chen, C.S. Lin, Real-time detection of *Escherichia coli* O157:H7 sequences using a circulating-flow system of quartz crystal microbalance, Biosens. Bioelectron. 22 (2007) 2967–2975.
[125] Y.J. Liu, D.J. Yao, H.Y. Chang, C.M. Liu, C. Chen, Magnetic bead-based DNA detection with multi-layers quantum dots labeling for rapid detection of *Escherichia coli* O157:H7, Biosens. Bioelectron. 24 (2008) 558–565.
[126] S.V. Schrumpf, R. Buresch, M. Schinkinger, A simple nucleic acid hybridization/latex agglutination assay for the rapid detection of polymerase chain reaction amplicons, J. Microbiol. Methods 68 (2007) 568–576.
[127] S.W. Dutse, N.A. Yusof, Microfluidics-based lab-on-chip systems in DNA-based biosensing: an overview, Sensors 11 (2011) 5754–5768.
[128] N.V. Zaytseva, V.N. Goral, R.A. Montagna, A.J. Baeumner, Development of a microfluidic biosensor module for pathogen detection, Lab Chip 5 (2005) 805–811.
[129] C. Lui, N.C. Cady, C.A. Batt, Nucleic acid-based detection of bacterial pathogens using integrated microfluidic platform systems, Sensors 9 (2009) 3713–3744.
[130] J. Mairhofer, K. Roppert, P. Ertl, Microfluidic systems for pathogen sensing: a review, Sensors 9 (2009) 4804–4823.
[131] C. Roh, Facile inhibitor screening of hepatitis C virus NS3 protein using nanoparticle-based RNA, Biosensors 2 (2012) 427–432.
[132] L.T.H. Kao, L. Shankar, T.G. Kang, G. Zhanga, G.K.I. Tay, S.R.M. Rafei, C.W.H. Lee, Multiplexed detection and differentiation of the DNA strains for influenza A H1N1 2009 using a silicon-based microfluidic system, Biosens. Bioelectron. 26 (2011) 2006–2011.

Biographies



Dr. Renu Singh received her Ph.D. degree (2013) from Guru Gobind Singh Indraprastha University, New Delhi, in collaboration with National Physical Laboratory, CSIR, New Delhi, and All India Institute of Medical Sciences, New Delhi, India in biotechnology. She is currently employed as Research Scientist in Ulsan National Institute of Science and Technology (UNIST), South Korea and working on the topic carbon-nanotubes based airborne virus detection sensor system for swine influenza virus H1N1 detection and removal of proteins, antibodies and biofilms using carbon dioxide aerosols. She has research experience of 8 years in the area of development of biosensors based on nanomaterials, nanobiocomposites, and conducting polymers for health care.



Dr. Maumita Das Mukherjee received her Ph.D. degree (2012) from University of Delhi, Delhi in Chemistry. She is currently working as Assistant Professor in Amity Institute of Applied Sciences, Amity University, Noida, Uttar Pradesh, India. She has research Experience of 8 years in the area of development of biosensors based on nanomaterials, nanobiocomposites, conducting polymers for health care and glass and glass-ceramic materials.



Dr. Gajjala Sumana received her Ph.D. (1998) from Jiwji University in chemistry. She is currently working as scientist in Department of Science & Technology Centre on Biomolecular Electronics, Biomedical Instrumentation Section, National Physical Laboratory, New Delhi. She has a research experience of 10 years in controlled drug delivery, liquid crystal polymers, polymer dispersed liquid crystals and biosensors.



Prof. Rajinder K. Gupta received his Ph.D. degree Org. Chem. from Delhi University in Organic Chemistry of Natural Products. He earned his second Ph.D. in Microbiology/Biotechnology from University of Idaho, USA. He has over 99 research publications to his credit and has more than three decades of experience in academia, and industry (pharmaceutical, agrochemical, polymer and commercial test house). He is now Professor and Dean, School of Biotechnology, Guru Gobind Singh Indraprastha University, New Delhi, India. His current areas of research include identification of bioactive agent from actinomycetes & plants, biotransformations, and production of nanomaterials using microorganisms (nanobiotechnology).



Dr. Seema Sood received her MBBS from Lady Hardinge Medical College, New Delhi in 1987 and her M.D. (Microbiology) from Lady Hardinge Medical College, New Delhi. She is currently employed as Assistant Professor in the Department of Microbiology, AIIMS, New Delhi. She is currently working towards introducing novel technologies for the diagnosis of Infectious Diseases, with her focus being Sexually Transmitted Diseases.



Dr. B.D. Malhotra received his Ph.D. degree from University of Delhi, Delhi, India in 1980. He has published more than 245 papers, has obtained 10 patents, has edited/co-edited books on biosensors and polymer electronics, and is currently Professor and Head, Department of Biotechnology, Delhi Technological University, Delhi, India. He has research experience of about 30 years in the field of biomolecular electronics and has guided 21 Ph.D. students till date. His current research activities including biosensors, conducting polymers, Langmuir–Blodgett films, self-assembled monolayers, nanomaterials, and nanobioelectronics, etc.

International Journal of Thermal Technologies
E-ISSN 2277 – 4114
©2014 INPRESSCO®, All Rights Reserved
Available at http://inpressco.com/category/ijtt/

Research Article

Blending of Ethanol in Gasoline:Impact on SI Engine Performance and Emissions

Amit Pal[Á*]

[Á]Deptt of Mechanical Engineering, Delhi Technological University, Formerly Delhi College of Engineering, Delhi, 110042

Accepted 20 February 2014, Available online 01 February 2014, **Vol.4, No.1 (March 2014)**

Abstract

In this work the performance and emission characteristics of a 4 stroke, 4 cylinder spark ignition MPFI engine was investigated with different ethanol gasoline (Gasohol) blends. Ethanol can also be used in C. I. engines as ethanol blended (Desihol) diesel, but due to its easy miscibility with Gasoline and having a higher octane number, ethanol is preferably blended with gasoline. Due to the higher ethanol blend usability constraints, in this work the investigation was kept limited to the low (5-15 % ethanol) ethanol gasoline blends. The present paper aims at discussing the low ethanol gasoline blends and gasoline (E0/G100), which were tested on a Maruti Suzuki Wagon R engine with a SAJ eddycurrent dynamometer unit. The performance parameters like brake power and thermal efficiency and exhaust emission parameters like CO, HC, NOx and CO_2 were recorded. The results of this investigation prove the applicability of low ethanol blended Gasoline as clean fuel to reduce CO, HC and NOx emissions. Performance parameters show a marginal increase in BHP and thermal efficiency a little increase in specific fuel consumption, whereas the usefulness of the inherent oxygen content in the ethanol molecule has been proved through the occurrence of a higher peak cylinder pressure and a higher exhaust gas temperature.

Keywords: *Bio-Gasoline, Exhaust emissions, Ethanol blend, Performance testing, Gasohol*

1. Introduction

Despite discovery of new sources of unconventional sources of energy, due to inadequacies in the supply of other forms of commercial energy relative to demand, Gasoline remains the primary energy source in India and is preferred as an automotive fuel. It is evident that (MoPNG, GOI report 2011-12), its consumption has been increasing sharply from 3.5 Million Metric Tons (MMt) in the year 1950-51 to 84.3 MMt in 1997-98 to about 130 MMt in 2001 and it were about 175 MMt in 2006-07. Among the potential alternative fuels, ethanol is the most feasible alternate fuel in near future. The reasons for its preference in Indian scenario are following:

First, they can be produced from "cellulosic biomass", such as trees and grasses or from different agricultural products. Thus they represent really a zero emission technique as they eat up a lot of CO_2 in the process of theirproduction.

Secondly, ethanol (CH_3CH_2OH) is made up of a group of chemical compounds whose molecules contain a hydroxyl group, OH, bonded to a carbon atom; so, the oxygen content of this fuel favours further combustion of gasoline. And most importantly these are home grown; therefore they not only reduce the burden of arranging the foreign currency but also generate a massive opportunity of rural employment generation.

The countries like Brazil, Sweden and USA have marked their presence in the Bio-Gasoline based alternative auto fuel sector by the invention of the flexible fuel vehicle technologies and application of ethanol gasoline blends as high as E85 to E100 (Frank et al. 1998), (Pikunas et al. 2003). The economic and environmental constraints have compelled a country like India to imply a compulsory utilization of just E10 as fuel in the light duty vehicles. While there is no shortage of sugarcane in India, which is one of the prime sources for automotive ethanol fuel, being the 2nd largest producer in the world, India still lacks the technological advancement in terms of engine modifications and material compatibility problems. Ethanol besides being a renewable bio–mass based alternative fuel has other added performance based properties like the higher octane number, inherent oxygen content, and a higher latent heat of vaporisation which allows a higher power to be extracted from the engine both in the modified and unmodified state.

The addition of the anhydrous ethanol fuel to gasoline merely is enough to reflect that the properties of the blend generated inclines towards those of ethanol fuel (Milan Pospisil et al. 2009), (Karabulut et al., 2009), (Black and Frank, 1991). Because of inherent oxygen content of about 3.5% in an ethanol molecule, when the blend powers an unmodified S I engine the overall blend mixture burns lean nearing a stochiometric A/F ratio of 17.2 (Agarwal, 2006), (Demirbas, 2006), (Brinkman and Norman, 1981). This is

*Corresponding author: **Amit Pal email: amitpal@dce.ac.in**

one of the chief contributing reasons to the increased power, thermal efficiency and peak cylinder pressures. The inherent oxygen molecule contributes to an increase in the research octane number of the blend. The higher Octane Number allows the compression ratio of the engine to be increased again contributing to a higher power output. Because of its chemical structure the alcohol molecule contains fixed oxygen. This results in a lower calorific value of 26.8 MJ/kg of ethanol as compared to 44.5 MJ/kg for gasoline and hence higher fuel consumption with gasohol fuel. A lower flame temperature reduces heat losses from the engine and increases the thermal efficiency. Ethanol's stoichiometric flame temperature is 2197 K as compared to 2266 K for gasoline, contributes to higher efficiency for a blend fuelled engine (Powell, 1975), (Kremer, 1996,).

The comparison of various properties of Ethanol and Gasoline fuel is summarised in Table 1. Ethanol has a wider flammability limit of 3.5-26 volume % as compared to 1.4-7.6 volume % for gasoline, and hence is on the richer side. A wide rich flammability limit may be useful because rich air: fuel ratios can be used to maximize power by injecting more fuel per charge. A wide flammability limit on the lean side is useful in extending the operating range of the lean burn engines. Gasoline is composed of a mixture of large number of hydrocarbons having boiling point ranging from 30^0C to about 200^0C. Ethanol in contrast has a BP of 78^0C. The alcohols lack the light end fractions essential for cold starting of SI engines (Kremer, 1996), (Fikret and Bedri, 2004). Although ethanol itself has an RVP less than that of Gasoline, its addition to Gasoline markedly increases the RVP of the blend, which can lead to increased evaporative emissions. It is generally accepted that the peak RVP of ethanol blends occurs at around 5-10% ethanol concentration, and is about 6.5% above the RVP of neat Gasoline (Murphy and McCarthy, 2004).

Table 1 The Comparisons of The Gasoline and Ethanol thermodynamic Properties

Properties	Ethanol	Gasoline
Chemical Formula	C_2H_5OH	mC_nH_{2n}
Boiling Point, deg C @ 1 bar	78	30-225
LHV,MJ/kg Fuel	26.8	44.5
Octane number (Recearch)	111	90-98
Octane number (Motor)	94	82
Stoichometric A/F, mass	8.94	15.04
Flammability limit in air vol%	3.5-26	1.4-7.6
Adiabatic flame temp, Kelvin	2197	2266
Auto-ignition temp, Kelvin	792	753
Molecular weight	46	112
Spacific Gravity at 15.5 ◦ C	0.794	0.71-.75
Latent heat of Vapourisation,kcal/kg	204	70-100
Flame velocity, cm/sec	48	43
Vapour pressure at 58 ◦C bar	0.21	0.8

Several problems associated with ethanol have however put a restriction on the use of ethanol gasoline blends with higher ethanol percentage.Pure ethanol has a moderate volatility. Its high boiling point (78°C) induces difficulties of vaporization in ambient or cold conditions. Moreover, as it has been outlined previously, as ethanol has a very high latent heat of vaporization (3 times higher than typical gasoline). This property induces driveability difficulties. Due to the increased RVP of the ethanol gasoline blends the volatility of the fuel becomes higher as compared to baseline gasoline. Under such conditions the increased vapour formation in the fuel tank and the fuel carrying hoses lead to hot startability and vapour lock problem. (Murphy and McCarthy, 2004]

Ethanol contains acetic acid that can corrode aluminium alloys. It also adsorbs the lead in alloys causing the surface to become porous. Ethanol can chemically attack some of the resins used to make fibreglass tanks causing them to dissolve. In doing so, the ethanol causes leaks, heavy black deposits on engine intake valves, and deformation of push rods, pistons, and valves. Once absorbed into rubber, the oxygen in alcohol fuels breaks the rubber's carbon-carbon double bonds in the rubber and embrittle the rubber and cause swelling. This problem is associated mainly with the rubber fuel hoses and the rubber gaskets, the carburettor bowl. An additional problem with rubbers in fuel systems is the temporary attachment of hydrocarbons in the rubber to the hydrocarbons of the fuel.

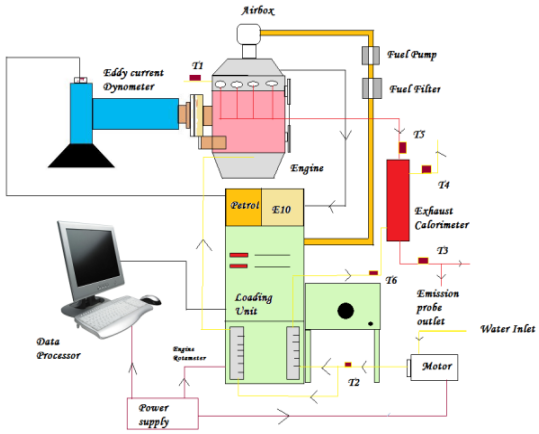


Figure 1: Schematic details of the test setup

As a result, the hydrocarbons in the rubber may add to a fuel's hydrocarbon content, creating increased emissions (Kumar et al. 2008). If too much water is introduced into an ethanol blend, the water and most of the ethanol (around 60% - 70%) will separate from the Gasoline and the remaining ethanol. Thus water being the densest of them all collects at the bottom of the fuel tank causing just water to be pumped to the carburettor leading to a momentary stalling of the engine (Murphy and McCarthy, 2004). Ethanolblends increase the solubility of the gum in gasoline and this may partly account for the increased intake system deposit-forming tendency. Dissolved gum causes suspended materials to plug filters. In order to overcome the above shortcomings and harness the advantageous potential associated with higher percentage of ethanol blended gasoline blends in an unmodified SI engine, some material changes may be incorporated. Viton B, Viton GFLT, Viton GF are all acceptable materials to be used in an ethanol vehicle. Nylon and Teflon

components such as the fuel hoses that connected the main fuel supply to the main stainless steel fuel lines and the in-tank fuel pump reservoir are compatible with blends up to E85 (Sheehy,2010) and (Sriram Bata,1993). Compatible fuel injectors would be constructed of compatible polymers and Viton o-rings on the interior and exterior.

2. Objectives & Experimental Setup

The primary objective of the study is to investigate the performance and emissions of a standard S I engine originally designed to run on gasoline. The study is carried out with the following objectives:

- To study quantitatively the CO, HC, NOx and CO_2 emissions with different ethanol gasoline blends when engine is operated under E-5 to E-15 blends in comparison with the baseline gasoline.
- To investigate into the performance based parameters like thermal efficiency, brake power output and brake specific fuel consumption with different ethanol gasoline blends.

Experimental Setup

The experimental setup for the present work consists of the following: Maruiti Suzuki make 4 cylinder inline, 4 stroke gasoline engine with the following specifications as given in Table 2. Some additional components like, Saj engine dynamometer unit working on the eddy current principle with water cooing and loading unit, and AVL DiGAS 444, 5 gas analyzer for exhaust gas emission analysis. The schematic setup is shown in the Figure1. It is attached with necessary instruments for crank-angle measurements. These signals are interfaced to computer through engine indicator for pθ−pV diagrams. Windows based Engine Performance Analysis software package "Engine soft" is used for on line performance evaluation. Another important unit is the exhaust outlet unit which comprises of the outlet tailpipe, exhaust heat balance measurement unit and a secondary outlet for the fitment of the gas analyzer probe for emission measurement.

4. Materials and Methods

Gasoline used in the study was purchased from nearby IOCL Gasoline pump, while Ethanol (99.8% purity) was taken from local chemical supplier. Samples were prepared on volume % basis. Measurements for the performance and emissions parameters were taken at various loads.

Table 2: The Set up specifications

Characteristics	Value
Make	Suzuki
Cylinder	4
Power	44.5kW@5000rpm
Torque	59Nm@2500rpm
Bore	72mm
Displacement	1100mm

4. Comparative Performance & Emissions Curves for Gasoline & Ethanol Blends

Using ethanol blend in gasoline engine can favourably reduce fine particulate matter (PM), carbon monoxide and global warming. Here in this performance evaluation test we are showing different curves b/w load (kiloWatt) v/s thermal efficiency (%), Bsfckg/kWhr, CO (%), HC (ppm) and NO_xin ppm.

Brake Thermal efficiency v/s power

Figure 2 shows the results of thermal efficiency v/s power, ethanol blends of 7.5 to 12.5% gives the most optimum thermal efficiency, especially at higher power, the gains are more. Still the gain in absolute are small and a higher compression ratio is need to be investigated to utilise the anti knock characteristics of ethanol blends. Also an increase in the power may be attributed to the increased volumetric efficiency of the engine due to the higher latent heat of vapourisation of ethanol of 207 Kcal/kg as compared to 70-100 kCal/kg of gasoline. Also due to the higher latent heat of vapourisation the combustion temperatures for the blended ethanol fuel decreases and the amount of thermal load on the engine. Therefore for engines designed to run on gasoline, marginal thermalefficiency improvement can be obtained.

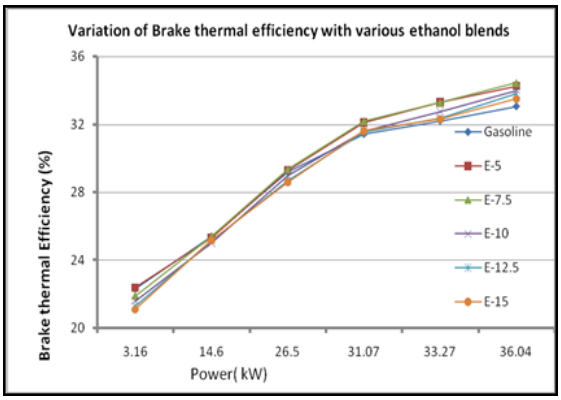


Figure 2: Variation of Brake Thermal Efficiency with Various Ethanol Blends

Brake Specific Fuel Consumption v/s power

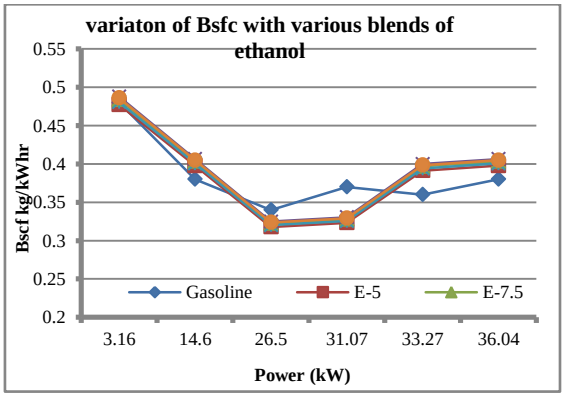


Figure 3: Bsfc v/s Power (Gasoline Ethanol Blend)

Considering the trend of bsfc v/s power, Figure 3 show that for all the ethanol blends the combustion efficiency improves but at higher blends bsfc increases slightly due to lower specific heat of the ethanol and this increase is significant at higher power. Though we have found an increase in bsfc with ethanol blends over gasoline when the engine was run at higher loads and this further increased with increase in blend % of ethanol.

CO emissions

The addition of ethanol to gasoline causes an increase in the oxygen available for combustion in the intakecharge thereby making the air fuel mixture lean in an unmodified engine, hence the charge burns more completely Use of ethanol blends in gasoline engines reduces the CO emissions vis-à-vis gasoline also at higher loads the drop in CO emissions is higher, this canbe seen from Figure 4. With E10 and above the combustion completed much earlier duringthe expansion stroke, thereby decreasing the probability of CO emissions due to flame quenching caused by downward movement of the piston.

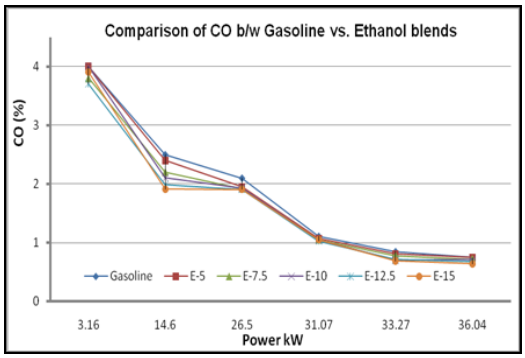


Figure 4: CO v/s Power for Gasoline Ethanol Blends

HC emissions

The HC emissions reduction is observed throughout the power range in case of ethanol blends as compared to gasoline as it is evident from Figure 5. Since the entry of the fuel vapour to the crevices, flame quenching and absorption by the oil layer would be more or less similar for all the ethanol blends. Thisshows a decrease in HC emissions with gasohol.

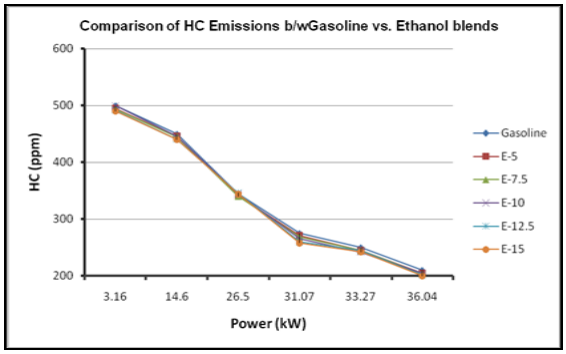


Figure-5: HC v/s Power for Gasoline Ethanol Blends

NO_x emission

There is no considerable difference w. r. t. NO_x emission, when the engine was run on gasoline and ethanol blends as clear from Figure 6. In some cases there is a little decrease in NOx emissions with the ethanol blends. NOx emissions with E10 and above were observed to be lower as compared to gasoline with the engine equivalence ratio maintained in the range of 0.85-0.95 by the engine lambda sensor. It is found that as the blend percentage is increased the maximum NOx emissions take place at higher value of equivalence ratio i.e. at much richer mixtures than stochiometric because of the inherent oxygen content in ethanol.

Hence for the ethanol gasoline blends the tendency of nitrogen to oxidize to NO and NO_2 will be lesser as compared to gasoline. Also ethanol flame's lower luminosity reduces the heat loss by radiation and leads to lower NOx emission from the engine.

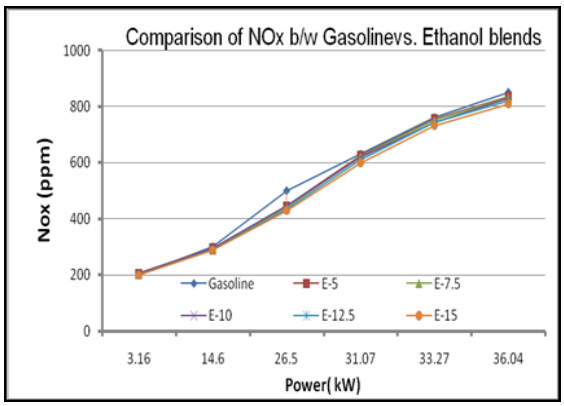


Figure 6: NOx v/s Power for Gasoline Ethanol Blends

Conclusions

The following conclusions can be summarized from the above analysis.

- The inherent oxygen content of ethanol is the chief contributor to the increased power output and thermal efficiency with the ethanol gasoline blends. Additionally a higher latent heat of vaporisation and a higher flame velocity also contribute to the power based performance.
- Higher boiling point of ethanol and a wider range of flammability limit have led to the development of cold start technologies as the most important technologies with the ethanol usage.
- CO, HC and NOx emissions with Bio-Gasoline are found to be reduced owing to more complete combustion of the air fuel charge under lean burning conditions created by the ethanol molecule. Higher Peak cycle pressures and greater exhaust gas temperatures also can't be ignored if an ethanol fuel performance based evaluation is to be done.
- The low energy content of ethanol is its most limiting factor in its acceptance for fuel economy and performance reasons
- The unmodified SI Engine performance and emission based benefits are limited by the aldehyde emissions, swelling of the fuel hose rubber components, gaskets

and the galvanic corrosion, gum deposits associated with the fuel tanks are some of the issues associated with the Ethanol fuel and thus can't be overlooked.

- Finally if in future India wishes to extract the emission based benefits of higher ethanol gasoline blends ,may be E85, then specific engine based modifications will have to be incorporated to reap the benefits of using a clean air fuel.

References

Ministrye of Petroleume and Naturale Gas, Government of India, New Delhi,(Economic Division) report (2011-12), Basic Statistics on Indian Petroleume& Natural Gas, Available at www. http:// Petroleume.nic.in/petstat.pdf, Accessed on 04-11-2013 20:30 P

Frank Rosillo-Calle and Luis A. B. Cortez, (1998), Towards ProAlcool II—a review of the Brazilian bioethanol programme, Biomass and Bioenergy, Volume 14, 23 March, pp 115-124

PikunasAlvydas., PukalskasSagirdas., GuabysJuozas., Gediminas Vilnius, (2003), Influence of composition of Gasoline – Ethanol blends on parameters of internal combustion engines, Journal of KONES, Internal Combustion Engines, Vol 10, 3-4.

Milan Pospíšil, ZlataMužíková, Gustav Šebor, (2007), Volatility and distillation properties of Ethanol Gasoline Blends, Svojstva ISSN 0350-350X, GOMABN 46, 4,335-353, Professional paper.

Karabulut, H., Yucesu, H. S., Cınar, C. and Aksoy F., (2009), The effects of ethanol–unleaded gasoline blends on engine performance and exhaust emissions in a spark-ignition engine, Renewable Energy 34, 2101–2106

Black, Frank, (1991), An Overview of the Technical Implications of Methanol and Ethanol as Highway Motor Vehicle Fuels, SAE Paper 912413

AgarwalAvinash Kumar, (2006), Bio fuels (alcohols and biodiesel) applications as fuels for internal combustion engines, Progress in Energy and Combustion Science, 27 November 2006.

DemirbasAyhan, (2006), Progress and recent trends in bio fuels, progress in energy and combustion science, 22 August 2006

Brinkman, Norman, D., 1981, Ethanol Fuel-A Single-Cylinder Engine Study of Efficiency and Exhaust Emissions, SAE Paper 810345.

Powell, T., 1975, Racing Experiences with Methanol and Ethanol-Based Motor-Fuel Blends, SAE Paper 750124.

Kremer FG, Jordim J L F , Maia D. M., 1996, Effect of alcohol composition on gasoline vehicle emissions. SAE paper no. 962094.

YukselFikret and YükselBedri, 2004, The use of ethanol–gasoline blend as a fuel in an SI engine, Renewable Energy, Volume 29, June 2004, Pages 1181-1191.

Kumar, Alok. Khatri, D. S. and Babu, MKG. 2008, Experimental investigation on the performance, combustion and emission characteristics of alcohol blended gasoline in a fuel injected SI engine, SAE 2008-28-0068.

Murphy J. D. And McCarthy K., 2004, Ethanol production from energy crops and wastes for use as a transport fuel, Applied Energy, October 2004.

Nersasian, A., 2004, The Volume increase of fuel handling rubbers in Gasoline/Alcohol blends", SAE paper 800789

Methanol Fuel Blending and Materials Compatibility Report for Methanol Institute 4100 North Fairfax Drive Suite 740, Arlington, VA 22203 Date: August 27, 2010 Rev A Prepared by Philip Sheehy, PhD Karen Law.

Sriram, Bata, 1993, A Performance Study of Iso-Butanol-Methanol-and Ethanol-Gasoline Blends Using a Single Cylinder Engine, SAE Paper 932953.

CALCULATION OF POTENTIAL ENERGY TERM IN VARIABLE MOMENT OF INERTIA NUCLEAR SOFTNESS (MINS) MODEL

Hardik P. Trivedi*

Pallavi Bhatt*

Anil Kumar **

Lalit Kumar Gupta***

Jai Prakash Gupta***

Than Singh Saini****

Krishna Chandra*****

ABSTRACT

In this paper, we have calculated Potential Energy Term in Variable Moment of Inertia Nuclear Softness which shows the variation of potential energy term for the different even-even nuclei in the region of I-quadrant based on the valence particle and hole pairs consideration [8]{Ce (N=90), Nd (N=92), Dy (N=92) & Dy (N-94)} with spin (J). The value of potential energy term is increasing almost linear with increasing spin (J) for all the nuclei.

Key Words: *(1) Ground State Moment of Inertia (θ_0), (2) Softness Parameter (σ) and (3) Stiffness Constant (C)*

*Department of Physics, Mewar University, Chittorgarh (Raj.), INDIA,

**Deptt. of Physics, Vivekananda College of Tech. and Management, Aligarh-202 002 INDIA,

***Department of Physics, D. S. College, Aligarh -202 001 (UP), INDIA,

****Department of Physics, Delhi Technological University, Delhi-42 INDIA,

*****Department of Physics, Goldfield Institute of Technology & Management, Faridabad, INDIA

INTRODUCTION

Now, it has been experimentally [1] suggested that the ground state bands for even-even nuclei away from closed shells can be expected throughout the Periodic Table. Theoretically, a number of models [2-7] have been proposed to correlate such a data. In this attempt, the variable moment of inertia (VMI) model proposed by Mariscotti *et al;* [2] is one of the earliest and very popular among the nuclear science community. In this model, the excitation energy of the state J is defined as the sum of the rigid rotational energy (with moment of inertia 'θ' varying with angular momentum 'J') and a potential energy term (harmonic in angular momentum dependent moment of inertia θ_J about its mean ground state value θ_0. Latter this VMI model extended by Klein and his associates [5, 6] on the basis of the predictions of the Interacting Boson Model [IBM-1] in to two generalizations of VMI model, namely, the Variable An harmonic Vibrator Model (VAVM) and the Generalized VMI (GVMI) model. Batra *et al;* [7-10] extended VMI model by taking in to account the concept of nuclear softness. This extended version of VMI generally called VMINS model. In this present work we studied the importance of potential energy term in VMINS model.

Methods

In the original variable moment of inertia (VMI) [2] model, the excitation energy of the member of the ground-state band with angular momentum J is given by

$$E(J) = \frac{\hbar^2}{2I} J(J+1) + \frac{c}{2}(I - I_0)^2 \qquad \text{----------} \quad \text{(i)}$$

Here the potential term is added to the usual rotational term. The coefficients c and I_0 are parameters, characteristic for each nucleus. Where I_0 is called the ground state moment of inertia and c is denoted as stiffness parameter.

Gupta *et al;* [7, 8] expressed the Variable Moment of Inertia (VMI) model for the ground state band in even-even nuclei in terms of his Nuclear Softness (NS) model [3]. In NS model the variation of moment of inertia θ with J is given by

$$\theta = \theta_0(1 + \sigma J) \qquad \text{----------} \quad \text{(ii)}$$

Where θ_0 is the ground state moment of inertia and σ is the softness parameter. After putting the value of Moment of Inertia (I) in terms of Nuclear Softness Parameter (σ) in equation (i) we get the following expression:-

$$E(J) = \frac{\hbar^2 J(J+1)}{2\theta_0(1+\sigma J)} + \frac{C}{2}\sigma^2\theta_0^2 J^2 \qquad \text{---------- (iii)}$$

Equation (iii) has three parameters

(a) Ground State Moment of Inertia (θ_0)

(b) Softness Parameter (σ)

(c) Stiffness Constant (C)

Two of the parameters Ground State M I (θ_0) and Stiffness Parameter (C) are same as 'I_0' and 'c' in original VMI model, while the Softness Parameter (σ) is different parameter which represents the softness of a particular nucleus. The first term in right hand side of equation (iii) has two parameters (i.e. θ_0 & σ), while the second term has three parameters (i.e. C, θ_0 & σ). The parameters θ_0 and □ are calculated by following the conditions given in reference [9].

In the present work we study the second term of equation (iii) (i.e. Potential Energy Term, $E_{pot.}$) with spin 'J' of the nucleons and with ground state of moment of inertia and with nuclear softness parameters of different nuclei of quadrant-I.

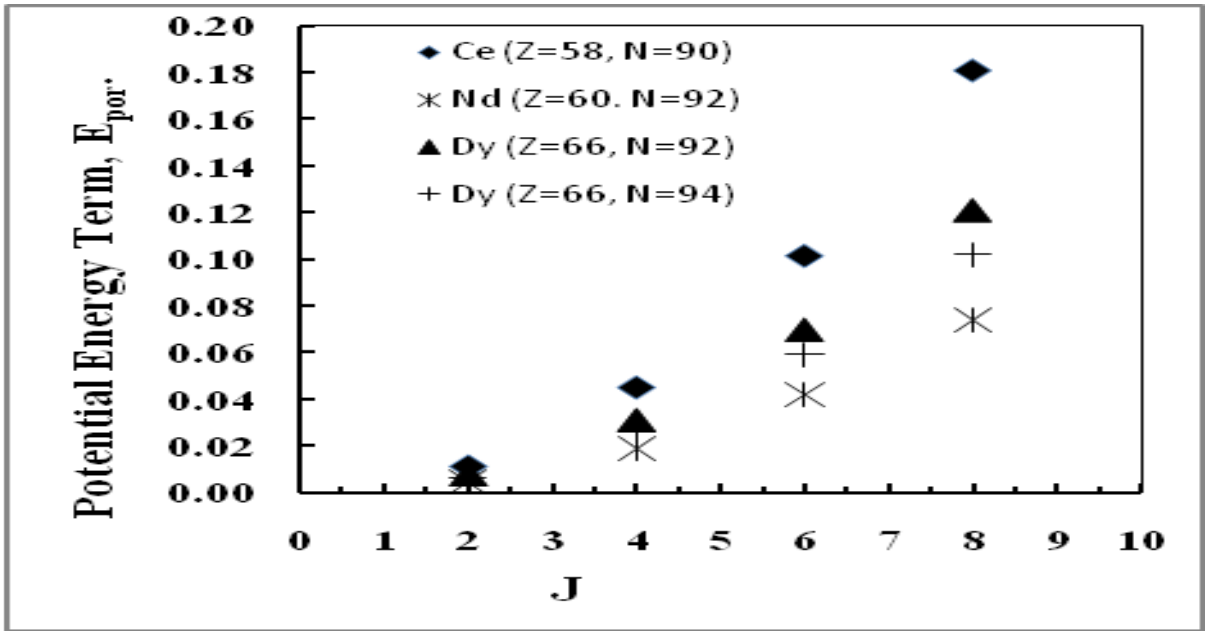


Fig.-(1): Variation of Potential Energy Term ($E_{pot.}$) with Spin (J).

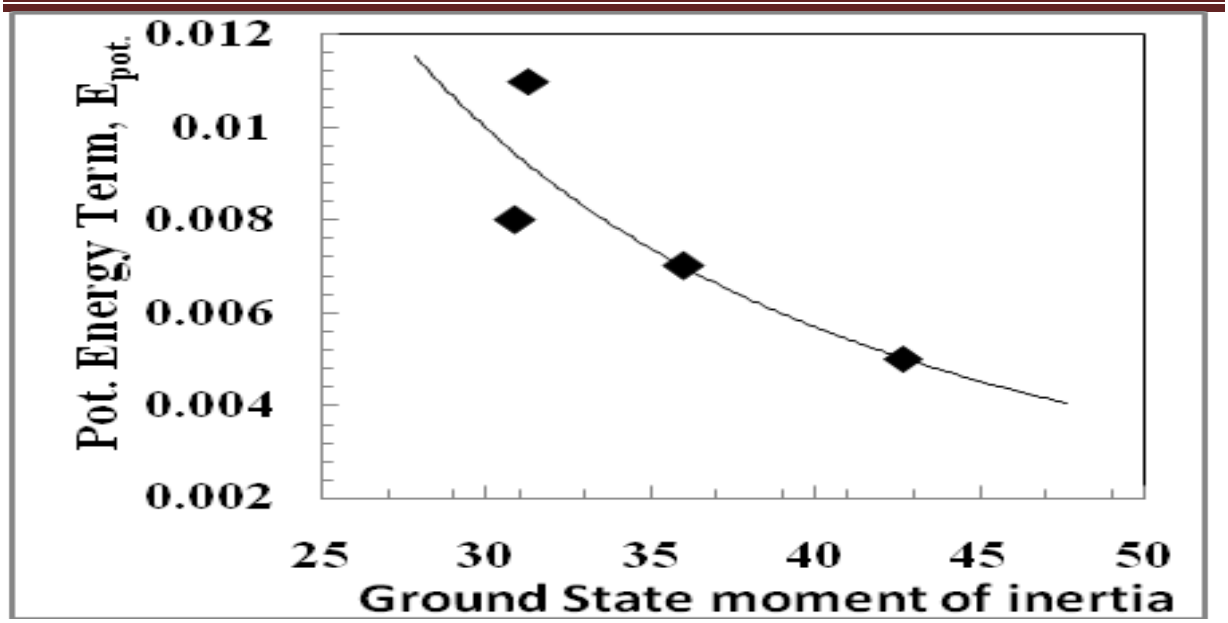


Fig.-(2): The Variation of Potential Energy Term ($E_{pot.}$) with Ground State Moment of Inertia.

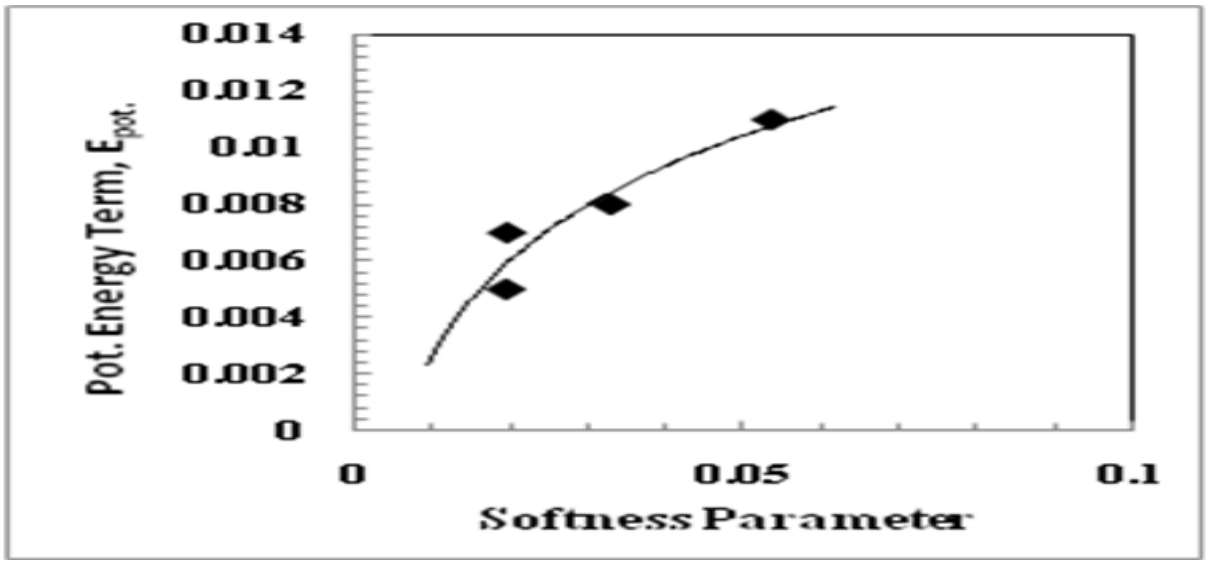


Fig.-(3): The Variation of Potential Energy Term ($E_{pot.}$) with Nuclear Softness Parameter.

RESULTS AND DISCUSSION

(a) Dependence of E_{pot} on Spin J

The variation of potential energy term for the different even-even nuclei in the region of I-quadrant based on the valence particle and hole pairs consideration [8]{Ce (N=90), Nd (N=92), Dy (N=92) & Dy (N-94)} with spin (J) has been shown in fig. (1). It is clear from fig. (1), that the value of potential energy term is increasing almost linear with increasing spin (J) for all the nuclei. In case of Dy (D=92) the potential energy term is less than that of Dy (N=94) for a particular value of spin (J).

(b) Dependence of E_{pot} on Ground State Moment of Inertia

In figure (2) the variation of potential energy, $E_{pot,}$ with ground state moment of inertia is shown. It is apparent from this figure that the potential energy term is decreases almost exponentially with ground state moment of inertia.

(c) Dependence of E_{pot} on Nuclear Softness Parameter

In figure (3) the variation of potential energy, E_{pot}, with nuclear softness parameter has shown. The nuclear softness parameter of nuclei is increases with nuclear softness parameter in the same way as that of decreases with ground state moment of inertia.

Acknowledgement

Hardik P. Trivedi. is very grateful to the Dr. A. K. Mahur, Associate Professor, Deptt. of Physics, VCTM, Aligarh for fruitful discussion and proper guidance.

REFERENCES

[1] M. Sakai, Quasi-Bands (Institute for Nuclear Study, University of Tokyo, Tokyo, 1982)

[2] M. A. J. Mariscotti, G. Scharff-Foldhaber and B. Buck, Phys. Rev. 178, 1864 (1969)

[3] R. K. Gupta, Phys. Lett. 36B, 173 (1971)

[4] M. Satpathy and L. Satpathy, Phys. Lett. 34B 377 (1971)

[5] D. Bonatsos and A. Klein, Phys. Rev. C29, 1879 (1984), Atomic data and Nuclear Data Tables 30, 27 (1984)

[6] A. Klein, Nucl. Phys. A 347, 3(1980)

[7] R. K. Gupta, *et al;* Nucl. Data for Sci. & Tech. (Mito, Japan), 729 (1988)

[8] J. S. Batra, *et.al;* Phys. Rev. C43, 1725(1991)

[9] J. B. Gupta, *et al;* Phys. Rev. C56, 6, 3417 (1997)

[10] J. H. Hamilton, *et.al;* Bull. Am. Phys. Soc. 32, 2130 (1987)

2014 International Conference on Signal Processing and Integrated Networks (SPIN)

Chaotic Map Based Steganography of Gray Scale Images in Wavelet Domain

Shalu Garg
Department of Electronics and Communication
Delhi Technological University
New Delhi, India
er.shalugarg@gmail.com

Monika Mathur
Department of Electronics and Communication
Delhi Technological University
New Delhi, India
mathur.monika2007@gmail.com

Abstract— ***In this study, we proposed a method of hiding the stego image in cover image by using a technique called fractional fourier transform with wavelet coefficients. Application of steganography is internet/web security. To maintain higher security Arnold transform is performed on host image with key, key is only known to a receiver/sender. For embedding, perform a fractional Fourier transform of cover image and secret image. Then apply DWT on both images. Cover image and secret image will added by using a technique called alpha blending which can add foreground with background color and wavelet coefficients of both images. Stego image will be extracted by applying IDWT (Inverse Discrete Wavelet Transform). For extracting, cover image will subtracted from stego image by using alpha blending. Secret image will be produced. By considering different aspects we have investigated the results of our scheme. This proposed method provides higher security, robustness against different attacks, good feasibility.***

Keywords— Steganography; Arnold transform; scrambling; alpha blending.

I. INTRODUCTION

Today digital contents are getting more and more commonly distributed by Internet than ever before. Steganography is an authenticated technique for maintaining secrecy of embedded data. Steganography provides hardness of detecting the hidden data and has a Potential capability to hide the existence of confidential data. In other words steganography is defined as a technique for hiding the secret information in a media in such a way that no one apart from the intended user can extract that message. Media can be a video, audio or can be a digital media. For this purpose we can use some other techniques also, like cryptography and water marking. For this purpose we selected 8 bit or 24 bit images as cover media. Cover image (original image) is defined as in which data to be hidden and cover image with secret information called stego image. 256 pixels are present in an image if it has dimensions of 256 x 256 in which each pixel is of 8 bit. RGB of 24 bit image where each pixel is of 24 bit. Gray Scale image is an image in which the value of each pixel is a single sample. That sample carries only intensity information. This image is also called a Black and White image. Grayscale images contain 16 shades of gray. Gray scale also called monochromatic, mono means one and color means chrome.

For hiding data we can use terms like watermarking and cryptography other than Steganography. Steganography and watermarking are basically exchangable terms both are using for same task that is hiding the information, but work in different domain. Watermarking can be invisible and visible but steganography always be invisible. Due to many factors steganography is different from other technique is higher capacity, security, feasibility, robustness and undetectibility. Steganography can be classified into different categories. Two broadly classified categories are spatial domain and transform domain. Spatial domain has less complexity but less robustness against attacks. In spatial domain pixel intensities of image is altered. LSB is defined as a technique used for embedding secret information in its pixel. But there are some drawback of LSB technique is explained as human eye is highly insensitive to edge, contrast, sharpening, texture where embedded information based on BPCS (bit plane complexity segmentation) and PVD (pixel value differencing). These methods are basically used for embedding more and more data. For maintaining higher security and authentication of this embedded data transform domain is used. In transform domain digital media converted into frequency domain by using different transform wavelet transform, fractional fourier transform, fourier transform, wavelet transform, cosine transform, counterlet transform. Transform domain has good robustness in comparison to spatial domain. Transform domain has high computational complexity but good robustness against attacks. Wavelet based steganograhy provides a good picture quality with high resolution. Steganography in transform domain has ability to tolerate signal processing operations and noises. In this less significant coefficients of cover image are used for embedding significant coefficients of secret data. In this DCT (discrete cosine transform) and DWT (discrete wavelet transform) techniques are frequently used.

Bhatnagar et al. [1] has proposed fractional wavelet packet transform to decompose an image, reference image is created by changing the frequency values of all sub-bands, singular values of reference image will modify with singular values of watermark image. Prabakaran et al. [2] has proposed high capacity and security based steganography scheme used

Arnold transformation to scrambled image, discrete wavelet transform, alpha blending. Shaker Hussain et al. [3] has reviews the current soft computing(SC) like neural network (NN), genetic algorithm(GA), support vector machine(SVM), fuzzy logic(FZ). SC is used for improving high quality of image, payload capacity, high imperceptibility. Saeid Fazli et al. [4] has proposed simple least significant bit insertion. This method will increase secret message capacity and security level. Khan [5] has proposed steganalysis based on neural networks to compute statistic features of images to get hidden information. Zong Liu et al. [6] has worked in wavelet domain by using laplace transform. Zhang et al. [7] has proposed steganography based on pixel differencing of images, that pixels used for data hiding. Sarreshtedarri et al. [8] has proposed high capacity method for transform domain work with wavelet transform provides large capacity without diminishing a picture quality of image. Malekmohamadi et al. [9] has proposed steganalysis using Gabor filter coefficients to train a multi layer perceptron neural network and a support vector machine classifier, Gabor filter used for showing differencing between clear image and altered image. This method provides high accuracy. Thanikaiselvan.V et al. [10] has proposed steganography based on integer wavelet transform (IWT) it provides high security, capacity, high visual quality. Banoci et al. [11] has done work with wavelet transform for providing high capacity and perceptibility. Raftari et al. [12] present a steganography technique based on integer wavelet transform and used Munkre's algorithm. In this stego data is hidden in frequency domain of cover image. MKhodaei et al. [13] has proposed steganography technique based on least significant bit insertion and pixel differencing of cover image.

In this paper we have purposed a new technique of embedding secret image in cover image by using Fractional wavelet transform (FRWT) with Arnold transform and alpha blending. Experimental analysis of this purposed method represents high efficiency, less computational complexity and high robustness against attacks.

II. Discrete Wavelet Transform (DWT): A Brief Review

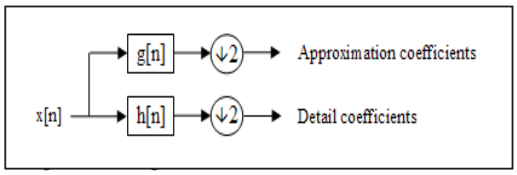
Assume the highest frequency components that exist in a signal will be Π radians. To provide sufficient amount of information of the signal, the signal will be sampled at Nyquist rate (which is twice the maximum frequency that exist in the signal). Next the signal is passed through the two filters is one half band low pass and one half band high pass band filters. The output of the high pass filter is preserved. After passing signal through a half band low pass filter, half of the samples can be eliminating. According to the Nyquist rate, the signal now has a highest frequency of Π/2 radians instead of Π radians. Simply discarding every other sample will subsample the signal by two, the signal will half the number of points. The scale of the signal is doubled. Low frequency basically removes high frequency components but leaves the scale unchanged and only sub-sampling process changes the scale.

DWT divides the signal into two parts, low frequency components called approximation coefficient and high frequency components called detailed coefficients. High frequency components basically contain edge components of the signal. On the other hand low frequency par further divided into two parts that is low frequency and high frequency. This process will going on as per required by the application.

$$y[n]=(x*g)[n]= \sum x[k]g[n-k] \quad (1)$$

$$y_{low}[n]=\sum x[k]g[2n-k] \quad (2)$$

$$y_{high}[n]=\sum x[k]h[2n-k] \quad (3)$$



III. Arnold Transform

It is defined as a chaotic map named after Vladimir Arnold basically used for scrambling the images so that data security can be maintained. Digital image is put as a matrix. After Arnold transform this image will be chaotic. Due to a correlation between elements discrete digital image is a class of special matrix. After Arnold transform new matrix can be obtained which provide image scrambling. Then set the image pixel coordinates. The order of image matrix is N, i, j € (0,1,2,.....,N-1) and the Arnold transform is as in (4).

$$\begin{bmatrix} i' \\ j' \end{bmatrix} = \begin{bmatrix} 1 & 2 \\ 1 & 1 \end{bmatrix} \begin{bmatrix} i \\ j \end{bmatrix} (Mod\ N) \quad (4)$$

The above transformation is one to one correspondence; the iteration can be done in image and image number is used as a secret key for extracting the secret image. This algorithm gives more security and robustness.

A. Properties

1. Arnold transform is invertible because the matrix has determinant.
2. It is area preserving.
3. It has a unique hyperbolic fixed point.

B. *FRWT (fractional wavelet transform)*

It is defined as the transform in which firstly take fractional fourier transform of images. Then DWT apply on these images. In fourier transform, it transfer a function in intermediate domain between time and frequency. Its application is defined as filter design, pattern recognition and signal analysis to phase retrieval. Basically fractional transform is domain signal. It's a rotation of time-frequency domain. Fractional fourier transform separates the real part

and imaginary part of images. After fractional fourier transform of images apply discrete wavelet transform on images and calculate detailed and approximation coefficients.

IV. Proposed Embedding Algorithm

In this section, we present our algorithm for gray scale images of dimension 256x256. The human eye has different visual sensitivity for different frequency. Low frequency component are basically used for embedding data. We are using FRWT (fractional wavelet transform) for hiding stego data in cover image. For higher security Arnold transform is used through which image can be scrambled. To embed stego image into original image Alpha blending is used in which we decide alpha factor (range b/w 0 to 1.0). Let x be the original gray scale image of size NxN and secret data in form of image of size MxM. Steps of embedding process are as follows:

Step1: First take cover image (C) of size NxN and secret image of size MxM. Then apply Arnold Transform with key on Secret image (S) through which image will scramble. Key will be known to only intended user. With the help of Arnold Transform we can attain high security.

Step2: Take fourier transform of cover image (C) and scrambled secret image (SS), which separate the real and imaginary part of images.

Step3: Real part of both images will transform into wavelet domain. 2D DWT of level1 will be applied on both images. Through which we extract approximation (LL) coefficient and detailed coefficient {LH, HL, HH}. Horizontal approximation coefficient is used for embedding data.

Step4: Extract the approximation coefficient of matrix A and detailed coefficient matrices HL, LH & HH of level1 of the cover image (C).

Step5: Extract the detailed coefficient of matrix A1 and detailed coefficient matrices HL1, LH2, HH2 of level1 of scrambled secret image (SS).

Step6: Apply Alpha Blending on image C and image SS which add approximation coefficients of image C and image SS.

Step7: Apply 2D IDWT (inverse discrete wavelet transform) to get stego image (SI).

The fig.2 shows embedding process.

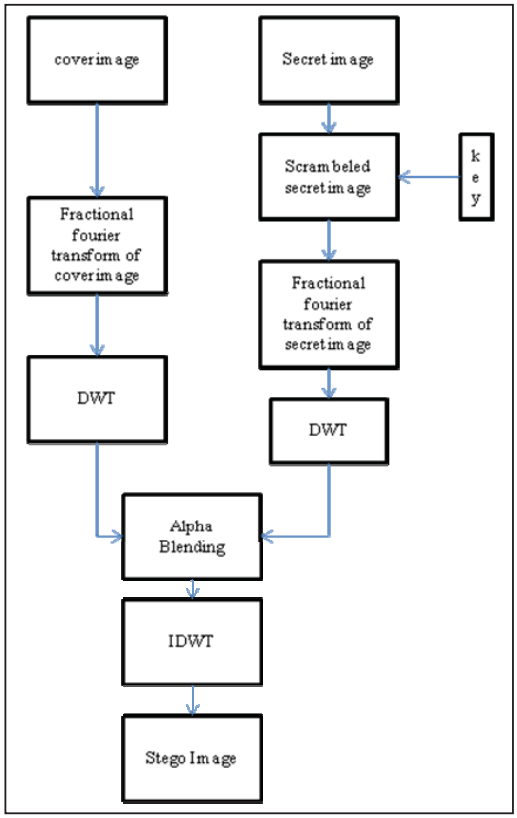


Fig. 2 Embedding code of modified secure steganography

V. Proposed Extracting Algorithm

Steps of Extracting Process:

Step1: Apply 2-D DWT of level 1 on both stego image (SI) and cover image(C).

Step2: Apply Alpha Blending on both SI and C.

Step3: Perform IDWT on separated wavelet coefficients and get scrambled secret image.

Step4: Take fourier transform of scrambled secret image.

Step5: Take inverse Arnold of scrambled secret image .

Step6: Recovered secret image (which is almost in similar to secret image).

The fig.3 shows embedding process.

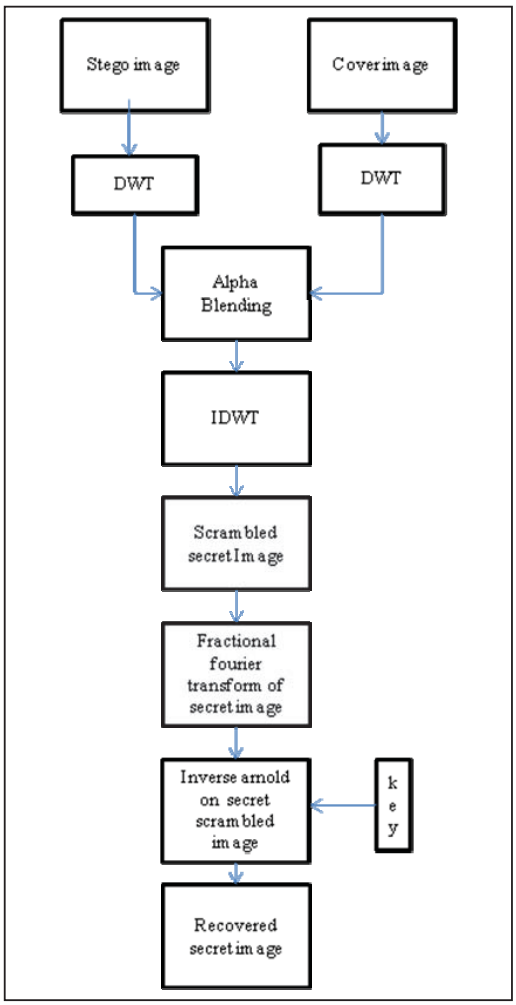


Fig. 3 Extracting code of modified secure steganography

VI. Experimental Results and Attack Analysis

The performance of purposed steganography method is implemented by using Matlab2010 and 7.10 version. Experimental result and attack analysis will be discussed in this section. In our experiment we considered different gray scale images of size 256 x 256images like cameraman, circles, Goldhill, peppers, Lena etc.

Figure 4(a) shows the cover image, 4(b) shows the secret image, 4(c) shows the secret scrambled image and 4(d) shows the final stego image and 4(e) shows the recovered secret image. The experimental results shows that secret image and recovered secret image are exactly similar to each other as PSNR value is very high i.e. 75.435.

A. Objective analysis

As a performance measure for image distortion due to embedding, the well-known peak-signal-to noise ratio (PSNR), which is categorized under difference distortion metrics, can be applied to stego images. The good visual quality of stego images (ie- images embedded with a secret image) is the most important property of steganography system because it is hard to detect by detectors. It is defined as:

$$PSNR = 10\log_{10}\left[\frac{255^2}{MSE}\right]$$

MSE is the mean square error representing the difference between the original cover image x sized M x N and the stego image x' sized M x N.

$$MSE = \frac{\sum_{M,N}\left[I_1(m,n) - I_2(m,n)\right]^2}{m \times n}$$

A large PSNR value means that the stego image is most similar to original image and vice versa. It is hard for the Human eyes to distinguish between original cover image and stego image when the PSNR ratio is larger than 30db. Other parameters for performance evaluation are SC (Structural Content) and NC(Normalized correlation).

Table1. MSE , PSNR ,SC , NC for test images

Cover image	Stego image	MSE	PSNR	SC	NC
Circles	Camera	0.0018	75.435	1.000	0.998
Lena	Godhill	0.0018	75.262	1.000	0.998
Camera	Circles	0.0018	74.794	1.000	0.997
Godhill	Lena	0.0018	74.449	1.000	0.998
Lena	Circles	0.0018	74.794	1.000	0.997
Circles	Lena	0.0018	74.449	1.000	0.997
Peppers	Lena	0.0018	74.997	1.000	0.997



Fig.4(a) Cover image



Fig.4(b) Secret image

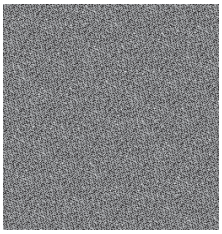


Fig.4(c) Scrambled secret image



Fig.4(d) stego image



Fig.4(e) Recovered Secret image

The *Correlation Coefficient* of two identical size images also tells the similarity between the images. If the value of Correlation Coefficient is near to 1, then two images are very similar. If value is 1 i.e. both are same images. Here we use it to compute the similarity measurement of originalsecret image and recovered secret image, which is defined as

$$corrcoeff = \frac{\sum_{i=1}^{N}\sum_{j=1}^{N}\left(w(i,j) * w'(i,j)\right)}{\sum_{i=1}^{N}\sum_{j=1}^{N} w^2(i,j)}$$

Where N×N is the size of secret image, $w(i,j)$ and $w'(i,j)$ represents the origina; and recovered secret images respectively.

B. Attack analysis

In order to measure the robustness of proposed scheme various attacks have been performed on test image. The scheme can withstand with number of attacks like Gaussian white' noise of zero mean and 0.001 variance, contrast variations, histogram attack, sharpening attack, median filtering attack. Recovered watermark with accuracy rate and correlation coefficient are shown below in figure 5 for camera man.



Fig.5 (a) Contrast variation



Fig.5(b) Addition of Gaussian white noise with 0 mean and 0.01 variance



Fig.5(c) Histogram attack



Fig.5(d) Sharpening effect

VII. CONCLUSIONS

In this, a robust steganography technique in the DWT domain is suggested and implemented using the MATLAB software. FRWT (Fractional wavelet transform) algorithm is used to embed secret data in low frequency range to achieve both robustness and higher security. For maintaining higher security Arnold Transform is used. With the Arnold transform a image can be scrambled and using inverse Arnold transform we can receive the unscrambled image back . By using FRWT computational time will reduced. The measured performance of the technique proves its robustness against several kinds of image processing attacks. Hence it can serve as a best means to prove the authenticity and ownership of intellectual images. So, common methods of attack, experimental results and analysis show that the proposed algorithm is effective and can be used in a practical system.

References

[1] A. Cheddad, J. Condell, K. Curran, P. McKevitt, "Digital image steganography: Survey and analysis of current methods," Elevier.

[2] S. Bhattacharyya, I. Banerjee, G. Sanyal, "A survey of steganography and steganalysis technique in image, Text, Audio, and video as cover .carrier," Journal of global research in computer science, vol. 2, no.4,Apr. 2011.

[3] C. K. Chan, L. M. Chang, "Hiding data in image by simple LSB substitution," Pattern Recognition, vol. 37, pp. 469–471, 2003.

[4] C. C. Chang, C. L. Chiang, J.Y. Hsiao, "A DCT-domain System forHiding Fractal Compressed Images," In AINA'05, Proceeding of the19th international Conf. on Advanced Information Networking and Applications, 2005.

[5] C. Y. Lin, Y.T. Ching, "A Robust Image Hiding Method Using Wavelet Technique," Journal of Information Science andEngineering, Vol. 22, pp. 163-174, 2006.

[6] A. A. Abdelwahab, A. L. Hassaan, "A Discrete Wavelet Transform based Technique for Image Data Hiding," 25th National RadioConference, pp. 1–9, Egypt, 2008.

[7] A. Nag, S. Biswas, D. Sarkar, P. P.Sarkar, "A Novel Technique for Image SteganograpyBased on DWT and Huffman Encoding, "International Journal of Computer Science and Security, (IJCSS), Volume (4): Issue (6),pp. 497-610,2011.

[8] L. Chun-Shien. Multimedia security: steganography and digital watermarking techniques for protection of intellectual property. USA: Idea Group Publishing, 2005, pp. 1-253.

[9] R.J. Anderson and F.A.P. Petitcolas. (1998, May). "On the limits of steganography." IEEE Journal of Selected Area in Communications. [On line]. 16(4), pp. 474-481.

[10] I.J. Cox, M.L. Bloom, J.A. Fridrich, and T. Kalkert. Digital watermarking and steganography.USA: Morgan Kaufman Publishers, 2008, pp. 1-591.

[11] N.F. Johnson and S. Jajodia. (1998, Feb.). "Exploring steganography: seeing the unseen."IEEE Computer Journal. [On line].

[12] A. Cheddad, J. Condell, K. Curran and P.M. Kevitt. (2010). "Digital image steganography: survey and analysis of current methods." Signal Processing Journal. 90(3),pp.727-752.Available: http://www.abbascheddad.net/Survey.pdf [Aug. 2011].

Applied Soft Computing xxx (2014) xxx–xxx

Contents lists available at ScienceDirect

Applied Soft Computing

journal homepage: www.elsevier.com/locate/asoc

Comparative analysis of statistical and machine learning methods for predicting faulty modules

Q1 Ruchika Malhotra

Department of Software Engineering, Delhi Technological University, Bawana Road, Delhi 110042, India

ARTICLE INFO

Article history:
Received 25 October 2011
Received in revised form 26 January 2014
Accepted 22 March 2014
Available online xxx

Keywords:
Software quality
Static code metrics
Logistic regression
Machine learning
Receiver Operating Characteristic (ROC) curve

ABSTRACT

The demand development of good quality software has seen rapid growth in the last few years. This is leading to increase in the use of the machine learning methods for analyzing and assessing public domain data sets. These methods can be used in developing models for estimating software quality attributes such as fault proneness, maintenance effort, testing effort. Software fault prediction in the early phases of software development can help and guide software practitioners to focus the available testing resources on the weaker areas during the software development. This paper analyses and compares the statistical and six machine learning methods for fault prediction. These methods (Decision Tree, Artificial Neural Network, Cascade Correlation Network, Support Vector Machine, Group Method of Data Handling Method, and Gene Expression Programming) are empirically validated to find the relationship between the static code metrics and the fault proneness of a module. In order to assess and compare the models predicted using the regression and the machine learning methods we used two publicly available data sets AR1 and AR6. We compared the predictive capability of the models using the Area Under the Curve (measured from the Receiver Operating Characteristic (ROC) analysis). The study confirms the predictive capability of the machine learning methods for software fault prediction. The results show that the Area Under the Curve of model predicted using the Decision Tree method is 0.8 and 0.9 (for AR1 and AR6 data sets, respectively) and is a better model than the model predicted using the logistic regression and other machine learning methods.

© 2014 Published by Elsevier B.V.

Q2 1. Introduction

As the size and complexity of the software is increasing day by day, it is usual to produce software with faults. The identification of faults in a timely manner is essential as the cost of correcting these faults increases exponentially in the later phases of the software development life cycle. Hence, testing is a very expensive process and one-third to one-half of the overall cost is allocated to the software testing activities [47]. There are several approaches being proposed to detect the faults in the early phases of the software development [47]. This motivates the development of fault prediction models that can be used in classification of a module as fault prone or not fault prone.

Several static code metrics have been proposed in the past to capture various aspects in the design and source code, for example [17,22,35]. These metrics can be used in developing the fault prediction models. The prediction models can then be used by the software organizations during the early phases of software development to identify faulty modules. The software organizations can use these subset of metrics amongst the available large set of software metrics. The metrics are computed from the proposed model to obtain the information about the quality of the software and can be assessed in the early stages of software development. These quality models will allow the researchers and software practitioners to focus the available testing resources on the faulty areas of the software, which will help in producing a improved quality, low cost and maintainable software. The static code metrics have been advocated as widely used measures in the literature [9,36].

The machine learning (ML) methods have been successfully applied over the years on a range of problem domains such as medicine, engineering, physics, finance and geology. These methods have also started being used in solving the classification and control problems [1,11–13,34,56]. In the existing literature, the researchers have used various methods to establish the relationship between the static code metrics and fault prediction. These methods include the traditional statistical methods such as logistic regression (LR) [8,26,32,39] and the machine learning (ML) methods such as decision trees [16,25,27,29,30,33,42,46,49,52], Naïve

E-mail address: ruchikamalhotra2004@yahoo.com

http://dx.doi.org/10.1016/j.asoc.2014.03.032
1568-4946/© 2014 Published by Elsevier B.V.

UNCORRECTED PROOF

Please cite this article in press as: R. Malhotra, Comparative analysis of statistical and machine learning methods for predicting faulty modules, Appl. Soft Comput. J. (2014), http://dx.doi.org/10.1016/j.asoc.2014.03.032

Bayes [6,9,10,38,41,49], Support Vector Machines [52,54], Artificial Neural Networks [28,33,38]. However, few studies compare the LR models with the ML models for software fault prediction using the static code metrics. Hall et al. [18] concluded that more quality studies should be conducted for software fault prediction using ML methods and Menzies et al. [36] advocated the use of public data sets for software fault prediction. It is natural for the software practitioners and potential users to wonder, "Which ML method is best?", or more realistically, "Is the predictive capability of the ML methods comparable or better than the traditional LR methods?". For this reason, this paper compares the model predicted using the LR method with the models predicted using the widely used ML methods and rarely used ML methods (Cascade Correlation Network (CCN), Group Method of Data Handling Polynomial Method (GMDH), Gene Expression Programming (GEP)). The evidence obtained from the data based empirical studies can help the software practitioners and researchers in obtaining the most powerful support for accepting/rejecting a given hypothesis [2]. Hence, conducting empirical studies to compare the models predicted using the LR and the ML methods is important to develop adequate body of knowledge so that the well formed and widely accepted theories can be produced.

The main motivation of the paper is threefold: (1) to show the performance of the ML methods such as Support Vector Machines (SVM), Decision Tree (DT), CCN, GMDH and GEP for software fault prediction; (2) to compare and assess the predictive performance of the models predicted using the ML methods with the model predicted using the LR methods; and (3) to evaluate the performance capability of the ML methods using public data sets, i.e. across two systems.

Thus, in this work we (1) build fault proneness models and (2) empirically compare the results of the LR and the ML methods. In this paper, we investigate the below issues:

1. How accurately and precisely do the static code metrics predict faulty modules?
2. Is the performance of the ML methods better than the LR method?

The validation of the models predicted using the LR and the ML methods is carried out using Receiver Operating Characteristic (ROC) analysis. We use the ROC curves to obtain the optimal cut off point that provides balance between the faulty and non faulty modules. The performance of the models constructed to predict faulty or non faulty modules is evaluated using the Area Under the Curve (AUC) obtained from the ROC analysis [11]. In order to perform the analysis we validate the performance of these methods using public domain AR1 and AR6 data sets. The AR1 and AR6 data sets consist of 121 and 101 modules, respectively. These data sets were developed using C language [35]. The data are obtained from the Promise data repository [35] and collected by Software Research Laboratory (Softlab), Bogazici University, Istanbul, Turkey [19]. Thus, the main contributions of the paper are: first, we performed the comparative analysis of the models using the LR method with the models predicted using the ML methods for prediction of faulty modules. Second, we analyze public domain and industrial data sets, hence analysing valuable data in an important area. Third, we analyze six ML methods and apply ROC analysis to determine their effectiveness.

The paper is organized as follows: Section 2 presents the research background that summarizes the static code metrics included and describes the sources from which the data is collected. Section 3 describes the descriptive statistics and the performance measures used for model evaluation. The results of model prediction are presented in Section 4 and the models are validated in Section 5. Section 6 summarized the threats to validity of the models and the conclusions of the work are given in Section 7.

2. Research background

In this section we present the dependent and independent variables used in this paper (Section 2.1). We also describe the data collection procedure in Section 2.2.

2.1. Dependent and independent variables

Fault proneness is the binary dependent variable in this work. Fault proneness is defined as the probability of fault detection in a module [2,4,7]. We use the LR method, which is based on probability prediction. The binary dependent variable is based on the faults that are found during the software development life cycle.

For this study, we predict fault prone modules from static code metrics defined by Halstead [17], and McCabe [35]. The software metrics selected in this paper are procedural and module based metrics, where a module is defined as the smallest individual unit of functionality. We find the relationship of the static code metrics with fault proneness since they are "useful", "easy to use", and "widely used" metrics [36].

First, the static code metrics are known as useful as they have shown higher probability of fault detection in past [36]. The results in this study also show that the correctly predicted percentage of faulty modules was high. Second, the metrics like lines of code and the metrics given by Halstead and McCabe [17,35] can be computed easily and at low cost, even for very large systems [30]. Third, many researchers have used the static code metrics in the literature [8,25–30,32,33,38,39,41,42,46,49,52,54]. It has been stated in [36] that "Verification and Validation textbooks advise using static code complexity metrics to decide which modules are worthy of manual inspections". Table 1 presents the static code metrics chosen in this study.

2.2. Empirical data collection

This study makes use of two public domain data sets AR1 and AR6 available in the Promise data repository [45] and donated by Software Research Laboratory (Softlab), Bogazici University, Istanbul, Turkey [23]. The data in AR1 and AR6 are collected from embedded software in a white-goods product. The data was collected and validated by the Prest Metrics Extraction and Analysis Tool [44] available at http://softlab.boun.edu.tr/?q=resources&i=tools. The data in AR1 and AR6 was implemented in the C programming language. Both the data sets were collected in 2008 and donated by Softlab in 2009. The AR1 system consists of 121 modules (9 faulty/112 non faulty). The AR6 system consists of 101 modules (15 faulty/86 non faulty). Both the data sets comprise of 29 static code attributes (McCabe, Halstead and LOC measures) and 1 fault information (false/true). Table 2 summarizes the distribution of faulty modules in the AR1 and AR6 data sets. The table shows that 7.44% of modules were faulty in the AR1 data set and 14.85% of modules were faulty in the AR6 data set.

3. Research methodology

In this section, steps taken to analyze the static code metrics are described.

3.1. Descriptive statistics and outlier analysis

Before further analysis can be carried out, the data set must be suitably reduced by analysing it and then drawing meaningful

UNCORRECTED PROOF

Please cite this article in press as: R. Malhotra, Comparative analysis of statistical and machine learning methods for predicting faulty modules, Appl. Soft Comput. J. (2014), http://dx.doi.org/10.1016/j.asoc.2014.03.032

Table 1
Software metrics.

McCabe [26]	Cyclomatic_Complexity Design_Complexity Essential_Complexity
Halstead [13]	Num Operands (N_1) Num Operators (N_2) Num Unique Operands (n_1) Num Unique Operators (n_2) Error Estimate Length: $N = N_1 + N_2$ Level: $L = V^*/VV^* = (2 + n_1^*)\log_2(2 + n_2^*)$ Volume: $V = N^* \log_2(n_1 + n_2)$ Content: $I = \tilde{L} * V \qquad \tilde{L} = \frac{2}{n_1} * \frac{n_1}{N_2}$ Difficulty: $D = 1/L$ Effort: $E = V/\tilde{L}$ Program time: $T = E/\beta$
Lines of code (LOC)	Blank Code_and_Comments Comments Executable Total
Miscellaneous	Branch_Count Call_Pairs Condition_Count Cyclomatic_Density Decision_Count Decision_Density Design_Density Edge_Count Essential_Density Maintenance_Severity Modified_Condition_Count Multiple_Condition_Count Node_Count Normalized_Cylomatic_Complexity Parameter_Count Percent_Comments

Table 2
Data used in the study.

System	Language	Total LOC	Total modules	% Faulty
Embedded software from white-goods product (AR1)	C	2467	121	7.44
Embedded software from white-goods product (AR6)	C	2078	101	14.85

conclusions from it. Descriptive statistics such as minimum, maximum, mean, standard deviation can be effectively used as measured for comparing different experimental studies. The independent variable having low variance will not differentiate modules very well and hence are unlikely to be useful. Therefore, such variables are to be excluded from the analysis.

Outliers are defined as the data points that are located away from the sample space. Outlier analysis is essential for identifying those data points that are over influential and must be analyzed for exclusion from the data set. In this study we found the Univariate and multivariate outliers. We used Mahalanobis Jackknife distance to identify the multivariate outliers. The details on outlier analysis can be found in [3].

3.2. Evaluating the performance of the models

The performance measures used to assess the quality of the predicted model in this work are described in this section.

3.2.1. Sensitivity and specificity

The correctness of the LR and the ML methods are analyzed using performance measures such as the sensitivity and the specificity. The sensitivity of the model is defined as the percentage of the faulty modules correctly predicted and the specificity of the model is defined as the percentage of the non faulty modules correctly predicted. The sensitivity and specificity should be high in ideal situation. The sensitivity and the specificity as determined by the ROC analysis (see Section 3.2.3 for details) are reported for each model predicted in this paper.

3.2.2. Precision

The precision is defined as the ratio of number of modules correctly classified to be faulty/non faulty to the total number of modules.

3.2.3. Receiver operating curve analysis

The performance of the models predicted in this work is analyzed using the ROC analysis [21]. During the development of the ROC curves, many cutoff points between 0 and 1 are selected and the sensitivity and specificity at each cut off point is calculated.

The Area Under the ROC Curve (AUC) is a combined measure of the sensitivity and specificity [14]. The AUC is used for comparing the predictive capability of the models predicted using the LR and the ML methods.

3.2.4. Cross validation

The prediction accuracy of the models can be assessed by applying them to different data sets. Hence, we performed k-cross validation of the models developed [51]. In this method the data set is randomly divided into k subsets. Each time $k-1$ subsets are used as the training sets and one of the k subsets is used as the validation set. Finally, we get the probability of occurrence of faults for each of the module. The results were validated with the value of k equal to 10.

4. Analysis results

In this section we describe the analyses performed to find the effect of the static code metrics and the fault proneness of the modules. We first employed the LR [24] method, which is the widely used statistical method to construct the fault proneness models. We then employed six machine learning methods (ANN, DT, SVM, CCN, GMDH, and GEP) to predict the fault proneness of the modules. These methods have been rarely applied in predicting fault prone/not fault prone modules.

In these methods we applied multivariate analysis. Multivariate regression analysis is used to determine combined effect of static code metrics and fault proneness [1].

During the multivariate analysis we did not found any of the outlier to be influential. In order to validate our results we used two data sets AR1 and AR6.

4.1. Descriptive statistics

Tables 3 and 4 show "min", "max", "mean", "std dev", "variance", "25% quartile" and "75% quartile" for all metrics considered in this study. The data was prepared by removing the outliers and metrics which did not had at least six values from the analysis.

4.2. Logistic regression (LR) analysis

The research methodology and the results of analysing the relationship between the static code metrics and the fault proneness using the LR method is presented in this section.

4.2.1. Logistic regression (LR) modeling

The LR method is the most widely used statistical technique [4] in the literature for predicting categorical dependent variable from

UNCORRECTED PROOF

Please cite this article in press as: R. Malhotra, Comparative analysis of statistical and machine learning methods for predicting faulty modules, Appl. Soft Comput. J. (2014), http://dx.doi.org/10.1016/j.asoc.2014.03.032

Table 3
Descriptive statistics for static code metrics (AR1 data set).

Metrics	Minimum	Maximum	Mean	Std. deviation
total_loc	2	95	20.388	19.601
blank_loc	0	9	0.206	1.040
comment_loc	0	30	4.760	6.114
code_and_comment_loc	0	2	0.074	0.293
executable_loc	2	82	15.421	15.262
unique_operands	1	47	12.454	10
unique_operators	2	19	8.330	4.156
total_operands	1	118	23.743	24.096
total_operators	3	184	36.876	36.343
halstead_vocabulary	3	62	20.785	13.453
halstead_length	4	302	60.619	60.326
halstead_volume	4	1210	205.132	240.713
halstead_level	0.03	1	0.257	0.245
halstead_difficulty	1	33.33	7.798	6.377
halstead_effort	4	40,333.33	2861.796	5926.754
halstead_error	0	0.4	0.068	0.08043
halstead_time	0.22	2240.74	158.988	329.264
branch_count	0	76	9.603	13.09611
decision_count	0	38	4.802	6.548
call_pairs	0	19	2.239	3.413
condition_count	0	38	4.396	6.527
multiple_condition_count	0	10	0.992	1.604
cyclomatic_complexity	1	28	4.570	4.857
cyclomatic_density	0.13	0.6	0.312	0.104
decision_density	0	2	0.683	0.582
design_complexity	0	19	2.239	3.413
design_density	0	6	0.6818	1.206
normalized_cyclomatic_complexity	0.03	0.5	0.254	0.104
formal_parameters	0	3	0.331	0.568

Table 4
Descriptive statistics for static code metrics (AR6 data set).

Metrics	Minimum	Maximum	Mean	Std. deviation
total_loc	1	98	20.574	19.8889
blank_loc	0	48	1.079	6.4026
comment_loc	0	31	5.128	6.486
code_and_comment_loc	0	11	0.277	1.429
executable_loc	0	89	15.257	15.313
unique_operands	1	50	13.525	10.931
unique_operators	2	21	8.584	4.421
total_operands	1	109	24.405	22.906
total_operators	3	160	37.465	34.849
halstead_vocabulary	3	97	22.821	16.935
halstead_length	4	267	61	57.380
halstead_volume	4	1101	207.43	231.414
halstead_level	0.03	591	11.248	78.0381
halstead_difficulty	0.04	33.33	7.701	5.956
halstead_effort	4	18,666.67	2561.309	4013.737
halstead_error	0	14,775	275.563	1951.752
halstead_time	0.17	1037.04	142.270	223.001
branch_count	0	820.83	22.929	107.864
decision_count	0	27	4.208	5.757
call_pairs	0	20	2.643	3.598
condition_count	0	24	3.277	5.069
multiple_condition_count	0	9	0.950	1.802
cyclomatic_complexity	1	19	3.841	3.732
cyclomatic_density	0.09	10	0.448	1.299
decision_density	0	3	0.671	0.688
design_complexity	0	20	2.470	3.443
design_density	0	7	0.851	1.421
normalized_cyclomatic_complexity	0	0.38	0.197	0.079
formal_parameters	0	2	0.261	0.460

the set of independent variables (a detailed description is given by [4,24]). In this study, independent variables are the static code metrics and the dependent variable is fault proneness. The LR method is divided into two categories: (i) Univariate LR and (ii) Multivariate LR.

The univariate LR is a statistical method determines the relationship between each static code metric and fault proneness. The multivariate LR is used to construct a model by using all the static code metrics in combination for predicting faulty/non faulty modules. In the LR method there are two stepwise selection methods including forward selection and backward elimination [4]. In the forward stepwise method, the entry of each variable is examined stepwise at each step. The backward elimination method enters all the independent variables in the model at a time. The metrics are then removed one at a time from the model until a stopping criteria is satisfied. In this work we have applied the backward

UNCORRECTED PROOF

Please cite this article in press as: R. Malhotra, Comparative analysis of statistical and machine learning methods for predicting faulty modules, Appl. Soft Comput. J. (2014), http://dx.doi.org/10.1016/j.asoc.2014.03.032

Table 5
Multivariate analysis for LR model (AR1 data set).

Variable	Halstead difficulty	Constant
B	0.140	−3.997
SE	0.044	0.686
p-Value	0.002	0.000
	−2 log likelihood: 53.645	
	R^2 statistic: 0.37	

Table 6
Multivariate analysis for LR model (AR6 data set).

Variable	Halstead effort	Decision count	Constant
B	0.000	0.388	−2.702
SE	0.000	0.121	0.466
p-Value	0.036	0.001	0.000
	−2 log likelihood: 62.025		
	R^2 statistic: 0.46		

elimination method on the static code metrics selected significant in the univariate analysis.

For the model predicted, the Coefficients (Ai's), the statistical significance (*p*-value), Maximum Likelihood Estimation (MLE), and the R^2 statistics are reported. The higher value of the R^2 statistic depicts that more is the effect of the independent variables on the dependent variable and higher is the prediction accuracy of the model. However, as stated in [6,55], "we should not interpret the value of R^2 in logistic regression using the usual heuristics for linear regression R^2s since they are built upon very different formulas". Hence, high value of R^2s rarely occur in the LR analysis. The details can be found in [2].

A test of multicollinearity was performed on the models predicted in this paper. The presence of the multicollinearity makes the interpretation of the model difficult. Let the covariates of the model predicted be *Y*1, *Y*2, ... *Yn*. The maximum eigenvalue and the minimum eigenvalue (e_{max} and e_{min}, respectively) is calculated using the principal component analysis method. The conditional number is defined as $\lambda = \sqrt{e_{max}/e_{min}}$. The multicollinearity of the model is not tolerable if the value of the conditional number is greater than 30 [50].

4.2.2. Multivariate LR analysis

In this subsection we find the effect of the independent variables (static code metrics) on the dependent variable (fault proneness). The multicollinearity of the predicted models is acceptable as the conditional number for the models is below 30 (see Section 4.2.1). In Tables 3 and 4, we summarize the coefficient (*B*), statistical significance (*p*-value), R^2, and correctness. One metric was selected in the model predicted using AR1 (see Table 5). Table 6 shows two out of the selected static code metrics are included in the model predicted using AR6 data set. The value of R^2 statistic is 0.46.

Table 7 predicts accuracy of the model containing the static code metrics, using forward selection method. Two metrics Halstead effort and decision count are included in the model. During univariate analysis all the static code metrics chosen in this work were found to be significant.

Table 7
Predicted correctness of LR model.

Observed	AR1 Predicted (cutoff point = 0.06)			AR6 Predicted (cutoff point = 0.18)		
	0.00	1.00	Percent correct	0.00	1.00	Percent correct
0.00	77	35	68.70%	65	21	75.58%
1.00	2	7	77.80%	3	12	80.00%

The model is applied to all the system modules to compare the accuracy of predicting faulty and non faulty software modules. The cut off point is selected using the ROC analysis to avoid the selection of arbitrary cut off point in the analysis [21]. This will provide balance between the values of the sensitivity and the specificity. The results of the model predicted using the AR1 data set shows that the sensitivity and specificity are 77.8% and 68.7%, respectively. In case of the AR6 data set, out of 15 modules actually fault prone, 12 modules were predicted to be fault prone. The sensitivity of the model is 80.00% (refer Table 5). Similarly, 65 out of 86 modules were predicted to be not fault prone. Thus, the specificity of the model is 75.58%. This shows that the model accuracy is not low.

4.3. Machine learning methods

In this section, we present the results of models predicted using six ML methods.

4.3.1. Artificial Neural Network (ANN)

4.3.1.1. Architecture. We use Multilayer Feed Forward and back propagation algorithm to train the network using the ANN method. The network constructed using the ANN method consists of three layers, input layer with I nodes, hidden layer with H nodes, and output layer with O nodes. The nodes in the input layer are connected to each node in the hidden layer and there is no direct connection between the input and the output nodes. The ANN adjusts the weights between connection of each nodes repetitively by computing the difference between the predicted output and the actual network. The network learns by searching the connection weights that minimizes the error between the actual and the predicted output on the training data set [46]. In order to perform the ANN analysis, we used min–max normalization is used. The min–max normalization transforms the data in the range of 0–1 [20,50] using the following formula:

$$v' = \frac{v - \min_M}{\max_M - \min_M} \quad (1)$$

where $\min_M$ and $\max_M$ are the minimum and maximum values of an metric *M*.

The ANN model was trained with the learning rate of 0.005, with the aim to continue until the minimum sum of squared error is reached.

The principal components (P.C.) analysis was applied on the normalized metrics to produce domain metrics. The aim of the P.C. analysis is to transform the raw static code metrics to the measures which are not correlated to each other [31]. Given an $a \times b$ matrix of multivariate training data, where *a* represents system modules and *b* represents the static code metrics. The P.C. analysis reduces the column ($a \times p$ matrix) where *b* is reduced to *p* ($p < b$).

The following domain metrics were given as input to the ANN model using the AR1 data set:

- P1: Total operators, halstead length, halstead volume, halstead error, total operands
- P2: total operators, halstead length, halstead volume, halstead error, total operands
- P3: design density, normalized cyclomatic complexity, cyclomatic density, blank loc, design complexity
- P4: halstead level, decision density, unique operators, normalized cyclomatic complexity, cal pairs, code and comment loc, cyclomatic density, decision density, formal parameters, comment loc
- P5: formal parameters, code and comment loc, decision density, normalized cyclomatic complexity, condition count
- P6: blank loc, code and comment loc, decision density, halstead level, formal parameters

UNCORRECTED PROOF

Please cite this article in press as: R. Malhotra, Comparative analysis of statistical and machine learning methods for predicting faulty modules, Appl. Soft Comput. J. (2014), http://dx.doi.org/10.1016/j.asoc.2014.03.032

Table 8
ANN summary for AR6 data set.

Architecture	AR1	AR6
Layers	3	3
Input units	7	9
Hidden units	4	4
Output units	2	2
Training Algorithm	Back propagation	

- P7: cyclomatic density, design density, blank loc, halstead difficulty, code and comment loc
- P8: multiple condition count, code and comment loc, decision density, unique operands, comment loc
- P9: decision density, halstead difficulty, formal parameters, halstead level, blank loc

The following domain metrics were given as input to the ANN model using the AR6 data set:

- P1: Total operators, halstead volume, halstead length, total operands, unique operands
- P2: Halstead level, halstead error, cyclomatic density, blank LOC, Branch count
- P3: Design density, design complexity, call pairs, normalized cyclomatic complexity, comment LOC
- P4: Design density, unique operators, halstead difficulty, condition count, multiple condition count
- P5: Formal parameters, normalized cyclomatic complexity, condition count, cyclomatic complexity
- P6: Formal parameters, normalized cyclomatic complexity, decision density, design complexity, call pairs
- P7: Normalized cyclomatic complexity, design density, halstead difficulty, comment LOC, unique operands

Table 8 presents the architecture of the ANN model for the AR1 and AR6 data sets. The ANN method is non linear in nature, hence the traditional statistical tests applied in the LR method are not applicable here. Instead we used the AUC produced by the ROC analysis to heuristically analyze and assess the importance of the static code metrics (input variables) for model prediction purpose.

4.3.1.2. Artificial Neural Network (ANN) analysis. In this section, we present and assess the results produced by applying the ANN method for the fault prediction. The module with one or more faults was considered to be faulty. The input to the model predicted using the ANN method were the P.C.s given above.

Table 9 presents the accuracy of the model predicted using the ANN method. The cut off point for the AR1 and AR6 models are 0.05 and 0.11, respectively. In case of the AR1 data set, the sensitivity and specificity of the model is 77.8% and 68.7%, respectively. Out of 9 modules actually fault prone, 7 modules were predicted to be fault prone. The sensitivity of the model is 94.20%. Similarly 13 out of 15 modules were predicted not to be fault prone. Thus, the specificity of the model is 86.50%. This shows that the model accuracy is very high.

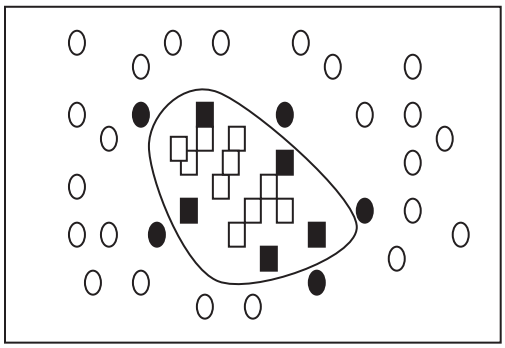


Fig. 1. Architecture of Support Vector Machines.

4.3.2. Support Vector Machine modeling

The SVM is a useful technique for classification of data and has been successfully applied in various modeling applications such as text classification, image analysis and face identification [59]. The SVM are capable of handling complex and large problems. Using the SVM method, an N-dimensional hyperplane is constructed that separates the input domain into binary or multi-class categories. This method constructs an optimal hyperplane which separates the categories of the dependent variable on each side of the plane [48]. The support vectors are present close to the hyperplane. The non linear relationships can be handled using the kernel function. The Radial Basis Function (RBF) maps the non linear relationships into a higher dimensional space so that the categories of the dependent variable can be separated. The *k*-means clustering is used to find the centers of the RBF network [43]. Fig. 1 depicts the architecture of the RBF kernel in the SVM method. The circles depict one category of the dependent variable and the rectangle depicts the other category of the dependent variable. The support vectors are depicted by the shaded portions of the rectangles and circles.

Given a set of $(a_i, b_i),\ldots,(a_m, b_m)$ and $b_i \in \{-1, +1\}$ training samples. $\alpha = (i = 1,\ldots,m)$ is a Lagrangian multipliers. $K(a_i, b_i)$ is called a kernel function and z is a bias. The discriminant function DF of two module SVM is given below [56]:

$$\mathrm{DF}(b) = \sum_{i=1}^{m} b_i \alpha_i K(a_i, a) + z \tag{2}$$

Then an input pattern a is classified as [56]:

$$a = \begin{Bmatrix} +1 & \text{if DF}(a) > 0 \\ -1 & \text{if DF}(a) < 0 \end{Bmatrix} \tag{3}$$

4.3.2.1. Support Vector Machine analysis results. In this section, we present results of employing the SVM method to predict the fault proneness of a module. In case of the AR1 model, out of 9 modules actually fault prone, 7 modules were predicted to be fault prone (see Table 10). The sensitivity of the model is 77.78%. Similarly, the specificity of the model is 66.07%. In case of the AR6 model, the sensitivity and specificity of the model is 73.33% and 73.26%, respectively. This shows that the model accuracy is less as compared to model predicted using the LR and ANN approach.

Table 9
Predicted correctness of ANN model.

Data set Observed	AR1 Predicted			AR6 Predicted		
	0.00	1.00	Percent correct	0.00	1.00	Percent correct
0.00	77	35	68.70%	81	5	94.20%
1.00	2	7	77.80%	2	13	86.50%

Table 10
Predicted correctness of SVM model.

Observed	AR1 (cutoff point 0.05) Predicted			AR6 Predicted		
	0.00	1.00	Percent correct	0.00	1.00	Percent correct
0.00	28	84	25.00%	63	23	73.33%
1.00	0	9	100%	4	11	73.26%

UNCORRECTED PROOF

Please cite this article in press as: R. Malhotra, Comparative analysis of statistical and machine learning methods for predicting faulty modules, Appl. Soft Comput. J. (2014), http://dx.doi.org/10.1016/j.asoc.2014.03.032

Table 11
Metrics included in DT models.

AR1	cyclomatic_complexity, branch_count, decision_count, condition_count, halstead_effort, halstead_time, comment_loc, executable_loc, unique_operators, multiple_condition_count, halstead_level, halstead_difficulty, total_operands, total_loc, total_operators, call_pairs, design_complexity, halstead_length, halstead_volume, halstead_error, decision_density, blank_loc, code_and_comment_loc, unique_operands, normalized_cyclomatic_complexity, cyclomatic_density.
AR6	cyclomatic_complexity, decision_density, design_complexity, code_and_comment_loc, call_pairs, halstead_error, halstead_level, halstead_difficulty, halstead_time, multiple_condition_count, cyclomatic_density, normalized_cyclomatic_complexity, formal_parameters, total_loc, blank_loc, executable_loc, unique_operators, total_operators, unique_operands, comment_loc, halstead_effort, total_operands, halstead_volume, and halstead_length metrics

4.3.3. Decision Tree (DT) method

In this section, we present the results for predicting faulty and non faulty modules using the DT method.

4.3.3.1. Decision Tree architecture. In the DT [42] method, each internal node in the tree represents the value of the independent variables and the terminal node represents the value of the dependent variable. The Classification and Regression Tree (CRT) algorithm splits the data into partitions based on the independent variables. At each step in the CRT algorithm the independent variable having the strongest relationship with the dependent variable is selected. In the CRT method, each parent node is split into only two child nodes. The aim of the CRT method is to maximize the within-node homogeneity.

4.3.3.2. Decision Tree model results. Table 11 shows the subset of the metrics included in the model predicted using the AR1 and AR 6 data sets. Table 12 presents the predicted correctness of the model developed using the DT method.

The sensitivity and specificity of the model predicted with respect to the AR1 data set is 77.7% and 89.3%, respectively. Similarly, the sensitivity and specificity of the model predicted with respect to the AR6 data set is 93.3% and 81.4%, respectively. The results show that the accuracy of the DT model is high as compared to the models predicted using the LR, SVM and ANN methods.

4.3.4. Cascade Correlation Network (CCN)

We used the correlation based feature selection (CFS) technique to select the uncorrelated and best predictors out of the set of the independent variables present in the training data set using correlation based heuristic [19]. All the possible combinations of the independent variables were searched to find the best combination of the independent variables. The CFS method ranks the metric subsets rather than the individual metric. The CFS is a heuristic that evaluates the predictive ability of the individual variables (static code metrics in our case) for predicting the dependent variable along with the correlation among the independent variables. In case of the AR1 data set, the predicted model shows better accuracy when the CFS technique was applied. However, in case of the AR6 data set, the model predicted showed lesser accuracy when subset of metrics were included using CFS. Hence, we did not use the CFS method in case of predicting model using the AR6 data set.

Table 12
Predicted correctness of DT model.

Observed	AR1 Predicted (cutoff point 0.08)			AR6 Predicted (cutoff point 0.18)		
	0.00	1.00	Percent correct	0.00	1.00	Percent correct
0.00	70	16	89.30%	70	16	81.40%
1.00	14	1	77.70%	14	1	93.30%

Table 13
Predicted correctness of CCN model.

Observed	AR1 Predicted (cutoff point = 0.10)			AR6 Predicted (cutoff point = 0.18)		
	0.00	1.00	Percent correct	0.00	1.00	Percent correct
0.00	86	26	76.79%	64	22	74.42%
1.00	1	8	88.89%	3	12	80.00%

The results of the correctness of predicted fault proneness model using the CCN approach is shown in Table 13. The sensitivity and specificity of the model predicted with respect to the AR1 data set is 88.89% and 76.79%, respectively. Similarly, the sensitivity and specificity of the model predicted with respect to the AR6 data set is 80% and 74.42%, respectively.

4.3.5. GMDH polynomial network

The GMDH networks are known as self organizing networks that mean the connections between the neurons are not fixed during the training process. In the GMDH network, the number of layers are automatically decided so that an network with maximum prediction accuracy and without overfitting is constructed [48].

Table 14 shows the output generated for the GMDH polynomial model. Output from neuron j is shown as $N(j)$. The final line shows the output of the network. In this case, the probability of faulty modules being true is predicted.

The results of correctness of predicted fault proneness model using the GMDH polynomial network approach is shown in Table 15. The sensitivity and specificity of the model predicted with respect to AR1 data set is 88.89% and 73.21%, respectively. Similarly, the sensitivity and specificity of the model predicted with respect to AR6 data set is 80% and 74.42%, respectively.

4.3.6. GEP analysis

Genetic algorithms (GA) are search based algorithms that have seen explosion of interest since 1980s. These are natural biological evolution algorithms and are much faster than the exhaustive search procedures. GEP was developed by Candida Ferreira in 1996 and they are 100–60,000 faster than the GA [15]. GEP mutate quickly the valid expressions as they use Karva language to encode the expressions. They use genes that have two sections the head and the tail. The head consist of functions, variables and constants and the tail consist of variables and constants. The terminals in the tail are used if there are not are enough terminal in the head. The following are the major steps for training data set in the GEP:

(1) Creation of initial population.
(2) Use of evolution to create well fitted individuals using mutation, transposition, inverse and recombination steps.
(3) Finding simpler functions.

In Table 16, we summarize the parameters to and determined by the GEP method. We used 4 genes per chromosome and addition function to link the genes.

The fitness function uses the following function, i.e. the number of faulty and non faulty modules predicted correctly with penalty for analysing the performance of the model. The aim of the GEP method is to maximize the value of the fitness function until the stopping criterion is met.

$$\text{Fitness} = \frac{\text{TFP} + \text{TNFP}}{\text{TFP} + \text{FNFP} + \text{FFP} + \text{TNFP}}$$

UNCORRECTED PROOF

Please cite this article in press as: R. Malhotra, Comparative analysis of statistical and machine learning methods for predicting faulty modules, Appl. Soft Comput. J. (2014), http://dx.doi.org/10.1016/j.asoc.2014.03.032

Table 14
GMDH polynomial output.

AR1	defects{true} = 0.029694-1.4561*halstead_error-6.685482* halstead_error2-0.006916*unique_operators+0.001303*unique_operators2+0.188474*halstead_error *unique_operators
AR6	N(5) = 0.044327+0.114179*multiple_condition_count-0.025803*multiple_condition_count2+0.034002*call_pairs- 0.004033*call_pairs2+0.018979*multiple_condition_count*call_pairs N(3) = -0.019685+0.002822*halstead_difficulty-0.000023*halstead_difficulty2+1.369638*N(5)+0.199649*N(5)2-0.04608* halstead_difficulty*N(5) N(10) = 0.056173-0.012912*cyclomatic_complexity+0.004474*cyclomatic_complexity2+ 0.086395*multiple_condition_count+0.003522*multiple_condition_count 2-0.012155*cyclomatic_complexity*multiple_condition_count N(8) = 0.00462-0.007771*total_loc-0.000003*total_loc2+2.216319*N(10)-1.249802*N(10)2+0.008383*total_loc*N(10) N(2) = -0.034398+0.690112*N(3)+0.691399*N(3)2+0.506948*N(8)+ 0.505133*N(8)2-1.36183*N(3)*N(8) faults{true} = -0.005575+0.00025*halstead_volume-9.274278e-007*halstead_volume2+1.025279*N(2)- 0.10709*N(2)2+0.00078*halstead_volume*N(2)

Table 15
Predicted correctness of GMDH model.

Observed	AR1 Predicted (cutoff point = 0.06)			AR6 Predicted (cutoff point = 0.16)		
	0.00	1.00	Percent correct	0.00	1.00	Percent correct
0.00	82	30	73.21%	64	22	74.42%
1.00	1	8	88.89%	3	12	80.00%

Table 16
GEP parameters.

Population size	50	50
Gene per chromosome	4	4
Gene head length	8	8
Generations required to train the model	349	442
Generations required for simplification	35	52
Linking function	Addition	
Fitness function	Number of correct predictions with penalty	

Table 17
Predicted correctness of GEP model.

Observed	Predicted (Cutoff point = 0.5)			Predicted (cutoff point = 0.13)		
	0.00	1.00	Percent correct	0.00	1.00	Percent correct
0.00	111	1	99.11%	84	2	97.67%
1.00	6	3	33.33%	7	8	53.33%

Table 18
Results of validation of LR model.

Observed	AR1 Predicted			AR6 Predicted		
	0.00	1.00	Percent correct	0.00	1.00	Percent correct
0.00	77	35	68.70%	65	21	53.50%
1.00	2	7	77.80%	3	12	53.50%

Table 19
Results of validation of ANN model.

Data set Observed	AR1 Predicted			AR6 Predicted		
	0.00	1.00	Percent correct	0.00	1.00	Percent correct
0.00	77	35	68.70%	58	28	67.40%
1.00	2	7	77.80%	5	10	66.70%

The results of correctness of predicted fault proneness model using the GEP method is shown in Table 17. The sensitivity and specificity of the model predicted with respect to the AR1 data set is 33.33% and 99.11%, respectively. Similarly, the sensitivity and specificity of the model predicted with respect to the AR6 data set is 53.33% and 97.67%, respectively.

Table 20
Results of validation of SVM model.

Data set Observed	AR1 Predicted			AR6 Predicted		
	0.00	1.00	Percent correct	0.00	1.00	Percent correct
0.00	35	77	31.25%	59	27	68.60%
1.00	1	8	88.89%	5	10	66.67%

Table 21
Results of validation of DT model.

Data set Observed	AR1 Predicted			AR6 Predicted		
	0.00	1.00	Percent correct	0.00	1.00	Percent correct
0.00	100	12	89.30%	70	16	81.40%
1.00	2	7	77.70%	1	14	93.30%

Table 22
Results of validation of CCN model.

Data set Observed	AR1 Predicted			AR6 Predicted		
	0.00	1.00	Percent correct	0.00	1.00	Percent correct
0.00	85	27	75.89%	63	23	73.25%
1.00	2	7	77.79%	4	11	73.33%

Table 23
Results of validation of GMDH model.

Data set Observed	AR1 Predicted			AR6 Predicted		
	0.00	1.00	Percent correct	0.00	1.00	Percent correct
0.00	78	34	66.67%	58	28	67.44%
1.00	3	6	69.64%	4	11	73.33%

5. Model evaluation

The models predicted in the previous section are applied on the same data set from which they are derived. The models predicted should be applied on the different data sets to gain insight about their prediction accuracy. Hence, we used 10-cross validation method on the LR, ANN, SVM, DT, CCN, GMDH, and GEP models following the procedure given in Section 3. For performing the 10-cross validation, the software modules were randomly divided into 10 partitions of approximately equal size (AR1: 9 partitions of 12 data points each and 1 partition of 11 data points, AR6:

UNCORRECTED PROOF

Please cite this article in press as: R. Malhotra, Comparative analysis of statistical and machine learning methods for predicting faulty modules, Appl. Soft Comput. J. (2014), http://dx.doi.org/10.1016/j.asoc.2014.03.032

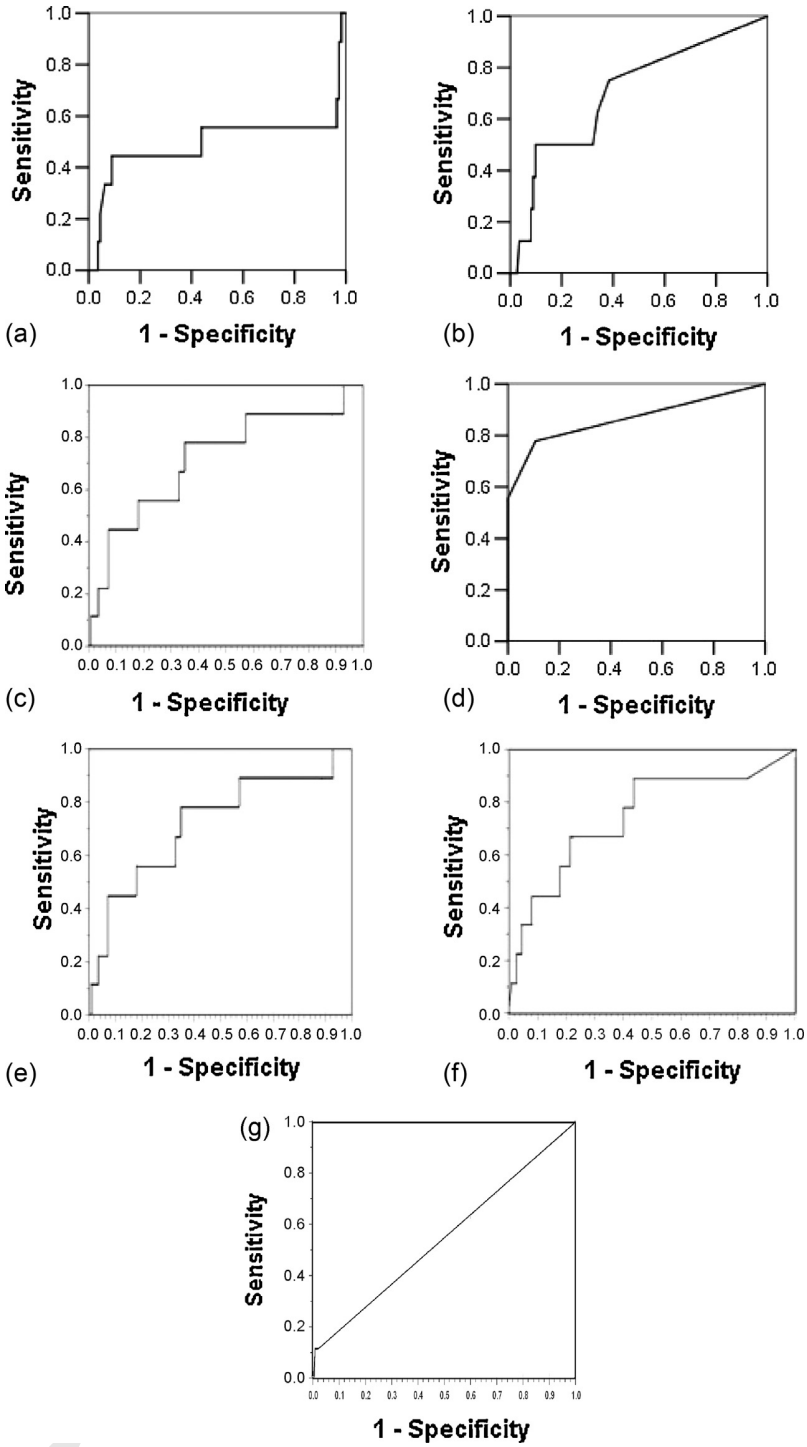


Fig. 2. ROC curve for AR1 data set (a) LR (b) ANN (c) SVM (d) DT (e) CCN (f) GMDH (g) GEP models.

9 partitions of ten data points each and 1 partition of 13 data points). Tables 18–24 show the accuracy of the models predicted using the ML methods. We present the results of the cross validation of predicted models via the LR, ANN, SVM, DT, CCM, GMDH, and GEP approaches in Tables 25 and 26.

As shown in Tables 25 and 26, the results of cross validation of the ML models were better as compared to the cross validation results of the LR model. The basis of comparison is the values of the AUC computed using the ROC analysis. The ROC analysis can be used to obtain the optimal cut off point that provides the balance between the number of faulty and non faulty modules. In Figs. 2 and 3, the ROC curves for the LR, ANN, SVM, DT, CCM, GMDH, and GEP models are presented.

In case of the AR1 data set, the AUC of model predicted using the LR method was 0.94 which is much lower than the models predicted using machine learning methods. Similar results were shown when we predicted model using the AR6 data set. The AUC of model predicted using the DT method is 0.865 in case of AR1 and 0.948

Please cite this article in press as: R. Malhotra, Comparative analysis of statistical and machine learning methods for predicting faulty modules, Appl. Soft Comput. J. (2014), http://dx.doi.org/10.1016/j.asoc.2014.03.032

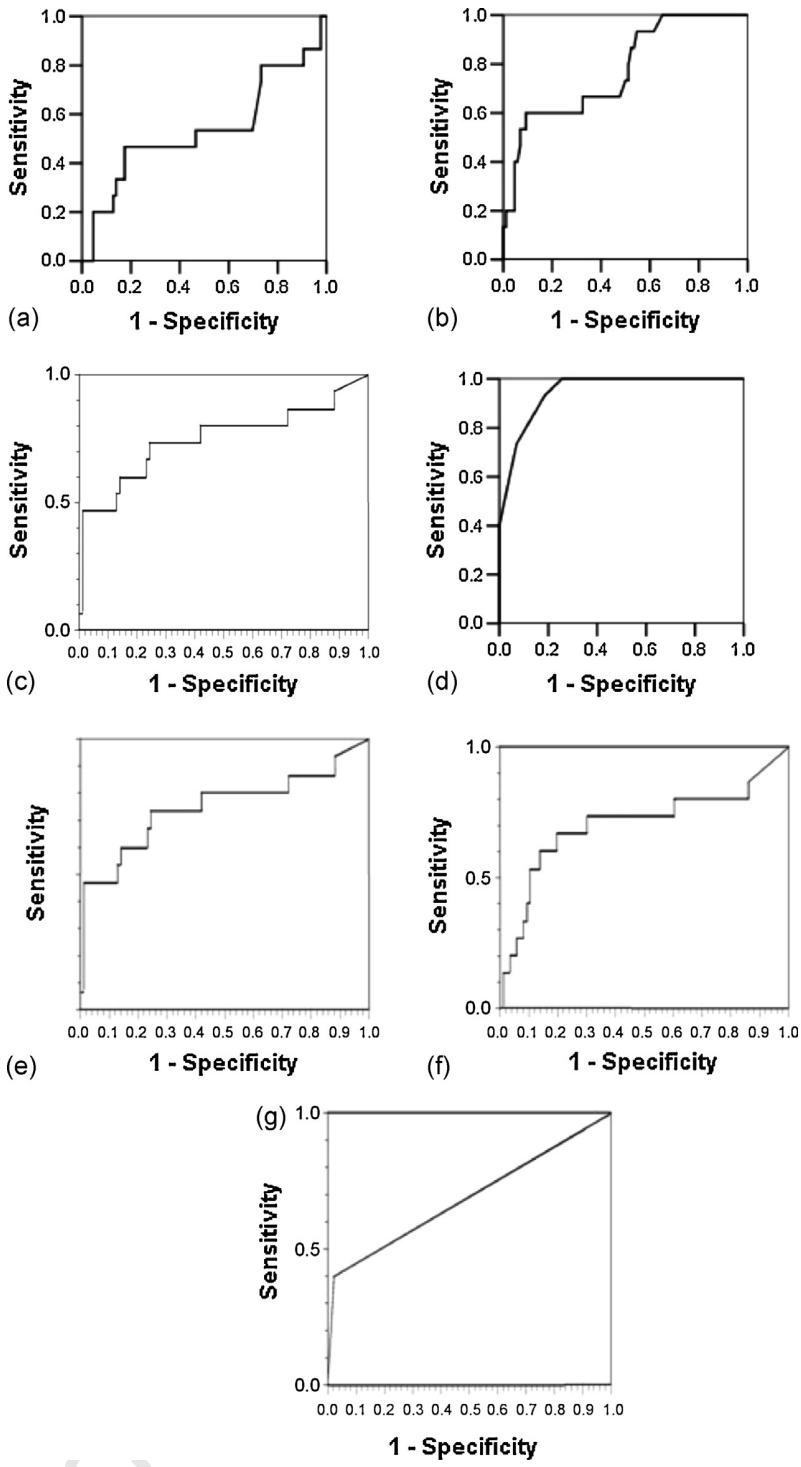


Fig. 3. ROC curve for AR6 data set (a) LR (b) ANN (c) SVM (d) DT (e) CCN (f) GMDH (h) GEP models.

in case of the AR6 data set. Thus, the model predicted using the DT method shows the highest values of AUC. In line with the other models predicted in literature, the findings of this study may also be validated externally. The models predicted using the DT method showed the best results. Although the LR models are widely used in construction of software quality models, but the results in this study show that the ML models show better predictive capability as compared to the LR model. Therefore, it appears that the model predicted using the ML methods might lead to construction of the optimum prediction models for developing fault prone models.

6. Threats to validity

The empirical studies consist of similar types of limitations which are summarized below:

Please cite this article in press as: R. Malhotra, Comparative analysis of statistical and machine learning methods for predicting faulty modules, Appl. Soft Comput. J. (2014), http://dx.doi.org/10.1016/j.asoc.2014.03.032

Table 24
Results of validation of GEP model.

Data set Observed	AR1 Predicted			AR6 Predicted		
	0.00	1.00	Percent correct	0.00	1.00	Percent correct
0.00	110	2	99.11%	84	2	97.67%
1.00	8	1	11.11%	9	6	40.00%

Table 25
Results of 10-cross validation of AR1 models.

Technique	Sensitivity	Specificity	Proportion correct	AUC	Cutoff point
LR	55.60	56.20	55.00	0.494	0.05
ANN	75.70	61.60	69.42	0.711	0.05
SVM	88.89	31.25	35.53	0.717	0.05
DT	89.30	77.70	88.84	0.865	0.08
CCN	77.89	75.89	76.03	0.786	0.10
GMDH	69.64	66.67	69.42	0.744	0.06
GEP	11.11	99.11	91.73	0.547	0.05

Table 26
Results of 10-cross validation of AR6 models.

Technique	Sensitivity	Specificity	Proportion correct	AUC	Cutoff point
LR	53.30	53.50	53.00	0.538	0.08
ANN	66.70	67.40	67.32	0.774	0.06
SVM	66.67	68.60	68.32	0.721	0.13
DT	93.30	81.40	83.16	0.948	0.11
CCN	73.33	73.26	73.27	0.758	0.10
GMDH	73.33	67.44	68.31	0.702	0.10
GEP	40.00	97.67	89.10	0.688	0.10

- The degree to which the results can be generalized to other research cannot be determined as we have used medium sized software in this paper.
- The study does not take into account the level of severity of faults hence the results cannot be used to determine the severity of the modules predicted to be faulty [14].
- The results in this study cannot be applied to the study having different dependent variable such as maintenance effort, testing effort, etc.

Hence, the results in this study can be used for future guidance for predicting faulty modules using the static code metrics. However, the results of this needs to be externally validated.

7. Conclusion and future work

The main goal of our study was to examine the regression (LR), and the ML methods (ANN, SVM, DT, CCN, GMDH and GEP) in order to find the combined impact of the static code metrics on fault proneness. Thus we employed six ML methods (ANN, SVM, DT, CCN, GMDH and GEP) methods to assess the relationship between the static code metrics and fault proneness. The primary contribution of this work is to assess the predictive capability of the ML methods. We also compare and analyze the performance of the models predicted using the LR method with the models predicted using the ML methods. To validate the results we used two public domain data sets AR1 and AR6. The AUC was used to determine the performance of the ML methods.

The AUC for the LR model was 0.494 and 0.538 for the models predicted using the AR1 and AR6 data sets, respectively. The AUC for DT model was 0.865 and 0.948, respectively. The models predicted using the ML methods outperformed the models predicted using the LR method for both AR1 and AR6 data sets. Thus, the models predicted using the DT showed the best results. This paper confirms that the models using the ML methods such as ANN, SVM, DT, CCN, GMDH and GEP have predictive ability for predicting faulty and non faulty modules.

Hence, the researchers and software practitioners can use the model predicted in this paper to predict faulty or non faulty modules in the early phases of the software development. The software practitioners can focus the available testing resources on the faulty portions of the software.

Replicated studies with large sized software should be carried out so that generalized results can be obtained. We may use the evolutionary or hybrid evolutionary algorithms for fault prediction in future.

Uncited references

[5,37,40,53].

References

[1] K.K. Aggarwal, Y. Singh, A. Kaur, R. Malhotra, Application of artificial neural network for predicting fault proneness models, in: International Conference on Information Systems, Technology and Management (ICISTM 2007), New Delhi, India, March 12–13, 2007.
[2] K.K. Aggarwal, Y. Singh, A. Kaur, R. Malhotra, Empirical analysis for investigating the effect of object-oriented metrics on fault proneness: a replicated case study, Softw. Process Improv. Pract. 16 (1) (2009) 39–62 (John Wiley & Sons).
[3] V. Barnett, T. Price, Outliers in Statistical Data, John Wiley & Sons, 1995.
[4] V. Basili, L. Briand, W. Melo, A validation of object-oriented design metrics as quality indicators, IEEE Trans. Softw. Eng. 22 (10) (1996) 751–761.
[5] D. Belsley, E. Kuh, R. Welsch, Regression Diagnostics: Identifying Influential Data and Sources of Collinearity, John Wiley and Sons, New York, 1980.
[6] A. Bener, B. Turhan, Analysis of Naive Bayes' assumptions on software fault data: an empirical study, Data Knowl. Eng. 68 (2009) 278–290.
[7] L. Briand, W. Daly, J. Wust, Exploring the relationships between design measures and software quality, J. Syst. Softw. 51 (3) (2000) 245–273.
[8] M. Chapman, D. Solomon, The relationship of cyclomatic complexity, essential complexity and error rates, in: Proc. NASA Software Assurance Symp., 2002 http://www.ivv.nasa.gov/business/research/osmasas/conclusion2002/Mike_Chapman_The_Relationship_of_Cyclomatic_Complexity_Essential_Complexity_and_Error_Rates.ppt
[9] K. Dejaeger, T. Verbraken, B. Baesens, Prediction Models Using Bayesian Network Classifiers, 39, 2013, pp. 237–257.
[10] B. Diri, C. Catal, U. Sevim, Practical development of an Eclipse-based software fault prediction tool using Naive Bayes algorithm, Expert Syst. Appl. 38 (2011) 2347–2353.
[11] S. Dreiseitl, L. Ohno-Machado, Logistic Regression and Artificial Neural Network Classification models: a methodology review, J. Biomed. Inform. 35 (2002) 352–359.
[12] E. Duman, Comparison of decision tree algorithms in identifying bank customers who are likely to buy credit cards, in: Seventh International Baltic Conference on Databases and Information Systems, Kaunas, Lithuania, July 3–6, 2006.
[13] B. Eftekhar, K. Mohammad, H. Ardebili, M. Ghodsi, E. Ketabchi, Comparison of artificial neural network and logistic regression models for prediction of mortality in head trauma based on initial clinical data, BMC Med. Inform. Decis. Mak. (2005).
[14] K. El Emam, S. Benlarbi, N. Goel, S. Rai, A Validation of Object-Oriented Metrics, Technical Report ERB-1063, NRC, 1999.
[15] C. Ferreira, Gene expression programming: a new adaptive algorithm for solving problems, Complex Syst. 13 (2001) 87–129.
[16] L. Guo, Y. Ma, B. Cukic, H.S.H. Singh, Robust prediction of fault-proneness by random forests, in: 15th Int. Symp. Softw. Reliab. Eng., 2004.
[17] M. Halstead, Elements of Software Science, Elsevier, 1977.
[18] T. Hall, D. Bowes, The state of machine learning methodology in software fault prediction, in: 11th International Conference on Machine Learning and Applications, 2012.
[19] M. Hall, Correlation-based feature selection for discrete and numeric class machine learning, in: Proceedings of the 17th International Conference on Machine Learning, 2007, pp. 359–366.
[20] J. Han, M. Kamber, Data Mining: Concepts and Techniques, Harchort India Private Limited, 2001.
[21] J. Hanley, B.J. McNeil, The meaning and use of the area under a Receiver Operating Characteristic ROC curve, Radiology 143 (1982) 29–36.
[22] S. Henry, D. Kafura, Software structure metrics based on information flow, IEEE Trans. Softw. Eng. 7 (5) (1981) 510–518.
[23] http://softlab.boun.edu.tr
[24] D. Hosmer, S. Lemeshow, Applied Logistic Regression, John Wiley and Sons, 1989.

UNCORRECTED PROOF

Please cite this article in press as: R. Malhotra, Comparative analysis of statistical and machine learning methods for predicting faulty modules, Appl. Soft Comput. J. (2014), http://dx.doi.org/10.1016/j.asoc.2014.03.032

[25] A. Kaur, R. Malhotra, Application of random forest for predicting fault prone classes, in: International Conference on Advanced Computer Theory and Engineering, Thailand, December 20–22, 2008.
[26] T. Khoshgoftaar, An application of zero-inflated Poisson regression for software fault prediction, in: Proc. 12th Intl. Symp. Software Reliability Eng., November, 2001, pp. 66–73.
[27] T. Khoshgoftaar, E. Allen, Model software quality with classification trees, Recent Adv. Reliab. Qual. Eng. (2001) 247–270.
[28] T. Khoshgaftaar, E.D. Allen, J.P. Hudepohl, S.J. Aud, Application of neural networks to software quality modeling of a very large telecommunications system, IEEE Trans. Neural Netw. 8 (4) (1997) 902–909.
[29] T. Khoshgoftaar, N. Seliya, Fault prediction modeling for software quality estimation: comparing commonly used techniques, Empirical Softw. Eng. 8 (3) (2003) 255–283.
[30] A.G. Koru, H. Liu, Building effective defect-prediction models in practice, IEEE Softw. 22 (2005).
[31] C.R. Kothari, Research Methodology Methods and Techniques, New Age International Limited, New Delhi, 2004.
[32] S. Lessmann, B. Baesens, C. Mues, S. Pietsch, Benchmarking classification models for software defect prediction: a proposed framework and novel findings, IEEE Trans. Softw. Eng. 34 (2008) 485–496.
[33] R. Malhotra, Prediction of high, medium, and low severity faults using software metrics, Softw. Qual. Prof. (2013).
[34] F. Marini, R. Bucci, A.L. Magri, A.D. Magri, Artificial neural networks in chemometrics: history, examples and perspectives, Microchem. J. 88 (2) (2008) 178–185.
[35] T.A. McCabe, Complexity measure, IEEE Trans. Softw. Eng. 2 (4) (1976) 308–320.
[36] T. Menzies, J. DiStefano, A. Orrego, R. Chapman, Data mining static code attributes to learn defect predictors, IEEE Trans. Softw. Eng. 32 (11) (2007) 1–12.
[37] T. Menzies, J. Stefano, M. Chapman, Learning early lifecycle IV and V quality indicators, in: Proc. IEEE Software Metrics Symp., 2003.
[38] A.T. Mısırlı, A.B. Bener, B. Turhan, An industrial case study of classifier ensembles for locating software defects, Softw. Qual. J. 19 (2011) 515–536.
[39] N. Nagappan, T. Ball, Static analysis tools as early indicators of pre-release defect density, in: Proc. Intl. Conf. Software Eng., 2005, pp. 580–586.
[40] A. Nikora, J. Munson, Developing fault predictors for evolving software systems, in: Proc. Ninth Intl. Software Metrics Symp. (METRICS'03), 2003.
[41] A. Okutan, O.T. Yıldız, Software defect prediction using Bayesian networks, Empirical Softw. Eng. (2012).
[42] A. Porter, R. Selby, Empirically guided software development using metric-based classification trees, IEEE Softw. (1990) 46–54.
[43] Polyspace verifier1, 2005, http://www.polyspace.com/.
[44] Prest Metrics Extraction and Analysis Tool, Available from: http://softlab.boun.edu.tr/?q=resources&i=tools
[45] Promise, http://promisedata.org/repository/.
[46] Y. Singh, A. Kaur, R. Malhotra, Application of decision trees for predicting fault proneness, in: International Conference on Information Systems, Technology and Management-Information Technology, Ghaziabad, India, 2009.
[47] Y. Singh, R. Malhotra, Object Oriented Software Engineering, PHI Learning, 2012.
[48] P. Sherrod, DTreg Predictive Modeling Software, 2003.
[49] Q. Song, Z. Jia, M. Shepperd, S. Ying, J. Liu, A general software defect-proneness prediction framework, IEEE Trans. Softw. Eng. 37 (2011) 356–370.
[50] K. Srinivasan, D. Fisher, Machine learning approaches to estimating software development effort, IEEE Trans. Softw. Eng. (1995) 126–137.
[51] M. Stone, Cross-validatory choice and assessment of statistical predictions, J. Royal Stat. Soc. 36 (1974) 111–147.
[52] B. Twala, Software faults prediction using multiple classifiers, in: 2011 3rd Int. Conf. Comput. Res. Dev., 4, 2011, pp. 504–510.
[53] X. Wang, D. Bi, S. Wang, Fault recognition with Labeled multi-category, in: Third Conference on Natural Computation, Haikou, China, 2007.
[54] L. Yu, An evolutionary programming based asymmetric weighted least squares support vector machine ensemble learning methodology for software repository mining, Inf. Sci. 191 (2012) 31–46.
[55] Y. Zhou, H. Leung, Empirical analysis of Object-Oriented Design Metrics for predicting high severity faults, IEEE Trans. Softw. Eng. 32 (10) (2006) 771–784.
[56] L. Zhao, N. Takagi, An application of Support vector machines to Chinese character classification problem, in: IEEE International Conference on systems, Man and Cybernetics, Montreal, 2007.



Ruchika Malhotra is an assistant professor at the Department of Software Engineering, Delhi Technological University (formerly Delhi College of Engineering), Delhi, India. She was an assistant professor at the University School of Information Technology, Guru Gobind Singh Indraprastha University, Delhi, India. Prior to joining the school, she worked as full-time research scholar and received a doctoral research fellowship from the University School of Information Technology, Guru Gobind Singh Indraprastha, Delhi, India. She received her master's and doctorate degree in software engineering from the University School of Information Technology, Guru Gobind Singh Indraprastha University, Delhi, India. She has received *IBM Best Faculty Award 2013*. She is executive editor of Software Engineering: An International Journal. She is coauthor of a book on *Object Oriented Software Engineering* published by PHI Learning. Her research interests are in software testing, improving software quality, statistical and adaptive prediction models, software metrics, neural nets modeling, and the definition and validation of software metrics. She has published more for than 75 research papers in international journals and conferences. Malhotra can be contacted by e-mail at ruchikamalhotra2004@yahoo.com.

UNCORRECTED PROOF

Please cite this article in press as: R. Malhotra, Comparative analysis of statistical and machine learning methods for predicting faulty modules, Appl. Soft Comput. J. (2014), http://dx.doi.org/10.1016/j.asoc.2014.03.032

Volume 1 (2014) 151-165 ISSN 2347 - 3258
International Journal of Advance Research and Innovation

Computer Simulation of Trombe Wall for Porous and Non-Porous Strutcures

Vishav Kamal *, R. S. Mishra
Department of Mechanical Engineering, Delhi College of Engineering, New Delhi, India

Article Info

Article history:
Received 2 January 2014
Received in revised form
29 January 2014
Accepted 20 February 2014
Available online 15 March 2014

Keywords

Thermal performance passive systems,
Porous Walls,
Non Porous Walls,
Trombe Walls

Abstract

Computer simulation of porous Trombe wall has been carried out for providing comfortable thermal environment. During sunshine hours excess heat is stored within the porous absorber and there is stratification in the porous layer. For two different porous materials viz. marble and quartzite, explicit expressions for heat flux and thermal efficiency of the porous system have been developed. The experimental results have been validated with numerical computations using the developed model. It has been observed that Trombe wall contributes 20% to 30% of the total heating of the buildings depending upon type of material. The average thermal efficiency of the wall has been found to be 29.09% for brick wall, 37.27% for concrete wall, 45.35% for marble wall and 57.2% for quartzite wall respectively.. The results from presented mathematical model would help the designers of passive solar systems to use this model for selecting optimal constructive parameters of the non-porous Trombe wall.

1. Introduction

Energy from the Sun can be collected and utilized in many different ways which may be grouped into three basic categories such as direct thermal applications, solar thermal-electric applications and fuel from biomass. All of these technologies exist and have been well demonstrated. The recent rapid escalations in the costs of fossil fuels and increasing awareness regarding environmental pollution issues and the finite size of fossil resources have changed the scenario. Therefore, alternate energy sources have to be developed for supplementing and eventually replacing fossil resources. The other potential application of solar energy in providing comfortable thermal environment in the living space is based on passive heating and cooling concepts. For providing a non-fluctuating temperature in a living room, a massive wall is usually introduced between the glazing and the room. Usually this massive wall, known as Trombe wall, is made of either concrete or consists of water drums stacked over one another as shown in Fig.1

The concept of a Trombe wall with and without vents is used for providing comfortable environment in the living space [1,2]. It is, however, necessary to provide ventilation to let the fresh air flow for diluting the effects of moisture, dust and gases. The energy required for heating this ventilating air could be sizable and hence the idea of a 'Trombe wall' which is provided with circular pipes for the flow of air [3, 4]. This idea of ventilated Trombe wall is more useful in dairies and farms, where animals are confined to remove the odour, moisture, dust and gases produced by the animals in the confinement. The building must be ventilated continuously with fresh air for diluting these unhealthy products. In hot climatic conditions, the hot air may be used for heating the gravel for domestic purposes. This idea offers an application of solar passive systems like that of a storage wall provided with a network of circular pipes through which ambient air flows either by natural convection or forced convection mode. The natural convection heat transfer plays an important role in a significant group of constructive solutions of passive structures utilized in buildings [5-7]. The thermal performance of two passive cooling systems under hot and humid climate condition has been experimentally investigated by Chungloo and Limmeechokchai [8-10]. The experimental results were obtained from a test cell and a controlled cell with identical walls but different roof configurations. The applications of the two systems in hot and humid climate are found to

Corresponding Author,
E-mail address: vishav.kamal4@rediffmail.com
All rights reserved: http://www.ijari.org

sustain the room temperature of the test cell to be lower than the ambient temperature by 2.0-6.2oC and lower than the room temperature of the controlled cell by 1.4-3.0oC.

Various techniques have been developed and used to enhance the thermal storage effect of a Trombe wall, such as installing an absorber plate in the air gap and using a black surface on the heat storage wall. Insulated layers are installed outside the Trombe wall for reducing heat loss at night in a cold climate. But the heat storage capacity of the wall also reduces significantly by using outside insulated layer. A shading device is installed in the air gap in order to improve heat accumulation of the Trombe wall at day time and reduce its heat loss at night time [7]. In winter, the shading device can be opened at day time to allow the black massive wall to absorb solar heat directly and shut down at night to minimize heat loss of the wall. In summer, the shading device can be closed at day time to decrease the direct heat gain from solar radiation and prevent overheating. Chandel and Aggarwal [5] have carried out experimental studies on passive solar building and concluded that high cost conventional heating systems can be replaced by using solar heating with backup heaters. The present paper mainly deals with the study of few basic concepts utilized in the architecture of the building to maintain thermally comfortable environment without using any passive means of energy.

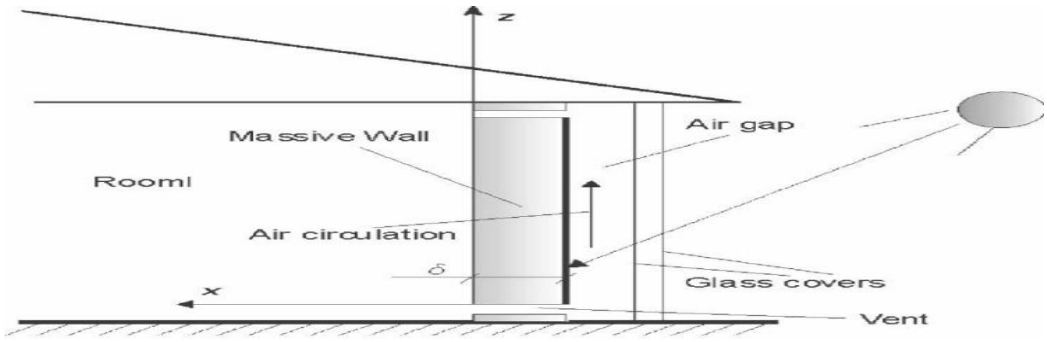


Fig: 1. Schematic diagram of 'Trombe Wall' System [1]

2. Literature Review

Akbarzadeh et al. [1] have made experimental flow visualization studies which provide a deeper insight into the fundamental flow mechanisms. The air velocity and temperature measurements have been used to explore the natural convection heat transfer processes involved in the thermo-circulation flow. The effects of the wall parameters such as wall-glazing distance and vent size on the thermal performance of the wall have been considered. They have correlated adequate experimental results by using expressions derived for natural convection processes occurring between vertical parallel plates, i.e. the vertical heated wall surface and the cooler vertical glazing panel. This type of fundamental heat transfer information is important as the overall performance of Trombe wall systems can be adequately modeled using the large range of simulation techniques presently available for thermal network analysis. The change in thermo circulation performance over the range of wall-glazing distance tested was not significant. Bansal and Thomas [2] have presented a steady state method for sizing four indirect gain passive solar heating systems, viz. mass wall system, water wall system, Trombe wall system and solarium. This method is developed for use by architects and builders who can quickly check if passive heating is feasible at a particular location by calculating the area of the passive building element. Blasco et al. [3] have studied the thermal performance of three passive systems viz. Trombe wall, direct gain and sunspace and two conventional constructive systems viz. with / without low energy measures for various situations (with / without night / day protection and ventilation) and climatic seasons (winter, summer, spring and autumn) and measured variables are solar intensity, outdoor temperature and indoor temperature taken from different points of the physical models. Chandel and Aggarwal [5] have evaluated the thermal performance of a passive solar bank building in Shimla (H.P.), India which incorporates a heat-collecting wall and a roof-top solar air heater with an electric heating backup, sunspaces and double-glazed windows.. Chel et al. [6] have investigated energy conservation, mitigation of CO_2 emissions and economics of retrofitting for a honey storage building with Trombe wall, located at Gwalior (India), for winter heating application. TRNSYS building simulation software was used to estimate the passive heating potential of Trombe wall

for a honey storage building. Chen et al. [7] have conducted experiments on the thermal performance of an advanced Trombe wall with shading in the air gap of a passive solar house in Dalian. They investigated the thermal performance in terms of temperatures, heat fluxes and their acquisition in a Trombe wall with shading effects. Chen and Liu [9] have studied heat transfer and flow in two types of solar composite walls with porous absorber. In order to analyze the performance of the flow and temperature field in the solar composite wall, an 'unsteady' numerical simulation model has been developed. Gan [11] has studied Trombe walls for passive cooling of buildings in summer using use CFD technique to simulate a Trombe wall for summer ventilation with solar heat gains and conduction heat transfer. The effect of parameters such as the channel width and height, heat gains and wall insulation that influence the performance of a Trombe wall has been investigated. It would also be desirable to increase heat exchanges within the channel using a fan as proposed by Boutin and Gosselin. Jaber and Ajib [12] have studied thermal, environmental and economic impacts of Trombe wall system for a residential building in Mediterranean region. They concluded that Trombe wall system does not reduce the maximum load. On the other hand, it reduced the annual heating energy consumption. Properly sized roof overhangs shade the Trombe wall during summer when the sun is high in the sky. Koyunbaba et al. [13] have made an attempt to validate the simulation model with experimental results of a prototype building integrated photo voltaic (BIPV) Trombe wall built in Izmir, Turkey. A transient energy analysis for determining the performance of a BIPV Trombe wall integrated to the façade of a room has been carried out. The mass flow rates for natural ventilation were calculated in the range of 0.013 kg/s for irradiance of 638.6 W/m^2 to 0.035 kg/s for irradiance of 750.88 W/m^2 for a typical day of February. The results showed that the heat stored in the wall during the day is transferred into the room during night time when there is no radiation. As the mass flow rate of air circulating in the air duct increases after the vents are opened, the thermal energy transferred to the wall from the room increases and it stabilizes above a given flow rate value. Koyunbaba and Yilmaz [14] have compared the thermal performances of single glass, double glass and a Si semi-transparent photo voltaic (PV) module integrated on the Trombe wall façade of a model test room built in Izmir, Turkey. A transient energy analysis for determining the thermal performance of the integrated Trombe wall has been carried out. Nayak et al. [15] have developed a mathematical model based on Fourier series solution for solving the heat conduction equation. The periodic approach leads to closed form solutions which are readily amenable to numerical computations on the computer. They have analyzed and compared the thermal performance of three typical passive heating systems viz. [16-17] Trombe wall with (forced) or without (natural) air circulation, water wall and solarium for two cases, viz. (i) when the glazing is left uncovered throughout and (ii) when the glazing is covered with an insulation during off sunshine hours. Ram and Garg [18] have presented a periodic analysis of the behavior of a ventilated south-facing Trombe wall / roof consisting of pipes, laid in a solid block. One surface of the block is exposed to the sun and the other surface is in direct contact with a room maintained at a constant temperature. Raman et al. [19] have described the development of a solar passive system which can provide thermal comfort throughout the year in composite climates. In the first phase, a passive model (passive model 1) comprising of two sets of solar chimneys was developed and monitored for its performance for one complete calendar year. The additional cost of providing passive components and wall insulation was estimated to be about 20% of the cost of a conventional room. The passive system described in this paper seems to have good potential keeping in view the increasing costs of electricity and deteriorating power situation. Shen et al. [20] have studied the thermal performances of passive solar systems, viz. a classical Trombe wall and a composite Trombe-Michel wall. The mathematical models were developed with the finite difference method (FDM) and with TRNSYS software. The results of simulation with FDM and with TRNSYS have been compared. The model for the composite wall developed with FDM was validated by experimentation. Smolec and Thomas [22] have developed a numerical code based on PASOLE in order to compare theoretical temperature distributions in a Trombe wall with experimental data. Sodha et al. [23] have used periodic analysis to evaluate the thermal flux entering an air-conditioned space for passive heating through the transwall. The thermal performance of the system has been evaluated in terms of the heat flux entering the air-conditioned space which is assumed to be maintained at 20^{o}C. The time-dependent thermal performance of the transwall can be predicted in order to understand its importance from a thermal load leveling viewpoint. Upadhya et al. [24] have presented a transient analysis of a transwall for an air-conditioned room. They have incorporated the effects of the wall design and climatic parameters on optimizing the water-wall thickness outside and inside the trap material while keeping the total thickness of the water column

constant. Zalewski et al. [25] have presented the results of a comparative study of four different types of solar walls. These results have been obtained using a numerical simulation model. An extensive experimental study has been conducted on a composite solar wall in order to validate the model. The model is then used to study the energy efficiency of solar walls in different locations and under different climatic conditions. Then the thermal performance of these walls during the summer period has been analyzed. These walls improve thermal efficiency for collecting solar energy and manage comfortable environments particularly in the summer to avoid overheating. The results of this study are fundamental in helping architects to decide the best suited configuration for each type of building. Zalewski et al. [26] have presented the results of an experimental study of a small-scale Trombe composite solar wall incorporating a phase change material (PCM). The phase change material, in the form of a brick-shaped package, was inserted into the wall. Because of the diverse position of the bricks, each brick reacts differently to solar radiation and heat transfers in the ventilated channel. Dragicevic and Lambic [27] have presented numerical analysis of efficiency of the modified Trombe wall system with forced convection. The analyzed system consists of a double glass glazing and a massive wall with opening and a central channel in it. A fan is provided at the bottom vent of the wall in order to increase the efficiency. The modified Trombe wall is more advanced as compared with simple Trombe wall with a relatively low thermal resistance which is considered as a reference in experimental analysis. The numerical results have shown that thermal efficiency of modified Trombe solar wall increases with the increase in both solar radiation intensity and air velocity in the entrance duct. The thermal efficiency of solar wall also increases with increasing air velocity in the entrance duct at constant solar radiation. Further, thermal efficiency of the system decreases with the rise in air inlet temperature in the entrance duct. The results have been compared with their experimental values and have been found to be in good agreement.. Ruiz-Pardo et al. [28] have reviewed the calculation methods for the evaluation and design of energy and thermal performance of buildings presented by the European and International Standard UNE-EN ISO 13790. These methods have a varied range of details for calculating the energy utilization of passive heating and cooling in different building zones as well as for calculating the heat transfer and solar heat gains of special elements such as ventilated Trombe walls. Fares [29] has studied the effects of changing Trombe wall components on the thermal load in the building. The parameters selected to study the effects are the wall type (thermal mass), thermal mass thickness, ratio of Trombe wall area to total wall area and the layer count of glass coat, viz. one layer, two layers or three layers. The thermal load, solar gain and auxiliary energy have been calculated considering the changes in these parameters. This research aims to attain and maintain the internal thermal comfort level using the passive solar heating system by considering changes in Trombe wall components. This leads to an optimal selection of Trombe wall components in order to reduce as much as possible the heating load in winter and the cooling load in summer. An important result is that an energy saving of 83% has been obtained when using such a Trombe wall. Stritih and Novak [30] conducted a numerical and an experimental study on a wall consisting of a transparent insulation material covering a solar collector made of black paraffin. An air channel behind the solar collector was used to supply the pre-heated air for the ventilation of the house. Their numerical analysis has shown that the optimum wall thickness was 50 mm and the melting point of paraffin was a few degrees above room temperature. Khalifa and Abbas [31] created a dynamic simulation computer model of a south-facing thermal storage wall. They examined two types of PCMs viz. the hydrated salt $CaCl_2.6H_2O$ and paraffin wax encapsulated in copper capsules with length to diameter ratio of 0.76. They concluded that a 0.08 m thick thermal storage wall made from the hydrated salt gave better thermal performance than a 0.20 m thick concrete wall and the 0.05 m thick wall made from paraffin wax. Fernndez-Gonzlez [33] has presented a summary of the thermal performance of five different passive solar test-cells (Direct Gain, Trombe wall, Water wall, Sunspace and Roofpond) and a control test-cell during the 2002-2003 heating season in Muncie, Indiana. The thermal storage wall had an area of 4.4 m^2 and included four vents each with an area of 0.1 m^2. He concluded that the Trombe wall produced an extremely stable indoor environment with a low variation in the operating temperature. Bhandari and Bansal [34] have used the concept of solar heat gain factor for calculating the net energy gain of passive heating elements and other components of a building due to incident solar radiation. Mishra & Kamal [35] carried out thermal analysis of Trombe wall for non porous structure out for providing comfortable environment conditions. Explicit expressions for heat flux and thermal efficiency of the non porous system using different thermal energy storage materials have been developed. The following data given in Table 1 have

been used for numerical computations in order to validate the experimental results.

Table: 1. Physical and Thermal Properties of Thermal Energy Storage Materials (Mishra & Kamal [35])

Sr. No.	Material	Thermal Conductivity k_m (W/m-K)	Density ρ (kg/m^3)	Specific Heat c_p (J/kg-K)
1	Brick	0.69	1600	840
2	Concrete	1.5	2243	837
3	Marble	2.7	2650	840
4	Quartzite	5.17	2635	732

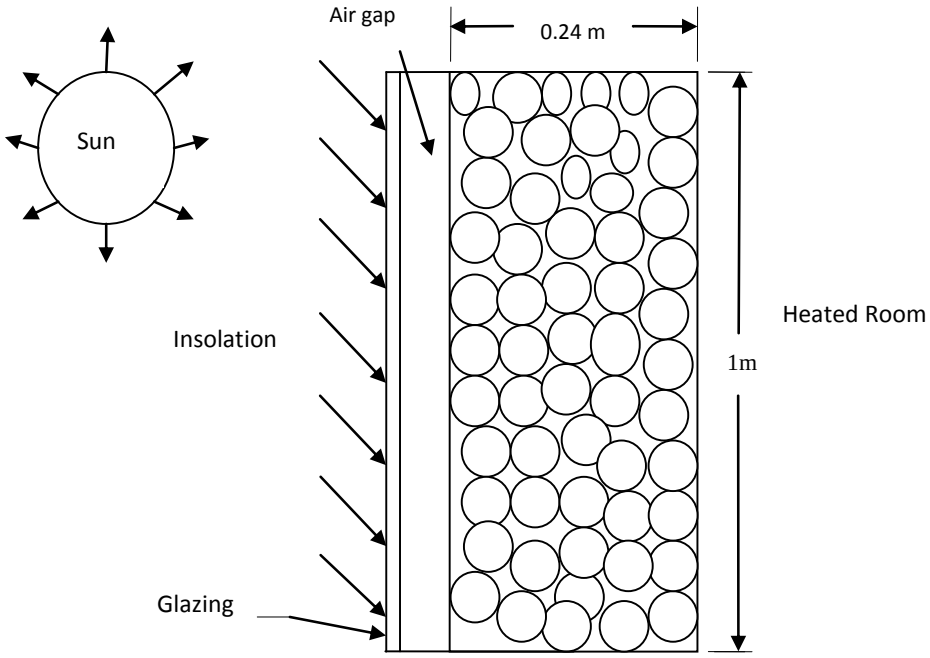


Fig: 2. Schematic diagram of a porous wall

Numerical computations have been carried out using the developed model which validates the experimental results. The thermal stratification in Trombe walls for non-porous structures is analyzed and it was observed that thermal energy storage wall made of quartzite gives better performance than other types of walls. This model is also useful for predicting thermal performance of other passive heating and cooling systems. Numerical simulation has been used to analyze the thermal performance of heat transfer and air flow in porous Trombe wall. For two different porous materials viz. marble and quartzite, explicit expressions for heat flux and thermal efficiency of the porous system have been developed. The experimental results have been validated with numerical computations using the developed model. Kamal and Mishra[36] carried out computer simulation of porous Trombe wall for providing comfortable thermal environment. During sunshine hours excess heat is stored within the porous absorber and there is stratification in the porous layer.

The porous absorber works as a thermal insulator when no sunshine as shown in Fig.2.

A study of thermal stratification in the porous and non-porous Trombe walls has not been carried in the literature so far. The literature further reveals that there has been a limited application of a numerical approximation technique such as finite element method for analyzing the solar thermal walls. Only finite difference method has been used to a certain extent by a few authors so far in their analysis. The performances of Trombe walls and Trans walls have been analyzed using an approximate numerical solution procedure based on finite element analysis for the different cases of these two types of walls.

3. Results And Discussions

Fig.3 shows the variation of specific heat of porous absorber with porosity for four different materials such as brick, concrete, marble and quartzite. As porosity of porous absorber increases, specific heat of porous absorber is also increasing. The specific heat of quartzite is much lower than that

of brick, concrete and marble. The density and thermal conductivity of porous absorber using brick, concrete, marble and quartzite decrease when porosity is increasing as shown in Figs.4 and 5 respectively.

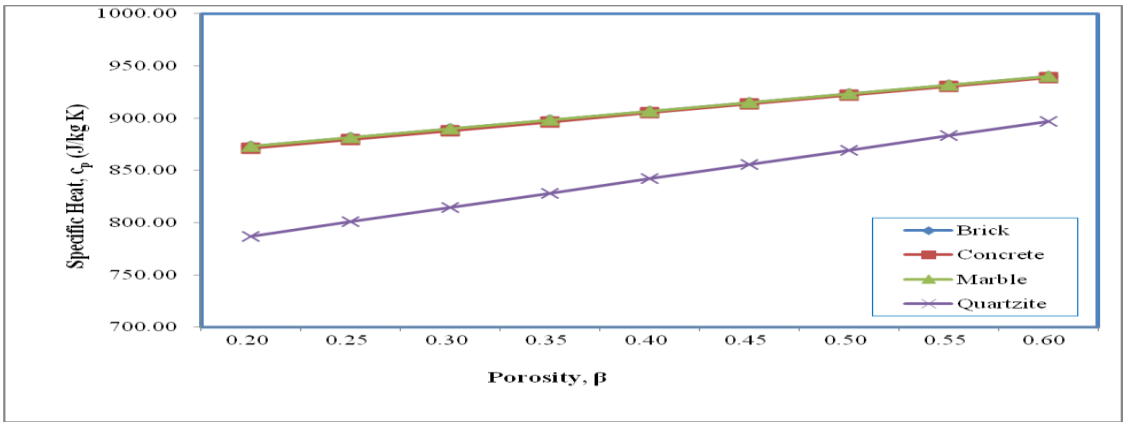


Fig: 3. Variation of Specific Heat with Porosity for different materials

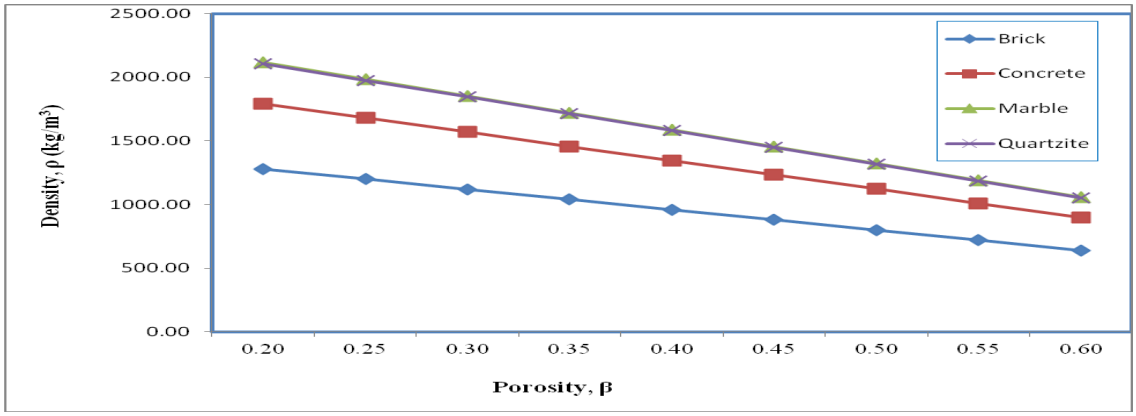


Fig: 4. Variation of Density with Porosity for different materials

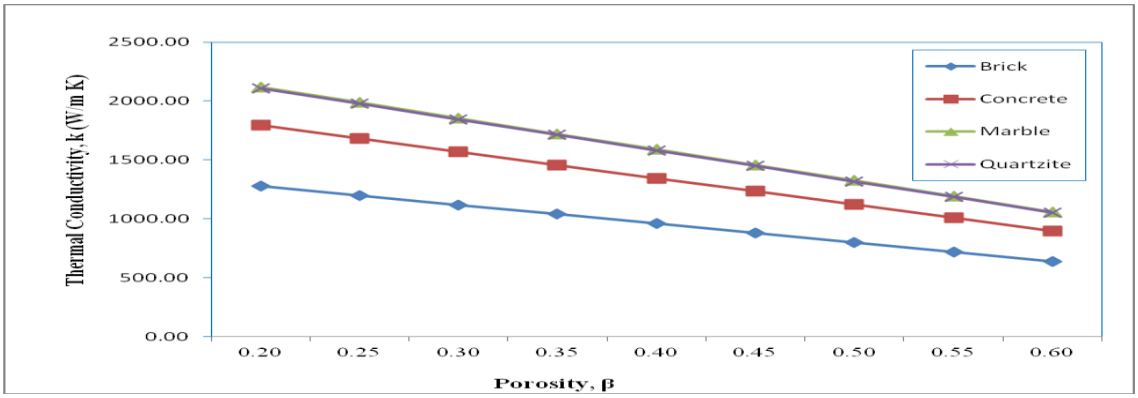


Fig: 5. Variation of Thermal Conductivity with Porosity for different materials

Fig. 6 shows the variation of fluid (air) temperature for different mass flow rates of air and ambient temperature with time of the day. It was observed that as mass flow rate of air increases, the fluid outlet temperature of porous collector decreases. Similarly Fig. 7 shows the variation of volumetric heat transfer coefficient with particle diameter of marble for different mass flow rates of air. It was observed that as mass flow rate of air increases, the volumetric heat transfer coefficient also increases for a given particle diameter.

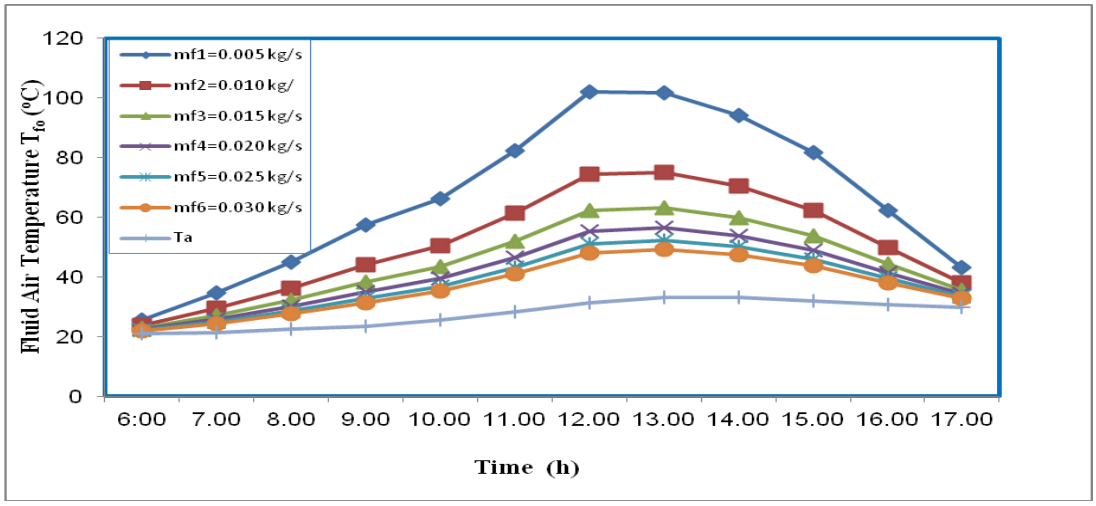


Fig: 6. Variation of Fluid (Air) Temperature for different Mass Flow Rates of air and Ambient Temperature with Time of the day

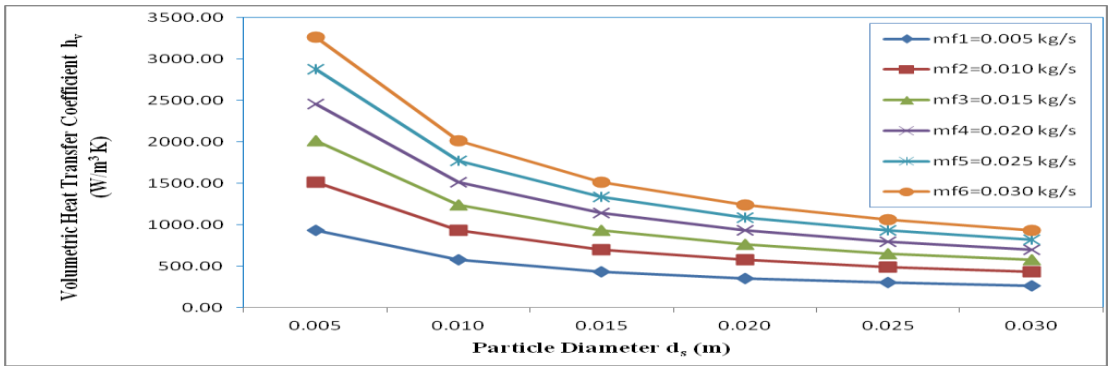


Fig: 7. Variation of Volumetric Heat Transfer Coefficient with Particle Diameter for different Mass flow Rates of air

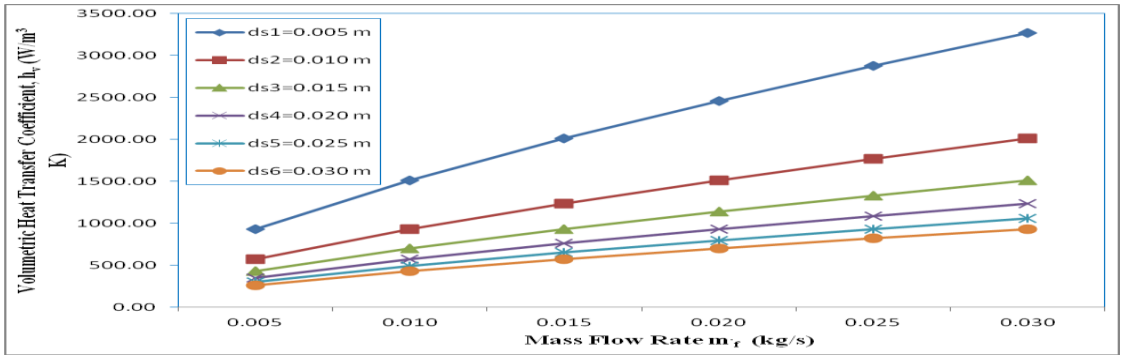


Fig: 8. Variation of Volumetric Heat Transfer Coefficient with Mass Flow Rate of air for different Particle Diameters

Fig. 8 shows the variation of volumetric heat transfer coefficient with mass flow rate of air for different particle diameters of porous marble. It was observed that as particle size increases, the volumetric heat transfer coefficient decreases for a given mass flow rate of air.

The variations of volumetric heat transfer coefficient and surface heat transfer coefficient for a given mass flow rate of air (0.010 kg/sec) and different porosities for different particle diameters of porous marble are shown in Fig. 9. It was observed that volumetric heat transfer coefficient decreases and

surface heat transfer coefficient increases with increasing particle diameter for a given mass flow rate of air. Fig. 10 shows the variations of volumetric heat transfer coefficient and surface heat transfer coefficient with particle diameter for different porosities and a given mass flow rate of air (0.010 kg/sec) for porous quartzite walls. It was observed that for a given mass flow rate of air, volumetric heat transfer coefficient is decreasing with increasing particle size while surface heat transfer coefficient first increases, reaching an optimum value before decreasing.

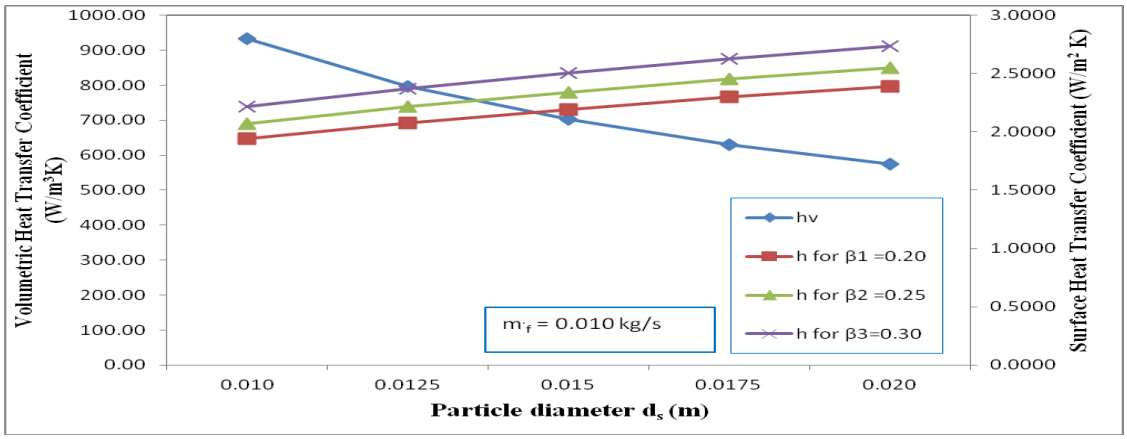


Fig: 9. Variations of Volumetric Heat Transfer Coefficient and Surface Heat Transfer Coefficient with Particle Diameter for different Porosities and a given Mass Flow Rate of air for Porous Marble walls

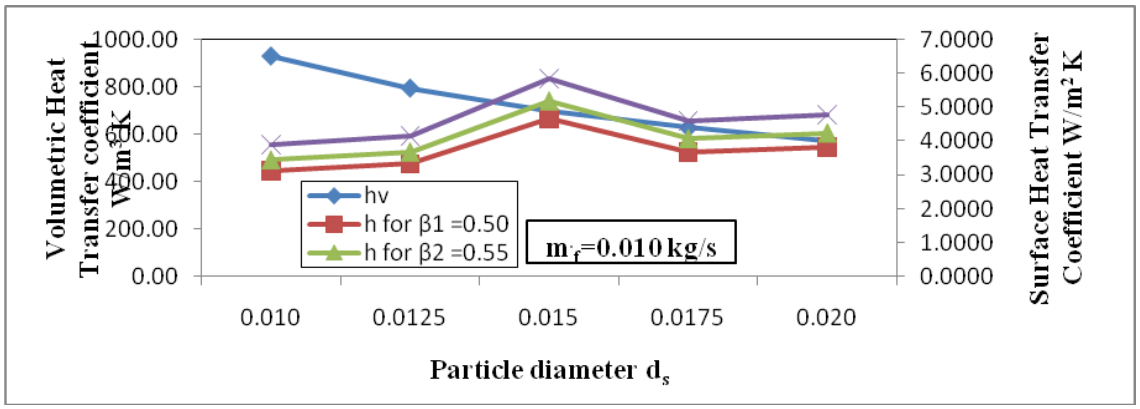


Fig: 10. Variations of Volumetric Heat Transfer Coefficient and Surface Heat Transfer Coefficient with Particle Diameter for different Porosities and a given Mass Flow Rate of air for Porous Quartzite walls

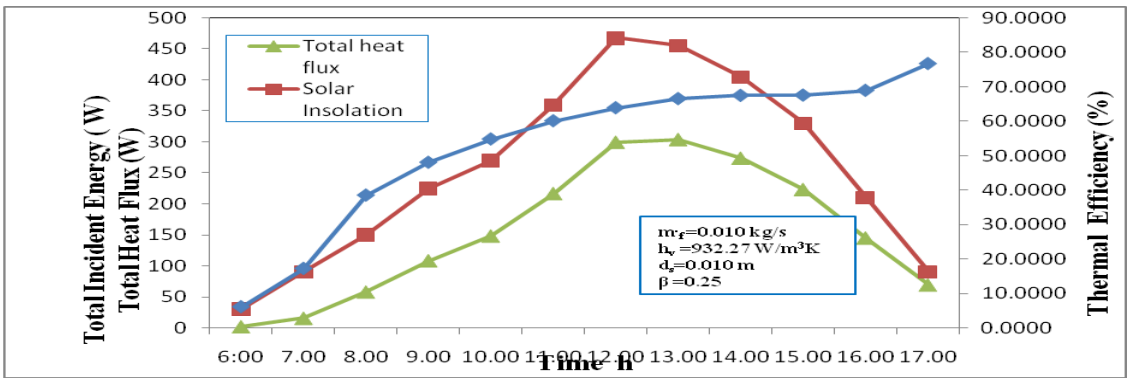


Fig: 11. Variations of Total Incident Energy, Total Heat Flux and Thermal Efficiency for Porous Marble wall with Time of the day at x=0.24 m

Figs. 11-13 show the variations of total incident energy, total heat flux and thermal efficiency of marble and quartzite walls with varying time. It was observed that marble and quartzite porous absorbers improve the thermal performance as compared to non porous Trombe walls made of the same materials. The average thermal efficiencies of porous Trombe walls made of marble and quartzite have been found to be 52.56% and 57.94% respectively.

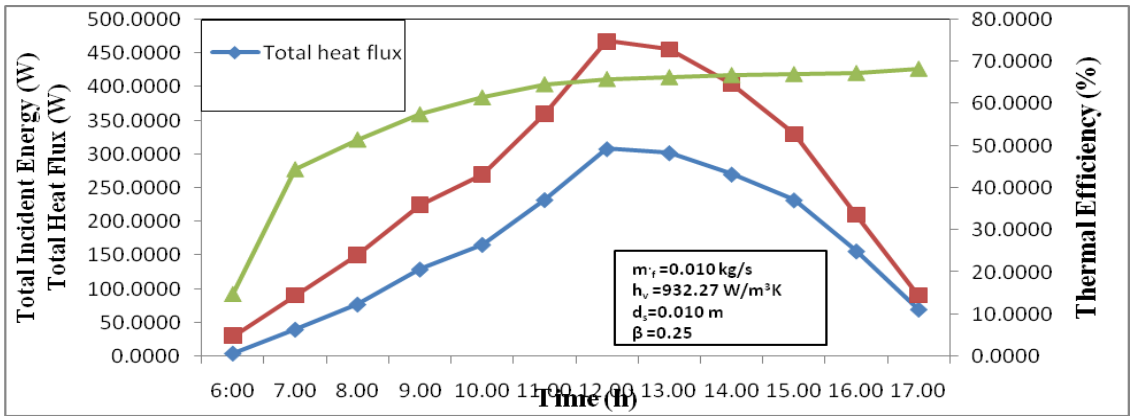


Fig: 12. Variations of Total Incident Energy, Total Heat Flux and Thermal Efficiency for Porous Quartzite wall with Time of the day at x=0.24 m

Figures 14, 15, 16 and 17 show the temperature stratification in the Trombe walls made of brick, concrete, marble and quartzite as thermal energy storage materials. It is observed that marble and quartzite showed the maximum temperature rise than brick and concrete. Figures 18, 19, 20 and 21 show hourly variations of heat flux with wall thickness across brick, concrete, marble and quartzite walls respectively. It is observed that marble and quartzite give more thermal energy storage than brick and concrete which can be utilized during off-sunshine hours Figures 14, 15, 16 and 17 shows the temperature stratification in the Trombe walls made of brick, concrete, marble and quartzite as thermal energy storage materials. It is observed that marble and quartzite showed the maximum temperature rise than brick and concrete. Figures 18, 19, 20 and 21 show hourly variations of heat flux with wall thickness across brick, concrete, marble and quartzite walls respectively. It is observed that marble and quartzite give more thermal energy storage than brick and concrete which can be utilized during off-sunshine hours

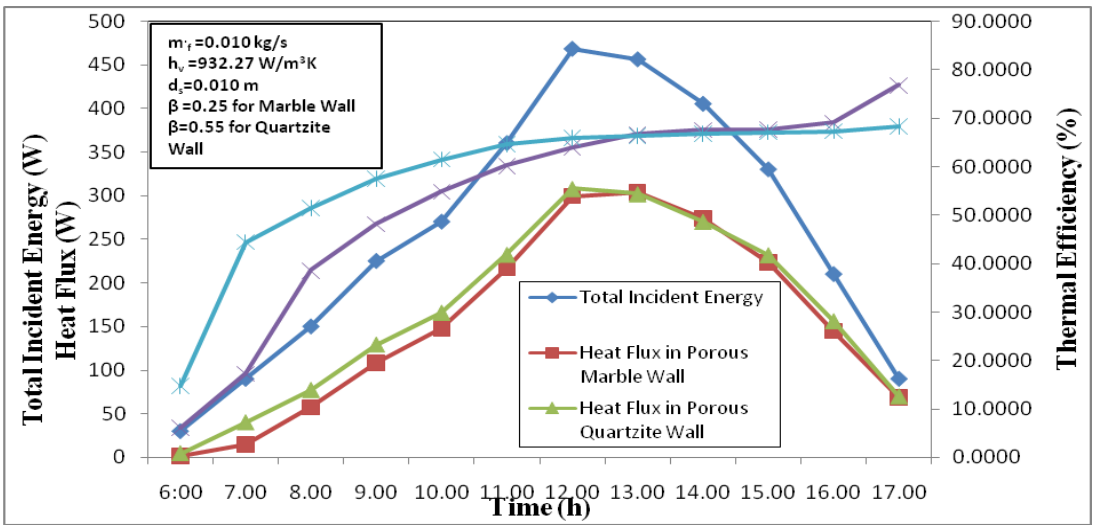


Fig: 13. Comparison between the variations of Total Incident Energy, Heat Fluxes and Thermal Efficiencies of Marble and Quartzite walls with Time of the day at x=0.24 m

From the techno-economic point of view, the locally available materials such as brick and concrete give lesser thermal energy storage. For a typical value of = 0.36 , i.e. at the inside surface of the wall, the hourly variations of sol-air temperature and temperatures in Trombe walls made of different thermal energy storage materials viz. brick, concrete, marble and quartzite [Table 1] are shown in Fig. 12 and hourly variations of solar insolation and heat fluxes in the Trombe walls are shown in Fig. 13. Figure 14 shows hourly variation of thermal efficiency for different thermal energy storage materials. It is observed that the average thermal efficiency of quartzite is maximum viz. 57.2% as compared with other materials. The thermal efficiency of marble and quartzite walls increases after 15:00 hrs due to energy storage in these walls which provides the heating effect inside the room during off-sunshine hours.

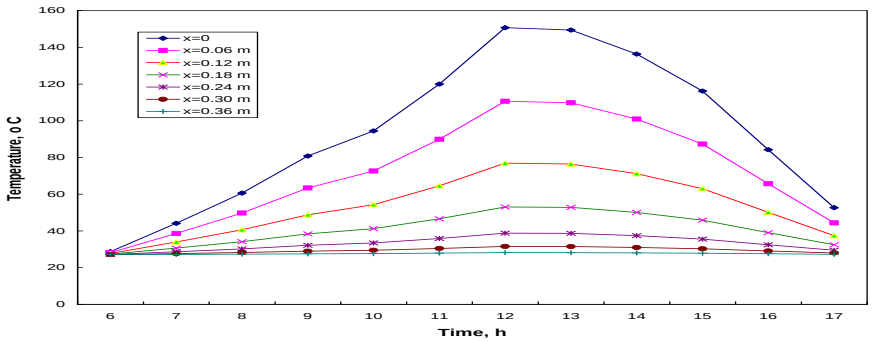


Fig: 14. Variation of Temperature across Wall Thickness for Brick Wall

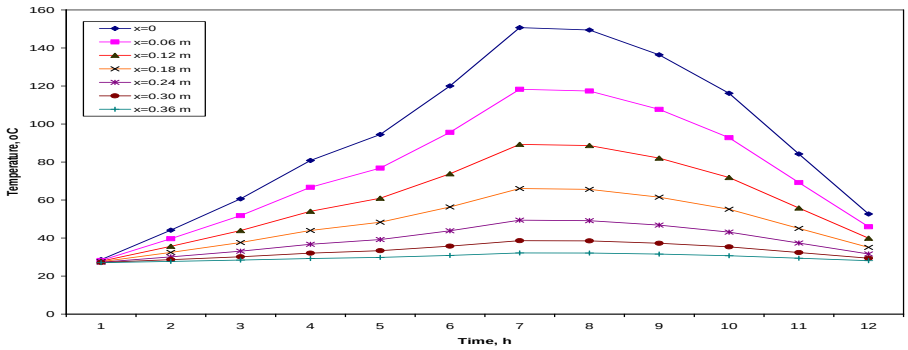


Fig: 15. Variation of Temperature across Wall Thickness for Concrete Wall

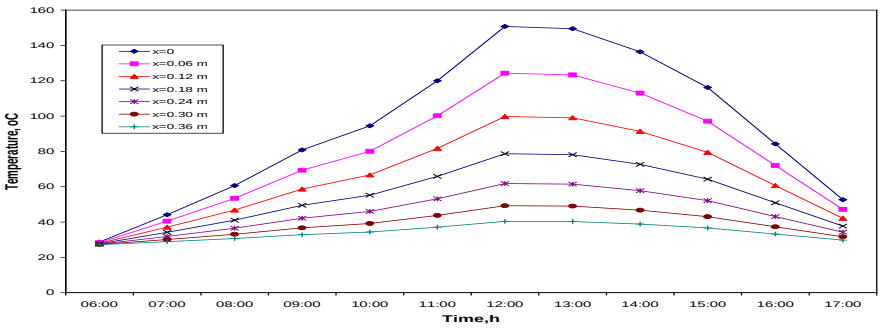


Fig: 16. Variation of Temperature across Wall Thickness for Marble Wall

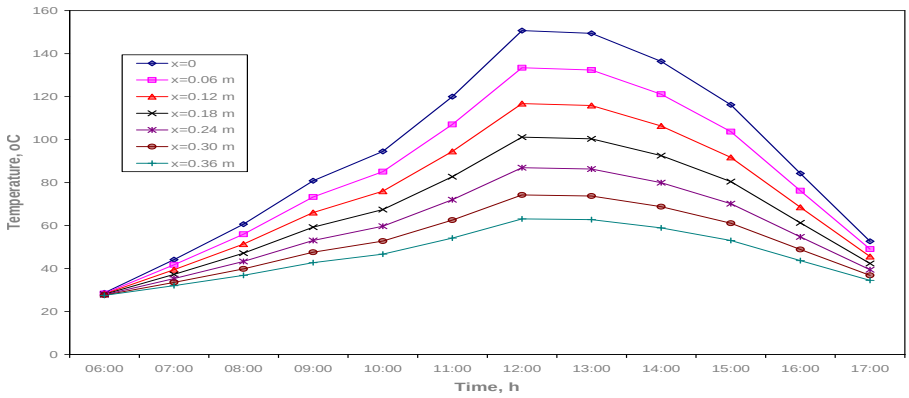


Fig: 17. Variation of Temperature across Wall Thickness for Quartzite Wall

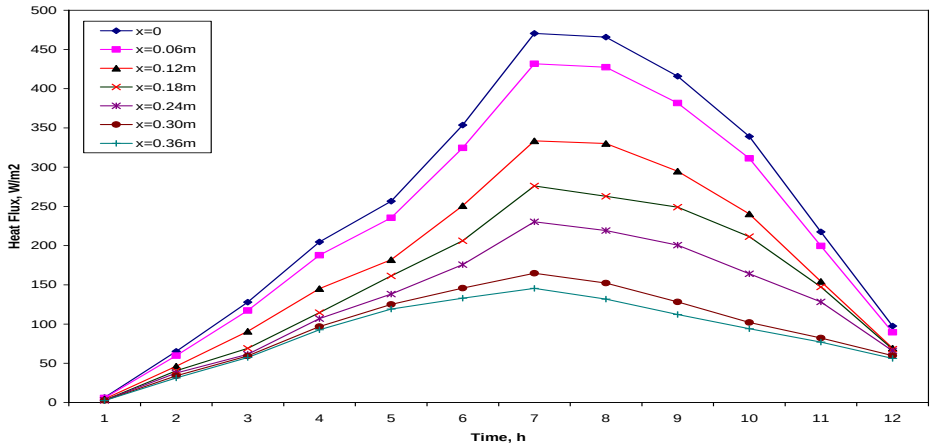


Fig: 18. Variation of Heat Flux with Wall Thickness across Brick Wall

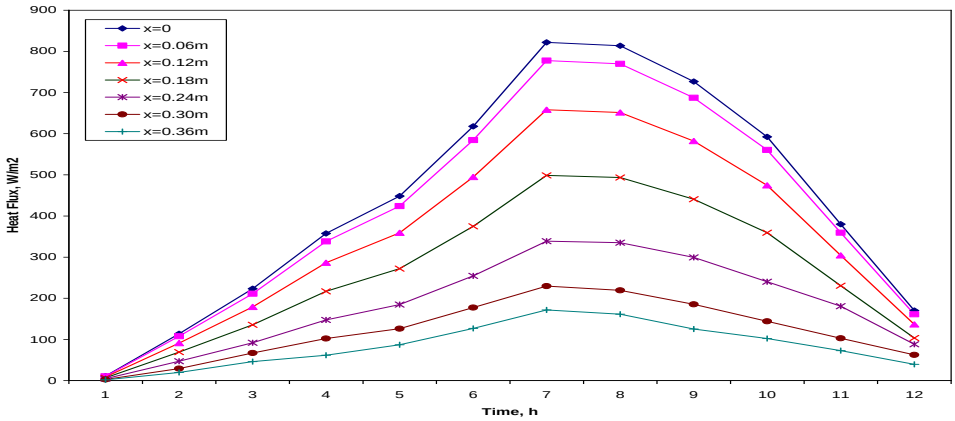


Fig. 19 Variation of Heat Flux with Wall Thickness across Concrete Wall

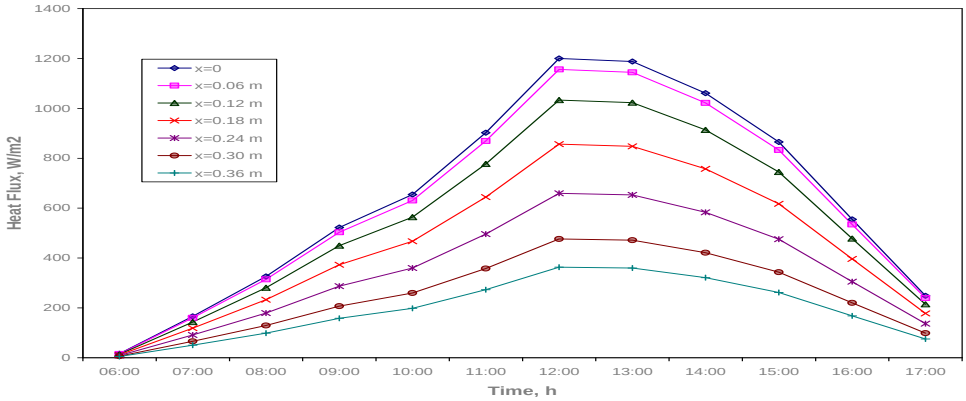


Fig: 20. Variation of Heat Flux with Wall Thickness across Marble wall

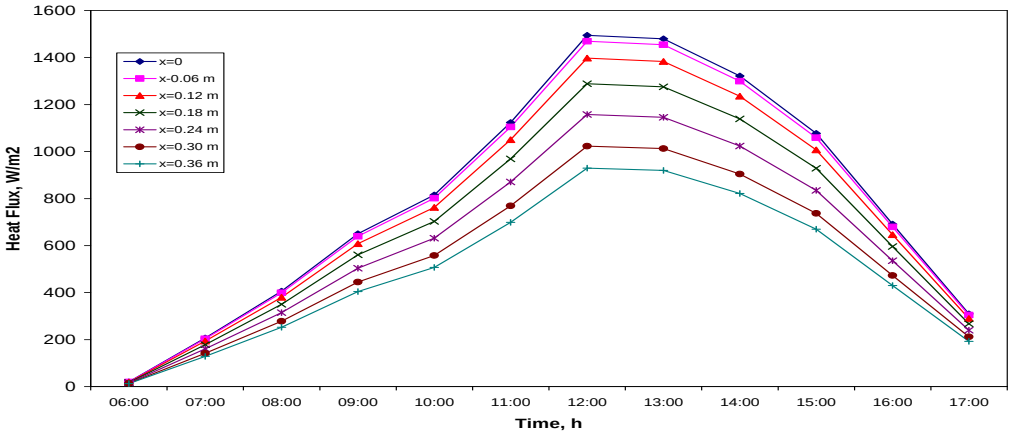


Fig: 21. Variation of Heat Flux with Wall Thickness across Quartzite Wall

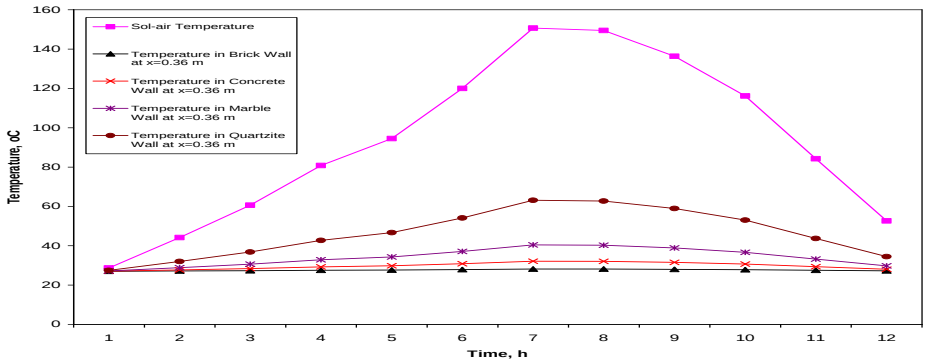


Fig: 22. Variation of Sol-air Temperature and Temperatures in Brick, Concrete, Marble and Quartzite Walls at x=0.36 m with Time of the day

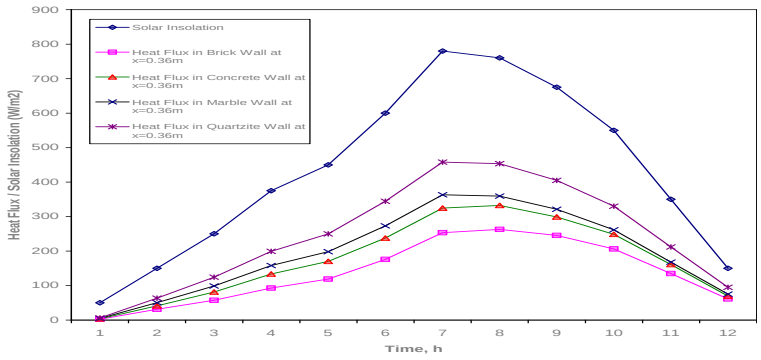


Fig: 23. Variation of Heat Fluxes in Brick, Concrete, Marble and Quartzite Walls at x=0.36 m and Solar Insolation with Time of the day

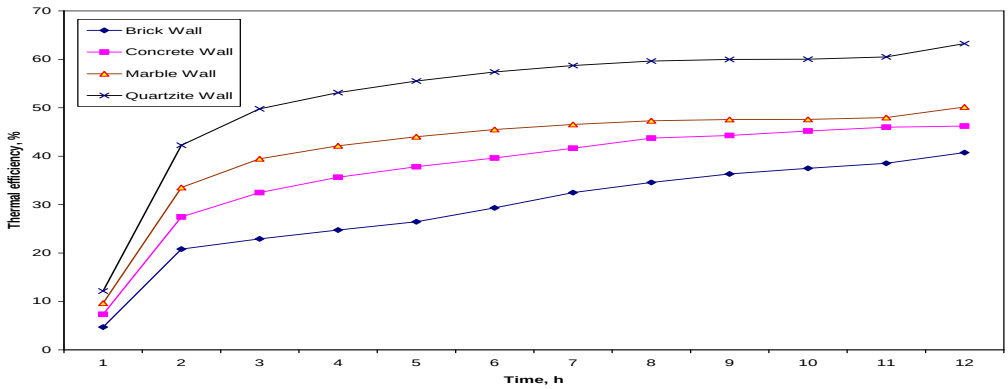


Fig: 24. Variation of Thermal efficiency with Time of the day for different wall materials

4. Conclusions and Recommendations

It has been observed that Trombe wall contributes 20% to 30% of the total heating of the buildings depending upon type of material. The average thermal efficiency of the wall has been found to be 29.09% for brick wall, 37.27% for concrete wall, 45.35% for marble wall and 57.2% for quartzite wall respectively.. The results from presented mathematical model would help the designers of passive solar systems to use this model for selecting optimal constructive parameters of the non-porous Trombe wall. A thermal model has been developed to study the effects of the porous absorber on heat transfer and air flow in porous Trombe wall for two types of absorbers viz. marble and quartzite. The average thermal efficiencies of porous Trombe walls made marble and quartzite have been found to be 52.56% and 57.94% respectively. The performance of passive heating or cooling systems is significantly influenced by the additional heating load in winter season and cooling load in summer season. Hence the porous Trombe wall can be designed by considering the annual net heating effect of the wall. The occurrence of overheating and inefficient use of solar energy can be avoided by considering the effects of particle size and porosity of the porous absorber on the air temperature in the heated room. The optimal constructive parameters of the porous structures can be selected by the designers of passive solar systems using the results from the presented mathematical model

References

[1] A. Akbarzadeh, W. W. S. Charters D. A. Lesslie, 1982, "Thermocirculation characteristics of a Trombe wall passive test cell", Solar Energy, 28(6), 461-46

[2] N. K. Bansal, P. C. Thomas, "A simple procedure for selection and sizing of indirect passive solar heating systems", Building and Environment, 26(4), pp. 381-387, 1991
[3] L. I. Blasco, L. Hoese, D. Pontoriero, "Experimental study of passive systems thermal performance", Renewable Energy, 19(1), pp. 39-45(7), 2000
[4] S. A. M. Burek, A. Habeb, "Air flow and thermal efficiency characteristics in solar chimneys and Trombe walls", Energy and Buildings, 39, 120-135, 2007
[5] S. S. Chandel, R. K. Aggarwal, "Performance evaluation of a passive solar building in Western Himalayas", Renewable Energy, 33, 2166-2173, 2008
[6] A. Chel, J. K. Nayak, G. Kaushik, "Energy conservation in honey storage building using Trombe wall", Energy and Buildings, 40, 1643-1650, 2008
[7] B. Chen, X. Chen, Y. H. Ding, X. Jia, "Shading effects on the winter thermal performance of the Trombe wall air gap: An experimental study in Dalian", Renewable Energy, 31, 1961-1971, 2006
[8] B. Chen, H. J. Chen, S. R. Meng, X. Chen, P. Sun, Y. H. Ding, "The effect of Trombe wall on indoor humid climate in Dalian", China, Renewable Energy, 31(3), 333-343
[9] W. Chen, W. Liu, "Numerical analysis of heat transfer in a passive solar composite wall with porous absorber", Applied Thermal Engineering, 28, 1251-1258, 2008
[10] S. Chungloo, B. Limmeechokchai, "Application of passive cooling systems in the hot and humid climate: The case study of solar chimney and wetted roof in Thailand", Building and Environment, 42, 3341-3351, 2007
[11] G. Gan, "A parametric study of Trombe walls for passive cooling of buildings", Energy and Buildings, 27(1), pp.37-43, 1998
[12] S. Jaber, S. Ajib, "Optimum design of Trombe wall system in Mediterranean region", Solar Energy, 85, 1891–1898, 2011
[13] V. Koyunbaba, Z. Yilmaz, K. Ulgen, "An approach for energy modeling of a building integrated photo voltaic (BIPV) Trombe wall system", Energy and Buildings, pages 9, 2011
[14] B. K. Koyunbaba, Z. Yilmaz, "The comparison of Trombe wall systems with single glass", double glass and PV panels, Renewable Energy, 45, 111-118, 2012
[15] J. K. Nayak, N. K. Bansal, M. S. Sodha, "Analysis of passive heating concepts, Solar Energy", 30(1), pp. 51-69, 1983
[16] N. P. Nwachukwu, W. I. Okonkwo, "Effect of an Absorptive Coating on Solar Energy Storage in a Trombe wall system", Energy and Buildings, 40, 371-374, 2008
[17] L. Pires, P. D. Silva, L. C. Goncalves, "Surface configuration relevance in the overall thermal resistance of a wall", Energy and Buildings, 37, 1068-1074, 2005
[18] S. Ram, H. P. Garg, "Heat flux through a Trombe wall / roof, Applied Energy", 19(1), pp.61-71
[19] P. Raman, S. Mande, V. V. N. Kishore, "A passive solar system for thermal comfort conditioning of buildings in composite climates", Solar Energy, 70(4), pp. 319-329, 2001
[20] J. Shen, S. Lassue, L. Zalewski, D. Huang, Numerical study on thermal behavior of classical or composite Trombe solar walls, Energy and Buildings, 39 (8), 962–974, 2007
[21] S. Shtrakov, A. Stoilov, "New approach for Finite Difference Method for Thermal Analysis of Passive Solar Systems", Department of Computer's systems, South – West University "Neofit Rilski", Blagoevgrad, BULGARIA, 17, 2005
[22] W. Smolec, A. Thomas, "Some aspects of Trombe wall heat transfer models", Energy Conversion and Management, 32(3), pp. 269-277, 1991
[23] M. S. Sodha, N. K. Bansal, S. Ram, "Periodic analysis of a Transwall: A passive heating concept", Applied Energy, 14(1), May, pp.33-48, 1983
[24] M. Upadhya, G. N. Tiwari, S. N. Rai, "Optimum distribution of water-wall thickness in a transwall", Energy and Buildings, 17(2), pp.97-102, 1991
[25] L. Zalewski, S. Lassue, B. Duthoit, M. Butez, "Study of solar walls – validating a simulation model", Building and Environment, 37, pp.109-121, 2002
[26] L. Zalewski, A. Joulin, S. Lassue, Y., Dutil, D. Rousse, "Experimental study of small-scale solar wall integrating phase change material", Solar Energy, 86, 208–219, 2012
[27] S. M. Dragicevic, M. R. Lambic, "Numerical study of a modified Trombe wall solar collector system", Thermal Science, 13(1), pp. 195-204, 2009
[28] A. Ruiz-Pardo, S. A. Dominguez, J. A. S. Fernandez, "Revision of the Trombe wall calculation method proposed by UNE-EN ISO 13790", Energy and Buildings, 42, pp.763-773, 2010

[29] A. Fares, "The effect of changing Trombe wall components on the thermal load", Energy Procedia, 19, pp. 47-54, 2012
[30] U. Stritih, P. Novak, "Solar heat storage wall for building ventilation", Renewable Energy, 8 (1-4), pp.268-271, 1996
[31] A. J. N. Khalifa, E. F. Abbas, "A comparative performance study of some thermal storage materials used for solar space heating", Energy and Buildings, 41, pp.407-415, 2009
[32] Y. Boutin, L. Gosselin, "Optimal mixed convection for maximal energy recovery with vertical porous channel (solar wall)", Renewable Energy, 34 (12), pp.2714-2721, 2009
[33] A. Fernndez-Gonzlez, "Analysis of the thermal performance and comfort conditions produced by five different passive solar heating strategies in the united states Midwest", Solar Energy, 81 (5), pp.581-593, 2007
[34] M. S. Bhandari, N. K. Bansal, "Solar heat gain factors and heat loss coefficients for passive heating concepts", Solar Energy, 53 (2), pp.199-208, 1994
[35] R. S. Mishra, V. Kamal, "Effect of thermal energy storage materials on the thermal performance of non-porous Trombe wall", International Journal of Applied Engineering Research, 5(18), pp.3085-3095, 2010
[36] V. Kamal, R. S. Mishra, "Thermal performance and analysis of thermal energy storage Trombe walls for porous structures", International Journal of Applied Engineering Research, 6(16), pp.1925-1936, 2011

Environmental Geotechnics

Consolidation of clayey gouge amid permeating rock masses
Trivedi, Banik, Sukumar *et al*.

Environmental Geotechnics
http://dx.doi.org/10.1680/envgeo.13.00043
Paper 13.00043
Received 20/05/2013; accepted 08/01/2014
Keywords: geoenvironment/geohydrology

ICE Publishing: All rights reserved

ice Institution of Civil Engineers
publishing

Consolidation of clayey gouge amid permeating rock masses

1 **Ashutosh Trivedi** PhD
Professor and Head, Department of Civil Engineering, Delhi Technological University, Delhi, India

2 **Tanmay Banik** BEng
GET, Triune Energy Services Pvt Ltd, New Delhi, India

3 **Tanay Sukumar** BEng
Fellow, Teach for India, Green Park Extn, New Delhi, India

4 **Naresh Kumar** MTech
Associate Professor, Department of Civil Engineering, Delhi Technological University, Delhi, India

5 **Akshay Jain** BEng
Sales Officer, Indian Oil Corporation Ltd, Ranchi, Jharkhand, India

6 **Amit Kumar** BEng
Officer Trainee, Indian Oil Corporation Ltd, Vijayawada, Andhra Pradesh, India








There are numerous occurrences of soil–rock–water interaction in the natural geo-environment involving saturated clayey gouge consolidating amid permeating rock masses and draining laterally through a network of joints. In this paper, the concept of two-dimensional drainage for consolidation along the vertical direction for saturated clay has been applied to a layer of gouge amid rock joints. Solutions for pore water pressure distribution and average degree of consolidation have been computed. The orthogonal directions along which the drainage has been assumed for the derivation of these expressions are vertical direction (as in Terzaghi's theory of one-dimensional consolidation) and lateral direction. Initially, such a case corresponds to a Dirichlet problem applied to a rectangular gouge lamina. The deformations appearing in the vertical direction are a result of the effects of drainage in the lateral and vertical directions together. An expression for the relationship of time factor with the average degree of consolidation as a function of dimensionless parameter relating rock mass characteristics has been proposed.

Notation

$a_v(x)$	coefficient of compressibility in x direction
$a_v(z)$	coefficient of compressibility in z direction
c''', c'', c'	coefficients of dimension less ratio r to obtain $\varphi(r)$
$C_h(x)$	coefficient of consolidation in x direction
$C_h(y)$	coefficient of consolidation in y direction
$C_h(z)$	coefficient of consolidation in z direction
E	deformation modulus of gouge material
E_{hv}	modulus ratio = E_h/E_v
E_h	deformation modulus in horizontal direction
E_v	deformation modulus in vertical direction
e	void ratio
e_0	initial void ratio
$2H$	descriptor of thickness of gouge
H_x, H_z	drainage path along vertical direction, thickness of gouge in z direction, and equivalent thickness of gouge amid a number of joints respectively
j	joints in rock mass
K	coefficient of permeability
K_{rm}	intrinsic permeability of rock masses
K_{uc}	intrinsic permeability of unconsolidated organic soils and clays
K_x	coefficient of permeability in x direction
K_y	coefficient of permeability in y direction
K_z	coefficient of permeability in z direction
k_h	coefficient of permeability along lateral direction
k_v	coefficient of permeability along vertical direction
$2L$	descriptor of lateral spread of gouge
L_x, L_y	drainage path along x direction and y direction respectively
n	porosity
r	dimension less ratio depending on r_c, r_k and r_s
r_c	ratio of coefficient of consolidation of clayey gouge to that of rock mass
r_k	ratio of intrinsic permeability of clayey gouge to that of rock mass
r_s	shape factor
T_f	final value of non-dimensional time factor at $U = 1$
T_{fs}	value of non-dimensional time factor where post primary consolidation offsets primary consolidation
T'_{fs}	variant of non-dimensional time factor T_{fs}
T_v	non-dimensional time factor
t_a	asperity height
U_{av}	average degree of consolidation

$U_{av}1$, $U_{av}2$, $U_{av}3$, $U_{av}4$	average degree of consolidation in Figure 3, at r = 0, 0·1, 1, 10 respectively
$U_{av}1$, $U_{av}2$	average degree of consolidation in Figure 4 for 1-D and 2-D drainage case, respectively
U_p	average degree of consolidation at the end of primary consolidation
U_s	average degree of consolidation at the end of post primary consolidation
U_z	degree of consolidation at depth 'z'
u	pore water pressure at time 't'
u_i	initial excess pore water pressure
v_x	component of velocity in x direction
v_z	component of velocity in z direction
β	joint inclination with the direction of loading
γ	bulk unit weight
γ_w	unit weight of water
γ_{xz}	shear strain in x–z plane
$\bar{\sigma}_x$	effective stress in x direction
$\bar{\sigma}_z$	effective stress in z direction
$\varphi(r)$	dimension less parameter depending on dimension less ratio, r

Introduction

Most of the rock masses in our planetary geo-environment are neither massive nor intact nearly to a hundred meters of earth crust. Several groups of interconnected discontinuities, under a set of geo-physical and geo-chemical forces, allow deposition of gouge and granular fragments. In a geo-mechanical stress environment, for a saturated ground water condition, the hydraulic and strain adjustment amid these formations is well anticipated. Therefore, the consolidation of randomised distribution of saturated clayey gouge is frequently encountered amid the permeating rock masses. The gouge material is defined as a fine hydro-geo-thermal deposit of clay and silt amid rock joints produced by soil–rock–water interaction and soil–rock–mineral alterations. Often, the fluid flow and deformability of the rock masses can be interpreted from in situ rock quality designation, number of joint (J), joint inclination (β), joint condition, gouge density, gouge thickness ($2H_z$) (Trivedi, 2010) and joint aperture ($2t_a$) (Hsu *et al.*, 2011; Klimczak *et al.*, 2010). The thickness of the gouge material ($2H_z$) and its lateral spread may vary in the range of several meters to a few millimetres with multiple drainage paths. In submerged conditions, these heterogeneous distributions of clayey gouge may be idealised as a lamina of variable permeability consolidating in the vertical direction and draining in plane strain conditions amid fractured rock masses. Figure 1 shows an example of a clayey gouge layer draining in the horizontal and vertical directions. The range of permeability of rock masses and that of silty–clayey gouge is shown in Table 1.

While the deformation of rock masses with gouge can be estimated reasonably well (Trivedi, 2010, 2013) from normal, shear stiffness (Zhang, 2010) and in situ rock mass characterisation, their time-dependent consolidation behaviour is yet to be computed by a physically idealised and numerically consistent method. Under varying salute and fluid transport conditions influenced by temperature, pressure and geo-environment, the saturated clayey gouge is expected to show a time-dependent volume change behaviour, which was ideally simplified in the seminal works of Terzaghi (1925, 1943) on one-dimensional (1-D) consolidation. Accordingly, the process of consolidation is defined as the decrease in pore fluid content of a saturated soil without its replacement by air. This definition attracted widespread interest in the scientific and engineering community, which had been involved in estimating the consolidation settlement of saturated clays for more than half a century using experimental and numerical techniques (Biot, 1941; Das, 2008; Di Francesco, 2011; Gibson *et al.*, 1967; Lambe and Whitman, 1969; Scott, 1963; Tewatia *et al.*, 2013; Wood, 2004).

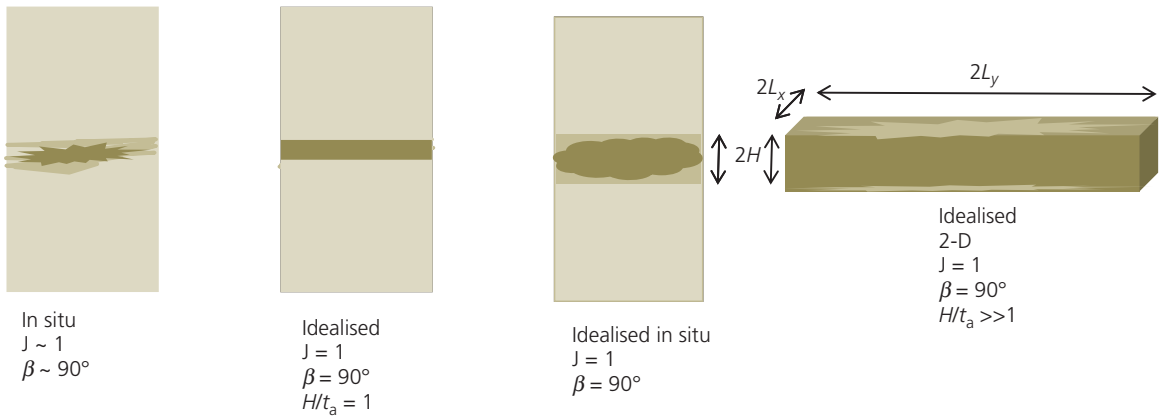


Figure 1. In situ and idealised saturated clay lamina amid permeating rock mass for single joint (J = 1) oriented normal to the direction of loading (β = 90°) at different asperity ratio (H/t_a); gouge thickness ($2H$) covers the asperity height ($2t_a$); the gouge is shown in dark shades

In situ profile	Coefficient of permeability: mm/sec	Physical effects
Well sorted gravels	>1	High permeability, pervious in nature
Sandy gouge	10^{-1}–10^{-4}	Medium to low permeability, semi-pervious
Highly fractured rock masses	10^{-2}–10^{-5}	Low permeability, pervious
Sand with silt and clay gouge	10^{-4}–10^{-6}	Low permeability, semi-pervious
Poorly weathered rock masses	10^{-5}–10^{-10}	Very low permeability, semi-pervious in nature, drainage is poor
Clayey gouge and organic soils	10^{-6}–10^{-11}	Very low permeability, impervious
Un-weathered rock mass	10^{-11}–10^{-13}	Impervious in nature

Interpreted from Bear (1972).

Table 1. Range of permeability as per soil and rock mass profile

In a classical work on consolidation theory, Biot (1941) assumed isotropy of the material, reversibility of stress–strain relations under final equilibrium conditions, linearity of stress–strain relations, small strain behaviour, incompressibility of pore water, possibility of air bubbles and that dissipation of pore water follows Darcy's law.

Biot (1941) agreed that among these basic assumptions, the isotropy and the reversibility of stress–strain are mostly subjected to serious criticism. However, he kept in mind that they also constitute the basis of Terzaghi's theory, which has been found quite satisfactory for the practical requirements of engineering. In fact, it can be imagined that the grains composing the soil are held together in a certain pattern by surface tension forces and tend to assume a configuration of minimum potential energy. This would especially be true for the colloidal particles constituting clay. It seems reasonable to assume that for small strains, when the grain pattern is not too much disturbed, the assumption of reversibility will be applicable. The assumption of isotropy is not essential, and anisotropy can easily be introduced by a mathematical induction in time factor due to the effects of 1-D and two-dimensional (2-D) drainage.

It might be of great importance to evaluate the influence of the state of initial stress in the soil before application of the load on the stress distribution and the settlement due to multi-draining systems. Such an influence may introduce an initial convexity in the time factor due to 1-D and 2-D drainage, which is captured in the present study by a non-dimensional ratio r and a parameter $\varphi(r)$. It is understood that this influence is significant for rock masses with high values of the parameter $\varphi(r)$.

As a consequence of the assumptions, there have been many estimates of 1-D, 2-D and three-dimensional (3-D) consolidation (McNamee and Gibson, 1960; Gibson *et al.*, 1970; Christian and Boehmer, 1970; Hansbo, 1981; Indraratna and Redana, 1997; Ai and Han, 2006; Ai and Cheng, 2009; Huang *et al.*, 2006; Zwanenburg, 2005; Sukumar *et al.*, 2013). Some of them based on Fourier transform became extensively popular owing to their natural simplicity. The consolidation scheme as that of saturated clayey gouge within permeable boundaries has rarely been considered in the past studies. Therefore, the solution to consolidation with permeable boundaries that originate amid rock masses has remained elusive. Therefore, it is proposed to derive a solution in the present study for 1-D consolidation with 2-D drainage for a clayey gouge layer sandwiched amid rock masses of higher permeability. The graphic representation of the degree of consolidation and time factor is shown using the software Mathematica (Wolform, 2013).

Based on discrete Fourier transform, Terzaghi (1943) proposed a solution for 1-D consolidation. Hansbo (1981) and Al-Tabbaa and Wood (1991) derived a relationship for the average degree of consolidation (U_{av}) and time factor (T_v) by assuming 2-D radial consolidation (Indraratna and Redana, 1997). The authors derived the 1-D consolidation with 2-D drainage equations for a layer of saturated clayey gouge of low permeability compared to the boundaries. The results obtained by 1-D consolidation 2-D drainage are significantly different from the case of radial consolidation (Hansbo, 1981; Al-Tabbaa and Wood, 1991). It is observed that there are innate similarities in the numerical representation of 1-D consolidation with 2-D drainage with that obtained by 1-D solutions, but at lower and moderately lower degree of consolidation, there appeared significant departures. The 1-D consolidation with 2-D drainage showed more realistic pore pressure distribution in the lateral and vertical directions for the sandwiched layer of saturated clayey gouge, where the rock masses are characterised by a non-dimensional parameter identified in the present text.

General theory for 1-D consolidation with 2-D drainage

It is assumed that a layer of clayey gouge is confined amid permeating rock masses. When a surcharge of load intensity $\Delta\sigma$ is transferred over this clay layer, the entire stress increase contributes to an increase in pore water pressure only and none to the stresses in the soil skeleton itself. This increase in pore water pressure equivalent to $\Delta\sigma$ appears at all depths of the saturated clay and dissipates gradually by 'squeezing out' through the relatively permeable sand stone layers and through the lateral sides, as shown in Figure 1. Normally, the thickness and spread of the gouge material ($2H_z$ and $2L_x$ respectively) should be larger than the asperity height ($2t_a$) such that ($H_z/t_a > 1$ and $L_x/t_a > 1$) while $L_y >> L_x$. The equivalent of joint fractures, gouge thickness and inclination of the gouge is considered in the z direction as

represented by $2H(= 2H_z)$. The gradual dissipation of pore water pressure causes an increase in the effective stresses at every depth of the layer, and a subsequent time-dependent settlement occurs in that layer.

The 3-D consolidation is given by the following differential equation:

$$\frac{\partial u}{\partial t} = c^2 \nabla^2 u \qquad 1.$$

where $\nabla^2 u = \frac{\partial^2 u}{\partial x^2} + \frac{\partial^2 u}{\partial y^2} + \frac{\partial^2 u}{\partial z^2}$.

Here, u represents the pore water pressure in vector space (x, y, z) in the soil sample at time t, after the application of surcharge. The ∇^2 is a Laplace operator in 3-D vector space. Like any other great work of science, the double integrands of Equation 1 provide an opening to a myriad of numerical, analytical and empirical interpretations. It allows a constant in the solution, which itself may be deduced as a function of time and space. Induction of such a function is often avoided deliberately as an input parameter in the differential equation for the purpose of simplicity in the solution. However, as an appearance due to the complementarity of observations, the effects become apparent in the post primary phase of consolidation and hence in time factor, where there are effects of particulate rotation, shear and compression. De Josselin de Jong and Virujit (1965) showed that the double integrand of Equation 1 with a constant in the solution reduces to only a function of time alone when deformations occur in the absence of rotations (Zwanenburg, 2005). These considerations allowed convergence of Biot's analytical solutions with that proposed by Terzaghi as also used in the present context.

In a simple initial form of 2-D vector space, if $\frac{\partial u}{\partial t} = 0$, Equation 1 may be represented as Dirichlet's problem as

$$c^2 \left(\frac{\partial^2 u}{\partial x^2} + \frac{\partial^2 u}{\partial z^2} \right) = 0 \qquad 2.$$

Here, c^2 is fully described on pore pressure u.

The effects of hydraulic and deformation anisotropy may be conveniently considered through C_{vz} and C_{hx} as $\frac{\partial u}{\partial t} \neq 0$

$$C_{hx} \frac{\partial^2 u}{\partial x^2} + C_{vz} \frac{\partial^2 u}{\partial z^2} = \frac{\partial u}{\partial t} \qquad 3.$$

If $C_{hx} = C_{vz} = c^2$, and $\frac{\partial u}{\partial t} = 0$, Equation 3 is converted into Dirichlet's problem, which permits induction of geometric anisotropy in 2-D space similar to Equation 2.

Incidentally, the 1-D consolidation problem can be solved with the same ease as is possible for the 2-D seepage problem. Terzaghi's model has a spring constant that is comparable to the deformation modulus for an elastic body; similarly, gouge lamina has orthogonal springs for isotropic elastic body. It retains Terzaghi's model of one constant for primary and a different constant for post-primary range. It is a model material with a hardening–softening character. These difficulties get resolved from the 2-D pore pressure dissipation model, similar to the solution of problems of transient heat transfer in two dimensions (Carslaw and Jaegar, 1986). Scott (1963) intuitively provided a simple solution for the average degree of consolidation of an infinitely long square prism that is shown to be a special case of the present study. Moreover, some approximate solution for the problem of transient flow in two dimensions is provided with reference to what is known of 1-D transient flow as per Terzaghi's theory of 1-D consolidation and 1-D drainage.

The surcharge applied has a value $\Delta\sigma$, which is initially equal to u_i (the initial value of pore pressure at time $t = 0$). The quantity c^2 is equal to the coefficients of consolidation c_v, and have the dimensions of L^2T^{-1}. The layer of clay is bounded at the sides (x direction) by permeable joints, top and bottom (z direction), by permeable rock mass. The extent of space in the y- direction is assumed infinite so as to have 1-D consolidation with 2-D drainage.

Equation 1 is reduced to the case of 1-D consolidation with 1-D drainage if the pore water pressure changes in the x- and y-directions are zero. Fourier analysis of the partial differential equation given by Equation 1 provided the following solutions for the case of 1-D consolidation with 1-D drainage:

$$u = \sum_{n=1}^{n\to\infty} \left(\frac{1}{H} \int_0^{2H} u_i \sin \frac{n\pi z}{2H} \mathrm{d}z \right) \sin \frac{n\pi z}{2H} \exp\left(\frac{-n^2\pi^2 T_v}{4} \right) \qquad 4.$$

The degree of consolidation at a given depth and time is a quantity defined as

$$U_z = \frac{u_i(z) - u_t(z)}{u_i(z)} \qquad 5.$$

In Equations 4 and 5, H represents the thickness of the longest drainage path in the layer (a two-way vertical drainage condition has been assumed; thus, H is half the thickness of the layer), and $u_t(z)$ is the pore water pressure at depth z at a given time t, and $u_i(z)$ is the initial pore water pressure at depth z. T_v is the non-dimensional time factor such that $T_v = c_v t/H^2$, where c_v is coefficient of consolidation, and $c_v = kE/\gamma_w$.

In isotropic condition, the coefficient of consolidation varies according to the isotropic hydraulic conductivity k. Here, the deformation modulus E, which is the inverse of the coefficient

of volume compressibility, and the unit weight of pore fluid γ_w are considered constant during the process of consolidation. The coefficient of volume compressibility is defined as the ratio of change in volume per unit volume of soil corresponding to the unit change in pressure.

While defining non-dimensional time factor T_v, c_v is induced such that c^2 is fully described over time t and descriptor of space H. Since the description of c_v is numerically holomorphic, therefore a fully described c_v in space entails $U_z = U_p$, where U_p is the limiting magnitude of primary consolidation such that the behaviour is poro-elastic. In the range of primary consolidation, according to Terzaghi (1925), there is a unique relation of T_v and U_z such that $T_v = (\pi/4)U_z^2$. Alternatively, the relationship of time factor with degree of consolidation is presumed nearly parabolic $T_v = (3/4)U_z^2$ (Schofield and Wroth, 1968; Wood, 2004). If the degree of consolidation is such that $U_z > U_p$, the consolidation is presumed to be in the post-primary range. As the magnitude of $U_z > U_p$, the deformation may not remain poro-elastic; therefore, the coefficient of consolidation is alternatively described over space and time.

Since the consolidation amid rock masses gradually proceed from primary to post primary and reach finality (U_z = 1), the modified convexities in the time factor either in primary, post primary or later range of consolidation should be captured using the concepts of 1-D consolidation with 2-D drainage. Because of the fact that the clay lamina amid rock masses have an apparent similarity (Figure 1) to drainage through a plane frame and secondly for simplicity of assumptions, a solution for 1-D consolidation with 2-D drainage is obtained numerically using a non-dimensional parameter, depending on shape factor, modulus and intrinsic permeability ratio.

Application of consolidation with 2-D drainage

The solutions obtained by Terzaghi (1925) remain valid for the situation where drainage takes place along the vertical direction. There are varied practical situations where drainage may take place along two directions as in the case of clay lamina sandwiched amid permeating rock masses (Figure 1). For consolidation settlement to occur, the thickness of the lamina must be greater than the asperity height of the rock joints. The gouge material is often deposited as a sheet of clay amid the rock joints, which show a diffusivity pattern for pore fluid similar to consolidation with 2-D drainage. Similarities may also be observed in the thermal conductivity through a metal sheet, which shows a 2-D diffusion pattern. Starting from the continuity equation for fluid flow and Darcy's law, the authors derived an expression that describes the dissipation of pore water pressure along more than one direction.

The expressions were derived for the case where dissipation takes place along the z direction and one of the two lateral directions, say, the x direction. The starting point for the derivation remains the same as for the expressions for consolidation as per Equation 1, that is, the continuity equation for fluid flow. Finally, the expressions are used to plot a relationship between pore pressure and space coordinates, which provide an interpretation to the 1-D consolidation 2-D drainage of a clay layer. The authors in proviso studied the relationship between the degree of consolidation and the time factor.

Terzaghi's theory of 1-D consolidation is meant for applications to the ideal case of excess pore pressure dissipation occurring along the vertical direction. In real-life situations, such cases are encountered where only lateral drainage is possible, yet vertical deformations are visible due to lateral dissipation of pore pressure, as shown in Figure 1. During the geotechnical investigation for several projects, the saturated clay layer is found to be sandwiched between relatively pervious rock masses. While movement of water is possible through the lateral direction, the settlement is a result of 1-D consolidation with 2-D drainage.

Theoretical descriptors for consolidation of gouge

Equation for consolidation with 2-D drainage

There are solutions available for 1-D consolidation by Terzaghi (1925), 2-D consolidation by Ai and Wu (2009) and Di Francesco (2011) and 3-D consolidation by Biot (1941), with varied assumptions. Further, there are numerous natural occurrences of varied structural shapes of gouge material amid rock masses with one of the relatively longer dimensions. Alternatively, the no-flow conditions may also exist due to the locking of gouge amid rock mass in one of the directions. It corresponds to the presence of 1-D consolidation with 2-D drainage of clay layers amid rock masses with all possible randomness in length and thickness. The presence of such a varied and random distribution of shapes of clay lamina amid rock masses induces variation in permeability in the orthogonal directions. Since there may be natural variation in the compressibility of rock masses along these directions, the ratio of coefficient of consolidation and shape factor provides a guiding parameter $\varphi(r)$ to evaluate the consolidation of clayey gouge. The authors assume the continuity equation for fluid flow, which is applicable to all flow situations.

At this stage, the following assumptions are considered to simplify the problem:

(*a*) The nature of the problem allows conceiving the quantity $\left[\frac{\partial^2 u}{\partial y^2}\right]$ in Equation 1 as zero, such that the drainage along one of the two lateral directions is negligible due to its extent, which is assumed infinite. At time $t = 0$, there is no compression and no flow along the y direction. There is a vertical surcharge (along z direction) and a confining stress along the x direction. Also, $c_{hx} = c_h$ and $c_{vz} = c_v$.

(*b*) Darcy's law is valid along both drainage directions on which stresses are applied, that is, $v_z = k_z \frac{\partial h}{\partial z}, v_x = k_x \frac{\partial h}{\partial x}$

(*c*) The gouge layer is completely saturated.

(*d*) The gouge layer is homogeneous.

(*e*) The gouge grains and water are isotropic and incompressible

(*f*) The primary consolidation controls deformation as long as the degree of consolidation is fully described by c_v and a dimensionless ratio r.
(*g*) The post-primary consolidation is said to control deformation as the degree of consolidation is alternatively described by c_v, r and a non-dimensional parameter $\varphi(r)$.

The consolidation with 2-D drainage equation is a particular case of the expression for consolidation given by Equation 3. It can be derived by applying the above assumptions to the continuity. The equations of static equilibrium in a x–z plane as per Ai and Wu (2009) and Ai and Cheng (2009) may be expressed as

6a. $$\frac{\partial \sigma_x}{\partial x} + \frac{\partial \tau_{zx}}{\partial z} = 0$$

6b. $$\frac{\partial \tau_{xz}}{\partial x} + \frac{\partial \sigma_z}{\partial z} = 0$$

where σ_x and σ_z are the total stresses in the x and z directions, respectively, and τ_{xz} is the shear stress. The relationships for strain and displacement can be expressed for an elastic media as

6c. $$\varepsilon_x = \left[\frac{1-v^2}{E}\right]\left[\sigma_x + u - \left\{\frac{v}{1-v}(\sigma_z + u)\right\}\right]$$

6d. $$\varepsilon_z = \left[\frac{1-v^2}{E}\right]\left[\sigma_z + u - \left\{\frac{v}{1-v}(\sigma_x + u)\right\}\right]$$

6e. $$\gamma_{xz} = 2(1+v)\tau_{xz}/E$$

where E is the deformation modulus, and ν is Poisson's ratio. The permeability of gouge is anisotropic because of their directional drainage restrain. Therefore, to consider the anisotropy of permeability in the consolidation calculation, the continuity equation for a plane strain medium with anisotropic permeability can be expressed as

6f. $$\frac{1}{1+e_0}\frac{\partial e}{\partial t} = (1/\gamma_w)\left(k_h \frac{\partial^2 u}{\partial x^2} + k_v \frac{\partial^2 u}{\partial z^2}\right)$$

where $\varepsilon_v = \varepsilon_x + \varepsilon_z$ is the volumetric strain, resulting in a change in void ratio ∂e. γ_w is the unit weight of water, and k_h and k_v are the permeability coefficients in the horizontal and vertical directions, respectively. As conceived in Equation 3, the continuity Equation 6f may be represented as

7a. $$c_h \frac{\partial^2 u}{\partial x^2} + c_v \frac{\partial^2 u}{\partial z^2} = \frac{\partial u}{\partial t}$$

7b. $$c_v = \frac{k_z(1+e_0)}{a_{v(z)}\gamma_w},\ c_h = \frac{k_x(1+e_0)}{a_{v(x)}\gamma_w}$$

For no changes in total stresses,

7c. $$a_{v(z)} = a_{v(x)}$$

It implies that the changes in void ratio in the vertical and horizontal directions are complimentary to the global changes in scalar product of change in stresses and compressibility.

Similarly, for the 1-D consolidation with 1-D drainage case

7d. $$\partial e \rightarrow f(\partial e_{(z)}) \rightarrow a_v \partial \bar{\sigma}_z$$

Solution for the 1-D consolidation with 2-D drainage

To solve Equation 7a, the pore pressure is assumed as $u(x, z, t)$ to be the product of three functions as

8. $$u(x, z, t) = F(x) \cdot F(z) \cdot G(t)$$

In differential form, it is represented as

9. $$\frac{\partial u}{\partial t} = F(x) \cdot F(z) \cdot G'(t)$$

10. $$\frac{\partial^2 u}{\partial x^2} = F''(x) \cdot F(z) \cdot G(t)$$

11. $$\frac{\partial^2 u}{\partial z^2} = F(x) \cdot F''(z) \cdot G(t)$$

Substituting Equations 9, 10 and 11 in Equation 8

$$F(x) \cdot F(z) \cdot G'(t) = c_h F''(x) \cdot F(z) \cdot G(t) + c_v F(x) \cdot F''(z) \cdot G(t)$$

Dividing this equation by $F(x) \cdot F(z) \cdot G(t)$,

$$\frac{G'(t)}{G(t)} = c_h \frac{F''(x)}{F(x)} + c_v \frac{F''(z)}{F(z)}$$

The left-hand side of this equation is dependent only on time t. Similarly, on the right-hand side of the equation, one expression is a

function of x only, whereas the other is a function of z only. Hence, for the equation to be true, both sides must be individually equal to a constant, say, $-B^2$. So

12. $G'(t) = -B^2 G(t)$

13. $$c_h \frac{F''(x)}{F(x)} + c_v \frac{F''(z)}{F(z)} = -B^2$$

The solution to Equation 12 is

14. $G(t) = A_1 e^{-B^2 t}$

where A_1 is a constant. Solving Equation 13

15. $$\frac{F''(x)}{F(x)} = -C^2, \frac{F''(z)}{F(z)} = -D^2$$

The values of C and D are such that

16. $c_h C^2 + c_v D^2 = B^2$

The solutions to Equation 15 are

17. $$F(x) = A_2 \cos Cx + A_3 \sin Cx,$$
$$F(z) = A_4 \cos Dz + A_5 \sin Dz$$

where A_2, A_3, A_4 and A_5 are constants.

Now substituting Equations 14 and 17 in Equation 8

18. $u = (A_2 \cos Cx + A_3 \sin Cx)(A_4 \cos Dz + A_5 \sin Dz) A_1 e^{-B^2 t}$

To obtain the particular solution, the constant terms in Equation 18 need to be evaluated, which is obtained by using Initial Value Condition (i) and Boundary Value Conditions (ii)–(v):

Initial Value Condition:

(*i*) $t = 0$, $u = u_i$

Boundary Value Conditions:

(*ii*) $u = 0$ at $z = 0$
(*iii*) $u = 0$ at $z = 2H$
(*iv*) $u = 0$ at $x = 0$
(*v*) $u = 0$ at $x = 2L$

Conditions (ii) and (iv) give $A_4 = 0$ and $A_2 = 0$ respectively. Conditions (iii) and (v) give $C = \frac{m\pi}{2L}$ and $D = \frac{n\pi}{2H}$, where m and n are integers. From the above relations, a general solution can be given in the form

19. $$u = \sum_{m=1}^{\infty} \sum_{n=1}^{\infty} A_{mn} \sin \frac{m\pi x}{2L} \sin \frac{n\pi z}{2H} e^{-B^2 t}$$

Substituting the obtained values of C and D in Equation 16

20. $$c_h \frac{m^2\pi^2}{4L^2} + c_v \frac{n^2\pi^2}{4H^2} = B^2$$

Substituting B^2 in Equation 19

21. $$u = \sum_{m=1}^{\infty} \sum_{n=1}^{\infty} A_{mn} \sin \frac{m\pi x}{2L} \sin \frac{n\pi z}{2H} \times \exp\left[-\left(c_h \frac{m^2\pi^2}{4L^2} + c_v \frac{n^2\pi^2}{4H^2} \right) t \right]$$

According to boundary condition (i), at $t = 0$, and $u = u_i$

22. $$u_i = \sum_{m=1}^{\infty} \sum_{n=1}^{\infty} A_{mn} \sin \frac{m\pi x}{2L} \sin \frac{n\pi z}{2H}$$

The solution for this equation is given by the double integral

23. $$A_{mn} = \frac{1}{L \cdot H} \int_0^{2H} \int_0^{2L} u_i \sin \frac{m\pi x}{2L} \sin \frac{n\pi z}{2H} \, dx dz$$

Therefore, the general expression that is a solution to Equation (7a) is

24. $$u = \sum_{m=1}^{\infty} \sum_{n=1}^{\infty} A_{mn} \sin \frac{m\pi x}{2L} \sin \frac{n\pi z}{2H} \times \exp\left[-\left(c_h \frac{m^2\pi^2}{4L^2} + c_v \frac{n^2\pi^2}{4H^2} \right) t \right]$$

with A_{mn} as defined in Equation 23.

Particular expression for the case when u_i is constant with depth

For this case, initially the pore pressure

25. $u_i = u_0$

Taking u_i outside and evaluating the double integral, Equation 23 is expressed as

$$\int_0^{2H}\int_0^{2L} \sin\frac{m\pi x}{2L}\sin\frac{n\pi z}{2H}\,dx\,dz = \frac{4LH}{mn\pi^2}(1-\cos m\pi)(1-\cos n\pi) \quad (26.)$$

Using Equation 23 and 26, A_{mn} is derived as

$$A_{mn} = \frac{4u_0}{mn\pi^2}(1-\cos m\pi)(1-\cos n\pi) \quad (27.)$$

Therefore, the solution for this case is given by substituting A_{mn} from Equation 27 into Equation 24. Since the terms $(1 - \cos n\pi)$ and $(1 - \cos m\pi)$ vanish for even values of m and n, the solution is given by

$$u = \sum_{k=0}^{\infty}\sum_{l=0}^{\infty}\frac{16u_0}{mn\pi^2}\sin\frac{m\pi x}{2L}\sin\frac{n\pi z}{2H} \times\exp\left[-\left(c_h\frac{m^2\pi^2}{4L^2}+c_v\frac{n^2\pi^2}{4H^2}\right)t\right] \quad (28.)$$

where $m = 2k + 1$, $n = 2l + 1$.

Expression for degree of consolidation for a particular depth

At a given time and depth, the degree of consolidation is as given in Equation 3. Using Equation 28 for the particular case as described by Equations 25 to 28, the degree of consolidation is computed as

$$U_z = 1-\sum_{k=0}^{\infty}\sum_{l=0}^{\infty}\frac{16}{mn\pi^2}\sin\frac{m\pi x}{2L}\sin\frac{n\pi z}{2H} \times\exp\left[-\left(c_h\frac{m^2\pi^2}{4L^2}+c_v\frac{n^2\pi^2}{4H^2}\right)t\right] \quad (29.)$$

where $m = 2k + 1$, $n = 2l + 1$.

Through a few basic operations, Equation 29 is expressed in terms of the time factor T_v, as defined in Equations 2 and 3 as

$$\left(c_h\frac{m^2\pi^2}{4L^2}+c_v\frac{n^2\pi^2}{4H^2}\right)t = \frac{c_v t}{H^2}\left(\frac{c_h}{c_v}\cdot\frac{H^2}{L^2}\cdot\frac{m^2\pi^2}{4}+\frac{n^2\pi^2}{4}\right) = T_v\left(r\cdot\frac{m^2\pi^2}{4}+\frac{n^2\pi^2}{4}\right) \quad (30.)$$

where $r = \frac{c_h}{c_v}\cdot\frac{(2H)^2}{(2L)^2}$.

Therefore, Equation 29 may be rewritten as

$$U_z = 1-\sum_{k=0}^{\infty}\sum_{l=0}^{\infty}\frac{16}{mn\pi^2}\sin\frac{m\pi x}{2L}\sin\frac{n\pi z}{2H} \times\exp\left[-T_v\left(r\cdot\frac{m^2\pi^2}{4}+\frac{n^2\pi^2}{4}\right)\right] \quad (31.)$$

where $m = 2k + 1$, $n = 2l + 1$ and $r = \frac{c_h}{c_v}\cdot\frac{(2H)^2}{(2L)^2}$.

Relationship between average degree of consolidation and time factor

This section computes the relationship for the particular case as described by Equations 25 to 28.

The degree of consolidation for every layer, as given in Equation 3, when averaged over all layers in the case of 1-D consolidation with 2-D drainage, provides following expression as

$$U_{av} = 1-\frac{\frac{1}{4L\cdot H}\int_0^{2H}\int_0^{2L}u\,dx\,dz}{\frac{1}{4L\cdot H}\int_0^{2H}\int_0^{2L}u_i\,dx\,dz} \quad (32.)$$

To compute the value of U_{av}, the initial pore pressure is integrated over the two directions as

$$\int_0^{2H}\int_0^{2L}u_i\,dx\,dz = 4u_0L\cdot H \quad (33.)$$

Further, from Equation 28

$$\int_0^{2H}\int_0^{2L}u\,dx\,dz = \int_0^{2H}\int_0^{2L}\sum_{k=0}^{\infty}\sum_{l=0}^{\infty}\frac{16u_0}{mn\pi^2}\sin\frac{m\pi x}{2L}\sin\frac{n\pi x}{2H} \times\exp\left[-\left(c_h\frac{m^2\pi^2}{4L^2}+c_v\frac{n^2\pi^2}{4H^2}\right)t\right]dx\,dz \quad (34.)$$

where $m = 2k + 1$, $n = 2l + 1$. The double integral above is evaluated to give

$$\int_0^{2H}\int_0^{2L}u\,dx\,dz = L\cdot H\sum_{k=0}^{\infty}\sum_{l=0}^{\infty}\frac{256u_0}{(mn\pi^2)^2} \times\exp\left[-\left(c_h\frac{m^2\pi^2}{4L^2}+c_v\frac{n^2\pi^2}{4H^2}\right)t\right] \quad (35.)$$

Finally, using the evaluated integrals from Equations 33 and 35 in Equation 32, the expression for the average degree of consolidation is expressed as

$$36.\quad U_{av} = 1 - \sum_{k=0}^{\infty}\sum_{l=0}^{\infty} \frac{64}{(mn\pi^2)^2} \exp\left[-\left(c_h \frac{m^2\pi^2}{4L^2} + c_v \frac{n^2\pi^2}{4H^2}\right)t\right]$$

where $m = 2k + 1$, $n = 2l + 1$.

Expressing in terms of T_v, as described in Equation 30, average degree of consolidation is expressed as

$$37.\quad U_{av} = 1 - \sum_{k=0}^{\infty}\sum_{l=0}^{\infty} \frac{64}{(mn\pi^2)^2} \exp\left[-T_v\left(r \cdot \frac{m^2\pi^2}{4} + \frac{n^2\pi^2}{4}\right)\right]$$

where $m = 2k + 1$, $n = 2l + 1$, $r = \frac{c_h}{c_v} \cdot \frac{(2H)^2}{(2L)^2}$.

Evolution of approximate expressions

It is evident that the relationship shown in Equation 37 involves two infinite steps of summation, and hence, a handy alternate relationship is required. Further, observation of test data reveals that the deformations in the post primary phase of consolidation are not necessarily poro-elastic. Hence, two sets of approximate relationship between U_{av} and T_v are proposed.

The following approximate equations may be used for the case of constant u_i with depth:

$$38.\quad U_{av} = 1 - \left(1 - \sqrt{\frac{4T_v}{\pi}}\right)\left(1 - \sqrt{\frac{4rT_v}{\pi}}\right) \text{ for } U_{av} < U_p$$

$$39.\quad T_v = T_f - \frac{T_{fs}}{r+1}\{\log(1 - U_{av}) + 2\varphi(r)\} \text{ for } U_{av} > U_p$$

Equation 38 represents a relation among the average degree of consolidation, time factor and non-dimensional ratio (r) as used in Equation 37. The non-dimensional ratio (r) introduces varied levels of convexities in the $U_{av} - T_v$ relationship. It emphatically establishes a gradual numerical departure by way of non-dimensional ratio (r) in $U_{av} - T_v$ relationship obtained so far in the works of Terzaghi (1925, 1943) and Scott (1963). Equation 39 has an initial intercept for time space evolution for post-primary consolidation. Ideally, the final value of time factor T_f is undefined, yet some terminal values derived from experimental observations of 1-D consolidation are more frequently used in practice. T_{fs} represents an empirical observation of time factor where post primary consolidation offsets primary consolidation. This transformation corresponds to a granular adjustment at particulate level when the proximity of the grains is promoted by lateral drainage and implies convergence influenced by material characteristics.

As Equation 39 draws meaning similar to consolidation theory as per Terzaghi (1925), $T_f = 1{\cdot}781$ and $T_{fs} = 0{\cdot}933$. In the present study, the terminal value of T_f is rounded off for simplicity to 1·782, whereas the terminal value of T_{fs} is acceded by trials among the values 0·930 to 0·860 respectively. The non-dimensional parameter $\varphi(r)$ is a function of the dimensionless ratio r. For limiting values of dimensionless ratio r, the non-dimensional parameter $\varphi(r)$ is a second-degree polynomial function of the form

$$40.\quad \varphi(r) = c'''r^2 + c''r^1 + c'r^0$$

The coefficients of Equation 40, namely, c''', c'' and c', take values in the present range of analysis as -3×10^{-6}, 0·9574 and 1·0497 respectivly. The variation of the non-dimensional parameter $\varphi(r)$ with the dimensionless ratio r is given in Table 2.

r	$\varphi(r)$	r	$\varphi(r)$	r	$\varphi(r)$
0·0	1·000	0·8	1·807	7·0	7·720
0·1	1·127	0·9	1·902	8·0	8·670
0·2	1·228	1·0	2·000	9·0	9·625
0·3	1·324	2·0	2·950	12·0	12·480
0·4	1·421	3·0	3·900	15·0	15·344
0·5	1·520	4·0	4·850	39·0	39·196
0·6	1·617	5·0	5·810	100·0	96·455
0·7	1·712	6·0	6·765	1000·0	955·455

Table 2. Variation of non-dimensional parameter $\varphi(r)$ with dimensionless ratio r

Results and discussion

In Equation 31, the authors have derived the expression for 1-D consolidation with 2-D drainage. The plot among U, x and z are shown in Figures 2(a) and 2(b). The plots have been drawn using Mathematica Wolfram (2013). An observation of the 3-D plot provides an understanding into the manner in which pore water pressure is dissipated at different time factors in the consolidating layer. The wavy lines appear in the plots because only a limited number of terms of the Fourier expansion have been used to evaluate the relationship. Using the code, the authors have also plotted the relationship between the average degrees of consolidation with respect to time factor according to Equation 37, in Figure 3.

In Equation 37, the dimensionless ratio (r) is equal to $\frac{c_h}{c_v} \cdot \frac{(2H)^2}{(2L)^2}$. If $r = 1$, the situation corresponds to isotropy, which further consists of geometric isotropy and consolidation isotropy defied by a shape factor (r_s) and a consolidation factor (r_c) respectively. Therefore, the dimensionless ratio ($r = r_s * r_s$) is resolved into a function of the shape (a shape factor, $r_s = \frac{(2H)^2}{(2L)^2}$) and a consolidation ratio r_c, depending on the ratio of coefficient of consolidation of gouge in the horizontal and vertical directions such that $r_c = \frac{c_h}{c_v}$. The consolidation ratio r_c is equivalent to the scalar product of

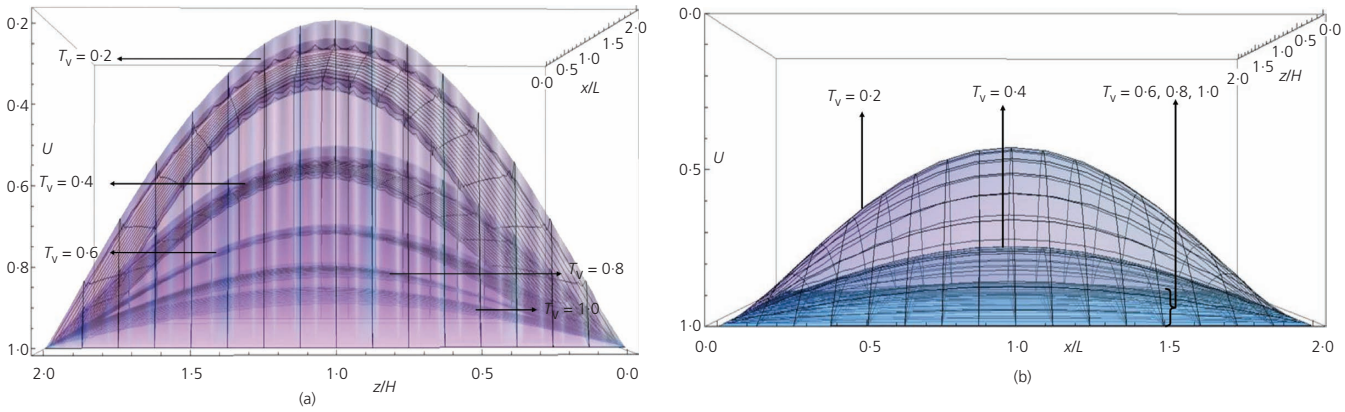


Figure 2. (a) Variation of U, x/L and z/H for $r = 0$, i.e., the case of one-dimensional consolidation, showing plots for five different values of T_v (T_v = 0·2, 0·4, 0·6, 0·8, 1·0); (b) variation of U, x/L and z/H for $r = 1$, showing plots for five different values of T_v (T_v = 0·2, 0·4, 0·6, 0·8, 1·0)

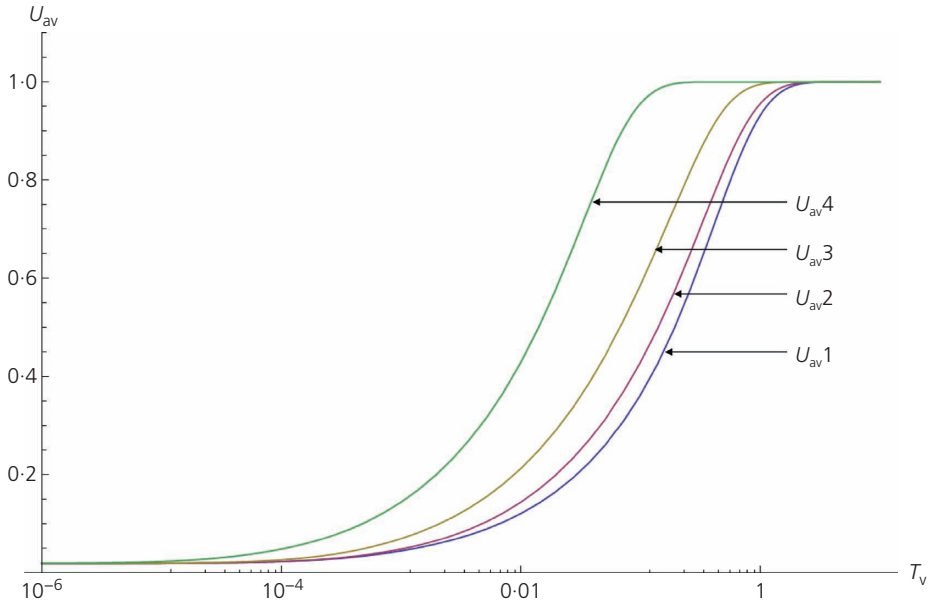


Figure 3. Variation of U_{av} and T_v for different values of r as $U_{av}1(T_v)$, $U_{av}2(T_v)$, $U_{av}3(T_v)$ and $U_{av}4(T_v)$, refer to r = 0, 0·1, 1, 10, respectively

modulus ratio and intrinsic permeability ratio $\left(E_{hv}\frac{k_{uc}}{k_{rm}}\right)$ under the same range of pressures. k_{rm} and k_{uc} are the intrinsic permeabilities of rock mass and that of clayey gouge respectively. The intrinsic permeability depends on the area of the fracture network and takes the dimensions of surface of contact (L^2T^0). The intrinsic permeability does not depend on the properties of pore fluid.

The deformation isotropy depends on the modulus ratio ($E_{hv} = E_h/E_v$), which is considered equal to unity for the case of isotropic deformation. The modulus ratio is defined as a ratio of deformation modulus of rock masses consisting of clay gouge in the horizontal and vertical directions. The variance in the values of modulus ratio and intrinsic permeability brings tortuosity in the consolidating clayey gouge.

The value of modulus ratio and intrinsic permeability can be readily estimated from rock mass investigations (Hsu *et al.*, 2011; Jiang *et al.*, 2009; Klimczak *et al.*, 2010; Liu *et al.*, 1999) and characterisation. The rock masses are typically characterised to

obtain modulus using rock quality designation (RQD). The RQD is empirically related to the joint condition and gouge thickness (Trivedi, 2013).

The typical values of effective porosity, intrinsic permeability of intact rocks, rock masses, gouge materials and consolidation anisotropy (O'Kelly, 2005) of clays are given in Tables 3, 4, 5 and 6 respectively for ready reference. Therefore, selectively the value of r is picked up in a practical range as $r = 0$ to 10. For higher values of $r \geq 10$, the dissipation pattern is free draining. The variation of average degree of consolidation with time factor is shown in Figure 3, where $U_{av}1(T_v)$, $U_{av}2(T_v)$, $U_{av}3(T_v)$ and $U_{av}4(T_v)$, refer to the function U_{av}, for $r = 0$, 0·1, 1, 10 respectively.

In situ profile	Effective porosity[a]: %	Physical effects
Unconsolidated clays, silt, sand and gravel	Up to 25	Pervious
Consolidated clastic rocks	5–15	Semi-pervious
Hard massive rocks	1–2	Impervious

[a] Interpreted from Franciss (2010).

Table 3. Effective porosity of massive rocks and gouge

Relationship with Terzaghi's expression for 1-D consolidation

Terzaghi's equation for 1-D consolidation gives this expression for U_{av} and T_v:

$$U_{av} = 1 - \sum_{k=0}^{\infty} \frac{8}{m^2\pi^2} \exp\left[-T_v \frac{n^2\pi^2}{4}\right] \quad 41.$$

where $m = 2k + 1$.

The expression proposed in Equation 37, albeit for 1-D consolidation with 2-D drainage, may be reduced to the case of 1-D consolidation with 1-D drainage by putting $r = 0$ (since $c_h = 0$ for this case). Equation 37 reduces to

$$U_{av} = 1 - \sum_{k=0}^{\infty} \sum_{l=0}^{\infty} \frac{64}{(mn\pi^2)^2} \exp\left[-T_v \frac{n^2\pi^2}{4}\right] \quad 42.$$

Although Equations 41 and 42 appear different, the plots for the degree of consolidation against time factor for both equations were

In situ profile	Intrinsic permeability[a]: mm^2	Physical effects	Range of intrinsic permeability ratio[b]
Highly fractured rock masses	10^{-1}–10^{-4}	Pervious	10^{-3}–10^{3}
Oil reservoir rocks	10^{-5}–10^{-7}	Semi-pervious	10^{-2}–10^{2}
Fresh sand stone	10^{-8}–10^{-9}	Semi-pervious	10^{-1}–10^{1}
Fresh lime stone, dolomite	10^{-10}–10^{-11}	Impervious	10^{-1}–10^{1}
Un-weathered rock mass, fresh granite	10^{-12}–10^{-13}	Impervious	10^{-1}–10^{1}

[a] Interpreted from Bear (1972).
[b] Ratio used for consideration of numerical inputs in the present study.

Table 4. Intrinsic permeability of rock masses (k_{rm})

In situ profile	Intrinsic permeability[a]: mm^2	Physical effects	r[b]
Peat	10^{-5}–10^{-6}	Semi-pervious	0·1–10
Layered clay	10^{-7}–10^{-9}	Semi-pervious	0·1–10
Un-weathered clay	10^{-10}–10^{-13}	Impervious	0·01–10

[a] Interpreted from Bear (1972).
[b] Ratio used for numerical inputs in the present study.

Table 5. Intrinsic permeability of unconsolidated organic soils and clays (k_{uc})

In situ profile	Permeability ratio	Physical effects	r[a]
Organic silt with peat	1·2 to 1·7[b]	Semi-pervious	1–2
Boston blue clay	0·7 to 3·3[c]	Semi-pervious	0·1–5
Singapore marine clay	2·0 to 3·0[d]	Semi-pervious	1–5

[a] Representative range for numerical input in the present study.
[b] Tsien (1955).
[c] Haley and Aldrich (1969).
[d] Chu *et al*. (2002).

Table 6. Horizontal and vertical permeability ratio

found to be nearly coinciding beyond 10% of consolidation, as shown in Figure 4, drawn using Mathematica, but, in fact, they originate differently. Therefore, the expression derived in Equation 37 has a solution extendible as 1-D consolidation. The present solution appears close to Terzaghi's solution, as shown in Figure 4.

Convergence of 1-D consolidation with 2-D drainage and 1-D drainage

Using $r = 0$ in Equations 38 and 39

$$43.\quad \text{For } U_{av} < U_p,\ U_{av} = 1 - \left(1 - \sqrt{\frac{4T_v}{\pi}}\right) = \sqrt{\frac{4T_v}{\pi}} \Rightarrow T_v = \frac{\pi}{4}U^2$$

According to Terzaghi (1925), for 1-D consolidation, $U_p = 0{\cdot}526$.

Also

$$44.\quad \text{For } U_{av} > U_p,\ T_v = T_f - T_{fs}\{\log(1-U) + 2\}$$

According to Terzaghi (1925), for 1-D consolidation, $T_f = 1{\cdot}781$ and $T_{fs} = 0{\cdot}933$.

T_f and T_{fs} are limiting values of time factor corresponding to $U_{av} = 1$ and degree of consolidation in the range of post primary consolidation (Tables 7 and 8). Equations 43 and 44 are similar to the approximate relations proposed by Terzaghi for 1-D consolidation.

Figures 5(a) and 5(b) show the convexity in time factor due to the effect of $r = 0$ and $0{\cdot}1$, respectively. The effect of 2-D drainage indicates convergence with the plot of primary consolidation with the post primary effect at U_{av} as early as 30% and 2% for $r = 0$ (for $T_{fs} = 0{\cdot}880$) and $r = 0{\cdot}1$ (for $T_{fs} = 0{\cdot}86$), respectively.

Application of 1-D consolidation with 2-D drainage for the special case for rock masses, $r = 1$

Using $r = 1$ in Equations 38 and 39

$$45.\quad \left(1 - \sqrt{\frac{4T_v}{\pi}}\right)\left(1 - \sqrt{\frac{4T_v}{\pi}}\right) = 1 - U \text{ for } U_{av} < U_p$$

$$46.\quad T_v = T_f - T'_{fs}\{\log(1-U) + 4\} \text{ for } U_{av} > U_p$$

Equation 45 is similar to the results proposed by Scott (1963) for 1-D consolidation and 2-D drainage. Incidentally, it corresponds to the solutions proposed by the present study for $r = 1$. Additionally, Equation 46 provides a solution for the time factor in the post primary phase of consolidation settlements with $T'_{fs} = \frac{T_{fs}}{r+1} = 0{\cdot}4665$.

Equations 45 and 46 show the relation of time factor and average degree of consolidation for the 2-D drainage case at $r = 1$. There can be varied applications of Equation 37 in petroleum engineering,

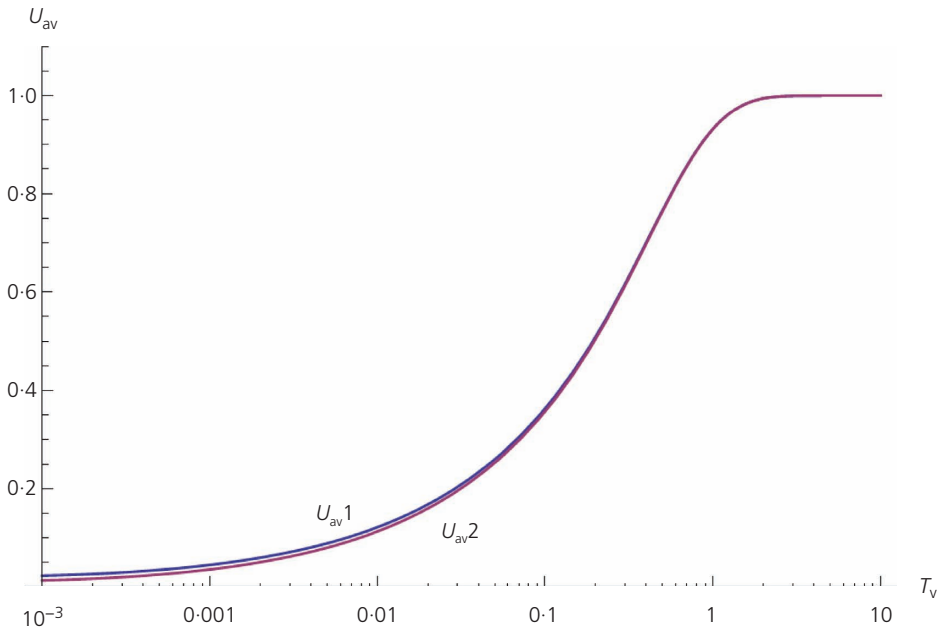


Figure 4. Plot for degree of consolidation U_{av} and time factor T_v for $r = 0$ ($U_{av}1$ from Equation 41 for 1-D consolidation nearly superimposes over $U_{av}2$ from Equation 42, the plot for 1-D consolidation with 2-D drainage)

r	U_{av}
0[a,b]	$1-\left(1-\sqrt{\frac{4T_v}{\pi}}\right)$
0·1[a]	$1-\left(1-\sqrt{\frac{4T_v}{\pi}}\right)\left(1-\sqrt{\frac{0{\cdot}4T_v}{\pi}}\right)$
1[a,c]	$1-\left(1-\sqrt{\frac{4T_v}{\pi}}\right)^2$
10[a]	$1-\left(1-\sqrt{\frac{4T_v}{\pi}}\right)\left(1-\sqrt{\frac{40T_v}{\pi}}\right)$

[a] Present work.
[b] Terzaghi (1925) for 1-D drainage $U_{av}=1-\left(1-\sqrt{\frac{4T_v}{\pi}}\right)$.

[c] Scott (1963) for 2-D drainage $U_{av}=1-\left(1-\sqrt{\frac{4T_v}{\pi}}\right)^2$.

Table 7. Variation of degree of consolidation of clayey gouge ($U_{av} < U_p$) amid rock masses with variation of time factor and dimensionless ratio (r)

r	T'_{fs}	T_{fs}	T_v
0·0[a, b]	0·9330[a], 0·8800[b]	0·840–0·930	$T_f-T'_{fs}\{\log(1-U)+2\}$[a, b]
0·1[b]	0·8481	0·860–0·940	$T_f-T'_{fs}\{\log(1-U)+2{\cdot}254\}$[b]
1·0[b]	0·4665	0·890–0·950	$T_f-T'_{fs}\{\log(1-U)+4\}$[b]
10·0[b]	0·0848	0·923–0·960	$T_f-T'_{fs}\{\log(1-U)+21{\cdot}246\}$[b]

[a] Terzaghi (1925), T_f = 1·781 for 1-D consolidation with 1-D drainage.
[b] Representative expressions in the present study, for 1-D consolidation with 2-D drainage.

Table 8. Approximation of time factor for post primary consolidation of clayey gouge ($U_{av} > U_p$) amid rock masses with variation of dimensionless ratio r using Equation 46

soil and rock mechanics, with a few typical examples shown in Equations 38 to 46. Tables 7 and 8 show the relationship between time factor and dimensionless ratio (r) for the degree of consolidation of clayey gouge using 1-D consolidation 2-D drainage equation. The dimensionless ratio (r) is a function of the shape of saturated clay lamina, deformation modulus of mass material and intrinsic permeability ratio.

Figures 5(c) and 5(d) show the convexity in time factor due to the effect of using r = 1 and 10, respectively. The effect of 2-D drainage indicates convergence with the plot of primary consolidation with the post primary effect at U_{av} as early as less than 1% for r = 1 (T_{fs} among 0·90 and 0·88) and 10 (T_{fs} among 0·924 and 0·923), respectively.

The effect of the variation of dimensionless ratio (r) relative to the rock mass characteristics is shown in Table 9.

Steps for implementation of present technique to obtain the time factor

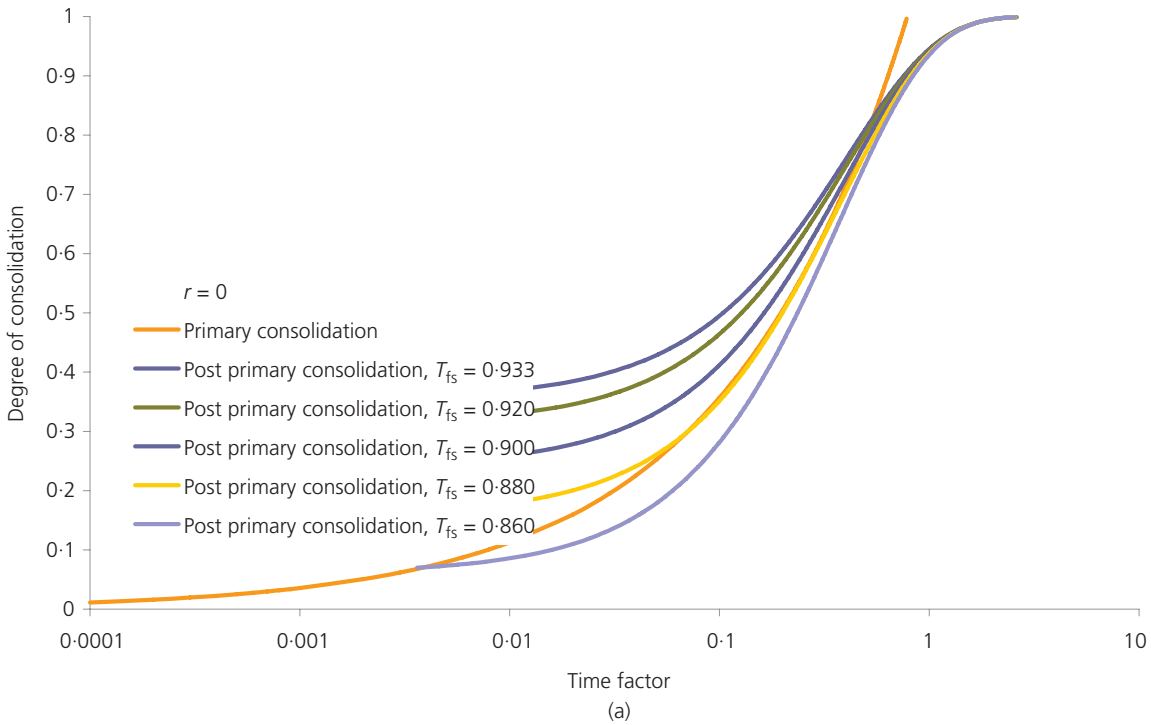
The steps followed to find out the consolidation of clayey gouge amid rock mass using 1-D consolidation 2-D drainage equation are the following:

- Prepare the bore log sheet containing important information, namely, area and depth of sampling at requisite interval, unit weight, overburden pressure, number of joints, orientation of joints, maximum, minimum and mean thickness of gouge, void ratio of gouge, water table and *RQD*.
- Assign values of thickness and spread of gouge material ($2H_z$ and $2L_x$, respectively) to obtain the shape factor. It should be larger than the asperity height ($2t_a$) such that ($H_z/t_a > 1$ and $L_x/t_a > 1$) while $L_y >> L_x$.
- Evaluate the overburden, confining pressure and consider modulus ratio E_{hv} according to the values of *RQD*, number of joints, joint inclination, gouge spread and thickness and asperity height.
- Evaluate the intrinsic permeability ratio for clay gouge and rock material.
- According to the values of $2H_z$ and $2L_x$ respectively, find out the final value of dimension less ratio (r) from the shape factor, modulus ratio, E_{hv} and intrinsic permeability ratio.
- Estimate values of non-dimensional parameter $\varphi(r)$ (use Equation 40) for an appropriate value of dimensionless ratio (r).
- Operate the dimensionless ratio (r) and non-dimensional parameter $\varphi(r)$ in Equations 38 and 39 to get the time factor corresponding to any degree of consolidation at any value of intermediate dimension less ratio (r) obtained from rock mass and gouge characteristics shown in Table 9.
- Using approximate analysis consequent to the value of non-dimensional parameter $\varphi(r)$, use the corresponding plots for the primary or post primary consolidation to obtain the time factor.

Comments on the applicability of the present study

The present study for the evaluation of consolidation of clayey gouge amid rock masses should be applied to the field conditions carefully owing to the following reasons:

- This study neither intends to make any comment on the merits of either 1-D, 2-D or 3-D consolidation nor provides any resolve to the extent of elastic, plastic or elasto-plastic deformation during the process of consolidation. It has no scope to offer any resolve to time impending discussions on the scientific relevance of the proposed solutions by either Terzaghi's or Biot's or any other great work. Rather, it provides a simple numerical tool to estimate consolidation settlement with frequently encountered 2-D drainage condition for gouge amid permeating rock masses from rock mass characteristic and drainage features.



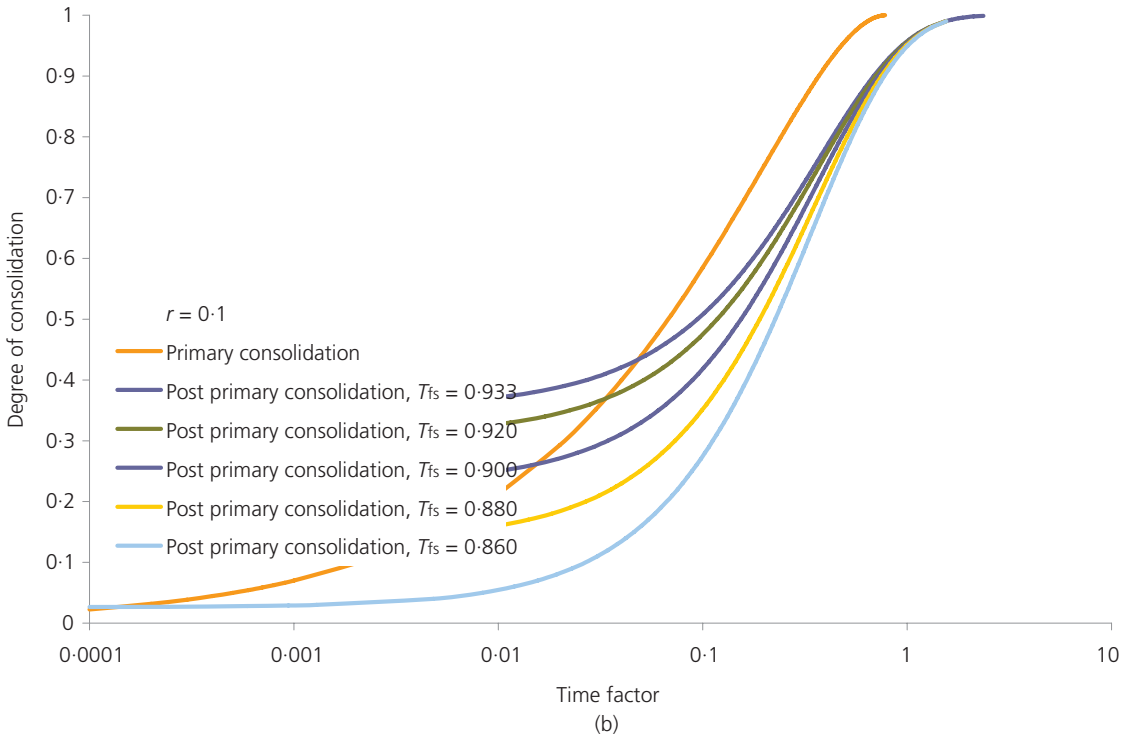
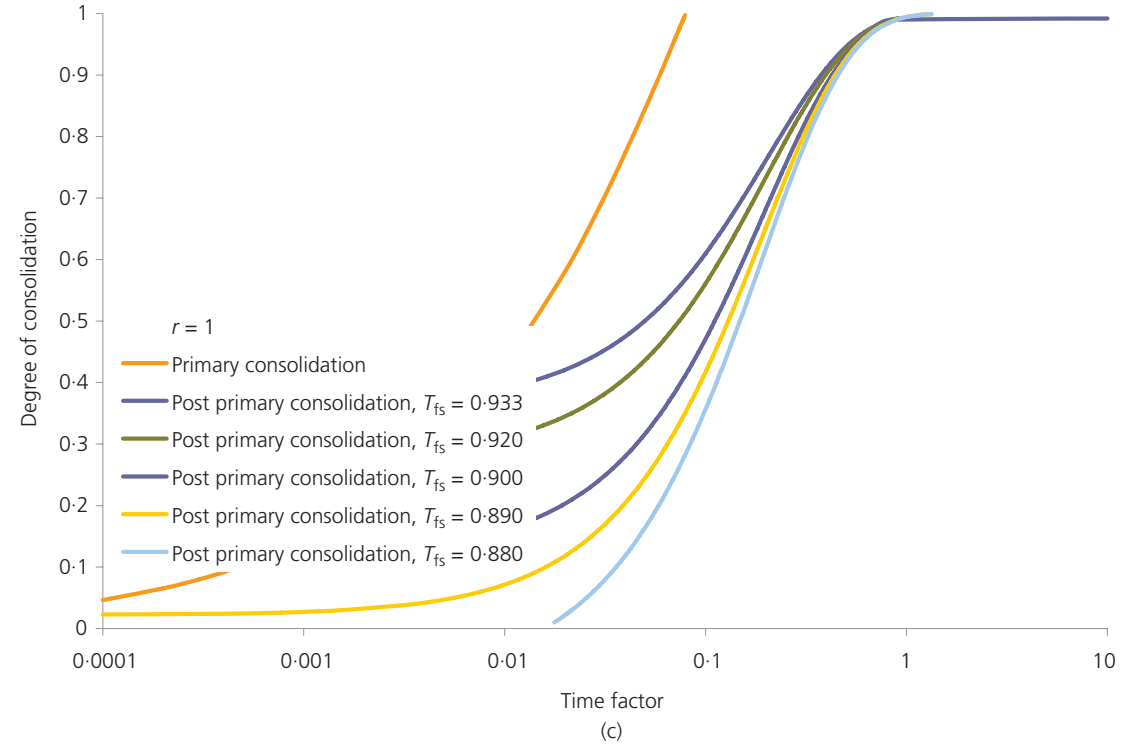


Figure 5. (a) Convexities in time factor due to primary and post primary consolidation at $r = 0$; (b) convexities in time factor due to primary and post primary consolidation at $r = 0{\cdot}1$; (c) convexities in time factor due to primary and post primary consolidation at $r = 1$; (d) convexities in time factor due to primary and post primary consolidation at $r = 10$ (continued overleaf)



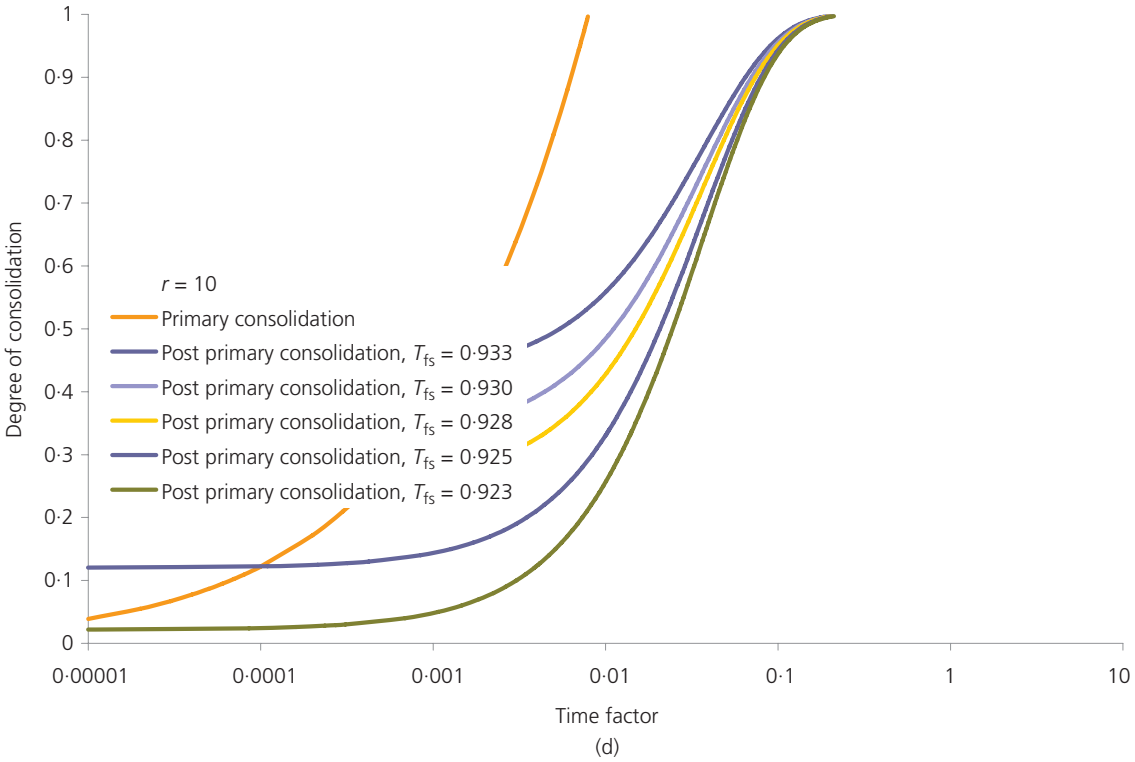


Figure 5. (continued)

r	Rock mass characteristic parameters		
	Shape of clay lamina	Deformation modulus	Intrinsic permeability
$r << 1$	Disturbed geometric isotropy. Thickness of gouge layer is significantly lower compared to the lateral spread, i.e., $2H_z << 2L_x$, and $2L_x << 2L_y$.	Anisotropy in deformation modulus may exist as $E_v >> E_h$ for 2-D consolidation. For 1-D consolidation and 2-D drainage, $E_v = E_h$.	Hydraulic anisotropy possible, intrinsic permeability of adjoining rock mass and intrinsic permeability of gouge material may be such that $K_V >> K_H$.
	$C_v/H_z^2 > C_h/L_x^2$		
$r = 1$	Geometric isotropy for a self-limiting, spherically consolidating element with permeable boundary may exist. Thickness of gouge layer is comparable to the lateral spreads, i.e., $2H_z = 2L_x$, and $2L_x = 2L_y$.	Possible initial isotropy in deformation modulus. The horizontal and vertical deformation modulus may be such that $E_v = E_h$.	Hydraulic isotropy possible, intrinsic permeability of clay gouge nearly equal to that of adjoining rock mass.
	$C_v/H_z^2 = C_h/L_x^2$		
$r >> 1$	Disturbed geometric isotropy. Thickness of gouge layer is significantly higher compared to the lateral spread, i.e., $2H_z >> 2L_x$, and $2L_x << 2L_y$.	Anisotropy in deformation modulus may exist as $E_v << E_h$ for 2-D consolidation. For 1-D consolidation and 2-D drainage, $E_v = E_h$.	Hydraulic anisotropy possible, intrinsic permeability of adjoining rock mass and intrinsic permeability of gouge material may be such that $K_V << K_H$.
	$C_v/H_z^2 < C_h/L_x^2$		

Table 9. Rock mass characteristic parameters controlling consolidation of clayey gouge

- The main aim of this study is to propose a solution for the consolidation of gouge material amid rock masses based on three variable systems, namely, degree of consolidation, time factor and dimensionless ratio r, which is interpreted from rock mass characteristics. The dimensionless ratio r in itself has features of rock mass, gouge and contact characteristics.
- Taking a cue from Terzaghi's work, the consolidation settlement is divided into primary and post primary phases where the time factor may be evaluated using dimensionless ratio r and a non-dimensional parameter $\varphi(r)$ respectively, which are related to the rock mass, gouge and contact characteristics.
- The present study further considers the single horizontal gouge layer draining vertically through the rock mass and laterally through the vertical joints while the in situ gouge may be draining through the oriented joints and through a number of layers of uneven thickness. The presence of thick asperities may significantly undermine the actual thickness of gouge participating in the consolidation process.
- The lateral protrusion of the gouge material is assumed to be restricted by the lateral pressure exerted by the adjoining block; while in practice, such protrusion may happen, which may lead to additional settlements.
- The horizontal gouge layer may be draining vertically through open joints and laterally through the rock mass opposed to the assumption. In these circumstances, the non-dimensional parameter must be selected carefully.
- The non-dimensional parameter is assumed to remain constant throughout the consolidation process, which may not remain so in the actual case while the deformations are progressive and mutual adjustment of rock mass and gouge material leads to redistribution of pressure.
- The modulus ratio estimated from rock mass investigations needs to be considered on the scale of horizontal and vertical strength ratios, which may vary due to gouge thickness, and joint orientation.
- There may be significant variation in the estimate of intrinsic permeability ratio within the rock mass itself and extent of contact.
- The length of drainage path is considered a straight line in the direction of drainage in the orthogonal directions while in situ conditions may co-generate orthogonal equipotential and flow paths.

One or many situations as listed in the comments on the applicability of the present study frequently appear in the geo-mechanical environment. They may call for suitable adjustments in the numerical parameters proposed in this study or a separate numerical scheme.

Conclusions

Solutions to the partial differential equation for pore water pressure distribution and average degree of consolidation have been obtained for consolidation of saturated clayey gouge amid permeating rock masses. The clay lamina amid rock masses have an apparent similarity to 2-D drainage; therefore, a solution for the 1-D consolidation with 2-D drainage is obtained numerically using a dimensionless ratio (r) and a non-dimensional parameter $\varphi(r)$, depending on shape factor, modulus and intrinsic permeability ratio. An expression for the time factor with average degree of consolidation in 1-D and 2-D drainage cases has been shown to be a consistent numeric sub-set of the proposed solutions in relation to the newly proposed dimensionless ratio (r) and non-dimensional parameter $\varphi(r)$. It is shown that with higher values of dimensionless ratio (r), the dominance of primary consolidation becomes apparent. The increasing values of dimension less ratio (r) are essentially associated with decreasing time factor and hence reduced time taken for completion of primary consolidation as captured numerically by the present study.

Acknowledgements

The authors sincerely compliment the reviewers, assessors and editors for their savant inputs, comments and questions, which improved the presentation of this paper. The authors thankfully acknowledge the support of Delhi Technological University in conducting this study.

REFERENCES

Ai ZY and Cheng ZY (2009) Transfer matrix solutions to plane-strain and three-dimensional Biot's consolidation of multi-layered soils. *Mechanics of Materials* **41(3)**: 244–251.

Ai ZY and Han J (2006) A solution to plane strain consolidation of multi-layered soils. Soil and Rock Behavior and Modeling, ASCE Geotech. Sp. Pub., *Proceedings of the Geo-Shanghai International Conference, Shanghai, China*, June 6–8, pp. 276–283.

Ai Z and Wu C (2009) Plane strain consolidation of soil layer with anisotropic permeability. *Applied Mathematics and Mechanics* **30(11)**: 1437–1444.

Al-Tabbaa A and Wood DM (1991) Horizontal drainage during consolidation: insights gained from analyses of a simple problem. *Geotechnique* **41(4)**: 571–585.

Bear J (1972) *Dynamics of Fluids in Porous Media.* Dover, ISBN 0-486-65675-6.

Biot M (1941) General theory of three-dimensional consolidation. *Journal of Applied Physics* **12(2)**: 155–164.

Carslaw HS and Jaeger JJC (1986) *Conduction of Heat in Solids*. Clarendo Press, Oxford, UK.

Christian JT and Boehmer JW (1970) Plane strain consolidation by finite elements. *Journal of the Soil Mechanics and Foundations Division, ASCE* **96**: 1435–1457.

Chu J, Bo MW, Chang MF and Choa V (2002) Consolidation and permeability properties of Singapore marine clay. *Journal of Geotechnical and Geoenvironmental Engineering, ASCE* **128(9)**: 724–732.

Das BM (2008) *Advanced Soil Mechanics*. Routledge, Oxford, UK.

De Josselin de Jong G and Verruijt A (1965) Primary and secondary consolidation of a spherical clay sample. *Proceedings of the 6th International Conference on Soil Mechanics and Foundations Engineering*, Montreal Vol. 1, pp. 254–258.

Di Francesco R (2011) Exact solutions of two-dimensional and tri-dimensional consolidation equations. *Physics.Geo.Ph arXiv:1103.6084*, **(1)**: 1–8.

Franciss FO (2010). *Fractured Rock Hydraulics.* CRC Press, London.

Gibson RE, England GL and Hussey MJL (1967) The theory of one dimensional consolidation of saturated clays. *Geotechnique* **17**: 261–273.

Gibson RE, Schiffman RL and Pu SL (1970) Plane strain and axially symmetric consolidation of a clay layer on a smooth impervious base. *Quarterly Journal of Mechanics and Applied Mathematics* **23**: 505–520.

Haley X and Aldrich X (1969) Engineering properties of foundation soils at Long Creek-Fore River areas and Black Cove. *Report to Maine State Highway Company*. Report no. 1.

Hansbo S (1981) Consolidation of fine-grained soils by prefabricated drains. *Proceedings of the 10th International Conference on Soil Mechanics and Foundations Engineering* (Balkema AA (ed)). Publications Committee of ICSMFE, Rotterdam, The Netherlands, pp. 677–682.

Hsu S, Lo H, Chi S and Ku C (2011) Rock mass hydraulic conductivity estimated by two empirical models. *Developments in Hydraulic Conductivity Research* (Dikinya O (ed)). InTech Europe, pp. 1–27.

Huang W, Fityus S and Bishop D (2006) Finite-element parametric study of the consolidation behavior of a trial embankment on soft clay. *International Journal of Geomechanics, ASCE* **6(5)**: 328–341.

Indraratna B and Redana IW (1997) Plane-strain modelling of smear effects associated with vertical drains. *Journal of Geotechnical and Geoenvironmental Engineering, ASCE* **123(5)**: 474–478.

Jiang X-W, Wan L, Wang X-S, Wu X and Zhang X (2009) Estimation of rock mass deformation modulus using variations in transmissivity and RQD with depth. *International Journal of Rock Mechanics and Mining Sciences* **46(8)**: 1370–1377.

Klimczak C, Schultz RA, Parashar R and Reeves DM (2010) Cubic law with aperture-length correlation: implications for network scale fluid flow. *Hydrogeology Journal* **18(4)**: 851–862.

Lambe TW and Whitman RV (1969) *Soil Mechanics*. John Wiley & Sons, NY, USA.

Liu J, Elsworth D and Brady B (1999) Linking stress-dependent effective porosity and hydraulic conductivity fields to RMR. *International Journal of Rock Mechanics and Mining Sciences* **36**: 581–596.

McNamee J and Gibson RE (1960) Plane strain and axially symmetric problem of the consolidation of a semi-infinite clay stratum. *Quarterly Journal of Mechanics and Applied Mathematics* **13**: 210–227.

O'Kelly BC (2005) Consolidation anisotropy of some natural soft soils. *Proceedings of the International Conference on Problematic Soils, Cyprus*, Vol. 3, pp. 1183–1192.

Schofield A and Wroth P (1968). *Critical State Soil Mechanics.* McGraw Hill, London.

Scott RF (1963). *Principles of Soil Mechanics*. Addison-Wesley, London.

Sukumar T, Jain A, Kumar A and Banik T (2013) *Evaluation of settlement in 2-D consolidation*. BE-Major Project, Department of Civil Engineering, University of Delhi, New Delhi, India.

Terzaghi K (1925) *Erdbaumechanik auf Bodenphysikalischer Grundlage*. F. Deuticke, Vienna.

Terzaghi K (1943) *Theoretical Soil Mechanics*. John Wiley & Sons, NY, USA.

Tewatia S, Bose P and Sridharan A (2013) Fastest rapid loading methods of vertical and radial consolidations. *International Journal of Geomechanics, ASCE* **13(4)**: 332–339.

Trivedi A (2010) Strength and dilatancy of jointed rocks with granular fill. *Acta Geotechnica* **5(1)**: 15–31.

Trivedi A (2013) Estimating in situ deformation of rock masses using a hardening parameter and RQD. *International Journal of Geomechanics, ASCE* **13(4)**: 348–364.

Tsien SI (1955) Stability of marsh deposits. *Highway Research Bulletin* **15**: 15–43.

Wolfram S (2013) *The Mathematica Book*, Version 9. Cambridge University Press, Cambridge, UK.

Wood DM (2004) *Geotechnical Modelling.* Spoon Press, London.

Zhang L (2010) Method for estimating the deformability of heavily jointed rock masses. *Journal of Geotechnical and Geoenvironmental Engineering, ASCE* **136(9)**: 1242–1250.

Zwanenburg C (2005) *The influence of anisotropy on the consolidation behaviour of peat*. PhD thesis, Delft University of Technology, Delft University Press, Delft, the Netherlands.

WHAT DO YOU THINK?

To discuss this paper, please submit up to 500 words to the editor at journals@ice.org.uk. Your contribution will be forwarded to the author(s) for a reply and, if considered appropriate by the editorial panel, will be published as a discussion in a future issue of the journal.

IOSR Journal Of Environmental Science, Toxicology And Food Technology (IOSR-JESTFT)
e-ISSN: 2319-2402,p- ISSN: 2319-2399.Volume 8, Issue 2 Ver. IV (Mar-Apr. 2014), PP 44-48
www.iosrjournals.org

Critical Assessment of River Water Quality and Wastewater Treatment Plant (WWTP)

Allaa M. Aenab[1] & S. K. Singh[2]

[1] *PhD Student, Environmental Engineering Department, Delhi Technological University, Delhi, India.*
[2] *Professor, Dean & Head of Environmental Engineering Department, Delhi Technological University, Delhi, India.*

Abstract : *Water and wastewater systems in Iraq have thoroughly been damaged in the First and Second Gulf Wars. Moreover, the Hussein regime in Iraq left the water system to collapse, and caused it to be in desperate need of modernization, redevelopment and improvement.*

For the purpose of this study, samples were collected from two stations along with Diyala River in Baghdad City. The major sources of data are the Ministry of Environment and Ministry of Water Resources. We used Detection of Violation to determine the water quality of Diyala River and Al-Rustumiya Wastewater Treatment Plant (WWTP). Violation for Diyala River shows the parameters (BOD, SO_4, PO_4 & Cl) are 100% violations and that maximum level of pollution. Al-Rustumiya Wastewater Treatment Plant was having very high level of violation for the years (2005, 2006 & 2007) and the values were between (55% - 87%).

Keywords: *Water Quality, Water Pollution, River Pollution, WWTP, Detection of Violation, Water resource and Diyala River.*

I. INTRODUCTION

In the capital city of Baghdad, The surface water suffering from effect of conservative pollutants. Baghdad city has two rivers, the main river Tigris River and Diyala River in boundary of Baghdad City (Jassir Diyala) eastern of Baghdad as is shown in Figure 1 [6].

Diyala provincial council confirmed at the beginning of 2013, that 60% of the pollution in the province's rivers and streams are a result of the citizen's actions and demanded the spreading of environmental preservation awareness to maintain the necessary components of life [10].

Most streams and rivers in Diyala province suffer from an exponential increase in environmental pollution rates resulting from numerous factors namely the negligence of citizens and the infractions of many service administrations that bump their waste directly into the rivers. Diyala River is considered to be one of the main rivers in the province stretching through more than 150 km. The river springs from Iran and it is considered to be one of Tigris most important feeders.

Today most Iraqis have limited access to essential basic services, including electricity, water supply, sanitation, and refuse collection. Serious environmental and health risks associated with contaminated water supplies, inappropriate handling of solid waste, and disposal of sewage threaten to further burden the already stressed health system [5]. Approximately 30% of Baghdad's population is not connected to a sewage collection and treatment system. Sewage treatment plants are operating at 50% of the installed capacity, and untreated sewage is being discharged into rivers and waterways. This problem is exacerbated by the illegal discharge of septic sewage collected from houses into rivers or onto land. Leakage from sewer pipes is also contaminating both the potable water networks and the underground water, which is further adding to the health and environmental problems. According to CARE International, the U.S.-based charity, 300,000 ton of raw sewage escapes into the Tigris River daily. Diseases associated with poor sanitation, unsafe water, and unhygienic practices had increased to alarming rates. It is estimated that water-related diseases are responsible for approximately 25% of all deaths of children in Iraq; approximately 109 per 1,000 children die before the age of 1 [3]. Al-Rustamiya sewage treatment plant (WWTP) serves the east side of Baghdad City (Rusafa) and is considered one of the largest projects in Iraq. It consists of three parts (old project F0, first extension F1, and second extension F2) that treat wastewater and the effluent is discharged into Diyala River and thus into the Tigris River [1].

Sewage is created by residences, institutions, commercial and industrial establishments. It can be treated close to where it is created (in septic tanks, onsite package plants or other aerobic treatment systems), or collected and transported via a network of pipes and pumping stations to a treatment plant. Industrial sources of wastewater often require specialized treatment processes. Wastewater treatment is the process of removing the contaminants from it by physical, chemical and biological processes. Its objective is to produce a treated effluent and a solid waste or sludge suitable for discharge. This sludge may also be reused [1].

Environmental issues Iraq are also facing very serious environmental problems, including poor water

quality, air pollution, waste management, contaminated sites and the deterioration of key ecosystems. With environmental problems neglected to a large extent prior to the war as well, the decades of war, conflicts and economic sanctions have further worsened the environmental conditions. The problems are aggravated by the country's weak environmental governance structure [4].

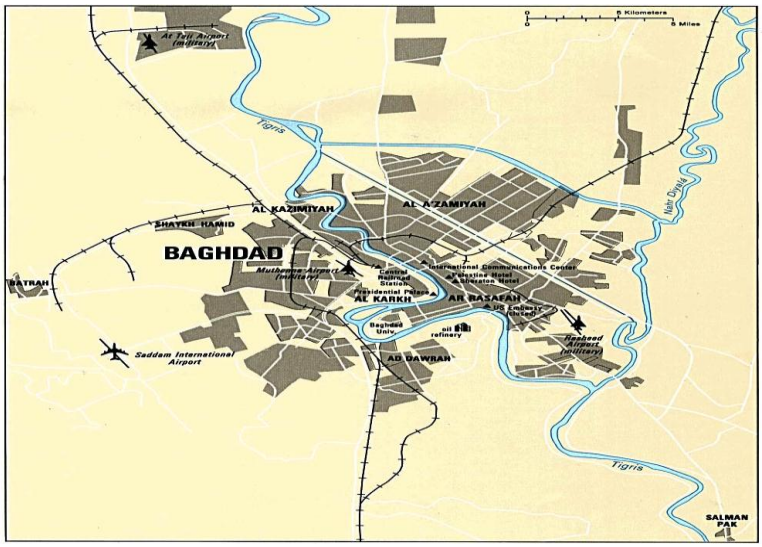


Figure (1) Map of Tigris & Diyala Rivers within Baghdad City

II. Objective and Approach

This study is an attempt to evaluate the current water quality status in Baghdad, Iraq and conduct an environmental assessment of the real status of water quality in Diyala River within Baghdad border and analyzed as follows:

- Evaluation of Diyala River water quality.
- Refine or create Diyala River specific water quality standards pursuant to International standards including development of appropriate reference conditions.
- To provide an early warning system for downstream users about adverse water quality conditions.

III. Materials and Methods

A) Study Area

The Diyala River is a major tributary of the Tigris River that runs through Iran and Iraq which drains an area of 32,600 km^2 [8]. The Diyala River originates near Sanandaj in the Zagros Mountains in Iran, forming the Iran- Iraq border for over 30 km. With a total length of 574 km [12], the river has a drainage area of 32,600 km^2, of which 25% are located in Iran and 75% in Iraq [11]. The Diyala joins the Tigris 15 km south of Baghdad [12].

Despite the construction of a major reservoir in the upper Diyala catchment in 1962, no significant impact on flow volumes and flow regime can be detected. As with the other Tigris tributaries, 1963 is the wettest year within the period of record. Since 1999 below-average flow volumes mark a dry period in the catchment, which potentially indicates intensified stream regulation. However, no long-term trend is detectable over the whole period of record from 1931 to 2011. The Diyala streamflow is very similar to that of the Lesser Zab. It is characterized by peak flows in April and a low-flow season from July until November. The Derbendikhan Dam was constructed in 1962 as a multi-purpose dam on the upper course of the Diyala in Iraq. Besides flood protection and power generation, the dam secures domestic water supply and irrigation water [2]. The 17,850 km^2 catchment area lies mainly in Iran [9]. Iraq built the Hemrin Dam in the early 1980s, creating Lake Hemrin with a storage capacity of over 2 BCM. Inflows originate primarily from the Wand River in Iran and runoff from Iraq is only generated during the rainy season.

B) Data Procurement and Methods

Water samples were collected from selected two stations (Di6 & Di7) along with Diyala River from January 2004 to December 2007. The samples were collected from just under water surface for analysis of selected parameters included: pH, biological oxygen demand (BOD_5), nitrate (NO_3), phosphate (PO_4), Total Dissolved Solids (TDS), Total Hardness (TH), Magnesium (Mg), Calcium (Ca), Chlorides (Cl), Sulphates (SO_4), Sodium (Na) and electrical conductivity (EC).

Violations of the permissible water or wastewater quality standards may be detected by plotting the cumulative frequency distribution (cfd) for the desired parameter and then checking the value against the standard. The cfd will plot as a straight line on normal probability graph paper. To apply this method, the following steps are necessary [7]:

- Arrange the data in ascending order.
- Give each values a rank (position) number of symbols i). This number will run from 1 to n, (n) being the number of points in the data set.
- Calculate cfd_i for each point from as shows in table (1):

$$cfd_i(\%) = \frac{i}{n+1} * 100$$

- Plot the value of each data point against its cfd on normal probability graph paper.

IV. RESULTS

A) Violation of Diyala River

Table (1) shows all the parameters (BOD, SO_4, PO_4 & Cl) are 100% violations for the years (2004, 2005, 2006 & 2007) in Diyala River within Baghdad City.

Table (1) Summary of Violation in Diyala River

NO.	Year	Parameter	Violation	Station
1	2004	BOD	100%	Di6 and Di7
2	2004	SO_4	100%	Di6 and Di7
3	2004	PO_4	100%	Di6 and Di7
4	2005	BOD	100%	Di6 and Di7
5	2005	SO_4	100%	Di6 and Di7
6	2005	PO_4	100%	Di6 and Di7
7	2005	Cl	100%	Di6 and Di7
8	2006	BOD	100%	Di6 and Di7
9	2006	SO_4	100%	Di6 and Di7
10	2006	PO_4	100%	Di6 and Di7
11	2006	Cl	100%	Di6 and Di7
12	2007	BOD	100%	Di6 and Di7
13	2007	SO_4	100%	Di6 and Di7
14	2007	PO_4	100%	Di6 and Di7
15	2007	Cl	100%	Di6 and Di7

B) Violation of Al-Rustumiya Wastewater Treatment Plant

Performance assessment of wastewater treatment plants and efficiency of removal

The extent and efficiency of removal of the impurities are presented in table (2), (3) and (4).

Table (2) Efficiency of removal for Al-Rustumiya WWTP

Time	PO_4	NO_3	SO_4	BOD	O&G
April 2005	21%	34%	0%	88%	63%
May 2005	32%	61%	43%	97%	96%
September 2005	71%	53%	0%	87%	70%
January 2006	0%	0%	27%	53%	72%
March 2006	70%	57%	0%	86%	16%
April 2006	0%	37%	37%	75%	50%
May 2006	74%	0%	0%	97%	98%
June 2006	20%	50%	27%	95%	68%
August 2006	10%	15%	14%	26%	90%
February 2007	25%	0%	9%	58%	95%
March 2007	33%	57%	0%	0%	92%
May 2007	0%	65%	14%	81%	0%
August 2007	54%	59%	48%	92%	0%
September 2007	55%	0%	17%	0%	84%

Table (3) Al-Rustumiya wastewater treatment plant before treatment

	Before treatment					
Time	**PO_4 (mg/l)**	**NO_3 (mg/l)**	**SO_4 (mg/l)**	**T.D.S (mg/l)**	**BOD (mg/l)**	**O&G (mg/l)**
Standard limit						
August 2004	6.6	8.37	576	1718	288	4.4
April 2005	8.1	17.4	414	1598	1500	21
May 2005	5.63	10	795	1820	1350	29.8
September 2005	5.6	12.4	620	1320	420	25
January 2006	8.87	17.05	740	1866	458	31
March 2006	21.4	40.1	480	1690	222	23.8
April 2006	4.96	12.4	560	1070	84	8
May 2006	15.97	13.15	385	1240	432	6.8
June 2006	10.71	8.9	582	1488	180	5
August 2006	7.344	4.43	1000	2792	102	4
February 2007	5.41	5.05	616	2020	300	81.6
March 2007	8.7	13.2	577	1684	459	20
May 2007	4.38	15.3	403	1828	576	8.2
August 2007	8.73	13	576	1683	457	21
September 2007	8.5	7	322	1440	42	18.4

Table (4) Al-Rustumiya wastewater treatment plant after treatment

	After treatment					
Time	**PO_4 (mg/l)**	**NO_3 (mg/l)**	**SO_4 (mg/l)**	**T.D.S (mg/l)**	**BOD (mg/l)**	**O&G (mg/l)**
Standard limit	**3**	**50**	**400**		**40**	**3 to 10**
August 2004	6.6	8.37	514	1718	288	4.4
April 2005	6.4	11.4	496	1398	168	7.7
May 2005	3.8	3.9	450	1560	38	1.2
September 2005	1.6	5.8	740	1330	54	7.4
January 2006	17.7	40.09	540	1784	215	8.6
March 2006	6.4	17.1	710	1674	30	19.8
April 2006	7.65	7.75	348	851	21	4
May 2006	4.1	15.06	390	1220	9.6	0.1
June 2006	8.568	4.4	420	1376	8.4	1.6
August 2006	6.61	3.76	860	1248	75	0.4
February 2007	4.025	18.1	556.5	1936	125	4
March 2007	5.81	5.625	788	2140	870	1.5
May 2007	6.24	5.3	345	1464	108	14.4
August 2007	3.95	5.3	295	1330	34.2	37
September 2007	3.8	9.4	266	1200	45	2.8

Violation of standard of post treatment disposal

Table (5) presents the violation of post treatment standards. Substantial violation in many parameters indicates the shortfall in the level of treatment offered by Al-Rustumiya treatment plant.

Table (5) Summary of Violation in WWTP's

NO.	Year	Parameter	Violation	WWTP
1	2005	BOD	65%	Al-Rustumiya
2	2005	SO_4	75%	Al-Rustumiya
3	2005	PO_4	60%	Al-Rustumiya
4	2006	BOD	55%	Al-Rustumiya
5	2006	SO_4	68%	Al-Rustumiya
6	2006	PO_4	75%	Al-Rustumiya
7	2007	BOD	61%	Al-Rustumiya
8	2007	SO_4	55%	Al-Rustumiya
9	2007	PO_4	87%	Al-Rustumiya

V. CONCLUSION

The present study deals with the critical assessment of Diyala River water quality and performance of the water supply and sewerage systems in Baghdad. In the case of Diyala River were found to be high for the concentrations BOD, Cl, SO_4 and PO_4 and the concentrations of TH, Oil & Grease, Na, K, PH, NO_3, T.D.S, Ca, Mg, and Alk are within the limits. Diyala River is one of the major rivers of Baghdad and special attention must be taken towards enhancing the water quality standards. This is in turn closely related to the development of Iraq. Efforts are needed from the concerned authorities for renovation of water treatment plants and network in inaccessible and ware prone areas.

REFERENCES

[1] AbdulKarim Muneer AbdulRazzak, 2013. Performance Evaluation of Al-Rustamiya Wastewater Treatment Plant. Journal of Engineering, Number 4, Volume 19 April 2013Wikipedia foundation Inc, 2011. Text is available under the Creative Commons Attribution-ShareAlike License

[2] ACSAD and UNEP-ROWA (Arab Center for the Studies of Arid Zones and Dry Lands; United Nations Environment Programme-Regional Office for West Asia). 2001.

[3] Allaa M. Aenab, S. K. Singh, 2011. Critical Assessment of Environmental Quality of Baghdad, Iraq. Journal of Environmental Engineering, Vol. 138, No. 5, May 1, 2012. @ASCE, ISSN 0733-9372/2012/5-601-606/$25.00.

[4] Allaa M. Aenab, S. K. Singh, 2012. Evaluation of Drinking Water Pollution and Health Effects in Baghdad, Iraq. Journal of Environmental Protection, 2012, 3, 533-537 doi:10.4236/jep.2012.36064 Published Online June 2012 (http://www.SciRP.org/journal/jep).

[5] Allaa M. Aenab, S. K. Singh, 2012. Environmental Assessment of Infrastructure Projects of Water Sector in Baghdad, Iraq. Journal of Environmental Protection, 2012, 3, 1-10. doi:10.4236/jep.2012.31001 Published Online January 2012 (http://www.SciRP.org/journal/jep).

[6] Allaa M. Aenab, S. K. Singh, Adil Abbas Majeed Al-Rubaye, 2012. Evaluation of Tigris River by Water Quality Index Analysis Using C++ Program. Journal of Water Resource and Protection, 2012, 4, 523-527 doi:10.4236/jwarp.2012.47061 Published Online July 2012 (http://www.SciRP.org/journal/jwarp).

[7] Chapman & Hall, 1992. First edition 1992. UNESCO, WHO, UNEP. Printed in Great Britain at the University Press, Cambridge. ISBN 0-412-45610-9.

[8] Haitham A. Hussein, 2010. DEPENDABLE DISCHARGES OF THE UPPER AND MIDDLE DIYALA BASINS. Number 2 Volume 16 June 2010 Journal of Engineering.

[9] Ministry of Environment in Iraq, Ministry of Water Resources in Iraq and Ministry of Municipalities and Public Work in Iraq. 2006. Main Water Control Structures (Dams and Water Diversions) and Reservoirs (Annex III). In New Eden Master Plan for Integrated Water Resources Management in the Marshlands Area. New Eden Group. Italy-Iraq.

[10] Mohannad Mohammed, Safaa Abdul Hamid - June 12, 2013, Pollution reduces aquatic life in Iraqi Diyala River by 60%. Al-Sumaria NEWS. http://www.alsumaria.tv/news/77492/pollution-reduces-aquatic-life-in-iraqi-diyala-riv/en.

[11] Shahin, M. 2007. Water Resources and Hydrometeorology of the Arab Region. In Water Science and Technology.

[12] UN-ESCWA and BGR (United Nations Economic and Social Commission for Western Asia; Bundesanstalt für Geowissenschaften und Rohstoffe). 2013. Inventory of Shared Water Resources in Western Asia. Beirut. Shared Tributaries of the Tigris River Chapter 4. http://waterinventory.org/sites/waterinventory.org/files/chapters/Chapter-04-Shared-Tributaries-of-the-Tigris-web_1.pdf.

 International Journal on Electrical Engineering and Informatics - Volume 6, Number 1, March 2014

Design and Assemble of Low Cost Prepaid Smart Card Energy Meter – A Novel Design

Sudarshan K. Valluru

Department of Electrical Engineering, Delhi Technological University
(Formerly Delhi College of Engineering)
Bawana Road, Delhi-110042, India.
valluru.sk@ gmail.com.

Abstract: In India, presently distribution companies are collecting revenues from their consumers by metering and billing. The expenses for metering, billing, and collecting dues became complex as electricity is supplied to large number of consumers located in far-flung areas, resulted in high cost per unit. This may encourage consumers to fudge meter readings. To address these problems, distribution companies can opt prepaid smart card energy meter, which overcomes the whole problems associated with the present billing system and will make the consumer more conscious about usage electricity. This paper explores the design and assemble of smart card prepaid electricity meter system, which enables the consumer to buy required amount of energy and also provides information about their credit balance. A prototype of the system has been developed with the state-of-the-art digital and information technology and proven to be stable, reliable, tamper resistant, low cost, and easy maintenance.

Keywords: Smart Card, Micro controller AT89C51, MAX-232 Serial Communication, Liquid Crystal Display, Pre-paid Electricity Protocol

1. Introduction

Electricity is a major source of energy in the world and used in every civilized country for domestic, commercial and industrial purpose. Recently owing to raise in number of new housing, commercial and industrial developments in India, the number of consumers of electricity have been increased in the network distribution. The monthly power bill for consumers is calculated from post-paid meter reading based on the electricity consumption. But the disadvantage of this system is that meter readers are needed to visit every door to door to read the meter for billing purposes. This is a tiresome, lengthy and error prone process. Moreover, there is a chance for consumers as well as meter readers to do the corruption. In post-paid system [1], the monthly bill sent to the consumer by mail in the beginning of the month and all the consumers often need to gather in a long queue to pay the bills. This procedure is tiresome and time consuming.

In this paper, a prepaid metering (PPM) system [2] has been proposed. Each consumer has to install digitally designed prepaid electricity meter along with smart card in their home, office or industry. Based on the electricity utilization the credit will be deducted automatically from the smart card. When the credit goes below the threshold value, the meter gives warning icons and if credit reaches to zero the meter will automatically cut off the power supply. The consumer has to go to the vending station with the smart card and money to buy electricity. In the vending station, user can buy the credit to his smart card by paying the money. Then the consumer will insert the smart card to the meter and the meter will be recharged. In prepaid billing system, the consumer will be always conscious about the remaining credit and thus try to use electricity carefully and stop its misuse. Furthermore, in contrast with post-paid billing, the consumer can buy credit at any time in the month from the vending station.

Received: August 31st, 2013. Accepted: February 3rd, 2014

In the present proposed scheme there is no need of manual intervention to note meter reading which avoids hassle in billing and distributions companies make money promptly which certainly helps them to generate more revenue.

2. PPM System Architecture

Prepaid meters (PPM) will be installed in home, commercial or industries. For a specific region there will be a vending station also called cash dispensing unit (CDU) from where the consumer will buy credit. The vending stations hold the regional user data base and billing software. The communication between the meter and the vending station is done by smart card. All vending stations are connected with a central server called the master station through the Internet. Master station holds the integrated database of all the vending stations, user account creation software and overall system analysis tools. The overall architecture of the prepaid metering system is shown in Figure1.and brief description of several components of the system is discussed below.

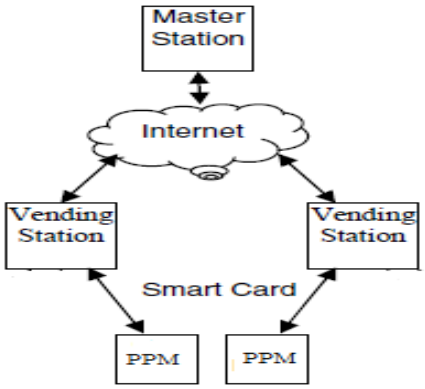


Figure 1. Architecture of the Prepaid Metering System

A. Master Station

Master station holds the integrated database of all the vending stations. Creation, edition and deletion of users account are also done from here. In the master station, the values of the meter settings variables are given. User transaction report or meter status report of any user can be generated from here. As the master station holds the integrated database of all the vending stations, the overall analysis of the system can be done from here.

B. Vending Station

Vending station is the office where the clients go to by credits and holds the database of all local users. Every user of the prepaid meter has smartcards, which establishes the connectivity between the PPM and the vending station. The Figure 2. shows the basic components of vending station mainly consist of server PC, smartcard reader/writer and slip printers to print receipts. When a client needs to buy credit, goes to the local vending station with the smart card and money. To keep the database of the vending station up-to- date, clients are advised to punch the smart card in the meter before coming to the vending station. When the card is punched, the meter's last status is copied to the smart card. In the vending station, the last status of the meter is firstly read from the smart card and save it in database. Then according to the client's demand, vending station writes the credit in the smart card. When the user returns home and punch the smart card in the meter, the credit is added with the remaining credit and the new meter settings are activated. Vending stations maintain relation with the master station through internet. Vending station uploads all the meter status and vending data to the master station and it downloads the latest meter settings from the master station.

C. Smart card Unit

A smart card reader/writer [3] is interfaced using the serial three wire bus protocol with the CPU to read/write data to smart card. The smart card reader's Reset and Clock pins are connected with two output ports of the CPU. The Data pin is connected with a port which can be configured both in input and output direction so that data can both be read and write to smart card. The SLE4428 type smart card has been used with 1KB of non-volatile EEPROM memory and it is write-protected by a 16 bit password. Different meter settings and meter status variables are mapped in different memory locations of the smart card.

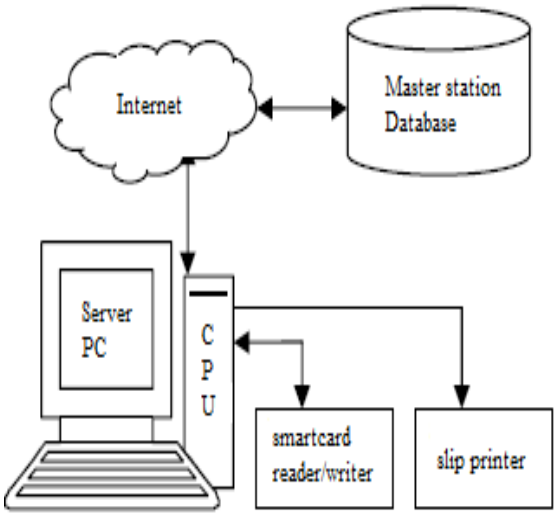


Figure 2. Block diagram of Vending Station

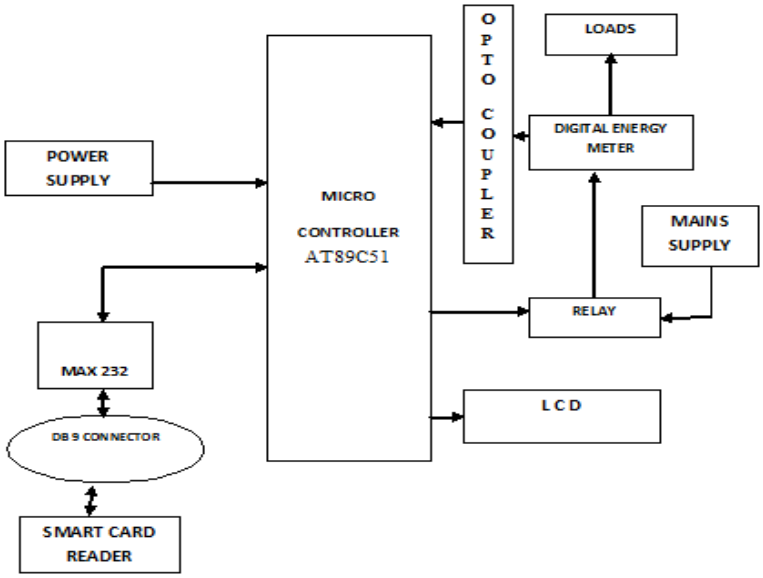


Figure 3. Block diagram of Prepaid Energy Meter

D. Prepaid meter

The most important constraint is design and assembles of prepaid energy meter. The block diagram of prepaid energy meter [4] is shown in Figure3.and its components are discussed below sections.

3. The Design of Intelligent Controller

This system is composed of software and hardware structures. The hardware structure consists of a digital energy meter module interfaced to an AT89C51 [5-11] low-power, high-performance CMOS 8-bit micro controller has 40-pin, a highly stable 24 MHz oscillator, 4 KB flash programmable and erasable read only memory (PEROM), 128 bytes of RAM, 32 I/O lines, two 16-bit timer/counters, a five vector two-level interrupt architecture, a full duplex serial port, on-chip oscillator and clock circuitry. In addition, the AT89C51 is designed with static logic for operation down to zero frequency and supports two software selectable power saving modes. The Idle Mode stops the CPU while allowing the RAM, timer/counters, serial port and interrupt system to continue functioning. The Power-down Mode saves the RAM contents but freezes the oscillator disabling all other chip functions until the next hardware reset.PIN P0.0-P0.7, P1.0- 1.7, P2.0 - P2.7,and P3.0-P3.7 may as general I/O and LCD analog output. In the16pin LCD, first pin grounded, Second pin connected to power supply and 3rd pin will be connected to variable pot to control the contrast of the LCD. LCD data lines are connected to port P0, The microcontroller pins P2.7, P2.6 and P2.5 are connected to the LCD control pins RS, R/W and EN respectively. The ALE, PSEN, EA pins are left isolated. For the execution of the program of micro-controller requires clock pulses of frequency 12MHz which generated by the crystal oscillator with grounding capacitance 33PF,therefore XTAL2 and XTAL1 pins of micro-controller are connected to the crystal oscillator. The RX(P3.0) and TX (P3.1) are connected to the 12 and 11 pins of MAX 232 serial communication via DB9 connector to interface the Smart Card Reader module, from that smart card the data regarding the amount is fed to the micro controller gets activated and starts to take the data from the 4N35 optocoupler. The micro controller P3.2 connected to the IRLED digital energy meter via optocoupler, with external interrupt0 the number units consumed is counted with the help of the counted pulses which are generated from the optocoupler. The IRLED blinks when there is a unit consumed gives the IR rays incident on optocoupler which itself drives the transistor base connected to P3.2. The micro-controller counts the number of units and simultaneously monitors the smart card reader for the presence of the card. The micro-controller reads the total purchased units from the smart card and unit's value has been reduced by one for each and every unit consumed. If the units in the smart card become zero then the micro-controller gives the signal to the relay to switch off the total supply to the energy meter. The P2.0 is connected to the relay through the transistor. The 40th pin (V_{cc}) and 20th pin (GND) of microcontroller connected to 5 V power supply and ground respectively. 9th pin will be connected to the reset and by pressing the reset pin the C-Language program in the micro-controller will be executed. Therefore the micro controller gets the data from the energy meter and SLE4428 card reader and also controls the total power supply of the system [12]. The design diagram of intelligent AT89C51micro controller, energy meter, Display and Relay Control Circuit is shown in Figure 4.

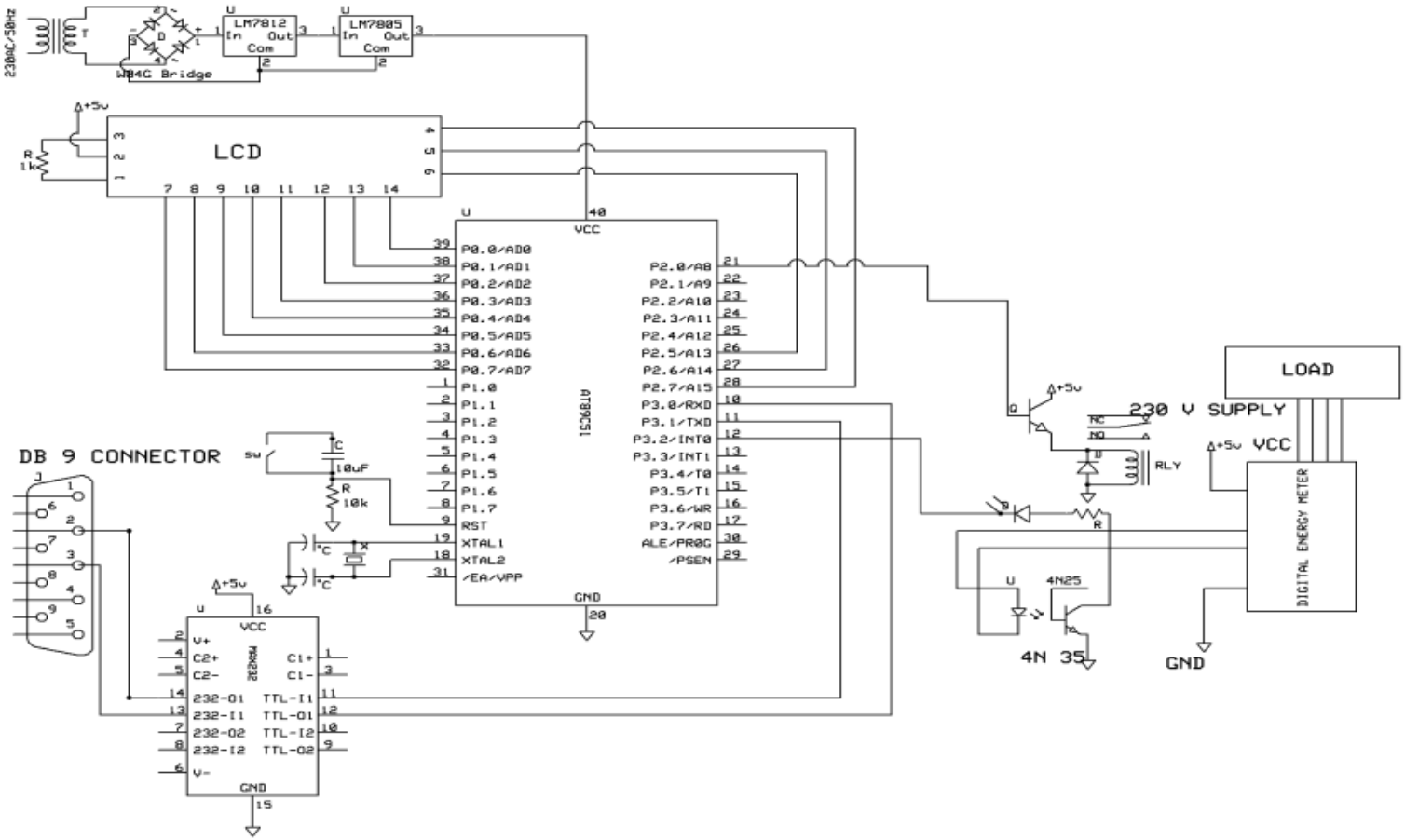


Figure 4. Display and Relay Control Circuit of Prepaid Energy Meter

A. The Design of Software

The main protocol has five phases for controlling the consumption of electricity based on proper authorisation by using smartcard; balance checking, decision making, decision process and termination. Control systems for working process main protocol [13] flow chart is shown in Figure5.and the other sub-modules of flow chart are omitted.

B. Prototype Development

Based on the design discussed above, prepaid smart card energy meter shown in Figure6 has been constructed and assembled in the laboratory; the meter technical specifications [14] are shown in Table 1. The test results are tabulated in Table 2 and precision experimentally obtained for this new meter better than 97%. This value is compatible with the commercially available energy meters in the market.

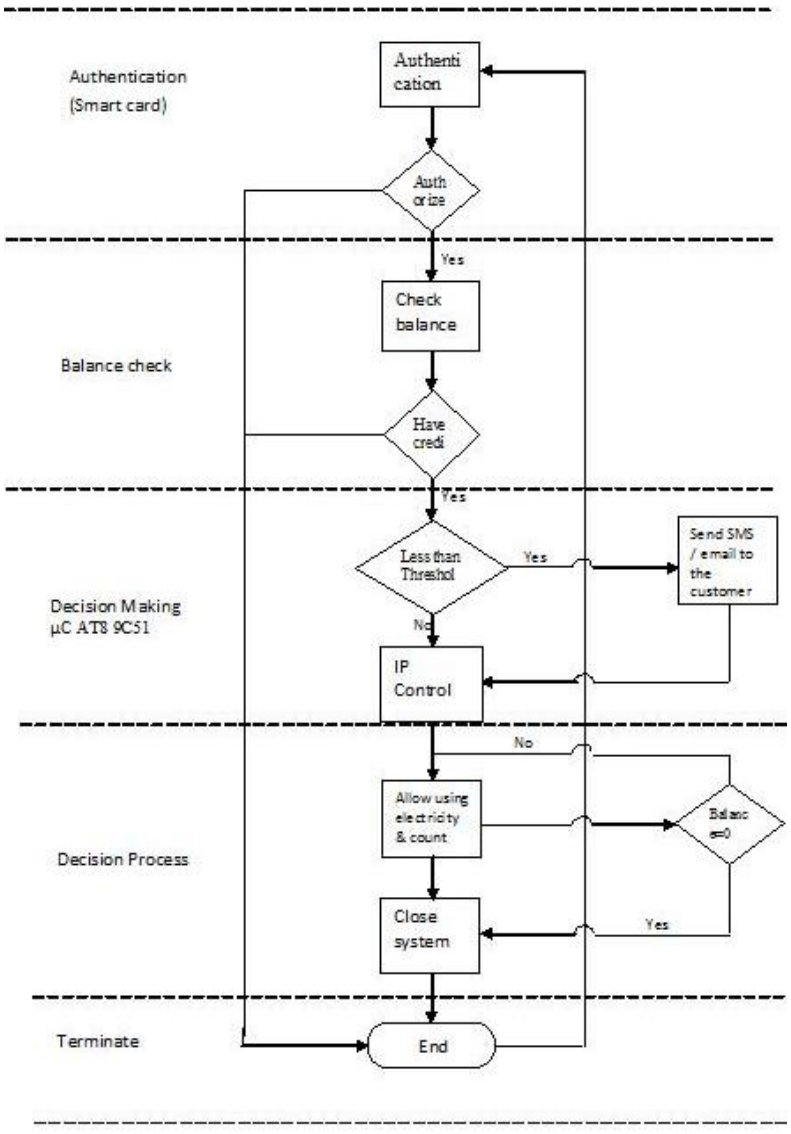


Figure 5. Pre-paid electricity protocol

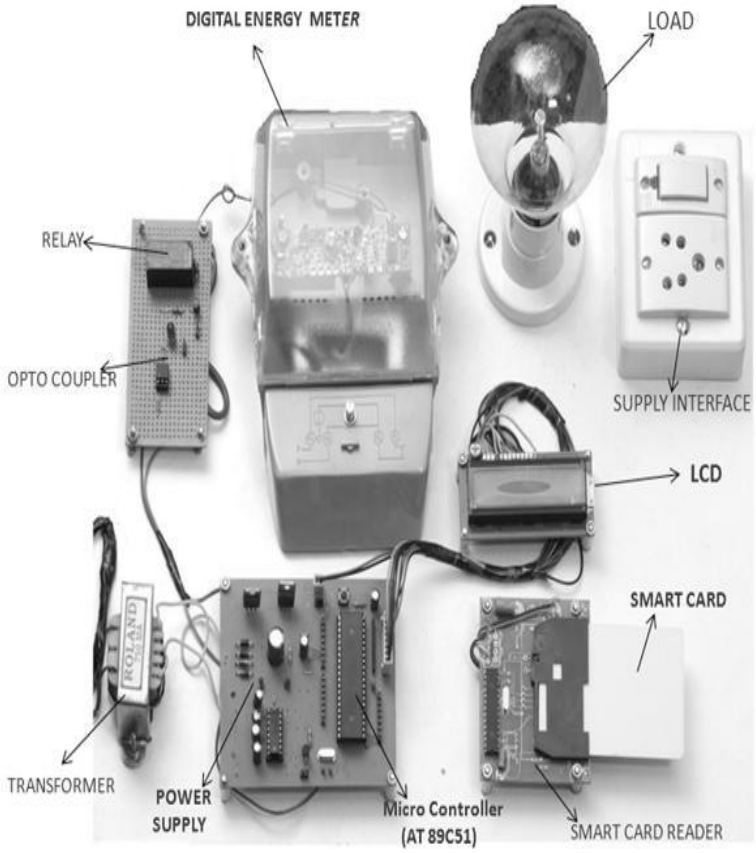


Figure 6. Proto type of Pre-paid smart card meter

Table 1.Technical Specifications

Type	Accuracy	Rated Voltage	Frequency	Display	Information Record
Contacted IC card Pre-Paid meter	Class 1.0	Single-Phase 230V	50Hz	LED display	The energy credited and used will be recorded

Table 2. Test results over 24 - hours

Lamp load(W)	Number of Hours	Load Measured by Standard Meter(kWH)	Load Measured by Pre-Paid Meter(kWH)	Deviation	Error (%)	Precision (%)
200	6	1.2	1.17	0.03	2.5	97.5
100	6	0.6	0.582	0.018	3.0	97
60	6	0.36	0.3528	0.0072	2.0	98
40	6	0.24	0.2328	0.0072	3.0	97
Mean	24	2.4	2.3376	0.0624	2.6	97.4

4. Conclusion

A prototype of the system has been developed and tested successfully. In this paper, the advantages of prepaid metering system and its design components have been discussed. The meter features includes with alarming of remainder, storing data up to 20 years. This prepaid metering system minimizes the human intervention in meter reading, bill calculations and bill delivery which ultimately reduces many defects than the currently existing post paid billing systems. This system was specially designed for India but can also be implemented in any other country. Of course, the basic principles implemented here can be easily extended to the case of three-phase meters. This is certainly beneficial to both consumers and power distribution companies.

References

[1] M I Tibbenham, "Implementing a Pre-payment System" *IEE International Congress on Metering and Tariffs for Energy Supply, Birmingham, UK, 1999, pp 251-257.*

[2] Muhammad Faheem Khan, Ahmed Zoha, and Rana Liaqat Ali ''Design and Implementation of Smart Billing and Automated Meter Reading System for Utility Gas'' *Proc. in IEEE Conference on Information and Emerging Technologies, 2007, pp1-6*

[3] KwanB H, M Moghawemi ''PIC Based Smart Card Prepayment System'' *Proc. in IEEE Student Conference on Research and Development, Malaysia,2002, pp 440-443*

[4] PAV. Loss, MM. Lamego, GCD. Sousa and JLF.Vieira, "A Single Phase Microcontroller Based Energy Meter", *Proc. in IEEE Instrumentation and Measurement, Technology Conference, Minnesota, 1998, pp 797-800.*

[5] Huang Ji-wu, Yang Hong-wei, Ming Feng " Study on an Application Using AT89c51 to Measure Frequency in UHF and VHF", *Wuhan University Journal of Natural Sciences, Vol 48 (1), 2002, pp 125-128.*

[6] Fuquan Pan, Lixia Zhang, Gang Sun, Jiyou Li, " Design of Vehicle Reversing Collision Avoidance Device based on Single Chip Computer" *2nd International Conference on Power Electronics and Intelligent Transportation System (PEITS), Shenzhen, 2009, pp. 223-226.*

[7] Wei Shutao, Chen Lin, Cui Lili and Wang Zhenxing "Interface Design of EEPROM and Signle Chip Micro Computer by IIC Bus" *International Conference on Information Management and Engineering, Kula Lumpur, 2009, pp 554-557.*

[8] Jishun Jiang, Lina Liu, Tian Jiang "Study of A New Type Field Irrigation Intelligent Controller" *Proc in 2nd IEEE International Conf. on Information Engineering and Computer science, 2010, pp1-4.*

[9] Wang Yuanzhe, Bai Liyuan, "Electric Cable Interface Temperature Monitoring and Early Warning System" *Second WRI Global Congress on Intelligent Systems, Wuhan, 2010, pp. 211-215.*

[10] Li Xiangyang, Luo Genghe, Yan Jie, Guo Yan Ling, "The communication interface design of AT89C51 preparation robot based on Serial" *International Conference on Electric Information and Control Engineering, Wuhan, 2011, pp 802-804.*

[11] Zhu Weiguo, Ruan Hailin "Design and Research of Solar Photovoltaic Power Generation Controller based on 89C51 microcontroller" *Advance Materials Research Vol. 345, 2012, pp. 66-69.*

[12] Tian Yew Lim and Tat-Wai Chan "Experimenting Remote Kilowatthour Meter Reading Through Low-Voltage Power Lines at Dense Housing Estates" *IEEE Transactions on Power Delivery, Vol. 17, No. 3, July 2002. pp. 708-711*

[13] Ross J. Anderson, S.Johann Bezuidenhout, "Cryptographic Credit Control in Pre-payment Metering Systems" *Proc. in IEEE Symposium on Security and Privacy, Oakland,USA, 1995 pp15-22.*

[14] Manual on Standardization of AC Static Electrical Energy Meters, Publication No: 304, Central Board of Irrigation and Power, New Delhi , 2008



Sudarshan K. Valluru is working as Associate Professor in Electrical Engineering department of Delhi Technological University (Formerly Delhi College of Engineering), Govt. of NCT of Delhi and has 18 years of academic experience. He received his B.Tech in Electrical and Electronics Engineering from Nagarjuna University, Andhrapradesh and M.Tech in Computer Applications in Industrial Drives from National Institute of Engineering, Mysore, Karnataka. So far he has published 4 papers in international and 1 in national referred journals, 2 papers in IEEE International conferences and 5 in national conferences. He is authored a book on Neural Networks, Fuzzy Logic and Genetic Algorithms (Jaico publishers 2010). His areas of interest are AI systems, Instrumentation and Control. He is a senior fellow member of Institution of Electronics and Telecommunication Engineers India, Member in Indian Society for Technical Education India, Institution of Engineers India and IEEE.

2014 International Conference on Signal Processing and Integrated Networks (SPIN)

Design of Stacked Miniaturized Slotted Antenna with Enhanced Bandwidth for WiMAX Application

Jimmy Gautam[1],N. Jayanthi[2]
[1]ECE Department, Amity University
Noida, UP, India
[2] ECE Department, Delhi Technological University
Delhi,India
jgautam@amity.edu, njayanthidce@yahoo.in

***Abstract*— In this paper, a dual-frequency stacked patch with asymmetric U- slot on lower patch and a rectangular slot on upper patch is presented. For wireless system and RF applications, the microstrip patch is one of the most chosen antenna structures because of its being cheaper and compact design. Dual-Band antennas are of a main interest as they can support several communication systems. The designed antenna is experimentally verified for the required performance with the help of IE3D software. Dual frequency operation is obtained by loading slots in rectangular patches and good impedance bandwidth is obtained by using Rogers Duroid 5880 with slight difference in dielectric permittivity for upper and lower patch. The impedance bandwidth (VSWR ≤ 2) is obtained as 4.29% for 3.4 GHz and 6.32% for 5.6GHz. Return losses obtained are -31 dB and -42dB at3.4GHz and 5.6 GHz respectively**

Keywords*— *Broadband techniques, Wireless communications, dual-band, WiMAX, patch antennas, stacked antenna

I. INTRODUCTION

Microstrip patch antennas are mainly implemented in wireless communication even though they have a narrow bandwidth. For making the bandwidth broader many broad banding techniques are used among which stacked antenna configuration plays a good role. Microstrip patch antenna is used because of its smart features such as low profile, light weight, conformal shaping, low cost, good efficiency, ease of manufacture and simple integration to circuits. However the main drawback of the microstrip patch antenna is its innately narrow impedance bandwidth. Thorough research has been done in recent years to build up bandwidth improvement techniques. In [9], a circularly polarize antenna is designed using asymmetric u slots. The bandwidth is obtained as 1% at 3.5 GHz and 3.1 % for 5.8 GHz. In [10], reactive loading is used in stacked configuration for improving the bandwidth. In [12], bandwidth is increase from 3.72% to a great extent by adding the slots in stacked antenna for dual band operation. In [13], an H shaped stacked patch antenna is designed and the bandwidth at lower and upper resonance is found 3.66% and 10.25% respectively. In [17], a compact double u slot patch antenna for WiMAX application is made in which the three band behaviour at 2.7, 3.2 and 5.3 GHZ is obtained. Also the bandwidth requirements for WiMAX standards 4.8 %, 3 % and 2.5 % respectively is obtained. The return loss for the triple band is -18.5 16 dB, -14.5 dB and -19 dB respectively. Also in [18], an I slotted patch antenna is proposed in which the bandwidth (VSWR ≤ 2) is 1.57% (1.222 GHz to 1.2414 GHz) for L2 and 6.27% (1.5617 GHz to 1.6626 GHz) for L1. In [19], L slotted rectangular patch antenna is designed for wireless applications and impedance bandwidth of 130MHz and 1.45GHz band is obtained in the proposed design.

U-slot stacked patch antenna structures joins two broadbanding methods where wider bandwidths can be achieved by using stacked configuration, bandwidth problem can be overcome. Various experiments are done with U-slot like in [9], [14], [17], [20] etc. The variation of U-slot dimensions such as width of slot, slot length, probe location etc. noticeably change the antenna performance. Mathematical procedures have not been developed to design U-slot patch antenna. The techniques are useful for initial designs and desired antenna behaviour can be achieved by tuning process.

II. DESIGN

For WiMAX applications, Antenna designing doesn't need size to be very bulky. These present communication systems have need of antennas with broadband and/or multi-frequency functional modes. The aim is to design a smaller size microstrip antenna and to maintain the layout as simply as achievable and a rectangular patch antenna was chosen for this purpose. For reducing the size and resonance frequency of the patch antenna can be done by increasing the path length of the surface current which is obtained by cutting slots in the radiating patch.

There are numerous techniques to reduce the size of the patch i.e. shorting wall, shorting pin, slot cutting etc [21]. Using shorting method, microstrip antenna becomes a compact antenna but it goes through from of poor gain and deprivation in the radiation pattern. Another way to decrease the resonance frequency of the microstrip antenna is to raise the path span of the surface current by introducing slots in the radiating patch.

To fine-tune the size, distance between the driven and the parasitic elements, and the location of the feed point of Co-axial probe, an iterative procedure is followed. According to this, to place the impedance loops at the centre of the Smith chart, a feeding point with high impedance is required, as well resonating frequency of parasitic patch should be same as of the driven element. Designing an antenna for WiMAX applications require antenna dimensions to keep it light in

978-1-4799-2866-8/14/$31.00 ©2014 IEEE

weight. In this design two different dielectric constants of 2.22 for lower patch and 2.2 for upper patch is used. The loss tangent of the dielectric substrate is 0.009.

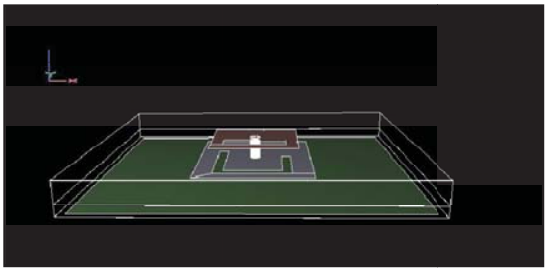


Fig. 1. 3D view of patch antenna

Figure 1 shows the 3D structure of proposed antenna. Slots are loaded on the conducting patch with dielectric medium kept between patch and ground plane. The antenna is excited using single coaxial feed arrangement. Using slots on the conducting patch element can cause meandering of the excited patch surface current paths. As a result resonant frequency is reduced, and which becomes the reason of reduction in antenna size comparatively to normal microstrip patch antenna at designed frequency. The final geometry of the upper patch and lower patch are shown separately in Figure 2.

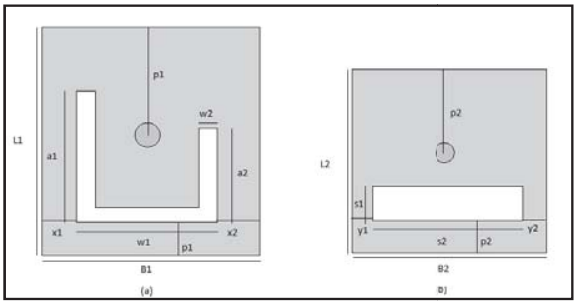


Fig. 2. Design of a) lower patch b) upper patch with probe feed

A singly fed patch radiates both left hand circularly polarized (LHCP) and right hand circularly polarized (RHCP) at the same level and polarity of bias magnetic field; however LHCP and RHCP have different resonant frequencies [2]. When (Lul>Lur), the antenna is left-hand circularly polarized (LHCP). Similarly, when (Lul<Lur), the antenna is right-hand circularly polarized (RHCP).In the proposed design, LHCP is used for the required circular polarization. Initial dimensions of the asymmetric U-slots for each layer were determined using the approach described in [15].

III. EQUATIONS

The length on patch is generally in the range of $0.3333\lambda_0 < L < 0.5\lambda_0$where λ_0 is the free space wavelength. The thickness of patch should be very less thanλ_0. The height of the substrate of the dielectric substrate should be in the range of $0.003 < h < 0.05\lambda_0$ and the value of dielectric constant should be less than$2.2 \leq \epsilon_r \leq 12$. The different formulas for the basic design are given as following [1]:

Patch width

$$w = \frac{c}{2\sqrt{\frac{(\epsilon_r + 1)}{2}}} \quad (1)$$

Patch length

$$L = L_{eff} - 2dL \quad (2)$$

Where

$$L_{eff} = \frac{c}{2f\sqrt{\epsilon_{reff}}} \quad (3)$$

$$dL = 0.412 \frac{(\epsilon_{reff} + 0.3)\left(\frac{W}{h} + 0.264\right)}{(\epsilon_{reff} - 0.258)\left(\frac{W}{h} + 0.8\right)} \quad (4)$$

$$\epsilon_{reff} = \frac{(\epsilon_r + 1)}{2} + \frac{(\epsilon_r - 1)}{2}\left(1 + 12\frac{h}{W}\right)^{-\frac{1}{2}} \quad (5)$$

$$L_g = 6h + L \quad (7)$$

$$W_g = 6h + W \quad (8)$$

Here ϵ_{reff} , L_{eff}, dL, L_g and W_g are effective dielectric constant, effective length, extended length on each end, ground length and ground width respectively.

In this effort, probe feed technique is selected to be used as its main benefit is that, the feed can be put at any location in the patch for matching with its input impedance (generally 50 ohm). Different graphs like return loss, VSWR, radiation pattern, smith chart and various other parameters are plotted using IE3D software

In the figure, ground size is kept to be 50x40 mm^2. Lower substrate thickness and upper substrate thickness is chosen to be of 1.534mm and 3.175 mm respectively. The size of lower patch is 19.1x21.2 mm2 and of upper patch is 14.5x12.7 mm2. The slot arms a1 and a2 are kept 11.9mm and 8.93 mm. gap between the arms (w1) is 12.7 mm and the width of slot w2 is 1.6mm.the slit length is 10.5 mm. the feed point location is set to (0, 1.1) for the best impedance matching by using a coaxial probe feed of diameter 1.6mm

IV. SIMULATED RESULTS

In figure 3, the return loss of the simulated antenna is shown which are about -31 dB at 3.4GHz frequency and -41 dB at 5.6GHz which is very much improved as in case of [9]. The bandwidth with respect to S11<-10dB is 146 MHz (4.29%) at 3.4GHz frequency and 355MHz (6.32%) at 5.6GHz. The VSWR is a way to measure impedance mismatch between the feeding system and the antenna. The higher the VSWR, the more is the mismatch. The minimum possible value of VSWR is unity and this refers to a perfect match. VSWR of the propose antenna can be easily seen in the figure 4 which is very near to 1. Antenna efficiency is about 83% for 3.4GHz and 98% for 5.6GHz. Radiation efficiency is also displayed along with antenna efficiency in figure 5.

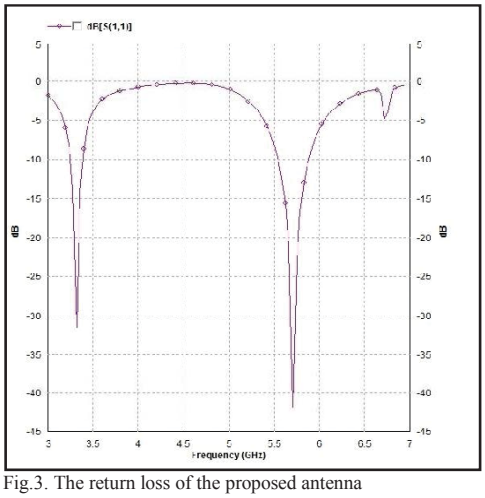


Fig.3. The return loss of the proposed antenna

The feed point should be positioned at that point on the patch, where the input impedance matches 50 ohms for the resonant frequency. Therefore, a trial and error technique is used to find the feed point.

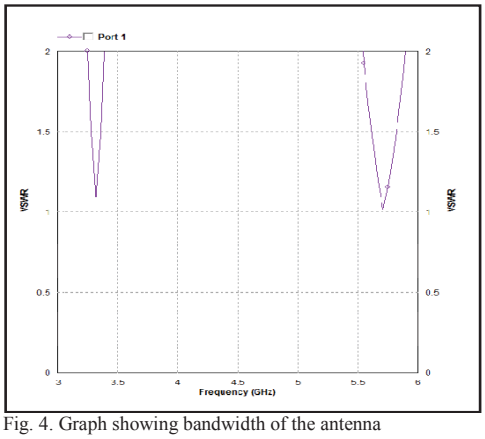


Fig. 4. Graph showing bandwidth of the antenna

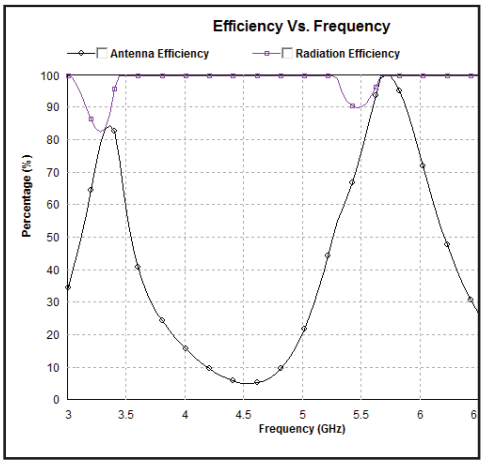


Fig. 5. Antenna efficiency of the antenna

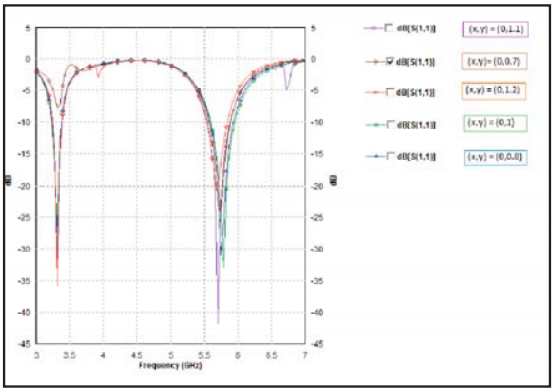


Fig. 6. Variation in return loss with location of probe

For different positions of the feed point, the return loss is noted and then comparison is done with other points and finally feed point is selected where the return loss is most negative. The variation in the graph in accordance with change in probe location is shown in figure 6 and also in figure 7 in terms of smith chart variations. Azimuth as well as Elevation 2D radiation pattern of electric field is shown in figure 8 using polar plots. The antenna gain obtained at 3.4 GHz and 5.6 GHz is 3.43dBi and 7.25 dBi respectively which can be seen clearly in figure 9.

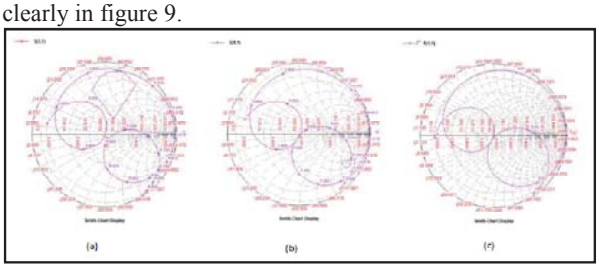


Fig. 7. Change in probe location a) (x,y)=(0,0.8), b) (x,y)=(0,1.2) c) (x,y)=(0,1.1)

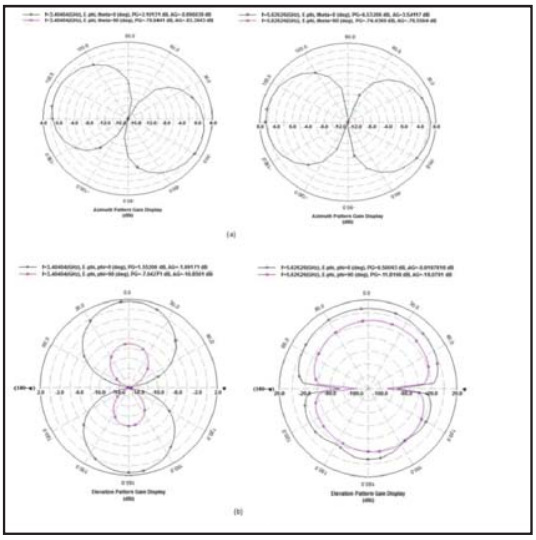


Fig. 8. 2D radiation patterns of the stacked antenna

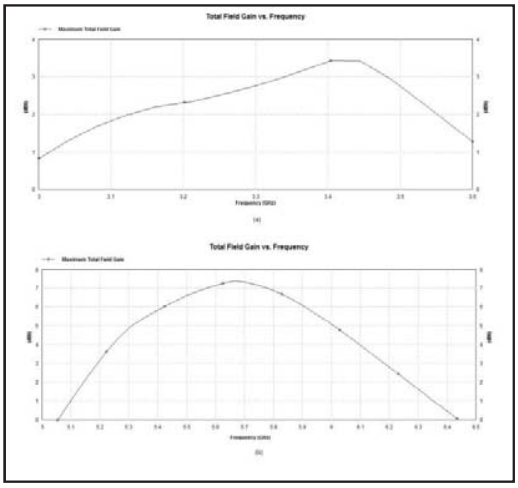


Fig. 9. Total field gain of the antenna for a) 3.4 GHz b) 5.6 GHz

V. CONCLUSION

The analysis of the designed patch antenna was performed using IE3D software. The parameters of the U-slot are optimized to provide different current paths for the two orthogonal modes required for circular polarization. In the design of the antenna, impedance matching is very important. It is concluded from the results that return loss of the stacked rectangular patch antenna at both the frequencies 3.4GHz and 5.6 GHz are much better. At 3.4GHz the return losses, bandwidth and gain obtained are -31 dB, 4.29% and 3.43dBi respectively .At 5.6 GHz return losses, bandwidth and gain are -42dB, 6.32% and 7.25 dBi respectively. All the simulation results show that the proposed stacked antenna performs very well with the two frequencies. The proposed antenna is well suited for WiMAX applications in 3.40-3.69 GHz and 5.25-5.85 GHz bands.

REFERENCES

[1] C. A Balanis, "Microstrip Antennas", Antenna Theory, Analysis and Design, Third Edition, John Wiley & Sons.

[2] D.M. Pozar, D. H. Schaubert," Microstrip Antennas, The Analysis and Design of Microstrip Antennas and Arrays" John Wiley & Sons, May 1995.

[3] T. Milligan," Modern Antenna Design", Second Edition, John Wiley & Sons

[4] C. Wu, k. L. Wu, Z. Bi, J. Litva, "Modeling of coaxial-fed microstrip patch antenna by finite difference time domain method", Electronics Letters 12th September 1991, Vol. 27, issue 19.

[5] J. R. James & P. S. Hall, "handbook of microstrip antenna", Peter Peregrinus Ltd., London, United Kingdom.

[6] R.Garg, P.Bhartia, I.Bahl, A.Ittipiboon, "Microstrip Antenna Design Handbook", Artech House Inc. Norwood, MA.

[7] S. Maci and G. Bif Ji Gentili," Dual-Frequency Patch Antennas", Department of Electronic Engineering University of Florence

[8] K. Wong," Compact and Broadband Microstrip Antennas", John Wiley & Sons.

[9] K.F. Lee, Fellow, IEEE, Atef Z. Elsherbeni, Fellow, IEEE, and Fan Yang, Senior Member, IEEE," Dual-Band Circularly Polarized Antennas Using Stacked Patches with Asymmetric U-Slots", IEEE Antennas and Wireless Propagation Letters, Vol. 10, 2011.

[10] J. Anguera , C. Puentez, and C. Borja," Dual Frequency Broadband Microstrip Antenna with A Reactive Loading and Stacked Elements", Progress in Electromagnetics Research Letters, Vol. 10, 2009.

[11] T.Fortaki, L.Djouane, F.Chebara, and A.Benghalia," On the Dual-Frequency Behavior of Stacked Microstrip Patches", IEEE Antennas and Wireless Propagation Letters, Vol. 7, 2008.

[12] H. F. Abu Tarboush, H. S. Al-Raweshidy and R. Nilavalan," Bandwidth Enhancement for Microstrip Patch Antenna Using Stacked Patch and Slot", Wireless Networks & Communications Centre (WNCC), School of Engineering & Design, West London U.K.

[13] J. A. Ansari, P. Singh, and S. K. Dubey," H-Shaped Stacked Patch Antenna For Dual Band Operation", Progress In Electromagnetics Research B, Vol. 5, 291–302, 2008.

[14] G. F. Khodaei, J. Nourinia, and C. Ghobadi," A Practical Miniaturized U-Slot Patch Antenna With Enhanced Bandwidth", Progress In Electromagnetics Research B, Vol. 3, 47–62, 2008.

[15] K.-F. Tong and T.P. Wong, "Circularly polarized U-slot antenna," IEEE Trans. Antennas Propag., vol. 55, no. 8, pp. 2382–2385, Aug. 2007.

[16] D. G. Fang," Antenna Theory and Microstrip Antennas", Taylor & Francis Group.

[17] H. F. Abu Tarboush, H. S. Al-Raweshidy and R. Nilavalan.," Compact double U-Slots Patch Antenna for Mobile WiMAX Applications", wireless Networks & Communications Group (WNCG) School of Engineering & Design, Brunel University, West London, UK.

[18] U. U. Hussine, Md. T. Islam Norbahiah Misran," A New I Slotted Compact Microstrip Antenna for L1 & L2 Bands". Proceeding of the 2011 IEEE International Conference on Space Science and Communication (IconSpace), Penang, Malaysia, July 2011.

[19] D. Yadav," L – Slotted Rectangular Microstrip Patch Antenna", 2011 International Conference on Communication Systems and Network Technologies.

[20] D. Chatterjee, "Effect of Substrate Permittivity and Thickness on Performance of Single-Layer, Wideband, U-slot Antennas on Microwave Substrates," Proceedings of the 20th Annual Review of Progress in Applied Computational Electromagnetics at Syracuse, New York, April 2004.

[21] K.-L. Wong," Compact and Broadband Microstrip Antennas", John

Wiley & Sons.

2014 International Conference on Reliability, Optimization and Information Technology -
ICROIT 2014, India, Feb 6-8 2014

Efficient Resolution Of Mixed Pixels Using Bio-Inspired Heuristics

Tanu Varshney, Lavika Goel
COE Department
Delhi Technological University
New Delhi, India

Daya Gupta
HOD,COE Department
Delhi Technological University
New Delhi, India

V.K.Panchal
DTRL
DRDO
New Delhi,India

Abstract—**In recent years, several nature inspired algorithms have been applied for remote sensing image classification. Each pixel is categorized into one of the several land cover classes such as water, vegetation etc. When a pixel is categorized into more than one class at a time then such pixels are called Mixed Pixels. Existence of mixed pixels lowers classification accuracy of satellite image. This paper focuses on resolving the Mixed Pixels, using sinusoidal migration model in Biogeography based optimization (BBO). The methodology proposed also involves excluding the redundant bands from multiband image to provide better decomposition of Mixed Pixels.**

Keywords- mixed pixels; nonredundant bands; sinusoidal migration in BBO

I. INTRODUCTION

Remote sensing is a technique of obtaining information about objects through the data that is collected without coming in contact with the object. Remote sensing systems record brightness values at different wavelengths that commonly include not only portions of the visible light spectrum, but also those outside the visible region such as near infrared, middle infrared bands. Satellite images, obtained in different wavelength bands contain spectral values. The spectral response is represented by the discrete digital number (DN) [1].

Generally pixels representing field boundaries comprise of more than one ground cover type. These pixels are referred to as the Mixed Pixels. Not every band may provide unique information for an area. Few bands may have redundant information. Hence, we propose to include the non redundant bands for efficient resolution of the Mixed Pixels. Our approach is based on population based bio inspired optimization technique known as Biogeography based Optimization (BBO). This paper focuses on the sinusoidal migration model for sharing of information among species because recent studies have shown that it better represents the natural migration phenomenon [2].

This paper has been divided into six sections. The second section gives detail of BBO and the mixed pixels. The third section discuss about the proposed framework. The fourth section discuss about the proposed methodology. The fifth section discuss about the results of the proposed approach. The last section presents concluding remarks.

II. BACKGROUND

A. *Biogeography based optimization*

BBO was first introduced by Dan Simon, in December 2008 [3]. Biogeography is the study of the distribution of biodiversity over space and time. The process of migration in BBO can be interpreted in two ways- one is the introduction of new species into the habitat which is known as Immigration. Another is the moving out of a species from a habitat which is known as Emigration. It is through the concept of immigration and emigration, the information is shared in BBO [4]. Areas that are well suited for biological species are said to have a high habitat suitability index (HSI). HSI denotes the fitness of a candidate solution. The variables that characterize habitability are called suitability index variables (SIVs) [5]. In BBO, a habitat denotes a candidate optimization problem solution. The candidate solution with high HSI is considered a good solution. The species migrate from a habitat with high HSI to a habitat with low HSI so as to improve the biological diversity of the habitat and hence improve the candidate solutions [6] [7].

B. *Mixed pixels*

It is generally assumed in remote sensing that each pixel in an image contains information related to only single ground object i.e. these pixels are considered to be pure. However, this may not be the case. The pixel may contain spectral response from more than one ground object known as mixed pixels. The pixels on the edge or boundary of discrete classes tend to contain mixed spectral response from each of these classes resulting in Mixed Pixels [8].

Increase in the spatial resolution may reduce mixed pixels but it is not always the case. This is because more pure pixels are set inside the boundaries, which in turn may reveal finer details of new features leading to more and new spectral classes. Another drawback is that the number of pixels can become very large, which may add to the cost of processing.

III. PROPOSED FRAMEWORK

Our proposed framework for resolving the mixed pixels is based on the following concepts of choosing few numbers of bands and migration of species based on sinusoidal curve.

A. *Redundancy in bands*

The data from seven band images (Fig. 1) is useful in

978-1-4799-2995-5/14/$31.00©2014 IEEE

assigning a specific class to each mixed pixel. However, some bands may contain redundant information which may not contribute to the resolution of mixed pixels. These bands can be excluded from the resolution process as keeping them requires extra memory and their inclusion makes the process of resolving pixels complex.

B. Sinusoidal MigrationModel

Earlier mixed pixels have been resolved using linear migration concept. In our proposed approach (Fig. 2), migration rates are obtained using sinusoidal migration concepts. The habitat to which immigration will occur, is decided on the basis of immigration rate [9]. For our problem, the habitat from which emigration will occur is restricted to the set of mixed pixels. Hence, only immigration rate is considered in the proposed algorithm.

$$\lambda = I/2[(\cos(\text{fitness} \times \pi) + 1] \quad (1)$$

I is the maximum immigration rate

The HSI is calculated from standard deviation using the selected bands as follows-

$$HSI = (\sum_{k=1\ to\ b} Sd(k))/b \quad (2)$$

$$Sd = \sqrt{((\sum_{i=1}^{m} dev(i))/m)} \quad (3)$$

$$dev(i) = (x_i - (\sum_{j=1}^{m} x)/m)^2 \quad (4)$$

b= number of selected bands (here b=3)
m = number of pixels in feature class
x = DN values in specific bands

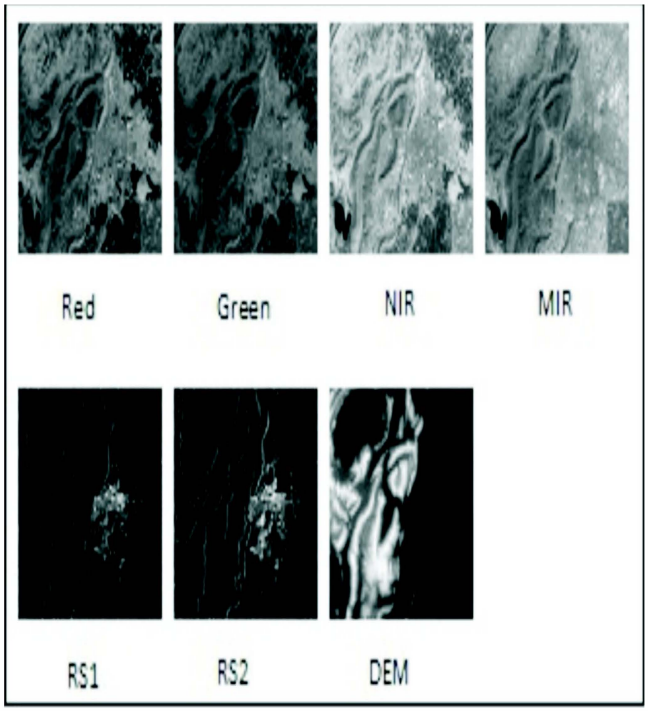


Figure 1. Seven Band images of Alwar, Rajasthan [7]

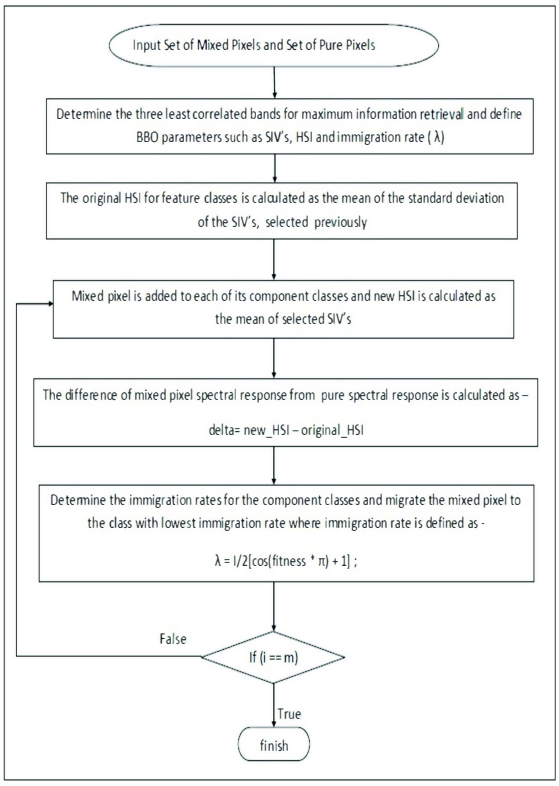


Figure 2. Our proposed algorithm

IV. METHODOLOGY

The image considered in this paper is multi-spectral multi-resolution and multi-sensor satellite image of Alwar area in Rajasthan [10]. This region is chosen as it contains large variety of land features like water, urban, vegetation, rocky and barren. The multi-spectral geo-referenced image-set consists of satellite images of dimension 472 X 546 pixels. The 4-spectral bands are in the visible bands namely: red, green, near- infrared (NIR) and middle infra-red (MIR) from LISS-III sensor of Indian Remote Sensing sat satellite Resourcesat-1.Also,two SAR images namely: low incidence S1 beam -200-270 (RS1) and other is High incidence S7 beam 450-490,(RS2) of the same area taken from Canadian Radarsat-1 satellite. The seventh band is digital elevation model (DEM) of the area. The ground is resolution of the image from LISS-III and Radarsat-1 image is 23.5m and 10m respectively. The DEM dataset is also generated from SAR interferometry using RS1 and RS2 and have 25-meter resolution [11].

Our dataset comprises of DN values of seven bands namely Red, Green, NIR, MIR, RS1, RS2, DEM of mixed pixels and training set for each seven bands. The training set has been provided by the expert. It consists of pure pixels of each feature class namely water, vegetation, urban, rocky and barren. Following is the dataset of few vegetation-barren mixed pixels (Table.3), pure vegetation (Table.1) and pure barren pixels (Table.2) which has been used in our approach.

Table 1 : Dataset of pure vegetation pixels

	A	B	C	D	E	F	G	H
1	RED	GREEN	NIR	MIR	RS1	RS2	DEM	DECISION
2	37	51	98	182	33	33	15	VEGETATION
3	35	49	95	179	20	30	15	VEGETATION
4	31	40	91	188	24	22	15	VEGETATION
5	37	51	98	182	30	35	15	VEGETATION
6	35	49	95	179	19	33	15	VEGETATION
7	31	43	87	199	23	26	15	VEGETATION
8	33	43	89	184	24	23	15	VEGETATION
9	29	43	89	186	26	26	15	VEGETATION
10	33	45	91	195	16	24	15	VEGETATION
11	29	41	93	182	23	19	15	VEGETATION

Table 2 : Dataset of pure barren pixels

	A	B	C	D	E	F	G	H
1	RED	GREEN	NIR	MIR	RS1	RS2	DEM	DECISION
2	115	91	182	126	20	15	30	BARREN
3	111	90	173	131	17	34	15	BARREN
4	121	91	182	118	26	17	40	BARREN
5	125	98	188	128	25	21	27	BARREN
6	130	94	186	128	24	33	25	BARREN
7	138	106	212	137	32	22	115	BARREN
8	170	127	234	159	37	45	100	BARREN
9	156	123	204	142	27	57	78	BARREN
10	113	86	190	113	24	28	53	BARREN
11	113	88	199	113	16	38	36	BARREN

Table 3: Dataset of urban-barren mixed pixels

	A	B	C	D	E	F	G	H
1	RED	GREEN	NIR	MIR	RS1	RS2	DEM	mixed
2	101	98	162	159	10	30	9	barren-veg
3	80	82	133	159	19	35	6	barren-veg
4	52	53	111	157	24	37	4	barren-veg
5	76	74	144	151	21	27	3	barren-veg
6	119	103	175	148	22	44	3	barren-veg
7	72	75	129	157	12	28	9	barren-veg
8	105	99	170	162	24	22	12	barren-veg
9	78	78	144	164	24	28	12	barren-veg

A. Problem definition

- The set of pure pixels denoting the land features on earth such as vegetation, rocky, water, urban and barren are analogous to the feature habitat.
- The seven bands are analogous to the SIV's . It is the SIV's that determine the fitness of the candidate solutions. The bands with relevant information for the mixed pixel are taken into consideration.
- HSI is calculated as the mean of standard deviations using DN values of feature habitat including least correlated bands.

B. Algorithm

The proposed algorithm has been implemented in MATLAB ver 7 [12]. The preprocessing steps include finding the subset of 'b' spectral bands to characterize the problem such that they are as much independent among themselves as possible. Thus, to determine right spectral bands, the eigen values for the correlation matrix are computed. The lower the eigen value, the less that factor contributes to the explanation of variances in the variables. Out of these, the number of eigen values that are greater than one are determined. This is the number of bands (SIV's) to be included in the algorithm.

In order to seek non redundant bands, correlation coefficient matrix is computed between vectors of seven bands for each feature class. Correlation quantifies the extent to which two quantitative variables, X and Y, go together. When high values of X are associated with high values of Y, a positive correlation exists. When high values of X are associated with low values of Y, a negative correlation exists. The bands with least value of correlation coefficient are chosen for further implementation in the proposed algorithm. The selected bands are then used to find HSI for pure pixels of each feature class. Then a mixed pixel is added to the both feature classes, to which it belongs. Their new HSI is calculated. The value of the difference between the two HSI's is normalized to [0,1] to obtain the fitness value. Using the fitness value, immigration rate is calculated for both feature classes after adding mixed pixel to it. Mixed pixel is migrated to the feature class whose immigration rate is less.

Input: The dataset of pure pixels as provided by the expert and the dataset of mixed pixels. The mixed pixel dataset includes pixels belonging to various classes such as urban-barren, rocky-vegetation, urban-vegetation etc.

Step 1: For each feature habitat, the correlation coefficient between every two bands is calculated for the seven bands using the correlation matrix. The least correlated bands are selected.

Step 2 : I and E are taken as unity initially. For every feature habitat, find Original_HSI using chosen bands as in (2) /*b= number of selected bands
r = numberof mixed pixels */

Step 3 : for(i=1 to r) do

a) Add Mixed pixel[i] to the pure pixels of the component feature classes say 'p' and 'q' to which this mixed pixel may belong.
b) Calculate New_HSI for each component class of mixed pixel as we calculated Original_HSI.
c) Delta = New_HSI – Original_HSI. Normalize Delta to get fitness value. Calculate λ for each component class as in (1).
d) If ($\lambda_p < \lambda_q$)
/*immigrate mixed pixel to feature class 'p'*/
else
/*immigrate mixed pixel to feature class 'q'*/
e) If(i!=r)
repeat step 3

Output : All the mixed pixels are resolved into their component classes (Fig. 3).

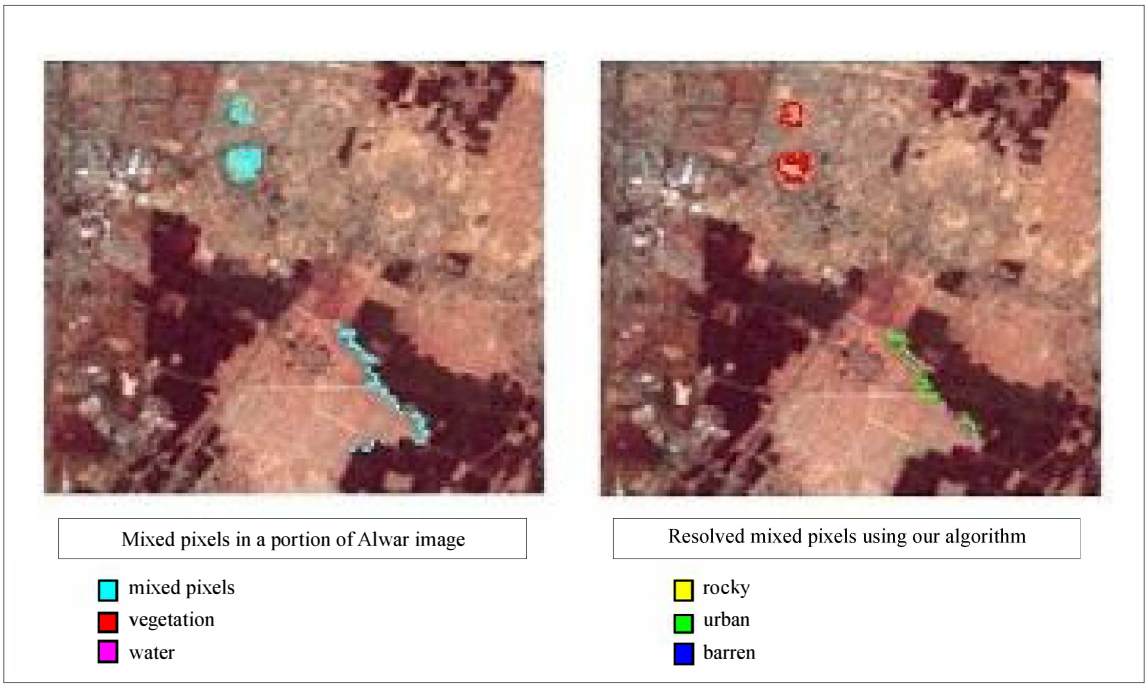


Figure 3. Resolved mixed pixels using our algorithm

Figure 3. Resolved mixed pixels using our algorithm

V. RESULTS AND DISCUSSION

This methodology resolves the mixed pixels more efficiently because it employs sinusoidal model which takes into account other factors as well, such as predator-prey relationships, population evolution etc. Figure 4 depicts the comparison ar

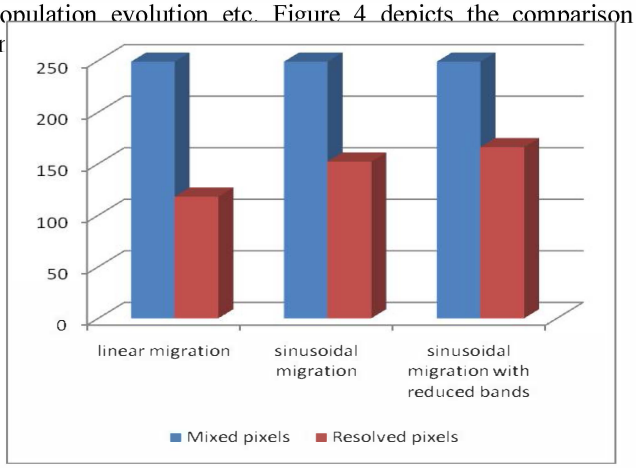


Figure 4. Analysis of sinusoidal migration Vs linear migration

Firstly, the results after including only sinusoidal model and including all the bands were analysed. This approach provides the better results than linear migration approach. However, application of sinusoidal approach after the removal of redundant bands, further improved the results.

Comparison of the resolved pixels with the original PSO/ACO classified image [13] shows that sinusoidal migration model incorporated with non redundant bands increases the efficiency of resolving Mixed Pixels by nearly 20% over the linear migration approach. The bar graph shows that more number of mixed pixels are resolved efficiently using our proposed approach. Sinusoidal migration resolves 66.67% mixed pixels as compared to linear migration which resolves nearly 47.38%. The result of few barren vegetation mixed pixels is as shown in Table. 4.

	A	B	C	D	E	F	G	H	I
1	RED	Green	NIR	MIR	RS1	RS2	DEM	mixed	decision
2	101	98	162	159	10	30	9	barren-veg	veg
3	80	82	133	159	19	35	6	barren-veg	veg
4	52	53	111	157	24	37	4	barren-veg	barren
5	76	74	144	151	21	27	3	barren-veg	barren
6	119	103	175	148	22	44	3	barren-veg	barren
7	72	75	129	157	12	28	9	barren-veg	veg
8	105	99	170	162	24	22	12	barren-veg	veg
9	78	78	144	164	24	28	12	barren-veg	veg

VI. CONCLUSION

The mixed pixels are resolved effectively using sinusoidal migration model because it matches the natural phenomenon more closely in a habitat. It takes into account predator/prey relationships, species mobility, evolution of particular species, and population size. These factors cause the migration curve to be a sinusoid. To avoid calculations involving redundant data, bands have been reduced. The reduced number of bands reduce computational overhead and memory space without

compromising the efficiency of the algorithm.

ACKNOWLEDGMENT

The authors would like to thank Nitish Gupta for providing required dataset and other helpful inputs on the topic.

REFERENCES

[1] Lillesand, T. M., Kiefer, R. W., & Chipman, J. W. (2004). *Remote sensing and image interpretation* (No. Ed. 5). John Wiley & Sons Ltd.

[2] Ma, H. (2010). An analysis of the equilibrium of migration models for biogeography-based optimization. *Information Sciences*, *180*(18), 3444-3464.

[3] Simon, D. (2008). Biogeography-based optimization. *Evolutionary Computation*, IEEE *Transactions on*, *12*(6), 702-713.

[4] Goel, L., Gupta, D., & Panchal, V. K. (2011). Information Sharing in Swarm Intelligence Techniques: A Perspective Application for Natural Terrain Feature Elicitation. *International Journal of Computer Applications*, 32(2).

[5] Panchal, V. K., Bhugra, D., Goel, S., & Singhania, V. (2011, April). Study on the behaviour of BBO over natural terrain features. In *Electronics Computer Technology (ICECT), 2011 3rd International Conference on* (Vol. 4, pp. 28-32). IEEE.

[6] Panchal, V. K., Goel, S., & Bhatnagar, M. (2009, December). Biogeography based land cover feature extraction. In *Nature & Biologically Inspired Computing, 2009. NaBIC 2009. World Congress on* (pp. 1588-1591). IEEE.

[7] Goel, L., Gupta, D., & Panchal, V. K. (2011, December). Performance governing factors of biogeography based land cover feature extraction: An analytical study. In *Information and Communication Technologies (WICT), 2011 World Congress on* (pp. 165-170). IEEE.

[8] Choodarathnakara, A. L., Kumar, T. A., Koliwad, S., & Patil, C. G. (2012). Mixed Pixels: A Challenge in Remote Sensing Data Classification for Improving Performance. *International Journal of Advanced Research in Computer Engineering & Technology (IJARCET)*, *1*(9), pp-261.

[9] Goel, L., Gupta, D., & Panchal, V. K. (2011). Hybrid bio-inspired techniques for land cover feature extraction: A remote sensing perspective. *Applied Soft Computing*, Elsevier publications, *12*(2), 832-849.

[10] Goel, L., Panchal, V. K., & Gupta, D. (2010). Embedding expert knowledge to hybrid bio-inspired techniques-an adaptive strategy towards focused land cover feature extraction. *International Journal of Computer Science & Information Security*, *8*(2), 244-253.

[11] Panchal, V. K., & Gupta, N. (2011, May). Swarm intelligence for mixed pixel resolution. In *IEEE Geo Sciences and Remote Sensing Symposium (IGRASS), pp-2801-2804*.

[12] MathWorks, Inc. (2005). MATLAB: the language of technical computing. Desktop tools and development environment, version7 (Vol. 9). MathWorks.

Energy and Exergy Analysis of A Wet Ethanol Based HCCI Engine Combined Cycle

Dr. Shailesh Kumar Trivedi, Dr. Ahmad Faizan Sherwani and Dr. Abid Haleem

Abstract--- *Homogeneous Charge Compression Ignition (HCCI) engine uses an advance combustion process with lean premixed air-fuel mixture and it works with high compression ratio like diesel engine. The charge is compression ignited and ignition occurs throughout the combustion chamber. Present system is proposed to meet the simultaneous demand of power and thermal energy from a sustainable fuel in efficient and environmental friendly manner. The paper describes the computational analysis of first and second law efficiencies of wet ethanol based HCCI engine with combined cycle cogeneration system by varying its turbocharger efficiency. An examination of results indicate that the first and second law efficiencies are increasing function with increase in efficiency of turbocharger compressor because it leads to higher HCCI engine work output due to efficient turbocharger.*

Keywords---*Cogeneration, First law efficiency, HCCI Engine, Second Law Efficiency, Turbocharger Efficiency, Wet Ethanol*

I. INTRODUCTION

HOMOGENEOUS Charge Compression Ignition (HCCI) is a new combustion process. Currently, it is a topic of research worldwide due to its potential to produce high efficiency with low emission. In an effort to combine the benefits of both SI and CI engines, Homogeneous Charge Compression Ignition engines are being developed. Efficient production of power in transportation sector through combustion engine is important work.In 1979, Onishi et al [1] discussed HCCI combustion and called it active thermo atmospheric combustion (ATAC) with two stroke engine. Further Thring R.H. [2] focused on the fundamental of premixed HCCI combustion in four stroke engines. The Homogeneous Charge Compression Ignition (HCCI) engine is an exciting concept because it uses a completely different form of ignition and combustion principles. Neither it uses spark plug to propagate turbulent flame as in gasoline engine, nor does it use high pressure fuel injector causing luminous diffusion flame as in diesel engine. The combustion in HCCI engine has multiple ignition points as in diesel engine rather than a single origin in gasoline engine. HCCI engines use high compression ratio and lean homogeneous mixtures which results the high efficiency and low NOx emissions [3].

The charge in HCCI engine is consumed by controlled auto ignition reactions. In ideal case, there is no occurrence of either the propagating flame front that characterizes SI combustion, or the diffusion burning that characterizes CI combustion. The vision of all engine designers is to find a combination of the diesel engine and the spark ignited engine that only take over the superior properties of these engines i.e. efficiency like a diesel engine and exhaust emissions that are as clean as from the SI engine. Christension et al [4] describes that the HCCI is the third alternative for combustion in internal combustion (IC) engines. They experimented with three different fuels i.e. Iso octane, ethanol and natural gas and compared the characteristics of HCCI combustion with SI combustion process and reported very little NO_X emission with HCCI and much better indicated efficiency than SI operation. This engine has multiple ignition points throughout the combustion chamber benefiting ultra low emission. Siewart [5] used a single cylinder diesel engine for evaluating HCCI engine by supplying externally prepared premixed, well vaporized air fuel mixture. Very low NO_X, near zero smoke, low combustion temperature and good thermal efficiency was obtained. Osberne et al[6] demonstrated a 99% reduction in NO_X emission for HCCI operation and HC emissions were comparable to other direct injection gasoline engine modes. Wet ethanol operated HCCI engine experimental work was made by Mach et al [7]. They investigated the effect the ethanol water fraction on the engine operating limits, intake temperature and exhaust emission.

The environmental impacts of automotive exhaust and depleting conventional fuels have lead to the development of new technology for the renewable fuel. Recently a lot of research is being carried out for the use of alternate fuels in HCCI engine. Mach et al [7] investigated 4-cylinder 1.9 liter engine running in HCCI mode fuelled with wet ethanol. They investigated the effect of ethanol water fraction on the engine's operating limits, exhaust emission, intake temperature and heat release rates. Saisirirat et al [8] investigated the auto ignition and combustion characteristics in HCCI using ethanol/n-heptane mixture with varying alcohol percentage up to 57% by volume. Diesel engine fuelled with alcohol/n-heptane blend was used at constant equivalence ratio of 0.3, with intake temperature at 80^0C operating at 1500 rpm. Wu et al [9] investigated the reduction in smoke and NO_X of a partial HCCI engine using premixed gasoline and ethanol as a fuel. The experiments were conducted under different engine speed of 1200, 1500 and 1800 rpm and at different loads. The results show the successful operation of HCCI engine with

Dr. Shailesh Kumar Trivedi, Dy. Director, DTTE, Ph D, Jamia Millia Islamia, Delhi, India

Dr. Ahmad Faizan Sherwani, Assistant Professor, Dept. of Mechanical Engineering, Faculty of Engineering and Technology, Jamia Millia Islamia, N. Delhi, India.

Dr. Abid Haleem, Professor, Dept. of Mechanical Engineering, Faculty of Engineering and Technology, Jamia Millia Islamia, N. Delhi, India. E-mail: haleem.abid@gmail.com

ISBN 978-93-83459-12-4 © 2014 Bonfring

ethanol resulting good efficiency and effectively reduced emissions

Numerical analysis of HCCI engine operating on wet ethanol was conducted by Frias et al [3] showing successful operation of HCCI engine with 35% ethanol in water. They obtained a very high brake thermal efficiency (38.7%). It was also emphasized that direct use of wet ethanol (35% ethanol in water mixture) improves the net energy balance in favour of wet ethanol production. The exergy analysis of HCCI engine was conducted by Trivedi et al [10] and Khaliq et al [11] to obtain the thermodynamic losses in terms of exergy destruction in all the components of HCCI engine by varying ambient temperature, turbocharger compressor efficiency and turbocharger pressure ratio. They found out that maximum exergy is destroyed in HCCI engine and in this way they have found out the reason of deviation between ideal and actual performance of wet ethanol operated HCCI engine.

II. COMBINED CYCLE COGENERATION SYSTEM

Conventional engines have low efficiencies, which imply that a greater part of the fuel energy is being converted to heat rather than shaft power and it is a continuous source of inefficiency and thermal pollution. Recovery of this waste heat for useful purpose of heating cooling and drying is one of the major objectives of engineers. All the engines exhaust a certain amount of heat through flue gases during the process of completing a power cycle as explained by laws of thermodynamics. The recovery of waste heat has become economically feasible and is being addressed today on very large scale and it is termed as cogeneration which is simultaneous production of power and useful heat. Various engineering applications throughout the world are also considering cogeneration system for improving efficiency and better utilization of resources as some of the rejected waste heat of the engine is put to good use. Cogeneration is the most promising commercially available technology.

Second low analysis of an automotive system and gas turbine based cogeneration system has been studied in the past by various investigators. Abusoglu and Kanoglu [12] analyzed the thermodynamic performance of an actual diesel engine cogeneration system. Exergy analysis was performed for this system to evaluate the exergy destruction in each component as well as exergetic efficiency. They found that the thermal efficiency of the overall plant is 44.2% and exergetic efficiency is 40.7%.Tuma et al [13] have derived the equations for calculation of the overall energetic and exergetic efficiency of a gas steam cycle cogeneration system. A comparison between energy and exergy efficiency has been performed. Oh et al [14] presented a most generalized exergy balance equation to evaluate the thermodynamic performance of gas turbine based cogeneration system. Their results revealed that recovery of waste heat at the gas turbine exhaust will make it more efficient and environment friendly. Tamura and Hagi [15] conducted an energetic analysis and investigated a natural gas fuelled homogeneous charge compression ignition engine cogeneration system and tested it by altering the intake air temperature, compression ratio etc. They found that the compression ratio is the most effective parameter in promoting the engine performance. Spentzas et al [16] discussed the benefits of a cogeneration in the automotive industry and examined several cogeneration prime movers of differing capabilities. Kanoglu and Dincer[17] conducted the performance assessment of various building cogeneration system through exergy analysis. They considered various cogeneration plants including steam turbine system, gas turbine system and diesel engine system etc. they further investigated the effects of certain operating parameters on the energy and exergy efficiencies of the system. It was finally concluded that exergy analysis is a useful tool in performance assessments of cogeneration systems and permits meaningful comparison of different cogeneration systems based on their merits. It was also concluded that use of cogeneration system leads to reduction in fuel and further reduction in environmental emission. Talom and Beyene [18] developed the mathematical model and also produced experimental test results for heat recovery from exhaust gases of an internal combustion engine to run absorption chillar. Their experimental results on the system, proved that the concept is feasible, and could significantly enhance system performance. They further suggested that the concept could be used for refrigeration and air conditioning of transportation vehicle. Descombes and Boudigues [19]presented some studies of cogeneration applications using gas turbines and thermal engines. They carried out a detailed study of thermodynamic modeling cycles with energy recovery and further concluded that the combined cycles with gas turbine and IC engine can generate a potential increase of about 10% of the energy efficiency.

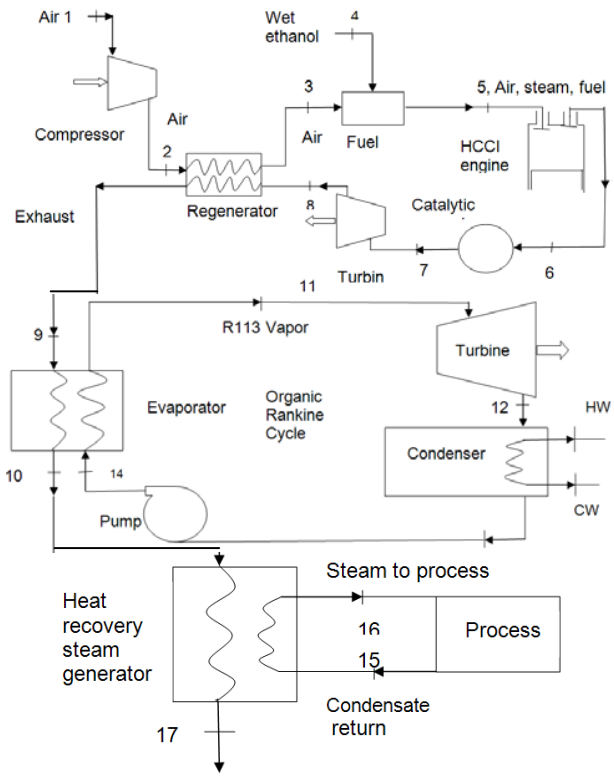


Figure 1: The schematic diagram of wet ethanol operated HCCI engine cogeneration system with organic Rankine cycle and process steam

ISBN 978-93-83459-12-4 © 2014 Bonfring

III. PROBLEM DEFINITION

Recovery of waste heat from gas turbines and internal combustion engines has been studied in the past however a little is reported on their exergy analysis in general and exergy analysis of cogeneration based HCCI engine in particular. This has provided us an area of research. The literature survey and the mathematical computational exergy analysis results so obtained substantiated a successful operation of HCCI engine with wet ethanol having good efficiencies and reduced emission. Exergy analysis of wet ethanol fuelled HCCI engine for cogeneration application is very much missing in the literature. Therefore in order to meet out the simultaneous demand of power and thermal energy from a sustainable fuel in efficient and environment friendly manner, an exergy analysis of wet ethanol fuelled engine in HCCI mode for cogeneration of power and heat has been carried out in this research paper. This paper describes the computational analysis of first and second law efficiencies and exergy destruction of wet ethanol based HCCI engine combined cycle cogeneration system by varying its turbocharger efficiency and pinch point. The magnitude of exergy destruction in various components of the cogeneration cycle has been evaluated by varying turbocharger compressor efficiency, pinch point, turbocharger pressure ratio, ambient temperature and effectiveness of regenerator.

IV. SYSTEM DESCRIPTION

A schematic diagram of the wet ethanol operated HCCI engine cogeneration system is shown in Figure 1. Ambient air enters the compressor which delivers air at high pressure and temperature followed by the regenerator, this raises the air temperature. Next liquid ethanol in water is injected into the vaporizer, where it evaporates and mixes with air. The evaporation process in the vaporizer produces a homogeneous mixture of ethanol, water vapor and air, which then enters the HCCI engine. The ethanol water air mixture inducted into the cylinder heats up as it mixes with residual gases within the cylinder. After combustion, exhaust gases enter the catalytic converter at a higher temperature and exit the converter at further higher temperature due to heat release from conversion of unburned fuel, hydrocarbon (HC) and carbon monoxide (CO) which were not reacted in the engine combustion chamber. Gases from catalytic converter at higher temperature flow into the turbine, generating power that drives the turbocharger compressor. After circulating through turbine, the exhaust gases exchange heat with the intake air in the regenerator and then leave the system at ambient pressure and higher temperature. These exhaust gases at higher temperature are assumed to be routed through the evaporator where heat transfer occurs between the exhaust stream and the organic working fluid (R113). In this study a counter flow heat exchanger (evaporator) configuration is considered to maximize heat transfer between the engine exhaust gases and the organic fluid. Thermodynamically this is preferred configuration because the temperature difference between the hot fluid and the cold fluid is minimized, thereby reducing the exergy destruction. The heated organic vapor is then expanded in the turbine, heat is rejected to the ambient in the condenser, and the cooled working fluid is pumped with pump, back in to the evaporator. Heat of hot exhaust gas is utilized in the heat recovery steam generator to generate steam and hence to produce the process heat. The hot exhaust entering the heat recovery steam generator is the waste heat source for the process heat production.

V. EXERGY DESTRUCTION MODEL

The scientific community is continuously developing new techniques for better utilization of resources. These resources are limited so there is need to take severe measures to eliminate waste and increase efficiency. The first law of thermodynamics deals with the quality of energy and asserts that energy cannot be created or destroyed. The second law deals with the quality of energy. It is concerned with the degradation of energy during a process, the entropy generation and the lost opportunity to do work. So it is used to optimize the complex thermodynamic systems.

Exergy is the maximum useful work that could be obtained from the system at a given state in a specified environment. Exergy is a property of the system-environment combination and the not the system alone. It represents the upper limit on the amount of the work a device can deliver without violating any thermodynamic laws. There will always be a difference, large or small, between exergy and actual work delivered by a device. This difference represents a scope for improvement in the system. The exergy destruction is the wasted work potential during a process as a result of irreversibilities. Development of exergy destruction model shows the analyst how the performance of a system departs from the ideal limit, to what extent each component contributes to this departure, and what can be done to design better (less irreversible) systems [20].

The general exergetic balance applied to a fixed control volume is given by Moran and Shapiro [21] as below in equation (1).

$$\sum \dot{Q}_j \left(1-\frac{T_0}{T_j}\right) - W + \sum_{in} \dot{m}_{in}\, e_{in} - \sum_{out} \dot{m}_{out}\, e_{out} - E_D = 0 \quad (1)$$

Where, $\dot{Q}_j$ is the heat transfer rate to the system, $\dot{W}$ the mechanical power produced by the system, $\dot{E}_D$ the irreversibility rate or exergy destruction, and e is the flow exergy associated with the stream of matter.

$$e = \sum_i [m_i((h_i - h_0) - T_0(s_i - s_0))] \quad (2)$$

Where, h_0& s_0 represent the specific enthalpy and specific entropy at dead state respectively. A system that is in equilibrium with its environment is said to be at the dead state. The properties of a system at dead state are denoted by subscript zero.

The relevant parameters required for the thermodynamic performance evaluation of the wet ethanol operated HCCI engine based cogeneration system may be considered as follows:

ISBN 978-93-83459-12-4 © 2014 Bonfring

- *First Law Efficiency* (η_f)

It can be defined as the ratio of all the energy in the useful product ($\dot{W}_{net}$ and $\dot{Q}_P$) to the energy of fuel input. Although it is an important quantity, it does not identify losses in utilization of fuel energy. By definition:

$$\eta_f = \frac{\dot{W}_{net} + \dot{Q}_P}{\dot{H}_f} \quad (3)$$

Where, $\dot{H}_f$ is the rate of heat supplied by the fuel.

$$\dot{W}_{net} = \dot{W}_{BT} + \dot{W}_{T,ORC} - \dot{W}_{P,ORC} \quad (4)$$

- *Power to Heat Ratio (energetic) Efficiency (RPH)*

The power to heat ratio compares the power output from the system to the heat output used as process heat. It is another parameter used to evaluate the thermodynamic performance of a cogeneration system which is defined as

$$R_{PH} = \frac{\dot{W}_{net}}{\dot{Q}_P} \quad (5)$$

In both, the first law efficiency and power to heat ratio, power and process heat are treated as equal. This reflects the first law of thermodynamics, which is concerned with quantity not energy quality. Thus η_f and R_{PH} are based on the first law of thermodynamics.

- *Second Law Efficiency* (η_{II})

Second law efficiency applies to the overall system. Power output is more valuable than the process heat according to the second law of thermodynamics. Unlike energy, the exergy is always destroyed in any real process. The amount of exergy supplied in the products to the amount of exergy associated with the fuel is more accurate measure of the thermodynamic performance of a system which is defined as

$$\eta_{II} = \frac{\dot{W}_{net} + \dot{E}_P}{\dot{E}_{fuel\ ,in}} \quad (6)$$

Where, $\dot{E}_{fuel\ in}$ is the exergy rate of fuel input and $\dot{E}_P$ is the exergy content rate of process heat which can be calculated as follows:

$$E_p = Q_p\left(1 - \frac{T_o}{T_p}\right) \quad (7)$$

VI. Result And Discussion

Cogeneration is applied to the wet ethanol operated HCCI engine system to enhance the system overall efficiency and to reduce the emissions. The properties of ethanol and related details are taken from Heywood [22] and Perry's chemical engineers hand book [23]. Processes in the engine are typical polytropic compression and expansion and near constant volume combustion as Otto cycle [6]. Equations used for evaluating performance parameters have been referred from Trivedi et al [10]. Fuel used is 35% ethanol in water mixture which improves the energy balance of ethanol production and it can efficiently run HCCI engine [3]. In order to increase the power output and to reduce the thermal pollution from the exhaust of HCCI engine, an organic Rankine cycle is employed. The thermodynamic equations to evaluate organic Rankine cycle (ORC) operating on R113 ($C_2Cl_3F_3$) are referred from Mago et al [24]. The analytical study conducted by Najjar and Radhwan [25] shows that R113 is the optimum choice because it gives the smallest and hence the most economical size of turbo expander. The result shows the use of exhaust heat as much as possible is an effective way to improve system power output and its efficiency. The primary purpose of wet ethanol operated HCCI engine combined cycle cogeneration system is to produce as much power as possible from the user's viewpoint. The process heat is a useful cycle by product. It is the final effort to obtain useful energy from input fuel. It increases the available energy of combined cycle cogeneration system. The thermodynamic equations to evaluate the process heat produced and temperature of the gas at the exit of HRSG are referred from Huang and Wang [26]. Wet ethanol fuel was considered for running HCCI engine cogeneration system. Fuel properties of ethanol, diesel, gasoline and natural gas are shown in table 2. Gasoline, diesel and natural gas are the mixture of hundreds of different hydrocarbon compounds, each having a dissimilar boiling point while ethanol fuel is essentially pure compound having simple molecular structure and a single boiling point. This causes gasoline, diesel and CNG to have a range of properties where as ethanol has a specific properties. The ethanol fuel has high octane number which allows for the use of higher compression ratios and improved thermal efficiency. Ethanol fuels are partially oxidized hydrocarbon. It burns efficiently and improves combustion efficiency. Higher heat of vaporization of ethanol greatly increases its evaporative cooling effect. This property tends to quench combustion. Vapor pressure is important for starting a cold engine because some of the fuel has to vaporize easily for the combustion in an engine.

Figure 2 shows the comparison of the behavior of HCCI engine, organic Rankine cycle, HCCI-ORC combined power cycle cogeneration system for its first law efficiency variation with the change in turbocharger compressor efficiency. The higher efficiency indicates the extent to which the system is well used for the intended task i.e. compression of ambient air and it also shows the capability of turbocharger to produce outcome effectively with minimum undesirable losses. So the compressor power requirement reduces with the increase in turbocharger efficiency. It is observed that the first law efficiency of HCCI engine increases with turbocharger efficiency due to production of more power by HCCI engine as the required compressor power reduces with increase in turbocharger efficiency and it further results in dropping of exhaust temperature from HCCI engine. This decrease in exhaust temperature renders lower energy content at the inlet of ORC evaporator resulting lower mass flow rate and finally lower power output yield from organic Rankine cycle. It leads

ISBN 978-93-83459-12-4 © 2014 Bonfring

to decreasing trend in ORC first law efficiency. The combined cycle cogeneration first law efficiency also increases with turbocharger efficiency. It is due to the fact that higher turbocharger efficiency results in higher engine output and lower process heat production and the contribution of the amount of power output is much higher than the amount of process heat production so the domination of HCCI works output over process heat results in increasing function of cogeneration system first law efficiency. The slightly increasing power to heat ratio is due to the fact that it is the ratio of marginally increasing work output of the cogeneration system and almost constant process heat from cogeneration HRSG.

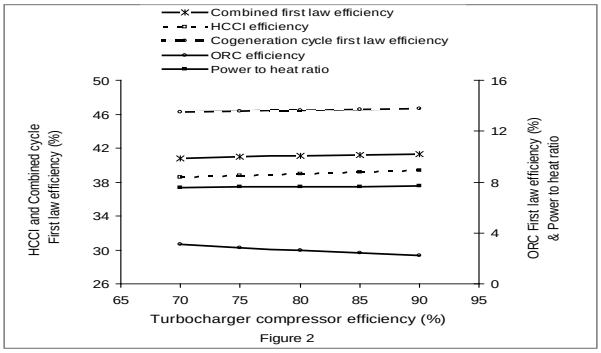


Figure 2

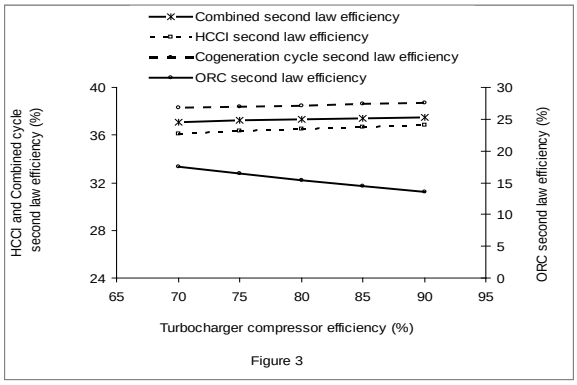


Figure 3

The effect of increase in turbocharger efficiency on second law efficiency of HCCI engine cogeneration system is shown in figure 3. The increase in turbocharger compressor efficiency finally leads to marginally reducing HCCI engine exhaust temperature and it shows lower value of exergy is expelled from the engine resulting slightly more work output and hence somewhat increasing trend of second law efficiency of HCCI engine. The similar trend in the second law efficiency of HCCI engine cogeneration system is also observed and it is due to the fact that the domination of increasing function of HCCI engine works output in the efficiency evaluation of overall cogeneration system. Further the reducing HCCI engine exhaust temperature is the heat source at the inlet of ORC evaporator and it has much lower exergy content than its energy content. That is why the second law efficiency of organic Rankine cycle is much higher than its first law efficiency. The overall decreasing trend in ORC second law efficiency is due to the fact that the decrease in net power output of ORC is more than the decrease in exergy content of the stack gases entering ORC evaporator.

VII. CONCLUSION

In this paper, we have evaluated the first and second law efficiencies of the HCCI engine cogeneration system. Here, the thermodynamic analysis of the wet ethanol operated HCCI engine cogeneration system is performed. Further the influences of turbocharger efficiency on the system performance and irreversibilities have been investigated. The fuel used is 35% ethanol in water mixture and this blend is formed in the process of ethanol production from biomass with nominal distillation energy consumption and further eliminating the need for energy intensive dehydration process. This study further explores the use of wet ethanol as a fuel for HCCI engines while using exhaust heat recovery to provide the high input energy required for igniting wet ethanol. The regenerator was used to preheat the intake air allowing HCCI combustion without electrical air heating. The thermal efficiency of the overall plant is found to be 46.47% and the exergetic efficiency is 38.5%.The main conclusions from the study can be summarized as follows:

- An examination of results indicate that the first and second law efficiencies are increasing function with pinch point of evaporator of organic Rankine cycle (ORC) as it provides higher exhaust gas temperature at the inlet of HRSG of cogeneration which further results in increasing the quantity of process heat for steam generation. It is concluded that the cogeneration cycle has a good thermal performance with first and second law efficiencies of 46.47% and 38.5% respectively for the mean operating conditions of T_0=300K, P_r=3, η_T=80%.
- The first and second law efficiencies are also increasing with increase in efficiency of turbocharger compressor because it leads to higher HCCI engine work output due to efficient turbocharger.
- Analysis of the results show that employing the HRSG in the engine enhances the first law efficiency of cogeneration system significantly and also second law efficiency appreciably
- HCCI engine cogeneration system offers thermodynamically efficient use of fuel as the waste heat is put to good use in ORC power production and HRSG process heat production.
- The organic Rankine cycle and heat recovery steam generator for process steam production is very effective to maximize exergy in HCCI engine application.
- Increasing the energy efficiency of the processes utilizing sustainable energy such as wet ethanol offers wide range of exceptional benefits.

It is always important to get a better insight and understanding of the sources of energy degradation so that a better and efficient system may be designed to achieve higher efficiency. This study contributes important information to the role of one of the operating variable and its influence on the thermodynamic performance of wet ethanol operated HCCI engine cogeneration system.

Heat recovery from automotive engines has been predominantly for turbo-charging or for cabin heating. Studies

ISBN 978-93-83459-12-4 © 2014 Bonfring

related to application of the recovered heat to run organic Rankine cycle (ORC) with HCCI engine is scarce. In this paper an ORC is attached with hot exhaust gases of HCCI engine. Mathematical model results suggest that the concept is thermodynamically feasible and could significantly enhance system performance of the engine. It will largely benefit considering the cost advantage particularly fuel cost in long run and emission control. This would definitely provide a right platform for rapid and qualitative development of internal combustion engines and will bring economic development.

REFERENCES

[1] S. Onishi, S.H. Jo, K. Shoda, P.D. Jo, S. Kato, Active thermo-atmosphere combustion (ATAC)-A new combustion process for internal combustion engines, SAE International, SAE Paper no. 790501, (1979).

[2] R.H. Thring, Homogeneous charge compression ignition (HCCI) engines, SAE International, SAE Paper no. SAE 892068, (1989)

[3] J.M. Frias, S.M. Aceves, D.L. Flowers, Improving Ethanol Life Cycle Energy Efficiency by Direct Utilization of Wet Ethanol in HCCI Engines, ASME Trans., Journal of Energy Resources Technology, 129, (2007), 332-337.

[4] M. Christension, B. Johansson, P. Einewell, Homogeneous charge compression ignition (HCCI) using isooctane, ethanol and natural gas-a comparision with spark ignition operation,SAE International, SAE Paper no. 972874, (1997).

[5] R.M. Siewart, Homogeneous charge compression ignition (HCCI) of gasoline like fuels in a single cylinder diesel engine, in: P. Duret (Ed), A new generation of engine combustion processes for the future, IFP International Congress,France, (2001), pp. 7-23.

[6] R.J. Osberne, G. Li, S.M. Sapsford, J. Stokes, T.H. Lake, M.R. Heikal, Evaluation of HCCI for future gasoline power trains, SAE International, SAE Paper No. 2003-01-0750, (2003).

[7] J.H.Mach, S.M. Aceves, R.W. Dibble, Demonstrating direct use of wet ethanol in a homogeneous charge compression ignition (HCCI) engine, Energy, 34, (2009), 782-787.

[8] P. Saisirirat, C. Togbe, S. Chanchaona, C. Foucher, M. Rousselle, and P. Dagaut,Auto- Ignition and Combustion Characteristics in HCCI and JSR Using 1-butanol/n-Heptane Blends, Proceedings of Combustion Institute, 33 (2), 2011, 3007-3014.

[9] H.W. Wu, R.H. Wang, D.J. Ou, Y.C. Chen, T.Y. Chen, Reduction of smoke and nitrogen oxides of a partial HCCI engine using premixed gasoline and ethanol with air, Applied Energy, 88(11), (2011), 3882-3890.

[10] S.K. Trivedi, A. Khaliq, P.B. Sharma, An examination of exergy destruction in wet ethanol operated HCCI engine based on first and second law analysis, in: Sharma et al (Eds) Proceedings of First International Conference on New Frontiers in Biofuel, DTU, New Delhi, India, 2010, pp295-305.

[11] A.Khaliq, S.K.Trivedi, I. Dincer, Investigation of wet ethanol operated HCCI engine based on first and second law analysis, Applied Thermal Engineering, 31(10), (2011), 1621-1629.

[12] A Abusoglu, M. Kanoglu, First and second law analysis of diesel engine powered cogeneration systems, Energy Conversion and Management, 49(8), (2008), 2026-2031.

[13] M. Tuma, J. Oman, M. Sekavenik, Efficiency of a combined gas steam process," Energ Convers Manage, 40, (1999), 1163-1175.

[14] S.D. Oh, H.S. Pang, S.M. Kim, H.Y. Kwak, Exergy analysis for a gas turbine cogeneration systems, ASME Trans., Journal of Engineering for Gas Turbines &d Power, 118, (1996), 782-791.

[15] M. Tamura, S. Hagi, An investigation of a natural gas fuelled homogeneous charge compression ignition engine for high performance cogeneration systems, SAE International, SAE Paper no. 2005-32-0005, (2005).

[16] S.N. Spentzas, M.J. Chimack, W.M. Worek, Optimization of a cogeneration system in the automotive industry, SAE International, SAE Paper no. 2006-01-0831, (2006).

[17] M. Kanoglu, I. Dincer, Performance assessment of cogeneration plants, Energy Conversion Management, 50(1), (2009), 76-81.

[18] H.L. Talom, A. Beyene, Heat recovery from automotive engine, Applied Thermal Engineering, 23(2-3), (2009), 439-444.

[19] G. Descombes, S. Boudigues, Modelling of waste heat recovery for combined heat and power applications, Applied Thermal Engineering, 29(13), (2009), 2610-2616.

[20] Y.A. Cengel, M.A. Boles, Thermodynamics: An Engineering Approach, 6th ed., Tata McGraw Hill Company Ltd, New Delhi, Special Indian Edition, 2008.

[21] M.J. Moran, H.N. Shapiro, Fundamentals of Engineering Thermodynamics, 6th ed., Willey New York, 2008.

[22] J. Heywood, Internal Combustion Engine Fundamentals, McGraw Hill, New York, 1988.

[23] D.W. Green, R.H. Perry, Perry's Chemical Engineer's Hand Book, 8th ed., McGraw Hill, New York, 2008.

[24] P.J. Mago, K.K. Srinivasan, L.M. Chamra, C. Somayaji, An examination of exergy destruction in organic Rankine cycles, International Journal of Energy Research, 32, (2008), 926-938.

[25] Y.S.H Najjar, A.M. Radhwan, Cogeneration by combining gas turbine engine with organic Rankine cycle, Heat Recovery System and CHP, 8(3), (1988)211-219.

[26] F.F. Huang, L. Wang, Thermodynamic study of an indirect fired air turbine cogeneration system with reheat, Transaction of ASME, 109, (1987), 16-21.

[27] C.R. Ferguson,A.T. Kirkpatrick, Internal Combustion Engines, John Wiley& Sons, NY, 2004.

ABOUT THE AUTHOR

Dr. Shailesh Kumar Trivedi is a Mechanical Engineer and presently posted as Deputy Director (TE/SD) at Directorate of Training and Technical Education, Govt. of Delhi, India. He is involved in the research of wet ethanol operated HCCI engine and its energy and exergy analysis. He received his Bachelor of Engineering from MNREC Allahabad and Master of engineering from Delhi College of engineering, Delhi. He recently completed his Ph. D. from Jamia Millia Islamia, New Delhi. He has published papers in the field of renewable energy, energy and exergy analysis, and thermal engineering in various international conference and international journals. He is a member of IE (India), member of ISTE and member of SESI.

Dr. Ahmad Faizan Sherwani is working as Assistant Professor, Department of Mechanical Engineering, Faculty of Engineering and Technology, Jamia Millia Islamia, since 2011 and has experience of over 12 years in research and teaching. Served various institutions as Delhi Technological University, UP Technical University at various positions. Expertise in the area of renewable energy, internal combustion engine, life cycle assessment. Published several research papers in international journal and conference in the area of solar energy and its application and use of alternative fuels in internal combustion engines. Has developed laboratory in Solar Systems at the department.



Dr. Abid Haleem is Professor of Mechanical Engineering Department, Faculty of Engineering & Technology since January, 2002. Presently he is Honorary Director Internal Quality Assurance Cell (IQAC) of Jamia Millia Islamia (A Central University by an Act of Parliament), New Delhi, India. He has served as Head, Mechanical Engineering and also Headed, MBA (Evening) program in his University. He has also been Honorary Visiting Professor at Department of Management Studies, IIT Delhi.

Professor Haleem has more than hundred research papers to his credit, published in good international and national journals. He is Regional Editor Asia Pacific, for Global Journal of Flexible Systems Management, published by Springer. He is on the advisory / research boards of various institutions. He is also involved in various institutional activities (focused institutions & universities) related to policy planning, administration, accreditation, curriculum design, admission, evaluation and examination process etc. He has produced more than fourteen Ph D.

ISBN 978-93-83459-12-4 © 2014 Bonfring

Volume 1 (2014) 232-236 ISSN 2347 - 3258
International Journal of Advance Research and Innovation

Experimental and Numerical Analysis of Negative Spring Back in V-Bending of if Steel

Rohit Shukla [a,*], Vijay Gautam [b]

[a] Department of Automobile Engineering, Delhi Technological University, Delhi, India
[b] Department of Mechanical Engineering, Delhi Technological University, Delhi, India

Article Info

Article history:
Received 1 January 2014
Received in revised form
20 February 2014
Accepted 28 February 2014
Available online 15 March 2014

Keywords
Spring Back,
IF Steel,
FEA

Abstract

One of the most sensitive features of sheet metal forming processes is the elastic recovery during unloading, called spring-back, which leads to some geometric changes in the product. This phenomenon will affect bend angle and bend curvature, and can be influenced by various factors. In this research, the effects of anisotropy i.e., the rolling direction of 0 o, 45 o and 90o of ultra low carbon steel Interstitial Free (IF) Steel in V- bending with a punch corner radii of 7.5mm, were studied by experiments and numerical simulations. Comparison between the experimental and the finite element simulation results are also presented and found to be in close agreement.

1. Introduction

The application of interstitial free (IF) or low carbon steel sheets for automotive use requires the control of spring-back because of their higher yield strength to elastic modulus ratio. After the press forming operations, the forming parts change their shapes to achieve the equilibrium with no external force. Spring-back is thus an elastically driven process that adjusts internal stresses to attain zero moment and force at each sheet location [1]. Also, under certain conditions, it is possible for the final bend angle to be smaller than the original angle. Such bend angle is referred to as spring-go or spring-forward [2]. The amount of spring-back/ spring-go is influenced by various process parameters, such as tool shape and dimension, contact friction condition, material properties, sheet anisotropy, and sheet thickness [3].

Many research conducted recently have shown the importance of spring-back in sheet metal industry, and studied how this permanent physical variation can be avoided. It is known that different spring-backs are possible regarding die design and convenience of the material. A combination of various materials and processes make it difficult to obtain the predicted spring-back. Material parameters such as elasticity, yield stress, hardening property, and process parameters such as the load applied, thickness of sheet metal, die angle, punch radius and die gap affect spring-back in a complex way [4].

In the research conducted by Tan et al. [4], a simple method is proposed to prevent the spring-back. In this method, sheet metal is exposed to a set of loading and unloading process. Each bending angle and the corresponding spring-back values are measured, and the output signal is computerized. Thus, the appropriate press depth of the punch, which corresponds to excessive bending, is determined.

The first objective of the research conducted by Shu and Hung [5] was to employ finite elements method to analyze the relation between coupled bending technique, springback and variables. Later, in order to reduce spring-back and find optimum shaping parameters, they combined the finite elements analysis and optimization techniques. The results obtained from the study were compared with the experimental data, and it was concluded that increasing die gap results in reduction of spring-back values. Yuan [6] tried to lessen spring-back, in the material subjected to plastic deformation, through redistribution of elastic stresses inside the material after the release of the affecting load.

In this paper, experimental and numerical studies of the effects of sheet anisotropy on spring-back/spring-go in V-die for Interstitial Free (IF) steel sheet have been conducted. The results of the experiments were also compared with those of the

Corresponding Author,
E-mail address: the.rohit.shukla@gmail.com
All rights reserved: http://www.ijari.org

finite element analysis. In addition, the results obtained from the two bending processes were also compared.

2. Methodology & Experimental Results

2.1 Mechanical Properties of IF Steel

The tension tests were carried out as per ASTM E 8M-04 (2004) on 10kN table top *UTM-Tinius Olsen* machine in metal forming laboratory at DTU Delhi. The extra low carbon steel sheets of IF grade was tested for the tensile propertites. The Sheet thickness is 1.2 mm which is denoted by the symbol A1. The Stress Strain curve is plotted for all the specimens.

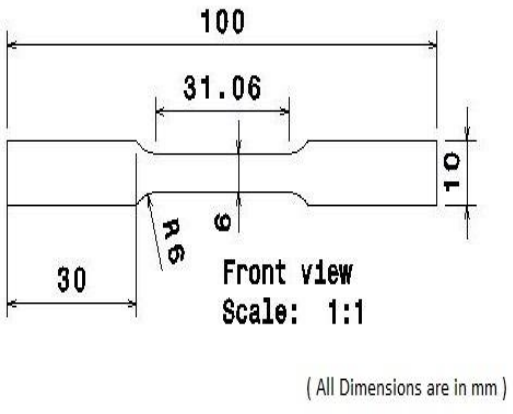


Fig: 1. Sample Size according to ASTM E8M-04 tested in UTM

The typical stress strain curve obtained from the tests is shown in figure 2. Since the departure from the linear elastic region cannot be easily identified, the yield strength was obtained using the 0.2 % offset method. UTS was determined for the maximum load and original cross sectional area of specimen.

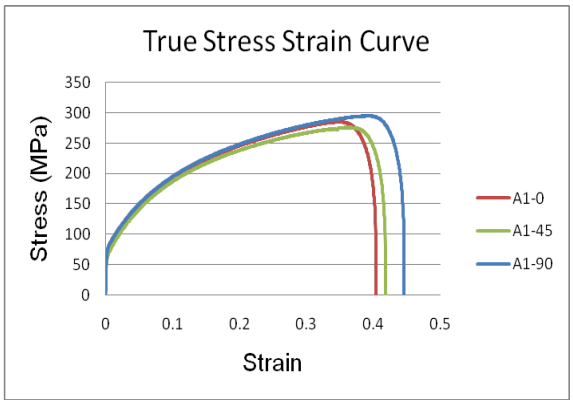


Fig: 2. True Stress Strain Curve for IF Steel

The strain hardening exponent (n) and the strength co efficient (K) values are calculated from the stress strain data in uniform elongation region of the stress strain curve. The plot of log (true stress) vs log (true strain) which is a straight line is plotted. The power law of strain hardening is given as :

$\sigma = K \epsilon^n$ (1)

Where, σ and Є are the true stress and the true strain respectively.

Taking log on both sides

$\log(\sigma) = \log(K) + n \log(\epsilon)$ (2)

This is an equation of straight line, the slope of which gives the value of "n" and "K" can be calculated taking the inverse log of the y intercept of the line (i.e log (K)).

The % elongation or the reduction in cross section area is used as a measure of ductility of material. % elongation values were calculated at the fracture. The elongation was measured by fitting together the fractured specimen.

Table: 1. Mechanical Properties of IF steel for all the samples in different rolling direction

IF-steel	0.2%-offset yield σ_y (MPa)	$\sigma_{(UTS)}$ (MPa)	Strain hardening exponent 'n'	Strength coefficient 'K'(MPa)	% Elongation
A1-0	123.33	205.55	0.343	428.37	48.88
A1-45	124.351	209.787	0.336	432.25	51.52
A1-90	124.28	207.57	0.32	414.47	48.75

2.2 Experimental Work for Spring Back or Spring Forward

In this experiment an offset was provided of the thickness of the blank i.e., 1.2 mm to allow the full displacement of punch and clearance of 0.5 mm was provided between the Die and lower surface of blank to prevent any type of excess punch holder force on blank to avoid the effect of sheet material on spring back, due to squeezing action of the bending section

(profile). As soon as the punch reached the last point of depth, it was removed and the punch load was relieved instantly. Figure 3 shows the diagrammatic view of complete setup.

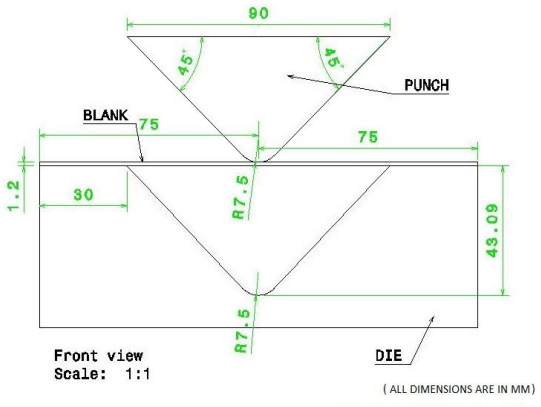


Fig: 3. The schematic diagram of complete Set-up

Here,

Φ_b = Initial Bend Angle

Φ_m = Measured Angle after experiment

Now, let $\frac{(180 - \Phi_b)}{2}$ (3)

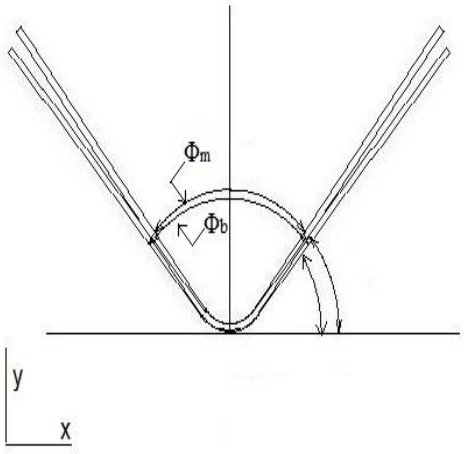


Fig: 4. Diagram to show Spring Forward

$$\theta_m = \frac{(180 - \Phi_m)}{2} \quad (4)$$

Therefore, the spring back of the IF Steel can be calculated by subtracting equation (4) from equation (3) , we get

$$\delta = \theta_b - \theta_m \quad (5)$$

Table: 2. Spring Forward data from performed experiment

IF-steel	Φ_{bE}	Φ_{mE}	θ_{bE}	θ_{mE}	$\delta_E = (\theta_{bE} - \theta_{mE})$ Springback(deg)
A1-0	90°	86.32°	45°	46.84°	-1.84°
A1-45	90°	86.58°	45°	46.71°	-1.71°
A1-90	90°	86.98°	45°	46.51°	-1.51°

3. Experimental Results Validation with Fea

The numerical model developed in this study considers a finite displacement of punch of PCR 7.5 mm on the blank to provide bending to the blank which was placed on the die. During bending process no blank holder forces acts on blank and thus after complete bending it is in perfect V Shape of different angle with respect to bend angle.

The clearance of 0.5 mm was provided between the Die and lower surface of blank to prevent any type of excess punch holder force on blank to avoid the effect of sheet material on spring back, due to squeezing action of the bending section (profile). As soon as the punch reached the last point of depth, it was removed and the punch load was relieved instantly. The Coefficient of friction between Blank and Punch is taken as 0.125 and coefficient of friction between Blank and Die is taken as 0.05. The Modulus of Elasticity is taken as 210 GPa and Poisson's ratio is taken as 0.3. The subsequent pages of this chapter show the bending of sheet.

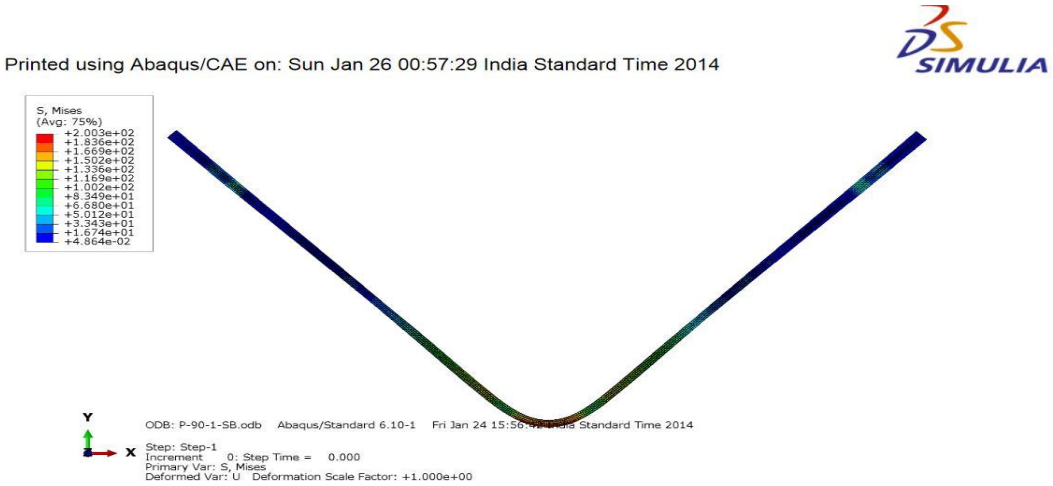


Fig: 5. Overlay Plot of the Specimen A1-0 of both spring Forward with Bend Angle

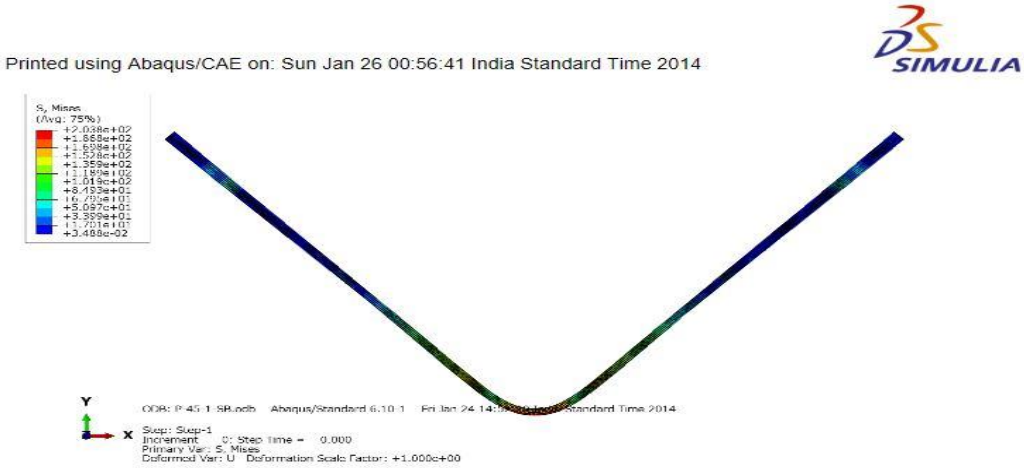


Fig: 6. Overlay Plot of the Specimen A1-45 of both Spring Forward and Bend Angle

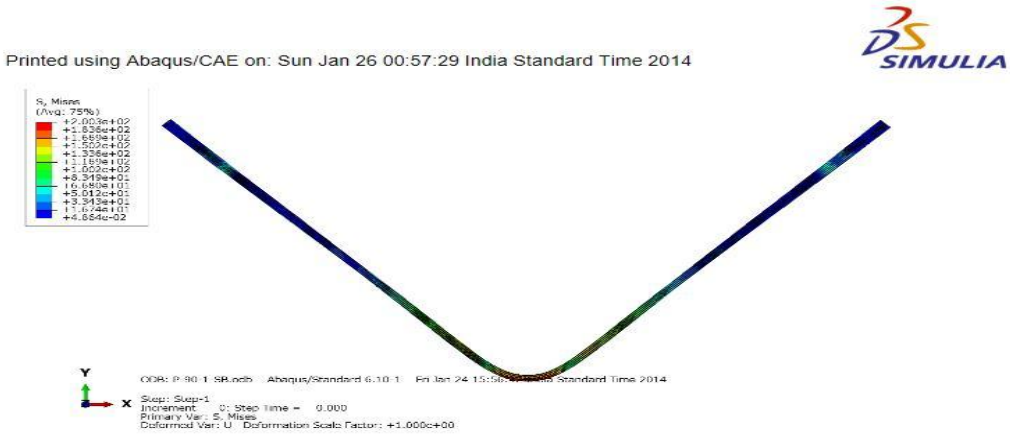


Fig: 7. Overlay Plot of the Specimen A1-90 of both Spring Forward and Bend Angle

Combined result of negative springback is formulated in Table 3 and comparison of negative springback obtained from experimental as well as from FEA is also shown.

Table: 3. Spring Forward data from FEA and its comparison with experimental values

IF-steel	ΦbFEA	ΦmFEA	θbFEA	θmFEA	δFEA	δE
A1-0	90°	87.65°	45°	46.17°	-1.17°	-1.84°
A1-45	90°	88.10°	45°	45.95°	-0.95°	-1.71°
A1-90	90°	88.40°	45°	45.80°	-0.80°	-1.51°

4. Conclusion

The mechanical properties of IF Steel were experimentally studied. IF steel depicts soft and ductile behavior with 49% of elongation on an average. The material is highly anisotropic affecting the bend angles with respect to rolling direction. During bending of sheet specimens, spring-forward takes place instead of spring back. At very small R/t ratios, this may even result in negative springback [7].

The Spring Forward has been studied in V-bending force and its effect on the negative Spring Back has been analysed using Abaqus CAE. The numerical model confers to the theoretical concepts of Bending and the results obtained are in agreement.

References

[1] W. Hosford, R. Caddell, Metal forming: Mechanics and Metallurgy, Prentice Hall, NJ, 1993

[2] S. Kalpakjian, S. R. Schmid, Manufacturing Engineering and Technology, Prentice Hall, NJ, 2001

[3] Ragail, D. Lazim, A. Nemes, Anisotropy and spring back in draw-bending of stainless steel 410: experimental and numerical study. J Mater Process Technol 2005; 166:116-27

[4] Z Tan, B Persson, C. Magnusson, Empirical model for controlling spring back in V-die bending of sheet metals. J Mater process Technol 1992; 34 (1-4); 449-55

[5] J. Shu, C. Hung, Finite element analysis and optimization of spring back reduction: the double bend technique. Int J Mach tool Manu 1996; 36(4):423-34

[6] WYD. Yuan, Generalized solution for the prediction of spring-back in marinated strip, J Mater Process Tedchnol 1996; 61(3):254-64

[7] Gedeon Mike, Elastic Springback, Technical Tidbits, Issue 11-2009

Volume 1 (2014) 166-173 ISSN 2347 - 3258
International Journal of Advance Research and Innovation

Experimental Investigation on Hydrodynamic Journal Bearing using SAE 10W30 Multi Grade Oil

Paras Kumar *, Ashish Kumar Gupta

Department Of Mechanical Engineering, Delhi Technological University, Delhi, India

Article Info

Article history:
Received 2 January 2014
Received in revised form
29 January 2014
Accepted 20 February 2014
Available online 15 March 2014

Keywords

Hydrodynamic Bearing,
Pressure distribution,
Thick film Lubrication,
Journal bearing,
Multi Grade oil

Abstract

This paper presents an experimental study of pressure distribution on hydrodynamic journal bearing with SAE 10W30 multi grade oil. Hydrodynamic Journal bearing test rig (HJBTR) is used to test the 40 mm diameter and 40 mm long bearing (l/d = 1) made of Bronze. Test bearing is located between two antifriction bearings and loaded mechanically. The space between the shaft and the bearing is filled with SAE 10W30. A constant load of 800 N is applied at various journal rotational speeds of 1000, 1500, 2000 rpm. Various parameters like frictional torque, oil temperature and pressure at 10 different sensors along circumferential direction were recorded from Hydrodynamic Journal Bearing Test Rig (HJBTR). These results were used for experimental calculations and theoretical verification using Raimondi and Boyd charts for practical design. The experimental plot of pressure ratio vs sommerfeld number indicates that the working conditions are in the stable hydrodynamic regime. Also experimental results were following the same trend as MCKEE's investigation curve.

1. Introduction

Hydrodynamic Journal bearing is a critical power transmission component that carry high load in different machineries. It is essential to study the performance characteristics under the different loading and operating conditions. The behaviour of Hydrodynamic Journal Bearing is also dependent on lubricant used and can be studied experimentally with the help of a test rig.

Numerous studies of the operating conditions of Hydrodynamic Journal Bearing have been made during the last decades. Ma and Taylor [1] carried out a theoretical and experimental study of thermal effects in a plain circular journal bearing under steady load. Baskar et al. [2] analysed the pressure distribution on hydrodynamic journal bearing under different Bio lubricants. Gethin [3] studied the thermal behavior of various types of high speed journal bearings and found good agreement with theoretical and the experimental results. Chun [4] examined the effect of Variable specific heat on maximum pressure, maximum temperature, bearing load, frictional loss journal. Now when the journal starts rotating, then at low speed and side leakage in high-speed journal bearing. Film pressure, load-carrying capacity attitude angle, end leakage flow rate, frictional coefficient and misalignment moment were calculated for different values of misalignment degree and eccentricity ratio. It was found that there are obvious changes in film pressure distribution, the highest film pressure, film thickness distribution, the least film thickness and the misalignment moment when misalignment takes place. Sep [5] investigated the oil flow velocity, pressure and temperature distribution of a journal bearing with a two-component surface layer. After all such studies, still the case is far from closed. There are a limited number of studies that carry out an in-depth examination of the true operating conditions of bearings in actual experiments upon the test rig with different oils. There is also a need for experimental studies to verify the theoretical ones.

Corresponding Author,
E-mail address: paraskum007@rediffmail.com
All rights reserved: http://www.ijari.org

2. Theory of Hydrodynamic Journal Bearing

Fig-1 shows the operation of Hydrodynamic Journal Bearing. When the journal is at rest, it touches the bush due to bearing load P at the lower most position and there is no oil film between the bush and the

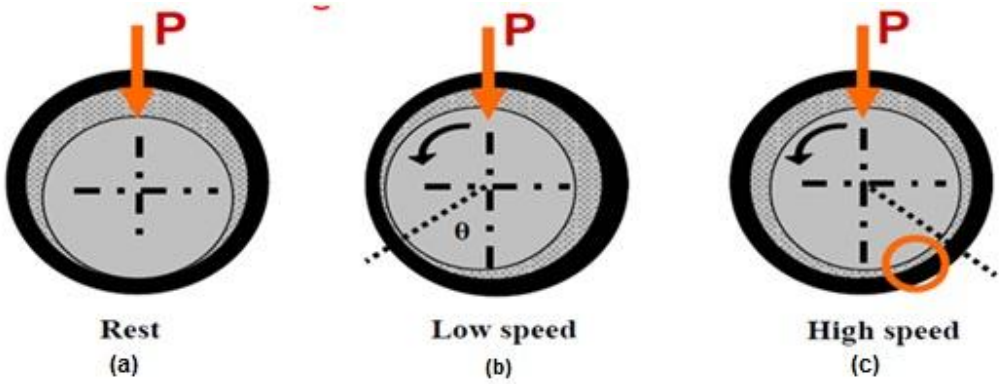


Fig: 1. Operation of journal bearing

condition, with the load P acting, it has a tendency to shift to its sides as shown in the Fig-1 (b). At this equilibrium position, the frictional force will balance the component of bearing load. In order to achieve the equilibrium, the journal orients itself with respect to the bush. The angle θ, shown for low speed condition, is the angle of friction. Normally at this condition either a metal to metal contact or an almost negligible oil film thickness will prevail. At the higher speed, the equilibrium position shifts and a continuous oil film will be created as indicated in the Fig-1 (c). This continuous fluid film has a converging zone, which is shown in the magnified view. It has been established that due to presence of the converging zone or wedge, the fluid film has sufficient pressure to support the heavy load. Hence, to build-up a positive pressure in a continuous fluid film, to support a load, a converging zone is necessary. Moreover, simultaneous presence of the converging and diverging zones ensures a fluid film continuity and flow of fluid. The Pressure distribution in Hydrodynamic Journal Bearing is shown in Fig-2.

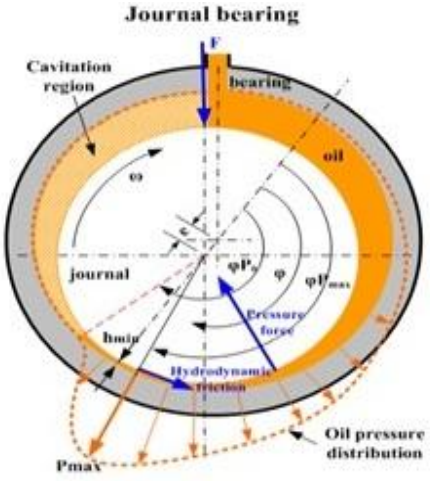


Fig: 2. Pressure distribution [12]

The action of the rotating journal is to pump the lubricant around the bearing. The lubricant is pumped into a wedge shaped space. A minimum film thickness occurs, not at the bottom but slightly displaced. This is explained by the fact that the film pressures in the converging half reaches a maximum somewhere to the left of the bearing center. The wedge shaped fluid film applies a perpendicular force to the bearing, whose one component is vertical which supports the load [6].

2.1 Petroff 'S Equation

In 1883, Petroff published his work on bearing friction based on simplified assumptions.

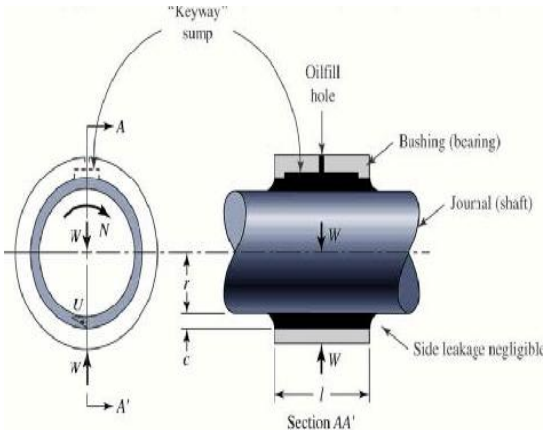


Fig: 3. Petroff's lightly loaded journal bearing [9]

With reference to Fig-3, an expression for viscous friction drag torque is derived by considering the entire cylindrical oil film as the "liquid block" acted upon by force W.

From Newton's law of Viscosity:

$$\tau = \mu \frac{U}{h} = \frac{2\pi r \mu N}{c} \quad (1)$$

The torque is the force times the lever arm and calculated as

$$T = (\tau A)(r) = \left(\frac{2\pi r \mu N}{c}\right)(2\pi r l)(r) = \frac{4\pi^2 r^3 l \mu N}{c} \quad (2)$$

Pressure (p)= W/2rl
Frictional torque is given by [7]

$$T = fWr = (f)(2rPl)(r) = 2r^2 flP$$

Substituting the value of torque from eq. (2) and (3) and the coefficient is expressed as

$$f = 2\pi^2 \frac{\mu N}{P} \frac{r}{c} \quad (4)$$

When the journal is not concentric i.e. there is some eccentricity "e" between the journal and bearing, then Petroff's equation takes the form:

$$f = K_1 \frac{\pi^2}{30} \left(\frac{\mu N}{P}\right) \left(\frac{r}{c}\right) \quad (5)$$

where,

$$K_1 = \frac{1}{\sqrt{1-\left(\frac{e}{c}\right)^2}} \quad (6)$$

2.2 McKee'S Investigation

The different regimes of operation were further investigated by McKee brothers. Fig-4 shows a plot of variation of Coefficient of Friction (f) with Bearing Characteristic Number $\left(\frac{\mu N}{p}\right)$.

The plot shows that initially there is a very high friction between the journal and bearing as there is no fluid film between the two. As the Journal speed is increased value of friction drops drastically. This region [From A to B] is referred as Boundary sometimes

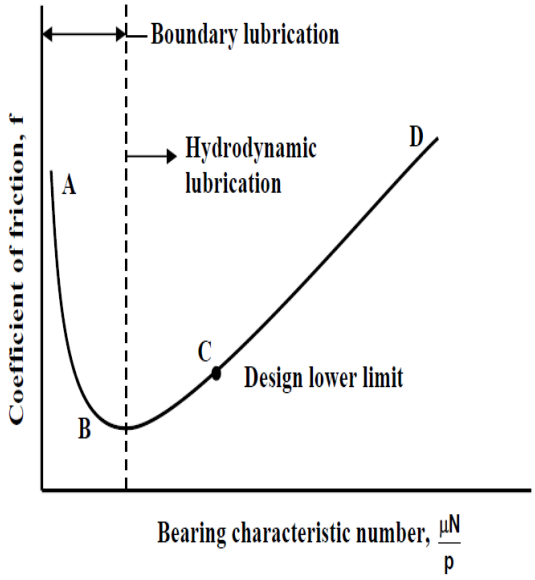


Fig: 4. Mckee's investigation curve [9]

termed as imperfect lubrication. Imperfect lubrication means that metal – metal contact is possible or some form of oiliness will be present. The portion from B to D is known as the hydrodynamic lubrication .The calculated value of bearing characteristic number should be somewhere in the zone of C to D. This zone is characterized as design zone.

For any operating point between C and D due to fluid friction certain amount of temperature generation takes place. Due to the rise in temperature the viscosity of the lubricant will decrease, thereby, the bearing characteristic number also decreases. Hence, the operating point will shift towards C, resulting in lowering of the friction and the temperature. As a consequence, the viscosity will again increase and will pull the bearing characteristic number towards the initial operating point. Thus a self control phenomenon always exists. For this reason the design zone is considered between C and D. The lower limit of design zone is roughly five times the value at B. On the contrary, if the bearing characteristic number decreases beyond B then friction goes on increasing and temperature also increases and the operation becomes unstable.

Therefore, it is observed that, bearing characteristic number controls the design of journal bearing and it is dependent of design parameters like, operating conditions (temperature, speed and load), geometrical parameters (length and diameter) and viscosity of the lubricant.

Volume 1 (2014) 166-173 ISSN 2347 - 3258
International Journal of Advance Research and Innovation

2.3 Reynols's Equation

Theory of hydrodynamic lubrication is based on differential equation derived by Osborne Reynold.

$$\frac{\partial}{\partial x}\left(\frac{h^3}{12\mu}\frac{\partial p}{\partial x}\right)+\frac{\partial}{\partial z}\left(\frac{h^3}{12\mu}\frac{\partial p}{\partial z}\right)=\frac{U}{2}\frac{\partial h}{\partial x} \quad (7)$$

The left hand side of the equation represents flow under the pressure gradient. The corresponding right hand side represents a pressure generation mechanism. In this equation it has been assumed that the lubricant is incompressible and Newtonian [8].

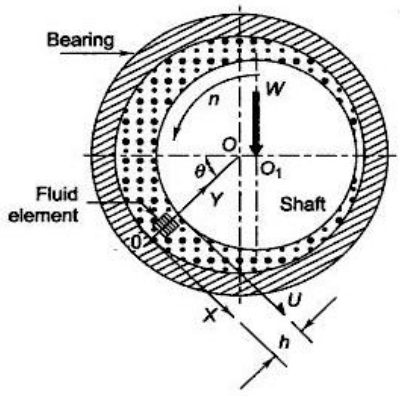


Fig: 5. Fluid element in X-Y plane

Solutions to Reynolds equation were developed in first decade of 20th century and were applicable for long bearings and give reasonably good results for bearings with(l / d) ratios more than 1.5. Ocvirk's short bearing approximation on the other hand gives accurate results for bearings with (l /d) ratio up to 0.25 and often provides reasonable results for bearings with (l / d) ratios between 0.25 and 0.75. Raimondi and Boyd have obtained computerized solutions for Reynolds equation. (7) and reduced them to chart form which provide accurate solutions for bearings of all proportions [9].

3. Experimental Setup

Experimental test was carried out using a Hydrodynamic Journal Bearing Test Rig (HJBTR) TR-660 shown in Fig-6, (designed by Ducom instruments Ltd, Bengaluru). It is versatile equipment for easy operation and measuring the pressure distribution on journal and also designed to ensure laminar oil flow in the bearing. The rig was designed to enable operation close to the limit of stability to be investigated. The lubricant was supplied to the bearing at an inlet port on the vertical centre line of the bearing, in the cavitated region of the bearing clearance; the oil exited the bearing in an axial direction and was collected at drain positions before being returned to the oil supply tank. 10 no's of pressure sensors are mounted on the face of bearing to measure Pressure distribution of the oil along the bearing circumference. Also loading arm is pivoted to get 1:5 loading ratio, exerts pressure on bearing through a roller when dead weights are placed on pan in the longer end. A counter weight is fixed on short end of lever to balance lever. This tester mainly consists of a rotating journal held in a special bearings in horizontal condition, it is rotated by AC motor and speed controlled by variable frequency drive. A bearing having l/d ratio=1 & c/r ratio=0.00135 is inserted over the journal and held in position by a loading lever. Bearing Pressure distribution on journal is displayed at different indexing angles on PC. When journal rotates, pressure created inside is measured & displayed on PC, depending on setting on PC the stepper motor rotates and indexes the bearing the value is measured and plotted on PC.



Fig: 6. Hydrodynamic Journal bearing test rig [11]

4. Experimental Parameters

The bearing performance characteristics were obtained for the following parameters:

1. Constant loading of 800N.
2. Journal speed variation from 1000 to 2000 rpm.
3. Lubricant used : Mobil 1 SAE 10W30
4. Ambient Temperature: 31℃-32℃.
5. Material for bearing : Bronze

The oil used contain viscosity modifier to stabilize its viscosity over a wide range of operating temperature. Typical properties are elaborated in the Table-1. From Hydrodynamic journal Bearing Test Rig (HJBTR), the values of frictional torque (T), oil inlet temperature, and pressure distribution were measured throughout the region. The measured parameters are shown in observation Tables- 2 and 3.

Table: 1. Typical Properties of Mobil 1 10W-30

S No.	Properties	Values
1.	SAE Grade	10W-30
2.	Viscosity @ 100ºC, cSt (ASTM D445)	10.1
3.	Viscosity, @ 40ºC, cSt (ASTM D445)	63.2
4.	Viscosity Index	146
5.	Sulfated Ash, wt% (ASTM D874)	0.8
6.	HTHS Viscosity, mPa.s @ 150ºC (ASTM D4683)	3.0
7.	Pour Point, ºC (ASTM D97)	-42
8.	Flash Point, ºC (ASTM D92)	232
9.	Density @15.6 ºC, g/ml (ASTM D 4052)	0.859

Table: 2. Observation Table

S No.	Load (N)	Journal Speed (rpm)	Frictional Torque (N-m)	Oil Inlet Temp. (°C)	Maximum Pressure (MPa)
1.	800	1000	0.72	38.30	0.999
2.	800	1250	0.77	39.60	0.998
3.	800	1500	0.78	39.90	0.994
4.	800	1750	0.82	41.60	0.989
5.	800	2000	0.84	42.90	0.984

Table: 3. Detailed pressure readings at 800 N Load

S No.	Journal Rotational Speed	Radial Pressure variation Distribution at 10 Different Sensors (MPa)									
	Rpm	P1	P2	P3	P4	P5	P6	P7	P8	P9	P10
1.	1000	0.876	0.781	0.768	0.800	0.866	0.971	0.999	0.896	0.742	0.734
2.	1250	0.875	0.775	0.748	0.783	0.860	0.968	0.997	0.892	0/740	0.735
3.	1500	0.878	0.766	0.739	0.765	0.858	0.960	0.994	0.890	0.742	0.737
4.	1750	0.877	0.766	0.737	0.762	0.855	0.951	0.991	0.890	0/739	0.734
5.	2000	0.876	0.764	0.735	0.759	0.848	0.942	0.984	0.888	0.738	0.737

5. Results and Discussion

The experimentation performed on the test rig with SAE10W30 oil at Constant load and varying rpm showed that the oil contains uniformly dispersed bubbles with a constant radius under atmospheric pressure. It was assumed that the bubbles remain spherical in the oil film and no interference, no break and combination between bubbles take place. Table 4 shows the comparison between theoretical (calculated by Raimondi and Boyd charts) and experimental (calculated by frictional torque obtained from test rig) values of coefficient of friction.

Table-4 Relative Error for Coefficient of Friction

S No.	Load (N)	Rpm variation	Coefficient of friction (experimental)	Coefficient of friction (theoretical)	% Error
1.	800	1000	0.0167	0.0121	29
2.	800	1500	0.0181	0.0135	31.8
3.	800	2000	0.0205	0.0162	23.4

Table 5 shows the comparison between theoretical and experimental values of pressure ratio (p/pmax.). The circumferential pressure distribution at different rpm is presented in Fig-7. Also variation of frictional coefficient (f) with bearing characteristic number (μn/p) is shown in Fig-8 and the variation of pressure ratio (p/pmax.) with sommerfeld number is shown in Fig-9. It is clear from the Fig-8 that with the increase in rpm, value of (f) increases throughout the region and thus it lies on the right side of the Mckee's curve. It also states a thick film lubrication and not any mixed or thin film lubrication. The value of torque (T) also increases with rpm and subsequently with coefficient of friction (f). The results obtained are in accordance with Raimondi and Boyd chart.

Table: 5. Relative Error for Pressure Ratio

S No.	Load (N)	Journal Rotational Speed (rpm)	Pressure ratio (P/Pmax.) (Experimental)	Pressure ratio (P/Pmax.) (Theoretical)	% Error
1.	800	1000	0.540	0.500	7.4
2.	800	1500	0.550	0.503	8.54
3.	800	2000	0.553	0.508	8.13

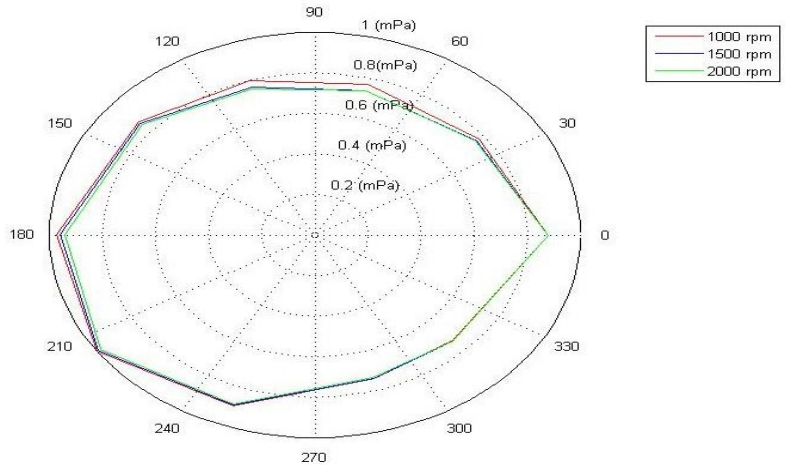


Fig: 7. Polar pressure distribution curve at 800N Load and different RPM

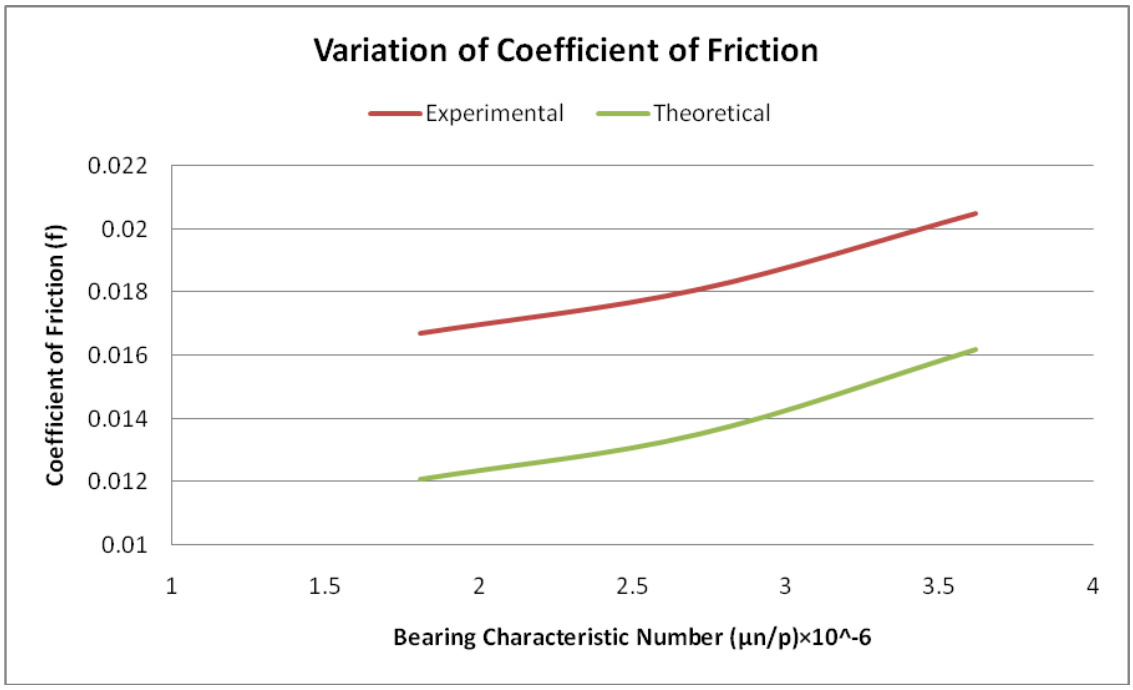


Fig: 8. Bearing characteristic Number $(\frac{\mu N}{P}) \times 10^{-6}$ vs Coefficient of friction (f)

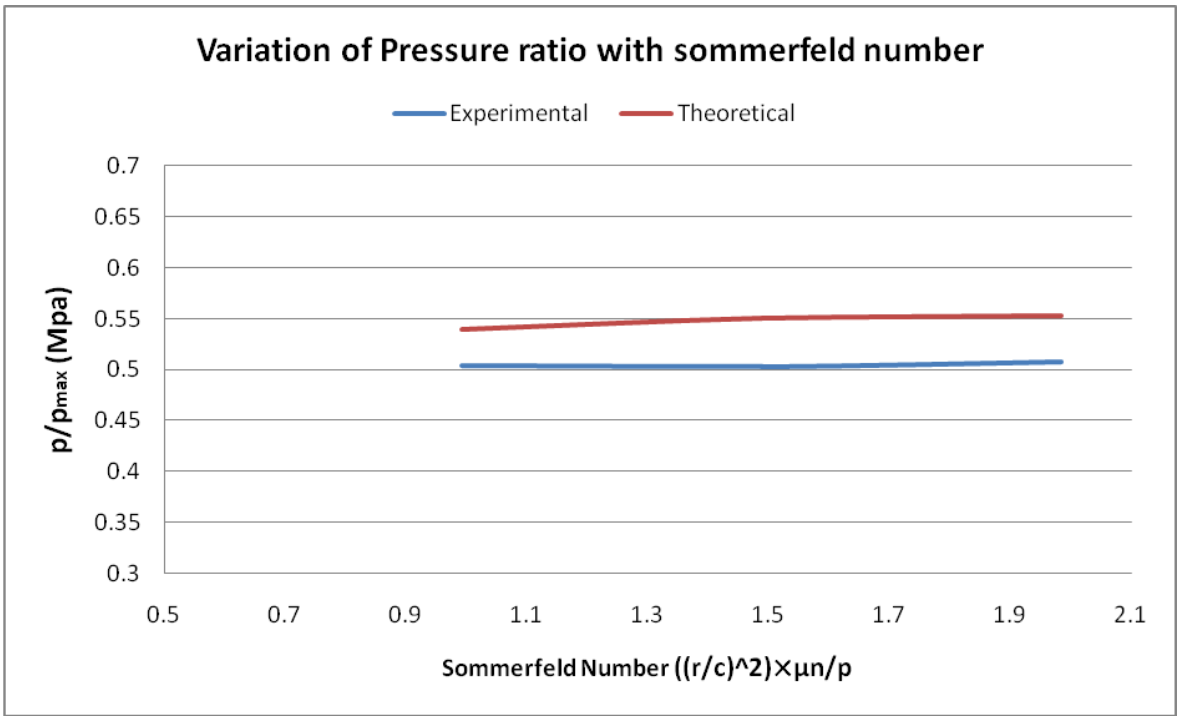


Fig: 9. Pressure ratio vs. Summerfield number

6. Conclusion

The experiment conducted showed that, at all operating conditions of 800N Load and different rpm, the plot of (μn/p) vs (f) lies on the right side of the Mckee's curve thus ensuring thick film lubrication in the entire region. There was no thin film or mixed lubrication. Also it was observed that there was a slight variation of pressure with increase in rpm. This confirms the stability of fluid film in the bearing. Torque increases with increase in rpm or coefficient of friction (f) due to addition of more fluid layers in the wedge shaped region. The variation of pressure distribution was in accordance with Raimondi and Boyd charts and also the experimental values matches with the theoretical values with a good degree of closeness. Overall theoretical trend was even followed at actual working conditions and thus design criteria are safe. Further the work can be extended by performing the experimentation with different types of lubricants to obtain a comparative study and choose their suitability according to conditions.

References

[1] MT Ma, CM Taylor, "A Theoretical and Experimental Study of Thermal Effects in a Plain Circular Steadily Loaded Journal Bearing," Transactions IMechE, 824(9), pp. 31-44, 1992.

[2] S Baskar, G Sriram "Experimental Analysis of Hydrodynamic Journal Bearing under different Bio lubricants," IEEE-International Conferences on Advances In Engineering, Science and Management (ICAESM-2012), March 30, 31 2012

[3] DT Gethin, "Thermo hydrodynamic Behaviour of High Speed Journal Bearings," Tribology International, 29(7), pp. 579-596, 1996

[4] SM Chun, "Thermo hydrodynamic lubrication analysis of high-speed journal bearing considering variable density and variable specific heat," Tribology International, 37, pp. 405-413, 2004

[5] J Sep, "Three dimensional hydrodynamic analysis of a journal bearing with a two component surface layer, "Tribology International, 38, pp. 97-104, 2005

[6] A. Buske, W. Rolli, ''Measurements of Oil-Film Pressure in Bearings Under Constant and Variable Loads,'' *Technical Note 1200*, NACA, pp. 43, 1949

[7] J. Bouyer, M. Fillon, "Experimental measurement of the friction torque on hydrodynamic plain journal bearings during start-up," *Tribology International* 44 (2011) 772–781, 2011

[8] V. B. Bhandari, Elements of Machine design, TMH Publications, 2007 edition

[9] K. Gopinath, MM Mayuram, nptel lectures, IIT Madras

[10] Christensen, Tonder "The hydrodynamic lubrication of rough journal bearings". Trans. ASME, *Journal of Lubrication*: Technology 1973; 95:166–72

[11] Ducom TR- 660 Instruction manual.

[12] www.substech.com/hydrodynamic journal bearing, search by google image

Applied Soft Computing 19 (2014) 322–332

Contents lists available at ScienceDirect

Applied Soft Computing

journal homepage: www.elsevier.com/locate/asoc

Generalized neural network and wavelet transform based approach for fault location estimation of a transmission line

Majid Jamil [a], Abul Kalam [a,*], A.Q. Ansari [a], M. Rizwan [b]

[a] Department of Electrical Engineering, Jamia Millia Islamia, New Delhi 110025, India
[b] Department of Electrical Engineering, Delhi Technological University, Delhi 110042, India

ARTICLE INFO

Article history:
Received 18 April 2013
Received in revised form
25 November 2013
Accepted 20 February 2014
Available online 13 March 2014

Keywords:
Generalized neural network
Wavelet transform
Artificial neural network
Transmission line protection
Transient signals

ABSTRACT

To maintain the efficient and reliable operation of power systems, it is extremely important that the transmission line faults need to be detected and located in a reliable and accurate manner. A number of mathematical and intelligent techniques are available in the literature for estimating the fault location. However, the results are not satisfactory due to the wide variation in operating conditions such as system loading level, fault inception instance, fault resistance and dc offset and harmonics contents in the transient signal of the faulted transmission line. Keeping in view of aforesaid, a new approach based on generalized neural network (GNN) with wavelet transform is presented for fault location estimation. Wavelet transform is used to extract the features of faulty current signals in terms of standard deviation. Obtained features are used as an input to the GNN model for estimating the location of fault in a given transmission systems. Results obtained from GNN model are compared with ANN and well established mathematical models and found more accurate.

© 2014 Elsevier B.V. All rights reserved.

1. Introduction

Faults can occur in any component of power systems including generator, transformer, buses and transmission lines. As the transmission line is one of the main components of power systems, therefore the detection of faults on transmission lines is the primary concern of the power systems, necessitating high speed fault clearance and improved transient stability [1].

Transmission line fault detection techniques can be classified into two main categories: techniques based on the fundamental power frequency component, and techniques utilizing the higher frequency components of the fault signals. Further these two categories of fault location techniques can be divided into two subgroups: to use single ended information or to use information from both ends using current and voltage data of the faulted line [2–5]. A number of mathematical models are available in the literature for identifying the types and location of the fault of transmission systems [2–8]. In recent study, the sampled current values at the relaying point i.e. single ended data have been used for classification and location of faults [11–13,16]. This technique is more attractive than the technique based on two terminals. Two terminals technique has drawbacks like requirement of communication links and synchronized sampling equipment which not only increase the cost but also affect the accuracy [3]. Therefore techniques using single ended data are preferred.

In fact correct fault location of a transmission line depends upon many factors such as on the geometry/configuration and the line parameters of the transmission network (i.e. whether the line is transposed/un-transposed, charging capacitance and shunt reactance being present neglected or taken into consideration for the transmission line model). In addition to that the accuracy of fault location also depends upon the resistance of the faulted path, the fault inception angle, the system loading level and on the amplitude of the dc offset and harmonics content in the transient signal of the faulted transmission line. Besides that transmission line being geographically wide distributed systems and exposed to the environment there is uncertainty about the fault events and the line parameters. Therefore, in such situation, where there is ambiguity and uncertainty about the fault events and the line parameters, it is difficult to deal with the transmission lines protection problems through strict mathematical approaches (deterministic approaches) effectively, and hence these factors introduce the considerable amount of error for the fault location estimation of the transmission system using conventional mathematical (deterministic approach) model of the transmission system.

To overcome these problems several intelligent techniques including fuzzy logic, artificial neural networks, neuro-fuzzy and

* Corresponding author at: Department of Electrical Engineering, Jamia Millia Islamia, Jamia Nagar, New Delhi 110025, India. Tel.: +91 9958281028.
E-mail address: kalam.a@rediffmail.com (A. Kalam).

http://dx.doi.org/10.1016/j.asoc.2014.02.020
1568-4946/© 2014 Elsevier B.V. All rights reserved.

combined wavelet-ANN have been developed and presented in the literature for fault identification and location of transmission system as discussed in [1] and [9–28]. Among aforesaid approaches it is seen that wavelet-ANN has been quite successful in identifying the types and location of fault. However, there are certain drawbacks of ANN like large training time, huge data requirement for training, unknown ANN structure, the relatively larger number of hidden nodes required, problem of local minima, etc. To overcome some of the problems of ANN and to improve it's training and testing performance, a new approach based on GNN in combination with wavelet transform is presented in this paper. The applications of GNN in the field of load forecasting, aircraft landing system, power system stabilizer, estimation of solar energy etc., are available in the literature [29–38]. However, the application of GNN with wavelet for the fault location estimation of transmission line is rarely available.

In the present work, single ended fault current signals are analyzed using wavelet transform. Obtained data is used as input parameters in GNN modeling for estimating the fault location of the three phase transmission system. The performance of the GNN model for the fault location estimation is evaluated on the basis of mean value of absolute relative error in percentage, considering the un-transposed transmission line model for the same network and parameters of power system as modeled in [6] and found to produce very accurate fault location result which is around 2.0%. While, the percentage error as reported in [6], which describes iterative method of fault location for the same power system network as considered in the proposed study is varies up to 4.81%. Whereas in [27] the percentage error is reported up to 6.5% using wavelet and fuzzy logic based technique for the fault location estimation of the transmission system.

Observations of all test results ascertain that the wavelet-GNN based model of fault location estimation performs excellent even at voltage zero crossing situation of fault inception angle and at different fault locations starting from relay end (sending end) to the end terminal of the transmission line for all kinds of phase to phase and phase to ground faults.

This paper is organized as follows: Wavelet transform used for pre-processing of fault current signals to obtain the features of fault current signals in terms of statistical feature i.e. standard deviation is presented in Section 2. Section 3 presents the generalized neural networks and fault location estimation based on GNN model. Section 4 describes the simulation studies. In Section 5 results are discussed. Section 6 presents conclusion followed by references.

2. Wavelet transform

The wavelet transform is a powerful tool for the analysis of transient phenomena because of its ability to extract time frequency information from the transient signal. Most of the transient signals based relay principle adopts the wavelet transform technology to construct the algorithms. Wavelet transform (WT) expands a signal into several scales belonging to different frequency regions by using translation (shift in time) and dilation (compression in time) of a fixed wavelet function known as mother wavelet. The discrete wavelet transform and multi resolution analysis provides a short window for high frequency components and long window for low frequency components and hence provides an excellent time frequency resolution [17].

Continuous wavelet transform (CWT) is defined as the sum over all time of the signal multiplied by scaled and shifted versions of the wavelet function $\psi(t)$. The CWT of a $x(t)$ signal is defined as

$$\mathrm{CWT}(x, a, b) = \int_{-\infty}^{\infty} x(t)\psi^* a,\ b(t)dt \tag{1}$$

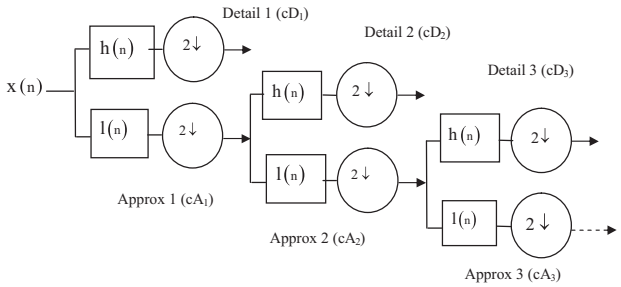


Fig. 1. Multi level wavelet decomposition scheme.

where $\psi_{a,b}(t) = |a|^{-1/2}\psi(t-b/a)$, the analyzing function $\psi(t)$ is known as the mother wavelet and $\psi_{a,b}(t)$ are its dilated and translated versions; the choice of a mother wavelet is flexible provided that it satisfies the following condition:

$$\int_{-\infty}^{\infty} \psi(t)dt = 0$$

This implies that a wavelet is compactly supported in both the time domain and frequency domain. The asterisk in (1) denotes a complex conjugate, $a, b \in \Re$, $a \neq 0$ ($\Re$ is a real continuous number system) are the scaling and shifting parameters respectively. $|a|^{-1/2}$ is the normalized value of $\psi_{a,b}(t)$ so that if $\psi(t)$ has a unit length, then its scaled version $\psi_{a,b}(t)$ also has a unit length.

Wavelet transform of sampled waveforms can be obtained by implementing the discrete wavelet transform which is given by:

$$\mathrm{DWT}(x,\ m,\ n) = a_o^{-m/2} \sum \left(x[k]\psi^* \left[\frac{k - n\, a_o^m b_o}{a_o^m} \right] \right)$$

where m, n and k are integer variables and it refers to a sample number in an input signal and a_o and b_o are the discrete steps of the scale and translation respectively.

2.1. Wavelet decomposition and multi resolution analysis

Multi-resolution analysis (MRA) is a time frequency analysis technique which has been found to be an effective signal processing tool in monitoring and analyzing power system disturbances including power quality assessment and system protection against faults [9]. It has also other desirable properties such as providing a substantial amount of data reduction and having a simple and fast algorithm. Therefore, DWT is most appropriate for fault detection and location problems in power systems. In this study phase A, phase B and phase C fault current signals, generated on a three phase transmission line considered as $x(n)$ in time domain is passed through high pass $h(n)$ and low pass filter $l(n)$. The outputs from both the filters are decimated by 2 to obtain the detail coefficient (cD_1) and the approximation coefficient (cA_1) which constitutes the level one decomposition of the original signal at stage first. The approximation coefficient (cA_1) is then sent to the second stage to repeat the procedure. Finally, the signal is decomposed up to the ninth levels. The details information and approximations at different levels are seen to provide useful clues regarding the faults locations on the transmission line [27]. A multi-level DWT decomposition scheme shown in Fig. 1 shows the essence of the procedure. The approximations and details at level-1, level-2 and level-3 have been represented using suffixes 1, 2 and 3 and so on.

2.2. Features extraction

In the present study wavelet transform is used to capture the useful fault signature of the faulty current signals of a given three

Table 1
Details wavelet coefficients at different frequency range for 100 kHz sampling frequency.

Wavelet coefficients up to ninth-levels of wavelet decomposition	Frequency band (Hz)
cD_1	25,000–50,000
cD_2	12,500–25,000
cD_3	6250–12500
cD_4	3125–6250
cD_5	1562.5–3125
cD_6	781.25–1562.5
cD_7	390.62–781.25
cD_8	195.31–390.62
cD_9	97.66–195.31

phase transmission line in terms of statistical features like standard deviation to be used as input to the GNN model. Three phase fault current signals recorded at the relaying point sampled at the rate of 100 kHz frequency are pre-processed passing through the multi level wavelet filter bank, selecting Db4 as mother wavelet, for different fault operating condition using MATLAB software. Since the selected sampling frequency is 100 kHz at the base frequency of 50 Hz, therefore ninth level wavelet detail coefficient includes second and third harmonics (97.66–195.31 Hz) which are predominant in case of transmission line faults and is useful for the fault classification and fault location estimation of the transmission line. The details coefficient at different frequency range for 100 kHz sampling frequency is shown in Table 1. Feature vectors in terms of standard deviation are obtained using Eq. (2), considering the ninth level detail coefficient denoted as: $[\sigma_A cD_9; \sigma_B cD_9; \sigma_C cD_9]$ for three phase fault current signals [25].

$$\text{Standard deviation } \sigma_\chi cD_i = \left[\frac{1}{N-1}\sum_{j=1}^{N}(cD_{ij} - \mu_\chi cD_i)^2\right]^{1/2}$$
$$\text{Mean } \mu_\chi cD_i = \frac{1}{N}\sum_{j=1}^{N} cD_{ij} \quad (2)$$

where χ represents phase A, phase B and phase C, $i = 1, 2, \ldots, l$ is the wavelet decomposition level from level 1 to level l, N = number of samples of wavelet details coefficient.

If the wavelet coefficients are used as inputs to the GNN, it will results in rather large number of inputs (equals to the N number of samples) posing difficulty for training and testing of GNN in connection with accuracy and speed [14]. Therefore, in order to overcome this problem but retaining important features of the wavelet signals, features are obtained in terms of standard deviation using ninth level detail coefficient which are predominant in case of transmission line faults.

3. Generalized neural network (GNN)

The general structure of the common neuron is an aggregation function and its transformation through a filter. It is shown in the literature [29–38] that the ANNs can be universal function approximators for given input–output data. The common neuron structure as shown in Fig. 2 has summation as the aggregation function with sigmoidal, radial basis, tangent hyperbolic or linear limiters as the thresholding function. The aggregation operators used in the neurons are generally crisp. However, they overlook the fact that most of the processing in the neural networks is done with incomplete information at hand. Thus, a GNN model approach has been adopted that uses the fuzzy compensatory operators [37] that are partly sum and partly product to take into account the vagueness involved.

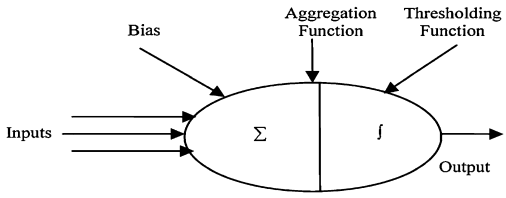


Fig. 2. Simple neuron model.

3.1. GNN model

Use of the sigmoidal thresholding function and ordinary summation or product as aggregation functions in the existing model fails to cope with the nonlinearities involved in real life problems. To deal with these, the proposed model has both sigmoidal and Gaussian functions with weight sharing. The GNN model has flexibility at both the aggregation and threshold function level to cope with the nonlinearity involved in the type of applications dealt with, as shown in Fig. 3. The neuron model described above is known as the summation type compensatory neuron model, since the outputs of the sigmoidal and Gaussian functions are summed up. Similarly, the product-type compensatory neuron models may also be developed. The neuron has both Σ and π aggregation functions. The Σ_1 aggregation function has been used with the sigmoidal characteristic function (f_1) while the π aggregation function has been used with the Gaussian function (f_2) as a characteristic function.

The output of the Σ_1 part with a sigmoidal characteristic function of the GNN is

$$o_\Sigma = f_1(s_net) = \frac{1}{1 + e^{-\lambda_s * s_net}} \quad (3)$$

where

$$s_net = \sum W_{\Sigma_i} X_i + X_{o\Sigma}$$

and λ_s is the gain scale factor of Σ_1

The output of the π part with Gaussian characteristics function of GNN is

$$o_\pi = e^{-\lambda_p * pi_net^2} \quad (4)$$

where

$$pi_net = \Pi W_{\Pi_i} X_i * X_{o\Pi}$$

and λ_p is the gain scale factor of π_1.

The final output of the neuron is a function of the two outputs and with the weights W and $(1 - W)$ respectively, and can be written in mathematical form as

$$o_{pk} = o_\pi * (1 - W) + o_\Sigma * W \quad (5)$$

The GNN model gives only one output. If a system requires more than one output, one GNN is used for each output.

The neuron model described above is known as the summation type compensatory neuron model, since the outputs of the

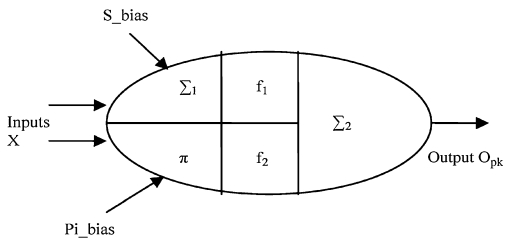


Fig. 3. GNN model.

sigmoidal and Gaussian functions are summed up. Similarly, the product-type compensatory neuron models may also be developed. It is found that in most of the applications, the summation-type compensatory neuron model works well and is the one used for the estimation of fault location of the transmission line.

3.2. Learning algorithm of a GNN model

The following steps are involved in the training of a GNN:

Step (1) Calculate the output of GNN as given in (3) and (4).
Step (2) After calculating the output of the GNN in the forward pass, as in the feed-forward neural network, it is compared with the desired output to find the error. Using a back-propagation algorithm, the GNN is trained to minimize the error. In this step, the output of the single flexible GNN is compared with the desired output to get the error for the i_{th} set of inputs.

$$\text{Error } E_i = (Y_i - O_i) \tag{6}$$

Step (3) Then, the sum squared error for the convergence of all the patterns is

$$E_p = 0.5 \sum E_i^2 \tag{7}$$

A multiplication factor of 0.5 has been taken to simplify the calculations.
Step (4) Reverse pass for modifying the connection strength.
(a) Weight associated with the Σ_1 and part Σ_2 of the GNN is

$$W(k) = W(k-1) + \Delta W \tag{8}$$

where $\Delta W = \eta\delta_k(o_\Sigma - o_\pi)X_i + \alpha W(k-1)$ and $\delta_k = \Sigma(Y_i - O_i)$

(b) Weights associated with the inputs of the Σ_1 part of the GNN are

$$W_{\Sigma_i}(k) = W_{\Sigma_i}(k-1) + \Delta W_{\Sigma_i} \tag{9}$$

where $\Delta W_{\Sigma_i} = \eta\delta_{\Sigma i}X_i + \alpha W_{\Sigma i}(k-1)$ and $\delta_{\Sigma j} = \sum\delta_k W(1 - O_\Sigma) * O_\Sigma$

(c) Weights associated with the input of the π – part of the GNN are

$$W_{\Pi i(k)} = W_{\Pi i(k-1)+\Delta W_{\Pi i}} \tag{10}$$

where $\Delta W_{\Pi i} = \eta\delta_{\Pi j}Xi + \alpha W_{\Pi i}(k-1)\delta_{\Pi j} = \sum\delta_k(1-W) * (-2 * pi_net) * O_\Pi$

α is the momentum factor for better convergence, and η is the learning rate. The range of these factors is from 0 to 1 and is determined by experience.

3.3. Wavelet-GNN model based fault location estimation

The fault current signals of three phase transmission line are filtered through wavelet transform. Obtained data from wavelet is used as input to GNN model. The input data is extracted features of fault current signals whereas the output of the GNN model is location of fault.

The neural network toolbox of MATLAB software is used for estimating the fault location of the transmission line. The flow chart of the proposed method is presented in Fig. 4. Firstly, the fault current signal is obtained at the sampling frequency of 100 kHz for each case, created for different fault operating conditions. Thereafter the multi-resolution analysis (MRA) based on Discrete Wavelet Transform (DWT) is used to capture the transient characteristics of the fault current signal. The information captured during the ninth level frequency bands by the details wavelet coefficients in terms of standard deviation is fed as input to the GNN and target as the fault location of the transmission line. Since the input and output data

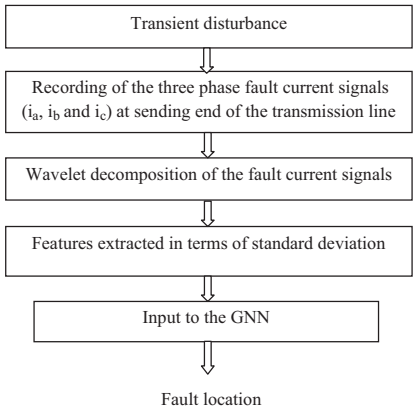


Fig. 4. Flow chart for fault location scheme.

are not of the same order of magnitude, therefore it is necessary to normalize the input and output data in the same order of magnitude. If actual data is directly used, this may cause a convergence problem during the learning process. To avoid such problem, the input and output data are scaled such that they remain within the range of (0.1–0.9). This process is known as normalization. Normalization has a major role in the training and testing of neural networks. The actual data is scaled using the following expression for the fault location estimation problem [37].

$$L_S = \frac{(Y_{\max} - Y_{\min})}{(L_{\max} - L_{\min})}(L - L_{\min}) + Y_{\min} \tag{11}$$

where L = the actual data; L_s = the scaled data which is used as input to the network; $L_{\max}$ = maximum value of particular data set; $L_{\min}$ = minimum value of particular data set; $Y_{\max}$ = upper limit (0.9) of normalization range; $Y_{\min}$ = lower limit (0.1) of normalization range.

The GNN model is developed for the fault location estimation of a given three phase transmission line as shown in Fig. 5. The neurons in the input layer receive three input signals representing the features of the three phase fault current signals in terms of standard deviation. The output layer, on the other hand consists of one output neuron representing fault location of the transmission line. The generalized neuron structure summation and product as aggregation functions have been incorporated and the aggregated outputs passed through a non-linear squashing/thresholding function. The Σ-part has the summation of weighted input with sigmoidal activation function f_1, while the π-part has the product of weighted input with Gaussian activation function f_2. The final output of the neuron is a function of the weighted outputs O_Σ and O_π.

The output of summation (Σ) part of the generalized neuron is

$$O_\sum = f_1\left(\sum W_{\sum i}X_i + X_{o\sum}\right) \tag{12}$$

The output of product (π) part of the generalized neuron is

$$O_\pi = f_2(\pi W_{\pi i}X_i + X_{o\pi}) \tag{13}$$

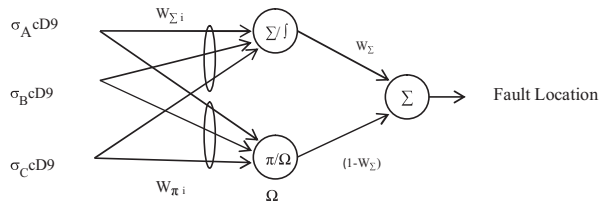


Fig. 5. Architecture of GNN model for the fault location estimation of transmission line.

Finally, the outputs are summed up to get the neuron output. The output of the neuron can be mathematically written as

$$Oi = O_{\Sigma} * W_{\Sigma} + O_{\pi} * (1 - W_{\Sigma}) \quad (14)$$

4. Simulation studies

The proposed fault location estimation approach is extensively tested on a 500 kV, 50 Hz transmission line of 300 km length connected between two sources as shown in Fig. 10. The parameters of the system under consideration are as follows:

Sending and receiving end source voltage

E_s = 500 kV; E_R = 475 ∠δ kV; where ∠δ is the receiving end phase voltage angle.

Sending and receiving end positive and zero sequence source impedance

$$Z_{s1} = 17.177 + j37.9404\Omega; \quad Z_{s0} = 2.5904 + j12.2773\Omega;$$

$$Z_{R1} = 15.31 + j38.2704\,\Omega; \quad Z_{R0} = 0.7229 + j12.6073\,\Omega;$$

Transmission line parameters

$$Z^1 = 0.15483 + j0.3050\,\Omega/\text{km};$$

$$Z^0 = 0.37432 + j0.9429\,\Omega/\text{km};$$

$$C_1 = 1.2097E - 8F/\text{km};$$

$$C_0 = 7.4982E - 9F/\text{km}.$$

In simulation studies, a large numbers of test cases are generated for different values of fault resistance (R_f) varying from 10 Ω to 1000 Ω for ground faults and for phase faults from 1 Ω to 10 Ω, which cover most of the high resistance faults. The variation of distance from the relay point to the end terminal (receiving end) in steps of every 5 km is considered, and the receiving end phase voltage angle (δ) of −15°, 15°, 30° and 90°. For simulation, fault is created at different fault inception angles (FIA) of 36°, 54°, 90° and 180°, considering 0.02 s simulation time. The fault inception angle specially voltage zero crossing situation has also been widely investigated. The data considered in the analysis is less than one cycle. The fault current signals are obtained at 100 kHz sampling frequency at the relaying point in order to be used in feature extraction using multi-resolution analysis based on DWT. For each fault operating condition, simulation of the program generates 59 data files that is a matrix of the order of 59 × 3 = 177 data. Out of which 80% data randomly chosen are fed to train the GNN and remaining 20% for testing. To validate the proposed wavelet-GNN model, the fault location results are compared with the other intelligent model like wavelet-ANN (presented in Appendix I), and with the mathematical based method (measuring symmetrical components of voltage and current shown in Appendix II) of fault location estimation.

5. Results

To show the effectiveness of the proposed model, an extensive series of simulation studies have been carried out for a wide variation of fault operating conditions. Due to the paucity of space, as an application example, current waveform and wavelet decomposition of phase A fault current signal for one type of fault (phase A to ground fault i.e. AG fault) due to the fault occurred at 240 km away from the relaying point operating at R_f = 100 Ω, FIA = 36°, δ = −15° is illustrated in Fig. 6. The characteristics features of fault current signals (extracted transient characteristics features of phase A, phase B and phase C fault current signals in terms of standard deviation considering the ninth level wavelet detail coefficient) corresponds to the different fault points along the line are depicted in column fifth to seventh of Tables 2 and 3. It is clear from the Fig. 6, that the detail signal at level-1 shows the distinctive features of the transient signal for faulted phase A i.e. just after the occurrence of fault sharp spikes appear in the detail signal which signifies the occurrence of fault. It is observed from the Tables 2 and 3, that the value of features vector (standard deviation) of the faulted phase decreases as the fault distance increases from the relay point. These distinguishable characteristics feature of the fault signals are applied as an input to the neural network, which help to determine the fault locations estimation of the transmission line. The column number eight and nine of Tables 2 and 3 respectively provides the estimated fault locations, and the training and testing performance of fault locations result using Wavelet-GNN model due to the fault occurred at the various locations of the line starting from the relay end to

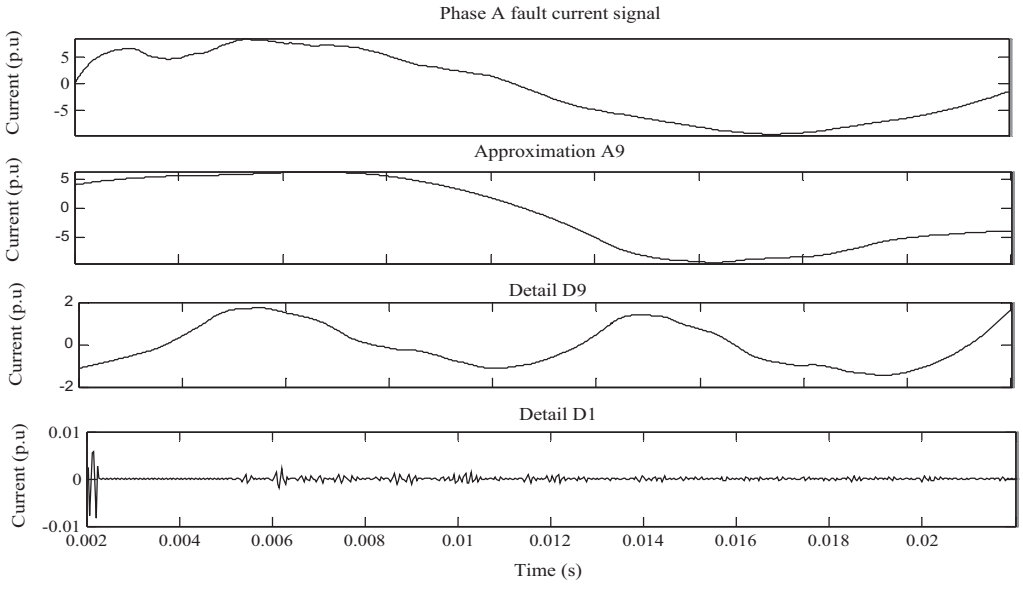


Fig. 6. Wavelet decomposition of phase A fault current signal for phase to ground (AG) fault due to the fault occurred at 240 km away from the relaying point operating at R_f = 100 Ω, FIA = 36° and δ = −15°.

Table 2
Training performance of AG fault operating at $R_f = 100\,\Omega$, FIA = 36° and $\delta = -15°$.

S. no.	Actual distance to fault from relaying point (km)	Fault location measuring zero sequence components of voltage and current		Normalized value of features vector in terms of standard deviation of phase A, phase B and phase C fault current signals						
		Computed distance (d) (km)	Absolute value of relative error in %	Applied as input to GNN					Applied as input to ANN	
				$\sigma_A cD_9$	$\sigma_B cD_9$	$\sigma_C cD_9$	Estimated fault location (km)	Absolute value of relative error in %	Estimated fault location (km)	Absolute value of relative error in %
1	10	9.35	6.50	0.8740	0.8978	0.1234	9.82	1.80	9.75	2.50
2	50	46.16	7.68	0.6917	0.8543	0.2918	49.39	1.22	48.41	3.18
3	120	109.45	8.79	0.4582	0.6892	0.5133	118.21	1.49	116.39	3.01
4	155	140.73	9.21	0.3691	0.5930	0.5948	153.43	1.01	151.42	2.31
5	200	180.56	9.72	0.2719	0.4451	0.6986	204.02	2.01	195.74	2.13
6	225	202.43	10.03	0.2236	0.3504	0.7527	222.91	0.93	220.16	2.15
7	240	215.45	10.23	0.1960	0.2906	0.7837	237.10	1.21	233.02	2.91
8	275	246.21	10.47	0.1344	0.1580	0.8568	270.77	1.54	269.28	2.08
9	280	250.43	10.56	0.1258	0.1413	0.8676	278.01	0.71	275.38	1.65
10	285	254.71	10.63	0.1172	0.1256	0.8782	284.57	0.15	277.13	2.76
11	295	263.28	10.75	0.1000	0.1000	0.9000	289.31	1.93	287.83	2.43

Table 3
Testing performance for AG fault operating at $R_f = 100\,\Omega$, FIA = 36° and $\delta = -15°$.

S. no.	Actual distance to fault from relaying point (km)	Fault location measuring zero sequence components of voltage and current		Normalized value of features vector in terms of standard deviation of phase A, phase B and phase C fault current signals						
		Computed distance (d) (km)	Absolute value of relative error in %	Applied as input to GNN					Applied as input to ANN	
				$\sigma_A cD_9$	$\sigma_B cD_9$	$\sigma_C cD_9$	Estimated fault location (km)	Absolute value of relative error in %	Estimated fault location (km)	Absolute value of relative error in %
1	35	32.46	7.26	0.7550	0.8764	0.2325	34.57	1.23	34.31	1.97
2	45	41.60	7.56	0.7122	0.8617	0.2725	44.60	0.89	43.81	2.64
3	60	55.28	7.87	0.6525	0.8383	0.3279	59.03	1.62	58.07	3.22
4	90	82.45	8.39	0.5476	0.7747	0.4274	89.06	1.04	89.12	0.98
5	100	91.43	8.57	0.5162	0.7483	0.4572	101.99	1.99	98.42	1.58
6	150	136.32	9.12	0.3810	0.6031	0.5842	152.49	1.66	153.50	2.33
7	160	145.18	9.26	0.3575	0.5821	0.6059	158.46	0.96	156.74	2.04
8	180	162.93	9.48	0.3132	0.5175	0.6529	181.89	1.05	178.15	1.03
9	220	198.05	9.98	0.2330	0.3702	0.7422	216.38	1.65	212.50	3.41
10	245	219.73	10.31	0.1870	0.2719	0.7942	243.41	0.65	242.97	0.83
11	260	233.10	10.35	0.1605	0.2143	0.8252	265.32	2.05	257.24	1.06

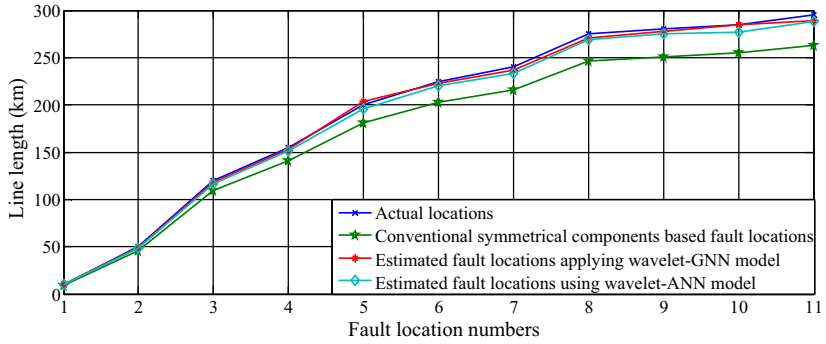


Fig. 7. Training output and performance comparison of wavelet-GNN model with ANN and conventional symmetrical method based fault location estimation for AG fault (phase A to ground fault) due to the fault occurred at the various locations of the line, operating at $R_f = 100\,\Omega$, FIA = 36° and $\delta = -15°$.

Table 4
Fault location results measuring sequence components of voltage and current for AG fault, operating at $R_f = 100\,\Omega$, FIA = 36° and $\delta = -15°$.

Fault location points	Actual fault location from relaying point	Sending end zero sequence component voltage (at Bus1)		Zero sequence component voltage at fault point (at Bus3)		Sending end zero sequence current component		Zero sequence impedance between Bus1 to Bus3 (p.u)	Computed fault location distance (d) (km)	Absolute value of relative error in %
		Mag. (p.u)	Angle (degree)	Mag. (p.u)	Angle (degree)	Mag. (p.u)	Angle (degree)			
1	15	0.08926	−142.26	0.12164	−141.49	5.78	−22.78	0.0056	14	6.65
2	35	0.08077	−145.51	0.14899	−144.19	5.25	−25.17	0.01298	32.46	7.26
3	105	0.05749	−153.21	0.20197	−150.95	3.77	−30.53	0.03837	95.93	8.64
4	170	0.04114	−156.46	0.20774	−153.28	2.7	−32.55	0.06164	154.1	9.35
5	180	0.03894	−156.38	0.20538	−153.31	2.55	−32.64	0.06517	162.93	9.48
6	215	0.03117	−156.26	0.18969	−152.79	2.05	−32.48	0.07747	193.67	9.92

Table 5
Fault location results measuring sequence components of voltage and current for ABG fault, operating at $R_f = 1000\,\Omega$, FIA = 180° and $\delta = 30°$.

Fault location points	Actual fault location from relaying point	Sending end zero sequence component voltage (at Bus1)		Zero sequence component voltage at fault point (at Bus3)		Sending end zero sequence current component		Zero sequence impedance between Bus1 to Bus3 (p.u)	Computed fault location distance (d) (km)	Absolute value of relative error in %
		Mag. (p.u)	Angle (degree)	Mag. (p.u)	Angle (degree)	Mag. (p.u)	Angle (degree)			
1	30	0.00518	−160.8	0.00899	−159.81	0.30171	−52.39	0.01261	31.53	5.1
2	40	0.00521	−154.55	0.01019	−155.05	0.29071	−51.88	0.01715	42.87	7.16
3	55	0.0052	−148.29	0.01188	−149.95	0.27432	−51.07	0.02437	60.92	10.76
4	215	0.00493	−109.94	0.01612	−134.82	0.11668	−35.45	0.09595	239.87	11.57
5	225	0.00485	−108.4	0.0154	−134.85	0.10793	−34.05	0.09774	244.35	8.6
6	235	0.00473	−107.04	0.01447	−135.34	0.09921	−32.62	0.09822	245.56	4.49

Table 6
Fault location results measuring sequence components of voltage and current for AB fault, operating at $R_f = 10\ \Omega$, FIA = 54° and $\delta = -15°$.

Fault location points	Actual fault location from relaying point	Sending end zero sequence component voltage (at Bus1)		Zero sequence component voltage at fault point (at Bus3)		Sending end zero sequence current component		Zero sequence impedance between Bus1 to Bus3 (p.u)	Computed fault location distance (d) (km)	Absolute value of relative error in %
		Mag. (p.u)	Angle (degree)	Mag. (p.u)	Angle (degree)	Mag. (p.u)	Angle (degree)			
1	170	4.75E−06	0	1.82E−05	0	0.00018	0	0.07537	188.43	10.84
2	180	4.63E−06	0	1.76E−05	0	0.00017	0	0.07731	193.27	7.37
3	210	4.21E−06	0	1.48E−05	0	0.00014	0	0.07775	194.37	7.44
4	215	4.02E−06	0	1.42E−05	0	0.00013	0	0.07842	196.04	8.82

Table 7
Fault location results measuring sequence components of voltage and current for ABC fault, operating at $R_f = 1\ \Omega$, FIA = 36° and $\delta = 15°$.

Fault location points	Actual fault location from relaying point	Sending end zero sequence component voltage (at Bus1)		Zero sequence component voltage at fault point (at Bus3)		Sending end zero sequence current component		Zero sequence impedance between Bus1 to Bus3 (p.u)	Computed fault location distance (d) (km)	Absolute value of relative error in %
		Mag. (p.u)	Angle (degree)	Mag. (p.u)	Angle (degree)	Mag. (p.u)	Angle (degree)			
1	175	7.64E−15	0	1.13E−14	0	4.51E−14	0	0.08025	200.62	14.64
2	225	7.51E−15	0	9.19E−16	0	8.54E−14	0	0.07722	193.04	14.20
3	230	4.63E−15	0	8.79E−15	0	5.18E−14	0	0.08029	200.73	12.73
4	270	2.39E−15	0	8.25E−15	0	5.80E−14	0	0.1012	252.99	6.30
5	275	2.11E−15	0	1.27E−14	0	9.28E−14	0	0.11398	284.95	3.62

Table 8
Comparisons of performance of wavelet-GNN model with ANN and conventional symmetrical method of fault location at various fault operating conditions for LG, LLG, LL and LLL faults.

Type of faults	Actual distance to fault from relaying point	Fault resistance	Fault inception angle	Receiving end phase voltage angle (δ)	Conventional method based fault location		Normalized value of features vector in terms of standard deviation of phase A, phase B and phase C fault current signals						
					Using zero sequence components of voltage and current		Fault location estimation applying feature vectors as input to GNN					Fault location estimation applying feature vectors as input to ANN	
	(km)	(ohm)	(degree)	(degree)	Computed distance (d) (km)	% Error	$\sigma_A D_9$	$\sigma_B D_9$	$\sigma_C D_9$	Estimated fault distance (km)	% Error	Estimated fault distance (km)	% Error
LG (AG)	15	100	36	−15	14	6.65	0.8487	0.895	0.1465	15.29	1.93	15.33	2.20
	35	100	36	−15	32.46	7.26	0.7550	0.8764	0.2325	34.08	2.63	35.58	1.65
	105	100	36	−15	95.93	8.64	0.5012	0.7344	0.4718	106.74	1.66	105.62	0.59
	170	100	36	−15	154.1	9.35	0.3349	0.5524	0.6291	167.24	1.62	165.47	2.66
	180	100	36	−15	162.93	9.48	0.3132	0.5175	0.6529	181.67	0.93	182.09	1.16
	215	100	36	−15	193.67	9.92	0.2426	0.3895	0.7316	218.99	1.86	218.53	1.64
LLG (ABG)	30	1000	180	30	31.53	5.10	0.6296	0.5756	0.4344	29.42	1.93	30.96	3.20
	40	1000	180	30	42.87	7.16	0.5363	0.4796	0.4984	39.44	1.40	38.95	2.62
	55	1000	180	30	60.92	10.76	0.4100	0.3597	0.5936	53.87	2.05	56.54	2.80
	215	1000	180	30	239.87	11.57	0.1029	0.2607	0.6804	219.21	1.96	220.14	2.39
	225	1000	180	30	244.35	8.60	0.1028	0.3081	0.6163	222.45	1.13	230.85	2.60
	235	1000	180	30	245.56	4.49	0.1243	0.3642	0.5451	240.64	2.40	241.03	2.57
LL (AB)	170	10	54	−15	188.43	10.84	0.2741	0.2728	0.8821	168.22	1.05	174.73	2.78
	180	10	54	−15	193.27	7.37	0.2562	0.2548	0.8632	183.03	1.68	176.52	1.93
	210	10	54	−15	194.37	7.44	0.2078	0.2064	0.7415	214.07	1.94	204.21	2.76
	215	10	54	−15	196.04	8.82	0.2004	0.199	0.706	219.47	2.08	209.42	2.60
LLL (ABC)	175	1	36	15	200.62	14.64	0.2472	0.2455	0.2454	172.11	1.65	179.41	2.52
	225	1	36	15	193.04	14.20	0.1745	0.1734	0.1735	231.11	2.72	231.02	2.68
	230	1	36	15	200.73	12.73	0.1683	0.1673	0.1679	227.33	1.16	233.49	1.52
	270	1	36	15	252.99	6.30	0.1239	0.1234	0.1243	265.33	1.73	277.26	2.69
	275	1	36	15	284.95	3.62	0.119	0.1185	0.1197	269.55	1.98	270.45	1.65

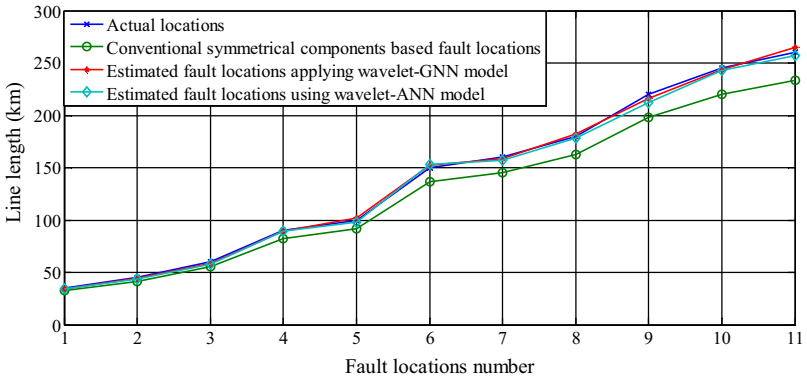


Fig. 8. Testing output and performance comparison of wavelet-GNN model with ANN and conventional symmetrical method based fault location estimation for AG fault (phase A to ground fault) due to the fault occurred at the various locations of the line, operating at $R_f = 100\,\Omega$, FIA = 36° and $\delta = -15°$.

the end terminal and it is found that the error varies from 0.15% to 2.05%. While using wavelet-ANN model it varies from 0.83% to 3.41% as depicted in column number eleven. Whereas in case of conventional symmetrical components based method of fault location as represented in column number four of Tables 2 and 3, it is found that the error varies from 4.05% to 10.75% which is considerably high. Graphically the comparisons of training and testing performance of fault locations result for the same are illustrated through Figs. 7 and 8. It is clearly seen from the graph that during training of wavelet-GNN model, both the actual and trained values are overlapping or very close to each other. This indicates that the network is trained successfully.

The task of estimation of fault locations is carried out for all kinds of phase and ground faults i.e. for line to ground (LG), double line to ground (LLG), line to line (LL) and double line to line (LLL) fault under different fault operating conditions as mentioned above. The performance of the models is evaluated on the basis of mean value of absolute relative error in percentage using the following formula

$$\text{Absolute relative error} = \frac{|\text{Actual fault location} - \text{Estimated fault location}|}{\text{Actual fault location}} \times 100$$

It is found that the mean value of absolute relative error using wavelet-GNN model is around 2%, while it is around 3% using wavelet-ANN model. Whereas in case of conventional symmetrical based fault location estimation method, it is in the range of 10%, considering the different fault operating conditions for all kinds of phase and ground faults. The comparative results of the wavelet-GNN based model of fault location estimation considering the same input parameters as in wavelet-ANN are depicted in Table 8. The comparison of fault locations using symmetrical components of voltage and current are also illustrated in Table 8, considering the same fault operating conditions as in GNN and ANN model. Observations of all test results ascertain that the wavelet-GNN based model of fault location estimation performs excellent even at voltage zero crossing situation of fault inception angle and at different fault locations starting from relay end (sending end) to the receiving end.

6. Conclusion

In the proposed study a GNN based fault location technique on three phase transmission line is presented. The fault current signals of the three phase transmission line are filtered through wavelet transform. The fault current signals are obtained at the sampling frequency of 100 kHz. MRA based on DWT is used to capture the transient characteristics of the fault current signals. The information captured during the ninth level frequency bands by the details wavelet coefficient in terms of standard deviation is fed as an input to the GNN and target as the fault location of the transmission line. The obtained results are compared with the conventional symmetrical components based method of fault location. To validate the proposed approach, it is applied to a large number of test cases generated for different fault operating conditions. The performance of the proposed wavelet-GNN model is also compared with ANN technique. It is found that the performance of the proposed GNN based model is better than the other method. As GNN requires less data to analyze. Therefore the time taken for identifying the location of the fault is quite less.

Acknowledgements

The authors would like to thanks to Prof. D.K. Chaturvedi, Department of Electrical Engineering, Dayalbagh Educational Institute (DEI), Deemed University, Agra (U.P.), India for giving us continuous support and suggestions in the development of GNN model for estimating the fault location of a given transmission systems.

Appendix I.

A multilayered feed forward neural network (FFNN) is chosen as shown in Fig. 9, for the fault location estimation of the transmission line considering the same input parameters and fault operating conditions as in wavelet-GNN based model of fault location estimation.

Appendix II.

In this study a faulted transmission line extending between two power systems as shown in Fig. 10, is considered to locate the fault distance '*d*' from the sending end of the transmission line to the fault point, due to the fault occurred under various fault operating

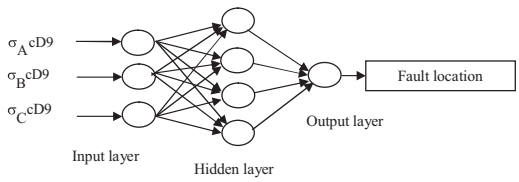


Fig. 9. Structure of Artificial neural network (ANN) for the fault location estimation.

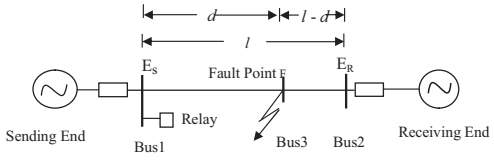


Fig. 10. Power system model.

conditions by measuring the sequence components of voltage and current at Bus1 and Bus3 using Eqs. (15)–(17).

The computed fault locations '*d*' in (km) for line to ground (LG), double line to ground (LLG), double line (LL), and double line to line LLL (symmetrical faults) faults are depicted in Tables 2–7 for different fault operating conditions.

$$Z_{13}^{0} = \frac{V_{sa}^{0}(F) - V_{3}^{0}(F)}{I_{13}^{0}} \tag{15}$$

$$Z_{13}^{1} = \frac{V_{sa}^{1}(F) - V_{3}^{1}(F)}{I_{13}^{1}} \tag{16}$$

$$Z_{13}^{2} = \frac{V_{sa}^{2}(F) - V_{3}^{2}(F)}{I_{13}^{2}} \tag{17}$$

where $V_{sa}{}^{0}(F) = 0 - Z_{13}{}^{0} I_{fa}{}^{0}$; $V_{sa}{}^{1}(F) = V_{sa}(F) - Z_{13}{}^{1} I_{fa}{}^{1}$; $V_{sa}{}^{2}(F) = 0 - Z_{13}{}^{2} I_{fa}{}^{2}$ and $Z_{13}^{0} = dZ^{0}$, $Z_{13}^{1} = dZ^{1}$, $Z_{13}^{2} = dZ^{2}$; $Z_{23}^{0} = (l-d)Z^{0}$, $Z_{23}^{1} = (l-d)Z^{1}$, $Z_{23}^{2} = (l-d)Z^{2}$; $V_{sa}{}^{0}(F)$, $V_{sa}{}^{1}(F)$ and $V_{sa}{}^{2}(F)$: zero, positive and negative components of sending end voltage; $V_{3}^{0}(F)$, $V_{3}^{0}(F)$ and $V_{3}^{0}(F)$: zero, positive and negative components of voltage at Bus3; $V_{sa}(0)$: pre-fault phase voltage at sending end; I_{fa}^{0}, I_{fa}^{1} and I_{fa}^{2}: zero, positive and negative components of current at fault point; Z_{13}^{0}, Z_{13}^{1} and Z_{13}^{2}: zero, positive and negative components of impedance between Bus1 and Bus3; Z_{23}^{0}, Z_{23}^{1} and Z_{23}^{2}: zero, positive and negative components of impedance between Bus2 and Bus3; l = total length of the transmission line in km; d = fault distance from relay to the fault point in km; Z^{0}, Z^{1} and Z^{2}: zero, positive and negative components of impedance of transmission line; base value selected for voltage (line to line) = 500 kV; Base value for power (VA 3 phase) = 100 MVA.

References

[1] M.J.B. Reddy, D.K. Mohanta, Performance evaluation of an adaptive network based fuzzy inference system approach for location of faults on transmission lines using Monte Carlo simulation, IEEE Trans. Fuzzy Syst. 16 (4) (2008) 909–917.

[2] T. Takagi, Y. Yamakoshi, M. Yamaura, R. Kondow, T. Matsushima, Development of a new type fault locator using the one terminal voltage and current data, IEEE Trans. Power Apparat. Syst. 101 (8) (1982) 2892–2898.

[3] H.-X. Ha, B.-H. Zhang, Z.-L. Lv, A novel principle of single ended fault location technique for EHV transmission lines, IEEE Trans. Power Deliv. 18 (4) (2003) 1147–1151.

[4] M.B. Djuric, Z.M. Radojevic, V.V. Terzija, Distance protection and fault location utilizing only phase current phasors, IEEE Trans. Power Deliv. 13 (4) (1998) 1020–1026.

[5] C. Wang, Q.-Q. Jia, X.-B. Li, C.-X. Dou, Fault location using synchronized sequence measurements, Int. J. Electr. Power Energ. Syst. 30 (2008) 134–139.

[6] S.M. Brahama, Iterative fault location scheme for a transmission line using synchronized phasor measurements, Int. J. Emerg. Electr. Power Syst. 8 (6) (2007) 1–14.

[7] Y. Liao, N. Kang, Fault location algorithms without utilizing line parameters based on the distributed parameter line model, IEEE Trans. Power Deliv. 24 (2) (2009) 579–584.

[8] C.E. de Morais Pereira, L.C. Zanetta, Fault location in transmission lines using one terminal postfault voltage data, IEEE Trans. Power Deliv. 19 (2) (2004) 570–574.

[9] S.R. Samantaray, P.K. Dash, G. Panda, Fault classification and location using HS-transform and radial basis function neural network, Electr. Power Syst. Res. 76 (2006) 897–905.

[10] J. Sadeh, H. Afradi, A new and accurate fault location algorithm for combined transmission lines using adaptive network based fuzzy inference system, Electr. Power Syst. Res. 79 (2009) 1538–1545.

[11] O.A.S. Youssef, Combined fuzzy logic wavelet based fault classification for power system relaying, IEEE Trans. Power Deliv. 19 (2) (2004) 582–589.

[12] D. Chanda, N.K. Kisore, A.K. Sinha, A wavelet multi resolution analysis for location of faults on transmission lines, Electr. Power Energ. Syst. 25 (2003) 59–69.

[13] A.H. Osman, O.P. Malik, Transmission line distance protection based on wavelet transform, IEEE Trans. Power Deliv. 19 (2) (2004) 59–69.

[14] P.S. Bhowmik, P. Purkait, K. Bhattacharya, A novel wavelet transform aided neural network based transmission line fault analysis method, Electric. Power Energ. Syst. 31 (2009) 213–219.

[15] J. Biswarup Das, V. Reddy, Fuzzy logic based fault classification scheme for digital distance protection, IEEE Trans. Power Deliv. 20 (2) (2005) 609–616.

[16] R.N. Mahanty, P.B. Dutta Gupta, A fuzzy logic based fault classification approach using current samples only, Electr. Power Syst. Res. 77 (2007) 501–507.

[17] S.R. Samantray, P.K. Dash, G. Panda, Distance relaying for transmission line using support vector machine and radial basis function neural network, Electric. Power Energ. Syst. 29 (2007) 551–556.

[18] H. Wang, W.W.L. Keerrthipala, Fuzzy neuro approach to fault classification for transmission line protection, IEEE Trans. Power Deliv. 13 (4) (1998) 1093–1102.

[19] C. Fan, K.K. Li, W.L. Chan, W. Yu, Study of protection scheme for transmission line based on wavelet transient energy, Electric. Power Energ. Syst. 28 (2006) 459–470.

[20] H. Osman, O.P. Malik, Protection of parallel transmission lines using wavelet transform, IEEE Trans. Power Deliv. 19 (1) (2004) 49–55.

[21] S. El Safty, A. El-Zonkoly, Applying wavelet entropy principle in fault classification, Electric. Power Energ. Syst. 31 (2009) 604–607.

[22] S. Ekici, S. Yildirim, M. Poyraz, Energy and entropy based feature extraction for locating fault on transmission lines by using neural network and wavelet packet decomposition, Exp. Syst. Appl. 34 (2008) 2937–2944.

[23] P. Chiradeja, A. Ngaopitakkul, Identification of fault types for single circuit transmission line using discrete wavelet transform and artificial neural networks, Proc. Int. Multi Conf. Eng. Comp. Sci. 2 (2009).

[24] N. Zhang, M. Kezunovic, Transmission line boundary protection using wavelet transform and neural network, IEEE Trans. Power Deliv. 22 (2) (2007) 859–869.

[25] B.K. Panigrahi, V.R. Pandi, Optimal feature selection for classification of power quality disturbances using wavelet packet based fuzzy k-nearest neighbour algorithm, IET Gener. Transm. Ditribut. 3 (2009) 296–306.

[26] A. Abdollahi, S. Seyedtabaii, Transmission line fault location estimation by Fourier and wavelet transforms using ANN, in: International Power Engineering and Optimization Conf., 2010, pp. 23–24.

[27] M. Jayabharata Reddy, D.K. Mohanta, A Wavelet fuzzy combined approach for classification and location of transmission line faults, Electric. Power Energ. Syst. 29 (2007) 669–678.

[28] M.P. Nikhli, A.A. Safavi, Path characteristic frequency based fault locating in radial distribution systems using wavelets and neural network, IEEE Trans. Power Deliv. 26 (2011) 752–781.

[29] D.K. Chaturvedi, S.A. Premdayal, A. Chandiok, Short-term load forecasting using soft computing techniques, Int. J. Commun. Netw. Syst. Sci. 3 (2010) 273–279.

[30] D.K. Chaturvedi, O.P. Malik, P.K. Kalra, Performance of a generalized neuron-based PSS in a multimachine power system, IEEE Trans. Energy Convers. 19 (3) (2004) 625–632.

[31] D.K. Chaturvedi, M. Mohan, P.K. Kalra, Improved generalized neuron model for short-term load forecasting, Soft Comput. 8 (2004) 370–379.

[32] D.K. Chaturvedi, R. Chauhan, P.K. Kalra, Applications of generalized neural networks in for aircraft landing control system, Soft Comput. 6 (2002) 441–448.

[33] D.K. Chaturvedi, P.S. Satsangi, P.K. Kalra, Fuzzified neural network approach for load forecasting, Eng. Intell. Syst. 1 (2001) 3–9.

[34] Manmohan, D.K. Chaturvedi, P.S. Satsangi, P.K. Kalra, Neuro fuzzy approach for development of new neuron model, Soft Comput. 8 (2003) 19–27.

[35] D.K. Chaturvedi, P.S. Satsangi, P.K. Kalra, Load frequency control: a generalized neural network approach, Int. J. Electr. Power Energy Syst. 21 (1999) 405–415.

[36] D.K. Chaturvedi, Soft Computing Techniques and its Applications in Electrical Engineering, Springer Verlag, Berlin, Heidelberg, Germany, 2008.

[37] D.K. Chaturvedi, Soft Computing Techniques and its Applications in Electrical Engineering, Springer Verlag, Berlin, Heidelberg, 2008.

[38] M. Rizwan, M. Jamil, D.P. Kothari, Generalized neural network approach for global solar energy estimation in India, IEEE Trans. Sust. Energ. 3 (3) (2012) 576–584.

SCIENTIFIC REPORTS



OPEN

SUBJECT AREAS:
SYNTHESIS OF GRAPHENE
DESIGN, SYNTHESIS AND PROCESSING
SOLAR CELLS
SYNTHESIS AND PROCESSING

Received
10 June 2013

Accepted
12 September 2013

Published
8 October 2013

Correspondence and requests for materials should be addressed to B.R.M. (brmehta@physics.iitd.ac.in)

In-flight gas phase growth of metal/multi layer graphene core shell nanoparticles with controllable sizes

Saurabh K. Sengar[1], B. R. Mehta[1], Rakesh Kumar[1] & Vinod Singh[1,2]

[1]Thin Film Laboratory, Indian Institute of Technology New Delhi, India-110016, [2]Department of Applied Physics, Delhi Technological University, Delhi, India-110042.

In this report, we present a general method for a continuous gas-phase synthesis of size-selected metal/multi layer graphene (MLG) core shell nanoparticles having a narrow size distribution of metal core and MLG shell for direct deposition onto any desired substrate kept under clean vacuum conditions. Evolution of MLG signature is clearly observed as the metal-carbon agglomerates get transformed to well defined metal/MLG core shell nanoparticles during their flight through the sintering zone. The growth takes place via an intermediate state of alloy nanoparticle (Pd-carbon) or composite nanoparticle (Cu-carbon), depending upon the carbon solubility in the metal and relative surface energy values. It has been also shown that metal/MLG nanoparticles can be converted to graphene shells. This study will have a large impact on how graphene or graphene based composite nanostructures can be grown and deposited in applications requiring controllable dimensions, varied substrate choice, large area and large scale depositions.

The observation of unique combination of properties, such as, mechanical strength, good thermal and electronic conductivity, zero band gap and ballistic electron transport in the 'ideal two dimensional' graphene structure have resulted in an unprecedented research interest[1–6]. In the last few years, graphene-metal nanoparticle composites have got attention due to possibility of tailoring the above mentioned properties resulting in improved, new and novel applications[7–18]. State of the art chemical vapor deposition allows the growth of graphene sheets on metal foils[19]. The restrictions of graphene growth only on few selected metal substrates and the requirement of transfer are the main nagging issues for using the graphene-metal nanostructures prepared by the above method in applications requiring large scale and large area deposition such as catalysis, Li ion batteries and solar cells[7–9,14,20]. The multistep chemical processes, used for growing graphene-metal composites involve simultaneous or separate reduction of graphene oxide with metal precursors yielding undefined configurations, high dispersibility and wide distribution of nanoparticle sizes and graphene thickness[21]. Chemical contamination incorporated into metal nanoparticles and graphene layers during reduction process is known to affect optical, electronic and catalytic properties[22–24]. The average nanoparticle size and distribution of Au nanoparticles grown by physical vapor deposition methods is linked to the number of graphene layers[25,26]. In physical methods of metal nanoparticles deposition, both particle density and particle size depend upon deposition time, and thus, nanoparticle size cannot be controlled independently. Further, in earlier reports on metal- carbon core shell nanoparticles prepared by arc discharge, metal carbide (in place of metal) core was found to be encapsulated in polyhedron carbon shells[27]. In another report, the graphite layer surrounding the metal nanoparticle was found to appear throughout the sample[28]. Broad size distribution and phase inhomogeneity are the other issues in these metal/graphite core shell nanoparticle prepared by arc discharge method[27,28]. Metal/graphite nanoparticles prepared by chemical methods have been reported to have low crystallinity, chemical contamination, and broad size distribution[29,30]. Therefore, these methods are not suitable for applications requiring controllable size, narrow size distribution and well defined graphene-metal interface such as biomedical and opto-electronic applications. In this report, a gas phase synthesis methodology for growing size selected metal/multilayer graphene (M/MLG) core shell nanoparticles with controllable size, narrow size distribution, well defined metal core and graphene shell is described.

Results

M/MLG core shell nanoparticles were fabricated using an integrated gas phase synthesis setup of which schematic diagram is shown in Fig. 1. The structural properties of the nanoparticles sintered at different temperatures during

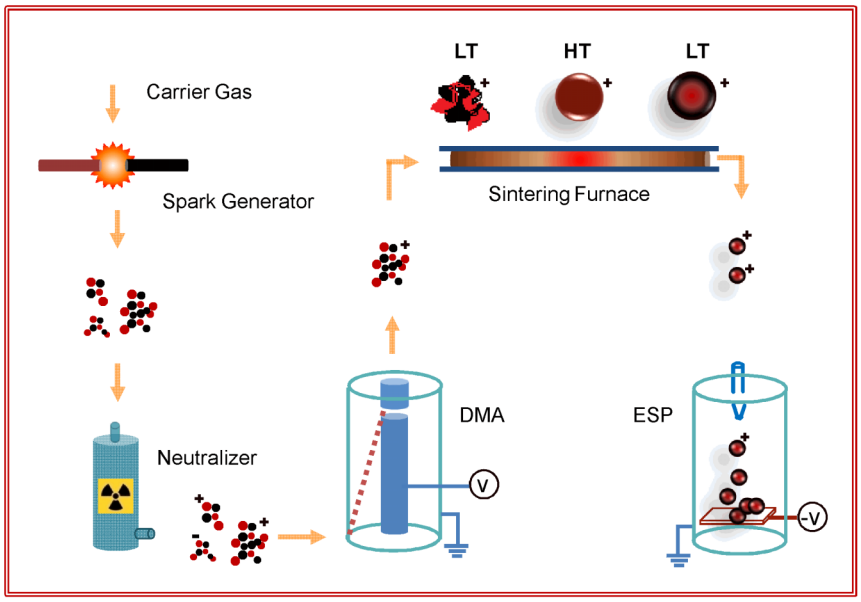


Figure 1 | Synthesis Methodology. Integrated gas phase synthesis setup for the growth of graphene-metal nanoparticles comprising of carrier gas assisted nanoparticle journey starting with formation of metal-carbon agglomerates in the spark generator, charging in the neutralizer, size selection in the DMA, sintering and subsequent cooling in the sintering furnace and deposition on desired substrate in the ESP as the final step. LT-low temperature, HT-High temperature zones.

in-flight sintering were carried out using glancing angle x-ray diffraction (GAXRD). GAXRD diffractograms of the Pd-C nanoparticles sintered at different temperatures are shown in Fig. 2a. The unsintered Pd-C agglomerates show high intensity peak at 2θ (d-value) of 39.36° (2.287 Å) corresponding to Pd-C solid solution in face centered cubic (FCC) phase having carbon atoms at interstitial positions[31]. In addition, a relatively low intensity peak at 40.04° (2.250 Å) corresponding to Pd FCC phase is also evident. A lattice parameter of 2.309 Å is reported in Pd-C nanoparticles due to the incorporation of carbon at the interstitial positions[31]. This behavior is similar to that observed in case of Pd-H system where hydrogen incorporation at the interstitial positions results in lattice expansion due to formation of β-palladium hydride phase[32]. In nanoparticles sintered at 300°C and deposited at RT, intensity of the Pd peak increases, accompanied by a decrease in Pd-C peak intensity and shift towards higher 2θ value. On further increasing the sintering temperature to 500°C, intensity of the Pd peak becomes higher than that of the Pd-C peak indicating that more and more of the carbon phase segregates out as the sintering temperature is increased. Finally, in nanoparticles sintered at 700°C, only Pd peak is observed with nearly complete segregation of carbon phase out of the Pd lattice. Unlike, Pd-C system, XRD peaks corresponding to the FCC Cu phase remains unchanged in all the samples sintered at different temperatures and stay at 43.275° (2.090 Å), as shown in Fig. 2b. This indicates that small carbon solubility has negligible effect on Cu lattice.

Morphological changes in Pd-C and Cu-C nanoparticles on sintering were studied using high resolution electron microscopy (HRTEM). HRTEM micrographs of the Pd-C nanoparticles sintered at different temperatures are shown in Figs. 3a–d (also see supplementary Fig. S1). It is clear from Fig. 3a that the initial agglomerates consist of 2–5 nm sized primary nanoparticles as revealed by lattice fringes (2.390 Å) corresponding to Pd-C alloy. On increasing the sintering temperature to 300°C, particles start merging as compaction process is initiated (Fig. 3b). Thereafter, at a sintering temperature of 500°C, compact, quasi-spherical and crystalline nanoparticles having carbon layers in the shell around the inner core are formed (Fig. 3c). Finally, sintering at 700°C results in the formation of nearly spherical, Pd/C core shell nanoparticles with carbon shell clearly visible in the HRTEM image (Fig. 3d). In the Pd/C core shell nanoparticle sintered

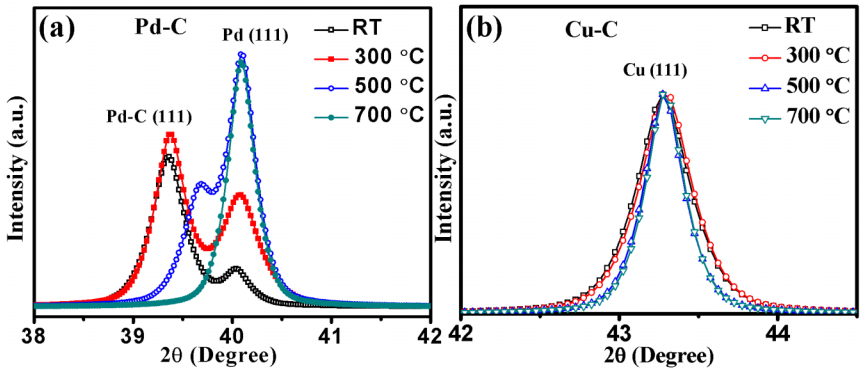


Figure 2 | Effect of in-flight sintering on structural properties. (a) X-ray diffractograms of Pd (111) peak show that initial Pd-C agglomerates get converted to Pd-C alloy nanoparticles before the segregation of carbon on surface of Pd nanoparticle core. (b) X-ray diffractograms of Cu-C do not show any lattice expansion indicated by Cu (111) peak due to very low solubility of carbon into Cu.

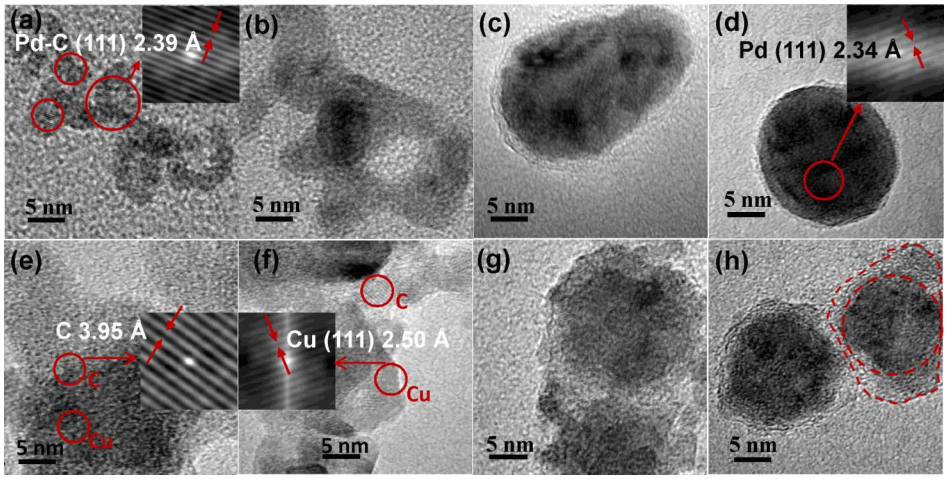


Figure 3 | Morphological changes on in-flight sintering. TEM images showing the compaction and conversion of (a–d) Pd-C and (e–h) Cu-C agglomerates to Pd/MLG and Cu/MLG core shell nanoparticles on sintering. HRTEM image of Pd-C agglomerates (a) showing Pd-C phase which gets converted to Pd phase (d) in the nanoparticle core on sintering at 700°C followed by subsequent cooling. MLG shell around the well formed metal nanoparticles is clearly visible in Figs. c and d. HRTEM images (e–f) of Cu-C nanoparticles show the presence of both Cu and C phases as confirmed by lattice fringes of selected regions in the micrographs (inset of e and f). Graphene shell layer around the well formed metal nanoparticles is clearly visible in Fig. g and h.

at 700°C a d-value of 2.340 Å is obtained from the lattice fringes of the Pd nanoparticle-core. The d-values of Pd-C and Pd phases using TEM are larger in comparison to those calculated from XRD. Slightly larger value of d-spacing as calculated by TEM in comparison to XRD may be due to the localized measurement in electron diffraction technique and a possibility of lattice expansion at smaller sizes[33–35]. The d-value obtained from XRD is the average value calculated from a larger sample having widely varying sizes of clusters especially in unsintered samples while the d-value obtained from HRTEM measurement corresponds to a specific nanoparticle. A large change in the lattice constant has been reported in a number of material systems[34,35]. Similar trends in the morphological changes of Cu-C nanoparticle system during the conversion of Cu-C agglomerates to Cu/C core shell nanoparticles are observed. In the HRTEM images (Figs. 3e–h) lattice fringes with inter-planar spacing of 3.95 Å and 2.50 Å are observed at different locations in case of agglomerated Cu-C particles. These values differ with the corresponding bulk values of 3.40 Å and 2.09 Å for graphite and Cu, respectively. These differences may be due to lattice expansion at smaller sizes of metal and carbon clusters in the agglomerates at RT[34,35]. Again the difference between the d-value of Cu calculated from XRD and HRTEM may be due to the localized measurement in HRTEM and widely varying cluster sizes in unsintered samples. On sintering at a temperature of 300°C, the compaction process gets initiated as shown in Fig. 3f. At 500°C sintering, formation of the Cu nanoparticle core and carbon shells is initiated (Fig. 3g). On further increasing the sintering temperature to 700°C quasi spherical metal nanoparticle core enveloped by well formed carbon shell around them is clearly observed in the HRTEM micrograph (Fig. 3h).

To investigate the nature of carbon, micro- Raman measurements of Cu-C and Pd-C nanoparticles sintered at different temperatures were carried out and are shown in Figs. 4a and b, respectively. In the initial Cu-C and Pd-C agglomerates without any sintering, no Raman peak in the entire measurement range of 1100–3200 cm^{-1} is observed. In the unsintered samples, carbon is present in the form of amorphous and nanosized carbon clusters or Pd-C clusters which are loosely connected to form agglomerates. A significant portion of carbon is present in the form of Pd-C and is expected not to show any D and G peak. In an earlier report, similar results on the absence of Raman D and G peaks in unsintered Ti-B-C films have been reported[36]. G peak is due to the relative motion of sp^2 carbon atoms while D peak is linked to the breathing mode of carbon rings (defects)[37]. As shown in Fig. 4a, G peak lie at 1584 cm^{-1} and I_D/I_G ratio is found to be 0.73 in the Cu-C nanoparticles sintered at 300°C. These values of G peak and I_D/I_G ratio correspond to either amorphous carbon or nanocrystalline graphite[37]. The absence of second order 2D peak which is the second order overtone of D peak in Cu-C samples sintered at 300°C indicates that it is amorphous

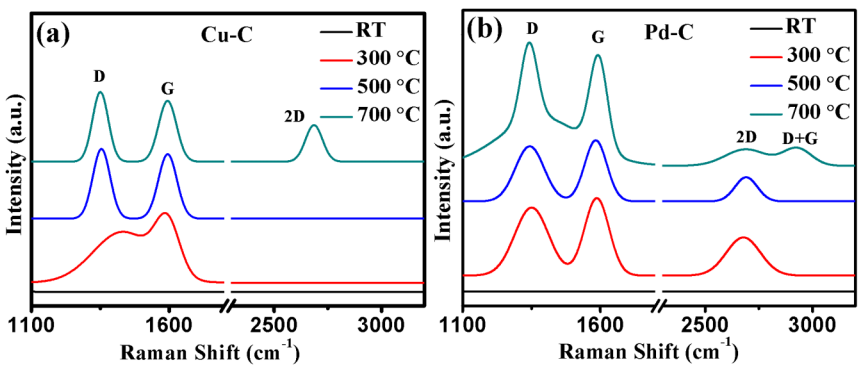


Figure 4 | Effect of sintering on Raman properties. Raman spectra of (a) Cu-C and (b) Pd-C nanoparticles sintered at increasing temperatures show that the initial amorphous carbon gets converted to MLG on sintering at 700°C.

carbon and not nanocrystalline graphite[37,38]. The possibility of diamond like carbon instead of amorphous carbon has been ruled out as the I_D/I_G ratio is >0.2[37]. On increasing the sintering temperature to 500°C, G peak appears at 1594 cm^{-1} while the I_D/I_G ratio increases to 1.08 in Cu-C nanoparticles. Finally on sintering at 700°C, G peak remains constant and I_D/I_G ratio increases to 1.15 in Cu-C nanoparticles. Further, in Cu-C nanoparticles sintered at 700°C, 2D peak appears at 2685 cm^{-1}. According to the 3-stage theory, G peak position near to 1600 cm^{-1} and a continuous increase in I_D/I_G ratio indicates that amorphous carbon gets converted to nanocrystalline graphite on increasing the sintering temperature[38,39]. Further, in Cu-C nanoparticles sintered at 700°C, I_G/I_{2D} ratio is found to be 1.66 while in bulk graphite I_G/I_{2D} ratio is reported to be ~4 which indicates that it is not nanocrystalline graphite but a stack of graphene nanolayers (MLG). As per literature, I_G/I_{2D} ratio of 1.66 represents a stack of 4–5 graphene nanolayers[40]. HRTEM micrograph (Fig. 3h) of Cu-C nanoparticles sintered at 700°C confirms this.

In Pd-C nanoparticles sintered at 300°C, three peaks at 1351 cm^{-1}, 1586 cm^{-1}, and 2678 cm^{-1} corresponding to D, G and 2D bands, respectively, are observed. In these nanoparticles, I_G/I_{2D} ratio is 2.05 and I_D/I_G ratio is 0.87. As discussed earlier, these conditions correspond to nanocrystalline graphite. On increasing the sintering temperature to 500°C, I_G/I_{2D} ratio increases to 2.41 while I_D/I_G ratio remains nearly same at 0.91. Finally at 700°C, I_G/I_{2D} ratio increases to 6.69 and I_D/I_G ratio increases to 1.11.

One of the advantages of the integrated gas phase deposition is that nanoparticle growth and deposition on to substrates are two independent steps. Nanoparticles having a controllable size and narrow size distribution can be grown by controlling the electrical mobility, which in turn can be changed by aerosol flow rate and DMA voltage. Size selected Cu/MLG core shell nanoparticles having an initial mobility equivalent diameter (Dm) of 68, 52, and 35 nm were grown using proper sintering conditions. It needs to be mentioned here that smaller mobility diameter particles require lower sintering temperature consistent with the normally observed depression in the melting point at lower sizes. It is observed from the HRTEM images in Figs. 5a and 5b that nanoparticle core is spherical and has a very well defined size (Dg) of 29.9 ± 2.9, 21.9 ± 1.7 and 18.3 ± 1.4 nm in the sintered Cu/MLG core shell nanoparticles (see supplementary Figs. S2 and S3). In Cu/MLG core shell nanoparticles having D_m = 35 nm, the average size of the Cu core and the thickness of the MLG shell are 14.5 ± 0.9 nm and 2.3 ± 0.6 nm, respectively, as shown in the size histograms in Fig. 5c. In case of Pd/MLG samples too, nearly same values of sizes are observed (supplementary Figures S2 and S3). From the comparison of HRTEM micrographs of Pd/MLG and Pd (without any carbon) nanoparticles it is clear that unlike Pd/MLG, Pd nanoparticles don't have any MLG like shell structure (supplementary Fig. S2). With increase in the size of the nanoparticle core, the width of the graphene shell is observed to decrease. This may be due to the difference in solubility of carbon in metal nanoparticle of different sizes. The Raman spectra of size selected core shell Cu/MLG nanoparticles having Dm values of 35, 52 and 68 nm is shown in Fig. 5d. The I_G/I_{2D} ratio for the Cu/MLG nanoparticles having Dm values of 35,52 and 68 nm comes out to be 1.66, 1.49 and 0.79, respectively. As discussed earlier, this indicates that properly sintered spherical shaped Cu/C nanoparticles have a shell comprising of multi

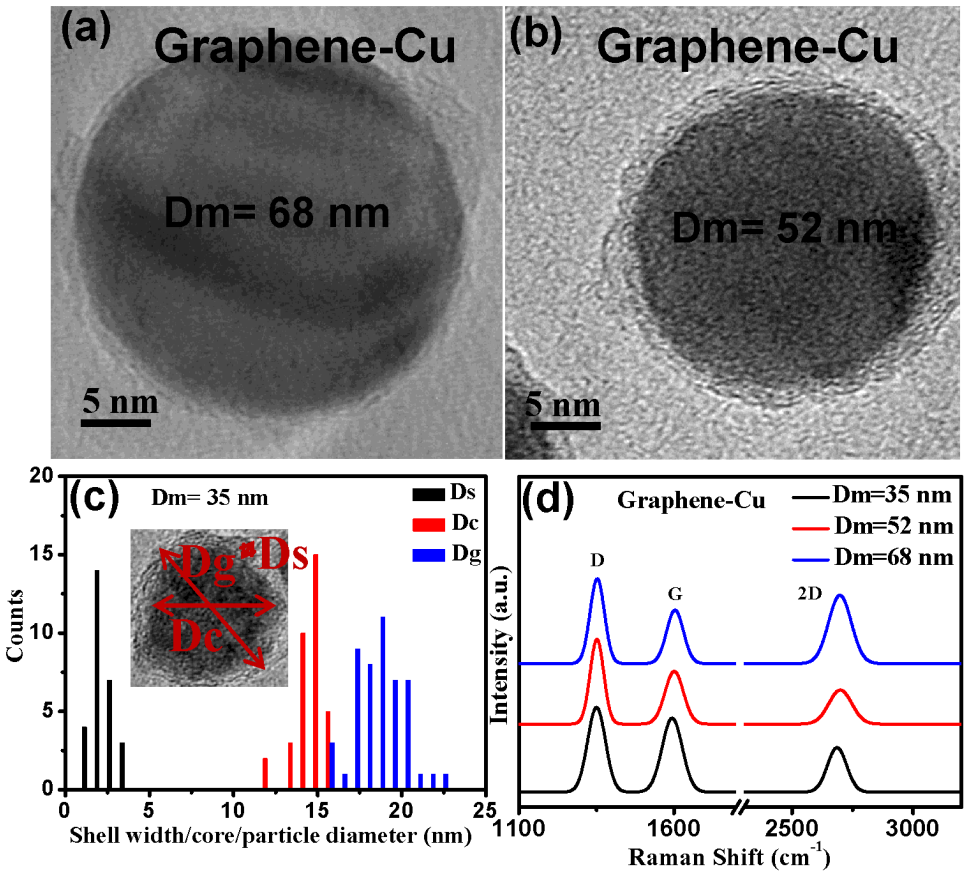


Figure 5 | Size selected Cu/MLG nanoparticles. [(a), (b)] HRTEM micrographs of Cu/MLG nanoparticles with mobility equivalent diameter (Dm) of 68 and 52 nm, respectively. (c) Histogram showing size distribution of shell thickness (Ds), Core diameter (Dc) and nanoparticle size (Dg) for Cu/MLG nanoparticle having Dm = 35 nm. Narrow size distribution, control of nanoparticle size by controlling electrical mobility diameter and well formed nanoparticle core and graphene shell are clearly visible. (d) Raman Spectra of size selected Cu/MLG nanoparticles for Dm = 35, 52 and 68 nm showing decrease in graphene layers with increase in nanoparticle size.

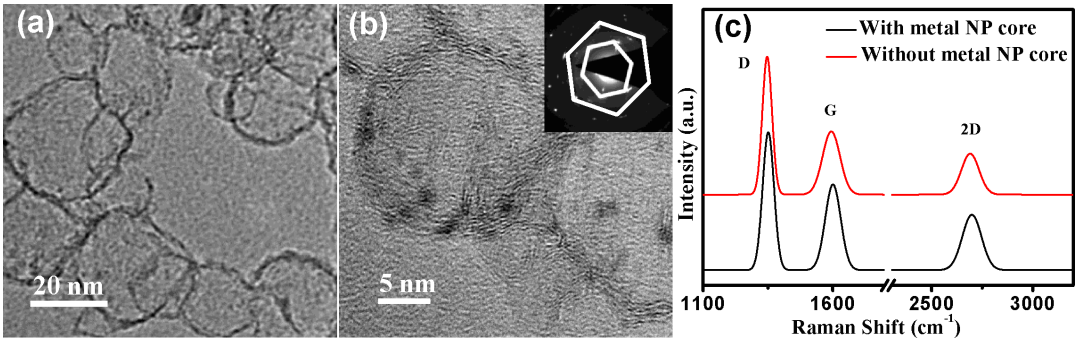


Figure 6 | Graphene nanoshells. [(a), (b)] HRTEM images of MLG shells formed by removing metal core via chemical etching. Inset shows SAED diffraction pattern of the MLG shells. (c) Comparison of Raman spectrum with and without Cu nanoparticle (NP) core confirms the preservation of MLG shell on chemical etching.

layer graphene. The continuously decreasing I_G/I_{2D} ratio indicates that the number of graphene nanolayers decrease on increasing the particle size. Decrease in number of graphene layers on increasing the Dm value is consistent with HRTEM of Cu/MLG core shell nanoparticles.

Wet chemical etching was used to remove the metal core in order to obtain the MLG shells (Fig. 6a) from the Cu/MLG core shell nanoparticles using $FeCl_3$ solution. After chemical etching MLG shell structures consisting of about 3–4 graphene layers can be easily seen in the HRTEM image (Fig. 6b). The selected area electron diffraction (SAED) patterns (Fig. 6b) with six fold symmetry confirm the MLG shell structure after removing the metal core. The Raman spectrum (Fig. 6c) shows an increase in I_D/I_G peak ratio from 1.59 to 2.18 after etching the Cu from the nanoparticle core which may be due to defects created during etching. To show the universality of the present method to spray coat the M/MLG nanoparticles onto any desired substrate, Cu/MLG core shell nanoparticles were deposited on to Si (polished and textured) and interdigitated Au electrodes (Au-Cr/SiO_2/Si). Scanning electron microscopy (SEM) images of Cu/MLG nanoparticles (Dm = 52 nm) grown on polished Si, textured Si and interdigitated Au electrodes fabricated on SiO_2/Si substrates are shown in Figs. 7a–c. Optical and electronic properties of the Cu/MLG nanoparticles were also studied. Reflectance spectrum of Cu/MLG nanoparticles (Dm = 52 nm) deposited on polished Si is shown in Fig. 7a (inset). Reflectance spectrum of Cu/MLG nanoparticles deposited on polished Si shows a large drop in total reflectance in comparison to the bare Si. Electronic properties of Cu/MLG nanoparticles were carried out in a field effect transistor (FET) structure where n-doped Si substrate is acting as back gate. The source-drain resistance versus back-gate voltage V_{BG} curve for the Cu/MLG

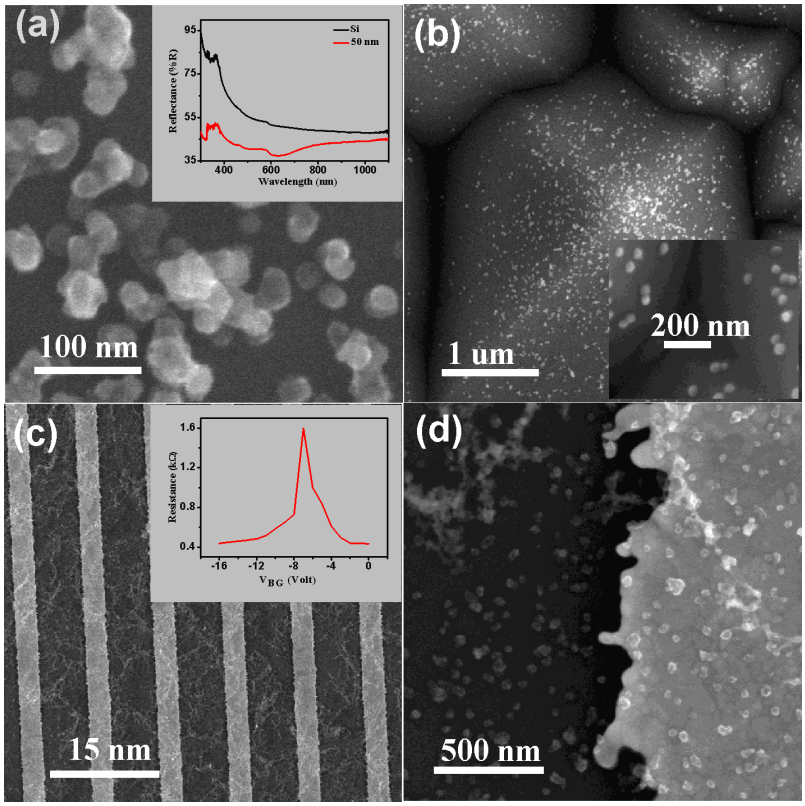


Figure 7 | Direct deposition of Cu/MLG core shell nanoparticles on substrates having different morphologies. SEM images of Cu/MLG nanoparticle (Dm = 50 nm) deposited on (a) polished, (b) textured Si substrates and (c, d) interdigitated Au electrodes. Inset of (a) shows the comparison of the reflectance spectra of Cu/MLG nanoparticle on Si and bare Si substrate. Inset of (c) shows gate voltage characteristics of Cu/MLG nanoparticles deposited in FET structure.

nanoparticles at room temperature is shown in Fig. 7c (inset). Dirac point at a negative gate voltage indicates unintentional n-type doping of the Cu/MLG nanoparticles[41].

Discussion

On the basis of the results of the structural, morphological and Raman studies, formation of M/MLG core shell nanoparticles in both the Pd-C and Cu-C material systems can be understood in terms of temperature dependence of carbon solubility in metals and the relative surface energy values. The solubility of carbon in different metals forming solid solution is given by the following equation based on Henrian behavior for the carbon activity[42].

$$\frac{x_c}{1-2x_c} = \exp\left(-\frac{\Delta H}{RT}\right)\exp\left(\frac{\Delta S}{R}\right) \quad (1)$$

Where x_c is the carbon content in mole fraction, ΔH is the partial molar enthalpy of carbon in solution, ΔS is the partial molar excess enthalpy of carbon in solutions, R is the gas constant and T is the absolute temperature. Using the reported values of ΔH (-30.9 kJ/mol) and ΔS (-0.136R) an increase from 3 ppm at RT to 15800 ppm at 700°C of carbon solubility in Pd lattice is calculated[43]. Observed shift (Fig. 2a) in XRD peak positions of Pd indicate that Pd-C solid solution is formed in the intermediate growth stage. Carbon solubility in Cu at RT and 700°C is calculated to be 1.5×10^{-4} ppm and 2.5 ppm, respectively, using the reported values of ΔH (-35.1 kJ/mol) and ΔS (-8.532R)[42]. Due to low carbon solubility in copper, no change in the XRD peak positions of the Cu (Fig. 2b) is observed in Cu-C system. Average surface energy of carbon in different phases (fullerene, graphite, and carbon black) is quite low (<250 mJ/m^2) in comparison to Pd (2.05 J/m^2) and Cu (1.83 J/m^2)[44,45]. In Pd-C system, a solid solution of Pd-C is formed on sintering, higher the sintering temperature more is the carbon solubility. As particles come out of the sintering zone, temperature decreases and hence carbon atoms segregate out of the Pd lattice and migrate to surface due to their low surface energy. Lattice fringes corresponding to Pd-C and Pd (Figs. 3e and 3h) are observed in unsintered agglomerates and nanoparticles sintered at 700°C, respectively. In case of Cu-C system, initially agglomerates consist of copper and carbon primary particles. At high temperatures Cu-C composite nanoparticle having Cu, C and mixed phases are formed, as confirmed by lattice fringes in the HRTEM images (Figs. 3a and 3b) of unsintered agglomerates and sintered agglomerates at 300°C. As Cu-C composite nanoparticle is sintered at higher temperature carbon segregates to the outer surface due to lower surface energy value while Cu segregates to the inner core. As both sintering and cooling takes place in-flight in the homogeneous gaseous medium, quasi spherical nanoparticles having Pd/Cu core and MLG shell are formed. It is necessary to mention that in both the material systems optimized sintering temperature is important for the growth of MLG shell around the spherical metal nanoparticle core. Under-sintering leads to incomplete compaction while over-sintering is observed to result in re-evaporation of metallic phases, both of which affect the size and size distribution of metal core and MLG shells. Large solubility values of C in Fe, Co and Ni at higher temperatures and large surface energy values of most of the metals (e.g. Pt, Ni, Co, W, Fe, Cr, and Ti) in comparison to carbon allows this method to be used as a general technique for M/MLG core shell nanoparticle growth[46]. Controlled growth of M/MLG core shell nanoparticles having a well defined size and narrow size distribution can be achieved by just manipulating the solubility and surface energy of two components with in-flight sintering temperature.

Gas phase deposition methods are ideally suitable for large scale and continuous deposition[47]. Recent report on the continuous growth of semiconductor nanorods onto size selected seed nanoparticles is a novel demonstration of the versatility of the gas phase deposition methods. A careful control of homogenous (Au nanoparticle) and heterogeneous nucleation (GaAs nanorods onto Au) in the gas has been utilized to grow Au-GaAs nanostructures[47]. The present method is a major step forward towards the advantage of depositing graphene based nanostructures in the gas phase mode in comparison to deposition of graphene layer on metal substrate and formation of graphene-metal nanoparticles by multi step chemical and physical processes. In the present study metal-carbon nanoagglomerates were formed by spark generation process using metal (Cu or Pd) and carbon as the two electrodes. Metal and carbon concentration in the intermediate alloy/composite nanoparticle was thus fixed by the relative ablation rates of the two materials during spark generation step[48]. It might be possible to vary the metal-carbon composition by preparing metal agglomerates and then sintering them in the presence of carbon precursor gases (e.g. CH_4). It is expected that this will result in a better control of number of graphene layers in the shell. Further, the M/MLG core shell nanoparticle prepared by the present method can also be incorporated into or onto growing thin films prepared by vacuum or plasma deposition techniques[49]. After etching the metal core, size-dependent electronic and magnetic properties of graphene shells can also be studied[50]. Moreover, the etching step for removing Cu or Pd core might be carried out in gas phase itself so that graphene shells can be deposited onto a desired substrate in the final step.

Synthesis of M/MLG nanoparticles having well defined dimensions and the possibility of their direct deposition on to different substrates will result in new and novel applications. MLG cap around the noble metal nanoparticles can result in significantly reducing the consumption of noble metals in large scale fuel cell applications[11–13]. Most recently, carbon-coated metal nanoparticles have shown exceptionally long term thermal and chemical stability against acidic erosion, reliable linking chemistry and biocompatibility, important for biomedical applications[51]. A well defined MLG shell can enhance the functionalization of drug molecules to metal nanoparticle core, which is useful in a number of drug delivery and bio imaging applications[52]. The enhanced surface contact between metal and graphene layers is known to result in enhancing the H_2 sensing response in graphene-Pd/Pt nanoparticles[15,16]. Graphene-metal (Au/Ag) nanoparticles with efficient molecule absorption property combined with strong surface enhanced Raman sensitivity are excellent substrates for nano-molar level molecular detection[53,54]. M/MLG nanoparticles may have superior electromagnetic interference shielding properties in comparison to individual metal or graphene layers[55]. M/MLG nanoparticles on solar cell surfaces may have superior antireflection properties due to anti-reflection (graphene layers) and surface plasmon (metal nanoparticles) effects[20,56]. SEM images of Cu/MLG core shell nanoparticles deposited onto textured silicon substrates show possible uniform growth on substrates having non-planar surface using the present method.

Methods

The schematic diagram of the integrated gas phase setup used for growing Cu/MLG and Pd/MLG core shell nanoparticles is shown in Fig. 1. It comprises of a spark generator for forming aerosol consisting of metal-carbon nanoagglomerates, particle charger for charging the agglomerates, DMA for selecting the agglomerates of constant mobility equivalent diameter (Dm), sintering furnace for compacting the agglomerates into M/MLG core shell nanoparticles and an ESP for depositing the M/MLG core shell nanoparticles onto any desired substrate. In the spark generator, electrical sparks are generated by applying a pulsating high voltage (~3 kV) to the carbon and Cu/Pd electrodes separated by a distance of 1.8 mm which is kept fixed during material ablation by an electrical stepper motor. Electrical sparks result in the ablation of the electrode material. Spark current controls the electrode ablation rate and can be changed by just varying the spark frequency. Due to very short duration of the pulsed discharge, evaporated material rapidly cools down, resulting in supersaturation, leading to the nucleation, condensation and finally to the formation of nanoagglomerates having a large size distribution. Average value of size and size distribution depends on the frequency and carrier gas flow. High purity nitrogen (N_2) (with 2% hydrogen) as a carrier gas is used in the complete process starting from the initial step of agglomerate formation to final step of nanoparticle deposition. In the particle charger, agglomerates were charged using a Kr-85 based radioactive isotope. Particle charger is basically a radioactive Kr-85 source which charges the nanoparticles both positively and negatively and is also called a neutralizer. DMA is used to

select the nanoparticles as per their Dm values which are controlled by the flow conditions and voltage applied to the DMA electrodes. By measuring the size distribution of agglomerates just after the spark generator, frequency was adjusted to obtain the peak at the desired Dm value. In the in-flight sintering step, compaction, alloy formation and phase separation processes resulted in the formation of M/MLG core shell nanoparticles. Finally, M/MLG core shell nanoparticles were deposited onto the Si substrates and TEM grids for further characterization.

Three different Pd-C/Cu-C agglomerates having Dm = 35, 52 and 68 nm were selected using the DMA. Diameter of C and Pd/Cu electrodes was kept fixed at 3.2 mm. Spark frequency was kept constant at 200 Hz throughout the experiment. Carrier flow (2% H_2 + 98% N_2) in the spark generator and aerosol flow in the sintering furnace were kept fixed at 2.5 l/m and 1 l/min, respectively. In the sintering furnace, agglomerates were sintered in-flight at 700°C, 820°C and 950°C, respectively. In the ESP, a constant voltage of 1 KeV was applied to the substrate with a fixed distance of 1.5 mm between the substrate and the nozzle.

TEM (FEI-Technai-G20 with a LaB6 filament, operated at 200 keV) was used to study the size and structural properties of nanoparticles. GAXRD (Philips X'Pert, PRO-PW 3040, CuKα) measurements at a glancing angle of 1° were carried out to investigate the structural properties. Micro-Raman measurements were performed to study the vibrational properties, using a Renishaw spectrometer at 514 nm of wavelength.

1. Du, X., Skachko, I., Barker, A. & Andrei, E. Y. Approaching ballistic transport in suspended graphene. *Nat Nano* **3**, 491–495 (2008).
2. Pati, S. K., Enoki, T. & Rao, C. N. R. *Graphene and Its Fascinating Attributes*. (World Scientific, Singapore, 2011).
3. Balandin, A. A. Thermal properties of graphene and nanostructured carbon materials. *Nat Mater* **10**, 569–581 (2011).
4. Lee, C., Wei, X., Kysar, J. W. & Hone, J. Measurement of the elastic properties and intrinsic strength of monolayer graphene. *Science* **321**, 385–388 (2008).
5. Miao, X. *et al.* High efficiency graphene solar cells by chemical doping. *Nano Lett.* **12**, 2745–2750 (2012).
6. Schedin, F. *et al.* Detection of individual gas molecules adsorbed on graphene. *Nat Mater* **6**, 652–655 (2007).
7. Scheuermann, G. M., Rumi, L., Steurer, P., Bannwarth, W. & Mülhaupt, R. Palladium nanoparticles on graphite oxide and its functionalized graphene derivatives as highly active catalysts for the Suzuki−Miyaura coupling reaction. *J. Am. Chem. Soc.* **131**, 8262–8270 (2009).
8. Li, Y. *et al.* Palladium nanoparticle-graphene hybrids as active catalysts for the Suzuki reaction. *Nano Res.* **3**, 429–437 (2010).
9. Siamaki, A. R., Khder, A. E. R. S., Abdelsayed, V., El-Shall, M. S. & Gupton, B. F. Microwave-assisted synthesis of palladium nanoparticles supported on graphene: A highly active and recyclable catalyst for carbon–carbon cross-coupling reactions. *J. Catal.* **279**, 1–11 (2011).
10. Seger, B. & Kamat, P. V. Electrocatalytically active graphene-platinum nanocomposites. role of 2-D carbon support in PEM fuel cells. *J. Phys. Chem. C* **113**, 7990–7995 (2009).
11. Zhou, Y.-G., Chen, J.-J., Wang, F.-B., Sheng, Z.-H. & Xia, X.-H. A facile approach to the synthesis of highly electroactive Pt nanoparticles on graphene as an anode catalyst for direct methanol fuel cells. *Chem. Commun.* **46**, 5951–5953 (2010).
12. Zhao, H. *et al.* Fabrication of a palladium nanoparticle/graphene nanosheet hybrid via sacrifice of a copper template and its application in catalytic oxidation of formic acid. *Chem. Commun.* **47**, 2014–2016 (2011).
13. Yang, J., Tian, C., Wang, L. & Fu, H. An effective strategy for small-sized and highly-dispersed palladium nanoparticles supported on graphene with excellent performance for formic acid oxidation. *J. Mater. Chem.* **21**, 3384–3390 (2011).
14. Ji, L. *et al.* Multilayer nanoassembly of Sn-nanopillar arrays sandwiched between graphene layers for high-capacity lithium storage. *Energy Environ. Sci.* **4**, 3611–3616 (2011).
15. Johnson, J. L., Behnam, A., Pearton, S. J. & Ural, A. Hydrogen sensing using Pd-functionalized multi-layer graphene nanoribbon networks. *Adv. Mater.* **22**, 4877–4880 (2010).
16. Kaniyoor, A., Imran Jafri, R., Arockiadoss, T. & Ramaprabhu, S. Nanostructured Pt decorated graphene and multi walled carbon nanotube based room temperature hydrogen gas sensor. *Nanoscale* **1**, 382–386 (2009).
17. Mao, S., Lu, G., Yu, K., Bo, Z. & Chen, J. Specific protein detection using thermally reduced graphene oxide sheet decorated with gold nanoparticle-antibody conjugates. *Adv. Mater.* **22**, 3521–3526 (2010).
18. Du, M., Yang, T. & Jiao, K. Immobilization-free direct electrochemical detection for DNA specific sequences based on electrochemically converted gold nanoparticles/graphene composite film. *J. Mater. Chem.* **20**, 9253–9260 (2010).
19. Li, X. *et al.* Large-area synthesis of high-quality and uniform graphene films on copper foils. *Science* **324**, 1312–1314 (2009).
20. Kumar, R., Sharma, A. K., Bhatnagar, M., Mehta, B. R. & Rath, S. Antireflection properties of graphene layers on planar and textured silicon surfaces. *Nanotechnology* **24**, 165402 (2013).
21. Bai, S. & Shen, X. Graphene-inorganic nanocomposites. *RSC Advances* **2**, 64–98 (2012).
22. Shin, H.-J. *et al.* Efficient reduction of graphite oxide by sodium borohydride and its effect on electrical conductance. *Adv. Funct. Mater.* **19**, 1987–1992 (2009).
23. Zan, R., Bangert, U., Ramasse, Q. & Novoselov, K. S. Interaction of metals with suspended graphene observed by transmission electron microscopy. *J. Phys. Chem. Lett.* **3**, 953–958 (2012).
24. Jiang, Y. *et al.* Facile electrochemical codeposition of "clean" graphene–Pd nanocomposite as an anode catalyst for formic acid electrooxidation. *Electrochem. Commun.* **19**, 21–24 (2012).
25. Luo, Z. *et al.* Size-selective nanoparticle growth on few-layer graphene films. *Nano Lett.* **10**, 777–781 (2010).
26. Zhou, H. *et al.* Thickness-dependent morphologies of gold on n-layer graphenes. *J. Am. Chem. Soc.* **132**, 944–946 (2009).
27. Ruoff, R. S., Lorents, D. C., Chan, B., Malhotra, R. & Subramoney, S. Single crystal metals encapsulated in carbon nanoparticles. *Science* **259**, 346–348 (1993).
28. Majetich, S. A., Artman, J. O., McHenry, M. E., Nuhfer, N. T. & Staley, S. W. Preparation and properties of carbon-coated magnetic nanocrystallites. *Phys Rev B* **48**, 16845–16848 (1993).
29. Zalich, M. A., Baranauskas, V. V., Riffle, J. S., Saunders, M. & St. Pierre, T. G. Structural and magnetic properties of oxidatively stable cobalt nanoparticles encapsulated in graphite shells. *Chem. Mater.* **18**, 2648–2655 (2006).
30. Ma, Y. *et al.* Chemical functionalization of magnetic carbon-encapsulated nanoparticles based on acid oxidation. *J. Phys. Chem. B* **110**, 20118–20122 (2006).
31. Yamamoto, T., Adachi, M., Kawabata, K., Kimura, K. & Hahn, H. W. Palladium carbide nanoparticles by gas flow reaction synthesis. *Appl. Phys. Lett.* **63**, 3020–3022 (1993).
32. Flanagan, T. B. & Oates, W. A. The palladium-hydrogen system. *Annu. Rev. Mater. Sci.* **21**, 269–304 (1991).
33. Smontara, A. *et al.* Structural (XRD and HRTEM) investigations of fullerite C60 and C70 samples. *Mater. Sci. Eng., C* **19**, 21–25 (2002).
34. Hailstone, R. K., DiFrancesco, A. G., Leong, J. G., Allston, T. D. & Reed, K. J. A study of lattice expansion in CeO2 nanoparticles by transmission electron microscopy. *J. Phys. Chem. C* **113**, 15155–15159 (2009).
35. Sun, C. Q. Size dependence of nanostructures: Impact of bond order deficiency. *Prog. Solid State Chem.* **35**, 1–159 (2007).
36. Sánchez-López, J. C. *et al.* Phase composition and tribomechanical properties of Ti–B–C nanocomposite coatings prepared by magnetron sputtering. *J. Phys. D: Appl. Phys.* **45**, 375401 (2012).
37. Ferrari, A. C. & Robertson, J. Interpretation of Raman spectra of disordered and amorphous carbon. *Phys Rev B* **61**, 14095–14107 (2000).
38. Ferrari, A. C. Raman spectroscopy of graphene and graphite: Disorder, electron–phonon coupling, doping and nonadiabatic effects. *Solid State Commun.* **143**, 47–57 (2007).
39. Jerng, S. K. *et al.* Nanocrystalline graphite growth on sapphire by carbon molecular beam epitaxy. *J. Phys. Chem. C* **115**, 4491–4494 (2011).
40. Calizo, I., Bejenari, I., Rahman, M., Liu, G. & Balandin, A. A. Ultraviolet Raman microscopy of single and multilayer graphene. *J. Appl. Phys.* **106**, 043509–043505 (2009).
41. Das, A. *et al.* Monitoring dopants by Raman scattering in an electrochemically top-gated graphene transistor. *Nat Nano* **3**, 210–215 (2008).
42. López, G. A. & Mittemeijer, E. J. The solubility of C in solid Cu. *Scr. Mater.* **51**, 1–5 (2004).
43. Okamoto, H. C-Pd (Carbon-Palladium). *J. Phase. Equ. Diff.* **28**, 313 (2007).
44. Skriver, H. L. & Rosengaard, N. M. Surface energy and work function of elemental metals. *Phys Rev B* **46**, 7157–7168 (1992).
45. Papirer, E., Brendle, E., Ozil, F. & Balard, H. Comparison of the surface properties of graphite, carbon black and fullerene samples, measured by inverse gas chromatography. *Carbon* **37**, 1265–1274 (1999).
46. Mattevi, C., Kim, H. & Chhowalla, M. A review of chemical vapour deposition of graphene on copper. *J. Mater. Chem.* **21**, 3324–3334 (2011).
47. Heurlin, M. *et al.* Continuous gas-phase synthesis of nanowires with tunable properties. *Nature* **492**, 90–94 (2012).
48. Tabrizi, N. S., Ullmann, M., Vons, V. A., Lafont, U. & Schmidt-Ott, A. Generation of nanoparticles by spark discharge. *J. Nanopart. Res.* **11**, 315–332 (2009).
49. Kala, S., Mehta, B. R. & Kruis, F. E. A dual-deposition setup for fabricating nanoparticle-thin film hybrid structures. *Rev. Sci. Instrum.* **79**, 013902–013907 (2008).
50. Potasz, P., Güçlü, A. D., Voznyy, O., Folk, J. A. & Hawrylak, P. Electronic and magnetic properties of triangular graphene quantum rings. *Phys Rev B* **83**, 174441 (2011).
51. Herrmann, I. K., Grass, R. N. & Stark, W. J. High-strength metal nanomagnets for diagnostics and medicine: carbon shells allow long-term stability and reliable linker chemistry. *Nanomedicine* **4**, 787–798 (2009).
52. Lu, A.-H., Salabas, E. L. & Schüth, F. Magnetic nanoparticles: synthesis, protection, functionalization, and application. *Angew. Chem. Int. Ed.* **46**, 1222–1244 (2007).
53. Lu, G. *et al.* Surface enhanced Raman scattering of Ag or Au nanoparticle-decorated reduced graphene oxide for detection of aromatic molecules. *Chem. Sci.* **2**, 1817–1821 (2011).
54. Wang, Y. *et al.* Gold on graphene as a substrate for surface enhanced Raman scattering study. *Appl. Phys. Lett.* **97**, 163111–163113 (2010).
55. Hong, S. K. *et al.* Electromagnetic interference shielding effectiveness of monolayer graphene. *Nanotechnology* **23**, 455704 (2012).

56. Atwater, H. A. & Polman, A. Plasmonics for improved photovoltaic devices. *Nat Mater* **9**, 205–213 (2010).

Acknowledgements

The support provided by Nanomission Programme of Department of Science and Technology, Department of Electronic and Information Technology, Government of India and Schlumberger Chair Professorship is acknowledged. One of the authors S.K.S. is thankful to Council of Scientific and Industrial Research, India for providing senior research fellowship.

Author contributions

S.K.S. carried out the majority of the research work towards synthesis and characterization of graphene-metal nanoparticles. R.K. carried out the electrical and optical measurements. V.S. assisted in the synthesis of nanoparticles on different substrates. The present study was conceived and supervised by B.R.M., Schlumberger Chair Professor, Thin Film Laboratory, Physics Department, I. I. T. Delhi, New Delhi, India.

Additional information

Supplementary information accompanies this paper at http://www.nature.com/scientificreports

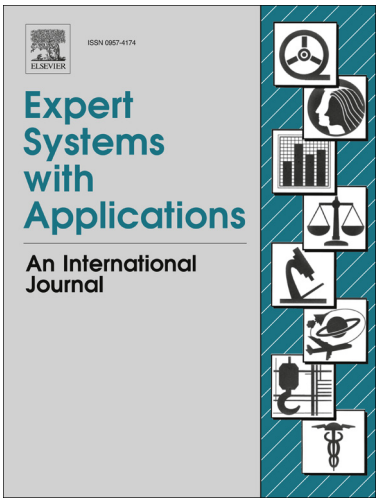
Competing financial interests: The authors declare no competing financial interests.

How to cite this article: Sengar, S.K., Mehta, B.R., Kumar, R. & Singh, V. In-flight gas phase growth of metal/multi layer graphene core shell nanoparticles with controllable sizes. *Sci. Rep.* **3**, 2814; DOI:10.1038/srep02814 (2013).



This work is licensed under a Creative Commons Attribution-NonCommercial-NoDerivs 3.0 Unported license. To view a copy of this license, visit http://creativecommons.org/licenses/by-nc-nd/3.0

Accepted Manuscript



Intelligent Video Target Tracking using an Evolutionary Particle Filter based upon Improved Cuckoo Search

Gurjit Singh Walia, Rajiv Kapoor

PII: S0957-4174(14)00141-9
DOI: http://dx.doi.org/10.1016/j.eswa.2014.03.012
Reference: ESWA 9225

To appear in: *Expert Systems with Applications*

Please cite this article as: Walia, G.S., Kapoor, R., Intelligent Video Target Tracking using an Evolutionary Particle Filter based upon Improved Cuckoo Search, *Expert Systems with Applications* (2014), doi: http://dx.doi.org/10.1016/j.eswa.2014.03.012

This is a PDF file of an unedited manuscript that has been accepted for publication. As a service to our customers we are providing this early version of the manuscript. The manuscript will undergo copyediting, typesetting, and review of the resulting proof before it is published in its final form. Please note that during the production process errors may be discovered which could affect the content, and all legal disclaimers that apply to the journal pertain.

ACCEPTED MANUSCRIPT

Intelligent Video Target Tracking using an Evolutionary Particle Filter based upon Improved Cuckoo Search

[1]Gurjit Singh Walia, [2]Rajiv Kapoor*

[1]***Scientist***, *Defense Research and Development Organization, Ministry of Defense, Delhi, India.*
[2]***Professor & Head***, *Department of Electronics and Communication, Delhi Technological University (formerly DCE), Bawana Road, Delhi, India.*

rajiv.kapoor@dce.ac.in **corresponding author*

Abstract:

The aim of this paper is to propose an evolutionary particle filter based upon improved cuckoo search algorithm which will overcome the sample impoverishment problem of generic particle filter. In our proposed method, improved cuckoo search (ICS) algorithm is embedded into particle filter(PF) framework. Improved cuckoo search algorithm uses levy flight for generating new particles in the solution and introduced randomness in samples by abandoning a fraction of these particles. The second important contribution in this article is introduction of new way for tackling scaling and rotational error in object tracking. Performance of proposed improved cuckoo particle filter is investigated and evaluated on synthetic and standard video sequences and compared with the generic particle filter and particle swarm optimization based particle filter. We show that object tracking using improved cuckoo particle filter provides more reliable and efficient tracking results than generic particle filter and PSO-particle filter. The proposed technique works for real time video objects tracking.

Key words: Visual Tracking, Particle filter, Sample impoverishment, Re-sampling, Cuckoo Search

1. Introduction

Visual tracking in video sequences is an emerging area of research in the field of computer vision. The visual tracking found its application to myriad areas such as security and surveillance, man-machine interaction, activity analysis, road traffic control, video indexing, video communication/compression and augmented reality etc. A number of innovations in the field of cluster computing, high quality video, object detection techniques and advancement multi sensors technology, open the new area of research in the field of video tracking. Visual tracking is complex due to: (1) loss information due to transformation of 3D world to 2D image; (2) occlusion of object subjected for tracking by multiple intermittent disturbances; (3) noise in images; (4) abrupt object motion change during tracking; (5) and real time restrictions. Under Bayesian framework, Visual tracking is considered as state estimation of dynamic system where both measurement and observation model bring in uncertainty [1-2]. The representative work under Bayesian framework can be categories into: (a) state estimation for linear and Gaussian model using Kalman filter and its variants such as unscented Kalman filter and extended Kalman filter ; (b) state estimation for non-linear and Non-Gaussian problems using Sequential Monte Carlo methods [3-5] also known as Condensation filter [6], Bootstrap filter [7], and particle filter [8-9].

ACCEPTED MANUSCRIPT

The main advantages of Sequential Monte Carlo methods (Particle filter) are reduction of sampling patches during tracking and its ability to handle multi modal distribution generated by cluttered environment. Although, there are a number of applications for particle filter due to its superiority over other tracking algorithm, it has some inherent problems which need to be addressed in order to increase the tracking accuracy.

1.1 The problems in visual tracking using particle filter and proposed framework

In spite of number of advantage, the efficiency of visual tracking using particle filter is greatly affected by its inherent shortcoming i.e. particle impoverishment, and by choice of reliable measurement model and observation (object) model. Number of researcher has contributed towards development of efficient object model and measurement models. Although, a simple object model [10-13] with 3-4 state parameter is considered to be efficient for real time application but amount of information provided is low which leads to pre and post processing of video data. For achieving additional information about object, more number of parameters gives more reliable information at the cost of high computational requirement [14]. In case of measurement model of particle filter, a number of methods are reported which either use single cue (e.g. edge, colour, motion etc.) or multiple cues which are fused using different data fusion techniques [15-17]. A review on video tracking indicates that a lot of work has been carried out for development of object and measurement model and there is very little scope for further improvement.

The most perturbing and perpetual problem of particle filter is the curse of dimensionality and degeneracy phenomenon, and solution of it leads to sample impoverishment. Theoretically, any posterior PDF can be estimated by selecting infinite number of particles but, in practice it is impossible to process infinite number of particle for estimation of PDF. In case of particle filter, particle degeneracy occurs when there is only few particle represent the true state of object and remaining contribute either little or none towards estimation of state due to their negligible weight. Processing these particles whose contribution towards state estimation is insignificance adds to computation power with no gain. Researchers addressed the degeneracy by number of methods such as re-sampling and good choice of proposal distribution. During resampling processes, particle whose contribution towards state estimation is little are replaced by particles whose weights are signification. But, suboptimal sampling mechanism in important sampling resampling leads to another problem of sample impoverishment. This will allure the particle in wrong likelihood area due to lack of diversity of particles after few state estimation. In present research work, we have provided solution for sample impoverishment problem in order to improve tracking accuracy i.e. better estimation of posterior probability distribution. The highlight of this work are :

- ***A method of object representation for object tracking.***
- ***Proposed ICS- PF for overcoming sample impoverishment of PF.***
- ***Better qualitative and quantitative performance over PSO-PF and PF.***
- ***Real time application due to less computational requirement.***

ACCEPTED MANUSCRIPT

The remaining of paper is organized as follows:

Section 2, recalls the Sequential Monte Carlo framework and Improved Cuckoo search via Levy flight optimization algorithm for video tracking. Proposed target representation model, along with used object model and measurement model are given Section 3. Section 4, introduced our novel improved cuckoo particle filter we named it as ICS-PF for tracking object in video sequences. The data set used for tracking experiment and performance of our proposed algorithm is presented in Section 5. Also, the results are compared with the best solution available in the literature. Finally, Section 6 sketches brief summary of our contributions and highlight future directions in this field. However, for better understanding of problem, it is absolutely necessary to have a quick review of related work carried out by different researchers.

1.2 Related Work

The sample impoverishment problem is addressed by number of researchers. One group is dealing with improvement in resampling process so that sample impoverishment is reduced. A number of resampling variants such as systematic re-sampling [18] , adaptive re-sampling [19], and residual re-sampling [20] were reported in the literature. But, most of these methods solve the problem to limited extend due to failure to replace particle which are statistically independent after re-sampling process. Another group of researchers were solving impoverishment problem through approximation of PDF. The algorithm introduced under this category are extended Kalman particle filter [21], unscented PF [22], approximation moments of the PDF [25, 26], or Gaussian sum filter [24]. However, most of these methods could not be applied automatically to any problem. Also, the solutions obtained through these methods are suboptimal due to approximation of PDF by a Gaussian and requirement of more computational power. Hence, solution for sample impoverishment problem which is both computational efficient and provide optimized solution is foremost requirement of video tracking.

In recent year, nature inspired optimization methods has been attempted by number of researchers. These methods aim at concentrating particles into high probable region of probability distribution function and at the same time introduce randomness in particles so as to improve sample impoverishment. Katsuji Uosaki et al. [27] solved particle degeneracy to some extend by exploring the similarity between sampling important resampling and evolutionary strategies. Evolutionary strategies propagate particles based upon selection which exploit the required fitness function. Also, more heuristic in these particles were introduced by mutation and recombination process. However, results were presented for one dimensional generic problem and applicability of approach for two dimensional models or video object tracking was not discussed. J. P. Zhong et al.[28] provided solution for sample impoverishment and degeneracy problem in particle filter by introducing Ant Colony optimization into particle filter framework. Results show that ACO rearrange the particle before update stage of particle filter for one dimensional generic economic problem. But performance for object tracking in video sequences was not reported. In [29], artificial fish swarm optimization was used for moving particles into region of high likelihood. The problem of particle destitution was resolved to some extent and results were reported for manoeuvring target tracking problem and robot localization. However, the qualitative analysis of results was not reported. S. Park et al. [30] introduced Genetic algorithm incorporated into particle filter for solving sample impoverishment problem. The proposed algorithm

ACCEPTED MANUSCRIPT

performs better during abrupt change in state because crossover and mutation operation of Genetic algorithm explore new area of proposal distribution and overcome interruption in measurement. Simulation of some complicated problem was presented in order to prove the proposed algorithm where abrupt changes were taken in the video sequences subjected for experiments. Hua Han et al. [31] embedded immune genetic algorithm in front of resampling step of particle filter in order to solve the sample impoverish problem of generic particle filter. The antibodies (Particles) were reproduced before resampling by mutation and crossover process of immune system. Further these antibodies were diversified for exploring new search area by regulatory mechanism of immune system such as promotion and suppression. The performance of proposed algorithm was presented on video object tracking and author claimed that proposed algorithm performs better in terms of efficiency and particle diversity than generic particle filter. However, qualitative performance measures were not presented also ability of algorithm for tracking multiple occluded objects in video is still need to be answered. Guofeng Tong et al .[46] proposed particle filter based upon particle swarm optimization for solving sample impoverishment problem. Their results show improvement over the generic particle filter. Further, PSO in particle filter framework was proposed by Jing Zhao et al [23] for tracking in video sequences using HOG and color histogram based feature vectors. The PSO was used as resampling algorithm which distributes the particles in high likelihood area in order to achieve diversity in particles. However, HOG is computational expensive and embedding it into particle filter framework need more computational power. In [32], authors solved sample impoverishment in particle filter by embedding cuckoo search via levy flight into particle filter framework. The results shows that particle filter based on cuckoo search via levy flight outperform simple particle filter and PSO particle filter. However, performance of cuckoo based particle filter only for generic one dimensional problem and classic bearing only tracking problem were reported by the author's. The applicability of particle filter based on cuckoo search for tracking object in video sequences was not addressed by Gurjit Singh Walia and Rajiv Kapoor [32]. Modified Potential Function As per latest published review [45] and survey of related literature, we have found that till now no one has reported particle filter based up on improved cuckoo search for video object tracking. Before the description of proposed algorithm, brief introduction of sequential Monte Carlo framework and improved cuckoo search algorithm is given in next section.

2. Sequential Monte Carlo Framework and Improved Cuckoo Search algorithm

Before, the introduction of our algorithm for tracking objects in synthetic and natural video sequences, we introduced the basic theory related to object tracking using particle filter. Similarly, improved cuckoo search algorithm which was introduced by [33-34] is illustrated.

2.1 Particle Filter

Particle filter was first introduced in 1993 by N.J. Gordon as bootstrap filter for estimation of non-linear and non-Gaussian states [37]. In particle filter, the state at each time instant is represented by sample based probability density function. Sequential Monte Carlo technique with important sampling is used for estimation of non-linear and non-Gaussian state. The objective of particle filter is to estimate the

ACCEPTED MANUSCRIPT

state of system by weighted mean of particles present in the neighbourhood of state space. It is a recursive process where the prior state is updated using online measurements (weights) to get the posterior state estimate. After the estimation of posterior state it act as prior for the next state estimation. Weights in particle filter are likelihood measure between posterior probability density and reference prior probability density. Although, particle filter theory is described at length in the literature, we introduced it briefly for the sake of completion of research paper.

For estimation of posterior state of the system, target model is selected which define the motion, scaling, rotation factor for the target. As shown in eq. (1), target state model is evolved as:

$$x_m = f_{m-1}\left(x_{m-1}, w_{m-1}\right) \qquad (1)$$

Here, $f_{m-1}:\mathbb{R}^k \times \mathbb{R}^n \to \mathbb{R}^k$ is the nonlinear function of target state with dimension of k; $w_{m-1} \in \mathbb{R}^n$ is white noise sequence of dimension n with zero mean (known PDF) represents the uncertainty in state prediction. Also, online discrete measurement $z_m \in \mathbb{R}^z$, m≥1 up to current time m are made according to measurement equation eq. (2).

$$z_m = h_m\left(x_m, u_m\right) \qquad (2)$$

Where, $h_m:\mathbb{R}^m \times \mathbb{R}^q \to \mathbb{R}^z$ is nonlinear function, and u_m is zero mean, white-noise sequence (PDF known) representing error in measurement. Recursive process of Particle filter consist of two steps as: 1) Prediction; 2) Updation, from the given online measurement sequences $z_m = \{z_i : i = 1,2,...,m\}$.

In prediction step, prior PDF at time instant m is determined as:

$$p(x_t \mid z_{t-1}) = \int p(x_m \mid x_{m-1})\, p(x_{m-1} \mid z_{m-1})\, dx_{m-1} \qquad (3)$$

Where in equation (3) prior PDF is obtained using system model eq.(1) and initial PDF at time m-1 i.e. $p\left(x_{m-1} \mid z_{m-1}\right)$. In update step, the problem is to estimate the posterior density $p\left(x_{0:m} \mid z_{1:m}\right)$ using the byes rules as defined in equation (4) at every time step given prior probability density function $p(x_1 \mid z_0) \equiv p(x_1)$, functional form of state (*f*)and measurement (*h)* model , and measurement up to that time instant. The same can be expressed as:

$$p\left(x_m \mid z_m\right) = \frac{p\left(z_m \mid x_{0:m}\right) p\left(x_m \mid z_{m-1}\right)}{p\left(z_m \mid z_{m-1}\right)} \qquad (4)$$

In particle filter, Equation (3) and (4) form the recursive process for state estimation. Considering the tracking problem, N random samples $\left[x_1^{(i)}\right]_{i=1,2,...N}$ are taken from initial given PDF $p(x_1)$. These samples are passed through system state model eq.(1) in order to obtain predicted N particles . The predicted particles are assigned normalized weights using equation (5).

$$w_j = \frac{p\left(z_m \mid x_m(j)\right)}{\sum_{j=1}^{N} p\left(z_m \mid x_m(j)\right)} \qquad where,\ j = 1,....N \qquad (5)$$

Because the target dynamics are assumed to be Markov chain, posterior can be represented :

$$p\left(x_m \mid z_{1:k}\right) \approx \sum_{j=1}^{N} w_m^j\, \delta(x_k - x_k^i) \qquad (6)$$

ACCEPTED MANUSCRIPT

Where $\delta(.)$ denotes Dirac delta function due to deterministic nature of equation (1) for given value of x_{m-1} and w_{k-1}. Finally, updated particles act as prior for the next state prior particles and this recursive process will continue till the last state prediction and updation. If we increase the size of particle, the accuracy of tracking will improve but it will require more processing power. In practice, a limited number of particles are taken for tracking application. Also, after little state estimation, number of particles whose weight is insignificant increases and keeping these particles whose contribution to estimation is negligible require more computational power. So, re-sampling is applied on updated particles in order to discard the particles with negligible weights [8]. In re-sampling, new samples $\left[*x_m^{(i)}\right]_{i=1,2,\ldots N}$ are generated by re-sampling N times form estimated PDF $p(x_k \mid z_{1:k})$ so that for any j $\Pr\left[*x_m^{(i)} = x_m^j\right]_{i=1,2,\ldots N} = w_m^j$. The pseudo code for particle filter is described as:

Algorithm 1: *Particle filter*

$[_{i=1}^{N}(x_m^i, w_m^i)] = P_Filter[_{i=1}^{N}(x_{m-1}^i, w_{m-1}^i), z_m]$ Where N = number of particle

1. For j= 1 : N
2. At time m=1
3. Randomly sample PDF $p(x_{m-1} \mid z_{1:m-1})$ for selecting N samples $\left[x_{m-1}^{(i)}\right]_{i=1,2,\ldots N}$
4. Assign weight to particle as per equation (5)
5. Calculate the sum of weight $W = \sum_{i=1}^{N} w_i$
6. Normalize the weight for particles.
7. Resample : Generate new samples $\left[x_m^{(i)}, w_m^{(i)}\right]_{i=1,2,\ldots N}$ based upon w_m^i after resampling of N updated particles so that $\Pr\left[*x_m^{(i)} = x_m^j\right]_{i=1,2,\ldots N} = w_m^j$
8. Estimate the state by $X_m = \frac{1}{N}\sum_{i=1}^{N} X_m^i$
9. set m+1← m, j+1← j
10. Go to step 3

2.2 Improved Cuckoo Search Algorithm

A new metaheuristic Cuckoo search blended with Levy flight was introduced by Xin-She Yang and Suash Deb in 2009 [38]. The algorithm is based upon intensification which caters for search best solution and diversification for exploring new search area. The objective of optimization is to increase reproductivity of cuckoo eggs by taking care of right time of laying eggs, action taken by cuckoo chicks that are just hatched. The assumption taken while developments of cuckoo optimization are:

a) Eggs are placed in randomly chosen nest.
b) Only the nests with best eggs present will survive in future generation.
c) Number of host nests (generally other species) is predefined, and probability that egg is discovered by host is estimated as $p \in [0,1]$.

In order to put diversification in cuckoo eggs, the cuckoo eggs are generated through Levy flight by equation (7).

ACCEPTED MANUSCRIPT

$$Z_i^{t+1} = Z_i^t + \alpha \text{ Levy}(\lambda) \quad (7)$$

Where, value of step size α depends upon the type of problem under consideration. The value of random step length is taken from levy distribution $t^{-\lambda}, [1 < \lambda \leq 3]$ which divide search into local and global search space and thus avoid local minima traps.

The value of key parameters P_a and α in cuckoo search established the search space either locally or globally. In general cuckoo search the values of these parameters are fixed and this may need more number of iteration for finding optimal solution. The solution to this was proposed by Ehsan Valian et al.[33] as improved cuckoo search algorithm(ICS) where the values of p_a and α are changed with each iteration according to their equations (8)-(10).

$$\text{Pa}(c) = \text{Pa_max} - \frac{c}{n}(\text{Pa_max} - \text{Pa_min}) \quad (8)$$

$$\alpha(c) = \alpha\text{max} \exp(c.d) \quad (9)$$

$$d = \frac{1}{n} \ln\{\frac{\alpha\text{min}}{\alpha\text{max}}\} \quad (10)$$

Where variable c is number of current iteration and chosen constant n is total number of iteration. In our experiment, we have considered stop criterion as total number of iteration performed for finding the best solution. Recently, ICS was used for reliability optimization problem [34] and results shows that ICS perform better than cuckoo search algorithm for finding optimal solution. The pseudo code for Improved Cuckoo Search is summarized as follows:

1. Create initial population of N host nest (Particles) $p_i ....where, i = 1,...N$
2. **While** termination< stop criterion **do**
3. Calculate the value of P_a an α using equations (8)-(10)
3. Use levy flights to generate the cuckoo randomly and find its fitness Fit_i
4. Choose at random a nest j from N host
5. **If** $Fit_i > Fit_j$
6. Change j with new solution
7. End if
8. A part of worst nest (P_a) are abandoned and new nest are generated
9. Arrange the solution and chose the current best
10 End **while**

The comparison of various metaheuristic techniques such as cuckoo search, ABC, PSO and differential evolution has been given by Pinar Civicioglu et al. [47] and between improved cuckoo search and cuckoo search by Ehsan Valian et al. [34]. From these review, one can conclude that improved cuckoo search is one of best optimization technique available for solving complex problem.

2.3 *Performance Measures for Object Tracking Algorithms*

Performance evaluation of tracking algorithm is absolutely necessary when these are implemented for real time systems. The interest of performance evaluation gain momentum with the start of workshop

ACCEPTED MANUSCRIPT

PETS i.e. performance evaluation of tracking and surveillance. Initial aim of this workshop is to provided standard dataset to research community which later shifted to metrics for evaluation and finally to online evaluation of tracking algorithms. Generally, ground truth is generated from pre-recorded videos. The various performance evaluation methods could be categorized as:

2.3.1 Quantitative Evaluation of Video Tracking:

Faisal Bashir and Faith Porikli [35] introduced performance measures based either on current frames of video sequences irrespective of object life span history or object take into account whole trajectory of object into consideration . For frame based metric , they count number of frames which are coincident [position of centroid of ground truth and tracker sequence] as a) True Negative(TN) object not present and system and ground truth result agree b) True Positive(TP) object is present and ground truth and tracker result agree c) False Negative (FN) ground truth contain at least one object and tracker does not contain any object or it not falling in bounding box of ground truth object d) False Positive tracker have at least one object but the ground truth does not have object or its object does not fall inside the tracker object.

In [36], N. Lazarevic-McManus et al. introduced F- measure for comparison of ground truth and tracker measured images. Also, the precision is defined as percentage of selected images which are correct or more precisely as a measure of amount of tracker estimation overlap with the ground truth image and recall is measures of percentage of correct frames that are selected or more precisely as a measure of amount of ground truth image covers tracker estimated images. These measures we also used for performance measure of our developed algorithm and found using equations (11) and (12).

$$\text{Precision} = = \frac{GT \cap T}{T} = \frac{\text{Number of correct correspondence}}{\text{Number of established correspondence}} = \frac{TP}{TP+FP} \quad \text{------ (11)}$$

$$\text{Recall} = = \frac{GT \cap T}{GT} = \frac{\text{Number of correct correspondence}}{\text{Number of actual correspondence}} = \frac{TP}{TP+FN} \quad \text{------ (12)}$$

Where GT is ground truth image and T is tracker estimated image. Harmonic mean which gives more conservative average of precision (P) and recall(R) is defined as F- measure for performance measure of motion detection algorithms. F measure found using equation (13):

$$F - Measure = \frac{1}{\alpha * \frac{1}{P} + (1 - \alpha)\frac{1}{R}} \quad \text{------(13)}$$

Also for most application, balanced F measure is considered with $\alpha=1/2$. Also, we used success rate as performance measures for tracker where it estimate the percentage of frames for which targeted object is correctly located in the frame in reference to ground truth frame.

2.3.2 Qualitative analysis of tracking algorithm

ACCEPTED MANUSCRIPT

Apart from quantitative measure for performance, a number of qualitative measures are reported in the literature and selection of measure also depends upon the objective for developed tracking algorithm. Most commonly reported qualitative measures is algorithm ability to handle entry of exit of object, occlusion etc.

3. Object Representation for catering Scaling and Rotation error, Motion Model, and Measurement Model

In tracking scenario, objects can be represented either by different shapes such as points, primitive geometric shapes, silhouette and contour etc. or by different appearance models such as probability density of object appearance, templates etc. Similarly there are different motion and measurement model for tracking scenario. In order to complete our research paper, we have discussed models which we have used for implementation of our proposed algorithm. Also, a new method for representation of object which will overcome rotation and scaling error is introduced.

3.1 Object Representation for Tracking

In our model, we represented object to be tracked by circular shapes. The object subjected for tracking is extracted through GMM background subtraction. The circle which inscribe the bounding box of detected object with radius R_{ref} and centre (X_{ref}, Y_{ref}) represent the reference object for tracking. Each of the particles (present experiment we have taken 100 particles) are represented by circle with fixed radius. The particles centre and reference centre are shown in figure 1. These centers are used for conversion of Cartesian coordinates into polar coordinates which are assigned to each particle in the state vector. The polar coordinates for each particle r(n) and angle θ(n) are calculated using equations from (14) to (22) where n varies from 1 to N (number of particles).

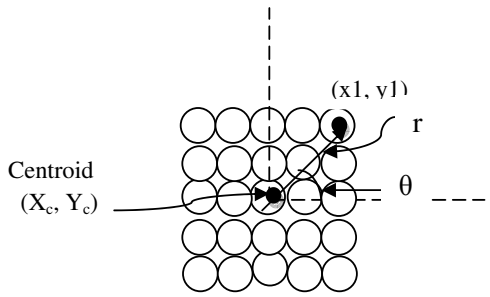


Figure: 1 Representation of Particle polar coordinate on Object

ACCEPTED MANUSCRIPT

$$Xrel(n) = Xc - X(n) \quad \text{--- (14)}$$

$$Yrel(n) = Yc - Y(n) \quad \text{--- (15)}$$

$$r(n) = \sqrt{Xrel^{2}(n) + Yrel^{2}(n)} \quad \text{--- (16)}$$

$$th(n) = (-1) * \tan^{-1}\left[\frac{Yrel(n)}{Xrel(n)}\right] \quad \text{--- (17)}$$

Where the value of θ's are calculated taking into consideration of relative magnitude of $X_{rel}(n)$ and $Y_{rel}(n)$. The pseudo code for calculation for θ(n) is as follows:.

If $X_{rel}(n) < 0$ & $Y_{rel}(n) <= 0$

$$\theta(n) = pi + th(n) \quad \text{--- (18)}$$

Elseif $X_{rel}(n) < 0$ & $Y_{rel}(n) > 0$

$$\theta(n) = pi + th(n) \quad \text{--- (20)}$$

Elseif $X_{rel}(n) >= 0$ & $Y_{rel}(n) > 0$

$$\theta(n) = 2 * pi + th(n) \quad \text{--- (21)}$$

Else $\theta(n) = th(n) \quad \text{--- (22)}$

Particle state is represented as state vector X(n),X'(n),Y(n),Y'(n),r(n),θ(n) where n=1,2,---,100 and X',Y' are speed in respective direction . The weighted sum of particles X'^{s} and Y'^{s} coordinates are taken before passing the state to observation model (equation (26)) as X_{int}, Y_{int} . The particles are passed through the observation model and weighted sum of particles X',Y' is again taken as X_{after} , Y_{after}. Based upon these values of X_{int}, Y_{int} and X_{after} , Y_{after} movement of centroid of object is calculated as X_{cen} and Y_{cen}. The effects of rotation and scaling error are catered through conversion of polar coordinates of particles , given the random walk, to Cartesian coordinates using equations from (23) to (24).

$$Xc = Xcen + r(n) \times \cos(\theta(n)) \quad \text{--- (23)}$$

$$Yc = Ycen - r(n) \times \sin(\theta(n)) \quad \text{--- (24)}$$

These steps are repeated for each state estimation of object. Using this proposed model for object representation , rotational and scaling error are catered for limited extend during object tracking. The results of the same are elaborated in the next section.

3.2 Motion Model

The different motion models for object tracking were introduced by different author as constant velocity model, random walk model or adaptive motion model. Multi component model was used for object tracking by Paul Brasnett et al. [39] and same we have used for our experiments. As reported, Constant velocity model for translation motion and random walk model for rotation and scale was used. The state of object at any time instant is represented by six components (X, X', Y, Y', r, θ) where X, Y are Cartesian coordinates of circle center and X', Y' are velocity in respective direction. The translation component X, Y were subjected to constant velocity and rotation and scaling were given random walk.

ACCEPTED MANUSCRIPT

The particles are represented by object model discussed above and each state of it is represented by state vector as:

$$S = (X, X', Y, Y', \theta, r) \quad \text{--- (25)}$$

The posterior probability distribution of state is estimated by state model equation (26) and target motion is predicted using this model at each time instant.

$$S_{t+1} = M \times S_t + n_t \quad \text{--- (26)}$$

Where, M and n_t are defined as

$$n_t \sim N(0, P) \quad \text{--- (27)}$$

$$M = \begin{bmatrix} \begin{pmatrix} 1 & H \\ 0 & 1 \end{pmatrix} & 0_{2\times 2} & 0_{2\times 1} & 0_{2\times 1} \\ 0_{2\times 2} & \begin{pmatrix} 1 & H \\ 0 & 1 \end{pmatrix} & 0_{2\times 1} & 0_{2\times 1} \\ 0_{1\times 2} & 0_{1\times 2} & 1 & 0 \\ 0_{1\times 2} & 0_{1\times 2} & 0 & 1 \end{bmatrix} \quad \text{--- (28)}$$

H is sampling interval and fixed at 0.9 for our experiments. P is zero mean covariance matrix and has separate covariance value for translation motion and rotational and scaling components as σ_x^2, σ_y^2, σ_r^2, σ_s^2.

3.3 Measurement Model

The measurement model is required for updation of predicted states so that changes in motion of object are catered faithfully. The different cues such as color, texture, edge, motion, thermal, or orientation etc. are used in the measurement model. Recently results on multiple cues for likelihood model were reported. Most of reported likelihood models are based on histogram because it can cater for small changes in appearance of object. For our proposed method, we have used color cue for estimating the likelihood between color histogram of each particle in object area and reference color histogram of the object. The color histogram of object at state t for circular region is represented as $h_t = \{h_{1,t}, h_{2,t}, h_{3,t}, \text{---}, h_{n,t}\}$ and found using equation (29). Where n is a total number bin for each channel. Here we have used RGB color model for our experiments with 8x8x8 bin histogram [40].

$$h_t = \sum_{i=1}^{n} \delta_i(p_u) \quad \text{--- (29)}$$

Where, p_u is histogram bin index assigned to intensity at particle location and δ_i is Kronecker Delta function at each bin location. The histogram for each channel at particle location is extracted separately. The various methods such as Bhattacharyya similarity distance, Hausdorff distance, fuzzy measure has been reported for measuring the similarity between reference histogram and predicted histogram. In our experiments, Bhattacharyya similarity distance [42] is computed for measuring the similarity between chosen color histogram and predicted state color histogram. If the reference color histogram is similar

ACCEPTED MANUSCRIPT

to predicted color histogram the similarity index is one. Based upon this estimated value of likelihood (similarity index), the weights are assigned to each of particles for estimating updated particles. Using these sub-models, complete particle filter framework for overcoming its inherent limitations by embedding improved cuckoo search algorithm is developed and same is presented in the next section.

4. The Evolutionary Particle Filter with Improved Cuckoo Search for Video Tracking

4.1 Proposed Algorithm:

In this manuscript, a novel approach is proposed for overcoming sample impoverishment problem of generic particle filter. The object is represented by n number of particles with each particle have state vector as (X, X', Y, Y', r, θ). The state vector has additional scale and rotation factor which will cater for scaling and rotation error. The detail of proposed algorithm is summarized in figure 2 below. As an illustration of algorithm, we have followed the generic particle filter framework for tracking. The state estimation process consists of prediction, updation and resampling. Apart from proposed method for tackling scaling and rotation effect, we have embedded improved cuckoo search algorithm in particle filter frames. The online video is acquired from digital camera at 25 fps or pre-recorded video could be taken for tracking. At first step we look forward for foreground object using background subtraction. For moving object segmentation we have applied Stauffer–Grimson algorithm [44]. We have used 3 Gaussian distribution and pixels which do not match with these Gaussian are declared as foreground. Once the object is detected, our tracker is initialized for tracking of object in subsequent frames. The particles are initialized on object and these are passed through the observation model. The predicted particles are further updated based on their weights assigned using Bhattacharya coefficient. The number of effective particles is calculated and resampling is performed if this number of less than threshold value in order to reduce particle degeneracy [41]. Before resampling of particles, new particles are generated using levy flight and particles are further randomized by abandoning particle based on improved cuckoo search algorithm. The improved cuckoo search algorithm needs on an average 3 iteration for finding optimum solution. The rotation and scaling effect are catered by re calculation of Cartesian coordinate of object from updated rotation and scaling factors. Finally, the state of object is estimated using weighted sum of all particles states and weights of particles are re initialized for estimation of new state of object.

ACCEPTED MANUSCRIPT

ACCEPTED MANUSCRIPT

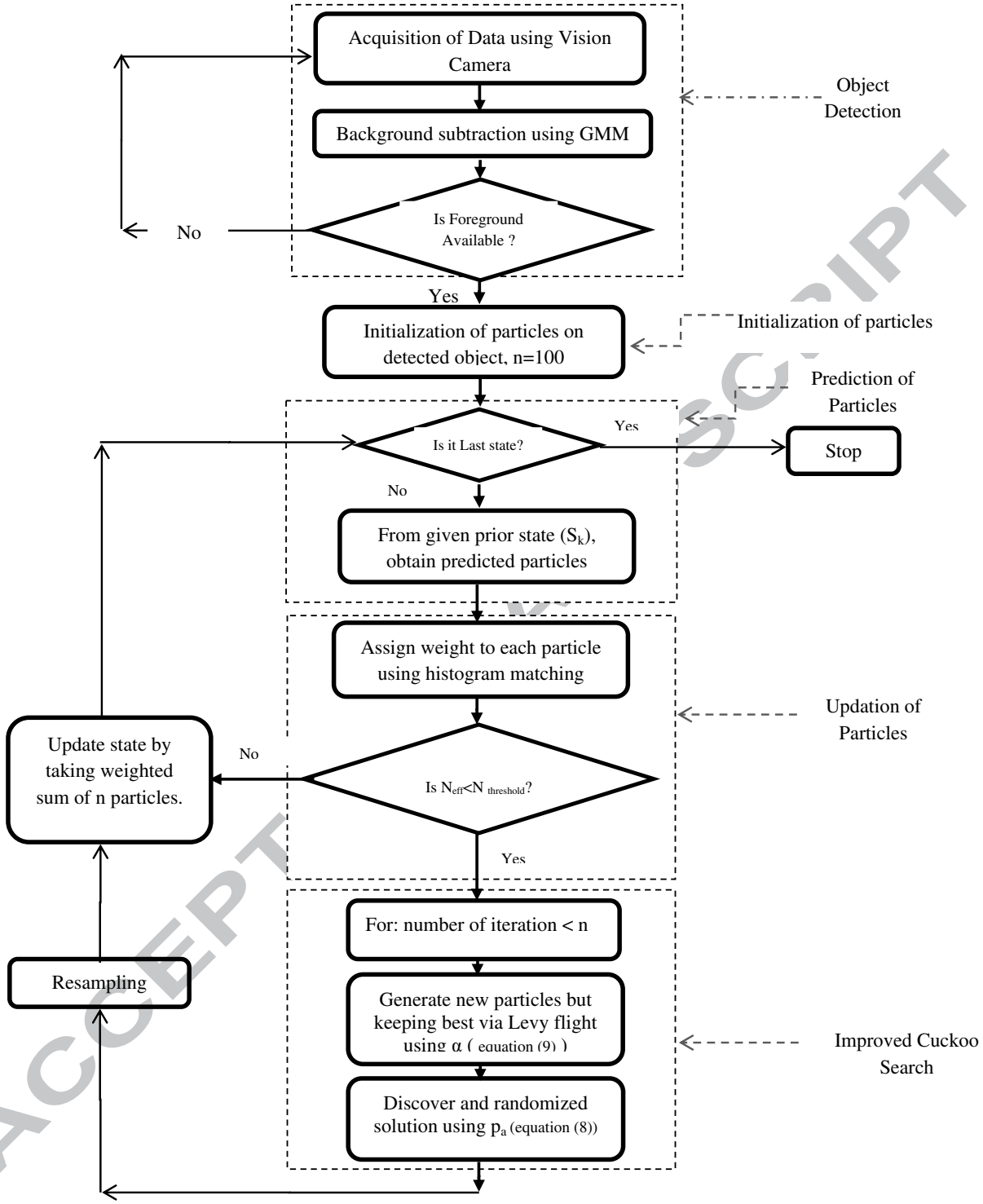


Figure 2: Evolutionary Particle filter using Improved Cuckoo Search

When all the states of objects are predicted or object goes out of field of view of camera, object tracker is stopped. The new object is again searched using GMM algorithm and tracker is reinitialized with new set of parameters for tracking newly detected object in video sequences.

ACCEPTED MANUSCRIPT

4.2. Implementation details

We have implemented our algorithm i.e. ICS-PF in MATLAB on a laptop with 2.0 GHz Intel Core2 Duo processor. The laptop is integrated to Sony camera for online capture of video stream for testing. For caviar data set we have taken the recorded video streams and performed our experiments. In all the experiments, the various parameters, we have used are listed in Table 1 apart from these fixed set of parameters other parameters are stated in the paper wherever it is used. For our experiment video, our algorithm runs at 25 frames per second. However, this processing rate could further be increased either by parallelization of source code or by running it on fast processor.

Table: 1
Salient parameters for tracking experiments

# of particle used	100
# of bins for histogram	8
Standard deviations of observation	$\sigma_x = .02$, $\sigma_y = .03$,
Model equation (26)	$\sigma_r = .02$, $\sigma_s = .02$

For PSO-particles filter, number of particles taken is 100. Number of iteration used is 5 and constants c1=2; c2=2;c3=2;c4=2. The model parameters are same as chosen for ICS-PF.

5. Experimental Results on Video Tracking

Under this section, the experiment results are presented. To illustrate the performance and effectiveness of proposed algorithm, we have performed experiments on two different sets of videos. In first sets of videos, we have taken video sequences from CAVIAR project [43] which are captured indoor under different lighting conditions. The test sequences in this data set contain variable environments with different level of illuminations, scaling and occlusions. In the second set of videos, we have taken five video sequences from our captured videos at Delhi Technological University. The videos are captured during day time in outdoor environment with shadow, partial occlusion, scaling and rotation factor included in the video sequences. We have conducted experiment on five set of these video sequences. In order to cater for randomness due to particle filter framework, we have run the algorithms for 10 runs each. Reported results are average of these runs. In all our experiments, we have taken N=100 number of particles on object subjected for tracking. The posterior state which is centroid of object is estimated as weighted mean of all the particles. In order to evaluate our algorithm, we have carried out both qualitative and quantitative analysis. The results of same are elaborated in following paragraphs where result of proposed method is compared with particle filter [37], PSO- particle filter [46].

5.1 Qualitative Analysis

In our first video set from CAVIAR project [43], we have analysed five video sequences and qualitative performance results for image sequence OneShopOneWait1cor.mpg are illustrated in Figure 3-4. In this video sequences, we are tracking white shirt person throughout the sequence using particle filter, PSO particle filter and our proposed algorithm. The person is started with entry near the camera view and it is

ACCEPTED MANUSCRIPT

moving away from the camera which introduced the effect of scaling. After few sequences, it is partially occluded by the other persons and again recovered from the occlusion. Also, as the person passes away from camera there is change of illumination effect and presence of shade in sequences. This information provides us various contextual information we would like to establish in video sequences.

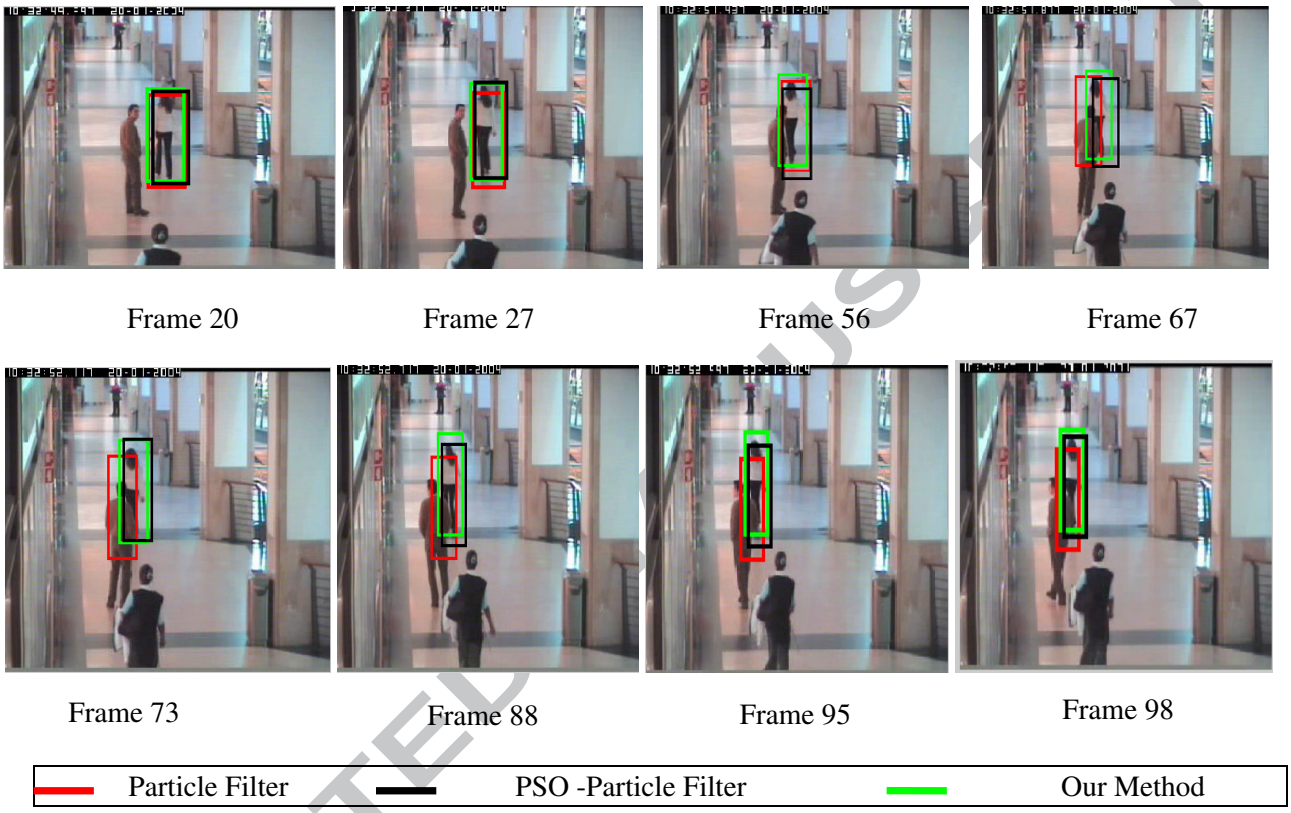


Figure 3: In Caviar OneShopOneWait1cor.mpg video sequence, our proposed method (improved cuckoo – PF) provides the best performance. Our method cater for change of illumination and scale in the scence (Object moving away from camera) . Between frame number 45 and 65 when partial occulsion occurs , our method perform better than PSO-Particle filter and Particle filter which is reflected in corresponding predicted rectangle on object(all see the corresponding error plots in figure 4).

The tracker performance with particle filter is greatly affected due to resampling which create sample impoverishment. In Figure 4 [(a)-(c)], comparison of number of particles at each frame number for particle filter(a) , PSO particle filter (b) and proposed method (c) illustrate that improved cuckoo search create more diversity of particles at different frames. Due more diversity in particles, the estimation of state of object is greatly improved. Even during occlusion of object, the number of different particles in our proposed method remains almost same whereas it is greatly decreased in other cases. The performance in terms of RMSE values of positional error w.r.to ground truth is also compared in figure 4(d). These RMSE values are plotted after taking 10 different runs of estimation of state in order to cater for randomness in results by particle filter estimation. The positional error due to our method is better than PSO-particle filter and particle filter.

ACCEPTED MANUSCRIPT

After number of estimation, positional error in particle filter is very high because almost all particles remain the same which may lead to wrong estimation of states.

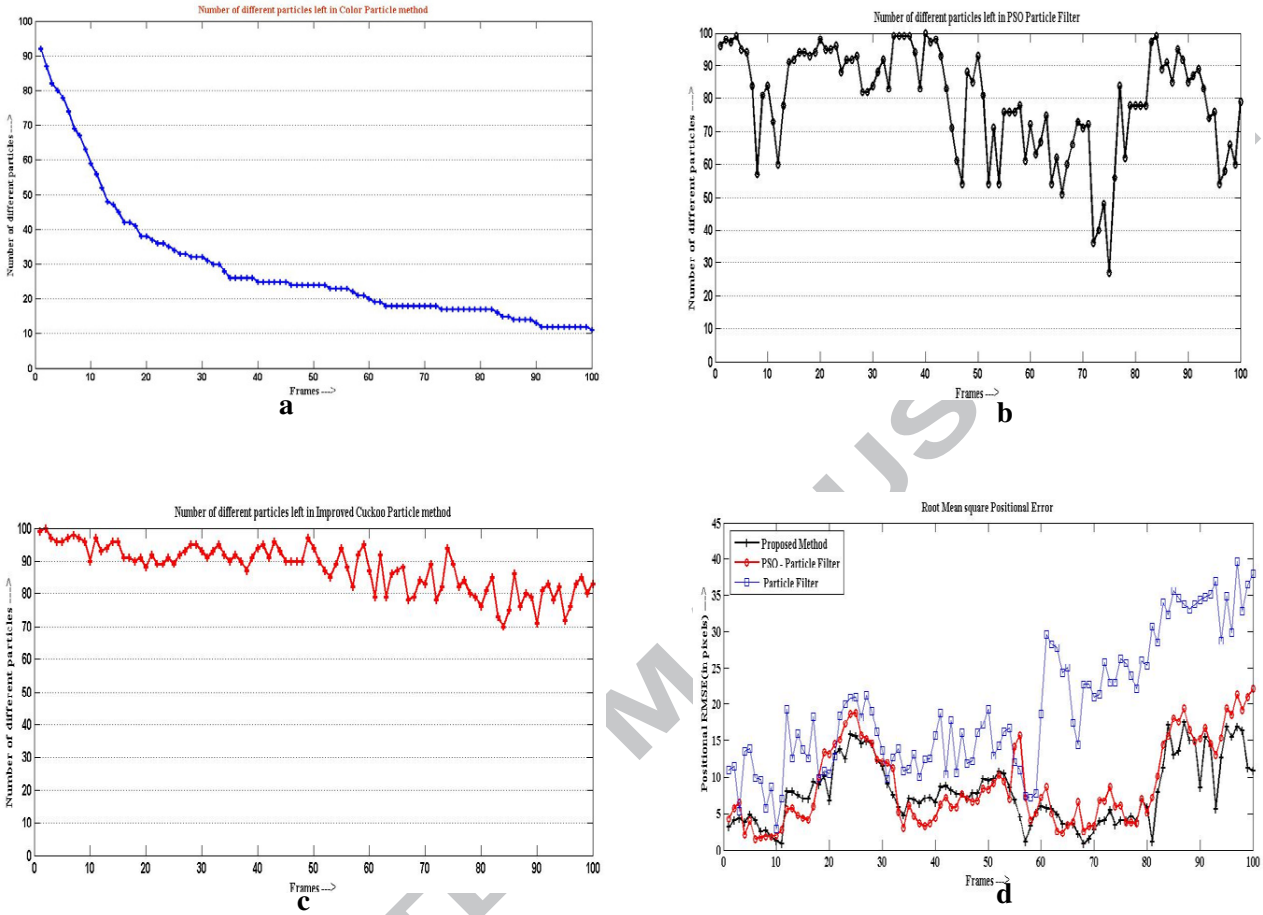


Figure 4 : In Caviar OneShopOneWait1cor.mpg video sequence, Number of different particles left after each posterior state estimation : (a) Particle filter b) PSO- Particle filter c) Proposed Method ; d) Comparison of RMSE value of positional erros plot w.r.t. ground truth position

ACCEPTED MANUSCRIPT

In second set of experiments, we have taken DTU ECE Main-1 video sequences. In this video two person are walking in different direction and have similar colour cloth. The condition of illumination is also changed intermediate stage. The persons are walking away from the camera which creates scaling effect. Total number of frames in this video is 437. There is complete occlusion between frames number 39 to 62.

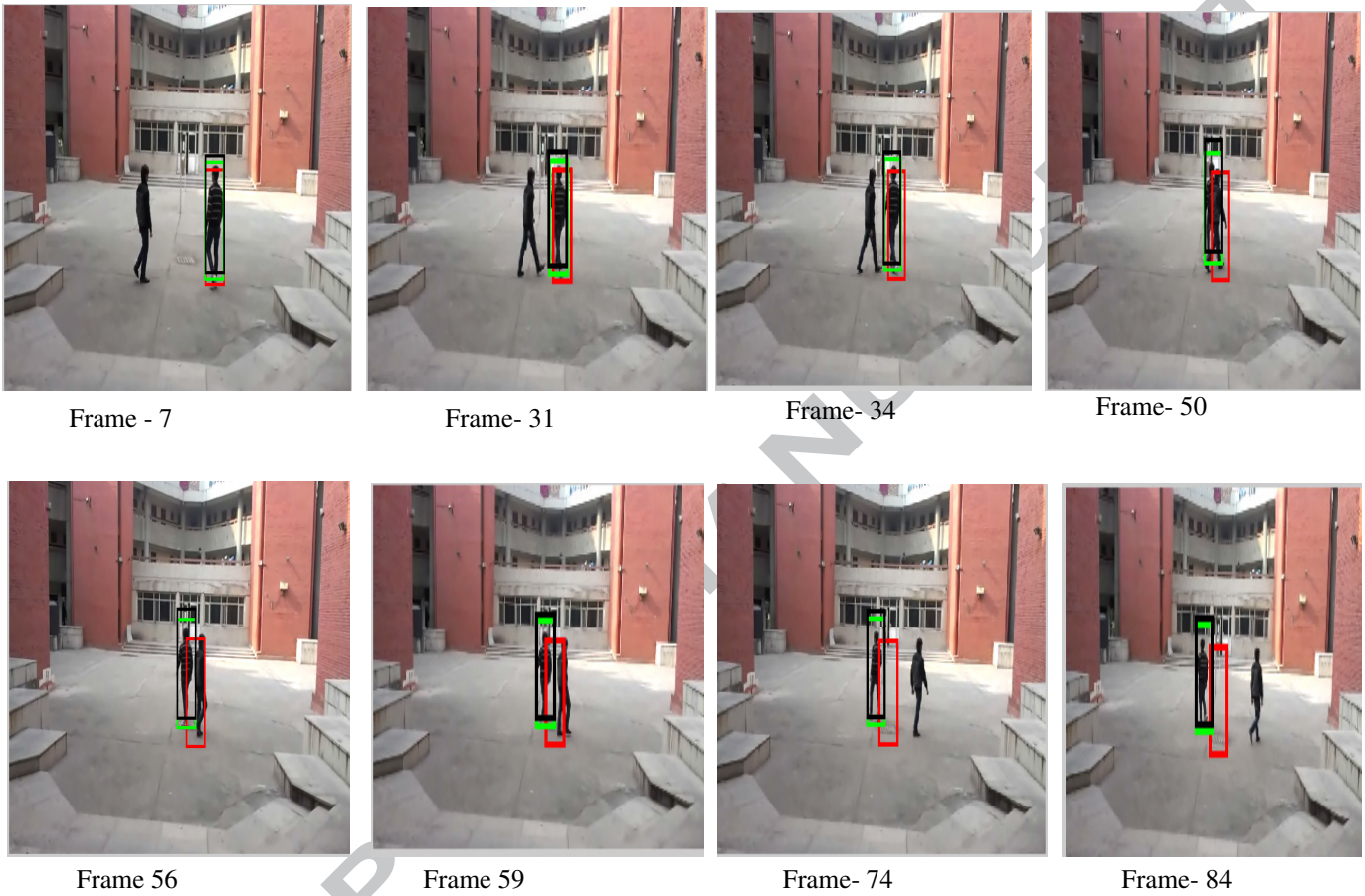


Figure 5: In **DTU ECE Main-1** video sequence, comparision of three different tracker performances concludes that our proposed method (improved cuckoo –PF) provides the best performance. The effect of change scale and occlusion is generated in this video and our method cater for these changes. Between frame number 39 and 62 when partial occulsion occurs , our method perform better than PSO-Particle filter and Particle filter which is reflected in corresponding predicted rectangle on object(all see the corresponding error plots in figure 6).

ACCEPTED MANUSCRIPT

The tracking results are shown in Figure 5 where particle filter is completely off the mark. The results of our proposed particle filter are better than PSO particle filter. The numbers of different particles at different frame number are shown in figure 5 (a). In generic particle filter, after few state predictions, almost all particles are same. Due to lack of diversity in particle on object space, tracking performance is greatly affected which is shown as RMSE estimation of x coordinate error figure 5 (b), y coordinate error figure 5(c) and positional error figure 5(d).

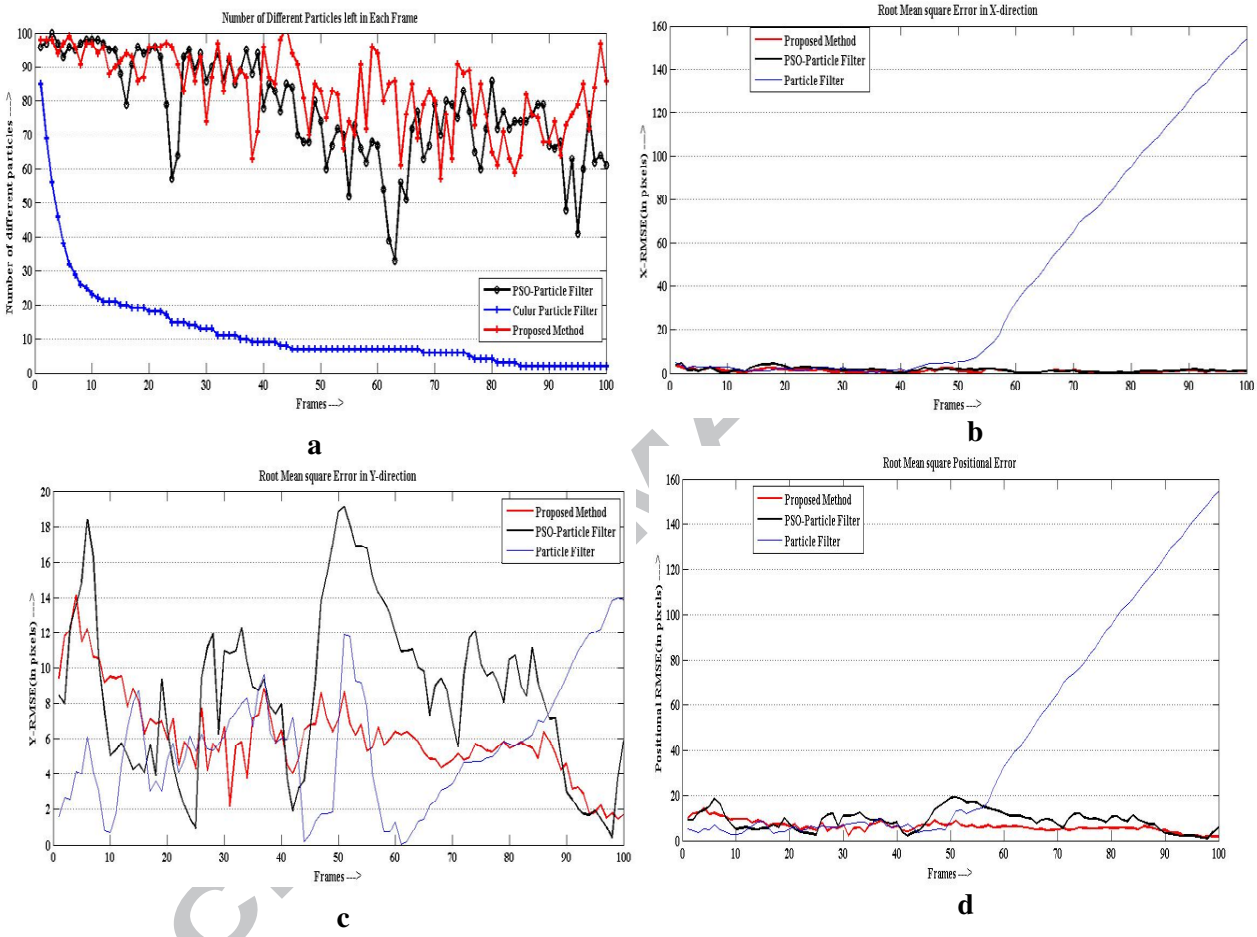


Figure 6 : In **DTU ECE Main-1** video sequence, a) Comparision of number of different particles left after each posterior state estimation ; Comparion of erros w.r.t ground truth position (b) RMSE X-error c) RMSE Y-error d) RMSE positional error

ACCEPTED MANUSCRIPT

As shown in figure 6 , after frame number 45 during occlusion, the number of different particle in particle filter is very less which will generate large amount of x coordinate error. The improved cuckoo search based particle filter recover from occlusion easily due of creation of inherent property of optimization where it create new partiles using levy flight and put randomness by abandoning a portion of particles. Although qualitative analysis results gives more illustrative results in terms of number of different particles at different frame number , occlusion handling ablity etc., details analysis for whole video stream is carried out by quantative analysis.

5.2 Quantative Analysis

We have performed the quantiative analysis of proposed method by four parameters as F-measure , recall , precison and success rate. These parameters are defined in section 2.3 . Experiments are conducted on two set of video sequences. In first set, we have taken standard CAVIAR project[43] videos and estimated the F measure and sucess rate . The average value of F-measure for OneShopOneWait1cor video for each frame for 10 runs of video is shown in Figure 7(a). The second set of experiments were conducted on vidoes from DTU data set where a few of videos are synthesis in order to include the effect of scaling , rotation and occlusion. The average value of F-measure for 10 runs for DTU ECE Main-1 is shown Figure 7(b).

ACCEPTED MANUSCRIPT

ACCEPTED MANUSCRIPT

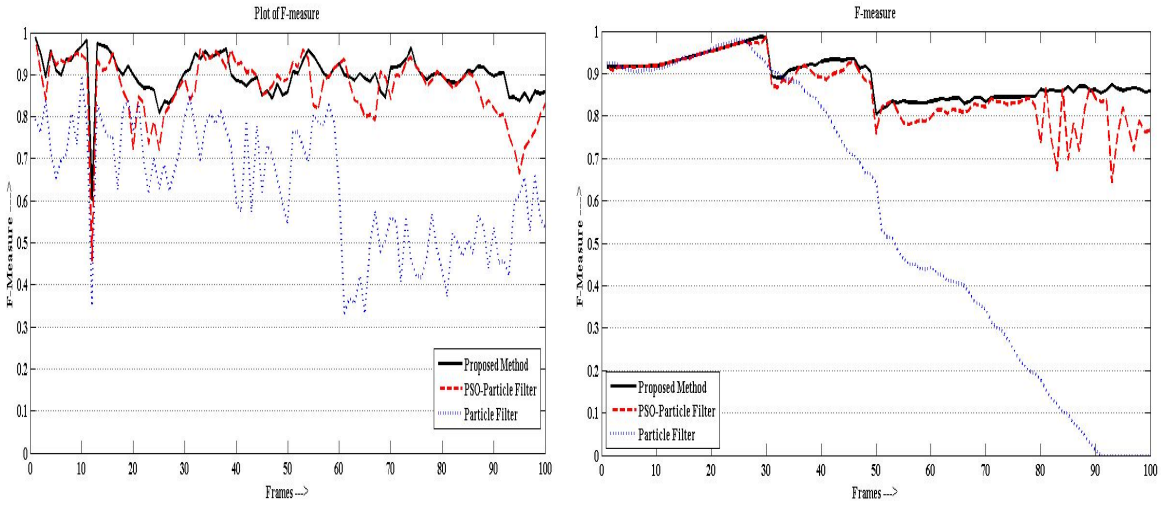


Figure 7: : a) F-Measure plot at each frame for **Caviar OneShopOneWait1cor.mpg** video sequence b) F-Measure plot at each frame for **DTU ECE Main-1** video sequence

In case of CAVIAR data set where five video sequences are taken as 1) OneShopOneWait1cor.mpg 2) OneShopOneWait2cor.mpg 3) OneStopEnter2cor.mpg 4) OneStopEnter1cor.mpg 5) OneShopOneWait2cor.mpg , The performance measures in terms of average success rate and average F-measure taken over five videos sequences is tabulated in table 2.

Table: 2

Performance measure calculated over all the 5 experiments for CAVIAR dataset

Sr No.	Qualitative Performance Measure	Particle Filter	PSO-Particle Filter	Proposed Method
1.	Average F-Measure	0.49	0.53	0.58
2.	Average Success Rate	87.1	89.45	95.30

The results show that there is significance improvement in F-measure and success rate of proposed method over the particle filter and PSO particle filter when CAVIAR data set is considered for tracking.

In case of DTU data set where five video sequences are taken as 1) DTU_ECE_Main-1.avi 2) DTU_PARK Main-2.avi 3) DTU_GATE_Main.avi 4) DTU_SCIENCE_Block.avi 5) DTU_HOST_Block.avi, The

ACCEPTED MANUSCRIPT

performance measures in terms of average success rate and average F-measure taken over listed five videos sequences is tabulated in table 3.

Table: 3

Performance measure calculated over all the 5 experiments for DTU Dataset

Sr No.	Qualitative Performance Measure	Particle Filter	PSO-Particle Filter	Proposed Method
1.	Average F-Measure	0.43	0.545	0.61
2.	Average Success Rate	75.4	87.5	94.30

The above results show that there is significance improvement in F-measure and success rate of proposed method over the particle filter and PSO particle filter when DTU data set is considered for tracking.

From the analysis of results, we can conclude that performance of our proposed algorithm is better than earlier PSO –particle filter and generic particle filter in terms of both F-measure and success rate. Also as shown in figure 7 , proposed algorithm better handle partial occlusion in video sequences. Further real time implementation of algorithms is studied on platform as discussed in section 4.2. The result for computational cost requirement is discussed in next section.

5.3 Computation cost

Under this experiments, the computational cost requirement is studied for particle filer , PSO particle filter and proposed method. The number of particles for all the experiment is fixed at 100. The time required to process one frame using proposed method is 0.0385 sec , PSO-Particle filter is 0.0427 sec and particle filter is 0.023 sec. One an average, proposed algorithm achieved good tracking accuracy with fewer number of iteration. However, this computational cost could further be reduced either by parallelization of source code or by running it on fast processor. Although our proposed algorithm takes more processing compared to particle filter, it could be used for real time tracking of object in video at 25 fps.

6. Conclusion and Future Work

This paper has presented a novel particle filter based upon ICS for object tracking under different environments. Sample impoverishment which is inherent problem of generic particle filter degrade its tracking performance to a large extend. In present paper, we have solved sample impoverishment problem of generic particle filter using meta-heuristic optimization technique. The proposed approach use ICS algorithm which use levy flight for generating new particles in the solution for speedily capture of local

ACCEPTED MANUSCRIPT

minimum and introduced randomness in sample at the same time by abandoning a fraction of these particles for avoiding local minimum traps. Also, a novel method for representing particles with will cater for tacking scaling and rotational error is proposed. During our experiments with synthetic and standard videos, we have seen that even after large number of prediction using our proposed algorithm, the number of different particles remains almost same as initial selection which leads to high accuracy in estimation. The proposed algorithm is tested on two set of videos for studying its robustness under different environments. In first set of videos, we have taken video sequences from CAVIAR project which are captured indoor under different lighting conditions. The test sequences in this data set contain variable environments with different level of illuminations, scaling and occlusions. In the second set of videos, we have taken five video sequences from our captured videos at Delhi Technological University. The videos are captured during day time in outdoor environment with shadow, partial occlusion, scaling and rotation factor included in the video sequences. The proposed algorithm is compared with generic particle filter and particle swarm optimization based particle filter while considering success rate and F-measure as qualitative performance measure. The positional error of object under partial occlusion is better handled by proposed algorithm due to more diversity of particles even under occluding situations. The results for different qualitative measures are evaluated using given ground truth (*.xml file) CAVIAR set and manual generated ground truth data for DTU data set. The computational requirement for improved cuckoo search algorithm is less than PSO particle filter due to less number of iteration requirement for convergence. From results obtained on standard data set video and synthetic video, we conclude that our proposed algorithm outperform the best solution available while considering success rate, F-measure, and robustness as performance metrics. Nevertheless that the developed algorithm is more time consuming than particle filter, it runs comfortably for real time videos captured at 25fps.

In future, we would look forward for tracking multiple people and guiding particles under ambiguous environments and uncertain conditions. Integrating more cues in this tracking framework so that dynamic shape of the object could be handled efficiently. Also, we are working on theoretical proof of our proposed concept.

7. Acknowledgements

The authors are grateful to the financial support by Delhi Technological University and Defence Research and Development Organization for this work.

8. References

[1] Toyama, K., Horvitz, E., “Bayesian modality fusion: Probabilistic integration of multiple vision algorithms for head tracking” Proc. Asian Conf. Computer Vision 2000.

[2] Sherrah, J., Gong, S, “Continuous global evidence-based Bayesian modality fusion for simultaneous tracking of multiple objects”. Int. Conf. Computer Vision, 2001, 42–49.

[3] R.M. Neal, “Probabilistic inference using Markov chain Monte Carlo methods”, Tech. Rep. CRG-TR-93-1, University of Toronto, (1993), URL: citeseer.ist.psu.edu/ neal93probabilistic.html.

[4] J.S. Liu, R. Chen, “Sequential Monte Carlo methods for dynamic systems” J. Am. Stat.Assoc. 93 (1998) 1032–1044.

ACCEPTED MANUSCRIPT

[5] A. Doucet, S. Godsill, C. Andrieu, "On sequential Monte Carlo sampling methods for Bayesian filtering" Stat. Comput. 10 (3) (2000) 197–208.
[6] Isard, M., Blake, A., "CONDENSATION – conditional density propagation for visual tracking" Int. J. Computer Vision, 5–28. 1998.
[7] N. Gordon, D.Salmond,C. Ewing, " Bayesian state estimation for tracking and guidance using the bootstrap filter", Journal of gauidance , Control and Dynamics 18(6),1995,1434-1443.
[8] Gordon, N., Arulampalam, M.S., Maskell, S., Clapp, T., 2002. A tutorial on particle filters for online nonlinear/non-Gaussian Bayesian tracking. IEEE Trans. Signal Process. 50.
[9] Nummiaro, K., Koller-Meier, E., Van Gool, L., "Object tracking with an adaptative colour-based particle filter" Image Vision Computer, 99–111, 2002.
[10] P. Perez, C. Hue, J. Vermaak, M. Gangnet, Color-based probabilistic tracking, ECCV '02: Proceedings of the 7th European Conference on Computer Vision—Part I, Springer-Verlag, London, UK, 2002, pp. 661–675.
[11] J. Vermaak, P. Perez, M. Gangnet, A. Blake, "Towards improved observation models for visual tracking: selective adaptation" Proc. Eur. Conf. Computer Vision, ECCV '02, Vol. 1, Copenhagen, Denmark, 2002, pp. 645–660.
[12] A.D. Jepson, D.J. Fleet, T.F. El-Maraghi, "Robust online appearance models for visual Tracking", IEEE Trans. Pattern Anal. Mach. Intell. 25 (10) (2003) 1296–1311.
[13] J. Odobez, D. Gatica Perez, S. Ba, "Embedding motion in model-based stochastic tracking", IEEE Trans. Image Process. 15 (11) (2006) 3514–3530.
[14] Y. Wu, T.S. Huang, "Robust visual tracking by integrating multiple cues based on co-inference learning", Int. J. Computer Vis. 58 (1) (2004) 55–71.
[15] M. Spengler, B. Schiele, "Towards robust multi-cue integration for visual tracking", ICVS '01: Proceedings of the Second International Workshop on Computer Vision Systems, Springer-Verlag, London, UK, 2001.
[16] C. Shen, A. van den Hengel, A.R. Dick, "Probabilistic Multiple Cue Integration for Particle Filter Based Tracking", in: C. Sun, H. Talbot, S. Ourselin, T. Adriaansen (Eds.), DICTA, CSIRO Publishing, 2003, pp. 399–408.
[17] P. Perez, J. Vermaak, A. Blake, "Data fusion for visual tracking with particles", Proc. IEEE 92 (3) (2004) 495–513.
[18] Isard, M., Blake, A.: 'Condensation/Conditional density propagation for visual tracking', Int. J. Computer Vis., 1998, 29, (1), pp. 5–28.
[19] Zhaoying Wang Zhentao Liu, Weiqun Liu, Yunbo Kong 'Particle Filter Algorithm Based on Adaptive Resampling Strategy' 2011 International Conference on Electronic & Mechanical Engineering and Information Technology, IEEE,pp3138-3141.
[20] Cho, J., Jin, S., Dai Pham, X., Jeon, J., Byun, J., Kang, H.: 'A real time object tracking system using a particle filter'. 2006 IEEE/RSJ Int. Conf. on Intelligent Robots and Systems, IEEE, 2006, pp. 2822–2827.
[21] Liang-Qun, L., Hong-Bing, J., Jun-Hui, L.: 'The iterated extended kalman particle filter'. IEEE Int. Symp. on Communications and Information Technology, ISCIT, 2005, vol. 2, pp. 1213–1216.
[22] Wan, E., Van Der Merwe, R.: 'The unscented Kalman filter for nonlinear estimation'. Adaptive Systems for Signal Processing, Communications, and Control Symp. 2000, AS-SPCC, The IEEE 2000, 2000, pp. 153–158.

ACCEPTED MANUSCRIPT

[23] Jing Zhao, Zhiyuan Li ,"Particle filter based on Particle Swarm Optimization resampling for vision tracking", Expert Systems with Applications, 37, 8910–8914, 2010.
[24] ALSPACH, D.L., and SORENSON, H.W: 'Non-linear Bayesian estimation using Gaussian sum approximation', IEEE Trans. On Automatic Control , Volume:17 , Issue: 4.
[25] WEST, M., HARRISON, P.J., and MIGON, H.S.: 'Dynamic generalised linear models and Bayesian forecasting, with discussion', *J. Am. Stat. Assoc.,* 1985, 80, pp. 73-97.
[26] MASRELIEZ, C.J.: 'Approximate non-Gaussian filtering with linear state and observation relations', *ZEEE Trans.,* 1975, AC-20.
[27] Katsuji Uosaki, Yuuya Kimura, Toshiharu Hatanaka "Nonlinear State Estimation by Evolution Strategies Based Particle Filters", 0-7803-7804-0, IEEE ,2003 , pp 2102-2109.
[28] J. P. Zhong, Y. F. Fung "A Biological Inspired Improvement Strategy for Particle Filter" 2009. ICIT 2009. IEEE International Conference on Industrial Technology, ISBN 978-1-4244-3507-4.
[29] Liang Xiaolong,Feng Jinfu and Li Qian , Lu Taorong, Li Bingjie "A Swarm Intelligence Optimization for Particle Filter", Proceedings of the 7th World Congress on Intelligent Control and Automation June 25 - 27, 2008, Chongqing, China.
[30] S. Park, J. Hwang, K. Rou, and E. Kim , "A New Particle Filter Inspired by Biological Evolution: Genetic Filter", World Academy of Science, Engineering and Technology 33 2007.
[31] Hua Han, Yong-Sheng Ding , Kuang-Rong Hao, Xiao Liang , "An evolutionary particle filter with the immune genetic algorithm for intelligent video target tracking" Elsevier , Computers and Mathematics with Applications, 62 (2011) 2685–2695, pp 2685-2695.
[32] Gurjit Singh Walia, Rajiv Kapoor, "Particle Filter Based on Cuckoo Search for Nonlinear State Estimation", *2013 3rd IEEE International Advance Computing Conference (IACC)* , pp 918-924 , IEEE xplore , IEEE , 2012, print ISBN 978-1-4673-4527-9.
[33] Ehsan Valian, Shahram Mohanna and Saeed Tavakoli , "Improved Cuckoo Search Algorithm for Global Optimization", International Journal of Communications and Information Technology, IJCIT-2011-Vol.1-No.1 Dec. 2011.
[34] Ehsan Valian, Saeed Tavakoli , Shahram Mohanna , Atiyeh Haghi, " Improved cuckoo search for reliability optimization problem", Computers and Industrial Engineering 64(2013) 459-468.
[35] F. Bashir, F. Porikli. "Performance evaluation of object detection and tracking systems", IEEE International Workshop on Performance Evaluation of Tracking and Surveillance (PETS), June 2006.
[36] N. Lazarevic-McManus , J.R. Renno, D. Makris, G.A. Jones " An object-based comparative methodology for motion detection based on the F-Measure" Computer Vision and Image Understanding 111 (2008) 74–85).
[37] N.J Gordon et al., "A novel approach for non-linear/Non-Bayesian state estimation", IEE proceeding-F Vol 140, No2, 1993.
[38] X.-S. Yang; S. Deb, "Cuckoo search via Lévy flights" In proceedings of World Congress on Nature & Biologically Inspired Computing (NaBIC 2009), pp. 210–214, 2009.
[39] Paul Brasnett , Lyudmila Mihaylova , David Bull , Nishan Canagarajah "Sequential Monte Carlo tracking by fusing multiple cues in video sequences", Image and Vision Computing 25 (2007) 1217–1227.
[40] P. Perez, J. Vermaak, and A. Blake, "Data fusion for tracking with particles," *Proceedings of the IEEE*, vol. 92, no. 3, pp. 495-513, March 2004.

ACCEPTED MANUSCRIPT

[41] N. Bergman, Recursive Bayesian estimation: navigation and tracking applications, Ph.D. dissertation, Linko¨ping University, Linko¨ping, Sweden, 1999.

[42] M.S. Khalid, M.U. Ilyas, M.S. Sarfaraz and M.A. Ajaz. "Bhattacharyya Coefficient in Correlation of Gray-Scale Objects" Journal of Multimedia, vol.1 no. 1, pp. 56-61, 2006.

[43] EC Funded CAVIAR project/IST 2001 37540, found at *http://homepages.inf.ed.ac.uk/rbf/CAVIAR/*.

[44] C. Stauffer and W. E. L. Grimson, "Adaptive background mixture models for real-time tracking," presented at Comput. Vision Pattern Recog. Conf., Fort Collins, CO, Jun. 1999, pp. 246–252.

[45] Tiancheng Li , Shudong Sun , Tariq Pervez Sattar , Juan Manuel Corchado, "Fight sample degeneracy and impoverishment in particle filters: A review of intelligent approaches", Expert Systems with Applications, 41 , 3944–3954, 2014.

[46] Guofeng Tong, Zheng Fang, Xinhe Xu, "A Particle Swarm Optimized Particle Filter for Nonlinear System State Estimation", 2006 IEEE Congress on Evolutionary Computation , July 16-21, 2006.

[47] Pinar Civicioglu , Erkan Besdok, "A conceptual comparison of the Cuckoo-search, particle swarm optimization, differential evolution and artificial bee colony algorithms", Artif Intell Rev 39:315–346, 2013.

[48] R Kapoor, A Dhamija, "Fast tracking algorithm using modified potential function", IET Computer Vision, Volume 6 , Issue 2, March 2012.

ACCEPTED MANUSCRIPT

ACCEPTED MANUSCRIPT

Highlights:

- ***A novel method of object representation for object tracking.***
- ***Proposed ICS- PF for overcoming sample impoverishment of PF.***
- ***Better qualitative and quantitative performance over PSO-PF and PF.***
- ***Real time application due to less computational requirement.***

ACCEPTED MANUSCRIPT

IRJSSE
Spreading Excellence

International Research Journal Of Sustainable Science & Engineering.

A Monthly Peer-Reviewed Journal

Thermodynamic performance evaluation of multi-evaporators single compressor and single expansion valve and liquid vapour heat exchanger in vapour compression refrigeration systems using thirteen eco friendly refrigerants for reducing global warming and ozone depletion.

Prof. R.S Mishra
Professor, Mechanical Engineering Department, Delhi College of Engineering, Bawana Road, Delhi , India.
E Mail: professor_rsmishra@yahoo.co.in

Abstract
The methods for improving first law and second law efficiency have been considered in this paper by using liquid vapour heat exchanger is investigated in this paper. Detailed energy and energy analysis of multi-evaporators at different temperatures with single compressor and single expansion valve using liquid vapour heat exchanger vapour compression refrigeration systems have been done in terms of performance parameter for R507a, R125, R134a, R290, R600, R600a, R1234ze, R1234yf, R410a, R407c, R707, R404a and R152a refrigerants. The numerical computations have been carried out for both systems. It was observed that first law and second law efficiency improved by 20% using liquid vapour heat exchanger in the vapour compression refrigeration systems. It was also observed that performance of both systems using R717 is higher but R600 and R152a nearly matching same values under the accuracy of 5% can be used in the above system .But difficulties using R152a, R600, R290 and R600a have flammable problems therefore safety measures are required using these refrigerants. Therefore R134a refrigerant is recommended for practical and commercial applications although it has slightly less thermal performance than R152a which is not widely used refrigerant for domestic and industrial applications

Keywords- Vapour compression refrigeration systems, Energy and Exergy Analysis, First and second law analysis,, Irreversibility analysis, VCR with LVHE

Nomenclature

COP	coefficient of performance (non-dimensional)	h	specific enthalpy (kJ/kg)
VCR	vapour compression refrigeration	P	pressure (kPa)
CFC	chlorofluorocarbon	IR	irreversibility (kW)
HCFC	hydrochlorofluorocarbon	E_x	exergy rate of fluid (kW)
Q	rate of heat transfer (kW)	m	mass flow rate (kg/s)
W	work rate (kW)	s	specific entropy (kJ/kgK)
T	temperature (K)	EF	exergy rate of fuel (kW)
δ	efficiency defect (non-dimensional)	EL	exergy loss rate (kW)
ΔT_{sc}	degree of subcooling	η	efficiency (non-dimensional)
EP	exergy rate of product (kW)	r	refrigerant, space to be cooled
EV	Expansion Valve	ex	exergetic
EP	Evaporator	ev	expansion valve

©-IRJSSE, ALL RIGHT RESERVED

Subscript

e	evaporator	c	condenser
comp	compressor	sc	subcooler
		k	kth component

1. INTRODUCTION

Technology of refrigeration is absorbs heat at low temperature sink and provides temperature below the surrounding by rejecting heat to the surrounding at higher temperature. The refrigeration system of two type such as air refrigeration system and vapour refrigeration system. Vapour refrigeration systems can be classified as vapour absorption system and vapour compression system. The vapour absorption system of two types such as NH3-H20 system and LIBR systems working on single effect, half effect, double effect and Tripple effect. The simple vapour compression system which consists of four major components compressor, expansion valve, condenser and evaporator in which total cooling load is carried at one temperature by single evaporator but in many applications like large hotels, food storage and food processing plants, food items are stored in different compartment and at different temperatures. Therefore there is need of multi evaporator vapour compression refrigeration system. The use suction heat exchanger or liquid vapour regenerative heat exchanger in vapor compression system is justified because superheating in liquid suction exchanger is preferable to superheating in evaporator itself

The systems under vapour compression technology consume huge amount of electricity, this problem can be solved by improving performance of system. Performance of systems based on vapour compression refrigeration technology can be improved by following:

The performance of refrigerator is evaluated in term of first law efficiency which is known as coefficient of performance (COP) which is the ratio of refrigeration effect to the net work input given to the system. The COP of vapour compression refrigeration system can be improved either by increasing refrigeration effect or by reducing work input given to the system. It is well known that throttling process in VCR is an irreversible expansion process. Expansion process is one of the main factors responsible for exergy loss in cycle performance because of entering the portion of the refrigerant flashing to vapour in evaporator which will not only reduce the cooling capacity but also increase the size of evaporator. This problem can be eliminated by adopting multi-stage expansion with flash chamber where the flash vapours is removed after each stage of expansion as a consequence there will be increase in cooling capacity and reduce the size of the evaporator.

Work input can also be reduced by replacing multi-stage compression or compound compression with single stage compression.

Refrigeration effect can also be increased by passing the refrigerant through subcooler after condenser to evaporator.

Vapour compression refrigeration system based applications make use of refrigerants which are responsible for greenhouse gases, global warming and ozone layer depletion. Montreal protocol was signed on the issue of substances that are responsible for depleting Ozone layer and discovered how much consumption and production of ozone depletion substances took place during certain time period for both developed and developing countries. Another protocol named as Kyoto aimed to control emission of green house gases in 1997[1]. The relationship between ozone depletion potential and global warming potential is the major concern in the field of GRT (green refrigeration technology) so Kyoto proposed new refrigerants having lower value of ODP and GWP. Internationally a program being pursued to phase out refrigerants having high chlorine content for the sake of global environmental problems [2].Due to presence of high chlorine content ,high global warming potential and ozone depletion potential after 90's CFC and HCFC refrigerants have been restricted. Thus, HFC refrigerants are used nowadays, showing much lower global warming potential value, but still high with respect to non-fluorine refrigerants. Lots of research work has been done for replacing "old" refrigerants with "new" refrigerants [3-8].

2. LITERATURE REVIEW

Reddy et al. [9] performed numerical analysis of vapour compression refrigeration system using R134a, R143a, R152a, R404A, R410A, R502 and

©-IRJSSE, ALL RIGHT RESERVED

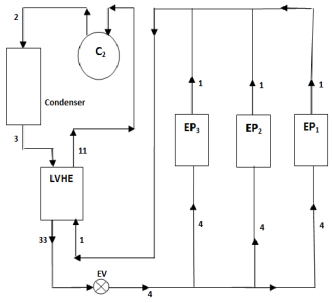
R507A , and discussed the effect of evaporator temperature, degree of subcooling at condenser outlet, superheating of evaporator
outlet, vapour liquid heat exchanger effectiveness and degree of condenser temperature on COP and exergetic efficiency. They reported that evaporator and condenser temperature have significant effect on both COP and exergetic efficiency and also found that R134a has the better performance while R407C has poor performance in all respect. **Selladurai and Saravana kumar [10]** compared the performance between R134a and R290/R600a mixture on a domestic refrigerator which is originally designed to work with R134a and found that R290/R600a hydrocarbon mixture showed higher COP and exergetic efficiency than R134a. In their analysis ,highest irreversibility obtained in the compressor compare to condenser, expansion valve and evaporator. **Nikolaidis and Probert [11]** studied analytically that change in evaporator and condenser temperatures of two stage vapour compression refrigeration plant using R22 add considerable effect on plant irreversibility. They suggested that there is need for optimizing the conditions imposed upon the condenser and evaporator. **Kumar et al. [12]** did energy and exergy analysis of vapour compression refrigeration system by the use of exergy-enthalpy diagram. They did first law analysis (energy analysis)for calculating the coefficient of performance and exergy analysis (second law analysis) for evaluation of various losses occurred in different components of vapour compression cycle using R11 and R12 as refrigerants. **Mastani Joybari et al.[13]** performed experimental investigation on a domestic refrigerator originally manufactured to use of 145g of R134a.They concluded that exergetic defect occurred in compressor was highest as compare to other components and through their analysis it has been found that instead of 145g of R134a if 60g of R600a is used in the considered system gave same performance
which ultimately result into economical advantages and reduce the risk of flammability of hydrocarbon refrigerants. **Anand and Tyagi [14]** did detailed exergy analysis of 2 ton of refrigeration capacity window air conditioning test rig with R22 as working fluid and reached to the conclusions , that irreversibility in system components will be highest when the system is 100% charged and lowest when 25% charged and irreversibility in compressor is highest among system components. **Arora and Kaushik[7]** developed numerical model of actual vapour compression refrigeration system with liquid vapour heat exchanger and did energy and exergy analysis on the same in the specific temperature range of evaporator and condenser and concluded that R502 is the best refrigerant compared to R404A and R507A and compressor is the worst component and liquid vapour heat exchanger is best component of the system in case of exergy transfer. **Ahamed et al.[17]** had performed experimental investigation of domestic refrigerator with hydrocarbons (isobutene and butane) by energy and exergy analysis. They reached to the results that energy efficiency ratio of hydrocarbons comparable with R134a but exergy efficiency and sustainability index of hydrocarbons much higher than that of R134a at considered evaporator temperature. It was also found that compressors shows highest system defect (69%) among components of considered in the system. **Ahamed et al. [15]** emphasized on use of hydrocarbons and mixture compressor shows much higher exergy destruction as compared to rest of components in the vapour compression refrigeration system and this exergy destruction can be minimized by using of nanofluid and nanolubricants in compressor. **Bolaji et al. [18]** had done experimentally comparative analysis of R32, R152a and R134a refrigerants in vapour compression refrigerator and concluded that R32 shows lowest performance whereas R134a and R152a showing nearly same performance but best performance was obtained of system using R152a. **Yumrutas et al. [19]**carried out exergy analysis based investigation of effect of condensing and evaporating temperature on vapour compression refrigeration cycle in terms of pressure losses, COP, second law efficiency and exergy losses. Variation in temperature of condenser as well as have negligible effect on exergy losses of compressor and expansion valve, also first law efficiency and exergy efficiency increase but total exergy losses of system decrease with increase in evaporator and condenser temperature. **Padilla et al. [20]** exergy analysis of domestic vapour compression refrigeration system with R12 and R413A was done. They concluded that performance in terms of power consumption, irreversibility and exergy efficiency of R413A is

©-IRJSSE, ALL RIGHT RESERVED

better than R12, so R12 can be replaced with R413A in domestic vapour compression refrigeration system. **Getu and Bansal [21]** had optimized the design and operating parameters of like condensing temperature, subcooling temperature, evaporating temperature ,superheating temperature and temperature difference in cascade heat exchanger R744-R717 cascade refrigeration system. A regression analysis was also done to obtain optimum thermodynamic parameters of same system. **Spatz and Motta [22]** had mainly focused on replacement of R12 with R410a through experimental investigation of medium temperature vapour compression refrigeration cycles. In terms of thermodynamic analysis, comparison of heat transfer and pressure drop characteristics, R410a gives best performance among R12, R404a and R290a. **Mohanraj et al. [23]** concluded through experimental investigation of domestic refrigerator they arrived on conclusions that under different environmental temperatures COP of system using mixture of R290 and R600a in the ratio of 45.2: 54.8 by weight showing up to 3.6% greater than same system using R134a, also discharge temperature of compressor with mixture of R290 and R600a is lower in the range of 8.5-13.4K than same compressor with R134a. **Han et al. [24]** Under different working conditions experimental results revealed that there could be replacement of R407C in vapour compression refrigeration system having rotor compressor with mixture of R32/R125/R161 showing higher COP, less pressure ratio and slightly high discharge compressor temperature without any modification in the same system. **Halimic et al. [25] had** compared performance of R401A, R290 and R134A with R12 by using in vapour compression refrigeration system, which is originally designed for R12.Due to similar performance of R134a in comparison with R12,R134A can be replaced in the same system without any medication in the system components. But in reference to green house impact R290 presented best results. **Xuan and Chen [26]** presented in this manuscript about the replacement of R502 by mixture of HFC-161 in vapour compression refrigeration system and conducted experimental study it was found that mixture of HFC-161 gives same and higher performance than R404A at lower and higher evaporative temperature respectively on the vapour compression refrigeration system designed for R404A. **Cabello et al. [27]** had studied about the effect of operating parameters on first law efficiency (COP), work input and cooling capacity of single-stage vapour compression refrigeration system. There is great influence on energetic parameters due change in suction pressure, condensing and evaporating temperatures.**Cabello et al. [28] discussed the** effect of condensing pressure, evaporating pressure and degree of superheating was experimentally investigated on single stage vapour compression refrigeration system using R22, R134a and R407C.It was observed that mass flow rate is greatly affected by change in suction conditions of compressor in results on refrigeration capacity because refrigeration capacity depended on mass flow rate through evaporator. It was also found that for higher compression ratio R22 gives lower COP than R407C. **Stanciu et al.[29]**did numerical and graphical investigation on one stage vapour compression refrigeration system for studied refrigerants (R22, R134a, R717, R507a, R404a) in terms of COP, compressor work, exergy efficiency and refrigeration effect. Effect of subcooling, superheating and compression ratio are also studied on the same system using considered refrigerants and also presented system optimization when working with specific refrigerant in the vapour compression .

Based on the literature it was observed that researchers have gone through detailed first law analysis in terms of coefficient of performance and second law analysis in term of exergetic efficiency of simple vapour compression refrigeration system with single evaporator. Researchers did not go through the irreversibility analysis.

This paper mainly deals with the thermodynamic analysis of simple VCR with liquid vapour heat exchanger using thirteen ecofriendly refrigerants.



©-IRJSSE, ALL RIGHT RESERVED

Fig.1 (a)-Schematic diagram of actual multievaporator with singlecompressor and single expansion valve and LVHE

To improve thermal performance of vapour compression refrigeration systems both multiple evaporator system by using liquid vapour heat exchanger for improving: First law efficiency (COP) , second law efficiency (Exergetic efficiency) and Reduction of system defect in components of system in terms of exergy destruction ratio which results into reduction of work input The multiple evaporators at the same temperature with single compressor and single expansion valve and liquid vapour heat exchanger vapour compression refrigeration system.

2.1 Mass of refrigerant flowing through each evaporator

$$m_1 = \frac{Q_1}{h_1 - h_4} \qquad (1)$$

$$m_2 = \frac{Q_2}{h_1 - h_4} \qquad (2)$$

$$m_3 = \frac{Q_3}{h_1 - h_4} \qquad (3)$$

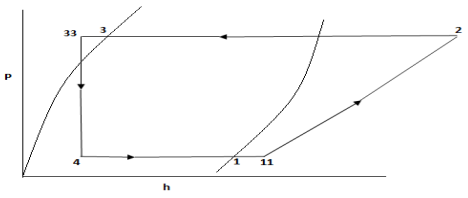


Fig.1 ((b) Pressure enthalpy diagram of actual multi evaporator with single compressor, and single expansion valve and LVHE

2.2 Work required to run the compressor

$$W_{comp} = (m_1 + m_2 + m_3)\,(h_2 - h_1) \qquad (4)$$

According to the first law of thermodynamics,
coefficient of performance (β) defined as the
ratio of the net refrigeration effect produced per
unit of work input. It is given as

2.3 Coefficient of performance

$$\beta = \frac{Q_1 + Q_2 + Q_3}{W_{comp}} \qquad (5)$$

Second law analysis (exergy analysis)

According to second law thermodynamic loss of work input required to drive the system due to irreversibility occur in various states (f_1 and f_2) for a steady flow system is given as components of the system. Irreversibility in each
component by neglecting the kinetic energy an potential energy of the system as per Eqs. (6)– (13) specified below

$$\Phi_{e1} = \chi_4 - \chi_1 + Q_1\left(1 - \frac{T_0}{T_1}\right)$$
$$= m_1(h_4 - T_0 s_4) - m_1(h_1 - T_0 s_1) + Q_1\left(1 - \frac{T_0}{T_1}\right) \qquad (6)$$

$$\Phi_{e2} = \chi_4 - \chi_1 + Q_2\left(1 - \frac{T_0}{T_1}\right)$$
$$= m_2(h_4 - T_0 s_4) - m_2(h_1 - T_0 s_1) + Q_2\left(1 - \frac{T_0}{T_1}\right) \qquad (7)$$

$$\Phi_{e3} = \chi_4 - \chi_1 + Q_3\left(1 - \frac{T_0}{T_1}\right)$$
$$= m_3(h_4 - T_0 s_4) - m_3(h_1 - T_0 s_1) + Q_3\left(1 - \frac{T_0}{T_1}\right) \qquad (8)$$

Compressor

$\Phi_{comp} = \chi_{11} - \chi_2 + W_{comp} = m\,((h_{11} - h_2) - T_o\,(s_{11} - s_2)) + m\,(h_2 - h_{11}) = m\,T_o\,(s_2 - s_{11})$ (9)

Condenser

$\Phi_c = \chi_2 - \chi_3 = m\,((h_2 - h_3) - T_o\,(s_2 - s_3))$ (10)

Expansion Valve

$\Phi_{ev} = \chi_{33} - \chi_4 = m\,((h_{33} - h_4) - T_o\,(s_{33} - s_4))$
$= m\,(T_o\,(s_4 - s_{33})$ (11)

Liquid vapour heat exchanger

©-IRJSSE, ALL RIGHT RESERVED

$\Phi_{lvhe} = (\chi_1 - \chi_{11}) + (\chi_{x3} - \chi_{x33}) = m((h_1 - T_o s_1) - (h_{11} - T_o s_{11})) + m((h_3 - T_o s_3) - (h_{33} - T_o s_{33}))$ (12)

3.1 Total destruction

$\Phi_{total} = \Phi_e + \Phi_{comp} + \Phi_c + \Phi_{ev} + \Phi_{lvhe}$ (13)

3.2 Second law efficiency

It is defined as the ratio of exergy in product in the work required to drive the system

$$\text{Exergy output} = (Q_1 + Q_2 + Q_3)\left|\left(1 - \frac{T_0}{T_1}\right)\right. \quad (14)$$

$$\eta_{ex} = \frac{Exergy\ Output}{Exergy\ Input} = (Q_1 + Q_2 + Q_3)\left|\right($$

EDR is the ratio of total irreversibility in the system to the exergy product .

$$EDR = \frac{\Phi_{total}}{(Q_1 + Q_2 + Q_3)\left|\left(1 - \frac{T_0}{T_1}\right)\right|} \quad (16)$$

3. RESULTS AND DISCUSSIONS

Using Engineering Equation Solver software [9] a numerical model is developed for tfirst law and second law analysis of the multi evaporators VCR for enhancing thermal performances. The performance parameters are calculated by assuming following specifications: Adiabatic efficiency of compressor(ζ_{comp}):75% Condenser temperature (T_c): 313K. Dead state temperature (T_0): 298K. Variation of evaporators temperature (T_e):223K to273K. Dead state enthalpy (h_0) and entropy (s_0) of the refrigerants have been calculated corresponding to the dead state temperature (T_0) of 298K. Degree of superheating of vapour refrigerant in liquid vapour heat exchanger before compression (ΔT_{sh}): 10K. Effectiveness of the liquid vapour heat exchanger is 100%. Degree of sub cooling of liquid refrigerant in the liquid vapor heat exchanger (ΔT_{sc}): 10K. Loads on the evaporators EP1, EP2 and EP3 are 35KW, 70KW and 105KW respectively.

Fig.2 presents the variation of first law efficiency (coefficient of performance) with the evaporator temperature at 313K condenser temperature. The COP will increase with evaporator temperature this is due to the fact that COP is the ratio of the net refrigeration effect of the work required to drive the compressor, compressor work will go down due to reduction in pressure on the other hand refrigeration effect will also enhance, So COP will increase. It was observed that COP of the system using R134a and R1234ze nearly matching same values.R134a and R1234ze show better COP than R-1234yf.Although R134a having a high global warming potential (GWP) and responsible for global warming. The maximum difference observed between COPs of R134a and R1234yf is (2%-6%).

Effect of increase in evaporator temperature on second law efficiency has shown in Fig. 3. As clear from Fig.3 that exergetic efficiency increase with increase in evaporator temperature but it should be cleared that this increment up to an optimal value of evaporator temperature after that exergetic efficiency goes down with increase in evaporator temperature. R1234ze shows the lowest value of exergetic efficiency among considered refrigerants. The percentage increase in second law efficiency of R1234ze as compared with R1234yf at 243K, 248K, 253K, 258K, 263K, 268K and 273K evaporator temperature are 4.57%, 4.33%, 4.07%, 3.80%, 3.55%, 3.30% and 3.06% respectively. System defect provides the information about of amount of loss of work input (energy) given to the system. As shown in Fig.4 that the highest system defect occurs in R1234yf.it was also observed that system defect in R1234ze only 1% higher than R134a, but with the increase in evaporator temperature this problem is eliminated. The maximum difference in system defect of R1234yf comparison with R134a is 3.7 % at 248K evaporator temperature. Fig.5 shows the effect of degree of sub cooling on COP. It is evident that sub cooling increases refrigeration capacity whereas there is no change in

©-IRJSSE, ALL RIGHT RESERVED

compressor work, hence COP increases. Both R134a and R1234ze presents maximum COP (3.18) by the 10K degree of sub cooling than R1234yf.Thus sub cooling responsible for the betterment for system performance. The effect of subcooling on second law efficiency shown Fig.6 reveals that both R134a and R1234ze shows better exergetic efficiency than R1234yf It is observed from Fig.7 and Fig.8 that trends of COP and exergetic efficiency are almost same for selected refrigerants, both COP and exergetic efficiency will decrease with increase in condenser temperature. Both COP and exergetic efficiency of R134a and R1234ze are 3.7 % and 3.9% at 314K condenser temperature higher than R1234yf.

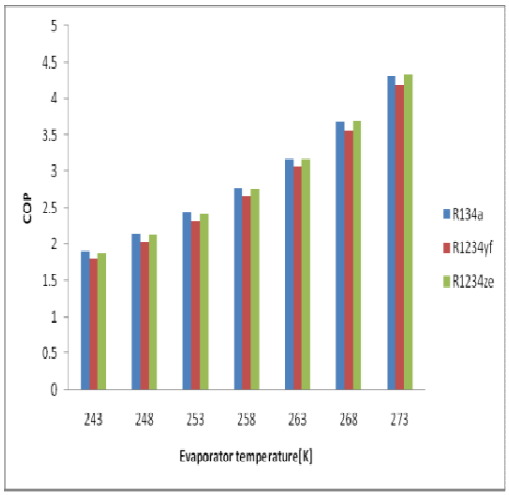


Fig.2- Variation of COP with evaporators' temperatures

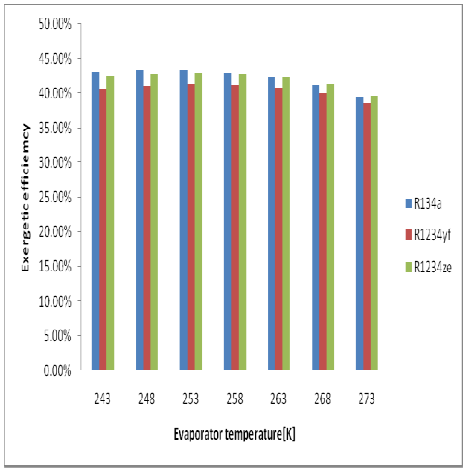


Fig.3- Variation of exergetic efficiency with evaporators' temperatures

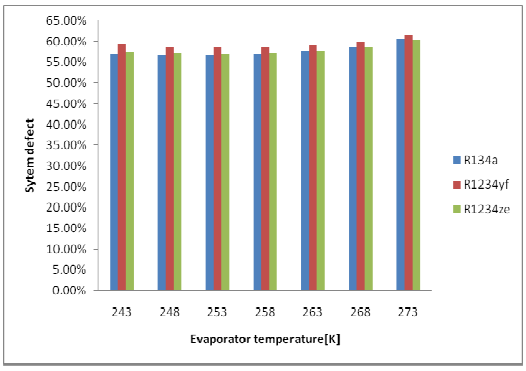
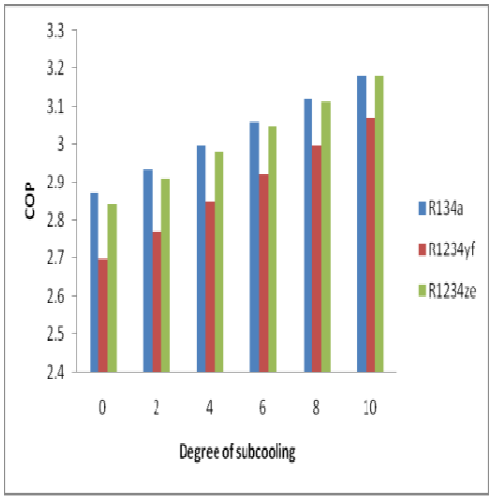


Fig.4- Variation of system defect with evaporator temperatures



©-IRJSSE, ALL RIGHT RESERVED

Fig.5- Variation of COP with degree of subcooling at condenser outlet

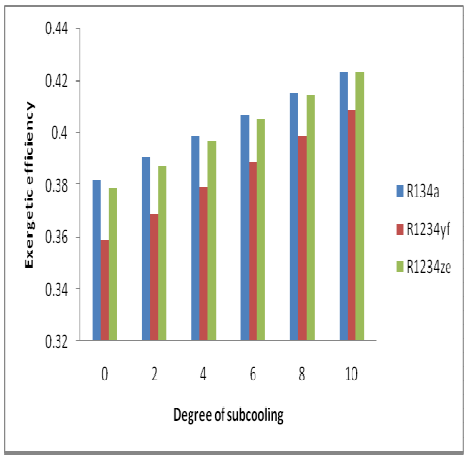


Fig.6- Variation of exergetic efficiency with degree of subcooling at condenser outlet

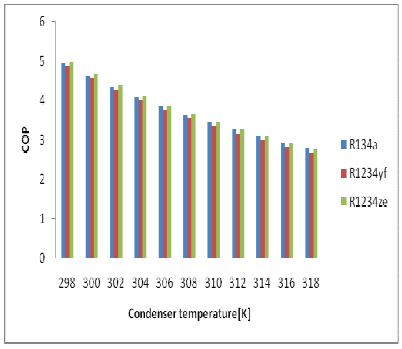


Fig.7- Variation of COP with condenser temperature

CONCLUSIONS:

In this paper, first law and second law analysis of an actual multi-evaporators vapour compression refrigeration system using ecofriendly refrigerants (R134a, R1234yf, and R1234ze) have been presented.

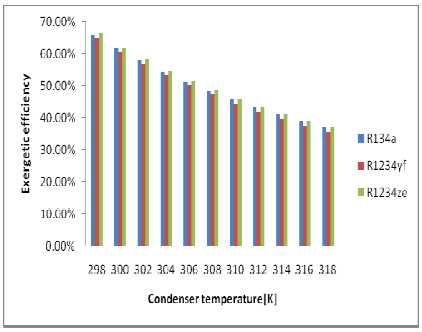


*Fig.8- Variation of exergetic efficiency with condenser temperature*Conclusion

First law and second law efficiency for R134a and R1234ze are matching the same values, both are better than that for R123yf and showing 2–6% higher value of COP and second law efficiency in comparison to R123yf. Both energetic and exergetic efficiency increase with increase in degree of subcooling It was found that energetic and exergetic efficiency greatly affected by changes in evaporator and condenser temperature. R1234ze is the best among considered refrigerant since it has 238 times lower GWP values than R134a and R1234ze is ecofriendly has both ODP and GWP are lowest.

Table-1:Multiple evaporator single compression single expansion valve vapour compression refrigeration system using ecofriendly refrigerants with LVHE

Ecofriendly REFRIGERANT	$COP_{WITH\ LVHE}$	EDR	EXERGETIC EFFICIENCY
R290	3.052	1.462	0.4062
R404A	2.747	1.735	0.3656
R410A	2.931	1.564	0.390
R134A	3.104	1.421	0.4131
R152A	3.227	1.328	0.4295
R600	3.234	1.324	0.4303
R600A	3.122	1.407	0.4155
R407C	2.62	1.868	0.3487
R507A	2.80	1.683	0.3727
R1234YF	2.964	1.535	0.3945
R1234ZE	3.086	1.435	0.4107
R717	3.205	1.345	0.4265
R125	2.628	1.859	0.3497

Table-2:Multiple evaporator single compression single expansion valve vapour compression refrigeration system using ecofriendly refrigerants without LVHE

REFRIGERANT	$COP_{WITHOUT\ LVHE}$	EDR	EXERGETIC EFFICIENCY
R290	2.97	1.53	0.3952
R404A	2.626	1.862	0.3495
R410A	2.858	1.63	0.3803
R134A	3.022	1.486	0.4022
R152A	3.177	1.365	0.4228
R600	3.161	1.377	0.4207
R600A	3.032	1.478	0.4035
R407C	2.541	1.958	0.3381
R507A	2.678	1.806	0.3564

©-IRJSSE, ALL RIGHT RESERVED

R1234YF	2.854	1.633	0.3798
R1234ZE	2.991	1.512	0.3980
R717	3.21	1.341	0.4271
R125	2.473	2.039	0.3291

RESULTS AND DISCUSSIONS and CONCLUSIONS

In this paper, first law and second law analysis of vapour compression refrigeration systems using multiple evaporators and single compressor and single expansion valve with thirteen ecofriendly refrigerants have been presented. The conclusions of the present analysis are summarized below:

1. The First law efficiency (COP) and Second law efficiency (Exergetic efficiency) of vapour compression refrigeration systems using liquid vapour heat exchanger and multiple evaporator and single compressor and single expansion valve is higher than without liquid vapour heat exchanger for above mentioned ecofriendly refrigerants.
2. The First law efficiency (COP) and Second law efficiency (Exergetic efficiency) of vapour compression refrigeration systems using R717 refrigerant is higher but is has toxic nature can be use by using safety measure for industrial applications.
3. COP and exergetic efficiency for R152a and R600 are nearly matching the same values.are better than that for R125 at 313K condenser temperature and showing higher value of COP and exergetic efficiency in comparison to R125.
4. For practical applications R-134a is recommended because it is easily available in the market has second law efficiency slightly lesser than R-152a which was not applicable for commercial applications.
5. The worst component from the viewpoint of irreversibility is expansion valve followed by condenser, compressor and evaporators, respectively. The most efficient component found to be subcooler. The R-152a has least efficiency defects for 313K condenser temperature.
6. The increase in dead state temperature has a positive effect on exergetic efficiency and EDR, i.e. EDR decreases and exergetic efficiency increases with increase in dead state temperature. Both R-152a and R-600 show the identical trends for exergetic efficiency are nearly overlapping. The exergetic efficiency for R-600 is higher than that of R-134a for the practical range of dead state temperature considered.

REFERENCES:

1. Johnson. E. Global warming from HFC. Environ. Impact Asses.1998; 18:485-492.
2. QiyuChen,R.C Prasad. Simulation of a vapour compression refrigeration cycles HFC134A and CFC12.Int Comm.Heat Mass Transfer.1999; 26:513-521.
3. M. Padilla, R. Revellin, J. Bonjour. Exergy analysis of R413A as replacement of R12 in a domestic refrigeration system. Int J Energy Conversion and Management.2010; 51:2195-2201.
4. H.O. Spauschus. HFC 134a as a substitute refrigerant for CFC 12. Int J of Refrigeration. 1988; 11:389-392.
5. J.U. Ahamed, R.Saidur, H.H.Masjuki. A review on exergy analysis of vapor compression refrigeration system. Int J Renewable and sustainable energy reviews.2011; 15:1593-1600.
6. R. Llopis, E. Torrella, R. Cabello, D. Sánchez. Performance evaluation of R404A and R507A refrigerant mixtures in an experimental double-stage of vapour compression plant. Int J Applied Energy.2010; 87:1546-1553.
7. AkhileshArora, S.C. Kaushik. Theoretical analysis of a vapour compression refrigeration system with R502, R404A and R507A. Int J Refrigeration.2008; 31:998-1005.
8. V. Havelsky. Investigation of refrigerating system with R12 refrigerant replacements .Int J Applied Thermal Engineering.2000; 20:133-140.
9. V. Siva Reddy, N.L Panwar, S.C Kaushik-Exergy analysis of a vapour compression refrigeration system with R134a,R143a,R152a,R404A,R407C,R410A,R502 and R507A.Clean Techn Environ Policy.2012;14:47-53.
10. R.Saravanakumar, V.Selladurai-Exergy analysis of a domestic refrigerator using eco-friendly R290/R600a refrigerant mixture as an alternative to R134a.Int J Therm Anal Calorim.2013;
11. C. Nikolaidis, D. Probert-Exergy method analysis of a two-stage vapour-compression refrigeration-plants performance. Int J Applied Thermal Engineering.1998; 60:241-256.
12. S.Kumar, M.Prevost, R.Bugarel- Exergy analysis of a vapour compression refrigeration system. Heat Recovery Systems & CHP.1989;9:151-157.
13. MahmoodMastaniJoybari,MohammadSadeghHata mipour, Amir Rahimi, FatemehGhadiriModarres-Exergy analysis and optimization of R600a as a replacement of R134a in a domestic refrigerator system. International Journal of refrigeration.2013; 36:1233-1242.
14. S.Anand ,S.KTyagi-Exergy analysis and experimental study of a vapour compression refrigeration cycle.Int J Therm Anal Calorim.2012; 110:961-971.
15. J.U Ahamed, R.saidur, H.H Masjuki, M.A Sattar-An analysis of energy, exergy and sustainable development of a vapour compression refrigeration system using hydrocarbon.International journal of Green energy.2012;9:707-717.
16. Camelia Stanciu, Adina Gheorghian, Dorin Stanciu, Alexandru Dobrovicescu- Exergy analysis and refrigerant effect on the operation and performance lomits of a one stage vapour

©-IRJSSE, ALL RIGHT RESERVED

compression refrigeration system.Termotehnica.2011;1:36-42.
17. J.U. Ahamed, R.Saidur, H.H.Masjuki. A review on exergy analysis of vapor compression refrigeration system. Int J Renewable and sustainable energy reviews.2011; 15:1593-1600.
18. B.O. Bolaji, M.A. Akintunde, T.O. Falade. Comparative analysis of performance of three ozone-friends HFC refrigerants in a vapor compression refrigerator. Int J Sustainable Energy & Environment.2011; 2:61-64.
19. RecepYumrutas, Mehmet Kunduz, Mehmet Kanoglu-Exergy analysis of vapor compression refrigeration systems. Exergy, An International Journal.2002; 2:266-272.
20. M. Padilla, R. Revellin, J. Bonjour. Exergy analysis of R413A as replacement of R12 in a domestic refrigeration system. Int J Energy Conversion and Management.2010; 51:2195-2201.
21. H.M Getu, P.K Bansal. Thermodynamic analysis of an R744-R717 cascade refrigeration system. Int J Refrigeration.2008; 31:45-54.
22. Mark W. Spatz, Samuel F. Yana Motta. An evaluation of options for replacing HCFC-22 in medium temperature refrigeration systems. Int J Refrigeration.2004; 27:475-483.
23. M. Mohanraj, S. Jayaraj, C. Muraleedharan, P. Chandrasekar.Experimental investigation of R290/R600a mixture as an alternative to R134a in a domestic refrigerator. Int J Thermal Sciences.2009; 48:1036-1042.
24. X.H. Han, Q. Wang, Z.W. Zhu, G.M. Chen. Cycle performance study on R32/R125/R161 as an alternative refrigerant to R407C. Int J Applied Thermal Engineering.2007; 27:2559-2565.
25. E. Halimic, D. Ross, B. Agnew, A. Anderson, I. Potts. A comparison of the operating performance of alternative refrigerants. Int J Applied Thermal Engineering.2003; 23:1441-1451.
26. Yongmei Xuan, Guangming Chen. Experimental study on HFC-161 mixture as an alternative refrigerant to R502. Int J Refrigeration. Article in Press.
27. R. Cabello, J. Navarro-Esbrı, R. Llopis, E. Torrella. Analysis of the variation mechanism in the main energetic parameters in a single-stage vapour compression plant. Int J Applied Thermal Engineering.2007; 27:167-176.
28. R.Cabello a, E.Torrella b, J.Navarro-
29. Esbr. Experimental evaluation of a
30. vapour compression plant performance using R134a, R407C and R22 as working fluids. Int J Applied Thermal Engineering.2004; 24:1905-1917.
31. Klein, S.A., AlvaradoF. Engineering Equation Solver, Version 7.441. F Chart Software, Middleton, WI.2005.
32. Dincer.I. Refrigeration Systems and Applications. Wiley, UK.2003:26.

©-IRJSSE, ALL RIGHT RESERVED

©-IRJSSE, ALL RIGHT RESERVED

Volume 1 (2014) 65-71 ISSN 2347 - 3258
International Journal of Advance Research and Innovation

Linde and Claude System Second Law Comparison for Liquefaction of Air

Devender Kumar *, R.S Mishra
Department Of Mechanical Engineering, Delhi Technological University, Shahabad, Delhi, India

Article Info

Article history:
Received 2 January 2014
Received in revised form
29 January 2014
Accepted 20 February 2014
Available online 15 March 2014

Keywords

Second law efficiency,
Energy,
Liquefaction mass

Abstract

The study deal with the anComparative analysis of two cryogenics system Linde Hampson and Claude. Thesecond law efficiency and the output which in form of liquefaction mass air are compared and through comparison result of systems it conclude that by joining extra accessories in system make a system efficient in output result but in other hand making system large , its cost and as well as useful energy destruction of overall system are degraded which seen in from of low second law efficiency. Two system giving same atmospherics input condition and varying compressor pressure considered. Final results show the output of Claude system is more than the Linde while seconde efficiency of ofLinde is 18 % more than the Claude at 300 bar compressor pressure.

Nomenclature

W=work
Q=Heat input
η_I=First law efficiency
η_{II}=Second law efficiency
h=Enthalpy
s=Entropy
X=Dryness fraction
T=temperature
P=Pressure
m=mass
Ɛ =Effectiveness of heat exchanger (approx. 80%)
η_{comp}=Efficiency of compressor (approx. 80%)
$\eta_{expander}$=Efficiency of expander (approx. 80%)
C=Specific heat capacity fluid or gas
W_t=Work of reversible isothermal compression
W_{comp}=Shaft work supplied to compressor per unit mass

1. Introduction

Cryogenics is a field of acquiring very low temperature, the temperature which sufficient to liquefy most of gaes but generally the temperature below -150 ^{0}C is considered in range of cryogenics. In early centuries the throttling effect of cooling and various expansion device attract the scientist toward achieving low temperature but oxygen use in medical science and it storage factor turn 18 centuries scientist to attain low temperature which can liquefy air and in turn harness the oxygen from that liquefaction. In end of 18 centuries various research are done cryogenics field but first scientist which got success is Linde and after that lots of scientist liquefy various gas on their scale. Various systems of cryogenics come in light in which Linde and Claude is widely used as system for liquefaction of air.

The system is made but how much they are efficient in industrial point of view is become matter of concern. Variousmethod are employs to minimize the cost without affecting the production rate are investigated in various mathematical techniques and simulation technique is widely used. In all this a best method second law exergy analysis of system which is based on the second law of newton of energy destruction.

Exergy analysis is basically defined as the how much part of energy we can fully utilize in our work. Useful part of energy is called exergy while unused part is anergy.First law efficiency simply defined as the ratio of output to the input of energy while Second law efficiency deal with the exergy and defined as the ration of exergy output to the exergy input.

Corresponding Author,
E-mail address: devenderdahiya@in.com
All rights reserved: http://www.ijari.org

$$\eta_I = \frac{Output\ enegy(W)}{Input\ energy(Q)}$$

$$\eta_{II} = \frac{Exergy\ output}{Exergy\ Input}$$

Lots of research are done to optimize and to increase the second law efficiency of system. And for this lots of new techniques are experimentally studied. Yang et al. [1] performed a comparative study on the trans critical carbon dioxide refrigeration cycles with a throttling valve and with an expander, based on the first and second laws of thermodynamics. Ignacio L´opezPaniagua [2] find New Simple Method for Estimating Exergy Destruction in Heat Exchangers. Yongliang Li [3] study An optimal design methodology for large-scale gas liquefaction. Antungalovic [4] do detail Analysis of Exergy Destruction of an

Evaporator or/and a Condenser. The main cause of low Second law efficiency directly link to the irreversibility of system so for which is just a form of exergy losses in any system. Irreversibility is the reason why the exergy received by the cold fluid and that released by the hot fluid are not equal. In fact, the total exergy loss in an exchanger is another characteristic of its exergetic behavior commonly referred to in the literature [5,6].and only part of the exergy loss can be avoided in practice [7]

2. Thermal analysis of Linde system

Linde system is first system which is use for liquefaction of air. In Fig 1(a).This system consist a compressor, heat exchanger, throttle valve and a separator. The air or gas which is used to liquefy is circulate in this closed cycle with perfect insulation to avoid large losses to occur due to system and outer surrounding temperature difference.Fig 1(b)show the temperature entropy diagram for Linde system.

$$\eta_{comp} = \frac{W_t}{W_{comp}} \quad (1)$$

$$W_t = mRT ln \frac{P_2}{P_1} \quad (2)$$

$$W_{comp} = h_2 - h_1 - T_1 (s_2 - s_1) \quad (3)$$

$$W_{reversible} = W_{actual} - T_0 s_{gen} \quad (4)$$

$$W_{actual} = \frac{W_{comp}}{x} \quad (5)$$

$$W_{reversible} = h_5 - h_1 - T_0 (s_5 - s_1) \quad (6)$$

Heat Exchanger

$$m_2(h_2 - h_3) = m_6(h_1 - h_6) \quad (7)$$

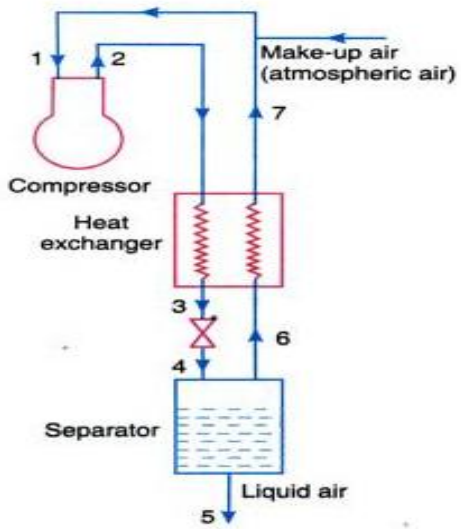


Fig: 1(a). Linde system for Liquefaction for gases

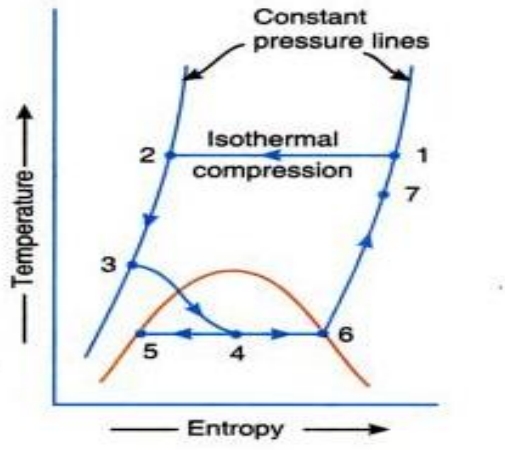


Fig: 1 (b). Tempertaure vs entropy of Linde system

$$m_2(h_2 - h_3) = (m_2 - m_5)(h_1 - h_6) \quad (8)$$

$$: m_6 = (m_2 - m_5) \quad (9)$$

$$\mathcal{E} = \frac{C_h (T_2 - T_3)}{C_{min} (T_2 - T_6)} \quad (10)$$

Throttling process:

$$h_3 = h_4 \quad (11)$$

Heat Balance of the separator

$$m_2h_4 = m_5h_5 + m_6h_6 = m_5h_5 + (m_2 - m_5)(h_6) \quad (12)$$

Second law analysis :

$$\eta_{II} = \frac{W_{rev}}{W_{actual}} \quad (13)$$

COP (coefficient of performance):

$$COP = \frac{h_2 - h_1}{h_2 - h_1 - T_1\,(s_2 - s_1)} \quad (14)$$

3. Thermal analysis of Claude system

Claude system not only used for liquefaction of air but other gas also can be liquefy with this system also .Fig 2(a) show a block diagram of Claude system having two heat exchanger ,two separator and two throttle valve with an expander. Fig 2 (b) shows temperature entropy diagram.

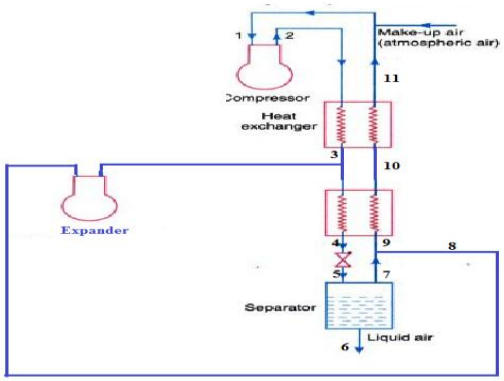


Fig: 2(a). Claude system for Liquefaction for gases

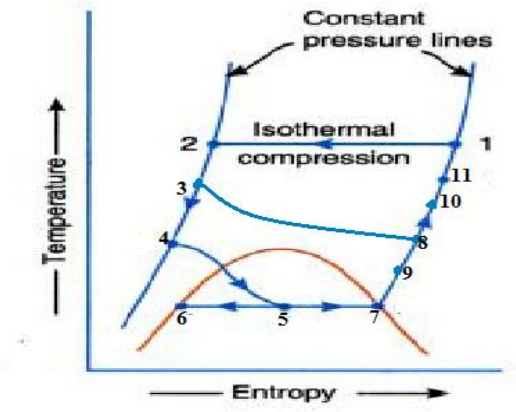


Fig: 2(b). Temperature vs entropy of Claude system

$$\eta_{comp} = \frac{W_t}{W_{comp}} \quad (15)$$

$$W_t = mRT\ln\frac{P_2}{P_1} \quad (16)$$

$$W_{comp} = h_2 - h_1 - T_1\,(s_2 - s_1) \quad (17)$$

$$W_{reversible} = W_{actual} - T_0 S_{gen} \quad (18)$$

$$W_{Total} = W_{comp} + W_{Expander} \quad (19)$$

First heat exchanger:

$$m_2(h_2 - h_3) = (m_2 - m_6)(h_1 - h_{10}) \quad (20)$$

Expander:

$$\frac{T_8}{T_8} = \left(\frac{P_8}{P_8}\right)^{\left(\frac{Y-1}{Y}\right)\eta_{expander}} \quad (21)$$

$$W_{Expander} = h_8 - h_3 \quad (22)$$

$$(m_4 - m_6 + m_8)h_9 = m_8h_8 + (m_4 - m_6)(h_7) \quad (23)$$

Second Heat exchanger:

$$m_4(h_3 - h_4) = (m_2 - m_6)(h_{10} - h_9) \quad (24)$$

Throttle valve:

$$h_4 = h_5 \quad (25)$$

Heat Balance of the separator

$$m_4h_5 = m_6h_6 + (m_4 - m_6)(h_7) \quad (26)$$

Second law analysis:

$$\eta_{II}(\%) = m_6\left(\frac{h_7 - h_6 - T_0(s_7 - s_6)}{W_c}\right)_{*100} \quad (27)$$

COP (coefficient of performance):

$$COP = \frac{h_1 - h_7}{h_2 - h_1 - T_1\,(s_2 - s_1)} \quad (28)$$

Table: 1.

Linde System (Air)			
COP	**η_2nd law (%)**	**m_Liq mass**	**P (Comp Pre)**
0.5612	8.891	0.04751	100
0.487	12.64	0.0778	200
0.4501	13.58	0.09048	300
0.4253	12.92	0.0911	400
0.4063	11.43	0.08433	500

Table: 2.

ClaudeSystem (Air)			
COP	η_2nd law (%)	m_Liq mass	P (Comp Pre)
0.5568	7.271	0.05007	100
0.4836	10.35	0.08203	200
0.4471	11.12	0.09533	300
0.4225	10.58	0.09603	400
0.4036	9.383	0.08913	500

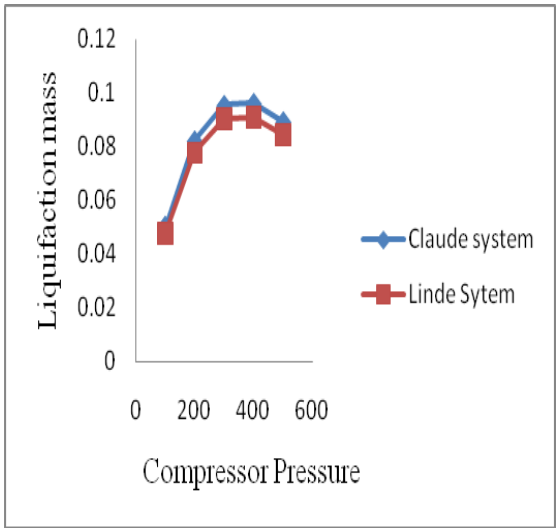


Fig: 2.5Liq mass vs compressor pressure

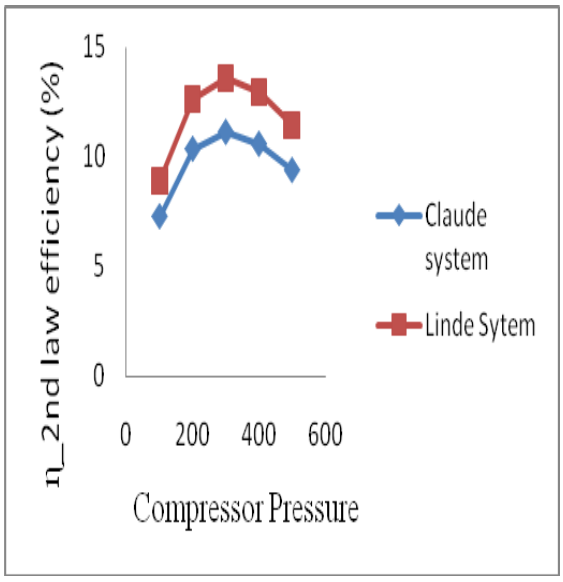


Fig: 2.6. Second law efficiency (%) vs compressor pressure

Table: 3.

Claude System (N)			
COP	η_2nd law (%)	m_Liq mass	P (Comp Pre)
0.5679	6.818	0.04781	100
0.4921	9.851	0.07971	200
0.4543	10.87	0.09531	300
0.4287	10.67	0.09914	400
0.4091	9.795	0.09534	500

Table: 4.

Linde System (N)			
COP	η_2nd law (%)	m_Liq mass	P (Comp Pre)
0.5721	8.521	0.04539	100
0.4954	12.3	0.07564	200
0.4571	13.57	0.09048	300
0.4314	13.32	0.09408	400
0.4116	12.2	0.0903	500

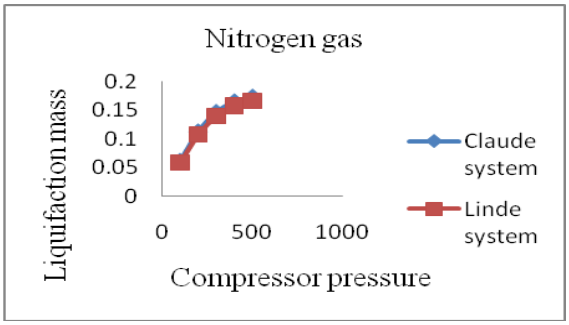


Fig:-

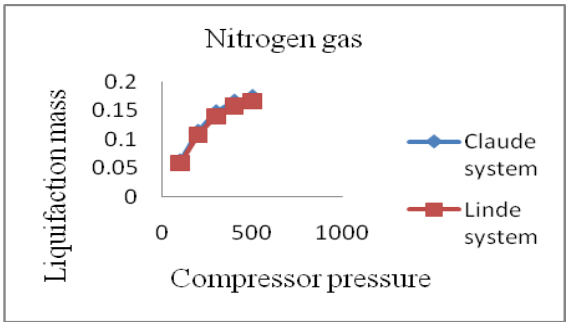


Fig:-

Table: 5.

Claude System (CH4)			
COP	**η_2nd law (%)**	**m_Liq mass**	**P (Comp Pre)**
0.5765	14.78	0.1164	100
0.5114	23.56	0.2091	200
0.4784	26.27	0.2492	300
0.4547	26.21	0.2615	400
0.4355	25.11	0.2617	500

Table: 6.

Linde System (CH4)			
COP	**η_2nd law (%)**	**m_Liq mass**	**P (Comp Pre)**
0.5829	17.43	0.1105	100
0.5161	27.8	0.1991	200
0.4825	31.24	0.2392	300
0.4585	31.31	0.2523	400
0.4392	30.08	0.2531	500

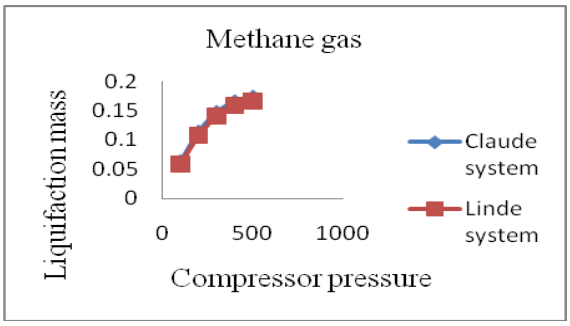


Fig:-

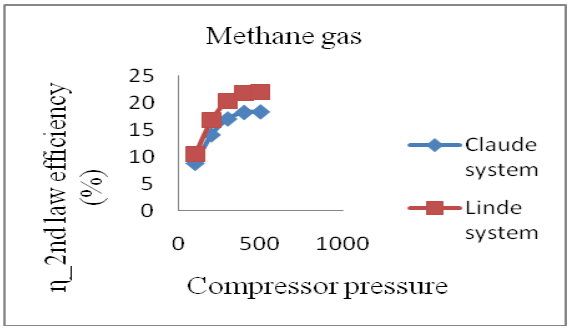
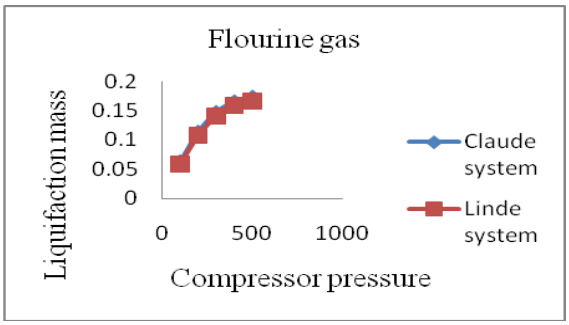


Fig:-

Table: 7.

ClaudeSystem (F)			
COP	η_2nd law(%)	m_Liq mass	P (Comp Pre)
0.5608	6.713	0.04466	100
0.489	10.57	0.08062	200
0.4541	13.01	0.1069	300
0.4311	14.22	0.123	400
0.4137	14.6	0.1316	500

Table: 8.



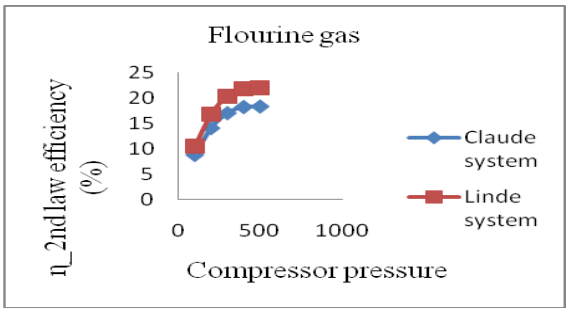


Fig:-

Table: 9.

Claude System (Ar)			
COP	**η_2nd law (%)**	**m_Liq mass**	**P (Comp Pre)**
0.3923	9.83	0.06649	100
0.343	15.62	0.1209	200
0.3191	18.82	0.1565	300
0.3032	20.07	0.1757	400
0.291	20.12	0.1835	500

Table: 10.

Linde System (Ar)			
COP	**η_2nd law (%)**	**m_Liq mass**	**P (Comp Pre)**
0.3955	11.1	0.06352	100
0.3454	17.61	0.1154	200
0.3212	21.24	0.1497	300
0.3051	22.7	0.1684	400
0.2928	22.79	0.1761	500

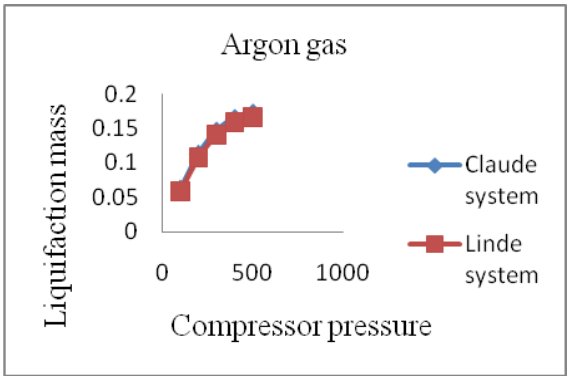


Fig:-

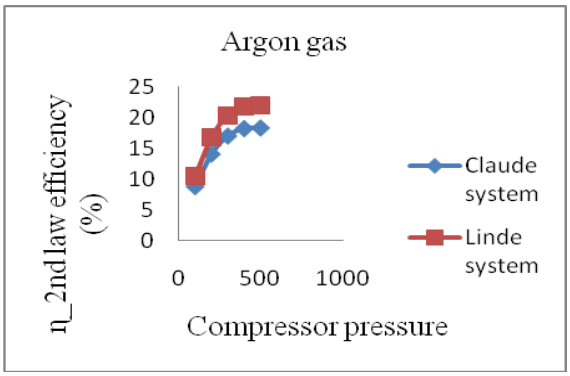


Table: 11.

Claude System (O2)			
COP	**η_2nd law (%)**	**m_Liq mass**	**P (Comp Pre)**
0.5395	8.732	0.06136	100
0.4719	14.01	0.1125	200
0.4392	16.97	0.1465	300
0.4174	18.17	0.165	400
0.4007	18.28	0.173	500

Table: 11.

Linde System (O2)			
COP	**η_2nd law (%)**	**m_Liq mass**	**P (Comp Pre)**
0.5441	10.47	0.05851	100
0.4755	16.77	0.1072	200
0.4422	20.34	0.1399	300
0.4202	21.83	0.158	400
0.4033	22.01	0.1659	500

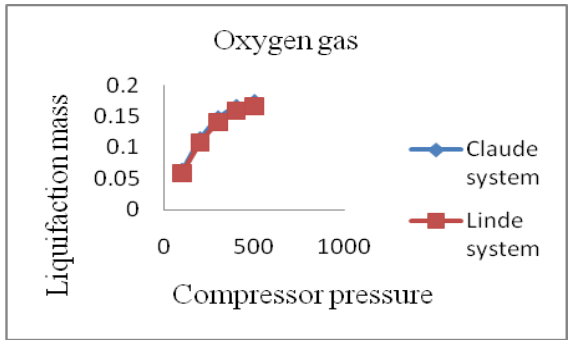


Fig:-

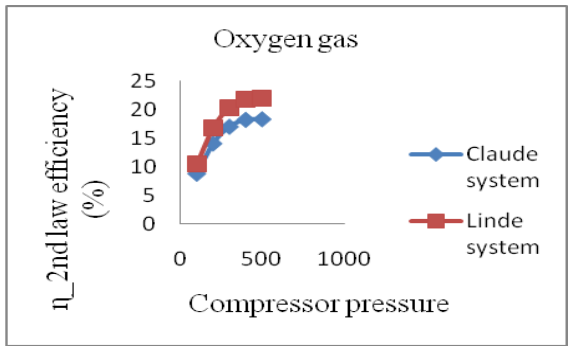


Fig:-

4. Results and discussion

For the analysis and comparison between two system Linde and Claude for liquefaction of air the inlet condition for both system is kept constant and compressor pressure are vary Computational numerical technique is used to get the following results.

1. In fig 5 the liquefaction mass of air is higher in Claude as compared to linde system ,so output of claude is more than the linde.The compressor pressure is not directly proportional to

liquefaction mass ,liquefaction mass is higher in range of 300 to 400 bar compressor pressure ,further increase in pressure degrade the quantity of liquefaction mass in both system

2. In fig 6 show that the second law efficiency of Linde system is more than the claude system and compressor pressure in range of 300 to 330 bar show highest efficiency for both system.

5. Conclusion

1. Linde system having less energy losses than claude system showing higher second law efficiency than claude system.
2. Output wise the claude system is better than linde system.
3. Compressor pressure range 300 to 350 show good result in both system at constant slandered atmospherics inlet conditions

References

[1] J. L. Yang, Y.T. Ma, M.X. Li, H.Q. Guan, "Exergy analysis of transcritical carbon dioxide refrigeration cycle with an expander", Energy 30 (2005) ISSN 1162-1175.

[2] Ignacio Lopez Paniagua, Javier Rodrıguez Mart´ın, Celina Gonzalez Fernandez, Angel Jimenez Alvaro and Rafael Nieto Carlier, "A new simple method for estimating exergy destruction in heat exchangers", Entropy (2013), 15, 474-489; ISSN 1099-4300

[3] YongliangLi, Xiang Wang, Yulong Ding, "An optimal design methodology for large-scale gas liquefaction", Applied Energy 99 (2012) 484–490, ISSN 0306-2619

[4] Antungalovic, Marijazivicand Matokokanovic, "Analysis of exergy destruction of an evaporator or/and a condenser", Strojarstvo 51 (1) 73-78 (2009), ISSN 0562-1887

[5] A. Franco, A. Russo, "Combined cycle plant efficiency increase based on the optimization of the heat recovery steam generator operating parameters", Int. J. Therm. Sci. 41 (2002), 843–859

[6] R. Saidur, J. Ahamed, H. Masjuki, "Energy, exergy and economic analysis of industrial boilers", Energy Policy 38 (2010), ISSN 2188–219

[7] T. J. Kotas, "The Exergy Method of Thermal Plant Analysis", 1995 Ed.; Krieger Publishing Company: London, UK, 1985

2014 International Conference on Signal Processing and Integrated Networks (SPIN)

Low Power D-latch design using MCML Tri-state Buffers

Radhika, Neeta Pandey, Kirti Gupta
Electronics and Communication Department
Delhi Technological University
New Delhi, India
radhikatanwar90@gmail.com, n66pandey@rediffmail.com,
kirtigupta_22@yahoo.com

Maneesha Gupta
Electronics and Communication Department
NSIT, Delhi University
New Delhi, India
maneeshapub@gmail.com

***Abstract*—This paper presents a low power D-latch designed using two low power tri-state MCML buffers. The proposed D-latch consumes less power as it makes use of low power tri-state buffers which promotes power saving due to reduction in the overall current flow in the circuit during the high impedance state. The proposed low power D-latch is simulated in PSPICE using 0.18µm TSMC CMOS technology parameters. The power consumption of the proposed D-latch is compared with the D-latch designed using switched based MCML tri-state buffers which indicate that the proposed low power D-latch is power efficient. The simulation result also proves that the low power D-latch consumes 50% less efficient than the other D-latch.**

Keywords—MCML, Tri-state Inverter, D-latch, Low Power

I. INTRODUCTION

In recent years, the growing demand for portable electronic devices require low power building blocks that enable long lasting battery life of the system [1]. This has lead to the development of low power digital circuits. D-latch is the basic circuit used for implementing many fundamental blocks whose performance strongly depends on the D-latch gate performance. D-latch acts as an integral part of various practical applications such as pre-scalars, frequency dividers, and sequential logic circuits [2-4].

MOS current mode logic (MCML) has emerged as a promising technology due to its various advantages over other logic styles [5]. At high frequency power dissipation in MCML circuits is significantly less as power dissipation in MCML is independent of its operation frequency. MCML style generates low switching noise as current supplied during switching is constant. They offer high performance due to low voltage swing, high noise margin and high switching speed [5-8]. Therefore, MCML style is appropriate for designing high performance digital circuits.

The paper first presents a brief introduction to MCML style in section II. Thereafter, Section III covers the review of MCML tri-state buffers. The D-latch design is presented in section IV and the proposed Low power D-latch design is also discussed. The proposed circuit is implemented, simulated and the results are discussed in section IV. All the simulations are performed in PSPICE using TSMC 180 nm CMOS technology parameters. Finally, the conclusions are drawn in section V.

II. MCML CIRCUITS

A MCML circuit consists of three main components which includes a pull-down network (PDN), a constant current source, and a load circuit [7]. The basic MCML block is shown in Fig. 1. Its PDN consists of source coupled NMOS transistor pairs. The constant current source generates the bias current I_{bias} while the load resistance R_L determines the output voltage swing [8].

The circuit works on the principle of current steering. MCML is completely differential logic i.e. all signals with their compliments is required [3]. Depending on the logic implemented by PDN, the current is steered through one of the two branches, providing complimentary output signals. When the voltage at input A of one transistor is low, the bias current I_{bias} is steered to the other transistor. The voltage at the output of the branch with no current reaches high ($V_{OH} = V_{OUT} - V_{OUT} = V_R$), conversely, for the other branch some voltage drops across load resistor and the output voltage in that branch become low ($V_{OL} = V_{OUT} - V_{OUT} = -V_R$). A basic MCML inverter/buffer circuit is shown in Fig.2.

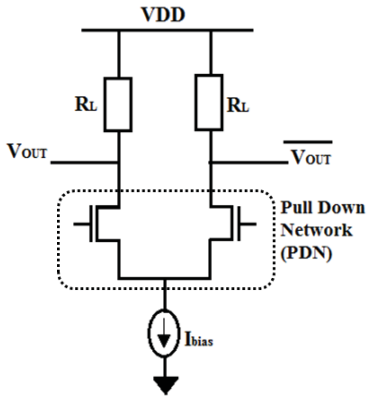


Fig. 1 Basic MCML Block

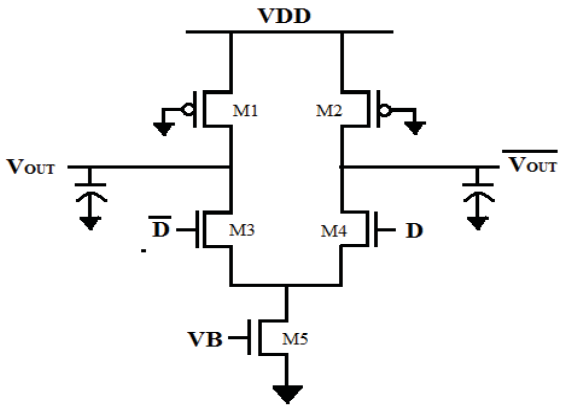


Fig. 2 the MCML Inverter

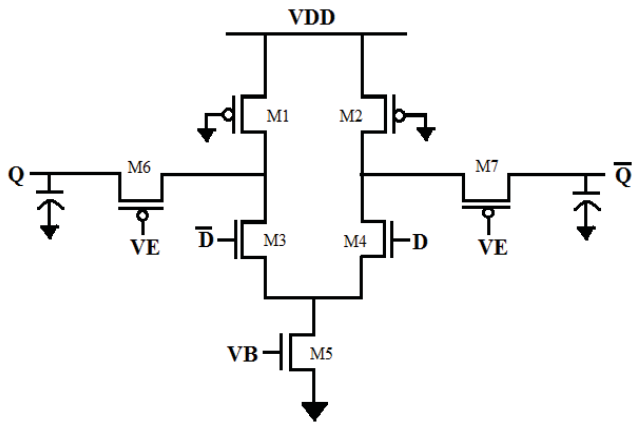


Fig. 3 Switched based MCML tri-state buffer

The load resistor can be modeled by PMOS transistors in triode region [8]. The PMOS load transistors (M1, M2) with grounded gate are always on transistors and are used as the load resistors in the MCML circuit. This offers static power dissipation in the circuit. The biasing current source I_{bias} can be modeled using NMOS transistor in saturation region. The voltage VB is used to bias the NMOS transistor (M5) to get the required biasing current. The differential input is applied to the NMOS transistor M3-M4 and depending upon the input logic applied complimentary outputs is available.

III. MCML TRI-STATE BUFFERS

A tri-state circuit has an extra terminal where enable is connected. It behaves as a normal gate when enabled and it goes in high impedance state when disabled [9]. In literature, two MCML tri-state inverters have been proposed which are shown in the following section.

A. Switched based MCML tri-state buffer

The MCML tri-state buffer that is shown in Fig.3 uses switch to incorporate enable circuitry. The switch based tri-state buffer (Fig. 2) consists of a MCML buffer (M1–M5) and two PMOS transistors (M6–M7) acting as switches [10]. The PMOS transistors are switched by the enable voltage VE that is applied at their gate terminal to switch the transistors ON and OFF. When VE signal is low, the buffer acts as normal gate. Conversely, when VE signal is high, the buffer enters the high-impedance state. During high impedance state, the transistors (M6-M7) are OFF but at the same time the transistors M1-M2 are ON. This leads to power dissipation in the circuit as all the current sources remain ON even in the high-impedance state.

B. Low Power MCML tri-state buffer

The low-power MCML tri-state buffer is shown in Fig. 4. This circuit makes use of modified MCML buffer (M1–M7) [11]. The enable signal is applied to the PMOS transistor that is acting as load resistor which efficiently turns ON/OFF the transistors (M1–M2, M5-M7) in the modified MCML buffer. The enable signal VE switches ON the load transistors (M1-M2) of the modified buffer and also controls the operation of current source (M5) via transistors M6 and M7. For low VE signal, the transistors M1 and M2 are turned ON and they act as load to the MCML buffer. At the same time, the transistor M7 charges the gate terminal of transistor M5 to the potential VBIAS as the transistor M6 is OFF. Therefore, the transistor M5 acts as a current source and provides the bias current Ibias to the MCML buffer. Thus, for low value of VE signal the circuit behaves as a normal MCML buffer. For high value of signal VE, the transistor M1, M2 and M7 are turned OFF whereas the transistors M6 conducts and pulls the gate terminal of transistor M5 to the ground potential.

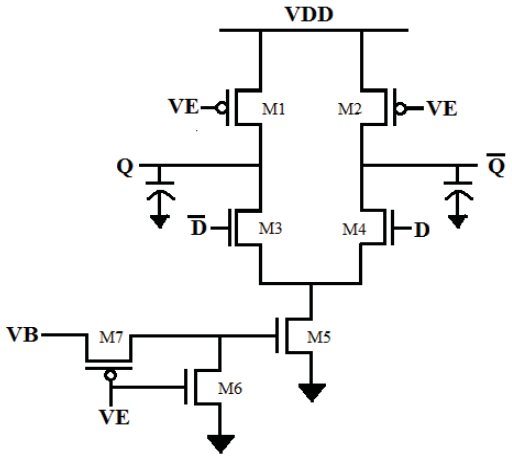


Fig. 4 Low Power MCML tri-state buffer

Thus, the output node is disconnected from the power supply VDD as well as ground leading to high-impedance at the output of the buffer. This circuit offers reduced power consumption as the circuit is deprived of current source in high impedance state. Therefore, the buffer can be utilized for low power circuit design.

IV. D-LATCH DESIGN

The D-latch design using tri-state inverters is given in [9]. The D-latch in [9] makes use of one inverter and two tri-state inverters shown in Fig.5 is based on CMOS. The clock signal is used to enable and disable the two inverters (I1 and I3) alternately so that one inverter is in normal mode and the other in high impedance mode or visa-versa. When clock signal is high then the input data is transferred to the output and when it is low the output state is preserved by the loop created by the two back to back inverters.

The proposed D-latch design using MCML based tri-state buffers require two buffers as MCML is differential logic and has both inverted and non-inverted outputs simultaneously. The D-latch design for MCML based buffers is shown in Fig.6. The clock signal is fed to the enable port of the two buffers operating alternately. When the clock signal is high, the buffer B1 is in normal state and the latch is transparent, thus the input is obtained at the output. The buffer B2 enters high impedance state and the loop breaks.

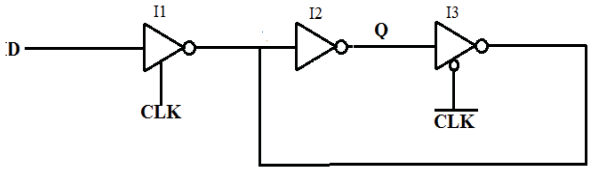


Fig. 5 D-latch design

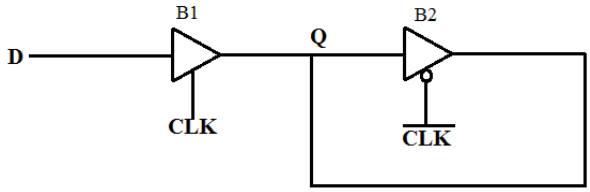


Fig.6 D-latch design using two tri-state MCML buffers

When the clock signal is low, the buffer B1 is in high impedance mode and thus there is no direct path between input and output. The buffer B2 is activated, thus completing the loop and the last output state is preserved till the next clock transition.

V. SIMULATION RESULTS

The low power D-Latch is simulated in PSPICE using CMOS TSMC 180 nm technology parameters with a voltage swing of 400 mV. The input parameters taken in the simulation of the circuits are shown in Table I.

TABLE I. SIMULATION ENVIRONMENT

Technology	180 nm
Temperature	27 ºC
Supply Voltage	1.8V
Output Load Capacitor	10 fF
Bias Current	50 µA
Input Data Frequency	166 MHz
Clock Frequency	500 MHz

The clock and data inputs that are fed to the circuit are shown in the Fig.7(a) and 7(b). The output waveforms of the proposed low power MCML D-latch is shown in Fig. 7(c). The above waveforms confirm to the functionality.

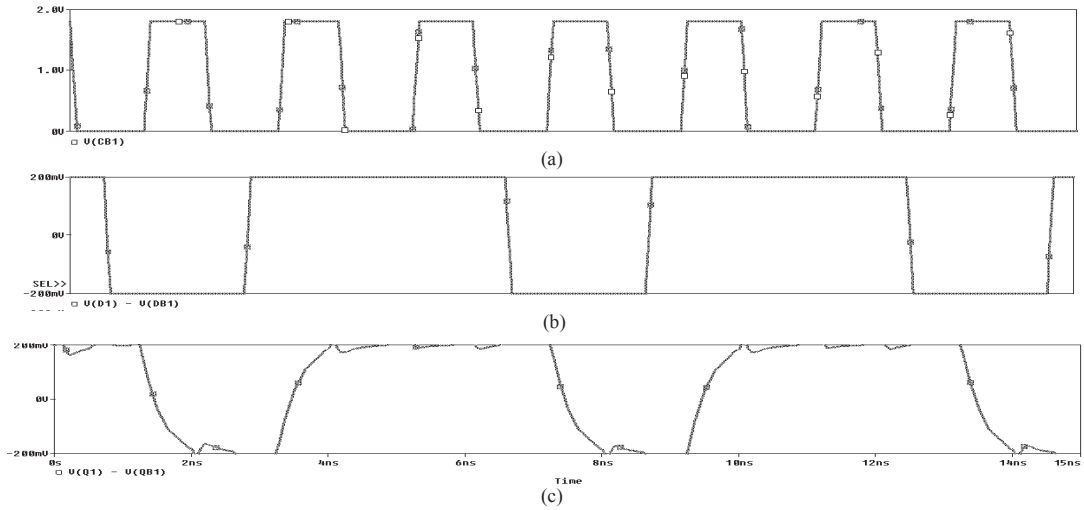


Fig. 7(a) Input Clock (b) Input Data (c) Output of the proposed D-latch

The performance of the proposed Low power MCML D-latch designed using low power MCML tri-state inverters is compared with MCML D-latch designed using switched based MCML tri-state inverters to verify the reduction in power dissipation with the use of the proposed circuit. The power comparison of both circuits is stated in Table II. Also, the delays associated with the Latches for high to low clock transition (H->L) and low to high clock transition (L->H) are also stated in Table III and Table IV.

TABLE II. POWER DISSIPATION (μW) OF LATCHES

Latch	Power
MCML D_Latch	200
Low Power MCML D-latch	100

.

TABLE III. DELAY (PS) OF MCML D- LATCH

	H->L	L->H
clk -> Q	275.8	271.6
D -> Q	306.8	302.9

TABLE IV. DELAY (PS) OF LOW POWER D-LATCH

	H->L	L->H
clk -> Q	305.1	320.1
D -> Q	201.6	206.7

VI. CONCLUSION

In this paper a Low power D-latch which uses two tri-state MCML buffers is presented. The proposed low power D-latch has been implemented and its performance is compared with D-latch designed using switched based tri-state MCML buffers. It is found that the proposed low power D-latch reduces the power consumption by 50%. It is also observed that the input data to stable output data (D->Q) delay of the low power D-latch is 34.28% and 31.76% less for high to low and low to high clock transition respectively as compared to the D-latch designed using switched based tri-state MCML buffers. An increment in clock edge transition to stable output data (C->Q) delay by 10.62% and 17.85% for high to low and low to high clock transition respectively is seen in the proposed latch in comparison to the other latch. The Proposed D-latch is suitable for portable devices where power is the major concern. MCML based circuitry makes the latch immune to noise and suitable for mixed signal environment.

REFERENCES

[1] J. M. Musicer, J. Rabaey, MOS Current Mode Logic for Low Power, Low Noise, CORDIC Computation in Mixed-Signal Environments, Proc. ISLPED, pp.102-107, July 2000.

[2] Vladimir Stojanovic, and Vojin G. Oklobdzija, "Comparative Analysis of Master-Slave Latches and Flip-Flops for High-Performance and Low-Power Systems," IEEE Journal of Solid State Circuits, Vol. 34, No. 4, April 1999.

[3] Muhammad Usama, Tad Kwasniewski, " Design and comparision of CMOS current mode logic latches", IEEE proceedings in International Symposium on Circuit and System, 2004.

[4] K. Gupta, N. Pandey, M. Gupta, "MCML D-Latch Using Triple-Tail Cells: Analysis and Design," Hindawi Publishing Corporation, Active and Passive Electronic Components, Volume 2013.

[5] T. K. Agarwal, A. Sawhney, A. K. Kureshi,M. Hasan, Performance Comparison of Static CMOS and MCML gates in sub- threshold region of operation for 32nm CMOS Technology, Proceedings of the International Conference on Computer and Communication Engineering, Malaysia pp. 284-287, 2008.

[6] M. Yamashina and H. Yamada, An MOS current mode logic (MCML) circuit for low-power sub-GHz processors, IEICE Trans. Electron., vol.E75-C, pp. 1181–1187, Oct. 1992.

[7] M. Mizuno, M. Yamashina, K. Furuta, H. Igura, H. Abiko, K. Okabe, A. Ono, H. Yamada, A GHz MOS, Adaptive Pipeline Technique using MOS Current-Mode Logic, IEEE J. Solid-state Circuits, Vol. 31, pp. 784-791, No. 6, June 1996.

[8] M. Alioto and G. Palumbo, Model and Design of Bipolar and MOS Current-Mode logic (CML, ECL and SCL Digital Circuits), Springer, New York,2005.

[9] Sung-Mo Kang, Yusuf Leblebici, "Cmos Digital Integrated Circuits," Tata McGraw-Hill Education, 2003.

[10] 10. Badel, S., & Leblebici, Y. (2007). Tri-state buffer/bus driver circuits in MOS current-mode logic. In Proceedings of Research in Microelectronics and Electronics Conference (pp. 237–240).

[11] Kirti Gupta, Neeta Pandey , Maneesha Gupta, "Low-power tri-state buffer in MOS current mode logic", An international journal on Analog Integrated Circuits and Signal Processing, volume-74, number-1, January 2013.

Volume 1 (2014) 50-64 ISSN 2347 - 3258
International Journal of Advance Research and Innovation

Methods for Improving First and Second Law Efficiencies of Vapour Compression Refrigeration Systems Using Flash-Intercooler with Ecofriendly Refrigerants

Kapil Chopra *, V. Sahni, R. S. Mishra
Department Of Mechanical Engineering, Delhi Technological University, New Delhi, India

Article Info

Article history:
Received 2 January 2014
Received in revised form
29 January 2014
Accepted 20 February 2014
Available online 15 March 2014

Keywords

Abstract

In the present thermodynamic analysis, the comparison and impact of environmental friendly refrigerants(R410a, R290, R600, R600a, R1234yf, R125, R717 and R134A)on multiple stage vapour compression refrigerator with flash intercooler and individual throttle valves (system-1) and multiple stage vapour compression refrigerator with flash intercooler and multiple throttle valves (system-2) has been carried out on the basis of energetic and exergetic approach. It wasobserved that for all selected ecofriendly refrigerants, energy and exergy efficiency of system-1is lower than sytem-2.For both systems R125 showed poorperformance in terms of energetic efficiency, second law efficiency and irreversibility whereas thermodynamic performances of hydrocarbon isobutene (i.e. R600) and R717 gives better performance in comparison of other selected ecofriendly refrigerants. AsR717 is toxic in nature and restricted to limited applications, and also R600 is flammable in nature, therefore R-134a is suggested better for practical applications for both systemswithout taking of any safety precautions. Although thermodynamic performance of R134a is only 2-3% lesser than R600 and R134A is easily available in the market

1. Introduction

Nowadays most of the energy utilize in cooling and air conditioning in industrial as well as for domestic applications, in addition to energy consumption, using of refrigerants in cooling and air conditioning having high GWP and ODP which are responsible for increasing global warming and ozone depletion. The primary requirements of ideal refrigerants are having good physical and chemical properties. Due to good physical and chemical properties such as non-corrosiveness, non-toxicity, non- flammability, low boiling point, Chlorofluorocarbons (CFCs) have been used over the last many decades, but hydro chlorofluorocarbons (HCFCs) and Chlorofluorocarbons (CFCs) having large amount of chlorine content as well as high global warming potential and ozone depletion potential, so after 90s refrigerants under these categories these kinds of refrigerants are almost prohibited [1].Most of the study has been carried out for the performance evaluation of vapour compression refrigeration system using energetic analysis, but with the help of first law analysis irreversibility destruction or losses in components of system unable to determined [2], so exergetic analysis is the advanced approach for thermodynamic analysis which gives an additional practical view of the processes [3-5]. The utility of second law analysis on vapour compression refrigeration systems is well defined because it gives the idea for improvements in efficiency due to modifications in existing design in terms of reducing exergy destructions in the components. In addition to this second law analysis also provides new thought for development in the existing system [6]. Xuan and Chen [7] presented in this manuscript about the replacement of R502 by mixture of HFC-161.Throug

Corresponding Author,
E-mail address: technokapilchopra@gmail.com
All rights reserved: http://www.ijari.org

h experimental study it was found that mixture of HFC-161 gives same and higher performance than R404A at lower and higher evaporative temperature respectively on the vapour compression refrigeration system designed for R404A.Cabello et al. [8] effect of condensing pressure, evaporating pressure and degree of superheating was experimentally investigated on single stage vapour compression refrigeration system using R22, R134a and R407C.It was observed that mass flow rate is greatly affected by change in suction conditions of compressor in results on refrigeration capacity because refrigeration capacity depended on mass flow rate through evaporator. It was also found that for higher compression ratio R22 gives lower COP than R407C.Spatz and Motta [9] focused on replacement of R12 with R410a through experimental investigation of medium temperature vapour compression refrigeration cycles. In terms of thermodynamic analysis, comparison of heat transfer and pressure drop characteristics, R410a gives best performance among R12, R404a and R290a.Han et al. [10] under different working conditions experimental results revealed that there could be replacement of R407C in vapour compression refrigeration system having rotor compressor with mixture of R32/R125/R161 showing higher COP, less pressure ratio and slightly high discharge compressor temperature without any modification in the same system. Cabello et al [11] had studied about the effect of operating parameters on COP, work input and cooling capacity of single-stage vapour

Nomenclature

LTE	low temperature evaporator	Φ	specific enthalpy (kJ/kg)
ITE	intermediate temperature evaporator	$\dot{\Psi}$	irreversibility rate(kW)
THE	high temperature evaporator	C	compressor
TR	ton of refrigeration	X	exergy rate of fluid (kW)
P	power (kJ/s)	$\dot{m}$	mass flow rate (kg/s)
F	flash intercooler	S	specific entropy (kJ/kgK)
$\dot{Q}$	rate of heat transfer (kW)	$\dot{EP}$	exergy rate of product (kW)
$\dot{W}$	work rate (kW)		
T	temperature (^{o}C)		
TV	throttle valve		
X	dryness fraction(non-dimensional)		
Subscript			
E	Evaporator	Tv	throttle valve
C	Compressor	Lsc	liquid subcooler
O	dead state	K	kth component
F	flash intercooler	Gen	generation
R	Refrigerant	cond	condenser

Refrigerant	Chemical formula	Molecular mass(g/mol)	NBP (^{o}C)	T_{cri} (^{o}C)	P_{cri} (MPa)	ASHRAE safety code
R410A	R-32/125	72.58	-60.9	72.5	4.95	A1
R290	$CH_3CH_2CH_3$	44.1	-42.2	96.7	4.25	A3
R600A	C_4H_{10}	58.122	-11.74	134.661	3.62	A3
R1234YF	$C_3H_2F_4$	114.04	-29.4	94.85	3.38	A2L
R600	C_4H_{10}	58.122	-0.49	151.98	3.79	A3
R134A	CH_2FCF_3	102.03	-26.1	101.1	4.06	A1
R125	C_2HF_5	120.02	-48.09	66.023	3.61	A1
R717	NH_3	17.03	-33.327	132.25	11.33	B2

Table: 1. Physical and environmental characteristics of considered refrigerants [2, 3]

compression refrigeration system. There is great influence on energetic parameters due change in suction pressure, condensing and evaporating temperatures. Arora and Kaushik [12] developed numerical model of actual vapour compression refrigeration system with liquid vapour heat exchanger and did energy and exergy analysis on the same in the specific temperature range of evaporator and condenser. They concluded that R502 is the best refrigerant compare to R404A and R507A, compressor is the worst and liquid vapour heat exchanger is best component of the system. Getu and Bansal [13] had optimized the design and operating parameters of like condensing temperature, sub cooling temperature, evaporating temperature, superheating temperature and temperature difference in cascade heat exchanger R744-R717 cascade refrigeration system. A regression analysis was also done to obtain optimum thermodynamic parameters of same system. Mohanraj et al [14]through experimental investigation of domestic refrigerator they arrived on conclusions that under different environmental temperatures COP of system using mixture of R290 and R600a in the ratio of 45.2: 54.8 by weight showing up to 3.6% greater than same system using R134a, also discharge temperature of compressor with mixture of R290 and R600a is lower in the range of 8.5-13.4K than same compressor with R134a.Padilla et al [15] exergy analysis of domestic vapour compression refrigeration system with R12 and R413A was done. They concluded that performance in terms of power consumption, irreversibility and exergy efficiency of R413A is better than R12.In this paper great emphasis put on saving of energy and using of ecofriendly refrigerants due to increase of energy crises, global warming and depletion of ozone layer. In this investigation the work input required running the vapour compression refrigeration system reduced by using compound compression and further decreased by flash intercooling between compressors.COP of system can also be enhanced by compressing the refrigerant very close to the saturation line this can be achieved by compressing the refrigerants in more stages with intermediate intercoolers. The refrigeration effect can be increase by maintaining the condition of refrigerants in more liquid stage at the entrance of evaporator which can be achieved by expanding the refrigerant very close to the liquid line. The expansion can be brought close to the liquid line by sub cooling the refrigerant and removing the flashed vapours by incorporating the flash chamber in the working cycle. The evaporator size can be reduced because unwanted vapours formed are removed before the liquid refrigerant enters in the evaporator. Multi-stage vapour compression with flash intercooler and individual throttle valves (system-1) consists of three compressors arranged in compound compression, individual throttle valves, condenser and evaporators as shown in Fig.1.Multiple evaporators at different temperatures with compound compression, flash intercooler and multiple throttle valves (system-2) consists of three compressors arranged in compound compression, multiple throttle valves, condenser and evaporators as shown in Fig.2.

2. Energy and Exergy Analysis

For carrying out energetic and exergetic analysis, computational models of system-1 and system-2 has been developed and impact of chosen refrigerants on these systems has been analyzed using Engineering Equation Solver software[16].In this investigation following assumptions are made:

1. Load on the low, intermediate and high temperature evaporators are 10TR, 20 TR and 30 TR respectively.
2. Dead state temperature (T_0): 25 ^oC
3. Difference between evaporator and space temperature (T_r-T_e):5 ^oC.
4. Adiabatic efficiency of compressor: 76%.
5. Dead state enthalpy (Φ_0) and entropy (s_0) of the refrigerants have been calculated corresponding to the dead state temperature (T_0) of 25 ^oC.
6. Variation in kinetic and potential energy is negligible.
7. Expansion process is adiabatic
8. Temperature of low, intermediate and high temperature evaporators are -10 ^oC, 0 ^oC and 10 ^oC respectively.
9. Condenser temperature : 40 ^oC
10. Degree of sub cooling : 10 ^oC

Exergy at any state is given as

$$X = (\Phi - \Phi_0) - T_0(s - s_0) \quad (1)$$

Energy analysis

First law of thermodynamic gives the idea of energy balance of system.

Mass flow analysis of system-1

$$\dot{m}_{c1} = \dot{m}_{e1} = \frac{\dot{Q}_{e1}}{(\Phi_1 - \Phi_{10})} \quad (2)$$

$$\dot{m}_{e2} = \frac{\dot{Q}_{e2}}{(\Phi_3 - \Phi_9)} \quad (3)$$

$$\dot{m}_{f1} = \frac{\dot{m}_{c1}(\Phi_2 - \Phi_3)}{(\Phi_3 - \Phi_9)} \quad (4)$$

$$\dot{m}_{c2} = \dot{m}_{c1} + \dot{m}_{e2} + \dot{m}_{f1} \quad (5)$$

$$\dot{m}_{e3} = \frac{\dot{Q}_{e3}}{(\Phi_5 - \Phi_8)} \quad (6)$$

$$\dot{m}_{f2} = \frac{\dot{m}_{c2}(\Phi_4 - \Phi_5)}{(\Phi_5 - \Phi_8)} \quad (7)$$

$$\dot{m}_{c3} = \dot{m}_{c2} + \dot{m}_{e3} + \dot{m}_{f2} \quad (8)$$

Energy consumption for sytem-1

$$P_{c1} = \frac{\dot{m}_{c1}(\Phi_2 - \Phi_1)}{60} \quad (9)$$

$$P_{c2} = \frac{\dot{m}_{c2}(\Phi_4 - \Phi_3)}{60} \quad (10)$$

$$P_{c3} = \frac{\dot{m}_{c3}(\Phi_6 - \Phi_5)}{60} \quad (11)$$

Energetic efficiency of system-1

$$\mathrm{COP} = \frac{\dot{Q}_e}{P_c * 60} \quad (12)$$

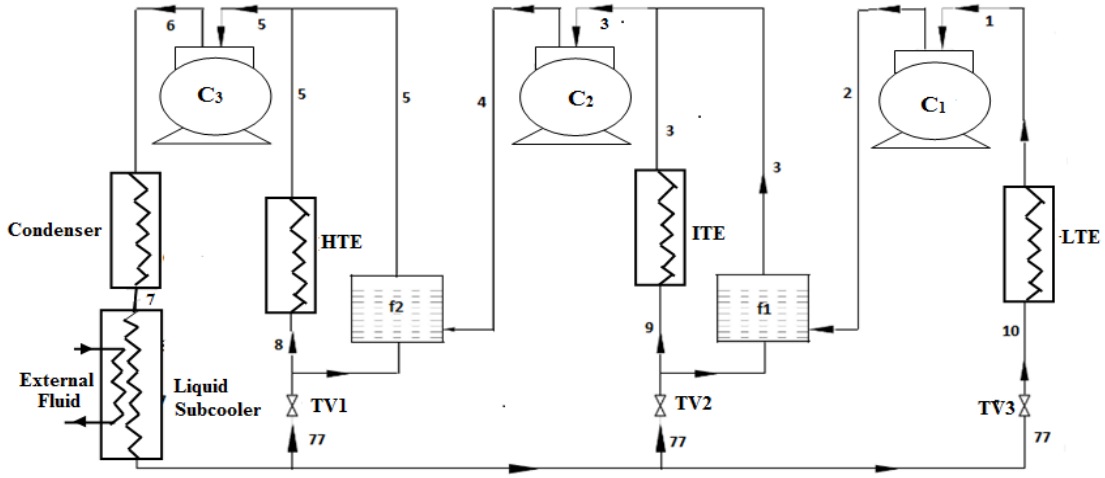


Fig: 1. Schematic diagram of multiple evaporators with compound compression, flash intercooler and individual throttle valves

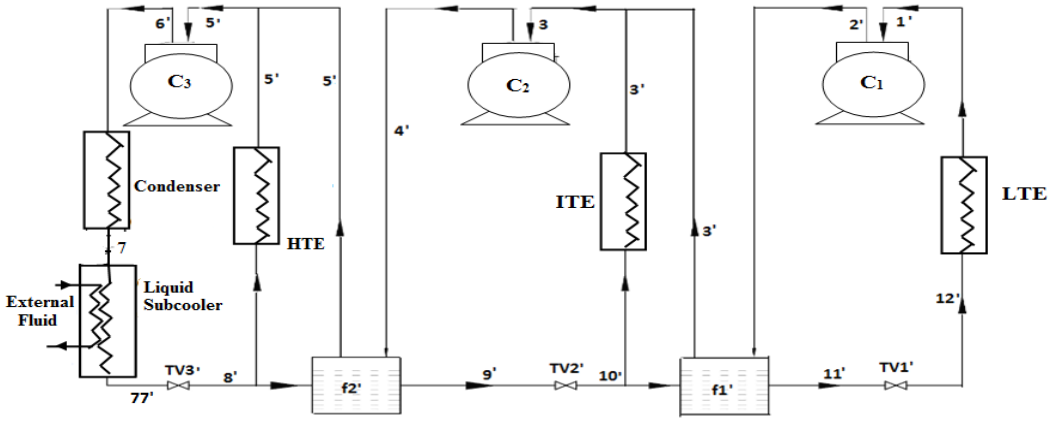


Fig: 2. Schematic diagram of multiple evaporators with compound compression, flash intercooler and multiple throttle valves

Rate of exergy loss due to irreversibility$(T_o \dot{S}_{gen})$ in various components of system-1

The concept of exergy was given by second law of thermodynamics, which always decreases due to thermodynamic irreversibility. Exergy is defined as the measure of usefulness, quality or potential of a stream to cause change and an effective measure of the potential of a substance to impact the environment [12].

Compressors

$$(T_o \dot{S}_{gen})_{c1} = \dot{W}_{c1} + \dot{m}_{c1}(X_2 - X_1) \quad (13)$$

$$(T_o \dot{S}_{gen})_{c2} = \dot{W}_{c2} + \dot{m}_{c2}(X_4 - X_3) \quad (14)$$

$$(T_o \dot{S}_{gen})_{c3} = \dot{W}_{c3} + \dot{m}_{c3}(X_6 - X_5) \quad (15)$$

$$\Psi_c = (T_o \dot{S}_{gen})_{c1} + (T_o \dot{S}_{gen})_{c2} + (T_o \dot{S}_{gen})_{c3} \quad (16)$$

Evaporators

$$(T_o \dot{S}_{gen})_{e1} = \dot{m}_{e1}(X_1 - X_{10}) - \dot{Q}_{e1}\left(1 - \frac{T_0}{T_{r1}}\right) \quad (17)$$

$$(T_o \dot{S}_{gen})_{e2} = \dot{m}_{e2}(X_3 - X_9) - \dot{Q}_{e2}\left(1 - \frac{T_0}{T_{r2}}\right) \quad (18)$$

$$(T_o \dot{S}_{gen})_{e3} = \dot{m}_{e3}(X_5 - X_8) - \dot{Q}_{e3}\left(1 - \frac{T_0}{T_{r3}}\right) \quad (19)$$

$$\Psi_e = (T_o \dot{S}_{gen})_{e1} + (T_o \dot{S}_{gen})_{e2} + (T_o \dot{S}_{gen})_{e3} \quad (20)$$

Condenser

$$\Psi_{cond} = (T_o \dot{S}_{gen})_{cond} = \dot{m}_{c3}(X_6 - X_7) - \dot{Q}_e\left(1 - \frac{T_0}{T_r}\right) \quad (21)$$

Throttle Valves

$$(T_o \dot{S}_{gen})_{tv1} = \dot{m}_{e1}(X_{77} - X_{10}) \quad (22)$$

$$(T_o \dot{S}_{gen})_{tv2} = (\dot{m}_{e2} + \dot{m}_{f1})(X_{77} - X_9) \quad (23)$$

$$(T_o \dot{S}_{gen})_{tv3} = (\dot{m}_{e3} + \dot{m}_{f2})(X_{77} - X_8) \quad (24)$$

$$\Psi_{tv} = (T_o \dot{S}_{gen})_{tv1} + (T_o \dot{S}_{gen})_{tv2} + (T_o \dot{S}_{gen})_{tv3} \quad (25)$$

Liquid sub cooler

$$\Psi_{lsc} = (T_o \dot{S}_{gen})_{sc} = \dot{m}_{c3}(X_7 - X_{77}) \quad (26)$$

Flash intercoolers

$$(T_o \dot{S}_{gen})_{f1} = \dot{m}_{f1}(X_9 - X_3) + \dot{m}_{c1}(X_2 - X_3) \quad (27)$$

$$(T_o \dot{S}_{gen})_{f2} = \dot{m}_{f2}(X_8 - X_5) + \dot{m}_{c1}(X_4 - X_5) \quad (28)$$

$$\Psi_f = (T_o \dot{S}_{gen})_{f1} + (T_o \dot{S}_{gen})_{f2} \quad (29)$$

Total irreversibility destruction in system-1

$$\sum \Psi_k = \Psi_e + \Psi_c + \Psi_{cond} + \Psi_{tv} + \Psi_{lsc} + \Psi_f \quad (30)$$

$$\dot{m}_{c1'} = \dot{m}_{e1'} = \frac{\dot{Q}_{e1'}}{(\Phi_{1'} - \Phi_{12'})} \quad (31)$$

$$\dot{m}_{e2'} = \frac{\dot{Q}_{e2'}}{(\Phi_{3'} - \Phi_{10'})} + \dot{m}_{c1'}\left(\frac{x_{10'}}{1 - x_{10'}}\right) \quad (32)$$

$$\dot{m}_{f1'} = \frac{\dot{m}_{c1'}(\Phi_{2'} - \Phi_{3'})}{(\Phi_{3'} - \Phi_{10'})} \quad (33)$$

$$\dot{m}_{c2'} = \dot{m}_{c1'} + \dot{m}_{e2'} + \dot{m}_{f1'} \quad (34)$$

$$\dot{m}_{e3'} = \frac{\dot{Q}_{e3'}}{(\Phi_{5'} - \Phi_{8'})} + \dot{m}_{c2'}\left(\frac{x_{8'}}{1 - x_{8'}}\right) \quad (35)$$

$$\dot{m}_{f2'} = \frac{\dot{m}_{c2'}(\Phi_{4'} - \Phi_{5'})}{(\Phi_{5'} - \Phi_{8'})} \quad (36)$$

Power required for running the compressors

$$P_{c1'} = \frac{\dot{m}_{c1'}(\Phi_{2'} - \Phi_{1'})}{60} \quad (37)$$

$$P_{c2'} = \frac{\dot{m}_{c2'}(\Phi_{4'} - \Phi_{3'})}{60} \quad (38)$$

$$P_{c3'} = \frac{\dot{m}_{c3'}(\Phi_{6'} - \Phi_{5'})}{60} \quad (39)$$

$$\text{Energetic efficiency} = \frac{\dot{Q}_{e'}}{P_{c'} * 60} \quad (40)$$

2.1 Rate of exergy loss due to irreversibilties $(T_o \dot{S}_{gen})$ in various components of system-2

Compressors

$$(T_o \dot{S}_{gen})_{c1} = \dot{W}_{c1} + \dot{m}_{c1}(X_2 - X_1) \quad (41)$$

$$(T_o \dot{S}_{gen})_{c2} = \dot{W}_{c2} + \dot{m}_{c2}(X_4 - X_3) \quad (42)$$

$$(T_o \dot{S}_{gen})_{c3} = \dot{W}_{c3} + \dot{m}_{c3}(X_6 - X_5) \quad (43)$$

$$\Psi_c = (T_o \dot{S}_{gen})_{c1} + (T_o \dot{S}_{gen})_{c2} + (T_o \dot{S}_{gen})_{c3} \quad (44)$$

Evaporators

$$(T_o \dot{S}_{gen})_{e1} = \dot{m}_{e1}(X_1 - X_{12}) - \dot{Q}_{e1}\left(1 - \frac{T_0}{T_{r1}}\right) \quad (45)$$

$$(T_o \dot{S}_{gen})_{e2} = \dot{m}_{e2}(X_3 - X_{10}) - \dot{Q}_{e2}\left(1 - \frac{T_0}{T_{r2}}\right) \quad (46)$$

$$(T_o \dot{S}_{gen})_{e3} = \dot{m}_{e3}(X_5 - X_8) - \dot{Q}_{e3}\left(1 - \frac{T_0}{T_{r3}}\right) \quad (47)$$

$$\Psi_e = (T_o \dot{S}_{gen})_{e1} + (T_o \dot{S}_{gen})_{e2} + (T_o \dot{S}_{gen})_{e3} \quad (48)$$

Condenser

$$\Psi_{cond} = (T_o \dot{S}_{gen})_{cond}$$

$$= \dot{m}_{c3}(X_6 - X_7) - \dot{Q}_e\left(1 - \frac{T_0}{T_r}\right) \quad (49)$$

Throttle Valves

$$(T_o \dot{S}_{gen})_{tv1} = \dot{m}_{e1}(X_{11} - X_{12}) \quad (50)$$

$$(T_o \dot{S}_{gen})_{tv2} = \dot{m}_{c2}(X_9 - X_{10}) \quad (51)$$

$$(T_o \dot{S}_{gen})_{tv3} = \dot{m}_{c3}(X_{77} - X_8) \quad (52)$$

$$\Psi_{tv} = (T_o \dot{S}_{gen})_{tv1} + (T_o \dot{S}_{gen})_{tv2} + (T_o \dot{S}_{gen})_{tv3} \quad (53)$$

Liquid sub cooler

$$\Psi_{lsc} = (T_o \dot{S}_{gen})_{lsc} = \dot{m}_{c3}(X_7 - X_{77}) \quad (54)$$

Flash intercoolers

$$(T_o \dot{S}_{gen})_{f1} = \dot{m}_{f1}(X_{10} - X_3) + \dot{m}_{c1}(X_2 - X_3) \quad (55)$$

$$(T_o \dot{S}_{gen})_{f2} = \dot{m}_{f2}(X_8 - X_5) + \dot{m}_{c2}(X_4 - X_5) \quad (56)$$

$$\Psi_f = (T_o \dot{S}_{gen})_{f1} + (T_o \dot{S}_{gen})_{f2} \quad (57)$$

Total irreversibility destruction in system-1

$$\sum \Psi_k = \Psi_e + \Psi_c + \Psi_{cond} + \Psi_{tv} + \Psi_{lsc} + \Psi_f \quad (58)$$

Exergetic efficiency

$$\text{Exergetic efficiency} = \frac{\text{Exergy of cooling load of}}{\text{Compressors wo}} \quad (59)$$

$$\text{Exergetic efficiency of system} - 1 = \frac{(\dot{Q}_{e1} + \dot{Q}_{e2} + \dot{Q}_{e3}) - T_0\left(\frac{\dot{Q}_{e1}}{T_{r1}} + \frac{\dot{Q}_{e2}}{T_{r2}} + \frac{\dot{Q}_{e3}}{T_{r3}}\right)}{P_c * 60} \quad (60)$$

$$\text{Rational efficiency of system} - 2 = \frac{(\dot{Q}_{e1} + \dot{Q}_{e2} + \dot{Q}_{e3}) - T_0\left(\frac{\dot{Q}_{e1}}{T_{r1}} + \frac{\dot{Q}_{e2}}{T_{r2}} + \frac{\dot{Q}_{e3}}{T_{r3}}\right)}{P_c * 60} \quad (61)$$

3. Results and discussions

Variation in low, intermediate and high temperature evaporator with coefficient of performance for considered refrigerants of system-1 and system-2 is shown by Fig.3-5 and Fig.6-8 respectively. Both systems (system-1& system-2) were analytically analyzed and it was observed that COP (energetic efficiency) of system-2 is higher than system-1.

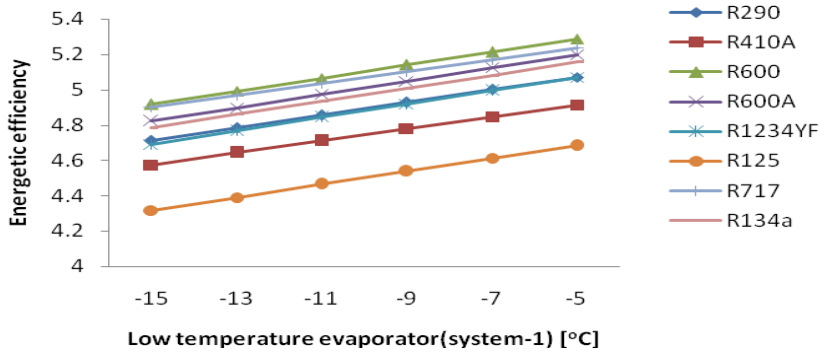


Fig: 3. Variation of low temperature evaporator of system-1with energetic efficiency

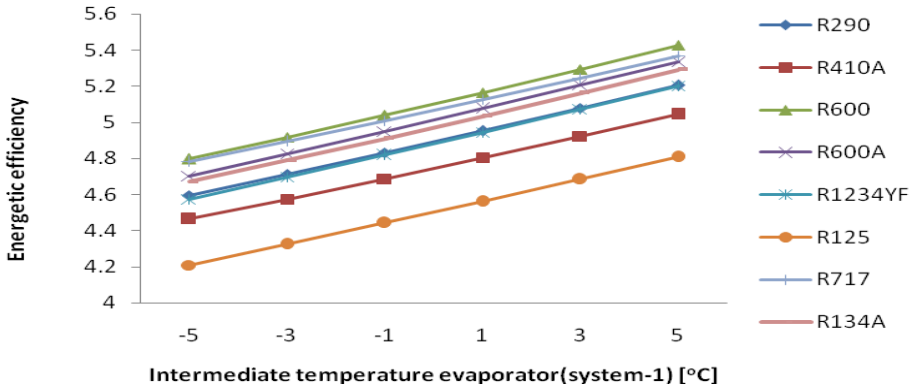


Fig: 4. Variation of intermediate temperature evaporator of system-1with energetic efficiency

The COP of both system-1 and system-2 increase with increase in evaporator temperature for chosen refrigerants. It was also observed that R600 and R717 show better performance and R125 gives poor performance in term of energetic efficiency than other refrigerants for both systems. The maximum percentage difference of COP was observed in high temperature evaporator of system-2 and system-1 is 9.59% for R125 at 15 ^{o}C,

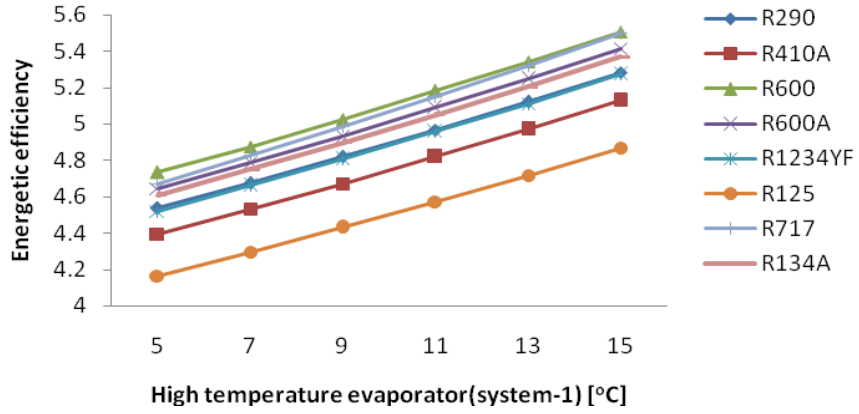


Fig: 5. Variation of high temperature evaporator of system-1with energetic efficiency

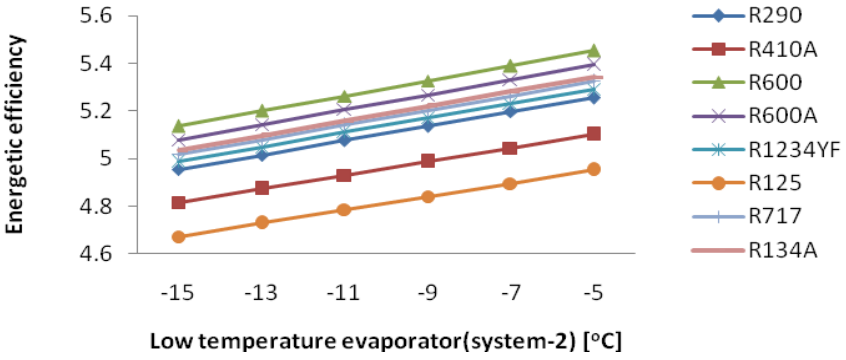


Fig: 6. Variation of low temperature evaporator of system-2 with energetic efficiency

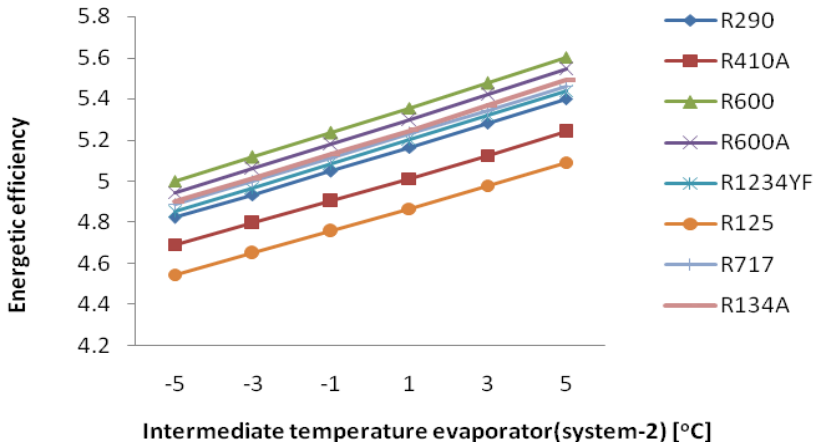


Fig: 7. Variation of intermediate temperature evaporator of system-2 with energetic efficiency

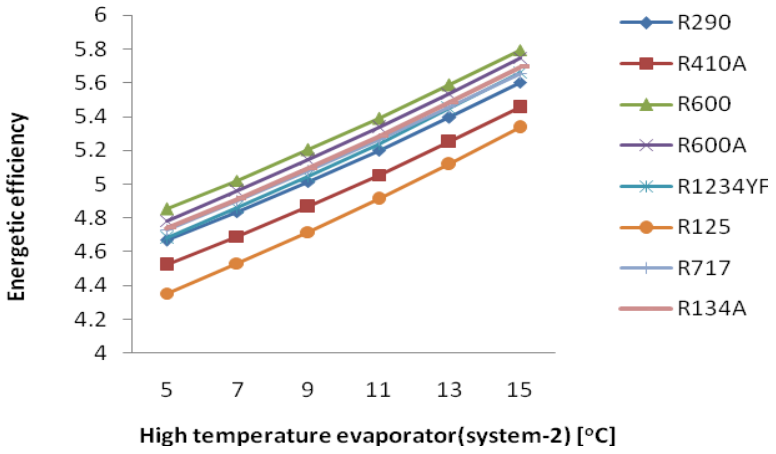


Fig: 8. Variation of high temperature evaporator of system-2 with energetic efficiency

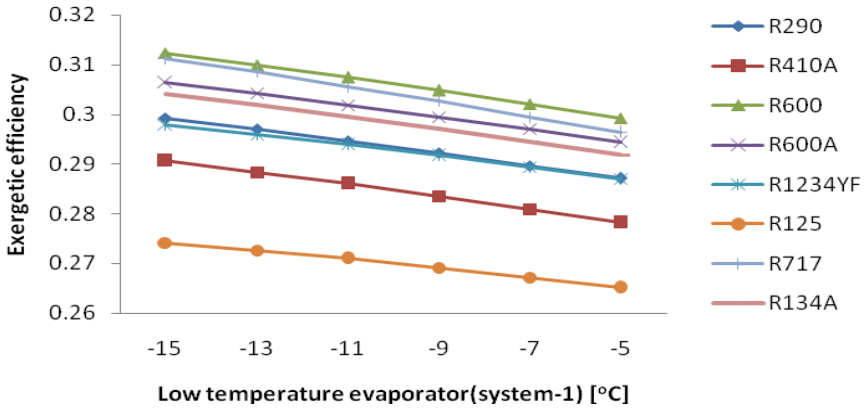


Fig: 9. Variation of low temperature evaporator of system-1with exergetic efficiency

The impact on second law efficiency (exergetic efficiency) with change in temperature of low, intermediate and high temperature evaporator of system-1 and system-2 shown by Fig.9-11and Fig.11-14 respectively. As variation in second law efficiency is reciprocal to coefficient of performance. It is also observed that second law efficiency decrease with increase in evaporator temperature. R600 and R125 have maximum and minimum second law efficiency for both systems similar to performance evaluation in terms of energetic efficiency. It was also found that temperature variation in low and intermediate evaporator put great impact on second law efficiency in comparison with high temperature evaporator, for both systems

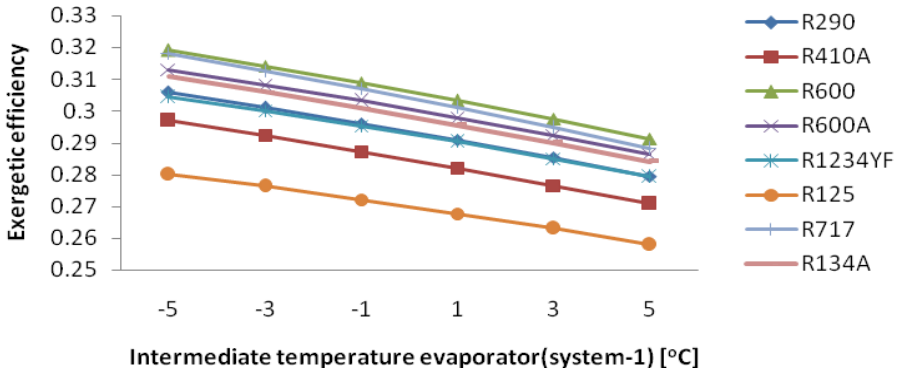


Fig: 10. Variation of intermediate temperature evaporator of system-1with exergetic efficiency

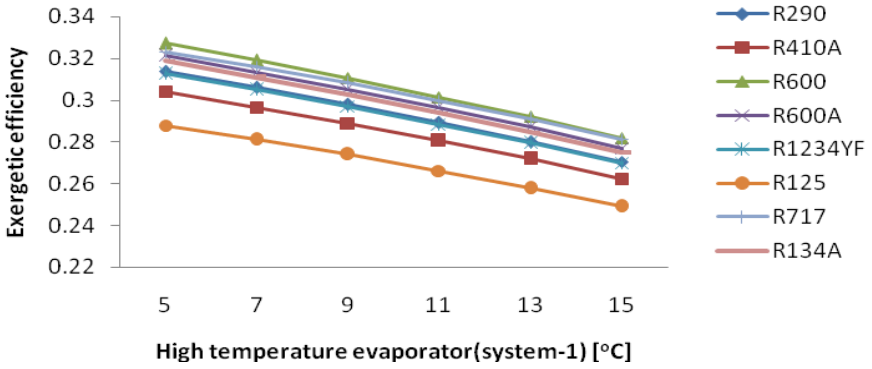


Fig: 11. Variation of high temperature evaporator of system-1with exergetic efficiency

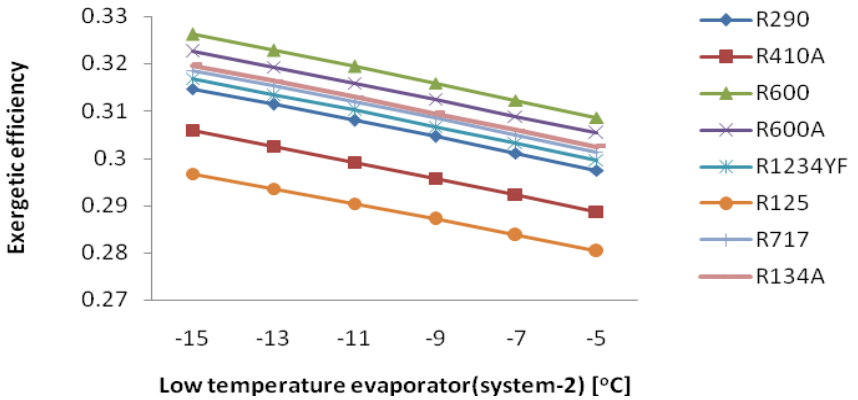


Fig: 12. Variation of low temperature evaporator of system-2 with exergetic efficiency

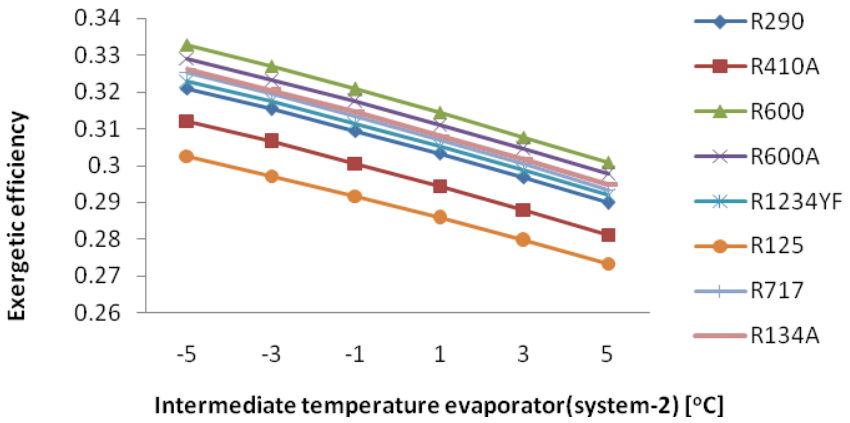


Fig: 13. Variation of intermediate temperature evaporator of system-2 with exergetic efficiency

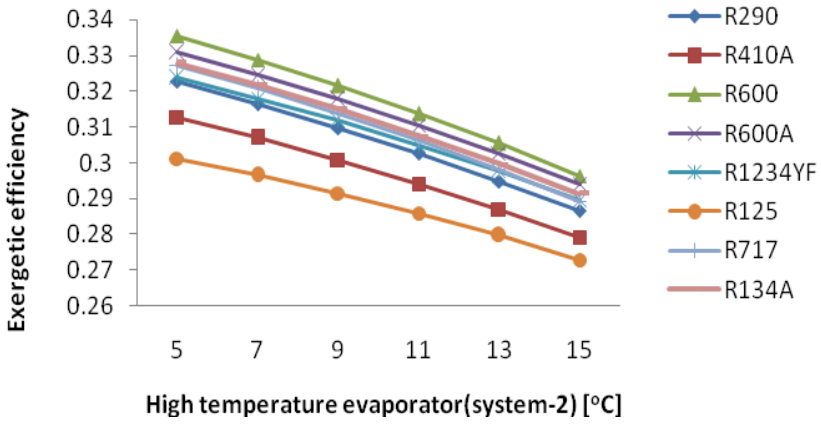


Fig: 14. Variation of high temperature evaporator of system-2 with exergetic efficiency

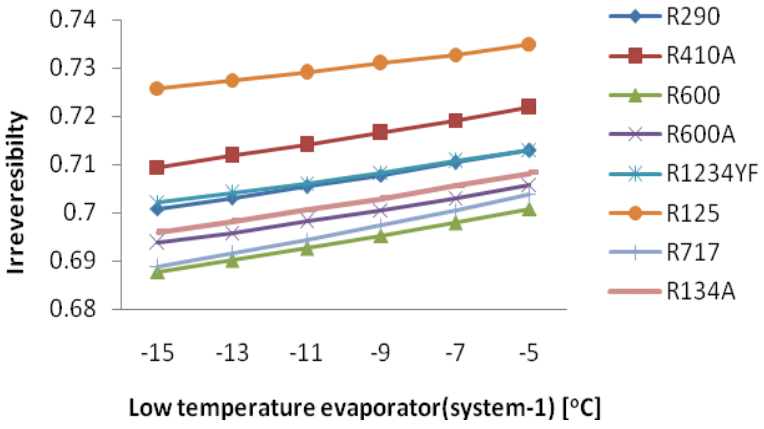


Fig: 15. Variation of low temperature evaporator with irreversibility of sytem-1

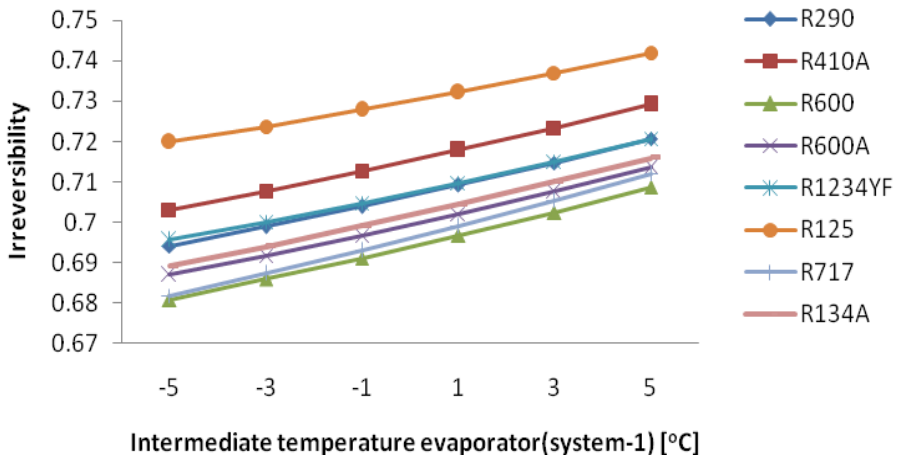


Fig: 16. Variation of intermediate temperature evaporator with irreversibility of sytem-1

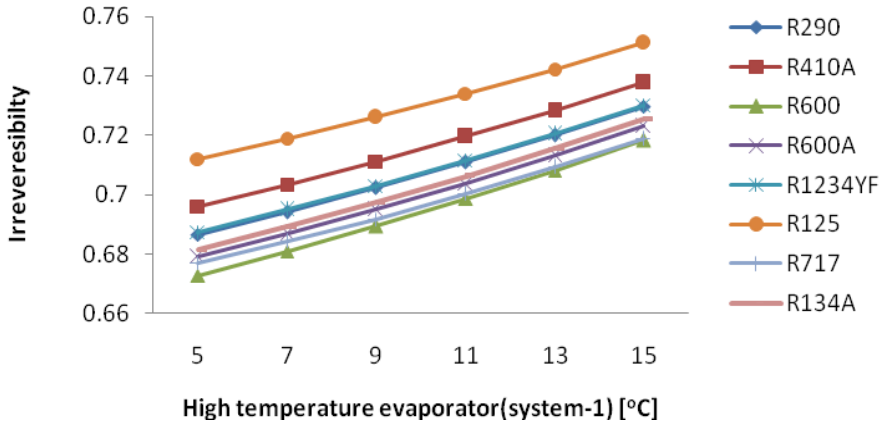


Fig: 17. Variation of high temperature evaporator with irreversibility of sytem-1

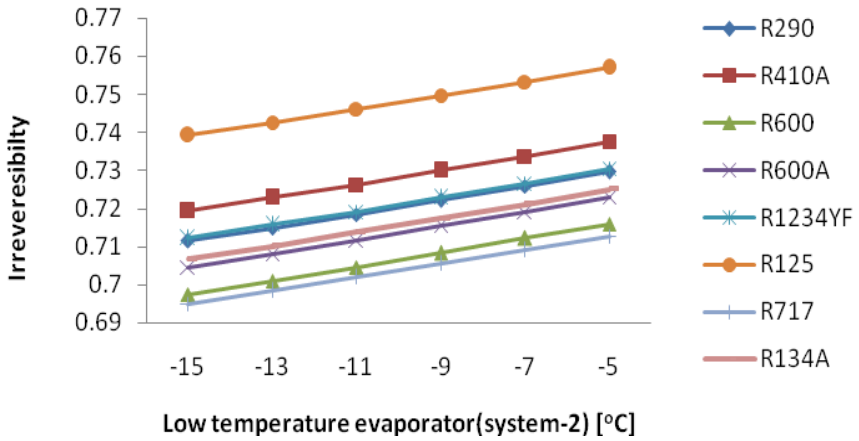


Fig: 18. Variation of low temperature evaporator with irreversibility of sytem-2

Irreversibility in system is work required to displace the atmosphere or lost work during the process. The irreversibility analysis of system-1 and system-2 is presented by Figs.15-17 and Figs.18-20 respectively. It was experienced that irreversibility of both system-1 and system-2 increase with increase in temperature of evaporator.R125 shows maximum irreversibility, on the other hand R600 and R717 show minimum irreversibility in systems compared with another selected refrigerants. It is also observed that irreversibility in system-1 is 1.4-2.1%, 1.3-2.2% and 1.6-2.0% using R600 and 1.8-3%, 1.7-3.1%, 2.2-2.7% using R125 is lower than system-2 for low, intermediate and high temperature evaporator respectively. This marginal irreversibility differences between system-1 and system-2 could be neglected.

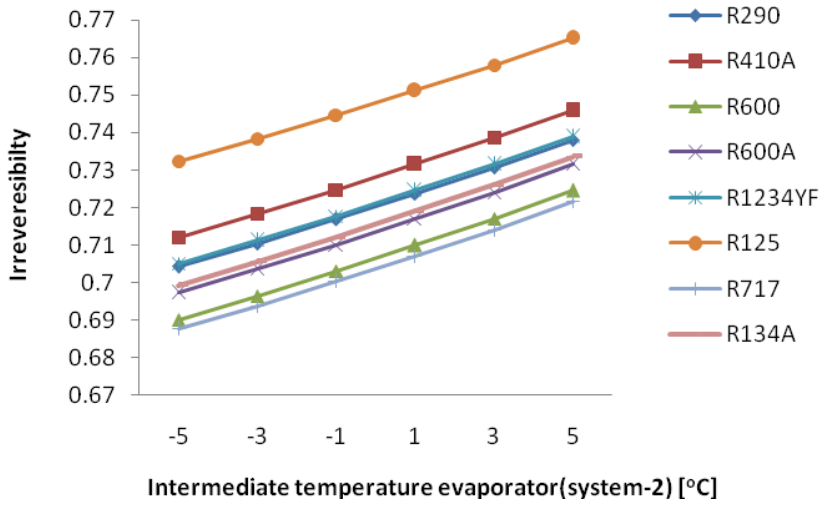


Fig: 19. Variation of intermediate temperature evaporator with irreversibility of sytem-2

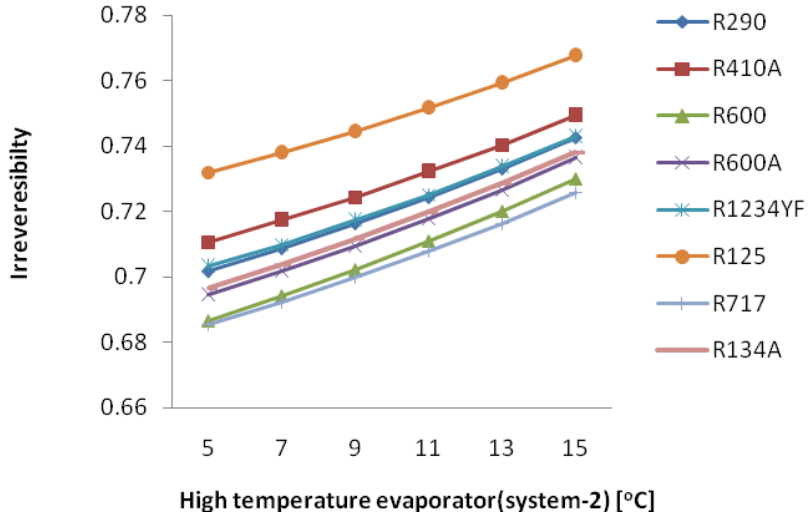


Fig: 20. Variation of high temperature evaporator with irreversibility of sytem-2

The impact of change in condenser temperature in range of 25 ^{o}C to 45 on coefficient of performance, second law efficiency and system irreversibility is shown in Figs.21-26 for sytem-1 and system-2 using ecofriendly refrigerants. This analysis reveals that COP and second law efficiency decreases with increase in condenser temperature on the other hand exergy destruction (system irreversibility) increase with increase in condenser temperature for system-1 & sytem-2

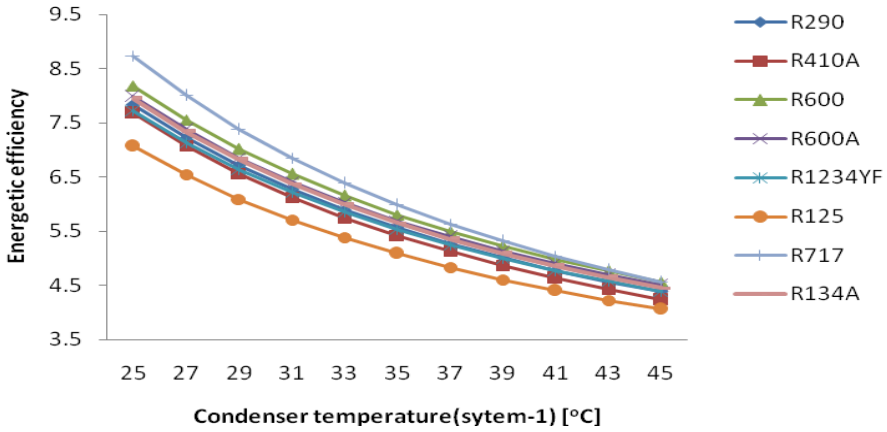


Fig: 21. Variation of condenser temperature with energetic efficiency of sytem-1

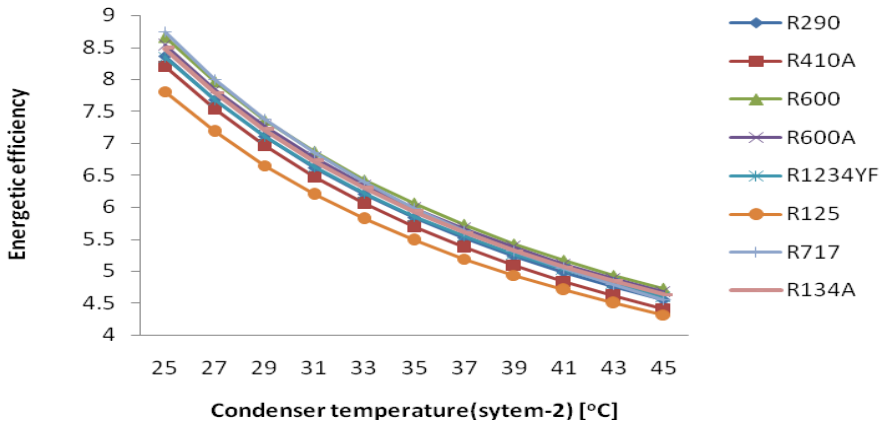


Fig: 22. Variation of condenser temperature with energetic efficiency of sytem-2

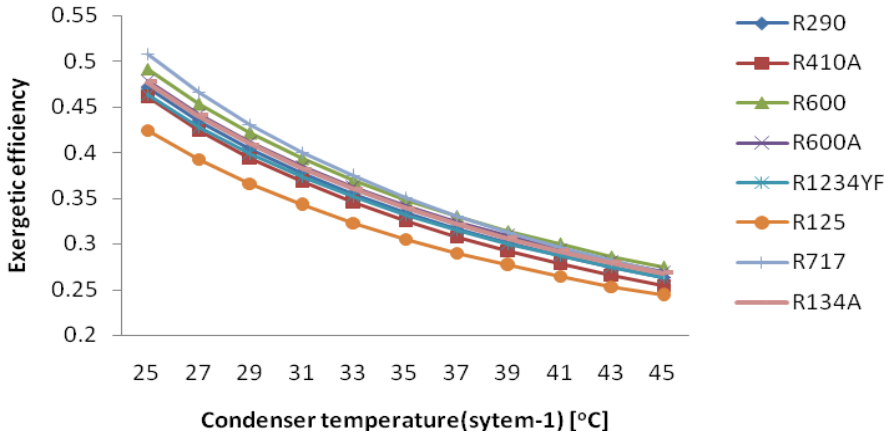


Fig: 23. Variation of condenser temperature with exergetic efficiency of sytem-1

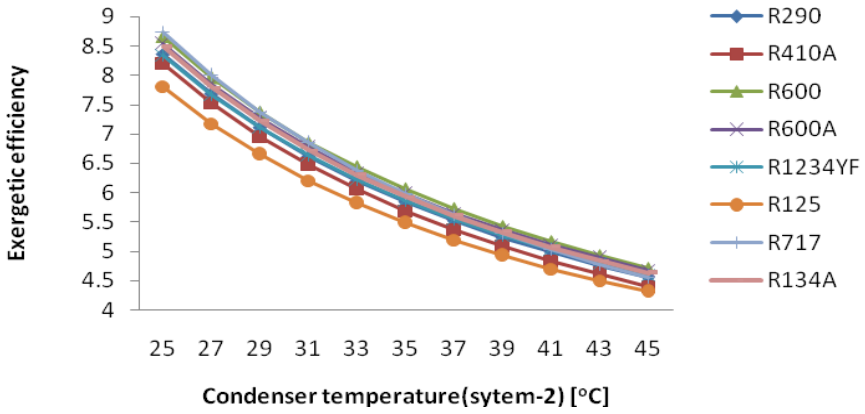


Fig: 24. Variation of condenser temperature with exergetic efficiency of sytem-2

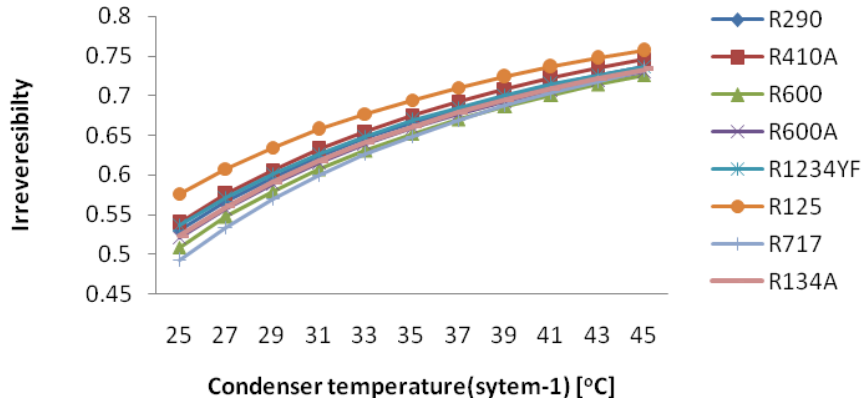


Fig: 25. Variation of condenser temperature with irreversibility of sytem-1

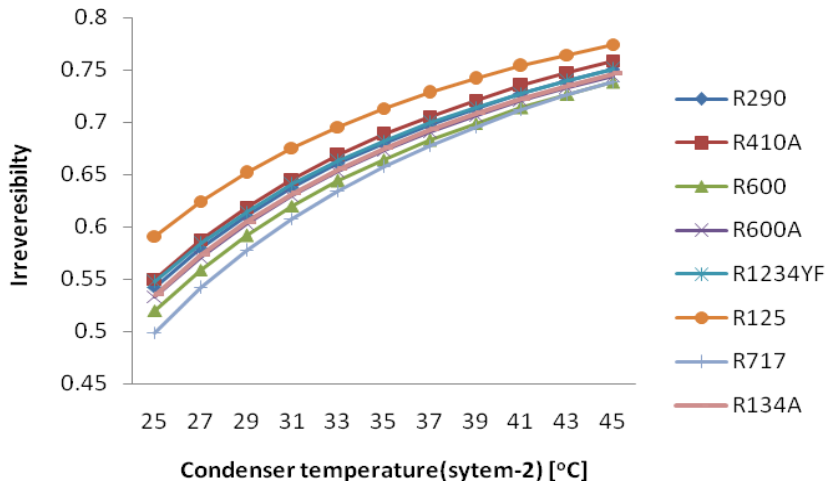


Fig: 26. Variation of condenser temperature with irreversibility of sytem-2

4. Conclusion

Thermodynamic analysis of multi-stage vapour compression refrigerator and flash intercooler with individual or multiple throttle valves has been carried out and numerical computation was done in terms of COP, second law efficiency and irreversibility destruction and following conclusions were made:

1. First law performance (Energetic) and second law performance (exergetic performance) of system-2 is higher than system-1 for selected temperature range of condenser and evaporators with chosen ecofriendly refrigerants.
2. For both systemsR125 shows minimum thermodynamic performance in terms of COP, second law efficiency and irreversibility in terms of exergy destruction in the components as well as in the both systems
3. Thermodynamic Performances in terms of COP and second law efficiency of R600and R717 better in comparison of other selected ecofriendly refrigerants for system-1 and system-2. ASR717 is toxic and limited to industrial applications, therefore R600 is recommended for both systems by taking safety precautions. Performance of R134a is slighly lesser than R600, therefore R134a can also be used for practical applications without taking of any safety precautions.
4. The maximum percentage difference of COP between system-2 and system-1 is 9.59% for R125 at 15 ^{o}C, high temperature evaporator. Irreversibility in system-1 is 1.4-2.1%, 1.3-2.2% and 1.6-2.0% using R600 and 1.8-3%, 1.7-3.1%, 2.2-2.7% using R125 is lower than system-2 for low, intermediate and high temperature evaporator respectively. This marginal irreversibility differences between system-1 and system-2 can be neglected.

References

[1] Camelia Stanciu, Adina Gheorghian, Dorin Stanciu, Alexandru Dobrovicescu, "Exergy analysis and refrigerant effect on the operation and performance limits of a one stage vapour compression refrigeration system, Termotehnia", 36-42, 2011

[2] V. Siva Reddy, N. L. Panwar, S. C. Kaushik Exergetic analysis of a vapour compression refrigeration system with R134a, R143a, R152a, R404A, R407C, R410A, R502 and R507A,Clean Techn Environ Policy,14:47–53, 2011

[3] J. U. Ahamed , R. Saidur, H. H. Masjuki, "A review on exergy analysis of vapor compression refrigeration system, Renewable and Sustainable Energy Reviews",15: 1593–1600

[4] D. Szargut, R. Petela, Egzergia(1965),WNT

[5] J. Szargut, D. Morris, F. Steward, "Exergy analysis of thermal, chemical and metallurgical processes". New York: Hemisphere Publishing Corporation. 1998

[6] R. Saidur, HH Masjuki, MY Jamaluddin, "An application of energy and exergy analysis in residential sector in Malaysia", Energy Policy, 35: 1050–63

[7] Yongmei Xuan, Guangming Chen, "Experimental study on HFC-161 mixture as an alternative refrigerant to R502", Int J Refrigeration, Article in Press

[8] R. Cabello, E. Torrella, J. Navarro, "Esbr, Experimental evaluation of a vapour compression plant performance using R134a, R407C and R22 as working fluids", Int J Applied Thermal Engineering.2004; 24:1905-1917

[9] Mark W. Spatz, Samuel F. Yana Motta, "An evaluation of options for replacing HCFC-22 in medium temperature refrigeration systems", Int J Refrigeration.2004; 27:475-483

[10] X. H. Han, Q. Wang, Z. W. Zhu, G. M. Chen, "Cycle performance study on R32/R125/R161 as an alternative refrigerant to R407C", Int J Applied Thermal Engineering.2007; 27:2559-2565

[11] R. Cabello, J. Navarro-Esbrı, R. Llopis, E. Torrella, "Analysis of the variation mechanism in the main energetic parameters in a single-stage vapour compression plant", Int J Applied Thermal Engineering.2007; 27:167-176

[12] Akhilesh Arora, S. C. Kaushik, "Theoretical analysis of a vapour compression refrigeration system with R502, R404A and R507A", Int J Refrigeration.2008; 31:998-1005

[13] H. M Getu, P.K Bansal, "Thermodynamic analysis of an R744-R717 cascade refrigeration system", Int J Refrigeration.2008; 31:45-54

[14] M. Mohanraj, S. Jayaraj, C. Muraleedharan, P. Chandrasekar, "Experimental investigation of R290/R600a mixture as an alternative to R134a in a domestic refrigerator", Int J Thermal Sciences.2009; 48:1036-1042

[15] M. Padilla, R. Revellin, J. Bonjour, "Exergy analysis of R413A as replacement of R12 in a domestic refrigeration system", Int J Energy Conversion and Management.2010; 51:2195-2201

[16] S. A. Klein, F. Alvarado, "Engineering Equation Solver, Version 7.441. F Chart Software, Middleton, WI, 2005

2014 International Conference on Signal Processing and Integrated Networks (SPIN)

MRDMS-Mobile Replicated Database Management Synchronization

Divyashikha Sethia
Department of Software Engineering
Delhi Technological University (DTU)
Delhi, India
divyashikha@dce.edu

Swati Mehta, Anant Chowdhary,Kartikeya Bhatt, Siddharth Bhatnagar
Department of Computer Engineering
Delhi Technological University (DTU)
Delhi, India

Abstract— **We consider a mobile replicated database that consists of several mobile nodes, each containing a replicated copy of a common database. The nodes are interconnected through a wireless network along with a fixed server which retains the primary copy of the database. In this work, we have proposed an efficient database synchronization algorithm - Mobile Replicated Database Management Synchronization (MRDMS) for networks with low bandwidth and poor connectivity. The algorithm has been designed and implemented so that any updates on databases can be performed on mobile nodes, even when they are offline. They can be synchronized later with a fixed server on availability of a network connection. A case study of Livestock Database has been used in this work. Our proposed algorithm can provide an efficient management of replicated database using simple mobile devices in a disconnected network for proper consistency and synchronization along with network utilization.**

Keywords— Distributed Database; Mobile; Replication; Synchronization

I. INTRODUCTION

Connectivity in today's time using mobile computing has laid its roots firmly and is growing rapidly day by day. Important information is transmitted; and is accessed through mobile devices. Mobile devices can be used for efficient management of data, even for the minutest work like that of management of livestock in a dairy. Unreliable network connectivity however, is a major drawback that needs to be taken into account especially in rural areas of developing countries. In these processes, the traditional client/server architecture needs to work with intermittent connectivity. Hence, data synchronization is an essential attribute that is required by mobile systems in the absence of a direct connection to the central servers.

Data Synchronization can be defined as keeping replicated copies of a data-set in coherence with each other. Synchronization can be real-time or non-real-time. Real time synchronization always requires a continuous data connection between the source and target devices. In this work, we look into the synchronization in disconnected networks; that is, non-real-time synchronization. Synchronization can be implemented using "Timestamps" or "Synchronization Flags". Since Synchronization flags are not suitable for multiple devices synchronizing with a single server, we use "Timestamps" to perform synchronization between multiple mobile devices and a fixed centralized server. For this non-real-time database synchronization, a way of performing synchronization is the "row-based" synchronization mechanism. However, for this solution, timestamps for each row need to be maintained; hence the chances of having a conflict are very high. This is because unique cells may not have been changed, and the overall timestamp of each row however, may still have been altered.

For instance, user A has edited two cells of a row at time t, and user B has edited two different cells of the same row at $t + \Delta t$. If user B synchronizes immediately, then the timestamp for that row will be set to $t + \Delta t$. Now, if user A synchronizes, his changes will not be updated on the server, because his change timestamp t is less than row timestamp $t + \Delta t$. This is incorrect as the cells that have been changed are not conflicting with each other.

Hence, to retain the changes made by all users, except when they are not on the same cell, we introduce a cell-based synchronization mechanism.

In our proposed algorithm, major computations are performed on the server which thus minimizes the computation requirement at mobile nodes; Further leading to a minimization of computations on small handheld devices. It uses a read-any/write-any replication scheme, that is – both the client and server can read and modify the database and then synchronize it, so that their copies are coherent with each other. Data availability is also increased due to the replication of database on mobile nodes. It performs authentication of each user accessing a local database as well as synchronization with the main server, and hence security is assured. Lastly, only modified rows need to be transferred between the local device and the server. This reduces the number of messages exchanged among the replicated nodes

The rest of the layout of the paper consists of section II, where we define our given problem statement followed by section III which states our proposed solution for the given problem statement. The proposed MRDMS algorithm is explained in section IV. The implementation and case details of the algorithm are depicted in section V. Section VI describes the various testing devices and parameters used in the testing process. Section VII introduces a brief outline of the previous

978-1-4799-2866-8/14/$31.00 ©2014 IEEE

works in this area. We finally conclude with section VIII, which describes the conclusion and the various avenues to be explored in future using the proposed algorithm.

II. PROBLEM STATEMENT

Network infrastructure in rural areas is often under developed. This results in poor bandwidth over most networks. Also, mobile devices that are used in rural areas need to be low cost devices(which in most cases have low end specifications).

Mobile devices are growing in numbers in developing countries like India, and can be used for inventory management of systems in a cost effective manner using mobile replicated databases. There is a requirement for an efficient synchronization to keep the database consistent.

In such a case, a synchronization algorithm needs to be developed having the following characteristics:

1) It should entail a minimum amount of data transfer

2) Changes made when the device is disconnected from the server, should be synchronized with the server whenever connectivity is available

3) The algorithm should be implemented easily through commonly available softwares such as an Apache server, and should be able to exchange data through popular formats such as JavaScript Object Notation (JSON).

Keeping these requirements in mind, an algorithm named Mobile Replicated Database Management Synchronization (MRDMS) has been designed, which is discussed in section IV.

III. PROPOSED SOLUTION

The traditional approach to synchronize data is row based timestamp comparison as discussed in section I. However, to increase efficiency, we have used cell based timestamp comparisons to reduce data transfer to a minimum. Each regular data table has a corresponding timestamp table with an identical schema. However, the timestamp table maintains timestamps for each cell barring the primary key of each table.

The Synchronization architecture is given in Figure 1. It is assumed that all devices have their respective times synchronized for the implementation of the algorithm.

Standard UNIX timestamps have been used. The core of the algorithm lies in the comparison of timestamps. If a cell on the server has a timestamp with a value greater than that on the mobile device being synchronized, then the copy of data on the server is more recent. If not, the copy of the data (cell) is more recent on the device.

In either case, the most recent copy of data (cell) is transferred to the party that requires it. Transfers are done through matrices. Matrices are convenient ways to structure data and furthermore, can be modeled as arrays. We model them as JSON arrays in our implementation.

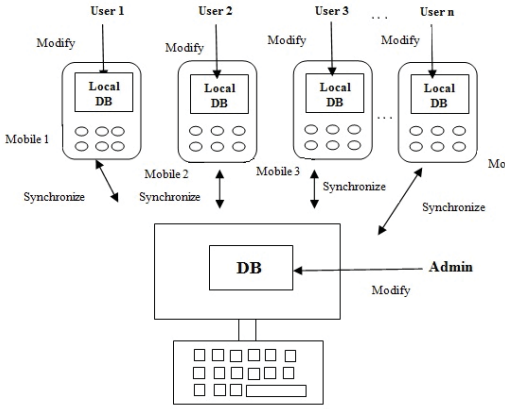


Figure 1: Synchronization Architecture

The algorithm has been implemented using basic HTTP POST requests, which are atomic in nature. That is, either the request goes through in its entirety or it doesn't at all. The request sent by a party is deemed to be successful if it leads to a response.

Each cell that can be viewed and updated must have a timestamp associated with it. Hence, a separate timestamp table for each regular table of data is maintained. Each cell of a regular table has its corresponding timestamp cell, which contains a timestamp value, which is the timestamp at which the cell was last updated.

Let table "abc" be a data table. Its corresponding timestamp table will be "abc_t". These are maintained on the server and are standard UNIX timestamps.

Each operation can be classified as an insert operation, a delete operation, or an update operation. We also assume that a column row_exists is set if an entry is valid and has value "-1" in case the entry (primary key) has been deleted.

Changes in data at either side are exchanged in 3-D matrix format-

[[[Table1 row1],[Table1 row2],….[Table1 row_n]], [[Table2 row1],[Table2 row2]…[Table2 row_n]]……Table_n].

Only changed rows are present in the matrix with the first column being the primary key. In case there is no change in any row of a table, the value "null" is set at that place. We use the terms LDB and MDB for Local Database on device and Master Database on the server, respectively. The algorithm is explained in detail in section IV.

IV. THE MRDMS ALGORITHM

We have proposed and implemented Mobile Replicated Database Management Synchronization (MRDMS) which is explained in detail along with a flow chart depicting the flow of data between the client and server devices.

The steps are as follows:

1) Each client device maintains a long variable

last_sync_timestamp (initialized with 0), which indicates the time at which this client last synchronized with the database on the server. This will get updated by the server's current timestamp after a successful synchronization attempt with the server.

2) Whenever a user makes changes at an LDB (local copy of the database), the timestamp at which the value of the concerned cell is changed, gets recorded in the corresponding timestamp table.
3) When a user synchronizes an LDB with the MDB (master database), a timestamp matrix of cells that have been changed, are then prepended with *last_sync_timestamp*, and are sent to the server through a wireless network.

Here is an example:

last_sync_time: [[["3", t1, t1, 0, 0] , ["5", t2, 0, t2, 0]] , null , [["4", t1, 0, 0, t1, 0, 0]]]

- Tables 1 and 3 of database have been changed; ***null*** value at the place of Table 2 indicates no change.
- Rows 3, 5 of "table 1" and row 4 of "table 3" have been changed
- Columns 1 and 2 of "row 3" of "table 1" have been edited at timestamp t1. The rest of the columns haven't witnessed any changes. Similar information can be inferred for the other rows.

4) If a user wants to update its database with "no change" in its LDB then only the value-*last_sync_time* is sent to server.
5) The matrix (mentioned in step 3) is encoded in a JSON string and is sent to the server using HTTP POST.
6) The server compares *last_sync_time* received from client with its corresponding timestamp tables and creates a similar matrix of the cells that have greater value, i.e. cells which have been updated, inserted or deleted after the user had last synchronized with the server. This would in turn bring the local database of the client up to date.
7) For any row, if a cell has a greater timestamp, as compared to the corresponding cell on the server, the server sets the special symbol "@" - for cells that the client need not update.
8) Also, the changes made by client at its local database will get reflected at server master database only if they have been performed more recently. This will be checked by the server by comparing the timestamp values sent by client with the corresponding timestamp values at server.
- If *server_cell_timestamp* > *client_cell_timestamp*, then the server has a value that is more recent, and it will be sent to the client.
- Else, the client has a more recently updated cell value. In this case, the server needs to update the value at its MDB, and it will need the requisite data from the client. This will be indicated with the special symbol "#" at the corresponding cell in the matrix that is being sent out to the client.
- An empty cell indicates a blank space.

9) The change matrix, which is obtained after performing the requisite comparisons, is prepended with the current time at the server and is then sent to the client.

Current_time_at_server
[[["3", "#", "klm", "@", "@"],
["5", "ghi", "@", "#", "@"]], null,
[["4", "#", "@", "@", "#", "@", "@"]]]

As we can see in Step 3 of the algorithm – the columns where a timestamp value is present in the timestamp matrix that has been sent by the client, a server response of "#" indicates that the server needs the value of that corresponding cell from the client in order to update its database (since the client's timestamp is greater).Whereas, if the response matrix contains a cell with a data value, for instance "klm" or "ghi" as mentioned in the example here, it indicates that the client needs to update its database according to these data values.
For cells which haven't been updated by the client (indicated by a "0" in the timestamp matrix), the server responds either with a value of "@"which indicates that there has not been any change at the server (the client does not need to change anything) or responds with some data value, which the client uses to update its database.

10) The client recognizes the special symbol "#", and sends a string value corresponding to that particular cell, to the server and makes no changes at cells corresponding to the places where "@" was received. It also updates the LDB for cells where string values were received.
11) The client's *last_sync_time* is updated according to the variable *Current_time_at_server*, at the server.
12) In this way, we are not sending actual data to server unless it is required.
13) To avoid inconsistencies at server due to insertion of new record by multiple devices, Insertions are handled a bit differently. We assume that insertions of new primary keys are made only when the mobile device under consideration is online – or is connected to the network. Insertions are carried out as follows:

a) The device requests the server for a new primary key.

b) The server checks any table for MAX_PRIMARY _KEY which supplies the maximum out of the set of all primary keys.
c) The server returns MAX_PRIMARY_KEY + 1 to the device.
d) The server creates a record with the previously returned primary key in all its regular data tables.
e) The device similarly creates a record with the received primary key.
f) The required information is now entered as any other update and upon a synchronization request from the device, the necessary data is sent to the server.

14) The value of last column *row_exists* of each table represents the different operations, i.e. "1" for insertion, "-1" for deletion, "0" for updating any row.

Figure 2 gives a pictorial representation of the flow of data between a client- server pair. Steps are numbered, and are followed by an alphabet – C: indicating the step was carried out at the client side; S: indicating the step was carried out at the server side.

Flow of Data in synchronization/deletion:

1. Client changes its local database and clicks "sync" button.
2. HTTP Post request containing *last_sync_time* and timestamp matrix is sent to server in JSON format.
3. The server decodes JSON and compares both *last_sync_time* and timestamp matrix with its own timestamp tables to collect all changes.
4. A JSON reply is sent containing *current_time_at_server* and requirement matrix (matrix containing "#" indicating data needed from client).
5. Client updates its database and *last_sync_time* accordingly.
6. Client sends *change_matrix c*ontaining data required by server.
7. Server updates its database.

V. Case Study And Implementation

The MRDMS algorithm has been implemented on a Server-Mobile Device setup. A standard Apache Server has been used, which has been set up using XAMPP, which is a free and open source cross-platform web server solution stack package. All requests on the server side have been processed using PHP/MySQL.

For testing purposes – an Android mobile Device (Sony Xperia S) has been used as the client device and a standard 802.11g wireless network.

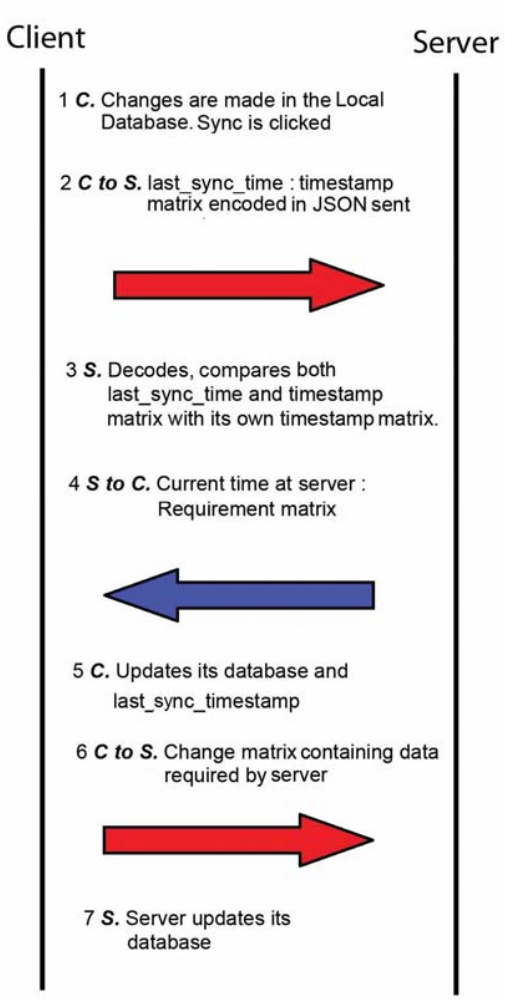


Figure 2: Flow of data between client and server

We have chosen the case study of a Livestock management system ranging over a large span of area, where the network is disconnected. This particular system has been chosen owing to the fact that for large areas(especially in rural areas) connections are slow and mobile devices are low end devices. It also serves as a prime example of a replicated database spread over a vast area, where parameters like animal health are of practical importance from the context of the algorithm as well as for those responsible for management of the livestock
Hence, such a system is a perfect test bed to study the algorithm in a practical environment.

The following tables are involved:

a) Age_info – to log all age related details of cattle
b) Health_records - to log all health related details of cattle
c) Info_table - to log general information about cattle
d) Lactation_info - to log all lactation related details of cattle

e) Reproduction_records - to log all age reproduction related details of a cattle

It is important to note that the very same tables exist on each of the client devices too. As explained earlier, each table has its corresponding timestamp table on the server. The corresponding timestamp tables are shown in Table 1.

The screenshots of the client device are in Figure 3 and the server side schema is shown as a part of Table 1.

TABLE 1: TABLES ON SERVER

Table Name	Corresponding Timestamp Table	No. of Columns
age_info	age_info_ts	6
health_records	health_records_ts	9
info_table	info_table_ts	12
lactation_info	lactation_info_ts	8
reproduction_records	Reproduction_records_ts	10
login_cred	-	2

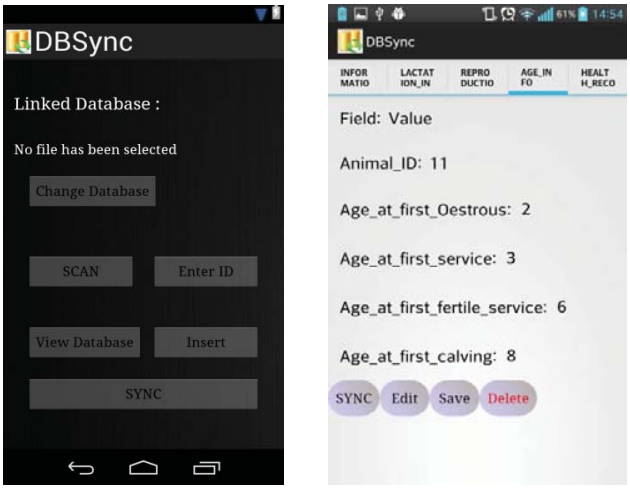


Figure 3: Screenshots of android application on mobile

VI. TESTING AND PERFORMANCE EVALUATION

Our testing bed consists of two client mobile devices and a fixed central server machine.

The algorithm has been stress tested using a comprehensive set of test cases ranging from single device testing to multi device testing, single modification, single delete, and single insertion to multiple of each. This has further been extended across devices created with a large number of permutations of possible test cases. The Insert-Delete test cases of multiple records across multiple devices have been the trickiest to handle. The algorithm also has capabilities to handle multiple updates followed by a single synchronization,and the corresponding conflict resolution on the server side due to this.

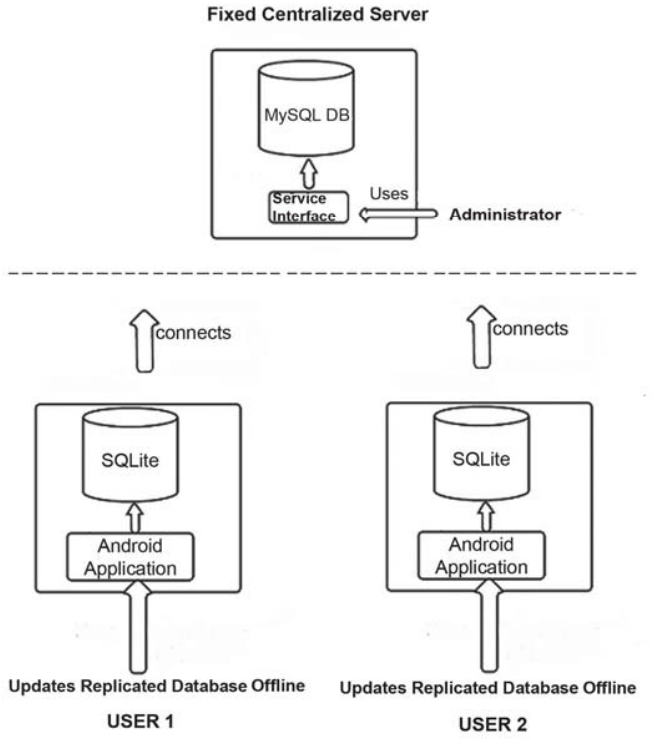


Figure 4: Test Bed structure

As shown in Figure 4, the Test Bed structure consists of two local devices and one server device with configurations as mentioned above. Each local device has an Android application implementing the algorithm and a SQLite database with the replicated database schema. The server has a MySQL database with the same schema as the SQLite databases and a PHP based server interface. Each of these devices has its own unique IP address and is connected to a wireless network created using a router.

Scalability is an important factor for the synchronization process described here. Scalability is commonly evaluated by performance of the given synchronization protocol. This is a function of time complexity of the protocol, where a short synchronization time reflects better performance. Performance of synchronization can also be evaluated in terms of following parameters:

Data Transmission Load: It is the amount of data exchanged between a source and its target devices. Data transmission Load affects the time consumed for each synchronization process, for a given throughput over a connection. Lesser the data to be transmitted, smaller is the time consumption – which suggests a better synchronization protocol. Our algorithm saves bandwidth and we even have numeric data in support of it.

Each table has "n" columns and "m" rows. There are "k" such tables and each cell of a table takes nearly 20 to 30 bytes of storage thus giving us a total of [k*m*n*(20 or 30 bytes of data)].

We, instead of sending the complete data, use a matrix and send only the required cells rather than the entire set of rows. We add an overhead of the matrix on the usual data sent. It may seem to actually waste bandwidth but in execution saves it. We send "k" matrices of mxn size with the each element size of 8 bits i.e. a total extra bit size of k*m*n*8 bits which is equal to k*m*n bytes of overhead.

The given bandwidth is assumed to be X Mbps. For the synchronization of only one table (10x10) where only one cell is edited the total data sent, according to our prototype algorithm ,was nearly 2000 bytes and for the same scenario our final version of the algorithm would send 100+20=120 bytes of data ,which is almost a 95% reduction in the usage of bandwidth.

Thus we can infer that our algorithm has been tested well and has been proven to be a well performing algorithm with low use of bandwidth.

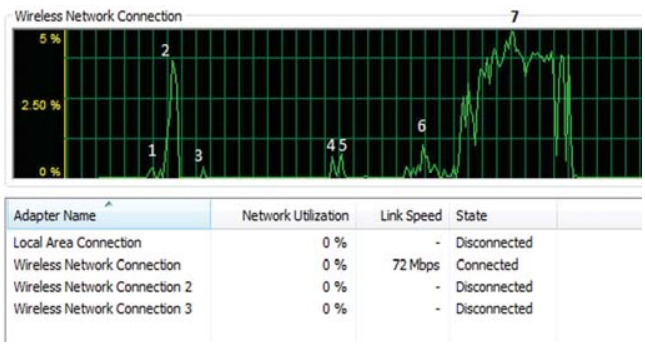
Computation Load: It is the processing load on the end device during a synchronization process. A lower computational load might not necessarily indicate a better protocol. But due to limited battery of hand held devices, a protocol with a high processing load on these devices may not be acceptable.

Our algorithm does not put any processing load on mobile devices.

Memory Usage: It is the amount of memory needed by the end device during synchronization. This point needs consideration as hand held devices in general, do not have large amounts of memory.

Our proposed MRDMS algorithm does not occupy any extra storage on mobile devices.

Figure 5: Network Utilization graph



We have used a 72Mbps router with a single user's bandwidth being limited to 256Kbps. In the network utilization graph shown above, we have tested our algorithm for all possible scenarios:

A) *Best Case:* The points {4,5} represent a synchronization scenario where the local device's database is the same as the server's copy of database. The points {4,5}actually symbolize the part of the algorithm where we only perform a matrix comparison on server end and reply with the change matrix. No data except for the matrices involved is transferred. Its performance is registered as less than 1% of the network usage.

B) *Average Case:* The points {1, 2, 3}represent a basic synchronization where only one row was required to be updated. The data transferred in this scenario is the data of one complete row transferred from client to server and the matrices involved. The performance is registered as less than 4% of the network usage.

C) *Worst Case:* The points {6,7} represent a scenario where the data of the whole table is transferred along with the matrices involved, which is the maximum possible data that can be transferred. The performance is registered as a maximum of 5% of the network usage.

VII. Related Work

Data consistency in replicated database systems is very important. This problem has been addressed by several works. In this section we introduce a few of these works that laid the groundwork for our algorithm to ensure this data consistency.

J. M. Monteiro [1] in 2007 proposed an update anywhere optimistic and centralized mechanism based on one-copy serializability and eventual consistency. However, for many database applications, serializability is too restrictive. This is the case of applications that access mobile databases. Indeed, the consistency degree may be traded for a potential gain in concurrency.

To overcome this problem, Alex Costa [2] in 2010 introduced a protocol, which guarantees data consistency of replicated databases in mobile computing based on dynamic monitoring and management of an acyclic conflict graph. His approach is known as the Temporal Serialization Graph Testing (TSGT) approach, which exploits temporal information with respect to the moment when a mobile transaction operation (read or write) is executed on a given database. This approach is based on transaction execution and is very complex to understand and implement.

D. W. K. Byung-Yun Lee, proposed the SyncML (Synchronization markup language) [3], scheme to synchronize contact and schedule information (personal information manager) between some type of handheld piece of equipment and a computer (personal, or network-based service), such as between a mobile phone and a personal computer. This is a complex but complete protocol specifically oriented to mobile systems, offering several synchronization modes. It uses XML format containing synchronization header and synchronization body to exchange

messages between client and server, which is complex, long and waste bandwidth with un-necessary xml tags, as compared to our matrix way of exchanging messages.

Inspired from SyncML, VicentSegu´ıPascual [4] in 2011, proposed an algorithm to synchronize contact information between the mobile and PC. It is simple and easy to implement, but not generic, since it only works with the contact information synchronization. It uses Synchronization Flags to mark the contact which needs to be synchronized. Synchronization flags do not work well when multiple devices reference the server.

Mi-Young Choi [5] proposed SAMD (Synchronization Algorithms based on Message Digest). The SAMD algorithm creates images at the server-side database. The rows needed for synchronization are selected by comparing two images using message digest tables by a mobile database. If the two images are dissimilar, the synchronization progresses according to the synchronization rule. It does not use triggers, stored procedures or timestamps, but standard SQL functions for synchronization. Two message digest tables need to be maintained at the server side and every time a hash comparison needs to be done which takes an extra storage and time. Calculation of message digests for every row whenever synchronization happens is also cumbersome. It performs synchronization based on SQL statements; users should be familiar with SQL to use the algorithm. The novelty of our MRDMS algorithm is – that it guarantees independence of the database vender and synchronization solution vender in a mobile business environment that has diverse mobile devices, mobile databases, and RDBMS. Madhu Ahluwalia [6] proposed synchronization of the source and target databases which is driven from the target's side and involve no changes to the source's schema or triggers. This algorithm groups tuples into partitions and compares hashes of matching source and target partitions before synchronizing only those partitions whose hashes do not match. This method works well when there are few changes to the database ;and row-level locking when fewer than 70% of the partitions are changed.

In 2012, Jan Sedivy [7] proposed a distributed, decentralized database for mobile devices, which was known as MC Synchronization (Mobile Cloud Synchronization).MC Synchronization allows users to save and synchronize data between their mobile devices and the cloud without any failure. It is an environment that handles a variety of situations, for instance, even when a data connection isn't available or when the user does not want to use the cloud. In such a case, the data is stored locally and the cloud database is updated when a network connection becomes available again. Data integrity is maintained via background synchronization in the database environment between the mobile and Web applications. However, it relies to a very large extent on Google's distributed file system which also necessitates that server database must reside on the Google app engine server. This imposes a serious restriction on the use of the protocol.

Based on these past works, we have developed a unique algorithm MRDMS that has a small overhead in communications and works efficiently for synchronization of replicated databases as discussed in section VI. It works with multiple updates on single fields of records across multiple devices both for separate and simultaneous syncing of devices with the server. It dynamically maintains data consistency and performs conflict resolution in an optimized manner. It provides synchronization integrity and minimizes data transfer to work with low bandwidth networks as well as with high bandwidth networks.

VIII. CONCLUSION

We have presented an algorithm, for synchronizing replicated databases on mobile devices with a centralized server along with minimum exchange of messages and hence maximum efficiency thus maintaining a consistency in the server database in an occasionally connected network. We have used timestamps to compare which user has recently made changes to a cell, thereby giving preference to a user who has recently made changes to a cell as compared to others. Comparison at cell level greatly reduces the occurrences of conflicts during synchronization. All the changes and time at which they are done by any user on their local databases are recorded and saved locally, which can then be synchronized with the server later at any time whenever network connectivity is available.

The MRDMS algorithm suggested in this work can be used for synchronization of replicated databases on mobiles to manage inventories in a large area with poor connectivity. A large disconnected area could mean a poor rural area in a developing country or a large urban area divided into distant locations which are not connected together and where inventories can be managed locally and later to be merged asynchronously and updates be done consistently. In this work we have taken an example of a livestock management system spread across a large area with poor connectivity. Other use cases could be attendance systems, agriculture etc.

Scalability is one parameter that this algorithm needs to be tested on in the future. Most of the testing until now has comprised of a maximum of 4 local devices. Stress testing of this algorithm with a greater number of devices would be required. The problem of device failure also needs to be addressed. The failure of the server has been addressed to some degree in our work, but recognizing local device failures need to be incorporated.

The algorithm, in the future is expected to incorporate replicated databases across many servers, each having a set of client devices. Currently, our client devices are limited to Android based devices, in the future, we hope to extend this to other platforms for a more generalized implementation, thus testing the robustness of our algorithm. Our algorithm possesses the characteristics of both Optimistic and Pessimistic Replication Algorithms. The repeated conflict resolution applied at the server end gives it pessimistic qualities, while no requirement for separate concurrency control mechanisms makes it optimistic. We hope to further improve its optimistic characteristics and efficiency by

introducing modification level conflict resolution, which would reduce the number of times conflict resolution is applied. Another future incorporation that we are working on is a security mechanism that maintains the integrity and authenticity of the data sent and received.

REFERENCES

[1] J. M. Monteiro, A. Brayner, S. Lifschitz, and M. Endler, "A Mechanism for Replicated Data Consistency in Mobile Computing Environment," Proceedings of the 22nd ACM Symposium on Applied Computing (SAC 2007), Seoul, Korea, 2007.

[2] Alex Costa, Jose Maria Monteiro, Angelo Brayner, "A Distributed Protocol for Ensuring Replicated Database Consistency in Mobile Computing Environments,"in SAC '10 Proceedings of the ACM Symposium on Applied Computing, 2010,pp.1688-1693.

[3] D.-W. K. Byung-Yun Lee, Tae-Wan Kim and H. Choi, "Data synchronization protocol in mobile computing environment using syncml," in 5th IEEE International Conference on High Speed Networks and Multimedia Communications, Nov. 2002,pp. 133–137.

[4] VicentSegu´ıPascual, FatosXhafa, "Contact Synchronization for the Android Platform," in International Conference on P2P, Parallel, Grid, Cloud and Internet Computing,2011,pp.156-162.

[5] Mi-Young Choi, Eun-Ae Cho, Dae-Ha Park, Chang-Joo Moon, Doo-Kwon Baik, "A Database Synchronization Algorithm for Mobile Devices," in IEEE Transactions on consumer Electronics, Vol. 56, No. 2, May 2010,pp. 392-398.

[6] MadhuAhluwalia, Ruchika Gupta, AryyaGangopadhyay,YelenaYesha, "Target-Based Database Synchronization", in SAC '10 Proceedings of the ACM Symposium on Applied Computing,2010,pp.1643-1647

[7] Jan Sedivy, Tomas Barina, Ion Morozan, Andreea Sand, "MC synchronization– Distributed,Decentralized Database for Mobile Devices," in Cloud Computing in Emerging Markets (CCEM), IEEE International Conference, October 2012,pp. 1-6.

[8] VicentSegu´ıPascual, FatosXhafa, "Contact Synchronization for the Android Platform," in International Conference on P2P, Parallel, Grid, Cloud and Internet Computing,2011,pp.156-162.

[9] Chia-Chi Teng, Kevin Brown, Craig Caro, Whitney Nielsen, Jason Wells, "A Service Oriented Livestock Management System Using Occasionally Connected Mobile-Cloud Architecture", in Systems Conference (SysCon), IEEE International,2012,pp.1-5.

[10] Adam Trevarthen and Katina Michael, "The RFID-Enabled Dairy Farm: Towards Total Farm Management," in 7th International Conference on Mobile Business, pp.241-250.

[11] MadhuAhluwalia, Ruchika Gupta, AryyaGangopadhyay,YelenaYesha, "Target-Based Database Synchronization", in SAC '10 Proceedings of the ACM Symposium on Applied Computing,2010,pp.1643-1647.

[12] Archana Sharma, Dr. VineetKansal, "Replication Management and Optimistic Replication challenges in Mobile Environment," in International Journal of Database Management Systems (IJDMS) Vol.3, No.4, November 2011

[13] Yasushi Saito, Marc Shapiro, "Replication: Optimistic Approaches," in Internet Systems and Storage Laboratory HP Laboratories Palo AltoW.

[14] Alexander Stage, "Synchronization and Replication in the context of Mobile Applications(Unpublished work style)," unpublished.

Physica B ■ (■■■■) ■■■–■■■

Contents lists available at ScienceDirect

Physica B

journal homepage: www.elsevier.com/locate/physb

Multiferroic properties of $BiFeO_3/BaTiO_3$ multilayered thin films

Savita Sharma [a,c], Monika Tomar [b], Ashok Kumar [d], Nitin K. Puri [c], Vinay Gupta [a,*]

[a] Department of Physics and Astrophysics, University of Delhi, Delhi 110007, India
[b] Physics Department, Miranda House, University of Delhi, Delhi 110007, India
[c] Department of Applied Physics, Delhi Technological University, Delhi 110042, India
[d] CSIR—National Physical Laboratory, Dr. K.S. Krishnan Marg, New Delhi 110012, India

ARTICLE INFO

Keywords:
Multilayer
Multiferroic
Ferroelectric
Ferromagnetic

ABSTRACT

Multilayered structures of multiferroic $BiFeO_3$ (BFO) and ferroelectric $BaTiO_3$ (BTO) have been fabricated using pulsed laser deposition (PLD). Ferromagnetic and ferroelectric properties of the multilayered system (BFO/BTO) have been investigated. It could be inferred that the magnetization increases with the incorporation of BTO buffer layer, which indicates a coupling between the ferroelectric and ferromagnetic orders. Vibrating sample magnetometer (VSM) measurements performed on the prepared multiferroic samples show that the magnetization is significantly increased (M_s=56.88 emu/cm^3) for the multilayer system with more number of layers (four) keeping the total thickness of the multilayered system constant (350 nm) meanwhile maintaining the sufficiently enhanced ferroelectric properties (P_r=29.68 μC/cm^2).

© 2014 Published by Elsevier B.V.

UNCORRECTED PROOF

1. Introduction

Multiferroic materials, in which both electric and magnetic polarizations coexist, have recently attracted the attention of research community because of its technological applications such as information storage and sensors taking advantage of two coupled ferroic properties [1]. Bismuth ferrite, $BiFeO_3$, (BFO) is one of the most important multiferroic materials, in which ferroelectricity (T_C: 850 °C) and antiferromagnetic (T_N: 370 °C) properties coexist at room temperature [2–4]. Weak ferromagnetism is additionally expected in this compound but as a result of a long range cycloidal spin structure there is no net magnetization. Net non-zero magnetization may be induced in BFO thin films by epitaxial strain [5], or by doping on the perovskite A-site or B-site [6,7]. Barium titanate, ($BaTiO_3$), (BTO) is also an interesting and widely studied perovskite material with excellent ferroelectric properties (T_C:120 °C). Since, pure-phase BFO with sufficiently enhanced ferroelectric properties is very difficult to obtain due to its large leakage current, BFO mixed with other ferroelectrics, such as $BaTiO_3$ (BTO) may result in enhanced multiferroic properties [8–10]. BFO–BTO systems have been widely studied in which both ferroelectric and ferromagnetic properties exist in the same phase at room temperature [10]. These materials have found a number of potential applications owing to their two coupled ferroic properties due to local off-centered crystal distortion and electron spin [10,2]. An alternative method has also been adopted to control the multiferroic properties of BFO by fabricating multilayered structures consisting of alternating BFO and BTO epitaxial layers. Magnetic properties of multiferroic bi-layer BFO/BTO thin films have already been studied. However not much efforts have been made to study both magnetic and ferroelectric properties simultaneously in BFO/BTO multilayered system and also the reported results for magnetization are not remarkable enough [11,12]. Pulsed laser deposition (PLD) technique is one of the most popular methods adopted for the growth of multicomponent oxide thin films because it ensures good stoichiometry, high deposition rate and purity, ease of fabrication of multilayered structures and epitaxial films at relatively low cost [13]. So, in the present study, two excellent ferroic materials with same structure (perovskite structure:ABO_3) BTO and BFO have been used to improve the multiferroic properties of the BFO/BTO multilayered structures prepared on $Pt/Ti/SiO_2/Si$ substrate using PLD technique. A systematic study of the magnetic and ferroelectric properties of the BFO/BTO multilayered system has been performed. The magnetization as well as ferroelectric properties of multilayered thin films have been correlated with the number of layers involved in the structure.

2. Experimental

Both BFO and BTO ceramic targets were prepared by conventional solid state reaction method. Bi_2O_3, Fe_2O_3 and $BaCO_3$, TiO_2

* Corresponding author.
E-mail address: drguptavinay@gmail.com (V. Gupta).

http://dx.doi.org/10.1016/j.physb.2014.03.089
0921-4526/© 2014 Published by Elsevier B.V.

powders of 99.9% purity were used for the fabrication of BFO and BTO targets, respectively. 20% Bi-excess was used in BFO target to avoid the Bi loss which occurs during the high temperature growth due to volatile nature of Bi. The powders were ball-milled separately, pressed into discs of one inch diameter and sintered at 850 °C and 1250 °C to make the BFO and BTO pellets, respectively. The pellets were polished and mounted on the target holders.

The ceramic targets were ablated using a Nd:YAG pulsed laser (wavelength of 266 nm at 4th harmonic) and the multilayered thin films of BFO/BTO were deposited on Pt/Ti/SiO_2/Si substrates. Pt metal thin layer of 70 nm thickness was deposited over the passivated Si (SiO_2/Si) substrate by E-beam evaporation technique, a buffer layer of Ti (20 nm) was deposited in-situ over SiO_2/Si substrate prior to Pt deposition to improve the adhesion of Pt on SiO_2/Si substrate. Typical PLD deposition conditions are summarized in Table 1. Total thickness of the multilayered structures was kept fixed at 350 nm with varying number and thickness of individual BTO and BFO layers at a substrate temperature of 750 °C. Thickness of (BFO/BTO) multilayered thin films was measured using surface profiler (Dektak 150). The number of layers were varied from two to four and whilst keeping BTO as the bottom layer (BFO/BTO/Pt/SiO_2/Si, BTO/BFO/BTO/Pt/SiO_2/Si and BFO/BTO/BFO/BTO/Pt/SiO_2/Si). For the ferroelectric measurements also passivated Si substrate having (1 0 0) orientation [SiO_2/Si (1 0 0)] has been used. The Pt/Ti bilayer has been fabricated on SiO_2/Si surface prior to the deposition of BFO/BTO multilayer system. The ferroelectric measurements have been made in MIM configuration where Pt/Ti deposited on SiO_2/Si was considered as bottom electrode. Au circular dots (600 μm diameter, 40 nm thickness) were deposited by thermal evaporation technique through a shadow mask for the top electrodes on the surface of multilayered thin films of BFO/BTO.

The schematic of the MIM capacitor configuration (Au/BFO/BTO/BTO/Pt/SiO_2/Si) is shown in Fig. 1.

For the magnetic measurements, multilayered thin film samples were prepared on Si (1 0 0) substrate separately under the similar deposition conditions. The corresponding magnetic hysteresis loops were measured at room temperature using the vibrating sample magnetometer.

Structural characterization of films was carried out using X-ray diffraction (XRD) analysis (Bruker D8). A Radiant Technology Precision ferroelectric workstation was used to measure the room temperature ferroelectric polarization hysteresis of the prepared samples in MIM capacitor configuration at a frequency of 1 kHz and at an applied bias of 10 V.

3. Results and discussion

Fig. 2 shows the XRD pattern of the prepared two layered (BFO/BTO/Si); three layered (BTO/BFO/BTO/Si) and four layered (BFO/BTO/BFO/BTO/Si) structures. For comparison, XRD patterns of the single layer BFO and BTO thin films fabricated under identical conditions have also been included. It may be seen that the individual films are polycrystalline having rhombohedral distorted structure for BFO and tetragonal structure for BTO. XRD pattern of the multilayered thin films (BFO/BTO/Si, BTO/BFO/BTO/Si and BFO/BTO/BFO/BTO/Si) reveals that all the peaks corresponds to either BFO or BTO only. The absence of any addition XRD peak clearly ruled out the possibility of the formation of any secondary phase in any of the prepared systems. Furthermore, splitting of the peaks at $2\theta=45^\circ$ corresponding to BTO can be easily observed for all the multilayered structures. The split XRD peaks so observed in the present case indicate that the BTO possess tetragonal structure. The XRD peak at $2\theta=54^\circ$ corresponds to (3 0 0) plane of BFO which has been found to shift towards the lower angle ($2\theta\sim54^\circ$) in all prepared multilayered structures (BFO/BTO) in comparison to the corresponding bulk value ($2\theta\sim55^\circ$). The observed shift is due to the induced tensile strain in the BFO unit cell due to presence of underneath BTO layer in the multilayered structure, that lead to slight expansion in the lattice parameter of BFO film.

Fig. 3 shows the typical ferroelectric P–E hysteresis loops of the mutilayered thin films at an applied bias of 10 V and 1 kHz frequency. It may be seen that the ferroelectric properties of the multilayered structures are enhanced with the increase in number of layers. Four layered system (Au/BFO/BTO/BFO/BTO/Pt/Ti/SiO_2/Si) exhibits the maximum saturation polarization of about 50.49 μC/cm^2. Such an enhanced response obtained in the multilayered structure may

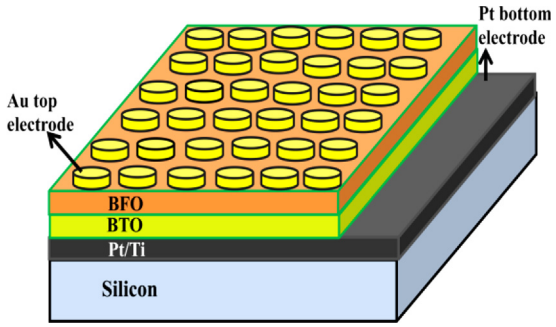


Fig. 1. MIM Capacitor configuration of the BFO/BTO Multilayer thin film with Au top electrodes deposited on Pt/Ti/SiO_2/Si substrates.

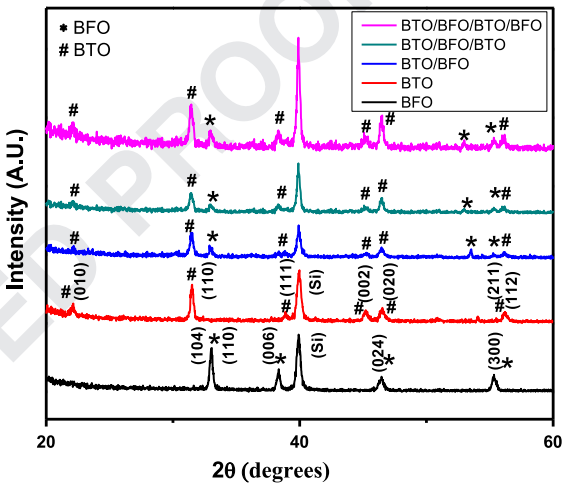


Fig. 2. XRD patterns of two layered (BFO/BTO/Si); three layered (BTO/BFO/BTO/Si) and four layered (BFO/BTO/BFO/BTO/Si) thin film structures along with the XRD patterns of BFO and BTO thin films.

Table 1
PLD processing conditions for the growth of BFO/BTO multilayered thin film.

Parameters	Deposited conditions
Targets	20% Bi-excess BFO, BTO
Substrate	Pt/Ti/SiO_2/Si
Substrate temperature	750 °C
Deposition pressure	200 mT
T–S distance	4.5 cm
Laser type	Nd:YAG (266 nm)
Pulse repetition rate	10 Hz
Fluence	120 mJ

UNCORRECTED PROOF

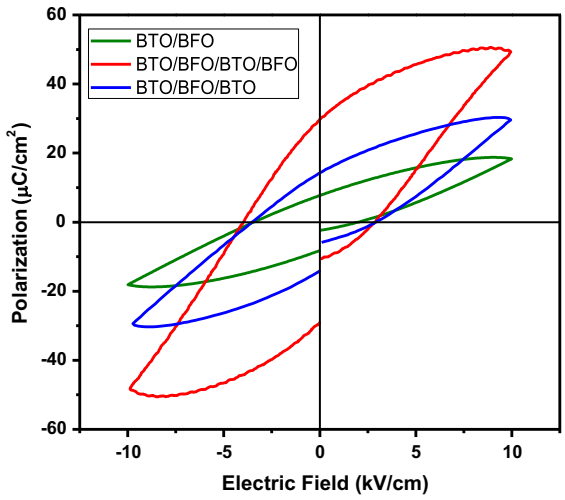


Fig. 3. PE hysteresis loops of the two layer, three layer and four layer multilayered thin film.

Table 2
Values of remnant polarization (P_r), saturation polarization (P_s), coercive field (E_c) and saturation magnetization (M_s) for the fabricated multilayered thin films.

Multilayered thin film structures	Remnent polarization (P_r) (μC/cm^2)	Saturation polarization (P_s) (μC/cm^2)	Saturation magnetization (M_s) (emu/cm^3)	Coercive field ($2E_c$) (kV/cm)
Bilayer BFO/BTO	7.62	18.60	28.47	5.42
Trilayer BTO/BFO/BTO	14.30	30.23	38.06	6.41
Four layer BFO/BTO/BFO/BTO	29.68	50.49	56.88	6.84

be related to the presence of BTO layer. Furthermore, the observed asymmetry in the hysteresis loops is attributed to the presence of different electrodes creating barrier at the interface of the metal with the insulating layer. The obtained values of P_r, P_s and E_c for all the multilayered structures are summarized in Table 2.

The magnetic hysteresis loops for the prepared multilayered structures at room temperature are presented in Fig. 4. It may be clearly seen that well defined magnetic hysteresis loops are observed for all the multilayered structures with continuous enhancement in remnant polarization (P_r) with the number of layers in the multilayered structure. The value of saturation magnetization for a four-layer system (BFO/BTO/BFO/BTO/Si) is found to be higher (56.88 emu/cm^2) than those reported earlier for the BTO/BFO multilayered thin film systems [12]. The enhanced magnetization obtained in the four layered system may be due to the intervening BTO layer which created constraint at each interface with the BFO film, resulting in a strong coupling between ferroelectric and magnetic orders. This results in an enhancement in the multiferroic properties of the multilayered structure that leads to an increase in the coercive field as well as the saturation magnetization [12]. It is interesting to note that the coercive field is same for all the samples. The values of saturation magnetization of all the structures are included in Table 2 for comparison.

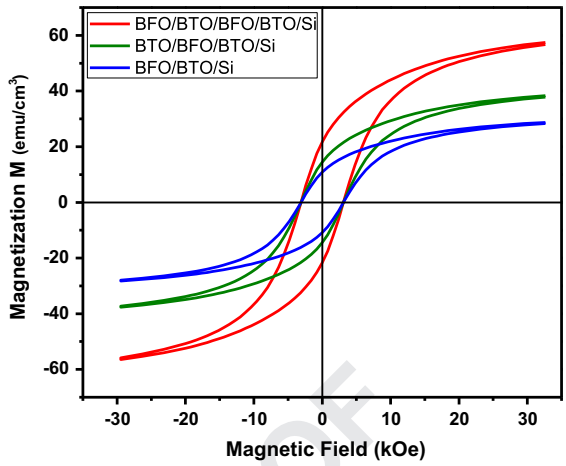


Fig. 4. Variation of room temperature magnetization with applied magnetic field (M–H) of BTO/BFO multilayered thin film structures.

4. Conclusion

In the present study, BFO/BTO multi-layered thin film structures have been fabricated using PLD technique. Multiferroic properties of multilayered thin films were studied and were found to exhibit both ferroelectricity and ferromagnetism simultaneously at room temperature which got enhanced (P_s=50.49 μC/cm^2 and M_s=56.88 emu/cm^3 for the four layer system) with the increase in the number of layers in the multilayered system. The enhanced magnetization and saturation polarization may be attributed to intervening BTO layer creating constraint and demonstrating multiferroic coupling between ferroelectric and magnetic orders.

Acknowledgements

Authors are thankful to Department of Science and Technology (DST) for the financial support. One of the authors (SS) is thankful to the Delhi Technological University (DTU) for the teaching assistantship.

References

[1] M. Figbig, T. Lottermoser, D. Frohlich, A.V. Golstev, R.V. Pisarev, Nature 419 (2002) 818.
[2] W. Eerenstein, N.D. Mathur, J.F. Scott, Nature 442 (2006) 759.
[3] P. Fischer, M. Polomska, I. Sosnowska, M. Szymanski, J. Phys. C: Solid State Phys. 13 (1980) 1931.
[4] S. Gupta, A. Sharma, M. Tomar, V. Gupta, M. Pal, J. Appl. Phys. 111 (2012) 064110.
[5] F. Bai, J. Wang, M. Wuttig, J.F. Li, N. Wang, A. Pyatakov, A.K. Zvezdin, L.E. Cross, D. Viehland, Appl. Phys. Lett. 86 (2005) 032511.
[6] V.A. Khomchenko, D. Kiselev, J.M. Vieira, R.M. Rubinger, N.A. Sobolev, M. Kopcewicz, V.V. Shvartsman, P. Borisov, W. Kleemann, A.L. Kholkin, J. Phys. Condens. Matter 20 (2008) 102003.
[7] V.A. Khomchenko, D. Kiselev, J.M. Vieira, Y.G. Pogorelov, J.P. Araujo, M. Maglione, A.L. Kholkin, J. Phys. D: Appl. Phys. 41 (2008) 155207.
[8] S.J. Kim, S.H. Han, H.G. Kim, A.Y. Kim, J.S. Kim, C.I. Cheon, J. Korean Phys. Soc. 56 (1) (2010) 439.
[9] N.G. Kim, Y.S. Koo, J.H. Jung, J. Magn. 11 (2006) 164.
[10] M. Kumar, A. Srinivas, S.V. Suryanarayana, J. Appl. Phys. 87 (2) (2000) 855.
[11] H. Toupet, V.V. Shvartsman, F. Lemarrec, P. Borisov, W. Kleemann, M. Karkut, Integr. Ferroelectr. 100 (2008) 165.
[12] P. Yang, K.M. Kim, J.Y. Lee, J. Zhu, H.Y. Lee, Integr. Ferroelectr. 113 (2009) 26.
[13] J. Schou, Appl. Surf. Sci. 255 (2009) 5191.

UNCORRECTED PROOF

Hindawi Publishing Corporation
Conference Papers in Science
Volume 2014, Article ID 683219, 5 pages
http://dx.doi.org/10.1155/2014/683219

Conference Paper

NO_2 Sensing Properties of WO_3 Thin Films Deposited by Rf-Magnetron Sputtering

Savita Sharma,[1,2] Monika Tomar,[3] Nitin K. Puri,[2] and Vinay Gupta[1]

[1] *Department of Physics and Astrophysics, University of Delhi, Delhi 110007, India*
[2] *Department of Applied Physics, Delhi Technological University, Delhi 110042, India*
[3] *Physics Department, Miranda House, University of Delhi, Delhi 110007, India*

Correspondence should be addressed to Vinay Gupta; drguptavinay@gmail.com

Received 8 February 2014; Accepted 11 March 2014; Published 10 April 2014

Academic Editors: P. Mandal, R. K. Shivpuri, and G. N. Tiwari

This Conference Paper is based on a presentation given by Savita Sharma at "National Conference on Advances in Materials Science for Energy Applications" held from 9 January 2014 to 10 January 2014 in Dehradun, India.

Copyright © 2014 Savita Sharma et al. This is an open access article distributed under the Creative Commons Attribution License, which permits unrestricted use, distribution, and reproduction in any medium, provided the original work is properly cited.

Tungsten trioxide (WO_3) thin films were deposited by Rf-magnetron sputtering onto Pt interdigital electrodes fabricated on corning glass substrates. NO_2 gas sensing properties of the prepared WO_3 thin films were investigated by incorporation of catalysts (Sn, Zn, and Pt) in the form of nanoclusters. The structural and optical properties of the deposited WO_3 thin films have been studied by X-ray diffraction (XRD) and UV-Visible spectroscopy, respectively. The gas sensing characteristics of all the prepared sensor structures were studied towards 5 ppm of NO_2 gas. The maximum sensing response of about 238 was observed for WO_3 film having Sn catalyst at a comparatively lower operating temperature of 200°C. The possible sensing mechanism has been highlighted to support the obtained results.

1. Introduction

Nitrogen dioxide (NO_2) is one of the most harmful gases to the ecosystem and provides a major contribution to air pollution [1]. The detection of NO_2 is crucial for monitoring environmental pollution resulting from combustion processes, particularly industrial emissions or vehicle exhaust [2]. Occupational Safety and Health Administration (OSHA, United States Department of Labour) declares the Permissible Exposure Limit (PEL) of NO_2 gas as 5 ppm for general industries and 20 ppm as Immediately Dangerous to Life or Health Concentrations (IDLHs) [3]. NO_2 gas is the main precursor for ozone layer depletion in lower atmosphere and also produces acid rain which is slowly damaging the ecosystem. Commercially, many NO_2 gas sensors are available in the market but they have poor sensitivity, high operating temperature, bulky size and are very costly. Thus, there is an urgent requirement of cheap, highly sensitive and selective NO_2 gas sensors which could be operated at lower operating temperature.

Gas sensors based on metal oxide semiconductors are used in a wide variety of applications including gas monitoring and detection applications [4–6]. Considerable research has been carried out on the development of chemical sensors based on semiconductor metal oxides such as SnO_2, ZnO, and TiO_2 because of their high sensitivity towards many reducing as well as oxidizing gases [7–9]. Tungsten trioxide has attractive electrical properties and reactivity to oxidizing gases making it one of the best candidates for gas sensing applications [10–12]. The tungsten trioxide (WO_3) thin films and nanostructures are seen to be an excellent candidate for NO_2 gas detection [13, 14] because the W transition metal is found to be with different oxidation states (W^{5+}, W^{6+}) enhancing the oxidizing power of NO_2 gas molecules onto the surface of WO_3 metal oxide. Thus, in the present work, WO_3 thin film based gas sensors have been exploited for the trace level (5 ppm) detection of NO_2 gas. Effect of different catalysts (Sn, Zn, and Pt) incorporated on the surface of SnO_2 thin film in the form of nanoclusters has also been studied for NO_2 gas detection.

Table 1: Deposition parameters for WO_3 thin film using Rf magnetron sputtering.

Target	W metal target (99.999% pure)
Substrate	IDE/corning glass; corning glass
Target to substrate distance	6 cm
Sputtering pressure	10 mT
RF power	50 Watt
Gas composition ($Ar : O_2$)	60 : 40

2. Experimental Details

WO_3 thin film has been deposited by Rf-magnetron sputtering technique using a 2-inch W metal target (99.999% pure) in a reactive gas ambient of Ar and O_2 gas mixture. WO_3 thin films were fabricated onto the corning glass substrates patterned with Pt interdigital electrodes (IDEs). The description of fabrication of Pt IDEs has been mentioned elsewhere [9]. The typical growth conditions used for the deposition of WO_3 thin film are summarized in Table 1. WO_3 thin films were deposited under the growth pressure of 10 mTorr with argon to oxygen ratio of 60 : 40 by applying a Rf power of 50 W.

For the formation of nanocrystalline WO_3 thin film, in situ annealing was carried out at a substrate temperature of 400°C for 1 hour in 60% Ar: 40% O_2 environment. In order to get the enhanced sensing response characteristics, Sn, Zn, and Pt metal catalysts were incorporated onto the surface of WO_3 thin film in the form of nanoclusters on separate sensors. Sn, Zn, and Pt were also deposited using sputtering technique using their respective metal targets under the sputtering pressure of 10 mT and in 100% argon gas ambient. Nanoclusters of metal catalysts were deposited using a shadow mask of uniformly distributed pores of 600 μm diameter onto the surface of WO_3 thin film. X-ray diffraction (XRD) study was carried out using Bruker D-8 X-ray diffractometer. Optical properties have been studied via UV-visible spectrophotometer (Lambda 35). WO_3 film thickness was measured using surface thickness profiler (DEKTAK 150). Gas sensing characteristics of the prepared WO_3 thin film based sensors were studied in a specially designed "Gas Sensor Measurement and Calibration System (GSMCS)." Changes in the sensor resistance were recorded after every second using a digital multimeter (Keithley 2700) interfaced with computer. The sensing response of prepared WO_3 thin film based structures was calculated using the relation: $S = R_g/R_a$, where R_g is the resistance of sensor in the presence of target NO_2 gas and R_a is the resistance of the sensor in the absence of target NO_2 gas.

3. Results and Discussion

Figure 1 shows the X-ray diffraction (XRD) spectra of WO_3 thin films deposited on corning glass substrate at a substrate temperature of 400°C. The XRD spectra show the formation of orthorhombic structure (JCPDS Card no. 35-0270) of WO_3 and do not show the presence of any other secondary phase indicating the growth of single phase and polycrystalline

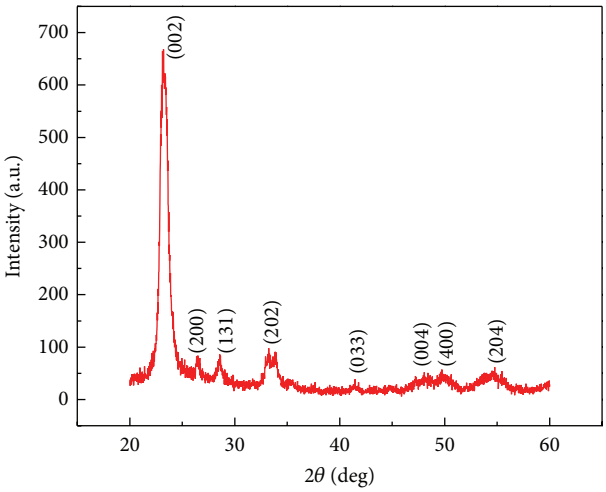


Figure 1: XRD patterns of the WO_3 thin film.

WO_3 thin films. It is observed from Figure 1 that reflection corresponding to (002) plane is dominant and is relatively intense indicating preferential orientation of the deposited WO_3 thin film. The crystallite size calculated from the Debye Scherrer formula is found to be 17.73 nm which is relatively small leading to increase in grain boundaries suitable for gas sensing applications.

UV-visible transmission spectra of annealed WO_3 thin film deposited over corning glass substrate were measured in the wavelength range of 190 to 1100 nm and are shown in Figure 2(a). It can be seen that the film is highly transparent (88%) in the visible region showing good optical quality and low absorption losses. The presence of fringes at higher wavelength confirms that the prepared WO_3 thin film is free from any inhomogeneity. The onset of sharp fundamental absorption edge at about 310 nm was observed in the deposited WO_3 thin films (Figure 2(a)).

The Tauc plot of $(\alpha h\nu)^2$ versus photon energy ($h\nu$) (where α is absorption coefficient, h is planks constant, and ν is frequency of the incident radiation) of the WO_3 thin film deposited at 10 mT sputtering pressure is shown in Figure 2(b). Optical bandgap of the WO_3 thin film was calculated from the linear portion of the Tauc plot. Linear region is clearly seen in Figure 2(b) at $h\nu > 3.5$ eV for WO_3 thin film which is in accordance with the well-known absorption law $\alpha h\nu \sim (h\nu - E_g)^{1/2}$ being characteristic for direct optical transitions. Estimated value of bandgap of the WO_3 thin film is found to be 3.90 eV and is close to the reported value [15].

Figure 3 shows the variation of sensing response of all the prepared WO_3 thin film based sensor structures (WO_3, WO_3/Sn, WO_3/Zn, and WO_3/Pt) as a function of temperature towards 5 ppm of NO_2 gas. It is observed that the value of resistance of the sensors in the presence of air (R_a) increases to a higher stable value (R_g) when target NO_2 gas is inserted into chamber due to the oxidising nature of NO_2. When the NO_2 gas is flushed out of the chamber, all the fabricated sensors retain their original high resistance value (R_a).

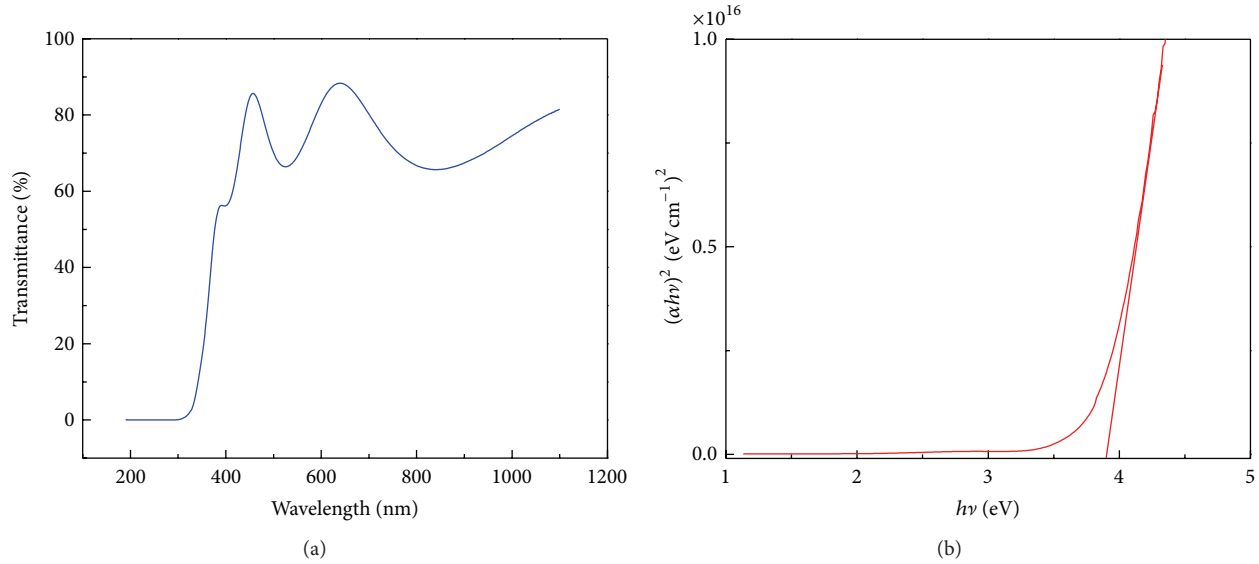


FIGURE 2: (a) UV-visible transmittance spectra of the WO_3 thin film prepared on corning glass substrate. (b) Tauc Plot of WO_3 thin film.

TABLE 2: Sensor response, response time, and recovery time at their respective operating temperatures for the fabricated sensor structures.

Sensor	Sensor response	Operating temperature (°C)	Response time	Recovery time
WO_3/Sn	238	200	32 sec	15.3 min
WO_3/Zn	173	250	5.2 min	18 min
WO_3/Pt	118	270	4.6 min	17 min

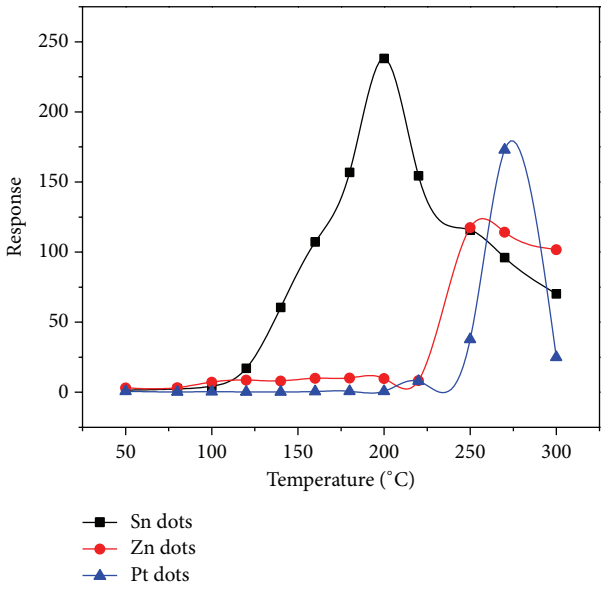


FIGURE 3: Variation of sensor response with temperature for the sensor structures: WO_3/Sn, WO_3/Zn, and WO_3/Pt towards 5 ppm of NO_2 gas.

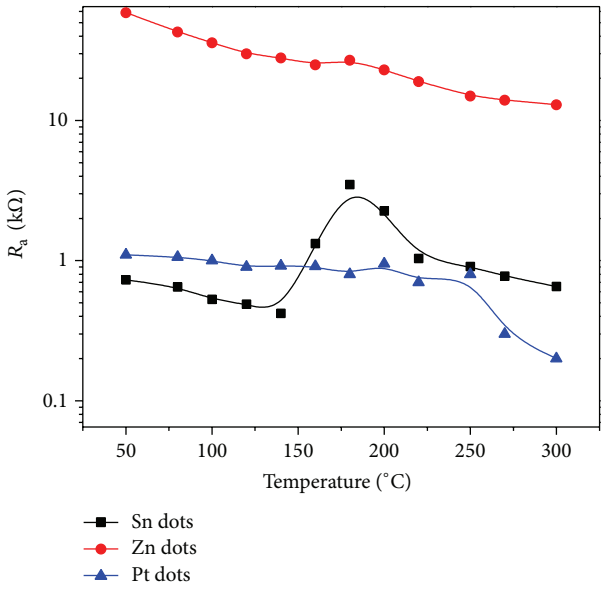


FIGURE 4: Variation of sensor resistance in air (R_a) with temperature for the sensor structures: WO_3/Sn, WO_3/Zn, and WO_3/Pt.

Figures 4 and 5 show the variation of sensor resistance in the presence of air (R_a) and in the presence of NO_2 gas (R_g), respectively, with temperature for all the prepared sensors (WO_3/Pt, WO_3/Sn, and WO_3/Zn nanoclusters). It can be observed from Figures 4 and 5 that the value of R_a and R_g decreases with increase in temperature. When NO_2 gas interacts with the sensor surface at a particular

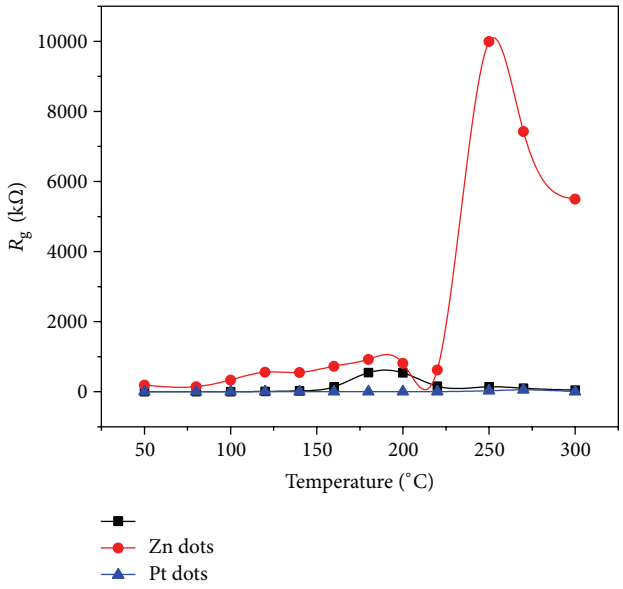


FIGURE 5: Variation of sensor resistance in the presence of 5 ppm NO_2 gas with temperature for sensor structures: WO_3/Sn, WO_3/Zn, and WO_3/Pt.

temperature, the value of resistance increases from R_a to R_g. The maximum increase in the value of R_g is observed for WO_3/Zn nanoclusters sensor structure; however, the higher value of R_a as compared to other sensor structures restricts the further enhancement in sensing response. Moreover, the maximum sensor response has been observed for WO_3/Sn sensor structure which may be attributed to the possible spillover of NO and O^- species onto the uncovered surface of WO_3 thin film. It can be observed from Figure 3 that the maximum sensing response of ~238 has been obtained for the WO_3/Sn sensor at a low operating temperature of 200°C. The obtained sensor response for all the sensors with response and recovery speeds at their respective operating temperatures is summarized in Table 2. It may be seen that the WO_3/Sn sensor exhibits comparatively high sensing response with fast response and recovery speeds at low operating temperature of 200°C. WO_3/Pt and WO_3/Zn sensors show a moderate response of 118 and 173, respectively, at high operating temperatures of 270°C and 250°C, respectively. For WO_3/Sn sensors, NO_2 gas reacts with free Sn sites as well in the similar way as with W sites and captures electrons thus giving a high sensor response [14]. NO_2 gas on interaction with Sn nanoclusters gets converted into NO and O^- species which spill over the WO_3 surface and captured electrons from WO_3 thin film thereby increasing sensing response.

4. Conclusion

The enhanced sensing response of 238 towards 5 ppm of NO_2 was obtained for WO_3/Sn sensor structure at a low operating temperature of 200°C as compared to other fabricated sensors, namely, WO_3/Zn, WO_3/Pt, and WO_3. Enhanced sensing response for WO_3/Sn sensor structure is attributed to the spillover of NO_2 species over WO_3 surface thus enhancing the adsorption of NO_2 gas on the sensor surface that leads to an increased sensor response.

Conflict of Interests

The authors declare that there is no conflict of interests regarding the publication of this paper.

Acknowledgments

The authors are thankful to the Department of Science and Technology (DST) and GAIL India Ltd. for the financial support to carry out this work. One of the authors (Savita Sharma) is thankful to the Delhi Technological University (DTU) for the teaching assistantship.

References

[1] B. T. Marquis and J. F. Vetelino, "A semiconducting metal oxide sensor array for the detection of NO_x and NH_3," *Sensors and Actuators B: Chemical*, vol. 77, no. 1-2, pp. 100–110, 2001.

[2] L. Shi, Y. Hasegawa, T. Katsube, K. Onoue, and K. Nakamura, "Highly sensitive NO_2 gas sensor fabricated with RF induction plasma deposition method," *Sensors and Actuators B: Chemical*, vol. 99, no. 2-3, pp. 361–366, 2004.

[3] http://www.osha.gov/.

[4] K. Potje-Kamloth, "Semiconductor junction gas sensors," *Chemical Reviews*, vol. 108, no. 2, pp. 367–399, 2008.

[5] D. E. Williams, "Semiconducting oxides as gas-sensitive resistors," *Sensors and Actuators B: Chemical*, vol. 57, no. 1–3, pp. 1–16, 1999.

[6] W. Göpel and K. D. Schierbaum, "SnO_2 sensors: current status and future prospects," *Sensors and Actuators B: Chemical*, vol. 26, no. 1–3, pp. 1–12, 1995.

[7] L. Liu, T. Zhang, L. Wang, and S. Li, "Improved ethanol sensing properties of Cu-doped SnO_2 nanofibers," *Materials Letters*, vol. 63, no. 23, pp. 2041–2043, 2009.

[8] Y. Wang, W. Jia, T. Strout et al., "Ammonia gas sensor using polypyrrole-coated TiO_2/ZnO nanofibers," *Electroanalysis*, vol. 21, no. 12, pp. 1432–1438, 2009.

[9] A. Sharma, M. Tomar, and V. Gupta, "SnO_2 thin film sensor with enhanced response for NO_2 gas at lower temperatures," *Sensors and Actuators B: Chemical*, vol. 156, no. 2, pp. 743–752, 2011.

[10] C. Zhang, M. Debliquy, A. Boudiba, H. Liao, and C. Coddet, "Sensing properties of atmospheric plasma-sprayed WO_3 coating for sub-ppm NO_2 detection," *Sensors and Actuators B: Chemical*, vol. 144, no. 1, pp. 280–288, 2010.

[11] C. Zhang, A. Boudiba, C. Navio et al., "Highly sensitive hydrogen sensors based on co-sputtered platinum-activated tungsten oxide films," *International Journal of Hydrogen Energy*, vol. 36, no. 1, pp. 1107–1114, 2011.

[12] A. Boudiba, C. Zhang, C. Navio, C. Bittencourt, R. Snyders, and M. Debliquy, "Preparation of highly selective, sensitive and stable hydrogen sensors based on Pd-doped tungsten trioxide," *Procedia Engineering*, vol. 5, pp. 180–183, 2010.

[13] P. V. Tong, N. D. Hoa, V. V. Quang, N. V. Duy, and N. V. Hieu, "Diameter controlled synthesis of tungsten oxide nanorod bundles for highly sensitive NO_2 gas sensors," *Sensors and Actuators B*, vol. 183, pp. 372–380, 2013.

[14] A. Sharma, M. Tomar, and V. Gupta, "Low temperature operating SnO_2 thin film sensor loaded with WO_3 micro-discs with enhanced response for NO_2 gas," *Sensors and Actuators B: Chemical*, vol. 161, no. 1, pp. 1114–1118, 2012.

[15] A. Paliwal, A. Sharma, M. Tomar, and V. Gupta, "Optical properties of WO_3 thin films using surface plasmon resonance technique," *Journal of Applied Physics*, vol. 115, no. 4, Article ID 043104, 2014.

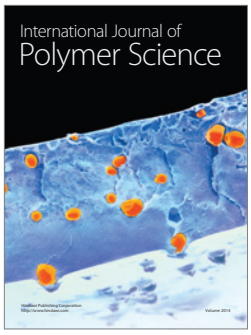


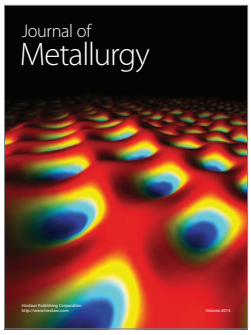




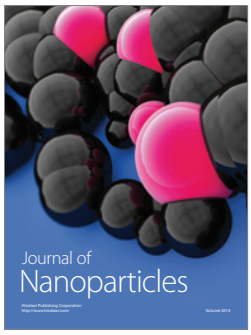


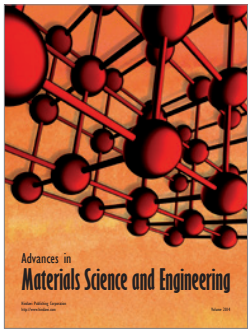


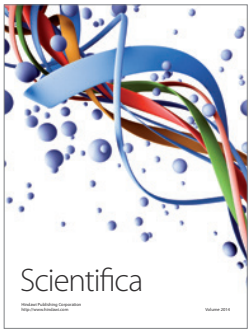


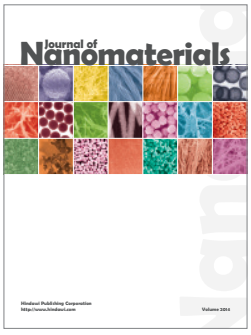


























Hindawi
Submit your manuscripts at
http://www.hindawi.com

International Journal of Current Engineering and Technology
E-ISSN 2277 – 4106, P-ISSN 2347 - 5161
©2014 INPRESSCO®, All Rights Reserved
Available at http://inpressco.com/category/ijcet

Research Article

Optimization of Process Parameters for Gas Tungsten Arc Welding of AA1100 Aluminium Alloy

Vijay Gautam[Á*]

[Á]Department of Mechanical Engineering, Delhi Technological University, Delhi, India.

Accepted 10 April 2014, Available online 15 April 2014, **Vol.4, No.2 (April 2014)**

Abstract

This paper aims at optimization of process parameters for gas tungsten arc welding (GTAW) of sheet samples of Aluminium alloy AA1100 using AC wave with Argon as inert gas. Tensile properties of parent and welded specimens were determined as per ASTM-E8M standard. Taguchi approach was applied to determine most influential control parameters which will yield better tensile strength of the joints of GTAW welded Aluminium alloy AA1100. Taguchi design was followed by ANOVA and Regression analysis to determine the effect of the individual parameters and a suitable combination was found out. The predicted optimum value of tensile strength of the weld joint is 91.35 MPa which was further confirmed by experiments and found to be in close agreement.

Keywords*: Aluminium alloy AA1100, Pulsed GTAW, Taguchi Approach, ANOVA, Regression, Tensile strength.*

1. Introduction

Aluminium is the world's most abundant metal and is the third most common element, comprising 8% of the earth's crust. The versatility of aluminium makes it the most widely used metal after steel. In any structural application of Aluminium alloys consideration of its weldability is of utmost importance as welding is largely used for joining of structural components. The preferred welding process of aluminium alloy is gas tungsten arc welding (GTAW) due to its comparatively easier applicability and better economy. GTAW process parameters are many and different for different materials, therefore for efficient use of the process it is required to optimize the parameters. Since a large number of experiments are required to be conducted to identify various parameters, therefore for successful optimization, design of experiments needs to be planned carefully. *Design of experiments*, is the design of all information-gathering exercises where variation is present, whether under the full control of the experimenter or not. Design of experiments is thus a discipline that has very broad application across all the natural and social sciences.

Taguchi method involves reducing the variation in a process through robust design of experiments. The overall objective of the method is to produce high quality product at low cost. The experimental design proposed by Taguchi involves orthogonal arrays to organize the parameters affecting the process and the levels at which they should be varied. Instead of having to test all possible combinations like the factorial design, the Taguchi method tests pairs of combinations. This allows for the collection of the necessary data to determine which factors most affect product quality with a minimum amount of experimentation, thus saving time and resources (Vuchkov , *et al* 2001), (Montgomery, 1997).

Kumar and Sunderrajan (2009) conducted experiments on optimization of pulsed GTAW welding process parameters and studied the effects on mechanical properties of AA 5456 aluminium alloy weldments using Taguchi technique. Ravisankar *et al* (2006) and Lakshminarayanan and Balasubramanian, (2008) implemented Taguchi approach to determine the most influential control factors which will yield better tensile strength of the joints of friction stir welded RDE-40 aluminium alloy.

Zhang and Zhang (1999) performed welding of Aluminium alloy AA6061 using Opposing Dual torch GTAW process. They disconnected the workpiece from the power supply and placing a second torch on the opposite side of the workpiece. Such a modification changed the direction of current flow, improved the weld penetration and reduced the heat input. This reduced the crack sensitivity of AA6061 and the alloy could be welded without filler metal.

Senthil Kumar *et al* (2007) studied influences of pulsed current tungsten inert gas welding parameters on the tensile properties of AA 6061 aluminium alloy. The use of pulsed current parameters was found to improve the mechanical properties of the welds compared to those of continuous current welds of this alloy due to grain refinement occurring in the fusion zone.

Luijendijk (2000) investigated welding of dissimilar Aluminium alloys and found that due to welding, the strength of the material in the HAZ was reduced. This reduction in strength was smaller for solution hardened

*Corresponding author: **Vijay Gautam**

and strain hardened alloys, than for precipitation hardened alloys.

Naa and Lee (2009) studied parameter optimization in the circumferential welding of aluminium pipes using a semi-analytical finite-element method.

In the present work Taguchi method was employed to optimize the GTAW process parameters of AA1100-O Aluminium alloy welds for obtaining maximum strength. Regression model was developed and Analysis of variance was employed to check the adequacy of developed models. The result was verified with Confirmation test.

2. Experimental Procedure

The base material employed in this study is 1.5 mm thick Al alloy cold rolled sheet in as annealed state. The base metal was tested for elemental composition using inductively coupled plasma atomic emission spectrometer (ICP-AES) and is shown in Table 1.

Table 1: Chemical Composition of Base and Filler material (wt %).

Elements	Cu	Mg	Si	Fe	Mn	Zn	Ti	Cr
% by weight	0.01	0.02	0.28	0.29	0.02	0.01	0.02	0.01

The filler metal used to weld Aluminium 1100 alloy under the trade name *EUTECROD 190* of size 1.6mm manufactured by Larsen and Turbo limited. The selection of filler material is based on the mechanical properties and resistance to cracking in the weld.

2.1 Selection of process parameters

The most important parameters which are having greater influence on the weld bead geometry are Current, Shielding gas flow rate and Welding Speed. A large number of trials have been conducted by varying one of the process parameters and keeping the others constant. The working range of current, flow rate and welding speed has been explored by inspecting bead appearance and the full penetration. The mode was AC and frequency was set at 175 Hz. The working range of the process parameters selected under the present study and the constant process parameters are shown in Tables 2 and 3 respectively.

Table 2: Working Range of Process Parameters

Symbols	**Process Parameters**	**Units**	**Lower Level**	**Higher Level**
C	Current	Amp	62	67
FR	Flow Rate	Lt/min	8	11
WS	Welding Speed	mm/sec	2.5	3.5

Table 3: Constant Process Parameters

Process Parameter	**Constant Value**
Polarity	AC
Open Circuit Voltage (V)	45
Filler Rod Diameter (mm)	1.6
Electrode Material	Tungsten (2% Thoriated)
Electrode Diameter (mm)	1.6

Number of process parameters considered under this study is 3 and the level of each parameter is 3. Each condition of experiments was conducted twice to reduce the noise/error effects. The selected orthogonal array L9 is presented in Table 4.

Table 4: L9 Orthogonal Array, Factors = 3 and Runs = 9

S.No.	**Current**	**Flow Rate**	**Weld Speed**
1.	62	8	2.5
2.	62	10	3.0
3.	62	11	3.5
4.	65	8	2.5
5.	65	10	3.0
6.	65	11	3.5
7.	67	8	2.5
8.	67	10	3.0
9.	67	11	3.5

2.2 Preparation of specimens by GTAW

The base metal sheets of dimension 100 mm x 50 mm x 1.5 mm as shown in the Fig.1 were prepared in the sheet metal shop using shearing machine. The butt joints were made using the experimental layout shown in Table 4. TRITON GTAW welding machine was employed for conducting the welding experiments. Before conducting the experiments the base metal sheets were cleaned with sand paper to remove the oxide layer. The sheets to be welded were kept on steel backing bar and ends were clamped to maintain the alignment and gap. Argon gas is used for shielding. The weld joint is completed in a single pass.



Fig.1 Butt welded specimen prepared by GTAW

2.3 Tensile properties of welded specimens

Specimens for tensile testing were prepared by wire cut EDM as per ASTM E8M standards (subsized scale 1:2) with the weld line in the middle of the specimens.

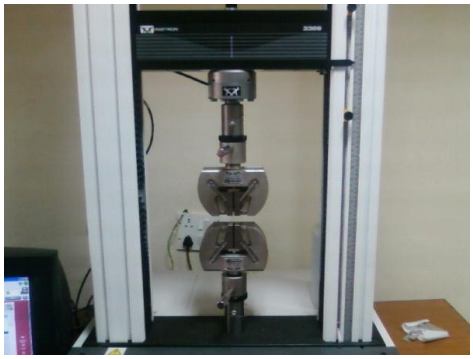


Fig.2 A 50kN UTM table top facility at DTU

Tensile testing was conducted using a computer controlled UTM of capacity 50kN Tonnes as shown in Fig. 2. The cross head speed of 2.54 mm/min was adopted for all the experiments. Each experiment was conducted thrice for better reproducibility of results.

The quality characteristics were evaluated for all the conditions and are presented in Table 5.

Table 5: Quality Characteristics Data

S.No.	Current (Amp.)	Flow Rate (Lt/min)	Weld Speed (mm/sec)	UTS1 (MPa)	UTS2 (MPa)
1.	62	8	2.5	70.3	71.0
2.	65	10	3.0	74.5	73.9
3.	67	11	3.5	62.8	61.3
4.	62	8	2.5	94.6	96.3
5.	65	10	3.0	88.4	87.7
6.	67	11	3.5	99.3	102
7.	62	8	2.5	76.3	74.2
8.	65	10	3.0	90.6	93.5
9.	67	11	3.5	88.4	86.1

3. Experimental Results

3.1 Optimization using Taguchi Technique

Minitab is leading statistical analysis software used for design and analysis of experiments to perform Taguchi technique, ANOVA and develop regression models. Minitab's logical interface makes it easy to use and its outstanding support features makes it easy to get results.

Table 6: Response Table for Signal to Noise Ratios Larger is better

Level	Current(A)	Flow(Lt/min)	Speed (mm/sec)
1	36.75	38.03	38.77
2	39.51	38.52	38.60
3	38.54	38.24	37.42
Delta	2.76	0.49	1.34
Rank	1	3	2

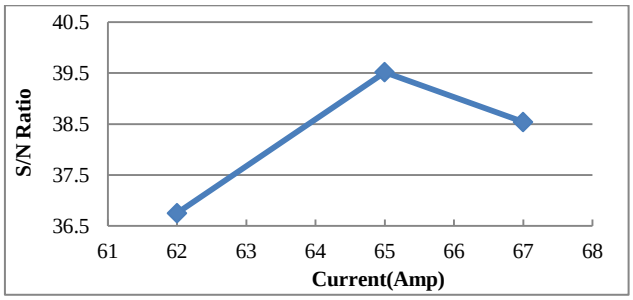


Fig.3 Main effect plot between S/N ratio and Current

The optimization of process parameters using Taguchi method permits evaluation of the effects of individual parameters independent of other parameters on the identified quality characteristic i.e. Ultimate tensile strength (UTS). The statistical analysis of variance (ANOVA) was carried out. Based on the ANOVA, the contribution of each parameter in influencing the quality characteristic is evaluated .The ANOVA also provides an indication of which process parameters are statistically significant. Signal to noise ratios are maximized using Larger the Better criterion and rank of each parameter influencing the ultimate tensile strength is found by using Taguchi method. Response for signal to noise ratio is shown in Table 6 and plots are shown in Fig. 3, 4 and 5. Similarly response for mean UTS is shown in Table 7 and plots are shown in Fig. 6, 7 and 8.

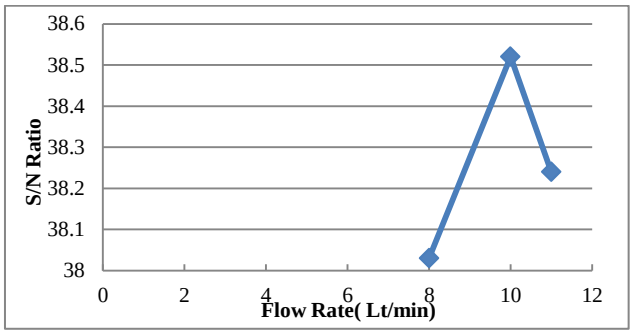


Fig.4 Main effect plot between S/N ratio and Flow rate

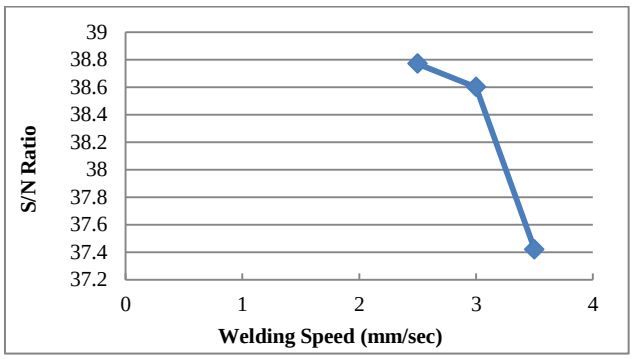


Fig.5 Main effect plot between S/N ratio and welding speed

Table 7: Response Table for Means (UTS)

Level	Current (Amp)	Flow (Lt/min)	Speed (mm/sec)
1	68.97	80.48	87.79
2	94.73	84.78	85.64
3	84.88	83.32	75.15
Delta	25.75	4.30	12.64
Rank	1	3	2

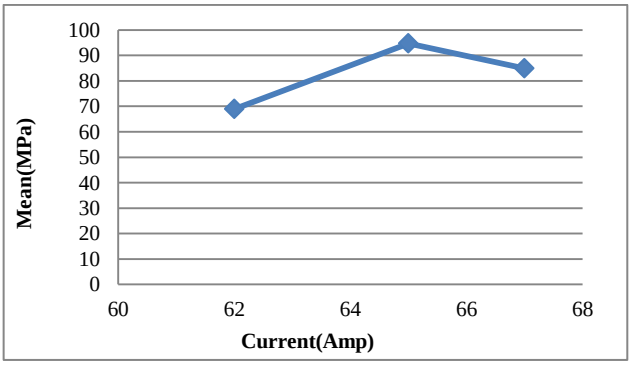


Fig. 6 Main effects plot between MeanUTS and current.

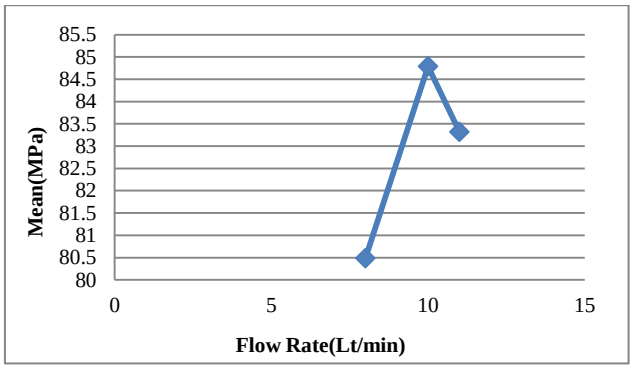


Fig. 7 Main effects plot between Mean -UTS and flow rate

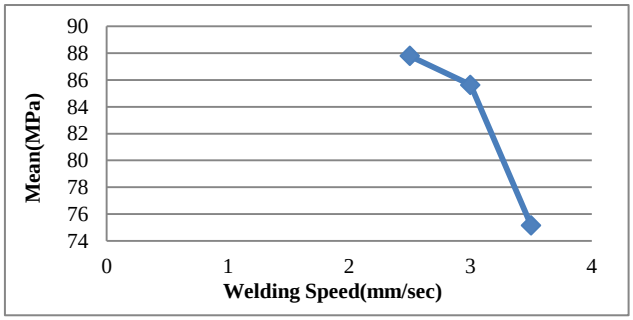


Fig. 8 Effects plot between Mean UTS and welding speed

3.2 Analysis of Variance

Results of ANOVA for mean UTS is shown in the Table 8, Where, DOF-Degrees of freedom (no of independent comparisons that can be made), Error- represents the unexplained variability in UTS, Seq SS- Sequential sum of Squares, Adj SS- Adjusted Sum of Squares, Adj MS-Adj Mean Squares.

Table 8: ANOVA for mean UTS

Source	DOF	Seq SS	Adj SS	F	P
Current	2	1013.41	506.71	296.62	0.003
Flow rate	2	28.74	14.37	8.41	0.106
Weld speed	2	274.37	137.19	80.31	0.012
Error	2	3.42	1.71		
Total	8	1319.94			

F value: The F-test is used to test if the variance measuring the differences between groups in a certain pre-defined grouping of observations is large compared to the variance measuring the differences within the groups: a large value would tend to suggest that grouping is *good* or *valid* in some sense, or that there are real differences between the groups. The formula for an F-test is:

$$F = \frac{(\text{explained variance})}{(\text{unexplained variance})},$$

Usually the change of welding process parameter has significant effect on response when the F ratio is large for ex like current in our case.

P value: The P value (alpha in the figure given below) for a F- test is the probability that a value chosen at random from a particular F distribution would be greater than or equal to the value of an observed value(the F-value)from the same distribution..For a particular confidence level, the value of P should be as small as possible for the model to be significant.

4. Results and Discussion

As per the ANOVA the optimum condition corresponds to C2 FR2 WS1 i.e. current at level 2(65 A), Flow rate at level 2(10Lt/min) and weld speed at Level 1(2.5 mm/sec). The coefficients of variables as shown in table 9 are calculated using the above model by MINITAB software and the regression equation developed is:

UTS = {- 123 + 3.61*(current) + 1.12*(flow rate) - 12.6* (welding speed)}

Table 9: Regression Analysis results

Predictor	Coeff.	SE Coeff.	T	P
Constant	-123.3	118.1	-1.04	0.344
Current	3.607	1.729	2.09	.091
Flow	1.119	2.849	0.39	0.711
Speed	-12.642	8.704	-1.45	0.206

Where, Coeff. is weight of predictor in the model, SE is Standard Error (Variability in estimates), T is Coeff. /SE (ex: -123.3/118.1 = -1.04), P is probability value for that level of T, and R-sq is validation criterion, i.e. in this case model accounts for 57% of the variance of the predictor i.e. the strength.

Table 10: ANOVA for testing regression

Analysis of Variance for testing significance of regression

Source	DF	SS	MS	F	P
Regression	3	751.7	250.6	2.21	0.206
Residual Error	5	568.2	113.6		
Total	8	1319.9			

Where, DF is degree of freedom, SS is Sum of squares, MS is Variance (=SS/DF) and P is contributed percentage.

5. Confirmation Test

The final step was to verify the improvement in the tensile strength by conducting experiment using optimal conditions.

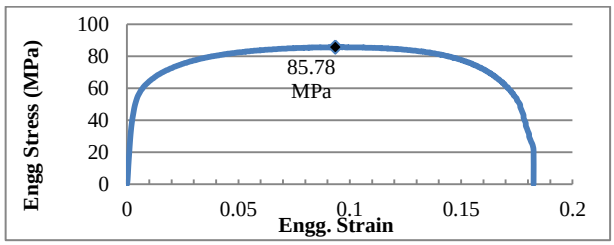


Fig. 9 Confirmation test conducted on butt welded Tensile specimen

Three specimens were tested for the set of optimized parameters and the tensile strength was found to be 85.78MPa as shown in Fig. 9, which is within the limits compared to the calculated value of 91.35 MPa obtained from the Linear equation.

Conclusions

From the above calculations and analysis we find that

- The current level for maximum strength was at 65 Amperes which could be explained as greater the value of current the easier it becomes to penetrate the hard oxide layer of Aluminium deposited on the sheet. On the other hand increase of current further would cause oxidation of Tungsten and causing its contamination.
- The flow rate was found to affect the tensile strength such that maximum strength was observed at flow rate of 10lt/hr. This could be explained as the flow rate is needed to prevent oxidation and shielding but again excess flow would be detrimental as it would cause cooling and turbulence in the weld pool.
- The speed would be optimized at level 1 i.e. 2.5 mm/sec which would facilitate proper fusion and strength.
- The value of R sq is obtained which is measure of amount of reduction in variability of tensile strength (dependent variable in this case) that the effect of parameters is 57% and the rest is unaccounted for. The unaccounted factors could be arc gap, feed angle of filler rod etc.
- There could be error in the measurements of the chosen parameters which could be beyond our control.

References

Vuchkov, I.N. and Boyadjieva, L.N. (2001), Quality Improvement with Design of Experiments: A Response Surface Approach Kluwer Academic Publishers.

Montgomery Douglas C. (1997), Design and Analysis of Experiments. New York: John Wiley & Sons; 1997.

A. Kumar and S. Sunderrajan (2009) Optimization of TIG welding process parameters on mechanical properties of AA5456 Aluminium alloy weldments, *Material and Design 30*, pp1288-1297.

V. Ravisankar, V. Balasubramanian, C. Muralidharan (2006), Selection of welding process to fabricate butt joints of high strength aluminium alloys using analytic hierarchic process, *Materials and Design 27*, pp 373-380.

A.K. Lakshminarayanan and V.Balasubramanian (2008), Process parameters optimization for friction stir welding of RDE-40 aluminium alloy using Taguchi technique, *Transactions of Non-ferrous Metals Society of China* 18, 548-552.

Y.M Zhang and S.B. Zhang (1999), Welding Aluminium Alloy 6061 with the opposing Dual-Torch GTAW Process, *Welding Research Supplement*, pp 202-206.

T. Senthil Kumar, V. Balasubramanian, M.Y. Sanavullah (2007), Influences of pulsed current tungsten inert gas welding parameters on the tensile properties of AA 6061 aluminium alloy, *Materials and Design 28* pp.2080-2092.

Luijendijk. I (2000), Welding of Dissimilar Aluminium alloys, *Journal of Material Processing Technology, 103*, pp.29-35.

S. J. Naa, H. J. Lee (2009), A study on parameter optimization in the circumferential GTA welding of aluminium pipes using a semi-analytical finite-element method, *Journal of Material Processing Technology*, 57 pp.95-102.

Performance Analysis of PID and Fuzzy PD+I Controller on Nonlinear Systems

Bharat Bhushan[1], Nupur Jha[2], Sangeeta Devra [3], Sarath S. Pillai [4]
Department of Electrical Engineering
Delhi Technological University
Delhi, India
Email[1]: bharatdce@yahoo.co.in
Email[2]: nj.nupurjha@gmail.com
Email[3]: sangeeta.devra@gmail.com
Email[4]: sspillai305@gmail.com

***Abstract*—This paper analysis the performance of Fuzzy PD+I and conventional PID controller on nonlinear systems. The nonlinear systems used are level control of a surge tank and cart pole system. Level control of a surge tank level system and angular position of cart pole system have been tracked using Fuzzy PD+I controller and conventional controller. Four type of membership functions Bell, Pi, Gaussian and Psigmoid are used in the fuzzy PD+I control of the nonlinear systems. Effects of different membership functions on the systems control have been compared with conventional PID controller. For four different membership functions besides control performance stability criterion also have been implemented using phase-plane method.**

Keywords— Fuzzy PD+I controller; Surge tank level system; cart pole system; PID controller; Phase plot.

I. INTRODUCTION

The Fuzzy logic gives a simple way to reach definite conclusion even when the input is based on vague, noisy, imprecise, ambiguous or missing information. It provides a multi-valued truth space in [0,1]. It is capable of generating inferences even when a partial matching occurs. Here we make use of Conventional PID and Fuzzy PD+I controller to control liquid level in a nonlinear Surge tank system [13] and to control the angular position in cart pole system.

Conventional proportional integral derivative (PID) controller is widely made use of in processes due to its simplicity in structure, ease to design and robust performance in wide range of operating conditions [9]. Conventional PID controller is the most popular control tool in many industrial applications as they can improve both the transient response and steady state error of the system at the same time [18].

Traditionally the parameters of Conventional PID controller, i.e. K_P, K_I& K_D, are usually fixed during operation. Such a controller is thus inefficient for controlling a system while a system is disturbed by the changes in the surrounding environment of the system or due to unknown facts [6, 17]. Integral action is necessary whenever a sustained error in steady state occurs. It will increase or decrease the control signal if there is a positive or negative error, even for small magnitudes of error. Thus, a controller with integral action will always return to the reference in steady state [12].

A fuzzy controller acts on three inputs: error, integral error and change in error. The integral action in the crisp PID controller combined with a fuzzy PD rule base as fuzzy PD+I (FPD+I) controller is an effective way to control the nonlinear systems.

In recent years, fuzzy logic control has been applied successfully in the area of nonlinear process control [1-4]. In direct fuzzy control applications fuzzy logic controller (FLC) estimates the necessary control action through rule inference by taking the linguistic description of the error behavior [5]. The literature tells that it has been successfully applied to various problems viz. temperature control of glass furnace [10-11], controlling the Yaw system for wind turbine generator [14] robot manipulator [16], Electro-hydraulic servo system [17, 18] inverted pendulum [19-20].

In this paper four types of membership functions have been considered. FPD+I controller have been implemented on nonlinear systems using four type of membership functions.

This paper is divided into several sections wherein Section II introduces the Conventional PID controller, Section III gives an account on Fuzzy PD+I controller section IV describes the nonlinear systems and section V shows the simulation results and discussion followed by conclusion in section VI and then references.

II. CONVENTIONAL PID CONTROLLER

The combinative action of proportional, integral and derivative [8] action is an effective tool for controlling processes. It is a generic control loop feedback mechanism (controller) widely used in industrial control system. An error value is calculated by the PID Controller as the difference between a desired set point and measured process variable. By adjusting the process control inputs the error is minimized by the controller.

The output of the controller is denoted by

$$U(n) = K_p\left(e(n) + \frac{1}{T_i}\sum_{j=1}^{n} e(j)T_s + T_d\frac{e(n)-e(n-1)}{T_s}\right) \quad (1)$$

The control signal u is a linear combination of the error e, its derivative and its integral. The parameter T_i is the integral

978-1-4799-2572-8/14/$31.00 ©2014 IEEE

time, K_P is the proportional gain, T_d is the derivative time and T_s is the sampling time.

III. FUZZU PD+I CONTROLLER

In this section, Fuzzy PD+I controller [12] have been described. Three inputs had been used, error(e), change in error(ce) that will be fed to the fuzzy controller while integral error will be used as conventional integral action . Figure 1 shows the structure of Fuzzy PD+I controller.

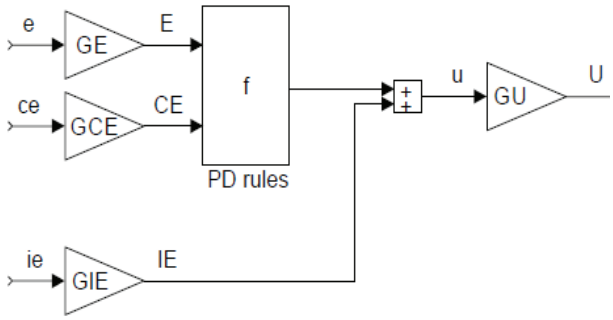


Figure 1.Fuzzy PID controller, FPD+I

The control signal U(n) after the gain GU, at the time instant n, is a nonlinear function of error, change in error, and integral error,

$$U(n) = \left[f(GE * e(n), GCE * \dot{e}(n)) + GIE \sum_{j=1}^{n} e(j)T_s\right] * GU \quad (2)$$

The function f is again the control surface of a PD rule base. The mapping is usually non-linear, but with a favorable choice of design, a linear approximation is

$$U(n) \approx \left[f\left(GE * e(n), GCE * \dot{e}(n)\right) + GIE \sum_{j=1}^{n} e(j)T_s\right] * GU \quad (3)$$

$$U(n) = GE * GU\left[e(n) + \frac{GCE}{GE} * \dot{e}(n) + \frac{GIE}{GE}\sum_{j=1}^{n} e(j)T_s\right] \quad (4)$$

Comparing equation (1) and (4) the gains are related as follows:

$$GE * GU = K_p \quad (5)$$

$$\frac{GCE}{GE} = T_d \quad (6)$$

$$\frac{GIE}{GE} = \frac{1}{T_i} \quad (7)$$

IV. NONLINEAR SYSTEMS

A. Surge Tank Level System

This section describes the Nonlinear Surge tank system [7, 13] in which the liquid level is to be controlled. The system can be modeled by the equation:

$$h(k+1) = max\left\{0.0001, h(k) + T\left(\frac{-\bar{d}\sqrt{19.6h(k)}}{|\bar{a}h(k)+\bar{b}|} + \frac{\bar{c}}{|\bar{a}h(k)+\bar{b}|}u(k)\right)\right\} \quad (8)$$

where *u(k)* is the control input (input flow) and it can both pull liquid out of the tank and put it in (can be positive or negative), *h(k)* is the output of the plant (liquid level) and T=0.1.

A(h(k)) = | $\bar{a}$ h(k)+ $\bar{b}$ |describes the cross-sectional area of the tank , $\bar{a}$ >0 and $\bar{b}$ >0. Here $\bar{a}$ = 0.01 and $\bar{b}$ = 0.2; g=9.8; $\bar{c}$ is the clogging factor Є [0.9, 1] for a filter in the pump actuator and symbolically if $\bar{c}$ =1, there is no clogging as the filter is clean. $\bar{d}$ is related to the diameter of the output pipe and its nominal value is taken as 1. We assume that the input to the plant saturates at +/- 50 for that controller generates an input $\bar{u}$(k).

B. Inverted Pendulum System

The aim of the controller is to stabilize the pendulum [7] in the upright position by applying the right amount of force. The system is described by the following equations:

$$(M+m)\ddot{x} + b\dot{x} - ml\sin(\theta)\dot{\theta}^2 + ml\cos(\theta)\ddot{\theta} = u \quad (9)$$

$$m\ddot{x}\cos\theta + ml\ddot{\theta} = mg\sin\theta \quad (10)$$

By approximating the system and converting into state space following state equations are obtained:

$$\frac{d}{dt}\begin{bmatrix}\Delta\theta\\ \Delta\dot{\theta}\\ \Delta x\\ \Delta\dot{x}\end{bmatrix} = \begin{bmatrix}0 & 1 & 0 & 0\\ \frac{g(M+m)}{lM} & 0 & 0 & \frac{b}{lM}\\ 0 & 0 & 0 & 1\\ \frac{-mg}{M} & 0 & 0 & \frac{-b}{M}\end{bmatrix}\begin{bmatrix}\Delta\theta\\ \Delta\dot{\theta}\\ \Delta x\\ \Delta\dot{x}\end{bmatrix} + \begin{bmatrix}0\\ \frac{-1}{lM}\\ 0\\ \frac{1}{M}\end{bmatrix}\Delta u \quad (11)$$

M (Mass of cart)=3Kg; *m*(mass of bob)=0.2Kg; *l*(length)=0.31m; *b*(frictional force)=0.1N/ms^{-1}.

V. SIMULATION RESULTS AND DISCUSSION

Here, liquid level in a surge tank system is controlled using both Conventional PID and Fuzzy PD+I controller. FPD+I controller has been implemented with four different membership functions viz. Bell shaped, Pi, Gaussian andPsigmoid functions. The result of each controller has been projected along with a comparative analysis. Here a plane is spanned by variables E and CE, which is a phase plane between error and its derivative. The sequence of errors and its derivative can be plotted; CE(t) against E(t), to form a phase trajectory. If the trajectory is ended in the centre (origin), then the plant stays on reference and not moving and that system is stable. For each membership function, phase plots have also been shown for stability analysis.

Four membership functions have been used: Gaussian, Bell, Pi and Psigmoid. The FPD+I controller uses these for different iterations. The result for each function applied on to the surge tank system and inverted pendulum were obtained. Three linguistic variables for each input have been used: Neg (negative), Pos (positive), and Zer (zero). There are two inputs: *e* and *ce*.The rules are as shown in the Table I.

TABLE I. FUZZY RULE BASE

e \ ce	Neg	Zer	Pos
Neg	Neg	Neg	Zer
Zer	Neg	Zer	Pos
Pos	Zer	Pos	Pos

Simulation results are obtained for surge tank level system and inverted pendulum system using conventional and FPD+I controller. Four membership functions were used for the FPD+I controller to study the effect on the nonlinear systems.

Reference input for surge tank is shown in Fig. 2 below and the reference for cart position and inverted pendulum is zero.

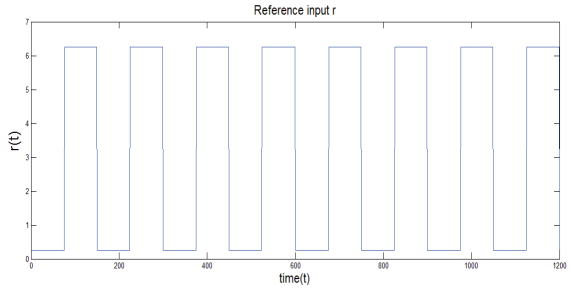


Figure 2.Reference Input

A. *Conventional PID*

The system was controlled with the Conventional PID controller with a fixed value for K_p, K_i & K_d.

The controlled output for the level of the liquid inside the tank is shown in Fig. 3. While angle and position of inverted pendulum by using the conventional PID controller are shown in Fig. 4 and 5 respectively.

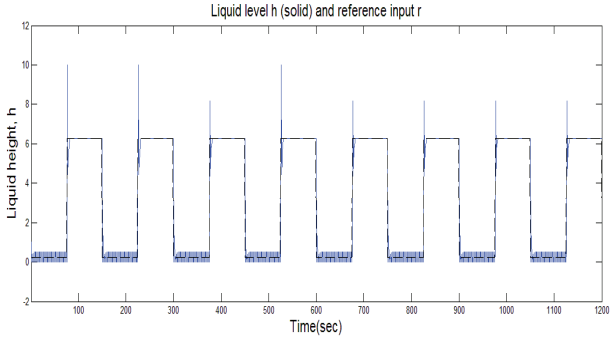


Figure3. The Controlled level of the liquid using PID

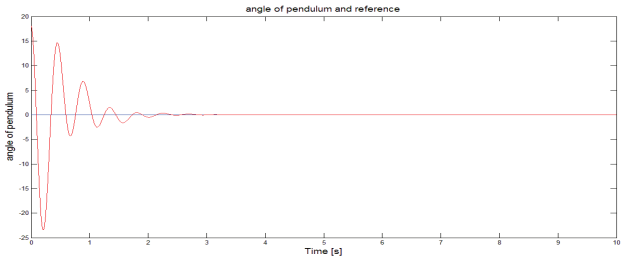


Figure4. The Controlled angle of pendulum using PID

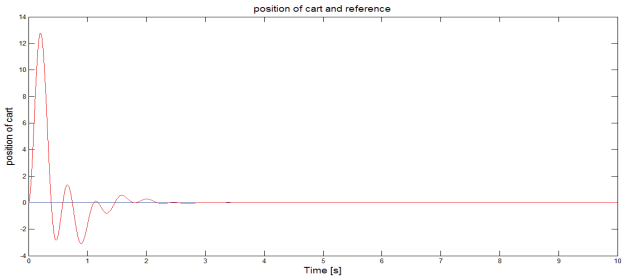


Figure5. The Controlled position of cart using PID

B. *FPD+I controller with Gaussian Membership Function*

The Gaussian membership function is shown in Fig. 6.

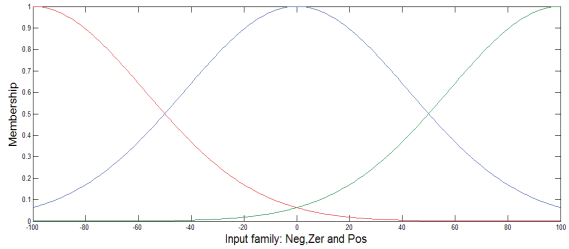


Figure6. Gaussian Membership Function

The output of the surge tank level and inverted pendulum systems obtained by using the FPD+I controller with gaussian membership function with respect to the reference input are shown in Fig. 7, 8 and 9.

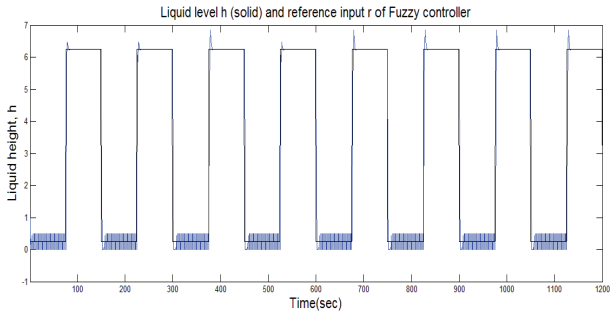


Figure7. The Controlled level output using Gaussian Membership function

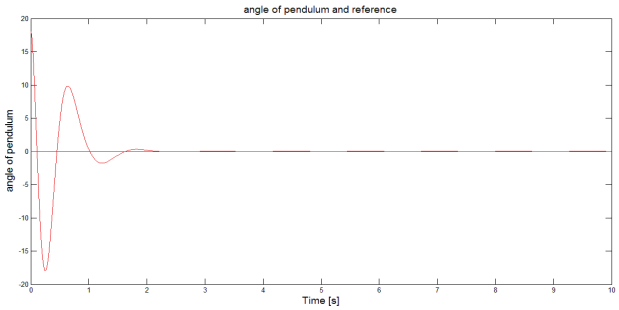


Figure8. The angle of pendulum using Gaussian Membership function

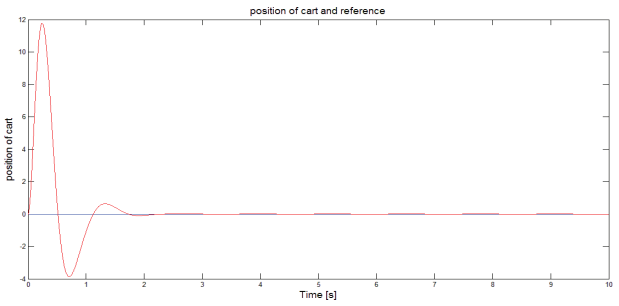
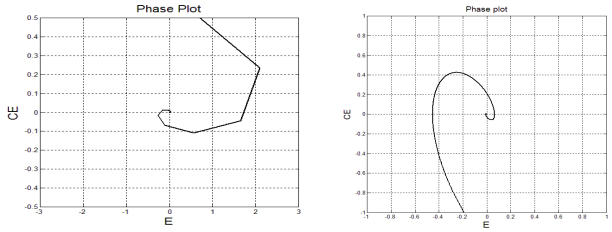


Figure 9 The position of cart using Gaussian Membership function

It can be seen clearly that the controller is able to control the level and angle of the systems efficiently and is also successfully able to track the reference input given to the systems.

The phase plots are obtained for both the nonlinear systems between CE and E which shows the system is stable as shown in Figure 10.



(a) (b)

Figure 10 .Phase Plot of (a) tank level; (b) Inverted pendulum for Gaussian MF

C. FPD+I controller with Bell Membership Function

The Bell membership function was used secondly in the FPD+I controller to analyze the effects on the control of the system. The Bell membership function is shown in Fig. 11.

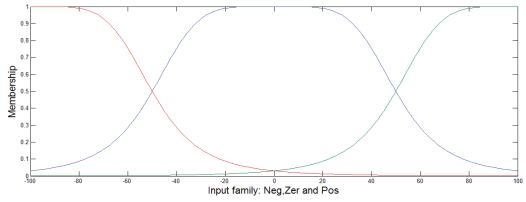


Figure11. Bell Membership Function

The output of the nonlinear systems obtained by using the Bell membership function with respect to the reference input are shown in Fig. 12, 13 and 14.

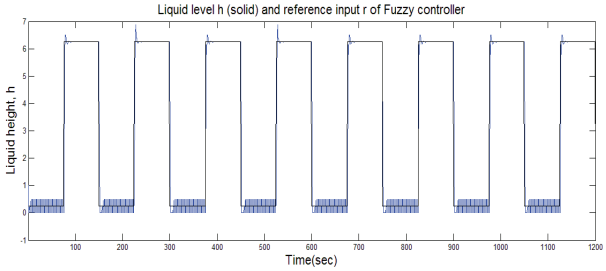


Figure12. The Controlled level output using Bell Membership function

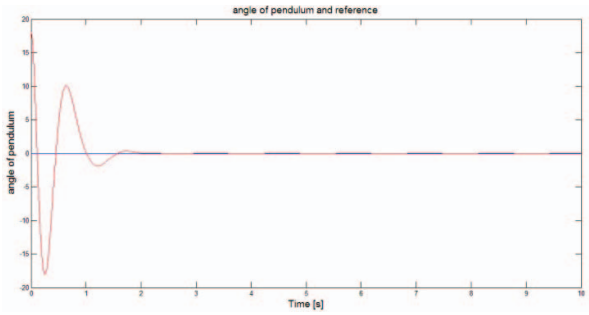


Figure13. The angle of pendulum using Bell Membership function

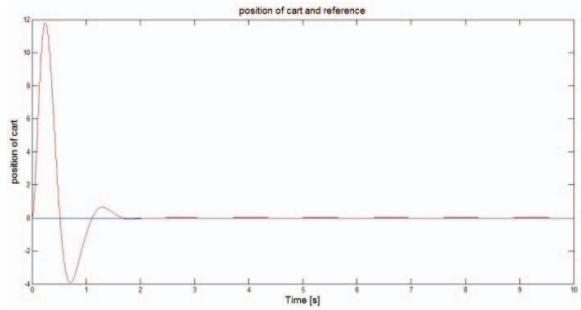
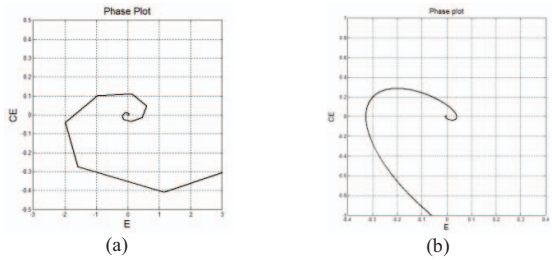


Figure14. The position of cart using Bell Membership function

The phase plots obtained for both the nonlinear systems between CE and E show that the systems are stable as shown in Fig. 15.



(a) (b)

Figure 15.Phase Plot of (a) tank level; (b) Inverted pendulum for Bell MF

D. FPD+I controller with Pi Membership Function

The Pi membership function was then used in the FPD+I controller to analyze the effects on the control of the nonlinear

systems. The Pi membership function was used is shown in Fig. 16.

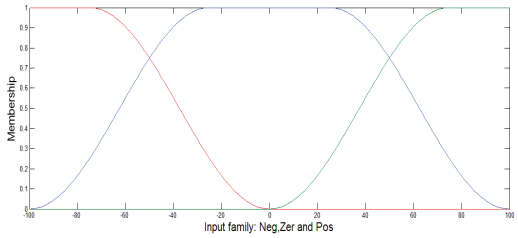


Figure16. Pi Membership Function

The output of the surge tank system obtained by using the Pi membership function with respect to the reference input is shown in Fig. 17.

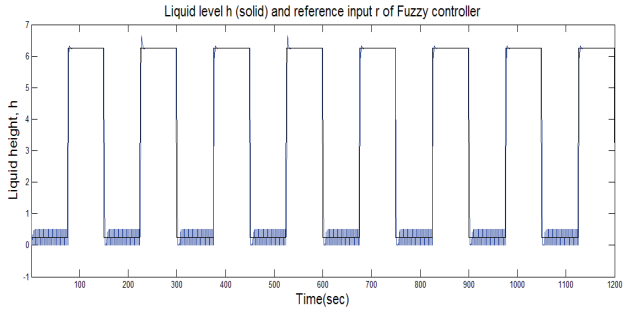


Figure17. The Controlled level output using Pi Membership function

The angle of pendulum and position of the cart obtained with FPD+I controller using Pi membership functions are shown in Fig. 18 and 19 respectively.

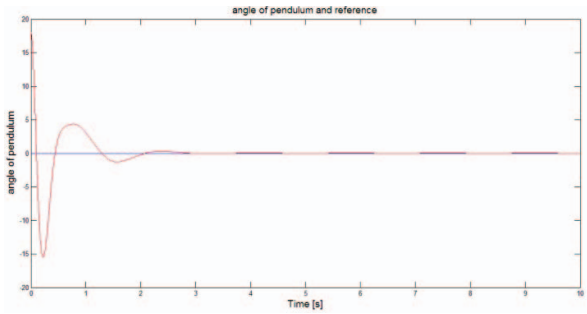


Figure18. The angle of pendulum using Pi Membership function

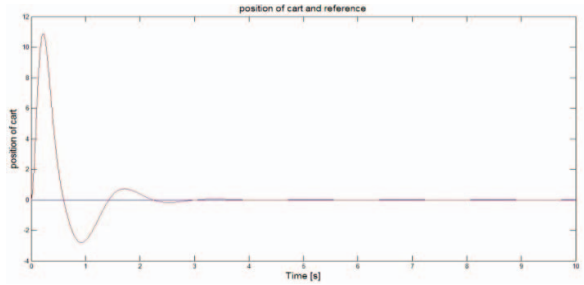
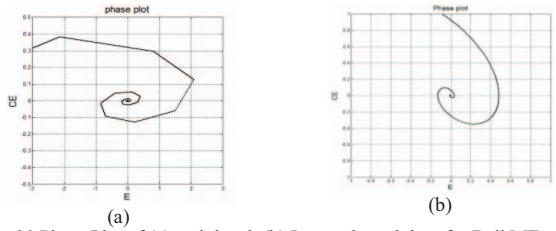


Figure19. The position of cart using Pi Membership function

The phase plots obtained for surge tank level system and inverted pendulum between CE and E using Bell membership functions are shown in Fig. 20, which show that both the nonlinear systems are stable.



(a) (b)

Figure 20.Phase Plot of (a) tank level; (b) Inverted pendulum for Bell MF

E. FPD+I controller with Psigmoid Membership Function

The Psigmoid membership function was used in the FPD+I controller to analyze the effects on the control of the nonlinear system using FPD+I controller. The Psigmoid membership function is shown in Fig. 21.

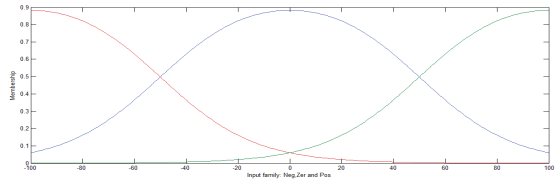


Figure 21.PSigmoid Membership Function

The output of the nonlinear surge tank system obtained by using the Psigmoid membership function with FPD+I controller with respect to the reference input is shown in Fig. 22.

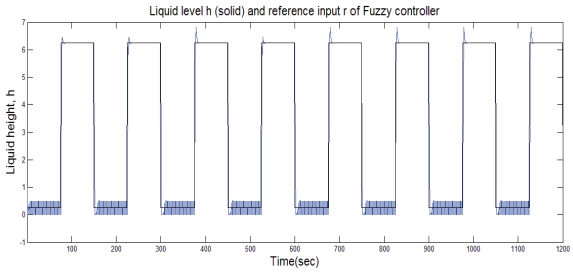


Figure22. The Controlled level output using Psigmoid Membership function

The outputs of the nonlinear inverted pendulum system obtained by using the Psigmoid membership function with FPD+I controller are shown in Fig. 23 and 24.

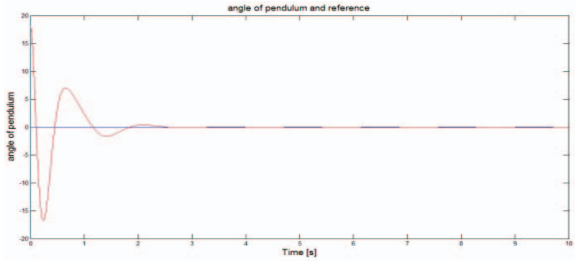


Figure23. The angle of pendulum using Psigmoid Membership function

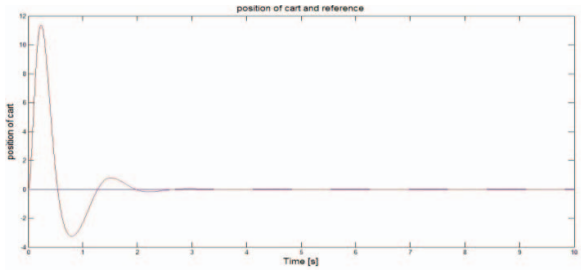
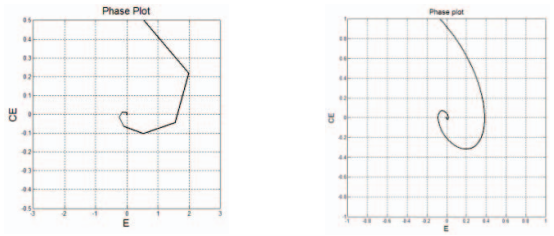


Figure24. The position of cart using Psigmoid Membership function

The phase plots obtained for surge tank level system and inverted pendulum system are shown in Fig. 25 which show that both the nonlinear systems are stable.



(a) (b)

Figure 25.Phase Plot of (a) tank level; (b) Inverted pendulum for Psigmoid MF

The results show that the response of Fuzzy PD+I controller with all membership functions used above gives low overshoot than the Conventional PID Controller. We have used four different membership functions with Fuzzy PD+I controller and they are giving better response than conventional PID controller. The performance tells that large number of processes can be efficiently controlled by using Fuzzy Controller rather than Conventional PID Controller.

On the effect of membership functions on the system, it can be commented that performance using Gaussian and Psigmoid membership functions is almost same for surge tank level system, but Fuzzy PD+I controller using Pi and Bell membership functions gives better output than the output obtained using Gaussian and Psigmoid membership functions for the same. But in the case of inverted pendulum results using Pi and Psigmoid gives better response than Gaussian and Bell. And in comparison to all performances Fuzzy Controller using Pi membership function gives best output. The FPD+I helps in determining the stability of the system which is evident from the phase plots above. The plots show that the trajectory converges to the origin which shows the system stability.

VI. CONCLUSION

The Conventional PID controller and FPD+I controller with different membership functions are implemented on nonlinear surge tank level control system and cart pole system using MATLAB. It is evident from the results that FPD+I perform better in four type of membership function than the PID controller. Effect of four different membership functions were studied and it is found that Fuzzy controller using Pi membership function gives best result compare to other three type of membership functions. . Phase plot of the system for all the four membership functions shows that both the nonlinear systems are stable.

REFERENCES

[1] C. J. Harris, C. G. Moore and M. Brown. IntelligentControl, Aspects of Fuzzy Logic and :Veural !Vets, WorldScientific: London, 1993.

[2] H. A. Malki, H. Li and G. Chen, "New Design and Stability Analysis of Fuzzy Proportional-Derivative Control Systems". IEEE Trans. on Fuzzy Systems. Vol. 2.pp. 245-254. 1994.

[3] C. W. de Silva. Intelligent Control-Fuzzy LogicApplications, CRC Press, New York, 1995.

[4] C-L. Chen and F-C. Kuo. "Design and Analysis of a Fuzzy Logic Controller", Int. J. Systems Sci., Vol. 26. pp.1223-1248, 1995.

[5] G.K.I.Mann, B.-G.Hu and R.G.Gosine, "Analysis and Performance Evaluation of Linear-Like Fuzzy PI and PID Controllers," Procc. Of 6th International Conference on Fuzzy Systems, IEEE, 1997, pp: 383-390.

[6] Parnichkun, M. and C. Ngaecharoenkul., "Hybrid of fuzzy and PID in kinematics of a pneumatic system," Proceeding of the 26th AnnualConference of the IEEE Industrial Electronics Society, Japan, 2000, pp:1485-1490.

[7] K.M.Passino, "Biomimicry for Optimization, Control, and Automation," 2005, Springer Publication.

[8] W. Chatrattanawuth, N. Suksariwattanagul, T. Benjanarasuth & J. Ngamwiwit, "Fuzzy I-PD Controller for Level control", SICE-ICASE International Joint Conference 2006, PP. 5649-5652.

[9] Asim Khan, N. Rapal, "Fuzzy PID Controller: Design, Tuning and Comparison with Conventional PID Controller," International Conference on Engineering of Intelligent Systems, IEEE, 2006, pp:1-6.

[10] O. Ziwei, S.Michael and W. Kexin, "The Experiment "Ball-in-tube" with Fuzzy PID Controller Based on Dspace," International Conference on Systems, Man and Cybernetics, IEEE, 2007,pp: 877-881.

[11] Qi Jianling, D. Zhenjie and Li Yezi, "Design of Fuzzy PID Controller and Application in Glass Furnace," The Eighth International Conference on Electronic Measurement and Instruments, ICEMI'2007,pp: 224-227.

[12] Jan Jantzen, "Foundations of Fuzzy Control", 2007, John Wiley & Sons.

[13] L. Behara and Indrani Kar, "Intelligent Systems and Control-Principles and Applications", 2009, Oxford University Press.

[14] F. CHEN and J. YANG, "Fuzzy PID Controller used in Yaw System of Wind Turbine," 3rd International Conference on Power Electronics Systems and Applications, 2009, pp: 1-4.

[15] R. Kannan, P. Ananthachristu Raj & P. Poongodi, "Design of Fuzzy Immune PID Controller for Liquid Level Control System", 2nd International Conference on Computer and Network Technology, IEEE, 2010, PP. 566-570.

[16] A.F.Amer, E.A.Sallan and W.M.Elawady, "Fuzzy Pre-compensated Fuzzy Self-tunig Fuzzy PID controller of 3 DOF Planar Robot Manipulators," International Conference on Advanced Intelligent Machatronics, IEEE/ASME, 2010, pp: 599-604.

[17] P.Pratumsuwan, S. Thongchai, and S. Tansriwong., "AHybrid of Fuzzy and Proportional-Integral-Derivative Controller forElectro-Hydraulic Position Servo System", Energy Research Journal, vol.1,issue 2, 2010, pp. 62–67.

[18] K. Sinthipsomboon, W. Pongaen and P. Pratumsuwan, "A Hybrid of Fuzzy and Fuzzy Self Tuning PID Controller for Servo Electro Hydraulic System," Conference on Industrial Electronics and Applications, IEEE, 2011, pp: 220-225.

[19] A.K. Yadav, P.Gaur, A.P. Mittal & M. Anzar, "Comparative Analysis of Various Control Techniques for Inverted Pendulum", India International Conference on Power Electronics (IICPE), IEEE, 2011, pp: 1-6.

[20] Dr. M P Nandakumar and R. Nalakath, "A Non-Linear PID Fuzzy Approach to Inverted Pendulum Controller with Evolutionary Parameter Optimisation," International Conference on Power, Signals, Controls and Computation, IEEE, 2012, pp: 1-6.

2014 International Conference on Reliability, Optimization and Information Technology -
ICROIT 2014, India, Feb 6-8 2014

Performance Analysis of Three-phase Four-wire Shunt Active Power Filter

Harsha Vanjani, U. K. Choudhury
Engineering Department
Ansal Institute of Technology,
Gurgaon, India
harsha.vanjani@aitgurgaon.org

Abstract—Active power filters are the emerging devices, which can diminish harmonic pollution effectively. Most of the proposed control strategies for power quality improvements have been reviewed with regard to performance and implementation. It has been seen that there has been a significant increase in interest of active power filters and its control methods. Mathematical model of Shunt Active Power filter is implemented with Instantaneous Reactive Power theory. Performance of Three-phase Four-wire Shunt Active Power Filter is analyzed here with Proportional and Integral controller and Proportional Integral and Derivative Controller. Simulation is done in MATLAB to verify the results.

Keywords—active power filter; PI controller; PID controller; total harmonic distortion; mathematical model

I. INTRODUCTION

Power quality is used to determine the fitness of electrical power consumed by various devices. The synchronization of the voltage frequency and the phase allows electrical systems to function in their intended manner without significantly affecting their performance or life. In other words, it describes the electric power that drives an electrical load and in turn, the load's ability to function properly. Power distortion occurs due to the nonlinear load which draws non-sinusoidal currents from the system. Passive filters have emerged as solution to this problem. However this solution has drawbacks:

i. If the conditions of the power system changing periodically, the passive filters can not perform properly because current harmonic absorbing capacity of the filter depends on variation of the power supply system.

ii. Passive filters are bulky and fixed tuned so with change in the system parameters its size and tuned frequency can not be changed easily.

iii. Passive filters are affected by frequency variation of the AC source and tolerances in filter components. The size of the component in tuned branch becomes infeasible because of large frequency variation.

The leading edge active power filters (APF) are smaller in size and it is adjustable in application as to passive filters. APF is self commutated inverter which compensates harmonics and reactive power effectively with extremely fast response. These APFs can be connected in series to compensate voltage harmonics and to compensate current harmonics it can be connected in parallel. Many control strategies have been reviewed and discussed so far [1]-[5]. Here Shunt Active Power Filter (SAPF) is discussed to compensate current harmonics of the supply system. Fig. 1 shows topology of SAPF.

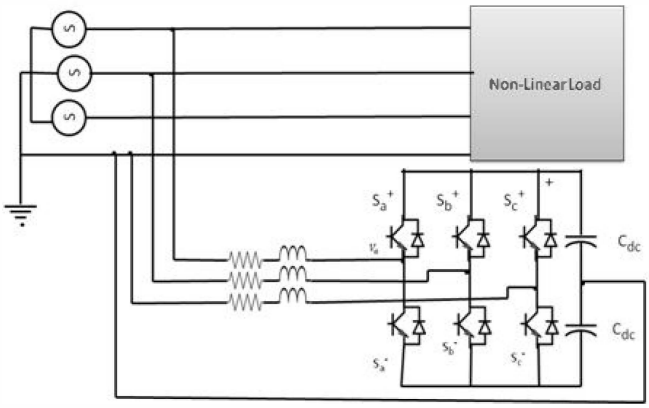


FIG. 1.THREE-PHASE FOUR-WIRE SAPF.

II. MATHEMATICAL MODEL OF SHUNT ACTIVE POWER FILTER

Shunt filters that were once only an idea are now actual live commercial projects with many of them deployed for operation. The controllers of these active shunt filters, in real time determine the reference current which is the harmonic current and simultaneously force a power converter to synthesize it , thereby making active filtering a selective and adaptive process. The active shunt filters also provides harmonic damping in power lines, so as to avoid harmonic propagation arising from harmonic resonances between the series inductances and shunt capacitors. Mathematical model is very essential part of the system. It relys on equations which are based on the performance of the particular system. For SAPF following nine equations are used here to determine performance.

For the circuit shown in Fig. 2 , applying KVL and KCL we can write the following dynamic equations of voltages and currents [6]:

$$\begin{cases} v_a = L_f \dfrac{di_{fa}}{dt} + R_f i_{fa} + v_{sa} \ldots\ldots\ldots\ldots (i) \\ v_b = L_f \dfrac{di_{fb}}{dt} + R_f i_{fb} + v_{sb} \ldots\ldots\ldots\ldots (ii) \\ v_c = L_f \dfrac{di_{fc}}{dt} + R_f i_{fc} + v_{sc} \ldots\ldots\ldots\ldots (iii) \end{cases}$$

978-1-4799-2995-5/14/$31.00©2014 IEEE

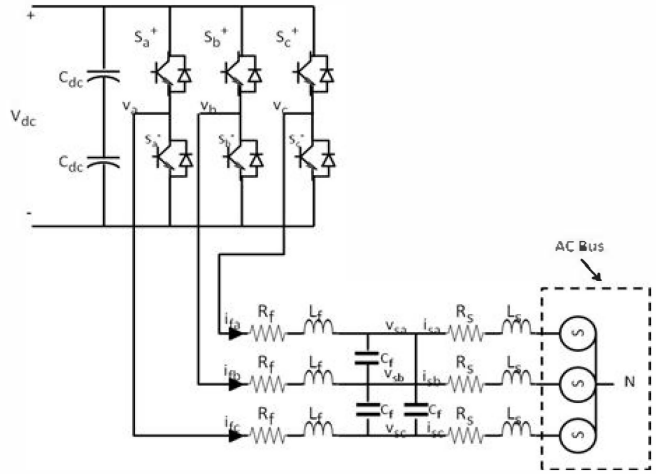


Fig. 2 : VOLTAGE SOURCE INVERTER AS A SAPF

$$i_{fa} = i_{sa} + C_f \frac{d[(v]_{sa} - v_{sb})}{dt} + C_f \frac{d[(v]_{sa} - v_{sc})}{dt} \ldots\ldots \quad (v)$$

$$(iv)@i_{fb} = i_{sb} + C_f \frac{d[(v]_{sb} - v_{sa})}{dt} + C_f \frac{d[(v]_{sb} - v_{sc})}{dt}$$

$$.(v)@i_{fc} = i_{sc} + C_f \frac{d[(v]_{sc} - v_{sb})}{dt} \quad (vi)$$

$$\begin{cases} L_s \frac{di_{sa}}{dt} + R_s i_{sa} = v_{sa} - e_a \ldots\ldots\ldots\ldots\ldots (vii) \\ L_s \frac{di_{sb}}{dt} + R_s i_{sb} = v_{sb} - e_b \ldots\ldots\ldots\ldots\ldots (viii) \\ L_s \frac{di_{sc}}{dt} + R_s i_{sc} = v_{sc} - e_c \ldots\ldots\ldots\ldots\ldots (ix) \end{cases}$$

III. REACTIVE POWER THEORY

The Instantaneous Reactive Power (IRP) p-q Theory is based on the Clarke Transform of voltages and currents in three-phase systems into α and β orthogonal coordinates. The power properties of three-phase systems are described by the IRP p-q Theory using two orthogonal α and β coordinates in terms of p and q instantaneous powers[7]. These are referred to as the instantaneous real and the imaginary powers (or more commonly as the instantaneous real and the reactive powers). The instantaneous imaginary (reactive) power q was introduced on the same basis as the conventional real power p in three phase circuits and then the instantaneous reactive power in each phase was defined with the focus on the physical meaning.

Properties of three-phase systems are expressed by the IRP p-q Theory in terms of only two, active and reactive, p and q, powers, while power properties of this typeof systems, even without harmonic distortion, rely on three independent phenomena:

- Permanent energy transmission
- The voltage and current phase shift
- Line current asymmetry due to the load imbalance.

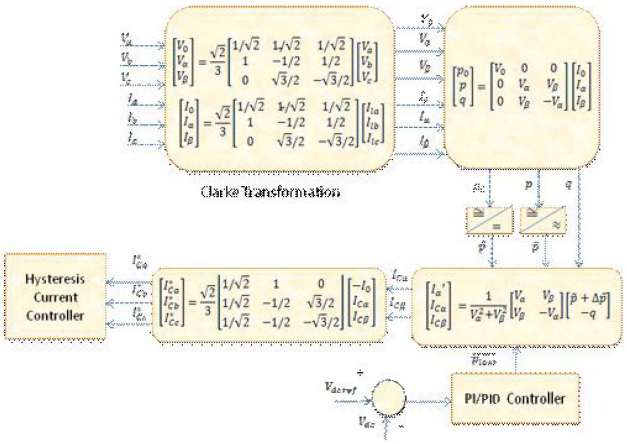


Fig. 3.Block Diagram of IRP theory for Three-phase Four-wire system.

The αβ0 transformation and Power calculation realizes following equations:

$$\begin{bmatrix} V_0 \\ V_\alpha \\ V_\beta \end{bmatrix} = \frac{\sqrt{2}}{3} \begin{bmatrix} \frac{1}{\sqrt{2}} & \frac{1}{\sqrt{2}} & \frac{1}{\sqrt{2}} \\ 1 & -\frac{1}{2} & \frac{1}{2} \\ 0 & \frac{\sqrt{3}}{2} & -\frac{\sqrt{3}}{2} \end{bmatrix} \begin{bmatrix} V_a \\ V_b \\ V_c \end{bmatrix} \ldots\ldots\ldots (x)$$

$$\begin{bmatrix} I_0 \\ I_\alpha \\ I_\beta \end{bmatrix} = \frac{\sqrt{2}}{3} \begin{bmatrix} \frac{1}{\sqrt{2}} & \frac{1}{\sqrt{2}} & \frac{1}{\sqrt{2}} \\ 1 & -\frac{1}{2} & \frac{1}{2} \\ 0 & \frac{\sqrt{3}}{2} & -\frac{\sqrt{3}}{2} \end{bmatrix} \begin{bmatrix} I_{1a} \\ I_{1b} \\ I_{1c} \end{bmatrix} \ldots\ldots\ldots (xi)$$

$$\begin{bmatrix} p_0 \\ p \\ q \end{bmatrix} = \begin{bmatrix} V_0 & 0 & 0 \\ 0 & V_\alpha & V_\beta \\ 0 & V_\beta & -V_\alpha \end{bmatrix} \begin{bmatrix} I_0 \\ I_\alpha \\ I_\beta \end{bmatrix} \ldots\ldots\ldots (xii)$$

A High Pass Filter with cut-off frequency 50Hz seperates $\tilde{p}$ from p and Low Pass Filter separate $\tilde{p}$ from p_0 The powers $\tilde{p}$ and p with q of load should be compensated to provide optimal power flow of the source. Thus, αβ current references are found to be,

$$\begin{bmatrix} I'_\alpha \\ I_{C\alpha} \\ I_{C\beta} \end{bmatrix} = \frac{1}{V_\alpha^2 + V_\beta^2} \begin{bmatrix} V_\alpha & V_\beta \\ V_\beta & -V_\alpha \end{bmatrix} \begin{bmatrix} \tilde{p} + \Delta\bar{p} \\ -q \end{bmatrix} \ldots\ldots (xiii)$$

Where, $\Delta\bar{p} = \overline{p_0} + \overline{p_{loss}}$ energy balance inside the active filter. p_{loss} can be calculated from PI/PID controller as shown in Fig. Finally, αβ0 inverse transform gives instantaneous currents for the hysteresis current controller of Voltage Source Inverter.

$$\begin{bmatrix} I^*_{Ca} \\ I^*_{Cb} \\ I^*_{Cc} \end{bmatrix} = \frac{\sqrt{2}}{3} \begin{bmatrix} \frac{1}{\sqrt{2}} & 1 & 0 \\ \frac{1}{\sqrt{2}} & -\frac{1}{2} & \frac{\sqrt{3}}{2} \\ \frac{1}{\sqrt{2}} & -\frac{1}{2} & -\frac{\sqrt{3}}{2} \end{bmatrix} \begin{bmatrix} -I_0 \\ I_{C\alpha} \\ I_{C\beta} \end{bmatrix} \quad \ldots (xiv)$$

Detailed layout of the Hysteresis Current controller is shown in fig. Here, Compensating currents are compared with standard reference currents which are given to the Hysteresis comparator to generate switching pulses [9].

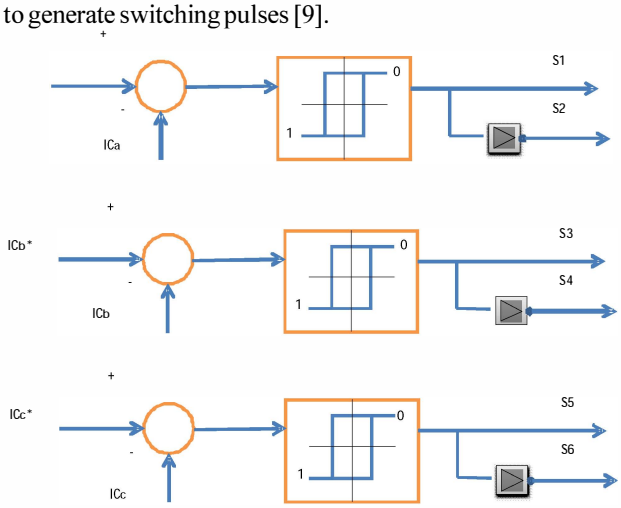


Fig. 4.Hysteresis Current controller.

IV. PI & PID CONTROLLER

SAPF consists of two sections i.e. reference current generation section and PWM current controller section. The PWM current controller is principally used for providing gating pulse to the active power filter. Many control schemes are there for reference current generation, such as p-q theory, Dead Beat controller, wavelet control, sliding mode control, delta-sigma modulation vector control, SFX control, repetitive control etc. Soft computing techniques are used to extract information from the process signal by using expert knowledge. It either seeks to replace a human to perform a control task or it borrows ideas from how biological systems solve problems and apply it to control processes. The main areas in soft computing are fuzzy logic, neural network, genetic algorithm, rough sets, etc. Here,

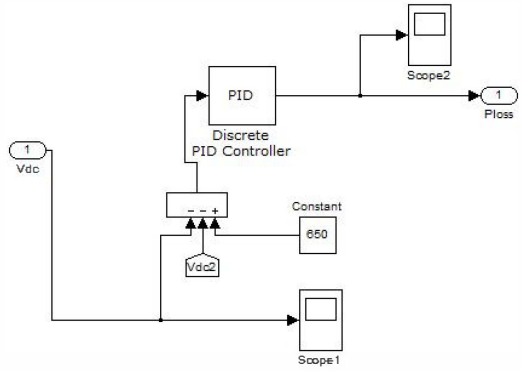


Fig. 5 Calculation of Ploss using PI/PID Controller.

performance of PI and PID controller is verified to set a general result for three-phase four-wire system[10]. Detailed structure of PI/PID controller is shown in fig. error is generated from the

PI/PID controller giving them Vdc actual and Vdc reference signal as input to the comparater [8].

Output of the controller is forwarded to generate reference current signal for SAPF.The input for a PI control is the difference between DC reference side capacitor voltage and sensed voltage (Vdc), a.k.a the error, e (at the nth sampling unit).

$$e = V_{dc,ref} - V_{dc}$$

To preserve the fundamental components this signal is passed through an LPF following which the PI controller estimates the magnitude peak reference current and controls the dc-side capacitor.The PI controller controls the DC bus voltage.Its transfer function is given as

$$H(s) = K_p + \frac{K_i}{s}$$

The principal of a PID controller is very much the same as that of a PI controller. It's control gain is a linear combination of the error itself (representing the present), integral of error (past) and the derivative of the error (representing the future).

$$H(s) = K_p + \frac{K_i}{s} + K_D(s)$$

Where Kp determines the dynamic response of DC-side voltage control, Ki determines it's selling time and KD is the derivative of the error representing the trends.

V.SIMULATION RESULTS

Simulation of this model has been done in MATLAB using simpowersystem block. When SAPF is not connected source current draws large amounts of harmonics in it and shape of the supply current becomes non-sinusoidal from sinusoidal as shown in fig 6.

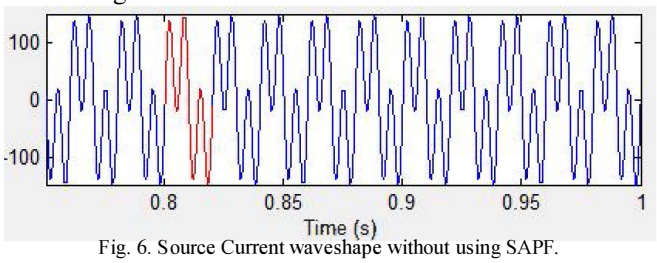


Fig. 6. Source Current waveshape without using SAPF.

With application of Three-phase Four-wire SAPF supply current becomes pure sinusoidal as shown in fig

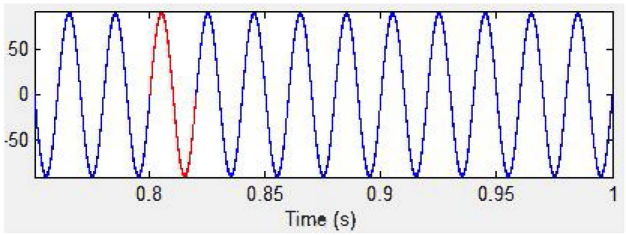


Fig. 7 FFT analysis after compensation with PI Controller, Kp=0.5, Ki=1.

Scope snap of the waveshape of current after compensation is given in fig. Waveshape of the supply voltage can be seen in fig.

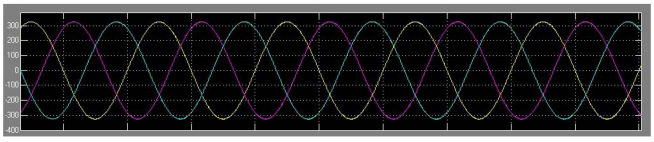


Fig. 8. Waveshape of Three-Phase Supply Voltage.

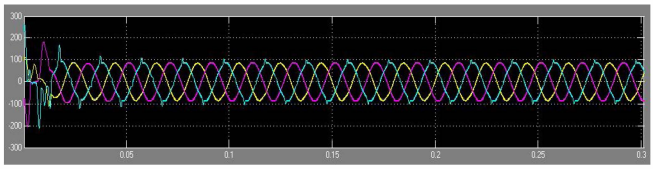


Fig. 9. Waveshape of supply current after compensation.

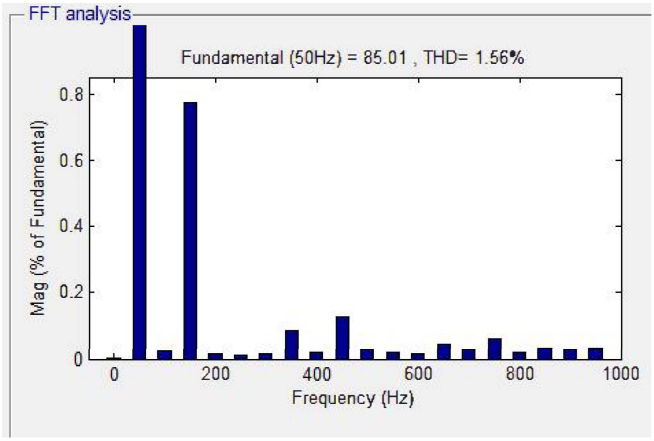


Fig. 10.FFT analysis after compensation with PI Controller, Kp=0.5, Ki=1.

FFT analysis tool in Powergui of MATLAB calculates %Total Harmonic Distortion (THD) factor which should be less than 5% according to IEEE-519 standatd. In this case PI controller is used to control and generate reference current signal for maintaining dc-link voltage of the Capacitor. Fig. shows performance of PI controller with Three-Phase SAPF. %THD is 1.56% in this case and settling time is

When Derivative part is introduced in controller its performance improves and %THD reduces

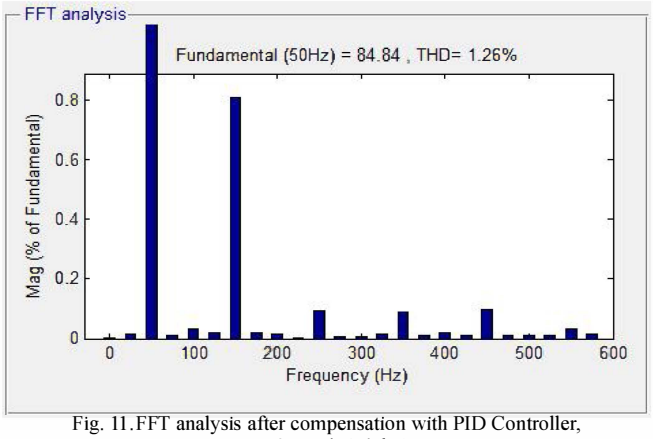


Fig. 11.FFT analysis after compensation with PID Controller, Kp=0.5, Ki=1, kd=1.

PI controller cannot predict the error in near future. This can be solved by introducing derivative mode which has ability to predict what will happen with the error in near future and thus to decrease a reaction time of the controller.

TABLE 1.

Performance Parameters	PI controller	PID controller
%THD	1.56%	1.26%
Time of Response	0.24s	0.22s

VI. CONCLUSION

The shunt active power filter (SAPF) has shown vitality in eliminating harmonics and reactive power and most of them are based on voltage source inverter. According to the PWM laws the DC-link voltage of the inverter must be kept constant for the APF to compensate the harmonics and reactive power efficiently. Since APF cannot maintain DC-link voltage itself, it relies on PI controller to manage this.The problem of DC-bus voltage control of three phase three leg voltage source inverter based four wire active filter control is treated. The performances of the PI and PID controller in DC□bus voltage control is verified through MATLAB simulation. The dc link PID control has better dynamic behavior than conventional PI control strategy and it reduces settlement time too. Table I shows results which satisfies requirements of IEEE-519 standard [11].

REFERENCES

[1] Harsha Vanjani, U. K. Choudhury, "Different Control Strategies applied for Active Power Filter" International Review of Automatic Control, vol.6, no.3, pp 280-285, May 2013.

[2] Bhim Singh, Kamal Al-Haddad, Ambrish Chandra, A Review of Active Filters for Power Quality Improvement, IEEE Transactions on Industrial Electronics, vol. 46issue 5, October 1999, pp. 960-971.

[3] M.El-Habrouk, M.K. Darwish, P. Mehta, Active Power Filters: A Review, IEE Proceedings Electric Power Applications, vol. 147 issue 5, September 2000, pp. 403-413.

[4] Vinod Khadkikar, Enhancing Electric Power Quality Using UPQC: A Comprehensive Overview, IEEE transactions on Power Electronics, vol. 2issue 5, May 2012,pp. 2284 - 2297.

[5] Shi Zhang, Daheng Li, Xu Wang, Control techniques for active power filters, International Conference on ELECTRICAL AND CONTROL ENGINEERING ~ ICECE 2010~, June25-27, 2010,Wuhan, China.

[6] Hirofumi Akagi, Edson Hirokhzu Watanabe, Mauricio Aredes, "Instantaneous Power Theory and Applications to Power Conditioning", IEEE press, 2007.

[7] Watanabe E.H. , Akagi H. , Aredes M., Instantaneous p-q power theory for compensating nonsinusoidal systems nonsinusoidal currents and compensation, International School on NONSINUSOIDAL CURRENTS AND COMPENSATION~ISNCC 2008~, June 10-13, 2008, Lagow, Poland.

[8] Zhang Qian, Wang Binbin, Zhu Haiyun, Ma Haibo, "Alterable Integral Control Algorithm for Shunt Active Power Filter", International conference on ADVANCED MECHATRONIC SYSTEMS~2011, Zhengzhou, China.

[9] T. Narongrit, K-L. Areerak and K-N. Areerak, "The Comparison Study of Current Control Techniques for Active

Power Filters", World Academy of Science, Engineering and Technology pp 471-476, 2011

[10] H.L.Jou, K. D. Wu, J. C. Wu, C. H. Li and M. S. Huang, "Novel power Converter Topology for Three-phase Four-wire Hybrid Powerfilter", IET Power Electronics, vol. 1 issue 1, March 2008, pp. 164-173.

[11] IEEE Std. 519-1992, "IEEE Recommended Practices and Requirements for Harmonic Control in Electrical Power Systems", 1993.



Harsha Vanjani, born on 22nd December 1983, brought up in India. Ms. Vanjani completed her B. Tech. In the field of electrical engineering in the year 2004 from Saurashtra University and M. Tech in power apparatus & systems in the year 2006 from Nirma University, Ahmedabad.

She is a dedicated academician working as Assistant Professor in Engineering Department at Ansal Institute of Technology. With over seven years of teaching experience in different engineering colleges, she is pursuing research in the field of Power Electronics. She has taught subjects like electromechanical energy conversion, circuits & systems, electrical measurement & measuring instruments, control engineering, power electronics & drives, electrical science, electrical machine design, power station practice, power quality management at Undergraduate level.



U.K Choudhury has done Ph.D. from Jamia Millia Islamia (Central University), M.Tech. from Delhi College of Engineering (presently known as Delhi Technological University) and B.E from University College of Engineering, Burla, Orissa,

He is working as Associate Professor in Ansal Institute of Technology. He has published papers in Referred Journals, International Conferences and National Conferences. He has also attended many seminars and workshops of national repute .His areas of interest are power system stability and application of artificial intelligence techniques in Power System.

With an experience of more than 14 years, Dr. Choudhury has worked in Industry, Govt. Institutes and reputed Engineering colleges in NCR region.

International Journal of Emerging Technology and Advanced Engineering
Website: www.ijetae.com (ISSN 2250-2459 (Online), Volume 4, Special Issue 1, February 2014)
International Conference on Advanced Developments in Engineering and Technology (ICADET-14), INDIA.

Physico-Chemical Characterization of Cathode Material, $Li_{1+x}(Mn_{0.4}Ni_{0.4}Fe_{0.2})_{1-x}O_2$ (x=0.2) for Lithium Ion Batteries

Rishibrind K. Upadhyay[1], Amrish K. Panwar[2]

***Abstract*-The alternative materials of well establish layered cathode material, $LiCoO_2$ are enormously in demand for lithium ion batteries due to the failure of Co based cathode at high temperature (>90 ^{0}C), toxicity and high cost. In past, $LiNi_{1/2}Mn_{1/2}O_2$ and $LiNi_{1/3}Co_{1/3}Mn_{1/3}O_2$ with less amount of Co has also been investigated extensively as cathode materials for better electrochemical performance in lithium ion batteries. In the present investigation, synthesis of alternative layered $Li_{1+x}(Mn_{0.4}Ni_{0.4}Fe_{0.2})_{1-x}O_2$ (x=0.2) cathode material has been carried out by sol-gel route of chemical synthesis with citric acid as chelating agent. After calcinations, precursor of $Li_{1+x}(Mn_{0.4}Ni_{0.4}Fe_{0.2})_{1-x}O_2$ (x=0.2) has been characterized by X-ray diffractometer (XRD), scanning electron microscope (SEM) for phase conformation, structural and morphological studies. The XRD results revealed that the synthesized material possesses layered structure with R3m space group. AC conductivity measurement of synthesized layered cathode material has also been attempted.**

***Keywords*-cathode materials, layered oxides, ordinate of LiCoO2, sol –gel route**

I. Introduction

Lithium ion batteries (LIBs) have become the highly promising power sources for consumer electronic devices, such as cellular phones, laptops, PDAs and electric vehicles/ hybrid electric vehicles due to their high energy density and light weight. There has been a growing development in lithium ion batteries due to very high demand of energy resources as these batteries play a vital role in our daily life. Earlier, there are various type of rechargeable batteries technology available in the market such as Lead acid, Ni-Cd, Ni–metal hydride etc.

Among these, lithium ion batteries have highest demand in market because of batter properties like little weight, high energy density, long cyclebility etc.

In 1990, Sony energy corporation fabricated first commercial device of lithium ion battery using layered $LiCoO_2$ as the cathode material due to its high energy density, better structural and high conductivity. But $LiCoO_2$ have also demerits such as toxicity, high cost and instability of cobalt at high potential windows greater than 4.3V [1, 2].

Hence, alternative ordinate of cobalt free cathode was investigated such as $LiNiO_2$ and $LiMnO_2$. However, these materials also have drawbacks such as thermal instability in $LiNiO_2$ and structural degradations during charge/ discharge cycle in $LiMnO_2$, which results in poor electrochemical performances [3, 4]. Further, other materials such as $LiMn_2O_4$ and $LiFePO_4$ investigated but problem occur during the operation at elevated temperatures, due to the Mn^{3+} dissolution and attack on battery electrode due to this performance of the cell decrease in terms of capacity fading and also these cathode materials have low conductivity [5]. Hence, research is still going on for establishment of high preference cathode material like layered structural material which would be low cost, environmental friendly, non-toxic and better electrochemical performance. New layered materials for lithium ion batteries such as $LiNi_{1/2}Mn_{1/2}O_2$ and $LiNi_{1/3}Co_{1/3}Mn_{1/3}O_2$ have been synthesized using co-precipitation synthesis route [6, 7]. Moreover, manganese based material i.e. Li_2MnO_3 was also developed but it has been observed that Li_2MnO_3 have poor electrochemical performance. In this investigation, a layered lithium manganese oxide in excess of Li as alternative cathode, $Li_{1+x}\{Mn_{0.4}Ni_{0.4}Fe_{0.2}\}1\text{-}xO_2$ (x=0.2) material has been prepared with Li, Mn, Ni and Fe compounds using a citric acid assisted sol-gel synthesis route. The prepared cathode material is advantageous for high capacity and thermal stability. Phase formation, particle distribution, morphology and particle size of $Li_{1+x}\{Mn_{0.4}Ni_{0.4}Fe_{0.2}\}1\text{-}xO_2$ (x=0.2) cathode material has been characterized by XRD, SEM and ac conductivity measurements.

II. Experimental

Synthesis of $Li_{1+x}\{Mn_{0.4}Ni_{0.4}Fe_{0.2}\}_{1-x}O_2$ (X=0.2) was carried out by stoichiometric amount of compounds lithium acetate [$Li(CH_3COO).2H_2O$], manganese Acetate [$Mn(CH_3COO)_2.4H_2O$], Nickel Acetate [$Ni(CH_3COO)_2.H_2O$] and Ferric nitrate [$Fe(NO_3)_3.9H_2O$]. All these compounds were dissolved in triply distilled water and then added to a continuously stirred aqueous solution containing citric acid as chelating agent.

International Journal of Emerging Technology and Advanced Engineering
Website: www.ijetae.com (ISSN 2250-2459 (Online), Volume 4, Special Issue 1, February 2014)
International Conference on Advanced Developments in Engineering and Technology (ICADET-14), INDIA.

The pH of the solution was kept between 6-7. The resultant solution was heated in the temperature range 80^0-90^0C with a continuous magnetic stirring until a transparent thin gel was obtained. Thin gel was further heated until a thick sticky precursor is formed. The resulting precursor was decomposed at 350^0C for 5 hours in an inert (Argon) gas environment in eliminate the organic moieties, such as carboxylic groups. The decomposed powder were ground, and kept into the furnace for calcinations at 750^0C for 12 hours in inert atmosphere to obtained nanocrystalline powders. The formation of desired phase of the synthesized powder was confirmed by X-ray diffraction measurement using CuKα_1 radiation in conjunction with nickel filter by Bruker make D8 ADVANCE model. The wide range XRD pattern was obtained between 10^0 and 80^0 at scan rate of 20 min^{-1}. The microstructural investigation such as morphology, particle size and distribution of particles in surface and subsurface region of the calcined powder was performed using Hitachi make model S-4700 of scanning electron microscope. Impedance measurements were carried out by making pellets of calcined powder of diameter, 1.0 cm and thickness, 1.28 mm at room temperature using LCR METER (Agilent 4284A) in the frequency range of 20Hz to1MHz. The flat surface of the pellet were coated with silver paste and then heated at 120^0C to remove moisture. All the measurement has been done at biased voltage 1V.

III. Results And Discussion

The synthesized $Li_{1+x}\{Mn_{0.4}Ni_{0.4}Fe_{0.2}\}_{1-x}O_2$ (X=0.2) powders were characterized using XRD for determination of crystal structure. Observed XRD pattern of $Li_{1+x}(Mn_{0.4}Ni_{0.4}Fe_{0.2})_{1-x}O_2$ (x=0.2) is shown in Figure 1. The indexed peaks reveal the hexagonal α-$NaFeO_2$ type structure with a space group of R3m, indicating that a layer of lithium is substituted with a layer containing lithium, manganese, nickel and iron atoms [8]. Two small peaks observed between 20^0 and 30^0 indicating the additional supper lattices, due to the short range ordering of lithium, manganese, nickel and iron at the atomic site 3a resulting the existence of a layered structure with Li_2MnO_3[9]. The radius of lithium ion, Li^+ (0.76Å) is greater than that of Nickel, Ni^{2+} (0.69 Å) and Mn^{4+} (0.53 Å, six fold coordination) as proposed by Shannon et.al [10] for the effect of ionic radii.

As the radius of Li^+ is larger, the substitution of Li^+ for metal ions causes the increase in lattice parameters.

Moreover, the c/a ratio of the sample is more than 4.90, it shows that the layered behavior of synthesized sample. This is well known that with increasing c/a ratio beyond 4.90, the ordering of the layered structure increases and the crystal structure becomes more hexagonal [11]. The ratio of the intensity of peaks indexed at (003) to (004) i.e. I(0 0 3)/I(1 0 4) is of about 0.84,which is also agreement with the value given by the Ohzuku [12]. That is the indication of mixing between Ni^{2+} and Li^+ cations.

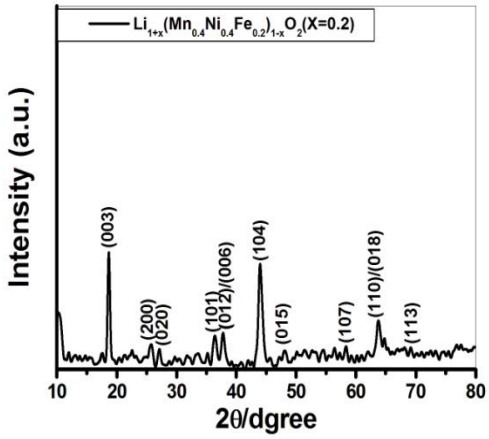


Figure 1: XRD patterns of $Li_{1+x}(Mn_{0.4}Ni_{0.4}Fe_{0.2})_{1-x}O_2$ (x=0.2) powers synthesized using citric acid assisted sol-gel method at 750ºC

The surface morphology of the layered powder prepared at 750 ^{0}C is shown in Figure 2 (a)-(d) at different Magnifications. As it is well-known that particle size and morphology of powders play a crucial role in determining the electrochemical performance of the material. From the figure 2, it is found that the uniformly distributed particles of prismatic shape and size lies between 100nm to 140 nm are observed. It was proposed that the small particles of 110 nm size with even distribution is beneficial for better Li+ diffusion and enhanced electronic transport at high current rates.[13,14].

"Sharpening Skills..... Serving Nation"

International Journal of Emerging Technology and Advanced Engineering

Website: www.ijetae.com (ISSN 2250-2459 (Online), Volume 4, Special Issue 1, February 2014)

International Conference on Advanced Developments in Engineering and Technology (ICADET-14), INDIA.

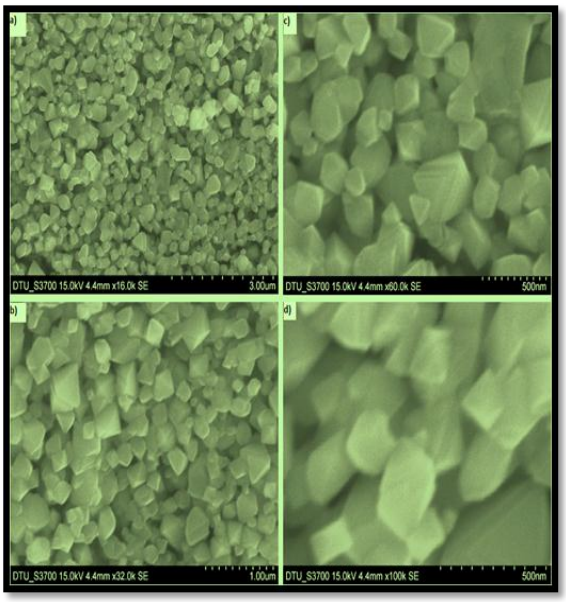


Figure 2: SEM images of $Li_{1+x}(Mn_{0.4}Ni_{0.4}Fe_{0.2})_{1-x}O_2$ (x =0.2) layered power calcinated at 750 ^{0}C

Impedance measurements have been carried out using LCR METER (Agilent 4284A) over the frequency range of 20Hz-1MHz at room Temperature. The real and imaginary parts of the measured impedance values were plotted in a complex plane and shown in Figure3(a). Bulk resistance (R) of the sample was calculated from the extrapolated semiconductor plot in the low frequency region on the X-axis. The electrical conductivity (σ) of the samples were calculated using the following relation:

$$\sigma = (1/R).(L/A)$$

Where L is the thickness of the sample and A the area of the cylindrical sample [15]. The electrical conductivity (ac) of the material at the room temperature is of estimated of the order of 10^{-6}S/cm. Figure 3(b) shows the variation of the real part of the impedance with the frequency. It may be revealed that the impedance is higher at lower frequency range, which indicates that the molecules are in the polarization state at the lower frequencies and on increasing the frequencies the molecules in the compound attain relaxation state.

It is also found that there is minor decrement in the impedance over the frequencies range of 20Hz-1MHz shows that the material can remain in the polarization state over the frequency range [16]. Hence, lithium intercalation into the host structure will be easy over the frequency range 20Hz-1MHz. Figure 3(c) shows that the variation in the resistance with the temperature. The resistance of the $Li_{1+x}\{Mn_{0.4}Ni_{0.4}Fe_{0.2}\}_{1-x}O_2$ (x=0.2) layered material decrease with the increasing temperature, which indicates the semiconducting behavior of the material.

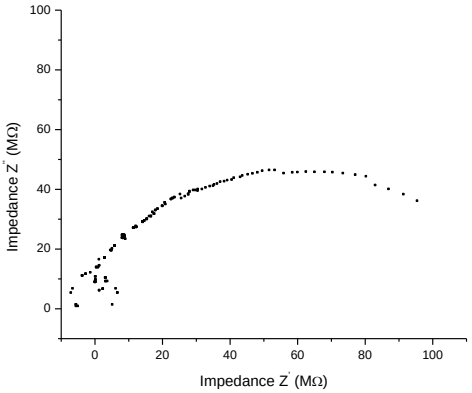


Figure 3 (a): The variation of real and imaginary parts of the measured impedances in complex plane.

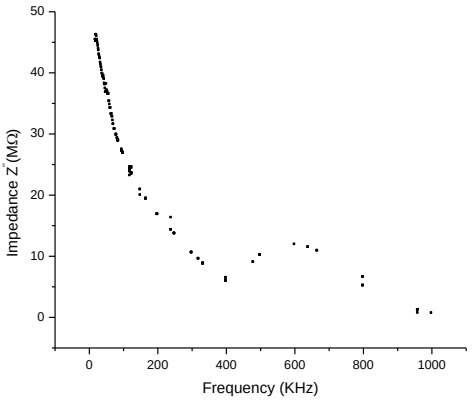


Figure 3(b): variation of the real part of the impedance with the frequency

IJETAE
EXPLORING RESEARCH AND INNOVATIONS
IKCE
"Sharpening Skills.....
Serving Nation"

International Journal of Emerging Technology and Advanced Engineering
Website: www.ijetae.com (ISSN 2250-2459 (Online), Volume 4, Special Issue 1, February 2014)

International Conference on Advanced Developments in Engineering and Technology (ICADET-14), INDIA.

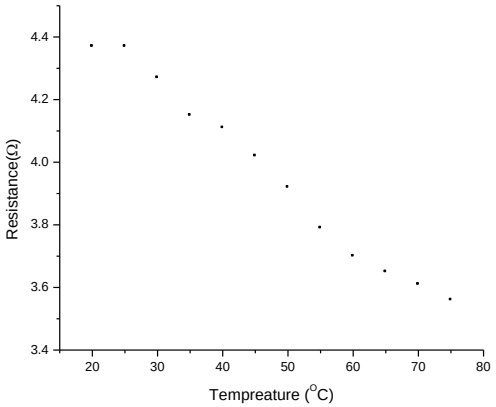


Figure 3(c): variation of the resistance with the temperature.

IV. CONCLUSIONS

A layered $Li_{1+x}(Mn_{0.4}Ni_{0.4}Fe_{0.2})_{1-x}O_2$ (x =0.2) composites cathode material for lithium ion batteries has been prepared using citric acid assisted sol-gel synthesis route. The layered materials containing iron could be one of the promising material for lithium ion batteries at low cost and eco-friendly energy resource at large scale. The phase formation of layered $Li_{1+x}(Mn_{0.4}Ni_{0.4}Fe_{0.2})_{1-x}O_2$ (x =0.2) with R3m space group has been confirmed by XRD. Scanning electron microscope (SEM) analysis reveals the existence of the uniformly distributed, prismatic shape of particles in the range of 100 nm-140 nm. Ac conductivity of the material at the room temperature is found of the order of 10^{-6}S/cm, in the semiconducting range. However, overall electrochemical performance will show the potentially of the prepared materials over other cathode materials, which has yet to be performed.

Acknowledgement

Authors are thankful to SERB, Department of Science and Technology (DST), New Delhi for financial support to carried out this work and also give sincere thanks to Mr. Sandeep Mishra for XRD and SEM characterizations in advance instrumentation centre, Delhi Technological University, Delhi 110042.

REFERENCES

[1] Ralph J. Brodd, Kathryn R. Bullock, Randolph A. Leising, Richard L. Middaugh, John R. Miller, and Esther Takeuchi "Batteries, 1977 to 2002" J. Electrochem. Soc., Vol.151(3) (2004), pp. K1-K11

[2] B. Ammundsen, J. Paulsen, "Novel Lithium- Ion Cathode Materials Based on Layered Manganese Oxides" Adv. Mater., Vol. 13 (2001), pp. 943–956

[3] G. Dutta, A. Manthiram, J.B. Goodenough, "Chemical synthesis and properties of $Li_{1-\delta-x}Ni_{1+\delta}O_2$ and $Li[Ni_2]O_4$" J. Solid State Chem., Vol. 96 (1992), pp. 123–131

[4] G. Vitins, K. West, "Lithium Intercalation into Layered $LiMnO_2$" J. Electrochem. Soc., Vol. 144 (1997), pp. 2587-2592

[5] O.K. Park, Y. Cho, S. Lee, H.C. Yoo, H.K. Song, "Who will drive electric vehicles, olivine or spinel?" J. Cho, Energy Environ. Sci., Vol. 4 (2011), pp. 1621-1633

[6] Y. Makimura, T. Ohzuku, "Lithium insertion material of $LiNi_{1/2}Mn_{1/2}O_2$ for advanced lithium-ion batteries " J.Power Sources, Vol. 119–121 (2003), pp. 156–160

[7] T. Ohzuku, Y. Makimura, "Layered lithium insertion material of $LiNi_{1/2}Mn_{1/2}O_2$: a possible alternative to $LiCoO_2$ for advanced lithium-ion batteries" Chem. Lett., Vol. 30 (2001), pp. 642-643

[8] M. Tabuchi, Y. Nabeshima, K. Ado, M. Shikano, H. Kageyama, K. Tatsumi, "Material design concept for Fe-substituted Li_2MnO_3-based positive electrodes" J. Power Sources, Vol. 174 (2007) , pp. 554–559

[9] Y. Sun, C. Ouyang, Z. Wang, X. Huang, L. Chen, "Effect of Co Content on Rate Performance of $LiMn_{0.5-x}Co_{2x}Ni_{0.5-x}O_2$ Cathode Materials for Lithium-Ion Batteries" J. Electrochem. Soc., Vol. 151 (2004), pp. A504-A508

[10] R. D. Shannon, "Revised effective ionic radii and systematic studies of interatomic distances in halides and chalcogenide", Acta Crystallogr., Vol. A32 (1976), pp. 751-767

[11] B. Ammundsen, J.Paulsen, I. Davidson, R. S. Liu, C. H. Shen, J. M. Chen, L. Y. Jang, J. F. Lee, "Local Structure and First Cycle Redox Mechanism of Layered $Li_{1.2}Cr_{0.4}Mn_{0.4}O_2$ Cathode Material" J. Electrochem. Soc., Vol. 149 (2002), pp. A431-A436

[12] T. Ohzuku, Y. Makimura, "Layered lithium insertion material of $LiCo_{1/3}Ni_{1/3}Mn_{1/3}O_2$ for lithium-ion batteries" Chem. Lett., Vol. 8 (2001) , pp.744-745

[13] C. Suryanarayana, C. C. Koch, "Nanocrystalline materials–Current research and future directions" Hyperfine Interact., Vol.130,(2000), pp. 5-44

[14] Z. Wang, Y. Sun, L. Chen, X. Huang, "Electrochemical Characterization of Positive Electrode Material LiNi1/3Co1/3Mn1/3O2 and Compatibility with Electrolyte for Lithium-Ion Batteries" J. Electrochem. Soc., Vol. 151 (2004), pp. A914-A921.

[15] F. Maia Luciana, C.M. Rodrigues Ana: "Electrical conductivity and relaxation frequency of lithium borosilicate glasses" Solid State Ionics., Vol. 168 (2004), pp. 87–92

[16] S. Nieto-Ramos, M.S. Tomer, S.Hernandez, F. Aliev: "Thin films of lithium intercalation complex oxides for cathodes" Thin Solid Films, Vol. 377 (2000), pp. 745–749

"Sharpening Skills.....
Serving Nation"

International Journal of Emerging Technology and Advanced Engineering
Website: www.ijetae.com (ISSN 2250-2459 (Online), Volume 4, Special Issue 1, February 2014)

International Conference on Advanced Developments in Engineering and Technology (ICADET-14), INDIA.

AUTHOR'S PROFILE



Rishibrind K. Upadhyay received his, B. Tech degree in Electronics & Communication from Dr B. R. Ambedkar University Agra and now, pursuing M.Tech in Nanoscience and Technology from Delhi Technological University, Delhi. He is doing M.Tech. Project on: "Alternative Cathode Material for Lithium Ion Batteries"



Dr. Amrish K. Panwar* is presently assistant professor in department of applied physics, Delhi Technological University, Bawana Road, Delhi. Besides of teaching assignment, he is actively involve in research and development work. His area of research includes: energy storage and conversion devices such as lithium/ sodium ion batteries (starting from materials synthesis to prototype device fabrication), study of nanosize multiferroic and thermoelectric materials, surface modification of low energy solids.

Rishibrind K. Upadhyay, Lithium-Ion Battery Technology Laboratory, Department of Applied Physics, Delhi Technological University (Formerly Delhi College of Engineering), New Delhi-110042, India, Mobile no. +91-8130146285 (Email: rishibrind1989@gmail.com)

***Dr. Amrish K. Panwar**, Assistant Professor, Department of Applied Physics, Delhi Technological University (Formerly Delhi College of Engineering), New Delhi-110042, India, Mobile no. +91-9891778307 (Email: panwaramar@gmail.com).

Volume 1 (2014) 127-133 ISSN 2347 - 3258
International Journal of Advance Research and Innovation

Portfolio Optimization: Indifference Curve Approach

Nand Kumar [a,*], Archana Singh [b], Ranganath M S [c], Amandeep Kaur [c]
[a] Department of Humanities and Applied Sciences, Dehli Technical University, New Delhi, India
[b] Delhi School of Management, Dehli Technical University, New Delhi, India
[c] Department of Mechanical Engineering, Delhi Technological University, New Delhi, India

Article Info

Article history:
Received 2 January 2014
Received in revised form
29 January 2014
Accepted 20 February 2014
Available online 15 March 2014

Keywords

Efficient Frontier,
Indifference Curve,
Risk-aversion Factor,
Investment Time Horizon,
Portfolio Optimization

Abstract

The study examines the monthly stock prices of 45 SENSEX companies for the period ranging from February 2002 to January 2012. Also the study includes the Indian G-SEC long term bonds with maturities ranging from 15 to 25 years. The set of all efficient portfolios is called the efficient frontier. All risk-averse investors who act to maximize expected utility have an optimal portfolio on this frontier. Based on the risk-aversion factor and the investment time horizon of each individual investor, an attempt is being made to select the optimal portfolio for that particular investor. Given a utility function for an individual investor, the portfolio optimization problem is to find the indifference curve which is tangent to the efficient frontier. The optimal portfolio for the investor lies at the point of tangency between the efficient frontier and the indifference curve. The findings of the study bring out the importance of the investor's time horizon and the risk-aversion factor in portfolio optimisation.

1. Introduction

Portfolio theory was first discovered and developed by Harry Markowitz in the 1950's (Markowitz, 1952). Markowitz formulated the portfolio problem as a choice of the mean and variance of a portfolio of assets. His work forms the foundation of modern finance. Post Markowitz theory related to portfolio is often called 'Modern Portfolio Theory'. Markowitz approach is based on the mean-variance analysis, where the variance of the overall rates of return is taken as a risk measure and expected value measures profitability. In contrast to expected utility maximisation, mean – variance analysis takes into account only the first two moments and there is no clear theoretical foundation. The special assumption under which mean- variance analysis is consistent with expected utility maximisation is the assumption of Von Neumann- Morgensten utility. [Modern portfolio Theory: Some main Results, Heinz H. Muller, Astin Bulletin, Vol18, no.2] Heinz H. Muller, in his article has summarised some main results in modern portfolio. He discusses Markowitz approach which shows that due to the correlation between the returns of the financial assets, diversification allows in general, only for a reduction but not for the elimination of the risk. Markowitz (1952) was the first who took the covariance between the rates of return into account.

John Norstad (1999, updated 2001) in his paper, 'An introduction to portfolio theory' has introduced the basic concept of portfolio theory, including the notions of efficiency, risk-return graphs, the efficient frontier iso-utility curve and asset allocation optimisation problems. He has developed the theory in both, a simplified setting by assuming returns are normally distributed over the time period and considering Random walk Model where returns are log-normally distributed. The assumption that the returns are normally distributed along with the assumption of negative exponential utility leads to portfolio maximisation problem. The log normal distribution in Random walk model is better approximation to the distribution of observed historical returns for common financial assets like stocks and bonds. Log normal returns are also consistent with Central Limit Theorem. In Random walk model, portfolio efficiency is determined by instantaneous expected returns and the standard deviations of these results. The additional assumption of Iso elastic-utility leads to portfolio optimisation problem that are linear in return and variance.

Researchers (Elton, Gruber, 1997) believe that there are two reasons for the persistence of mean

Corresponding Author,
E-mail address: nand.dce@gmail.com
All rights reserved: http://www.ijari.org

variance theory. First, mean variance theory itself places large data requirements on the investor, and there is no evidence that adding additional moments improves the desirability of the portfolio selected. Second, the implications of mean variance portfolio theory are well developed, widely known, and have great intuitive appeal.

Mean variance portfolio theory was developed to find the optimum portfolio when an investor is concerned with return distributions over a single period. MPT models an asset's return as a normally distributed function, defines risk as the standard deviation of return, and models a portfolio as a weighted combination of assets, so that the return of a portfolio is the weighted combination of the assets' returns. The primary principle upon which Modern Portfolio Theory (MPT) is based is the Random Walk Hypothesis which states that the movement of asset prices follows an unpredictable path. MPT assumes that investors are risk averse and rational. The implication is that a rational investor will not invest in a portfolio if a second portfolio exists with a more favourable risk-expected return profile – i.e., if for that level of risk an alternative portfolio exists which has better expected returns.

In Markowitz approach every mean-variance efficient portfolio is a combination of the riskless investment with reference to portfolio consisting of risky assets. It is important to note that special structure of the set of mean- variance, efficient portfolios provide the basis of the Capital Asset Pricing Model (Heinz H., Muller, et.al)

The Capital Asset Pricing Model (CAPM) is used to determine the expected rate of return of an asset. Sharpe - Lintner CAPM model assumes that there is a risk-less asset. The model takes into account the asset's sensitivity to non-diversifiable risk, often represented by Beta (β) as well as the expected return of the market and expected return of theoretical risk free asset. The assumption of existence of riskless asset is somewhat questionable, especially if one is interested in real return. The Black (1972) model derives the CAPM relationship without assuming the existence of riskless asset. The CAPM relationship obtained from Sharpe-Lintner model can be written as

$$E(R_i) - R_f = \frac{\text{Cov } R_i R_m}{\text{Var } R_m} [E(R_m - R_f)]$$

$$E(R_i) = R_f + \beta_i * E[R_m - R_f] \quad (1)$$

Where β_i is called the beta coefficient of assets

$E(R_i) - R_f$ is the risk premium on asset i.

$E(R_m - R_f)$ is risk premium on the market portfolio.

Indifference Curves defines the utility of the investors. For any given curve, the possible investments which plot on the curve will have the same expected utility, and the investor is therefore indifferent among them. The y-intercept of a curve is the value of **k**. This is the investor's certainty equivalent for all the other possible investments on the curve. The higher indifference curves have larger certainty equivalents and larger expected utility. Assuming that the investor has a negative exponential utility function, measured as a function of return rather than end-of-period wealth, the investor maximizes the following function over the feasible set or, over the efficient frontier:

$$k = R_P - \tfrac{1}{2}[(A\sigma^2_{pn}) / n] \quad (2)$$

Where, k gives the utility of the portfolio which is constant on a particular indifference curve. 'A' denotes the coefficient of risk-aversion, and σ^2_{pn} stands for the variance of portfolio for n-year.

The objective of this paper is to select an optimal portfolio, from a given set of portfolios, based on the investor's risk-aversion factor and the investment time horizon. Risk-aversion factor denotes the amount of risk that a particular investor is willing to tolerate. Investment time horizon defines the time-period for which a particular investor wishes to invest in the portfolio. The study is based on a simplified assumption that returns are normally distributed over the time period.

2. Research Methodology

In this paper we have considered the feasible set of investment alternatives consisting of all portfolios combining long-term G-SEC bonds and 45 SENSEX stocks. It is assumed that leverage and short sales are not allowed, so each portfolio consists of some percentage x of bonds and 100-x of stocks where,

$$0 < x < 100$$

The data set consists of monthly adjusted closing prices of the market (SENSEX), stock (45 stocks of SENSEX), and risk-free rate of return (from MIBOR) for the period from February 2002 through January 2012 (viz. 10 years). The sample period exhibits a mixed set of economic environment in Indian economy. Long-term GSEC bonds are the Government Securities with years of maturity ranging from 15 years to 20 years. Such bonds are considered to be the risk-free assets. In addition, the choice of the optimal portfolio is based on the investors' risk-aversion factor and the investment time horizon. The investment time horizon varies from one year to five years. It is assumed that two types of investors exist in the market. The first category includes the investors with low risk-aversion factor, i.e. investors' who can bear more risk for higher expected returns. The second

category of investors includes the one with high risk-aversion factor, i.e. investors' who are not willing to take large amounts of risk. So, the risk-aversion factor is chosen to be A=4 for investors who can bear more risk and A=40 for the investors who cannot take large amounts of risk.

In the present study, the capital asset pricing model (CAPM) is used to determine the expected rate of return on a stock. The model takes into account the asset's sensitivity to non-diversifiable risk, often represented by the quantity beta (β), as well as the expected return of the market and the expected return of a theoretical risk-free asset. The CAPM equation for the Security Market Line is given as

$$E(R_i) = R_f + \beta_i * [R_m - R_f] \quad (3)$$

Where, $E(R_i)$ is the expected return on security, R_f gives the risk-free rate, β_i denotes the systematic risk, and R_m is the expected return on market portfolio.

Market Returns are the returns that the investors generate out of the stock market. Here it has been calculated as below:

$$R_m = [(P_t - P_{t-1})/P_{t-1}]*100 \quad (4)$$

Where, P_t denotes the price of index in time period t, and P_{t-1} denotes the price of index in preceding time period t-1.A stock's market price is a function of the market's perception of the value of the future profits a company can create. Symbolically, return on stocks can be written as

$$R_s = ((P_t - P_{t-1})/P_{t-1})*100 \quad (5)$$

Where, R_s is the Percentage return on a stock.

Beta is a measure of the volatility, or systematic risk, of a security or a portfolio in comparison to the market. Beta is calculated using regression analysis. Symbolically

$$\beta = [Cov(R_s, R_m)]/\sigma_m^2) \quad (6)$$

Where, Cov (R_s, R_m) gives the covariance between security and market return and σ_m^2 gives the variance of market return. Return on bonds is calculated using Yield to Maturity (YTM) in Microsoft excel.

$$YTM = Rate(NPER, PMT, PV, FV) \quad (7)$$

Where, NPER denotes total number of payments, PMT denotes payment made each period, PV denotes present value, and FV denotes future value.

Risk for bonds is calculated in the same manner as the calculation of risk of stocks. Symbolically

$$\sigma = \sqrt{\frac{\Sigma(\bar{x} - x)^2}{n - 1}}$$

Where, σ gives the standard deviation (risk), X is the expected return, and n is used to denote number of observations.

Further, 21 feasible portfolios are constructed using the mix of stocks & bonds. The most conservative portfolio consists of 0% stocks & 100% bonds whereas the most aggressive portfolio consists of 100% stocks & 0% bonds. In between the conservative and aggressive portfolio the portfolios are assigned weights like 5% stocks & 95% bonds, 10% stocks & 90% bonds and so on

Portfolio return is the proportion-weighted combination of the constituent assets' returns. Symbolically

$$R_P = W_S R_S + W_B R_B \quad (8)$$

Where, R_P is the portfolio return, W_S and W_B gives the weight assigned to stocks and bonds, and R_S and R_B gives the return on stocks and bonds.

The feasible set of stocks and bonds plots as a curve between the risk and the expected return. The most conservative portfolio, 100% bonds, has both lower expected return and lower risk than does the most aggressive portfolio, 100% stocks. All of the portfolios which are more aggressive than the minimum variance portfolio are efficient. The set of all efficient portfolios is called the efficient frontier. All risk-averse investors who act to maximize expected utility have an optimal portfolio on this frontier.

The slope of the Efficient Frontier at any point depicts how much extra expected return is obtained by taking some more risk. This is called the Return/Risk Trade-off. It is a Measure of the Risk Adjusted Return and is also called as the Sharpe Ratio (S).

Return/Risk Trade-off = change in RP / change in σ_P

2.1. Result Analysis

Consider two investors; one with Risk Aversion A=4 and another with Risk Aversion A=40. The investor with A=4 is more risk tolerant (less risk averse) than the investor with A=40.

3. Based on Investment Time Horizon

Assuming the risk aversion factor, A=4

$$k = R_P - ½[(4*\sigma^2_{Rn}) / n] \quad (9)$$

Case I: - Investment Time Horizon, n = 1-year

$$R_P = k + (2*\sigma^2_{R1}) \quad (10)$$

Since the optimal portfolio lies at the point of tangency of the efficient frontier and the indifference curve, consider the curve with k=5.90%. This curve is tangent to the feasible set curve at approximately the portfolio which is 80% bonds and 20% stocks. This portfolio maximizes the investor's expected utility.

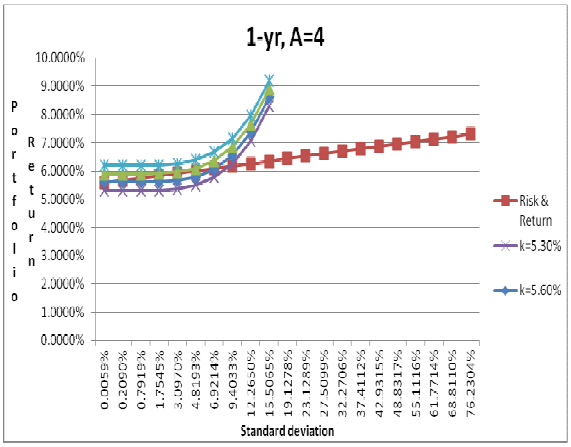


Fig: 1. Optimal Portfolio (n=1, A=4)

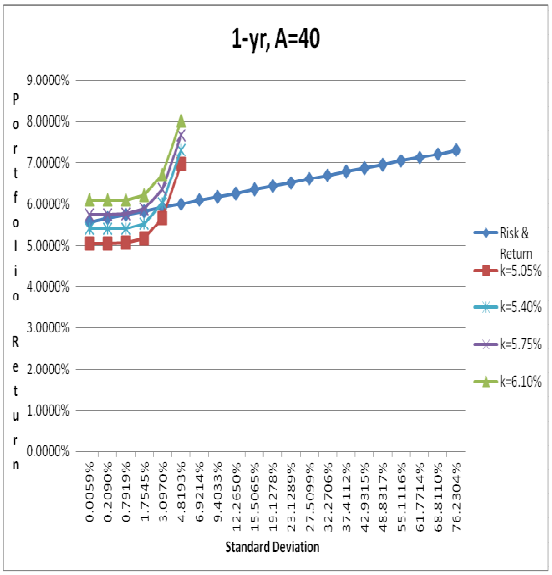


Fig: 2. Optimal Portfolio (n=1, A=40)

Case II: - Investment Time Horizon, n = 2-year

$R_P = k + \sigma^2_{R2}$ (11)

Consider the curve with k=5.90%. The optimal portfolio for our investor is clearly the 75% bond/25% stock portfolio, with a certainty equivalent of 5.90%. It is thus clear that as the investment time horizon increases, the indifference curve becomes a little flatter. Also, the investor is willing to accept a larger quantity of risk.

Case III: - Investment Time Horizon, n = 3-year

$R_P = k + [(2*\sigma^2_{R3}) / 3]$ (12)

The curve with k=6.00% is tangent to the feasible set curve at approximately the portfolio which is 70% bonds and 30% stocks. This portfolio is preferred to any of the portfolios on the bottom and second-to-bottom indifference curves.

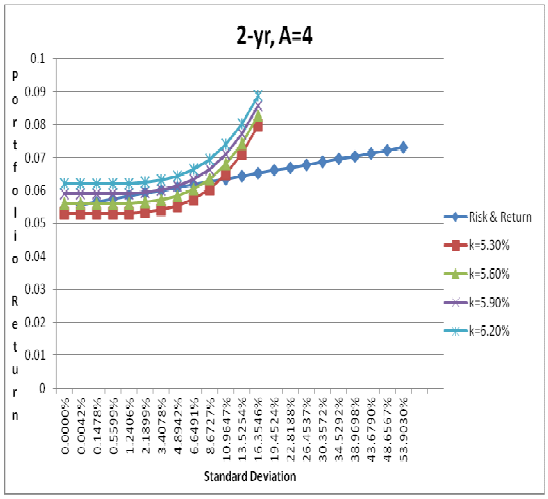


Fig: 3. Optimal Portfolio (n=2, A=4)

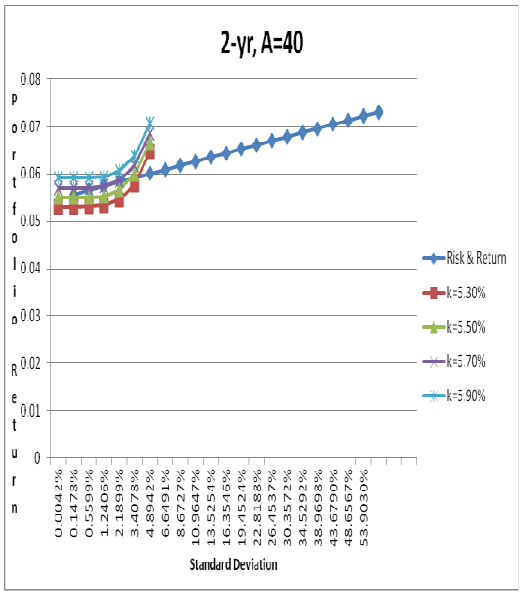


Fig: 4. Optimal Portfolio (n=2, A=40)

Case IV: - Investment Time Horizon, n = 4-year

$R_P = k + (\sigma^2_{R4} / 2)$ (13)

At k=6.10%, the point of tangency lies at approximately the portfolio which is 60% bonds and 40% stocks. This portfolio maximizes the investor's expected utility.

Case V: - Investment Time Horizon, n = 5-year

$R_P = k + [(2*\sigma^2_{R5}) / 5]$ (14)

Considering the curve with k=6.20%, the optimal portfolio for our investor is clearly the 55% bond/45% stock portfolio

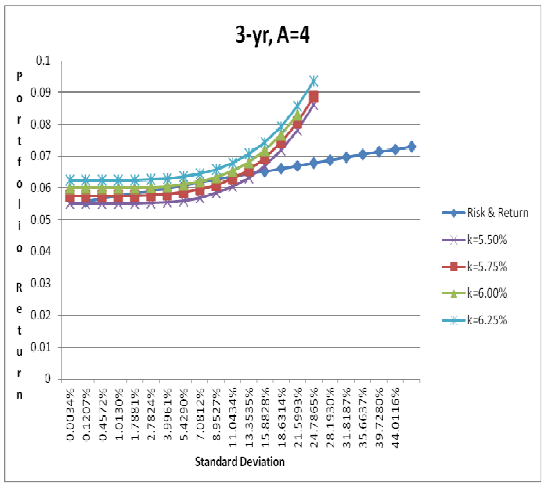


Fig: 5. Optimal Portfolio (n=3, A=4)

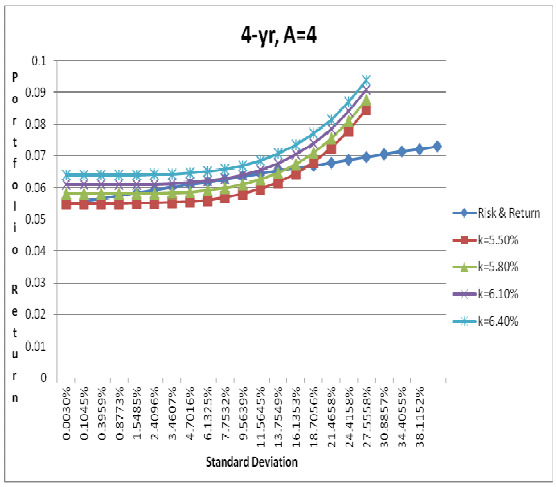


Fig: 7. Optimal Portfolio (n=4, A=4)

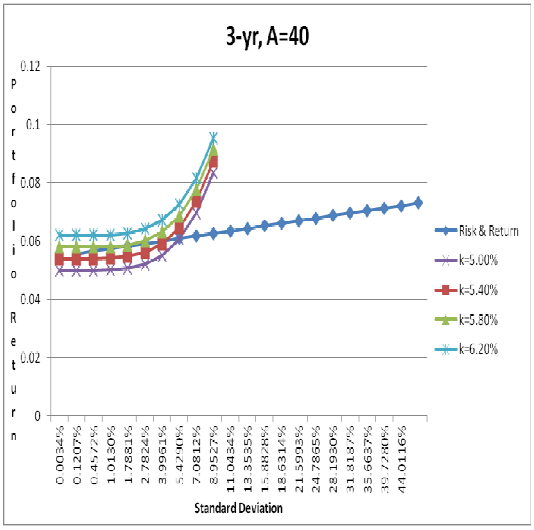


Fig: 6. Optimal Portfolio (n=3, A=40)

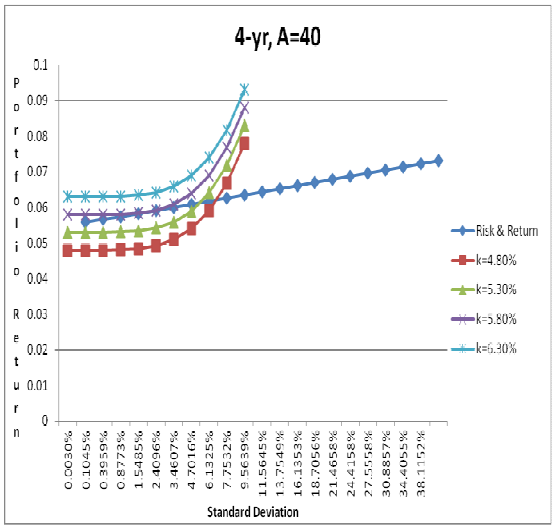


Fig: 8. Optimal Portfolio (n=4, A=40)

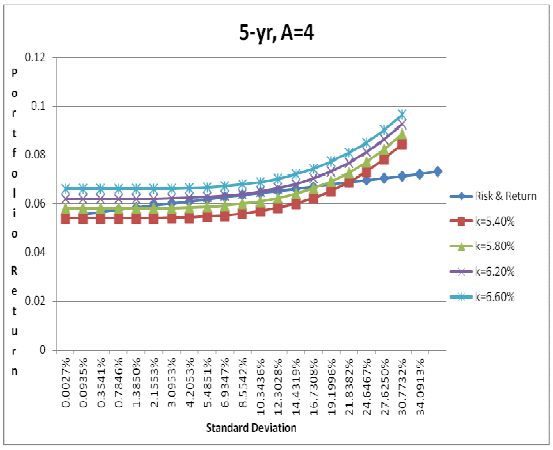


Fig: 9. Optimal Portfolio (n=5, A=4)

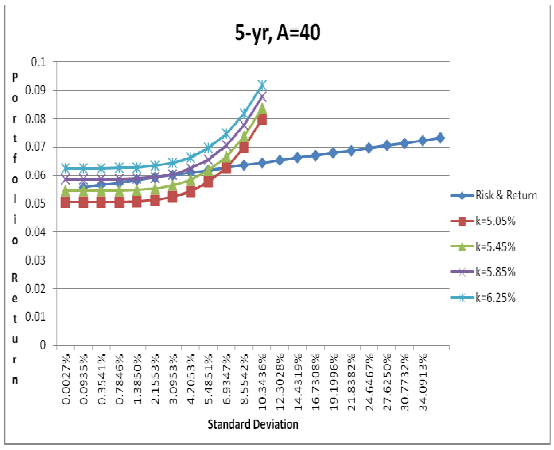


Fig: 10. Optimal Portfolio (n=5, A=40)

Thus, as the investment period of the investor increases from 1-year to 5-years, the risk taking capacity of the investor also increases. When the investment time horizon was 1-year, the optimal portfolio came out to be 80% bonds/20% stocks portfolio. On the other hand, when the investment time horizon was increased to 5-years, the optimal portfolio for the same investor became 55% bonds/ 45% stocks portfolio. Thus, with longer time horizon, the investor is willing to take a larger quantity of risk.

4. Based on Risk-Aversion Factor

Consider, for example, an investor with investment time horizon of 4-years. So, the utility function can be written as:

$R_P = k + ½[(A\sigma^2_{R4}) / 4]$ (15)

Case I: - Risk-Aversion Factor, A=4

$R_P = k + (\sigma^2_{R4} / 2)$ (16)

The curve with k=6.10% is tangent to the feasible set curve at approximately the portfolio which is 60% bonds and 40% stocks.

Case II: - Risk-Aversion Factor, A=40

$R_P = k + (5*\sigma^2_{R4})$ (17)

In this case, the investor (with A=40) is less risk-tolerant (more risk-averse). This means that the investor is not willing to accept a larger amount of risk. So, the investor is trying to be conservative by selecting an optimal portfolio of less risky assets. Here, the feasible set is the same, and the efficient frontier is the same, but the indifference curves are noticeably less flatter. The optimal portfolio, which is 80% bonds and 20% stocks, lies at the point of tangency of the curve with k=5.80%.

5. Conclusion

With the investment time horizon increasing, the indifference curve starts becoming flatter. So, this implies that the investor is willing to accept a larger quantity of risk. With the investment period of the investor increasing from 1-year to 5-years, the risk taking capacity of the investor also increases. The choice of the optimal portfolio changed from 80% bond/20% stock portfolio to 55% bond/45% stock portfolio.

More risk-averse investors prefer the investment which has lower risk, while less risk-averse investors prefer the investment with a higher expected return. The more risk-averse an investor is, the lower will be the optimal portfolio on the return/risk spectrum defined by the efficient frontier. For very small values of the coefficient of risk aversion A (near zero), the investor is primarily concerned with maximizing expected return, and has little concern for risk. Conversely, for very large values of A, the investor is primarily concerned with minimizing risk. With A increasing from 4 to 40, the investor becomes less risk-tolerant (more risk-averse). This means that the investor is not willing to accept a larger amount of risk. So, the investor is trying to be conservative by selecting an optimal portfolio of less risky assets

Thus, no rational investor will invest in any portfolio unless its utility exceeds the Risk Free Rate. Investor will not opt for risky portfolios unless their returns exceed the risk free rate by an amount that is sufficient to overcome the risk scaled by a factor related to his risk-aversion factor.

References

[1] M. Blume, I. Friend, "A new look at the CAPM", Journal of Finance, March (1973), 19-34,

[2] F. Black, M. C. Jensen, M. Scholes, "The CAPM: Some empirical tests, reprinted in M. C. Jensen, ed, studies theory of capital markets", Praeger, New york, 1972, 79-124

[3] W. F. Sharpe, "A simplified model for portfolio analysis, Management science, January 1963, 277-293

[4] F. Black, "Capital market equilibrium with restricted borrowing, Journal of business 45, 444-454, 1972

[5] Kraus Alan, Litzenberger Robert, "On the Distributional Conditions for a Consumption oriented Three Moment CAPM", Journal of Finance, 38(5), December 1976

[6] Fama F. Eugene, "The Behavior of Stock-Market Prices", The Journal of Business, 38(1), Jan., 1965

[7] J. Elton, Edwin, Gruber J. Martin, "Modern Portfolio Theory, 1950 to date, New York University stern School of Business Finance Department, Working Paper Series, 1997

[8] Hakansson H. Nils, "An Induced Theory of the Firm under Risk: The Pure Mutual Fund", Journal of Financial and Quantitative Analysis, 5(2), 1970

[9] Fama F. Eugene, "Efficient Capital Markets: A Review of Theory and Empirical Work", Journal of Finance, 25, May 1970

[10] Working Holbrook, "A Random Difference Series for Use in the Analysis of Time Series", journal of the American Statistical Association, 29(185), March, 1934

[11] Fama F. Eugene; Fisher Lawrence; Jensen C. Michael; Roll Richard, "The Adjustment of Stock Prices to New Information", International Economic Review, 10(1), Feb., 1969

[12] M. G. Kendall, A. Bradford Hill, "The Analysis of Economic Time Series: Prices", Journal of the Royal Statistical Society, 116, 1953
[13] Milgrom Paul, Stokey Nancy, "Information, Trade & Common Knowledge", Northwestern University, October, 1980
[14] Swisher Pete, Kasten W. Gregory, Post-Modern Portfolio Theory, FPA Journal, 2005
[15] Markowitz Harry, Portfolio Selection, the Journal of Finance, 7(1), March., 1952
[16] http://finance.martinsewell.com/stylized-facts/volatility/Fama1970.pdf
[17] http://www.travismorien.com/FAQ/portfolios/mptcriticism.htm
[18] http://pages.stern.nyu.edu/~eelton/papers/97-dec.pdf
[19] http://www.fcva.net/Documents%20and%20Files/Post-Modern%20Portfolio% 20 Theory.pdf
[20] http://www.signallake.com/innovation/FinanceNewSchool.pdf
[21] Modern portfolio theory: Some main results, Heinz H. Muller, Astin Bulletin, 18(2)
[22] http:// www.Norstad.org an introduction to portfolio theory.
[23] http://homepage.newschool.edu/~het/schools/finance.htm

Recommendation System for Highly Sparse Datasets: A Hybrid Approach

Himanshu Chadha
Khalsa College, University of Delhi
himanshuc@gmail.com
Ankita Jain
Aditi Singh
Ankur Ahuja
Delhi Technological University
aj.ankitajain.11@gmail.com
aditisingh94.8@gmail.com
a.ahuja.jr@gmail.com

In this paper we explore the problems encountered by traditional recommendation systems in dealing with a highly sparse dataset. Three existing approaches for recommender systems i.e. collaborative, content-based and demographic are discussed. Collaborative Filtering (CF) recommender systems utilize user-user similarity, content-based recommender systems use item similarity and demographic recommender systems make use of personal attributes' resemblance. We propose a new hybrid approach to overcome problems faced by traditional recommendation algorithms making use of FISM (Factored-Item-Similarity-Model) instead of conventional Pearson Similarity. We compare our proposed system with existing algorithms to show the increased quality of recommendation in highly sparse datasets.

Keywords- Recommender systems; user-user similarity;collaborative filtering; content-based filtering; demographic recommender system; hybrid recommender system.

1. Introduction

Due to the exponential growth in amount of data available, it is becoming increasingly difficult to provide users with relevant information. This has also aggravated the problem of filtering the relevant data according to the individual requirements of users and situations. These issues underscore the need for having an intelligent information extraction system or recommendation system which can filter the important information and predict whether a user would like a given resource. Recommender Systems use machine learning algorithms to predict user preferences. These recommender systems constitute of three basic parts- (i) background data, the information that the system has before the recommendation process begins, (ii) input data, the information that user must communicate to the system in order to generate a recommendation, and (iii) an algorithm that combines background and input data to arrive at its suggestions [1]. Some of the sites which use recommender systems are: Facebook-*'People You May Know'*, Amazon-*'Customers Who Bought This Item Also Bought'*, YouTube-*'Suggested Videos'*, Google Play Store-'*People also see this*'.

Let $\mathcal{U}$be the set of all users and $\mathcal{S}$ be the set of all possible items that may be recommended. Let r_{ui} denote the rating of the user *u* on the item *i*. Also, let z be a relevance function that measures the relevance of item *i* to user *u* i.e.

z:$\mathcal{U}$*$\mathcal{S}$->$\mathcal{T}$

Here,is a totally ordered set and the objective of the recommender system is to choose the item, for each specific user, which maximizes the value of relevance function.

CF Recommender System is the most widely used and most popular of all recommender system approaches. CF uses existing user-item rating information to exploit users and items similarities. Based on this, the items that have been preferred by similar users in the past are recommended to the user. CF systems can be classified as either memory-based or model-based [2]. Memory-based technique such as the TF-IDF [3] approach considers all the previously rated items by a user. Model-based approaches build a model from the collection of ratings. Dimensionality reduction techniques such as Singular Value Decomposition (SVD) [4], NSVD [5], SLIM [6], FISM [7] identify the *latent features* of items, thus helping the recommendation. CF systems focus on personal interest of an individual thus producing good quality recommendations. However, pure-CF systems suffer from the cold-start [2] problem and usually fail in sparse data conditions [6][7].

Content-based Recommendation Systems focus on recommending items on the basis of a user's profile and the history of items purchased. The focus is on two things, a user profile and a database describing the user purchases. Items are compared with the items already purchased by the user and recommendation to the user is based on the item-similarities. Item features are represented as weighted vectors which are then used to characterize user profile. This weight characterizes similarity present between the items purchased and the item

under consideration. A content-based recommender learns the profile of auser's interests based on the features present in objects that the user has rated [1]. User profiling is the key in content-based recommender systems. However this system provides less accurate results than a pure-CF system.

Demographic recommender systems use demographic data to identify the type of users that like a certain object and create *'stereotypes'*. Users' demographic features such as gender, age, country, education etc. are used to learn their behavior. These attributes categorize the user based on their personal attributes. Such data may be collected explicitly by asking the users to input the required demographic information. This technique does not suffer from cold start and the problems associated with data sparsity. But the predictions obtained with this technique are not always very accurate. User-item ratings are not used, so new users can get recommendations before they have rated any item thus eliminating new user problem. The method is also domain independent as it does not require any knowledge of the items and their features. This method, however, does not work well for users with unique tastes or preferences. Since demographic features require collection of personal information, it leads to users' privacy issues which may result in difficulty of data compilation.

In addition, there are some problems faced by all these stand-alone recommender systems. Data sparsity is one of the major issues. With users not always willing to give ratings to items they use or buy, sparsity of datasets is a common problem. Hence the ratings available for learning is very small compared to predictions made by system resulting in poor recommendations and reduced coverage [8]. This problem is popularly known as popularity bias. Cold-start problem is another major problem faced by these systems. Although demographic system doesn't suffer from the cold start problem, but the recommendations it generates are not very accurate and reliable.

Seeing the shortcomings of all these techniques, it is clear that good recommendations can't be produced with the use of these techniques individually. Hence, we propose the idea of a hybrid recommendation system. In this work, weighted [1] hybrid of all the three approaches is used. Despite the improvements achieved by the existing hybrid system [8], poor recommendations in case of highly sparse datasets still prevail. To overcome this problem of sparsity, the use of FISM algorithm along with content based and demographic approach is proposed.

2. Notations

In this paper, all matrices are represented by italicized upper case letters (e.g., *A, B*). Sets are denoted using calligraphic letters in upper case (e.g., $\mathcal{S}$). We use lower case calligraphic letters for representing vectors (e.g. a).Variables are denoted using italicized lower case letters (e.g.*x,y*).
$\mathcal{S}$ is used to denote the set of items.$a$and$b$ represent latent factor vectors. A predicted value is denoted using a tilde (~) sign over it (e.g., $\tilde{p}$).

3. Background

In this paper, a hybrid approach is developed using three existing algorithms. Whereas, the CF approach used is FISM (Factored Item Similarity Model), vector similarity is applied to discover feature correlation among all items and Euclidean similarity to explore user-user similarity based on resemblance of personal attributes of users.

III.1 CF Approach

The CF algorithm 'FISMrmse' was proposed by Kabburet. al.[7]. This algorithm predicts whether a user *u* would like item*i* as

$$\tilde{p}_{ui} = v_u + v_i + (n_u^+ - 1)^{-\theta} \sum_{j \in \mathcal{S}_u^+ \backslash \{i\}} a_j b_i^T ,$$

where $\tilde{p}_{ui}$ is the predicted feedback, $v_u$and v_i are bias corresponding to user *u* and item *i* respectively, n_u^+ is the total number of items rated by user *u*, θ is a user specified parameter whose value lies between 0 and 1, $\mathcal{S}_u^+$ is the set of items rated by user *u*, $\mathcal{S}_u^+\backslash\{i\}$ is $\mathcal{S}_u^+$ excluding item *i*, a_j and b_i are item 'latent factors' from matrices *A* and *B* respectively which are learned during process. *A*and *B* are low-rank $m \times k$ matrices representing latent factors of all the items *m*, such that, $k << m$. *k* represents cardinality of latent factors per item. b_i^TRepresents transpose of vectorb_i.

Note that in this method, $\mathcal{S}_u^+\backslash\{i\}$ is used which implies item *i*'s latent factors are not used for its own feedback prediction. Therefore, item *i*'s similarity with other items in set $\mathcal{S}_u^+$ is used to predict$\tilde{p}_{ui}$. θ controls the number of neighborhood items which are similar to item *i*. Such that θ = 1 implies all the items in $\mathcal{S}_u^+\backslash\{i\}$ are similar to item *i* and predicted feedback is the mean similarities between items in $\mathcal{S}_u^+\backslash\{i\}$ plus the biases. Similarly, if θ = 0, then the predicted feedback $\tilde{p}_{ui}$ is aggregate similarity between *i* and items in $\mathcal{S}_u^+\backslash\{i\}$ plus biases. Thus, if

item *i* is similar to few items, it can still get a high rating. Value of θ depends on the characteristics of dataset used.

The cost function for this model is given as

$$\Psi(\cdot) = \frac{1}{2}\sum_{u,i\in S} ||p_{ui} - \tilde{p}_{ui}||_F^2 + \frac{\beta}{2}\left(||A||_F^2 + ||B||_F^2\right) + \frac{\lambda}{2}||v_u||_2^2 + \frac{\gamma}{2}||v_i||_2^2,$$

Where, $||X||_F^2$ represents matrix Frobenius norm of *X*, $||X||_2^2$ represents entry-wise l_2-norm of *X*. β, λ, γ are regularization weights, used to avoid problem of over fitting. β is regularization weight for latent vector matrices *A* and *B*, λ for user bias vector v_u and γ for item bias vector v_i.

The matrices *A* and *B*, bias vectors v_u and v_i are learned by minimizing regularized cost function, that is,

$$\underset{A,B}{\text{minimize}}\, \Psi(\cdot)$$

To reduce computational requirements for optimization, a sampling strategy is employed. In this strategy, zeros are sampled and used along with all non-zero entries in *S*. Given constant sampling factor μ, and number of non-zero entries in *Snz(S)*, number of zeros sampled per iteration is equal to $\mu \cdot nz(S)$. This makes 'FISMrmse' computationally more efficient than other common approaches which compute cost function over all entries of *S*, that is, all zero and non-zero entries. In FISM, we use a binary matrix *S* such that entries with value 1 represent rated items and zero entries represent unrated items.

III.2 Content-Based Approach

We use basic stochastic gradient descent learning algorithm to tackle with the content based recommendation. The technique works in two parts or phases.

It works as follows, for a given dataset; we learn the weights of features associated with each training item. We then use these learned weights, along with the features of the item we need the predicted ratings for and find the desired result.

A. Weight Calculation

We use stochastic gradient descent for calculating the weights associated for calculating the desired ratings.

$$w_n^{(u)} = w_n^{(u)} - \alpha\left(\sum_{u:r(u,k)=1}\left((w^{(u)})^T x^{(k)} - y^{(u,k)}\right)x_n^k + \beta . w_n^{(u)}\right)$$

In the above equation, n^{th} item feature is depicted by *n*, user is depicted by *u* and item is represented by *k*. $y^{(u,k)}$is the user rating to the particular item *k* and $w_n^{(u)}$represents the weight assigned to feature *n* by user *u*. α is learning rate and β is regularization weight.$x^{(k)}$ Represents the feature vector of item *k* and $w^{(u)}$represents the weight vector corresponding to user *u*.$(w^{(u)})^T$ Represents transpose of vector$w^{(u)}$.

B. Rating Prediction Method

The weights calculated from the previous steps are multiplied by the feature vector of the item, whose ratings are to be predicted.

$$Predicted\ Ratings = W^T X,$$

Where, *W* represents weight matrix whose i^{th} column vector represents weight vector for user *i* and *X* represents item-feature matrix whose j^{th} column vector represents feature vector for item*j*.

III.3 Demographic Approach

Demographic recommender systems require identifying similarity among users. A number of measures are available to calculate this similarity. In this paper, Euclidean similarity is used to determine the extent to which a user is similar to another user. In other terms, Euclidean similarity aims at calculating the distance among users. Distance refers to the sum of differences in values of corresponding attributes of two users. If distance is more, it indicates that similarity between the two users under consideration is low. In collaborative techniques this attribute is the rating of an item by the user. On the other hand, in demographic technique, these attributes correspond to the personal information or attributes associated with the user.

Euclidean Distance between two points (in our case users) is calculated using Minkowski distance metric. It can be used in one-, two-, or higher-dimensional space. The formula of Euclidean distance between two users *X* and *Y* is calculated as

$$distance(x,y) = \sqrt{(x_1 - y_1)^2 + (x_2 - y_2)^2 + \cdots + (x_n - y_n)^2} = \sqrt{\sum_{i=1}^{n}(x_i - y_i)^2} \quad ,$$

Where, x_i and y_i are personal attributes of user *x* and user *y* respectively, *n* represents total number of attributes of a user.

4. Proposed Work

In this paper, we use $f(u,i)$to represent feedback of user *u* for item *i* as evaluated by FISM (CF), Demographic and Content Based methods collectively. The proposed algorithm works as follows:

1. Compute the similarity between items using rating data (CF), demographic data (Demographic), and feature data (Content Based), and store this information [8]. Vector similarity [9] between two items is used for measuring the similarity using demographic and feature vectors.
2. On the basis of this similarity, estimate the feedback (as in FISM) or rating (as in Demographic and Content Based) of all items for every user. These estimated values from each of the 3 methods are then normalized.
3. These normalized feedbacks are then assigned weights-ω_F to the feedback from FISM, ω_{CB} to the feedback from Content based method and ω_D to the feedback from Demographic method.

Final feedback of a user *u* for item is given as-

$$f(u,i) = \omega_F \times f_F(u,i) + \omega_{CB} \times f_{CB}(u,i) + \omega_D \times f_D(u,i),$$

Where,$f_F(u,i)$, $f_{CB}(u,i)$ and $f_D(u,i)$ are feedbacks of user *u* for item *i* as evaluated by FISM (CF), Demographic and Content Based methods respectively.

5. Evaluation

V.1 Data Sets

We evaluated the performance of our proposed system on Movie Lens dataset[1] and a restaurantdataset[2]. Movie Lens dataset contains 943 users, 1682 movies and 100,000 ratings ranging from 1 to 5.MovieLens dataset has been used in many research projects [8], [10], [11],[12]. The sparsity of this dataset is 93.7%-

$$\left(1 - \frac{non\ zero\ entries}{all\ possible\ entries} = 1 - \frac{100000}{943 \times 1682} = 0.937\right).$$

The second dataset we used contains 138 customers, 130 restaurants and 1161 ratings ranging from 0 to 2. The sparsity of this dataset is 93.5%.$\left(1 - \frac{non\ zero\ entries}{all\ possible\ entries} = 1 - \frac{1161}{130 \times 138} = 0.935\right)$.We considered zero entries as rated items for this dataset.

V.2 Evaluation Methodology & Metrics

To evaluate the performance of our system, we split our dataset into training and test sets using 5-fold Leave-One-Out-Cross-Validation. In each fold, we split the dataset into training and test set by randomly selecting one rated item of each user to be part of the test set, and using the remaining rating data for training. The training set is used to generate ranked top-N recommendation list of items for each user. This list of items is then compared with the items in the test set to determine the quality of recommendations produced.

Two metrics used to facilitate this evaluation are-Hit Rate (HR) and Average Reciprocal Hit Rank (ARHR) [13]. HR is defined using the following formula-

$$\text{HR}=\frac{\#hits}{\#users}$$

where, #users is the total number of users in the test set and #hits is the number of users for which item in the test set was also in the top-N list or the test item was successfully recalled.

[1]http://grouplens.org/datasets/movielens.

[2]http://archive.ics.uci.edu/ml/machine-learning-databases/00232.

The other measure i.e. ARHR is defined using the following formula-

$$\text{ARHR}=\frac{1}{\#users}\sum_{i=1}^{\#hits}\frac{1}{x_i},$$

Where, x_i is the position of the test item in the ranked list of recommendations for i^{th} hit. ARHR is a weighted version of HR. It measures how strongly an item is recommended.

6. Observations

A large number of experiments were done to decide the optimal values of the weights to be assigned to FISM (ω_F), Content Based (ω_{CB}) and Demographic model (ω_D) in our hybrid system. Many combinations of these weights were tried as shown in Table 1(for Restaurant dataset) and Table 2(for Movie Lens dataset) and the one giving the best HR value was chosen.

Table 1 *Estimation on HR for Different Sets of Weights (Restaurant), N=10*

S.No.	ω_F	ω_{CB}	ω_D	HR	ARHR
1.	0.8	0.1	0.1	0.07682	0.01922
2.	0.7	0.1	0.2	0.07536	0.01956
3.	0.7	0.2	0.1	0.07102	0.01896
4.	0.6	0.1	0.3	0.06814	0.01808
:	:	:	:	:	:
:	:	:	:	:	:
9.	0.5	0.2	0.3	0.06956	0.01770
:	:	:	:	:	:
:	:	:	:	:	:
20.	0.5	0.1	0.4	0.07392	0.01810
:	:	:	:	:	:
:	:	:	:	:	:
32.	0.1	0.1	0.8	0.06958	0.01752

Table 2 *Estimation on HR for Different Sets of Weights (MovieLens), N=10*

S.No.	ω_F	ω_{CB}	ω_D	HR	ARHR
1.	0.8	0.1	0.1	0.05366	0.01576
2.	0.7	0.1	0.2	0.05196	0.01570
3.	0.7	0.2	0.1	0.04516	0.01338
4.	0.6	0.1	0.3	0.05196	0.01522
:	:	:	:	:	:
:	:	:	:	:	:
9.	0.5	0.2	0.3	0.04368	0.01300
:	:	:	:	:	:
:	:	:	:	:	:
:	:	:	:	:	:
26.	0.4	0.1	0.5	0.04898	0.01426
:	:	:	:	:	:
32.	0.1	0.1	0.8	0.03840	0.01224

***Table* 3** *Performance Comparison of Stand-Alone Recommendation Systems with the Hybrid System.*

			Value of N						
			5	10	15	20	25	30	35
Movie Lens	HR	Hybrid	0.0347	0.057	0.083	0.1007	0.1233	0.1397	0.1596
		Euclidean	0.0165	0.0312	0.0488	0.0683	0.0908	0.1095	0.1289
		Demo							
		FISM(CF)	0.0117	0.0233	0.035	0.0424	0.0528	0.0591	0.0687
		PureCB	0.0087	0.0173	0.0237	0.0294	0.0358	0.0430	0.0481
	ARHR	Hybrid	0.0156	0.0184	0.0203	0.0212	0.0222	0.0228	0.0234
		Euclidean	0.0098	0.0116	0.013	0.0142	0.0151	0.0158	0.0164
		Demo							
		FISM(CF)	0.0051	0.0066	0.0075	0.0079	0.0084	0.0086	0.0088
		PureCB	0.0035	0.0046	0.0051	0.0054	0.0057	0.006	0.0061
Restaurants	HR	Hybrid	0.0392	0.0985	0.1275	0.1594	0.2203	0.242	0.3174
		Euclidean	0.0348	0.058	0.1101	0.1696	0.1884	0.1961	0.2724
		Demo							
		FISM(CF)	0.0304	0.0638	0.1014	0.1449	0.1826	0.2261	0.2639
		PureCB	0.0174	0.0526	0.0927	0.1333	0.1739	0.2116	0.2478

	ARHR	Hybrid	0.0182	0.0237	0.0262	0.0283	0.0312	0.0317	0.0345
		Euclidean	0.0196	0.0241	0.0278	0.0309	0.0328	0.0341	0.0357
		Demo							
		FISM(CF)	0.0133	0.018	0.0211	0.0234	0.0238	0.0265	0.0262
		PureCB	0.0095	0.0142	0.0172	0.0195	0.0213	0.0226	0.0237

7. Results

We conducted several experimental evaluations on the available datasets using our hybrid system and 3 standalone models namely FISM, Euclidean Demographic and Pure CB. We compare the performance metrics HR and ARHR against different values of neighborhood size (i.e. N) for these standalone models and our proposed hybrid system.

The general trend of the variation of HR and ARHR with N is shown in Figure 1 and Figure 2, respectively. It shows that the HR and ARHR values increase with the increase in neighborhood size.

For the restaurant dataset, the results of the comparison of HR and ARHR against different values of N for FISM, Euclidean Demographic, Pure CB and hybrid system are shown in Figure 3 and Figure 4 respectively. For the MovieLens dataset, these results are shown in Figure 5 and Figure 6.The results in Figure 3 and Figure 5 indicate that the HR values are better for our hybrid system compared to the other 3 standalone models.

The results in Figure 4 and Figure 6 show that the ARHR values are also better for our hybrid system than the other 3 models under consideration.

Producing good quality recommendations in case of a sparse dataset is quite important. Our hybrid system outperforms all the 3 standalone models both in terms of HR and ARHR for highly sparse datasets. This result is shown in Figure 7 and Figure 8. We considered 3 levels of sparsity- 93.75%(sparse), 95%(sparser) and 96.25%(sparsest)to check our system's performance on sparse datasets.

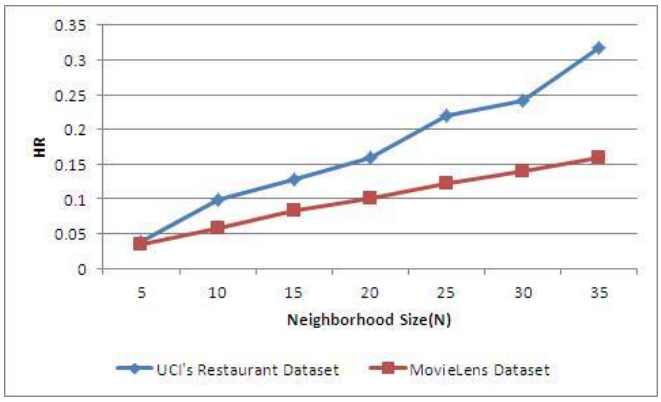


Figure 1 *Effect of Neighborhood Size (N) on HR*

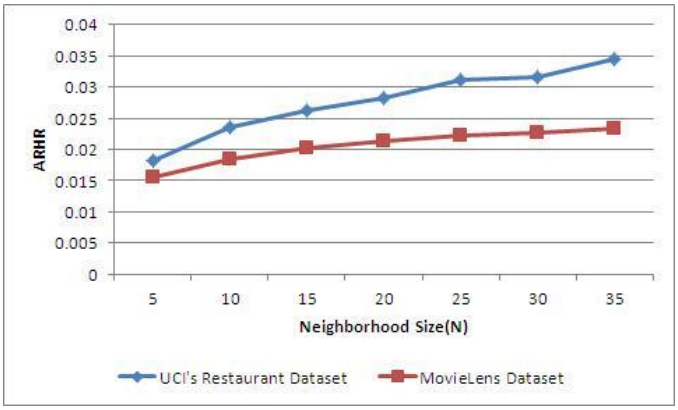


Figure 2 *Effect of Neighborhood Size (N) on ARHR*

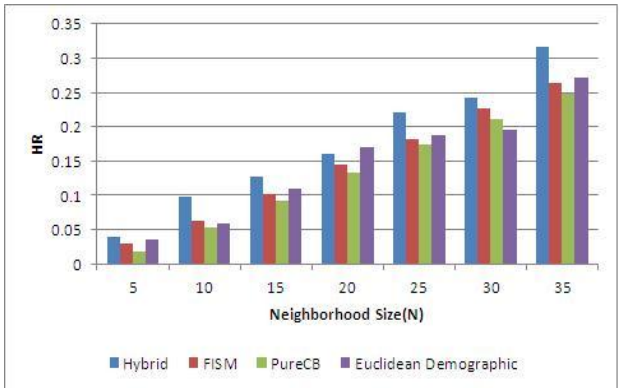


Figure 3 *Performance (HR) Comparison for Different Values of N-UCI's Restaurant Dataset*

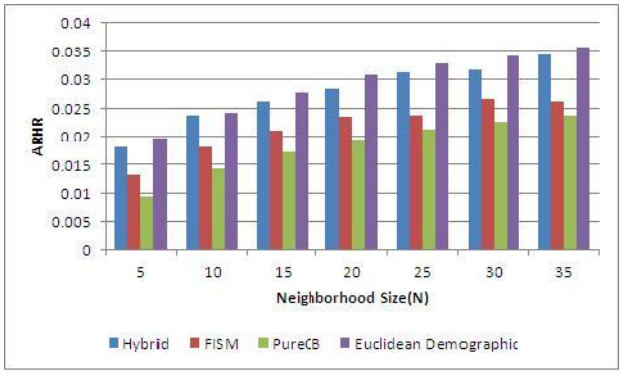


Figure 4 *Performance (ARHR) Comparison for Different Values of N-UCI's Restaurant Dataset*

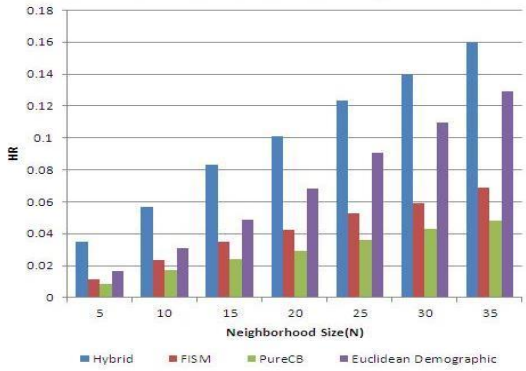


Figure 5 *Performance (HR) Comparison for Different Values of N-MovieLens Dataset*

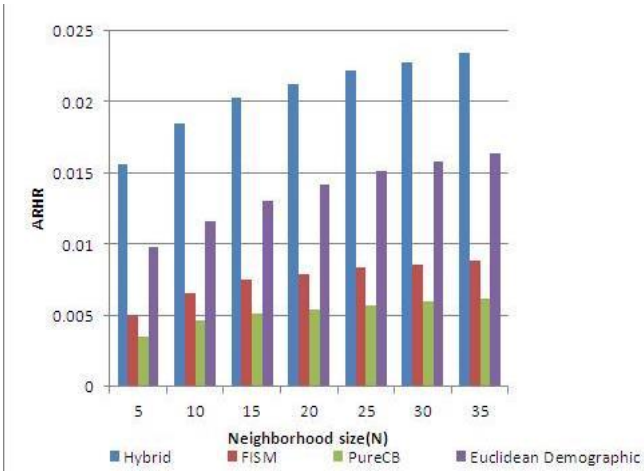


Figure 6 *Performance (ARHR) Comparison for Different Values of N-MovieLens Dataset*

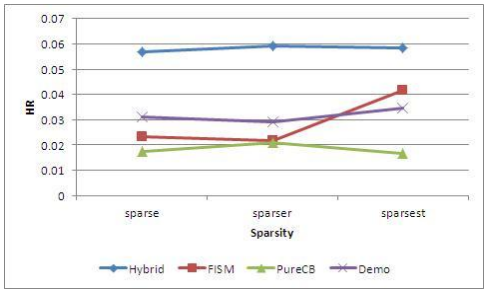


Figure 7 *Effect of Sparsity on HR - MovieLens Dataset*

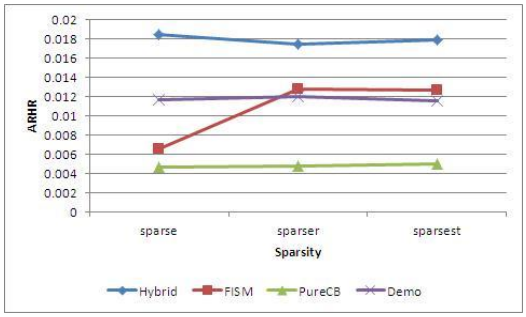


Figure 8 *Effect of Sparsity on ARHR -MovieLens Dataset*

8. Conclusion

In this paper, we have proposed a weighted hybrid recommendation approach by combining the feature, rating and demographic based information of items and users. We showed through our experimental results that our system gives better recommendation than traditional standalone approaches in case of highly sparse datasets as well.

9. References

1. R.Burke, "Hybrid recommender systems: Survey and experiments, User Modeling and User-Adapted Interaction," vol. 12, no. 4, 2002, pp. 331-370
2. A. T. GediminasAdomavicius, "Toward the next generation of recommender systems: A survey of the state-of-the-art and possible extensions," *IEEE Transactions on Knowledge and Data Engineering*, vol. 17, 2005, pp.734–749.
3. K. Lang, Newsweeder: "Learning to filter netnews," *in Proceedings of the Twelfth International Conference on Machine Learning*, 1995.
4. M. Vozalis and K. Margaritis, "Using SVD and demographic data for the enhancement of generalized collaborative filtering" *Information Sciences*, vol. 177, no. 15, 2007, pp. 3017-3037.
5. A. Paterek. Improving regularized singular value decomposition for collaborative filtering. *In Proceedings of KDD Cup and Workshop*, volume 2007, pages 5-8, 2007.
6. Xia Ning and George Karypis , "SLIM: Sparse Linear Methods for Top-N Recommender Systems". In *Data Mining (ICDM), 2011 IEEE 11th International Conference on*, pages 497-506. IEEE, 2011
7. SantoshKabbur, Xia Ning and George Karypis, "FISM: Factored Item Similarity Models for Top-N Recommender Systems. *Proceedings of the 19th ACM SIGKDD International Conference on Knowledge Discovery and Data Mining*, DOI: 10.1145/2487575.2487589 (2013).
8. Mustansar Ali Ghazanfar and Adam Prugel-Bennett, "A Scalable, Accurate Hybrid Recommender System". *In proceedings of Third International Conference on Knowledge Discovery and Data Mining,2010.*
9. J. S. Breese, D. Heckerman, and C. Kadie, "Empirical analysis of predictive algorithms for collaborative filtering," Morgan Kaufmann, 1998, pp. 43–52.
10. B. Sarwar, G. Karypis, J. Konstan, and J. Reidl, "Item based collaborative filtering recommendation algorithms," in Proceedings of the 10th international conference on World Wide Web. ACM New York, NY, USA, 2001, pp. 285–295.
11. M. Vozalis and K. Margaritis, "Using SVD and demographic data for the enhancement of generalized collaborative filtering," Information Sciences, vol. 177, no. 15, 2007, pp. 3017–3037.
12. M. Vozalis and K. Margaritis, "On the enhancement of collaborative filtering by demographic data," Web Intelligence and Agent Systems, vol. 4, no. 2, 2006, pp. 117–138.
13. M. Deshpande and G. Karypis. "Item-based top-n recommendation algorithms", ACM Transactions on Information Systems (TOIS), 22(1):143–177, 2004.

Reptiles Inspired Biomimetic Materials and Their Novel Applications

Kishor Kalauni and K. M. Gupta
Department of Applied Mechanics, Motilal Nehru National Institute of Technology, Allahabad -211004, India
Email: kishor.kalauni@gmail.com, kmgupta@mnnit.ac.in

Isha Bharti
Teaching-cum-Research Fellow, Department of Applied Physics, Delhi Technological University, Delhi-110042, India

***Abstract*—For all nature's sophistication, many of its clever devices are made from simple materials like keratin, calcium carbonate, and silica which nature manipulates into structures of fantastic complexity, strength, and toughness. In the past few decades, materials scientists have shown increasing interest in studying the whole variety of biological materials including hard and soft tissues, and to use discovered concepts to engineer new materials with unique combinations of properties. This paper aims at elaborating the development of such biomimetic materials by compiling the ongoing researches. In this regard, the research developments of some newer materials by other investigators have been presented here. Brief details of the development of Gecko feet inspired sticky-bot, Mini-viper model robot, Clothes that change colour, Snakes imitating robot, Robot scorpion are discussed. In these elaborations, it is shown that these biomimetic materials can be effectively used in a large variety of application in near future.**

***Index Terms*—gecko feet inspired sticky-bot, mini-viper model robot, clothes that change colour, snakes imitating robot, robot scorpion**

I. Introduction

Biomimetics is the word most frequently used in scientific and engineering literature that is meant to indicate the process of understanding and applying (to human designs) biological principles that underlie the function of biological entities at all levels of organization. Among the many fields of study of biomimetic, one area is the Mobile Robot. Biomimetics and bio-mimicry are both aimed at solving problems by first examining, and then imitating or drawing inspiration from models in nature. Biomimetics is the term used to describe the substances, equipment, mechanisms and systems by which humans imitate natural systems and designs, especially in the fields of defence, nanotechnology, robot technology, and artificial intelligence. Designs in nature ensure the greatest productivity for the least amount of materials and energy. They are able to repair themselves, are environmentally friendly and wholly recyclable. They operate silently, are pleasing in aesthetic appearance, and offer long lives and durability. Biomimetic materials inspired by biology from molecules to materials and from materials to machines. Some of mimicking of natures are adhesives that mimic gecko fingers, heat-sensing system that mimic viper, colour-changing clothes that mimic chameleons and constant state of balance inspired by snake. They are presented as examples of next generation bio-inspired materials. Biomimetic articulated robots are robots that imitate living creatures and have many modules. Various forms of bio-inspiration and related examples are listed below for a ready reference.

TABLE I. Various Forms of Bio-Inspiration and Related Examples

Biological example	Type of analogy	Biomimetic Materials
Gecko	Adhesion	Dry adhesives
Snakes	Sensing system, and Balancing system	Shape memory alloys (SMAs), Piezoelectric materials, and Electro-active polymers.
Chameleons	Colour changing	Choleric liquid crystals (CLCs)
Scorpion	Behavioural	Central pattern generators

II. Gecko Feet Inspired Biomimetic Products and Materials

Small lizards are able to run very fast up the walls and walk around clinging to the ceiling, very comfortably. Until recently, we could not understand as to how it could be possible for any vertebrate animal to climb up walls like the cartoon and film hero Spiderman. Now, years of research have finally uncovered the secret of their extraordinary ability. Little steps by the gecko have led to enormous discoveries with tremendous implications, particularly for robot designers. A few of them can be summarized as follows:

- Researchers in California believe that the lizard's "sticky" toes can help in developing a dry and self-cleaning adhesive.
- Geckos' feet (Fig. 1a) generate an adhesive force 600 times greater than that of friction. Gecko-like

Manuscript received December 1, 2013; revised February 25, 2014.

©2014 Engineering and Technology Publishing

doi: 10.12720/ijmse.2.2.122-125

robots could climb up the walls of burning buildings to rescue those inside.

- Dry adhesives could be of great benefits in smaller devices, such as in medical applications and computer architecture.
- Their legs act like springs, responding automatically when they touch a surface. This is a particularly appropriate feature for robots, which have no brain. Geckos' feet never lose their effectiveness, no matter how much they are used; they are self-cleaning and they also work in a vacuum or underwater.
- A dry adhesive could help hold slick body parts in place during Nano surgery.
- Such an adhesive could keep car tires stuck to the road.
- Gecko-like robots could be used to repair cracks in ships, bridges and piers, and in the regular maintenance of satellites.
- Robots modelled after the geckos' feet could be used to wash windows, clean floors, and ceilings. Not only will they be able to climb up flat vertical surfaces, but overcome any obstacles they meet on the way.



(a) (b)

Figure 1. (a) Gecko feet, and (b) Sticky-bot: Gecko inspired wall climbing robot [1]

The water's spreading out incredibly fast as drops fell on to the lizard's back and vanished. Its skin is far more hydrophobic. There may be hidden capillaries, channelling the water into the mouth. A subsequent examination of the thorny lizard's skin with an instrument called a micro-CT scanner confirmed, revealing tiny capillaries between the scales evidently designed to guide water towards the lizard's mouth. With this in mind, Cutkosky [2] endowed his robot with seven-segmented toes that drag and release just like the lizard's, and a gecko-like stride that snugs it to the wall. He also crafted Sticky-bot's legs and feet with a process, which combines a range of metals, polymers, and fabrics to create the same smooth gradation from stiff to flexible that is present in the lizard's limbs and absent in most man-made materials. Stickybot (Fig. 1b) is a four-legged robot capable of climbing smooth surfaces. He subsequently embedded a branching polyester cloth "tendon" in his robot's limbs to distribute its load in the same way evenly across the entire surface of its toes. Sticky-bot now walks up vertical surfaces of glass, plastic, and glazed ceramic tile, though it will be some time before it can keep up with a gecko. For the moment it can walk only on smooth surfaces, at a mere four centimetres per second, a fraction of the speed of its biological role model. The dry adhesive on Sticky-bot's toes isn't self-cleaning like the lizard's either, so it rapidly clogs with dirt. "There are a lot of things about the gecko that we simply had to ignore".

III. Viper as a Model in Its Defense

Dr. John Pearce, of the University of Texas Electrical and Computer Engineering Department, has studied Crotalines [3], better known as pit vipers. His research focused on the pit organs of these snakes. In front of the snake's eye (Fig. 2a) is a tiny nerve-rich depression, called the pit, which is used in locating warm-blooded prey. It contains a sophisticated heat-sensing system—so sensitive, that the snake can detect a mouse several meters away in pitch darkness. The researchers stated that when they unravel the secrets of the pit viper's search-and-destroy mechanism, the methods the snake employs can be adapted more widely to protect the country from enemy missiles.

The snake's pit is a thin membrane rich in blood vessels and nerve bundles. The membrane is so sensitive, and the variations in responses so minute that, to catch and study these signals has proved exceedingly difficult. To understand the functioning of the pit organ, it is necessary to work with delicate measurements and photomicrographs. The Mini-VIPER model robot in (Fig. 2b) weighs around 3.5 kilograms and is equipped with an array of sensors. Most of these conventional sensors, are strain sensors, thermal sensors, and optical sensors. More advanced actuation concepts are typically employed using active materials such as Shape memory alloys (SMAs), piezoelectric materials, and electroactive polymers. Small enough to move through tunnels and narrow alleys, it can be thrown into a building through a window and automatically begins scanning its environment. The robot is designed to protect infantry soldiers from explosives, booby traps and hostile forces lying in ambush.



(a) (b)

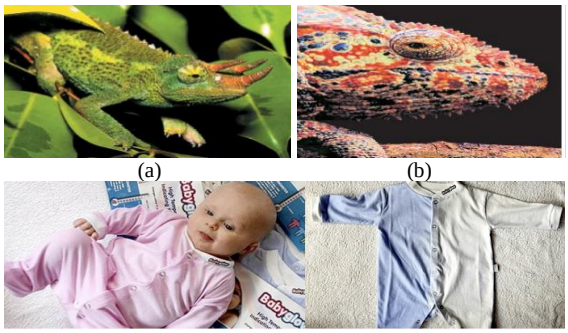
Figure 2. (a) Snake, and (b) the mini-viper model [4] photo: Elbit

IV. Chameleons Inspired Colour Changing Clothes

The impressive ability that chameleons (Fig. 3a-Fig. 3b) have to change colours to match their surroundings is both astonishing and aesthetically pleasing. The chameleon can camouflage itself at a speed that quite amazes people. With great expertise, the chameleon uses its cells called chromatophores which contain basic yellow and red pigments, the reflective layer reflecting blue and white light, and the melanophores containing the black to dark brown pigment melanin, which darkens its colour. The technology in colour-changing clothes (Fig. 3c) and the chameleon's ability to change colour may

©2014 Engineering and Technology Publishing

appear similar, but are in fact very different. Even if this technology can change colour, still it entirely lacks the chameleon's camouflage ability that lets it match its surroundings in moments. For instance, place a chameleon into a bright yellow environment, and it quickly turns yellow. In addition, the chameleon can match not only one single colour, but a mixture of hues.



(a) (b) (c)

Figure 3. (a-b) Chameleon's body with a system that lets it change colour to match its surroundings, and (c) Baby clothes that change colour with temperature [5].

The secret behind this lies in the way pigment-containing cells under the camouflage's skin expand or contract to match their surroundings. God has created the chameleon's body with a system that lets it change colour to match its surroundings, endowing it with a considerable advantage. Chameleons inspired for making clothes, bags and shoes that are able to change colours the same way as the chameleon does. Researchers envision clothing made from the newly developed fibre, which can reflect all the light that hits it, and equipped with a tiny battery pack. This technology will allow the clothing to change colours and patterns in seconds by means of a switch on the pack. Yet this technology is still very expensive. Scientists have designed choleric liquid crystals (CLCs) to alter the visible colour of an object to create the thermal and visual camouflage in fabrics. The colour of CLCs can be changed with temperature sensitive thermocouples [6]. The heating-cooling ability of thermocouples can be used to adjust the colour of the liquid crystals to match the object's background colour, providing camouflage or adaptive concealment.

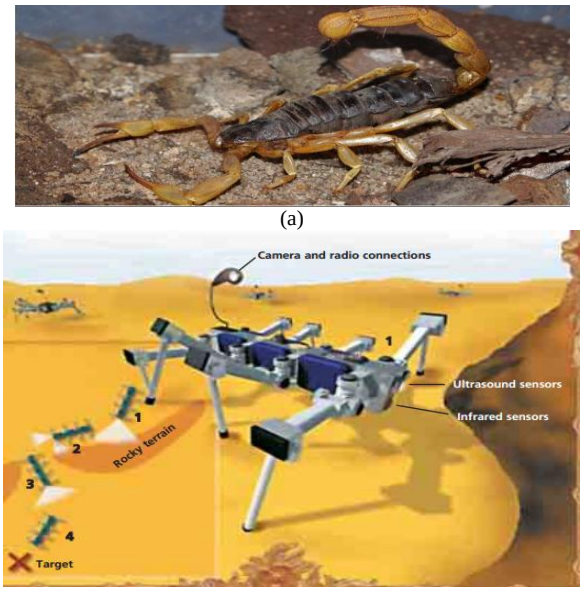
V. Snakes Imitating Robot to Overcome the Problem of Balance

For those engaged in robotics, one of the problems they encounter most frequently is of maintaining equilibrium. Even robots equipped with latest technology can lose their balance when walking. Robot experts attempt to build a balance-establishing learning that the snake (Fig. 4a) never loses its balance. Unlike other vertebrates, snakes lack a hard spine and limbs, and have been created in such a way as to enter cracks and crevices. They can expand and contract the diameter of their bodies, can cling to branches and glide over rocks. Snakes' properties inspired for a new robotic, interplanetary probe developed by NASA's Ames Research Centre which they called the "snake-bot" (Fig. 4b). This robot thus was designed to be in a constant state of balance, without ever getting caught up by obstacles.



(a) (b)

Figure 4. (a) Snake, and (b) Snake-bot [3]



(a) (b)

Figure 5. (a) Scorpion, and (b) Scorpion Robot [3]

VI. A Robot Scorpion Can Work in Harsh Desert Conditions

Sand or other abrasive particles have a way of eroding anything they encounter. Scorpions (Fig. 5a) have been able to survive harsh desert conditions ever since their creation. They live their entire lives subjected to blowing sand, yet they never appear to well, to erode. As a result, items such as helicopter rotor blades, airplane propellers, rocket motor nozzles and pipes regularly wear out and need to be replaced. A group of scientists recently set out to discover their secret, so it could be applied to man-made materials. In the United States, Defence Advanced Research Projects Agency (DARPA) is working to develop a robot scorpion (Fig. 5b) [3]. The reason the project selected a scorpion as its model is that the robot was to operate in the desert. The scientists subsequently applied what they observed in the scorpions' exoskeletons to man-made surfaces. They determined that the effects of erosion on steel surfaces could be significantly reduced, if that steel contained a series of small grooves set at a 30-degree angle to the flow of abrasive particles [7]. But another reason why DARPA selected a scorpion was that along with being able to move over tough terrain very easily, its reflexes are much simpler than those of mammals and can be imitated.

©2014 Engineering and Technology Publishing

Before developing their robot, the researchers spent a long time observing the movements of live scorpions using high-speed cameras, and analysed the video data. Later, the coordination and organization of the scorpion's legs were used as a starting point for the model's creation. The robot is controlled using a biomimetic approach of ambulation control. The approach is based on two biological control primitives, Central Pattern Generators and Reflexes. Using this approach, omni-directional walking and smooth gait transitions can be achieved. Additionally, the posture of the robot can be changed while walking. The robot was successfully tested in rough terrain with obstacles as high as the robot's body and in different terrains such as sand, grass, concrete and rock piles.

VII. Conclusions

From the above studies, the following conclusions have been drawn.

- Gecko feet inspires in developing a dry, and self-cleaning adhesive. A dry adhesive could help hold slick body parts in place during Nano surgery. Sticky-bot walks up vertical surfaces of glass, plastic, and glazed ceramic tile and also used repair cracks in ships, bridges and piers, and in the regular maintenance of satellites.
- After inspiring from viper a mini robot is designed to protect infantry soldiers from explosives, booby traps and hostile forces lying in ambush. Viper's search-and-destroy mechanism, the methods the snake employs can be adapted more widely to protect the country from enemy missiles.
- Smart and intelligent textiles are important developing area in science and technology because of their major commercial viability and public interest. Chameleons inspired for making clothes, bags and shoes able to change colours.
- Snakes' properties inspired for a new robotic interplanetary probe, which has a constant state of balance, without ever getting caught up by obstacles. The balancing problem can be overcome.
- By mimicking the scorpion, a robot is made for withstand harsh desert conditions. The robot can be asked to go to a specific region and, with a camera in its tail, send back to base images of the location

References

[1] K.-J. Cho, J.-S. Koh, *et al.*, "Review of manufacturing processes for soft biomimetic robots," *International Journal of Precision Engineering and Manufacturing*, vol. 10, no. 3, pp. 171-181, Jul. 2009.

[2] T. Mueller, "Biomimetics: design by nature," *National Geographic Magazine*, vol. 213, no. 4, pp. 68-91, 2008.

[3] H. Yahya, "Biomimetics: Technology imitates nature," *Global Publishing*, Mar. 2006.

[4] Y. Lappin, "Elbit unveils new defense products," in *Proc. Latrun Conference*, Latrun, Israel, Jul. 2010.

[5] Brian, "Baby clothes that change color with temperature," *Stories, Elemental/Exposing the Positive*, Oct. 14, 2010.

[6] A. V. Singh, *et al.*, "Bio-inspired approaches to design smart fabrics," *Materials & Design*, vol. 36, pp. 829-839, 2011.

[7] B. Coxworth, "Wear-resistant surfaces inspired by scorpions," *American Chemical Society journal Langmuir*, Jan. 26, 2012.



Kishor kalauni is a postgraduate student of Material Science and Engineering discipline in the Department of Applied Mechanics of Motilal Nehru National Institute of Technology, Allahabad, India. He obtained Degree in Mechanical Engineering in 2010. He has authored 3 research papers in reputed International Conferences. His major fields of study are Bio-composites and Biomimetic Materials.



Dr. K.M. Gupta is a Professor in the Department of Applied Mechanics, Motilal Nehru National Institute of Technology, Allahabad, India. He has over 35 years of teaching, research and consultancy experience. He obtained Postgraduation (M.E. with Honours) in 1977, and completed his Doctorate (Ph.D.) degree from University of Allahabad.

He has authored 30 books and edited 2 books on Engineering subjects, and a chapter in Scrivener Wiley published 'Handbook of Bio-plastics and Bio-composites Engineering Applications'. He has also authored 106 research papers in reputed International and National journals to his credit. He has presented his research papers in 16 International conferences abroad has also chaired 7 International Conferences in China, Singapore, Dubai, Bangkok etc.

Professor K. M. Gupta has acted as Editor-in-Chief of The International Journal of Materials, Mechanics and Manufacturing (IJMMM), has edited many International Journals and International Conferences. He has worked as reviewer for various International and National Journals, and has acted as Member of several Editorial Board. In recognition to his academic contribution at International level, Marquis Publication (USA) has included him in the list of 'World Who's Who in Science and Engineering 2007' and 'Who's Who in the World 2008'. The International Biographical Centre, a leading research institute (Great Britain) has also selected him as one of the '2000 Outstanding Scientists 2009' from across the world; and Rifacimento International Publisher has included his biographical-note in 'Reference Asia: Asia's Who's Who of Men and Women of Achievement. Earlier, he has served as Dean of Research & Consultancy, Head of the Applied Mechanics Department at Motilal Nehru National Institute of Technology Allahabad. He has acted as Chairman of various Research Selection Committees, of Research Project Monitoring Committees and other Administrative Committees of his Institute and other Universities. He has also served as Chairperson, Community Development Cell (CDC) of MNNIT for several years. Presently, Dr. Gupta is teaching Materials Science, Engineering Mechanics, Thermodynamics of Materials, Electrical and Electronic Materials etc. His research interests are in the fields of Materials Science, Composite Materials, Stress Analysis, Solid Mechanics etc.



Isha Bharti is from New Delhi, India, currently working as Teaching-cum-Research Fellow in the department of Applied Physics, Delhi Technological University. She completed her Masters (M.Tech.) in Nanoscience and Technology with specialization in Nanobiotechnology from Delhi Technological University in 2011. Her major field of study is synthesis and fabrication of Nanobiotechnological materials, luminescent materials for novel biomedical applications and diagnostic therapies, etc.

©2014 Engineering and Technology Publishing

Society of Plastics Engineers
PLASTICS RESEARCH ONLINE

10.2417/spepro.005409

Simple toughening of epoxy thermosets by preformed thermoplastics

Saurabh Chaudhary, Surekha Parthasarathy, Devendra Kumar, Chitra Rajagopal, and Prasun Roy

Reinforcing with microspheres avoids the need for solvent removal and improves impact strength and fracture toughness without compromising tensile properties.

Cured epoxy resins are widely used as the matrix material in fiber-reinforced plastics. However, they are inherently brittle in nature, which limits their use to less demanding applications where impact resistance is of secondary importance. Several toughening techniques exist, and one conventional approach involves blending with liquid reactive rubbers.[1,2] However, as a consequence of the inherently inferior mechanical properties of rubber, the resulting blends suffer from reduced modulus,[3] low glass transition temperature (T_g),[4] and high water absorption.

Thermoplastic-toughened epoxy resins avoid these disadvantages and are becoming more popular as a result,[5] but the thermoplastics are relatively difficult to process and require a separate solvent removal step. Therefore, we considered circumventing the issues associated with solvent removal and the low modulus of rubber by using preformed thermoplastics to toughen an epoxy matrix.

We prepared polystyrene (PS) thermoplastic microspheres by suspension polymerization. We subsequently formed aminopoly(styrene) (APS) by nitration followed by reduction, to aid compatibility between the microspheres and an epoxy matrix (see Figure 1).[6] We dispersed varying amounts of 100–200 mesh (75–150μm) microspheres in epoxy resin, using ultrasonication followed by room-temperature curing to prepare toughened compositions.

We found that the microspheres did not affect the thermal behavior of the base matrix. All compositions exhibited a glass transition temperature (T_g) of 66°C and could be used up to 250°C. Introducing PS and APS into the epoxy led to a remarkable improvement in mechanical properties (see Figure 2). The impact strength increased by 33% on adding 3% w/w APS, although the improvement was much less (~20% compared to neat epoxy) when PS was employed.

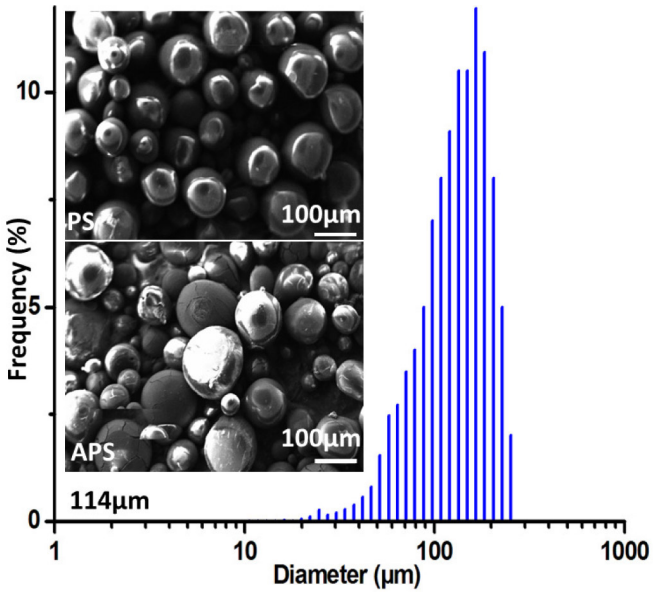


Figure 1. *Particle size distribution of thermoplastic microspheres. Inset shows scanning electron microscopy (SEM) images of polystyrene (PS) and aminopoly(styrene) (APS) microspheres.*

The optimal compositions contained 3% APS and exhibited an ~30% increase in fracture toughness and an ~70% increase in fracture energy. Higher loading caused the microspheres to agglomerate, which in turn reduced the impact strength and toughness.

We also studied the fractured surfaces of composites to gain insight into the underlying mechanisms behind the improved toughness of the base resin. The smooth and featureless surface of epoxy is characteristic of brittle fracture. In comparison, the fractured surfaces of the toughened composites are rather rough, and we observed characteristic features associated with microcracking, crack path deflection, particle yielding, crack pinning, particle bridging, and crack bowing

Continued on next page

(see Figure 3). Each of these plays its own significant role toward the overall toughening.

Our studies clearly indicate that amine functional groups in the microspheres help them disperse homogeneously within the epoxy matrix. The covalent interaction between the epoxy and amine groups in the APS improves compatibility and hence mechanical properties. The resulting morphology is more suitable for bearing dynamic loads compared with the inhomogeneous structure resulting from solution blending.

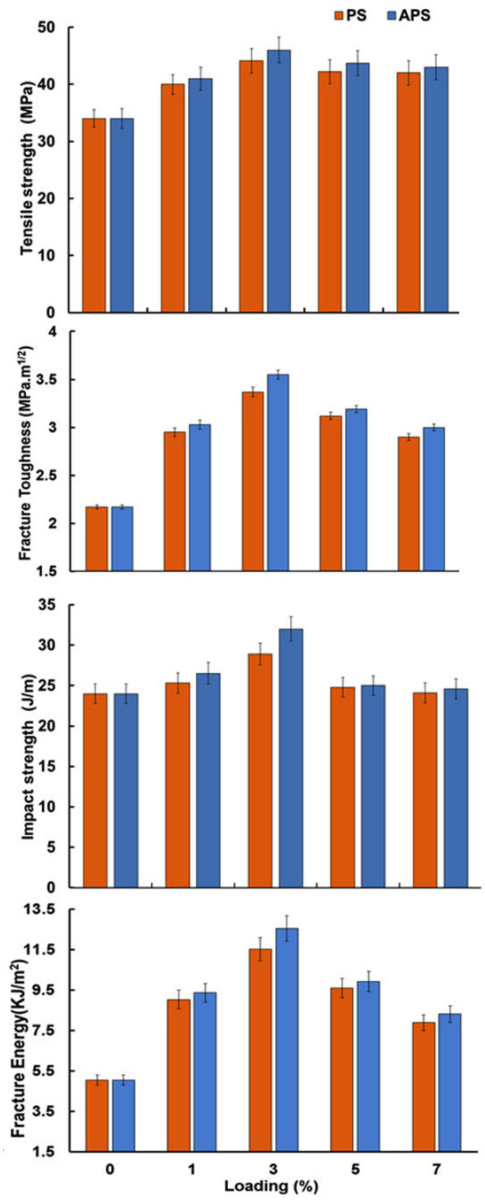


Figure 2. *Increase in mechanical properties of epoxy with loading of PS and APS microspheres.*

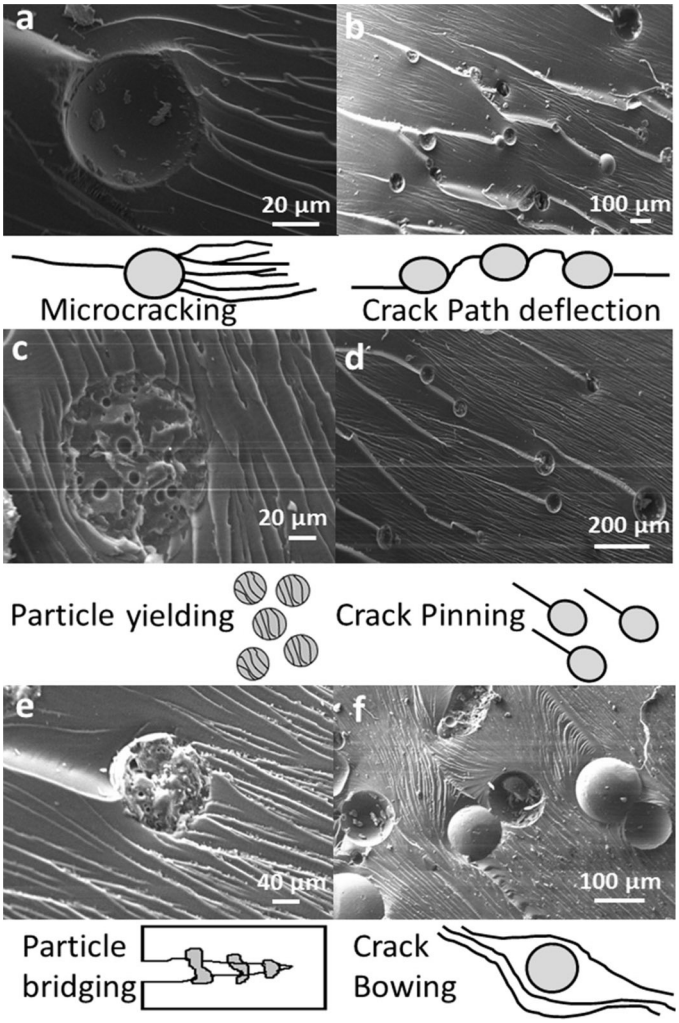


Figure 3. *Pictorial schematics of the underlying toughening mechanisms and SEM images of corresponding fracture surfaces. (a) Microcracking. (b) Crack path deflection. (c) Particle yielding. (d) Crack pinning. (e) Particle bridging. (f) Crack bowing.*

To summarize, we have demonstrated the potential of functionalized poly(styrene) microspheres to improve the dynamic properties of epoxy. Unlike toughening the epoxy with rubber, introducing these thermoplastic beads does not adversely affect the tensile properties of the base resin. We are now exploring other suitable engineering thermoplastics and the effect of their particle dimensions and morphology on the overall toughening of various thermosetting resins.

Continued on next page

Society of Plastics Engineers
PLASTICS RESEARCH ONLINE
10.2417/spepro.005409 Page 3/3

Author Information

Saurabh Chaudhary, Surekha Parthasarathy, Chitra Rajagopal, and Prasun Roy
Centre for Fire, Explosive and Environment Safety (CFEES)
Defence Research and Development Organisation (DRDO)
Delhi, India

Devendra Kumar
Department of Applied Chemistry and Polymer Technology
Delhi Technological University
Delhi, India

References

1. R. Bagheri and R. A. Pearson, *Role of particle cavitation in rubber-toughened epoxies: II. Inter-particle distance*, **Polymer 41**, pp. 269–276, 2000. doi:10.1016/S0032-3861(99)00126-3
2. S. Chaudhary, S. Parthasarathy, D. Kumar, C. Rajagopal, and P. K. Roy, *Poly(ethyleneterephthalate) glycolysates as effective toughening agents for epoxy resin*, **J. Appl. Polym. Sci. 131**, 2014. doi:10.1002/app.39941
3. P. Roy, N. Iqbal, D. Kumar, and C. Rajagopal, *Polysiloxane-based core-shell microspheres for toughening of epoxy resins*, **J. Polym. Res. 21**, pp. 1–9, 2014. doi:10.1007/s10965-013-0348-5
4. S. Chaudhary, S. Parthasarathy, D. Kumar, C. Rajagopal, and P. K. Roy, *Graft-interpenetrating polymer networks of epoxy with polyurethanes derived from poly(ethyleneterephthalate) waste*, **J. Appl. Polym. Sci.**, 2014. doi:10.1002/app.40490
5. I. A. Zucchi, M. J. Galante, and R. J. J. Williams, *Comparison of morphologies and mechanical properties of crosslinked epoxies modified by polystyrene and poly(methyl methacrylate) or by the corresponding block copolymer polystyrene-b-poly(methyl methacrylate)*, **Polymer 46**, pp. 2603–2609, 2005. doi:10.1016/j.polymer.2005.02.012
6. S. Chaudhary, P. Surekha, D. Kumar, C. Rajagopal, and P. K. Roy, *Amine-functionalized poly(styrene) microspheres as thermoplastic toughener for epoxy resin*, **Polym. Compos.**, 2014. doi:10.1002/pc.22927

© 2014 Society of Plastics Engineers (SPE)

SRF based Modeling and Control of Cascaded Multilevel Active Rectifier with Uniform DC-Buses

Amritesh Kumar, Dhruv Kumar, Daya Ram Meena
Dept. of Electrical Engineering
Delhi Technological University
New Delhi, India
amritesh@dce.ac.in, kdhruv92@gmail.com, dayaram5493@gmail.com

***Abstract*— Cascaded H-bridge (CHB) multilevel active rectifier system envisage attractive alternative for conventional method of active rectification and finds application in traction drive and locomotives. Further CHB structure can be utilize of high voltage transformer less rectification. Availability of multiple DC buses in CHB, needs DC bus regulation at each level. It becomes a challenging task in CHB due to interdependent control of each H-bridge. It is therefore proper control algorithm has to be designed for effective regulation and fast response. In view of this single phase synchronous reference frame (SRF) theory based voltage controlled phase shifted PWM controller has been modeled for active rectification with unity power factor operation. MATLAB based simulation results shows the efficient working of CHB multilevel active rectifier with proposed control algorithms and its effectiveness is verified by changing the loading conditions.**

Keywords*— Cascaded H-bridge (CHB); Multilevel; Phase shifted PWM; Synchronous reference frame (SRF).

I. INTRODUCTION

In the era of rapid industrialization spurt in electricity demand cannot be averted. But due to limited sources of generation energy efficient devices, systems, configurations and components are being encouraged to use. In many industries DC voltage is obtained by single or three phase diode rectifier for proper motor drive operation. This leads to poor power factor operation of the system. To tackle this issue active front end rectifier is being advocated in many literatures [1]. But due to limited range of IGBT's availability in the market, their uses are limited and for proper voltage operation transformers (step up/step down) are being used, that is being major sources of losses in the system. Moreover controlling of big traction motor drive becomes a challenging task as it requires high voltage rating IGBT's.

With the advancement in power electronics technology various multilevel topologies like diode clamped, flying capacitor (FC), cascaded H-bridge (CHB) based inverter is being advocated for traction motor drive. Out of various topologies, cascaded H-bridge (CHB) are much in research since last decade due to a modular structure and list number of other auxiliary components. Moreover the CHB active rectifier produces least harmonic content due to stepped waveform for voltage/current and further it decreases by the increasing the number of levels [2], [3]. Availability of separate DC buses in the CHB rectifier at each level finds attractive application for high voltage traction drive using CHB multilevel inverter, which requires separate DC sources [4].

Further in various metro rail coaches and electric trains auxiliary supplies for light, fan, charging are mainly maintained at 120 V DC. The supply is maintained at 120 V generally by proper rectification of AC voltage obtained after step down the AC input supply through transformer or using buck converter arrangement after rectification of AC source. Ultimately these arrangements incur extra cost in step down the voltage.

To tackle above issues, CHB based active rectifier is proposed in literature [5]. CHB structure not only provides isolated DC sources at each H-bridge, with proper control algorithm source current can also be maintained at unity power factor. Due to cascaded arrangement of each bridge, independent control is not possible for individual bridges in CHB as with single H-bridge active rectifier. So regulation of each dc bus becomes very important due to uneven switching of CHB at each level. These regulated dc bus can be connected to varied loads. In literature various PWM schemes are used for CHB rectifier operation [6], [7]. Some PI based control has also been proposed in literatures for proper dc bus regulation [8]. But these are based on instantaneous control and also control is complicated. Recently in some literature SRF based control has also been proposed for CHB active rectifier control [9]. To overcome the complicated control, a simple SRF based control logic has been proposed for proper power transfer and dc bus regulation. For unity power factor operation correct phase of the source voltage is sensed through PLL (Phase locked loop). The conventional 3 phase SRF theory has been modified for single phase system.

The proposed scheme modeled and simulated under MATLAB Simulink environment. The whole paper is discussed in following section (ii) System configuration; (iii) Control (iv) MATLAB based simulation, (v) Performance evaluation, (vi) Conclusion.

II. SYSTEM CONFIGURATION

The CHB rectifier is the best choice for working in high-voltage and high-power application because of its modularity and its simple layout. The structure can be expanded for any level of voltage just by increasing the number of bridges. Fig. 1

978-1-4799-2291-8/14/$31.00 ©2014 IEEE

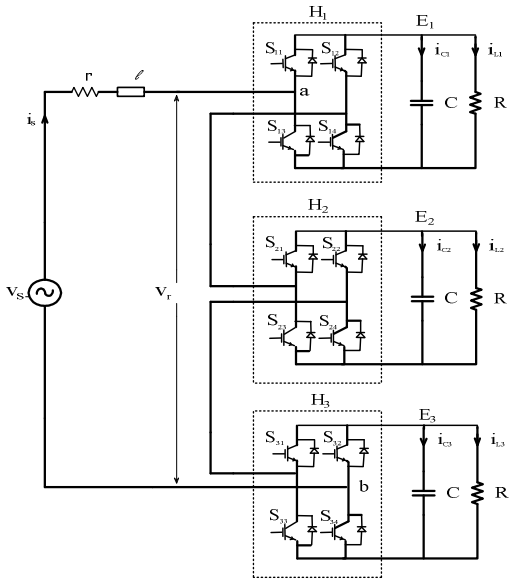


Fig. 1. Block diagram of proposed multilevel active rectifier

shows the block diagram of proposed single-phase 7 level multilevel active rectifier configurations comprising of 3 H-bridges. Each bridge includes four IGBT switches with anti-parallel diodes and a dc link capacitor across which resistive load is being connected. where, i_s is the input current, v_s is the source voltage, v_r is the rectifier input voltage, l and r shows coupling inductor and resistance respectively for proper active rectifier, E_1 , E_2 *and* E_3 are the dc-link voltages, C is the dc link capacitor.

This paper focuses on the single-phase ac/dc rectifiers with equal load at each bridge. It can be easily extended to three phase configuration. The ac/dc rectifier stage converts the single-phase 230V ac voltage to three dc-link voltages. The rectifier consists of three cascaded H-bridges with each dc-link voltage referenced to 120V. This transformer less H-bridge rectifier structure may be used for feeding different loads such as in metro and railway's auxiliary supplies for lighting, fan etc.

III. CONTROL THEORY

This paper presents a current driven voltage balance control method to resolve the voltage unbalance on the dc links of each H-bridge. The conventional synchronous reference frame (SRF) control algorithm has been modified to suit for single phase system also. In initial transformation source current i_s is assumed to be i_α and i_β is obtained after giving 90° delay to i_α , so that analysis can be made for single phase system as shown in Fig.2. For correct α-β to d-q transformation exact estimation of unit vectors (sinθ, cosθ) becomes essential i.e. being accomplished through PLL. After d-q transformation, the i_d component represents the real part and i_q represents the reactive component of the of the source current. This way SRF control gives decoupled control of real and reactive power component.

The source current is transformed into d-q component using equation (3) and passed through low pass filter (LPF) to obtain only dc components discarding any harmonics in the dc current.

Assuming current references as:

$$i_\alpha = A.\sin\omega t \qquad \ldots\ldots. (1)$$

After 90° delay in α component, β axis component becomes:

$$i_\beta = A.\sin(\omega t - \frac{\pi}{2}) \qquad \ldots\ldots. (2)$$

The α-β component is obtained then transformed to d-q by using equation (3)

$$\begin{pmatrix} i_d \\ i_q \end{pmatrix} = \begin{pmatrix} \sin\omega t & -\cos\omega t \\ \cos\omega t & \sin\omega t \end{pmatrix} . \begin{pmatrix} i_\alpha \\ i_\beta \end{pmatrix} \qquad \ldots\ldots. (3)$$

After transformation only α component is used as a modulating signal for phase shifted PWM scheme.

For a 7 level multilevel convertor, gating signals are generated by phase shifted modulation technique. Gating signals for each H-bridge are generated by comparing modulating signal with corresponding carrier waves as shown in Fig.3.

As the three H-bridges are in cascade, the voltage unbalance may be appear on dc links (E_1, E_2 and E_3 as shown in Fig.1) due to non-uniform PWM gating pulses in CHB control algorithm. This unbalance may rise the voltage across the capacitor or IGBT devices, In turn it may lead to trigger the system overvoltage protection in H-bridges. To avoid the problem of unbalance on dc links, each dc link voltages are sensed and compared with reference voltage (E_{ref}). The error of the estimated voltage is passed through PI controller to give appropriate real component of current (I_d) to be required for proper voltage regulation of each H-bridge. For unity pf operation I_q component of sources is compared with the zero reference current. Decoupled control of real and reactive component of voltage is obtained by taking account of voltage drop due to I_d and I_q component across the coupling inductor. The drop across coupling inductor due to i_q component is subtracted from V_{d1} to arrive at reference voltage V_d . Similarly drop across coupling inductor due to i_d component is added to V_{q1} to arrive at V_q reference. These d-q axis voltages are transformed back to V_α, V_β component using eq.(4).

$$\begin{pmatrix} i_\alpha \\ i_\beta \end{pmatrix} = \begin{pmatrix} \sin\omega t & \cos\omega t \\ \cos\omega t & -\sin\omega t \end{pmatrix} . \begin{pmatrix} i_d \\ i_q \end{pmatrix} \qquad \ldots\ldots. (4)$$

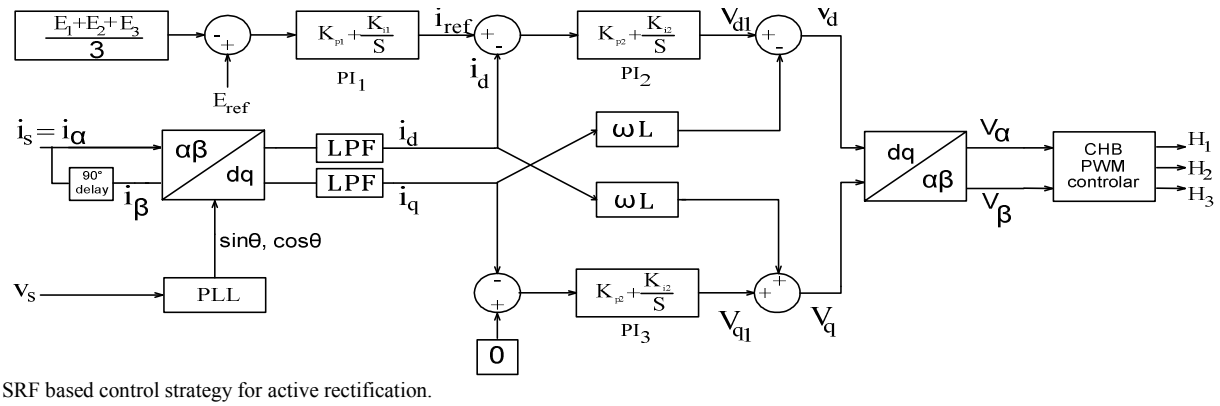


Fig. 2. SRF based control strategy for active rectification.

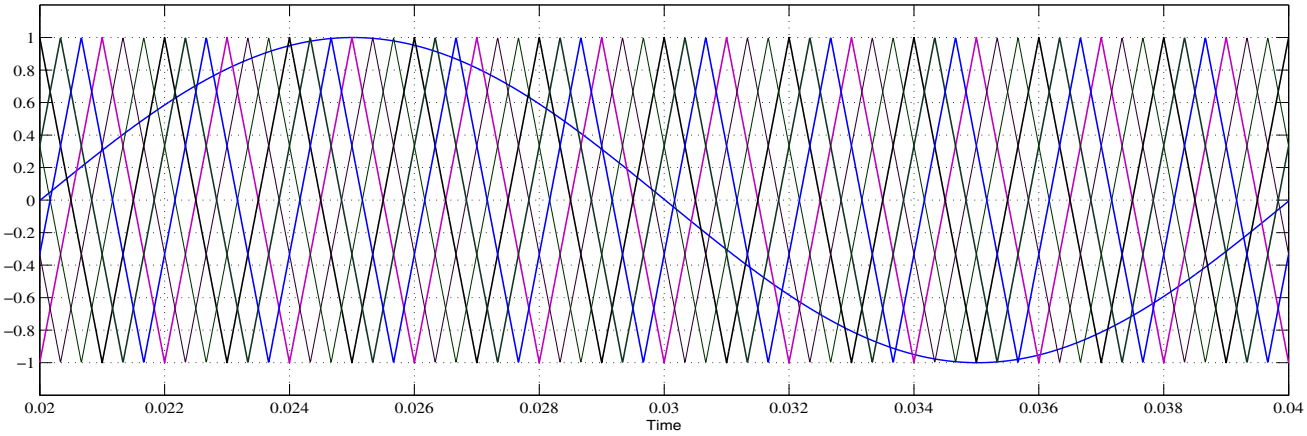


Fig. 3. Waveforms of phase shifted carrier signals and modulating signal.

Thereafter V_α component is used as modulating signal for phase shifted PWM.

IV. MATLAB BASED SIMULATION

The proposed CHB based rectifier is simulated under MATLAB Simulink environment as mentioned above. This paper focused on the voltage control of each DC link of H-bridge based multilevel active rectifier, and is simulated under MATLAB Simulink environment. The single phase synchronous reference frame (SRF) based theory of three-phase system is modified for the single phase system. Each of the DC bus is controlled through proportional integral controller modeled in Simulink as shown in fig. 4 and5. To verify the effectiveness of the control algorithm the load has been varied from 30 A to 50 A for each DC bus.

The detailed various parameters of the systems and various numerical values used in the model for proper tuning of different PI controllers are shown in the Table I, II.

TABLE I. SIMULATION PARAMETERS

Input AC voltage (single phase)	230V
Line inductance	2mH
Line resistance	0.1Ω
DC capacitor	4500μF
Load resister 1	10Ω
Load resister 2	15 Ω
DC link reference voltage	120V

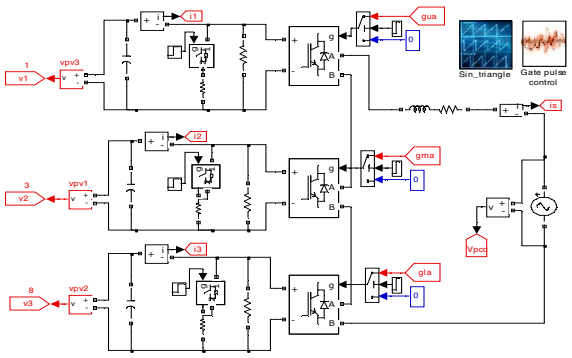


Fig. 4 . Simulation model of CHB active rectifier

TABLE II. VALUES OF PI CONTROLLERS

PI_1	K_p	0.8295
	K_i	4.839
PI_2	K_p	0.43
	K_i	43.318
PI_3	K_p	0.096
	K_i	8

V. RESULT

The proposed CHB based rectifier with unity power factor operation is simulated under MATLAB Simulink environment. Fig.7(a)-(f) shows the waveforms of voltage at the input of active rectifier (v_r), source voltage (v_s), source current (i_s), DC link voltage (E_1), DC link voltage (E_2), and DC link voltage (E_3). Initial transient conditions are not taken into account for analysis as it takes around 0.5s to each at steady state condition. At t=0.5s each dc link voltages has reached to 120 V, equal to reference being set for each dc-link as shown in Fig.7(d)-(f). In the same time source current is maintained at steady value of 21.21 A till t=1s. With each dc link maintained at 120 V, the active rectifier output voltage reach at the maximum peak of 360 voltages as shown in Fig.7 (a).

To verify the dynamic response of the control algorithm a load change command has been given at t=1s for each dc bus. It results into disturbance of the equilibrium state at t=1s, but again new steady state for each parameters has been reached at t=1.5s. With change in loading condition also voltage at each bus is maintained at 120 V same as reference voltage as shown in Fig.7(d)-(f). Due to increase in the load demand the steady

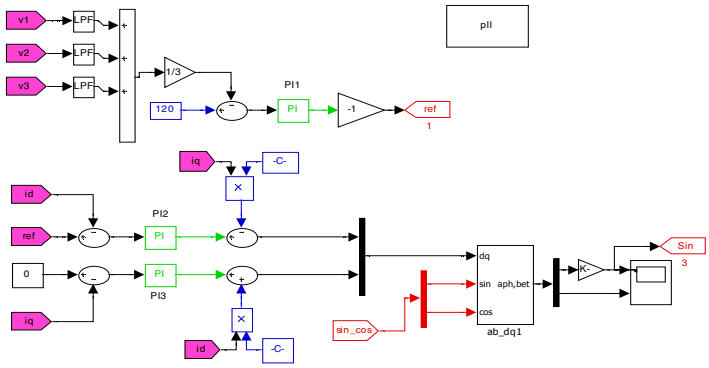


Fig. 5. Simulation model proposed SRF control scheme

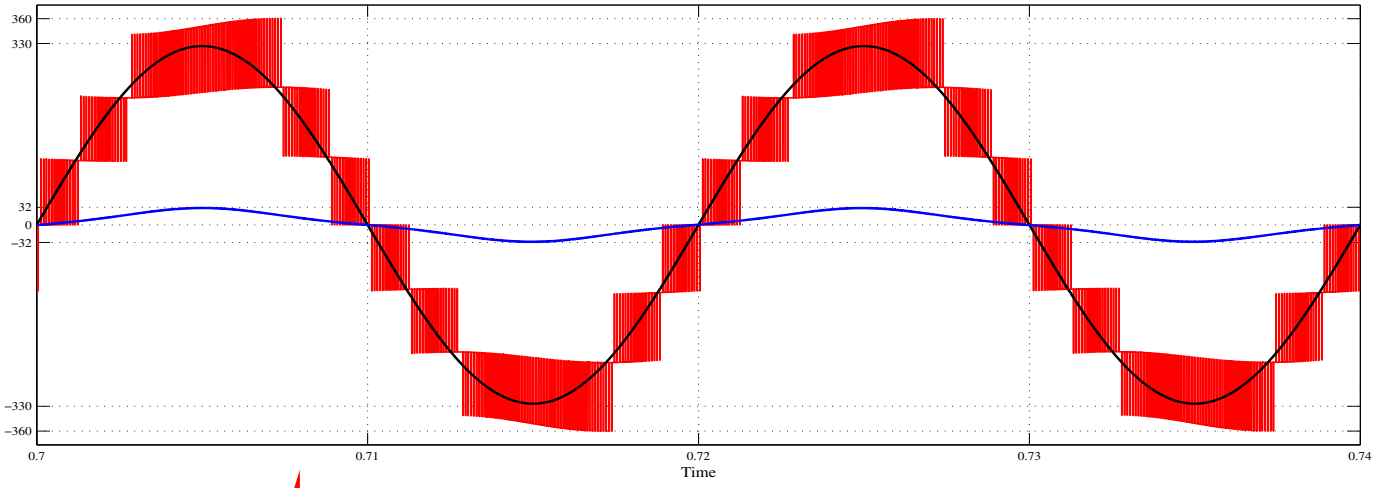


Fig. 6. AC terminal voltage (v_r),input current (i_s) and input voltage (v_s) showing unity power factor operation

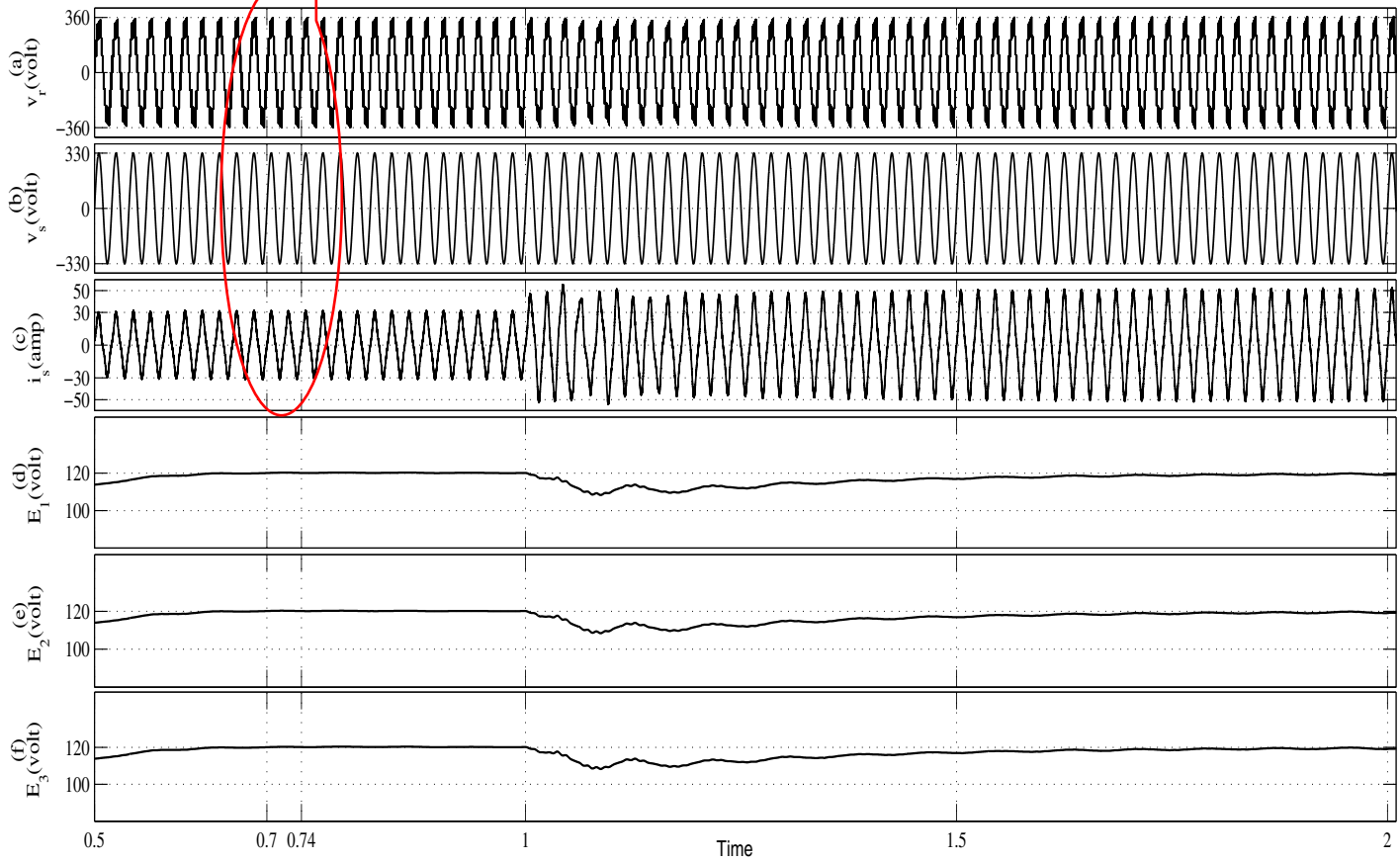


Fig. 7. Simulation results of AC terminal voltage (v_r),Input current (i_s) , Input voltage (v_s) and Different dc link voltage (E_1,E_2 and E_3)

state current value has reached to 35.36 A as shown in Fig.7(c).

To make analysis more clear zoomed waveforms of input voltage of active rectifier, source voltage, source current is shown in Fig.6. From the figure it's clear that source current is in phase with source voltage maintaining the system at unity power factor.

Fig.8 and Fig.9 shows the FFT analysis of multilevel input voltage and source current respectively. FFT of voltage source the THD around 22.51% and of the source current THD is 14.69%.

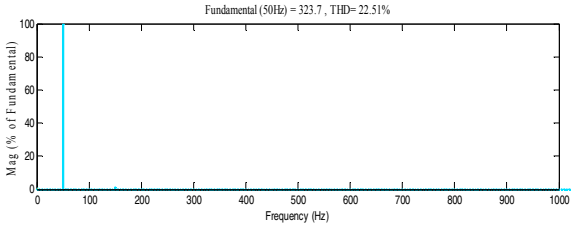


Fig. 8. FFT analysis of voltage

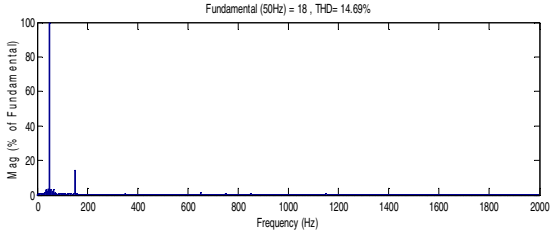


Fig. 9. FFT analysis of current

VI. CONCLUSION

SRF based simple control scheme for DC bus voltage balancing of each H Bridge of 7 level multilevel active rectifier have been successfully demonstrated through MATLAB simulation results. Voltage regulation at each bridge is achieved by simple proportional integral controller method. Dynamic response of the system is demonstrated through sudden load change in the load at each H-bridge. The result clearly demonstrates that use of CHB rectifier leads to reduction in THD and transformer less operation of the traction drive system. This will reduce overall cost and improve the efficiency. It also reduces stress on switches, switching losses and also it requires low capacity filters. Moreover with modular structure further levels can be increased without disturbing the structure.

REFERENCES

[1] Manias, S. ; Ziogas, P.D. ; Olivier, G., "An AC-to-DC Converter with Improved Input Power Factor and High Power Density," IEEE Trans. Industrial Electronics vol. IA-22, pp. 1073-1081, 1986.

[2] S. S. Fazel, S. Bernet, D. Krug, and K. Jalili, "Design and comparison of 4-kV neutral-point-clamped, flying-capacitor, and series-connected H-bridge multilevel converters," IEEE Trans. Ind. Appl., vol. 43, no. 4,pp. 1032–1040, Jul./Aug. 2007.

[3] Y. Cheng, C. Qian,M. L. Crow, S. Pekarek, and S. Atcitty, "A comparison of diode-clamped and cascaded multilevel converters for a STATCOM with energy storage," IEEE Trans. Ind. Electron., vol. 53, no. 5, pp. 1512–1521, Oct. 2006.

[4] Verma, V. ; Kumar, A. , "Power balanced cascaded multilevel inverter fed scalar controlled induction motor pump sourced from photovoltaic source," IEEE International Conference. pp.1- 6, 2012.

[5] C. Cecati, A. Dell'Aquila, M. Liserre, and V. G. Monopoli, "Design of H-bridge multilevel active rectifier for traction systems," IEEE Trans. Ind. Appl., vol. 39, no. 5, pp. 1541–1550, Sep./Oct. 2003.

[6] J. A. Barrena, L.Marroyo,M. A. R.Vidal, and J. R. T.Apraiz, "Individual voltage balancing strategy for PWM cascaded h-bridge converter-based STATCOM," IEEE Trans. Ind. Electron, vol. 55, no. 1, pp. 21–29, Jan.2008.

[7] Lin, B.-R. ; Yang, T.-Y., "Novel single-phase switching mode multilevel rectifier with a high power factor," IEE Proceedings Electric Power Applications vol. IA-22, pp. 447-454, 2005.

[8] Dell'Aquila, A. ; Liserre, M. ; Monopoli, V.G. ; Rotondo, P. "Overview of PI-Based Solutions for the Control of DC Buses of a Single-Phase H-Bridge Multilevel Active Rectifier," IEEE Trans. Industrial Electronics, vol. 44, pp. 857 - 866, 2008.

[9] Zhao, T. ; Wang, G. ; Bhattacharya, S. ; Huang, A. Q., "Voltage and Power Balance Control for a Cascaded H-Bridge Converter-Based Solid-State Transformer," IEEE Trans. Ind. Electron.Power Electronics, vol. 28, pp. 1523- 1532, Oct. 2013.

Journal of Statistical Theory and Applications, Vol. 13, No. 1 (March 2014), 27-37

Stochastic Comparisons of Residual Entropy of Order Statistics and Some Characterization Results

Ramesh C. Gupta [1], H.C. Taneja [2], and Richa Thapliyal [2]

[1] *Department of Mathematics and Statistics, University of Maine, Orono, ME 04469-5752, USA*
[2] *Department of Applied Mathematics, Delhi Technological University, Delhi-110042, India*

rcgupta@maine.edu, hctaneja@rediffmail.com, richa31aug@gmail.com

In this paper, we have presented some results for the residual and past entropies of order statistics. Results on the stochastic comparisons based on residual entropy of order statistics are presented. Characterization results for these dynamic entropies based on the sufficient condition for the uniqueness of the solution of an initial value problem have been considered.

Keywords: Order statistics, Residual entropy, Hazard rate, Past entropy, Stochastic comparisons, Characterization results.

1. Introduction

Let X be a non-negative continuous random variable with distribution function $F(\cdot)$ and probability density function $f(\cdot)$. Shannon (1948) introduced a measure of uncertainty associated with distribution function $F(\cdot)$ as

$$H(F) = -\int_0^\infty f(x)\ln f(x)dx = -E[\ln f(X)]\,, \tag{1.1}$$

where by convention $0\ln 0 = 0$.

The above differential entropy plays a central role in information theory. It measures the uncertainty associated with the distribution function F. It is obvious that this function $H(F)$ does not characterize the distribution function. In this connection, Ebrahimi (2001) presented some results that identify certain conditions based on the entropy under which the two random variables are stochastically equal.

The question now arises if the entropy of order statistics characterizes the distribution. For this purpose, Baratpour *et al.* (2007, 2008) explored some properties of the entropy of order statistics and record values and established some characterization results.

If we think X as life of a new unit, then $H(F)$ can be useful for measuring the associated uncertainty. However, for a used unit, $H(F)$ is no longer useful for measuring the uncertainty about the

Published by Atlantis Press
Copyright: the authors

remaining life of the unit. In such situations, if the unit has survived upto time t, we consider the uncertainty of the residual lifetime distribution as

$$\begin{aligned} H(F;t) &= -\int_t^\infty \frac{f(x)}{\overline{F}(t)} \ln \frac{f(x)}{\overline{F}(t)}\, dx \\ &= 1 - \frac{1}{\overline{F}(t)} \int_t^\infty f(x) \ln \lambda_F(x) dx \\ &= 1 - E[\ln \lambda_F(X) \mid X > t], \end{aligned} \tag{1.2}$$

where $\overline{F}(\cdot)$ is the survival function corresponding to $F(\cdot)$ and $\lambda_F(x)$ is its failure rate or hazard rate defined by $f(x)/\overline{F}(x)$. After the component has survived upto time t, $H(F;t)$ measures the expected uncertainty contained in the conditional density of $X-t$ given $X>t$ about the predictability of the remaining life of the component. Clearly for $t=0$, $H(F;0) = -\int_0^\infty f(x)\ln f(x)dx$ represents the Shannon uncertainty contained in X.

Analogous to the residual entropy, the entropy of $X|X \leqslant t$, called the past entropy at time t has also drawn attention in the literature. The past entropy is given by

$$\begin{aligned} \overline{H}(F;t) &= -\int_0^t \frac{f(x)}{F(t)} \ln \frac{f(x)}{F(t)} dx \\ &= 1 - \frac{1}{F(t)} \int_0^t f(x) \ln \tau_F(x) dx\,, \end{aligned} \tag{1.3}$$

where $\tau_F(x)$ is the reversed hazard rate of X given by $f(x)/F(x)$. Lately, the reversed hazard rate has drawn considerable attention, see for example Block *et al.* (1998), Di Crescenzo and Longobardi (2002, 2004) and Gupta and Gupta (2007).

A natural question arises: whether $H(F;t)$ and $\overline{H}(F;t)$ characterize the distribution. In this connection, Ebrahimi (1996) proved a characterization of a lifetime distribution in terms of the residual entropy. This was followed by Belzunce *et al.* (2004) who pointed out that the proof of Ebrahimi (1996) was not valid without some additional assumptions. Under the additional assumptions Belzunce *et al.* (2004) proved that $H(F;t)$ characterize the distribution. Recently Gupta (2009) presented a general result to determine whether $H(F;t)$ or $\overline{H}(F;t)$ determine the distribution.

Let $X_1, X_2, \ldots, X_n$ be n independent and identically distributed observations from a distribution F, where $F(\cdot)$ is differentiable with a density $f(\cdot)$ which is positive in an interval and zero elsewhere. The order statistics of the sample is defined by the arrangement of $X_1, X_2, \ldots, X_n$ from the smallest to largest denoted as $X_{1:n}, X_{2:n}, \ldots, X_{n:n}$. These statistics are widely used in reliability theory and survival analysis to study $(n-k+1)$-out-of-n system which works if and only if atleast $(n-k+1)$-out-of-n components are working. Series and parallel systems are particular cases of these system corresponding to $k=1$ and $k=n$, respectively.

In this paper, we shall explore the properties of the residual entropy of order statistics. We shall also consider the characterization results based on the entropy function of the order statistics based on residual lifetime distribution and the past life distribution. The organization of this paper is as follows: In Section 2, we present some basic results for the residual entropy and the past entropy based on order statistics together with some examples. Section 3 deals with the stochastic comparisons based on the residual entropy of order statistics. Section 4 contains some characterization results based on the entropy function of the residual lifetime distribution and the past life distribution. The proofs are based on using sufficient condition for the uniqueness of the solution of an initial value

Copyright: the authors

problem (IVP) encountered in the study of certain differential equation. Finally some conclusions and comments are given in Section 5.

2. Entropy of Order Statistics

Suppose X is a continuous random variable with distribution function $F_X(x)$. It is well known that $U = F_X(X)$ has a uniform distribution in $[0,1]$. Let $U_1, U_2, \ldots, U_n$ be a random sample from a uniform distribution $[0,1]$ and $W_1 < W_2 < \cdots < W_n$ be the order statistics, then W_i, $i = 1, 2, \ldots, n$ has a beta distribution with density function

$$g_i(w) = \frac{1}{B(i, n-i+1)} w^{i-1}(1-w)^{n-i}, \quad 0 \leqslant w \leqslant 1, \tag{2.1}$$

where $B(a;b) = \frac{\Gamma(a)\Gamma(b)}{\Gamma(a+b)}$.
The entropy of W_i is given by

$$H_n(W_i) = \ln B(i, n-i+1) - (i-1)[\psi(i) - \psi(n+1)] - (n-i)[\psi(n-i+1) - \psi(n+1)], \tag{2.2}$$

where, $\psi(z) = \frac{d \log \Gamma(z)}{dz}$ is the digamma function.
The entropy of the order statistics $X_{i:n}$ is given by

$$H(X_{i:n}) = H_n(W_i) - E_{g_i}[\ln(f(F^{-1}(W_i)))] \,, \tag{2.3}$$

where $g_i(w)$ is given by (2.1), refer to Ebrahimi *et al.* (2004).
The residual entropy of order statistics $X_{i:n}$ is given by

$$\begin{aligned} H(X_{i:n};t) &= -\int_t^\infty \frac{f_{i:n}(x)}{\overline{F}_{i:n}(t)} \ln\left(\frac{f_{i:n}(x)}{\overline{F}_{i:n}(t)}\right) dx \\ &= 1 - \frac{1}{\overline{F}_{i:n}(t)} \int_t^\infty f_{i:n}(x) \ln \lambda_{F_{i:n}}(x) dx \,, \end{aligned} \tag{2.4}$$

where $\lambda_{F_{i:n}}(x)$ is the hazard rate of the i^{th} order statistics.
Similarly, the entropy of the order statistics of the past life distribution is given by

$$\begin{aligned} \overline{H}(X_{i:n};t) &= -\int_0^t \frac{f_{i:n}(x)}{F_{i:n}(t)} \ln \frac{f_{i:n}(x)}{F_{i:n}(t)} dx \\ &= 1 - \frac{1}{F_{i:n}(t)} \int_0^t f_{i:n}(x) \ln \tau_{F_{i:n}}(x) dx \,, \end{aligned} \tag{2.5}$$

where $\tau_{F_{i:n}}$ is the reversed hazard rate of the i^{th} order statistics.

2.1. *Some Special cases*

In reliability engineering $(n-k+1)$-out-of-n systems are very important kind of structures. A $(n-k+1)$-out-of-n system functions if and only if at least $(n-k+1)$ components out of n components function. If $X_1, X_2, \ldots, X_n$ denote the independent lifetimes of the components of such system, then the lifetime of the system is equal to the order statistic $X_{k:n}$. The special case of $k = 1$ and n, that is for sample minima and maxima correspond to series and parallel systems respectively. Here, we calculate the residual and the past entropy of first order (sample minima) and n^{th} order (sample

Copyright: the authors

maxima) statistics, for an exponentially distributed random variable.

The residual entropy of $X_{1:n}$ can be obtained using (2.4) as

$$H(X_{1:n};t) = \left(\frac{n-1}{n}\right) - \ln n + \ln \overline{F}(t) - n\int_{F(t)}^{1} (1-u)^{n-1} \ln[f(F^{-1}(u))]du\,. \tag{2.6}$$

We calculate the residual entropy of the first order statistics $X_{1:n}$ for an exponentially distributed random variable with p.d.f. $f(x) = \theta e^{-\theta x}$, $\theta > 0$, $x \geqslant 0$. The p.d.f. of the i^{th} order statistics $X_{i:n}$, for $i = 1,2,\ldots,n$ is given by

$$f_{i:n}(x) = \frac{1}{B(i,n-i+1)}[F(x)]^{i-1}[1-F(x)]^{n-i} f(x), \tag{2.7}$$

for details refer to Arnold *et al.* (1992).

Putting $i = 1$ in (2.7) and using (2.6), we get that the residual entropy of the first order statistics for an exponentially distributed random variable is $1 - \ln n\theta$.

We calculate the past entropy of the n^{th} order statistics $X_{n:n}$ for an exponentially distributed random variable with p.d.f. $f(x) = \theta e^{-\theta x}$, $\theta > 0$, $x \geqslant 0$. Note that using (2.7), $f_{n:n}(x) = nF^{n-1}(x)f(x)$ and hence $F_{n:n}(x) = F^n(x)$. Putting these values in (2.8) we get

$$\begin{aligned}\overline{H}(X_{n:n};t) = &-\ln n - (n-1)\ln F(t) + \left(\frac{n-1}{n}\right) \\ &- \frac{n}{F^n(t)}\int_0^{F(t)} u^{n-1} \ln f(F^{-1}(u))du + n\ln F(t)\,.\end{aligned} \tag{2.8}$$

It can be easily seen that $f(F^{-1}(u)) = \theta(1-u)$. Putting this value in (2.9) and let $t \to \infty$, we get

$$\lim_{t\to\infty} \overline{H}(X_{n:n};t) = 1 - \ln n\theta + \gamma + \psi(n), \tag{2.9}$$

where $\gamma = -\psi(1) \approx 0.5772$, which is same as derived by Ebrahimi *et al.* (2004).

2.2. *Upper bound for dynamic entropies*

We derive the upper bound for the dynamic entropies under the condition that the pdf for the i^{th} order statistics is less than 1. Note that

$$\begin{aligned}H(X_{i:n};t) &= -\int_t^\infty \frac{f_{i:n}(x)}{\overline{F}_{i:n}(t)} \ln \frac{f_{i:n}(x)}{\overline{F}_{i:n}(t)} dx \\ &= \ln \overline{F}_{i:n}(t) - \frac{1}{\overline{F}_{i:n}(t)}\int_t^\infty f_{i:n}(x)\ln f_{i:n}(x)dx.\end{aligned}$$

We know that, for $t \geqslant 0$, $\ln \overline{F}_{i:n}(t) \leqslant 0$. Using this we get

$$\begin{aligned}H(X_{i:n};t) &\leqslant -\frac{1}{\overline{F}_{i:n}(t)}\int_t^\infty f_{i:n}(x)\ln f_{i:n}(x)dx \\ &\leqslant -\frac{1}{\overline{F}_{i:n}(t)}\int_0^\infty f_{i:n}(x)\ln f_{i:n}(x)dx\,.\end{aligned}$$

Hence

$$H(X_{i:n};t) \leqslant \frac{H(X_{i:n})}{\overline{F}_{i:n}(t)} \tag{2.10}$$

Copyright: the authors

with equality when $t \to 0$.

Next, we calculate an upper bound for the past entropy. We have

$$\begin{aligned}\overline{H}(X_{i:n};t) &= -\int_0^t \frac{f_{i:n}(x)}{F_{i:n}(t)} \ln\left(\frac{f_{i:n}(x)}{F_{i:n}(t)}\right) \\ &= \ln F_{i:n}(t) - \frac{1}{F_{i:n}(t)} \int_0^t f_{i:n}(x) \ln f_{i:n}(x) dx \,.\end{aligned}$$

For $t > 0$, we have $\ln F_{i:n}(t) \leqslant 0$

$$\begin{aligned}\overline{H}(X_{i:n};t) &\leqslant -\frac{1}{F_{i:n}(t)} \int_0^t f_{i:n}(x) \ln f_{i:n}(x) dx \\ &\leqslant -\frac{1}{F_{i:n}(t)} \int_0^\infty f_{i:n}(x) \ln f_{i:n}(x) dx.\end{aligned}$$

Hence

$$\overline{H}(X_{i:n}(t)) \leqslant \frac{H(X_{i:n})}{F_{i:n}(t)}. \tag{2.11}$$

The equality is obtained when $t \to \infty$.

3. Stochastic Comparisons Based on Residual Entropy of Order Statistics

We have the following definitions:

1. A non-negative random variable X is said to have increasing (decreasing) failure rate IFR (DFR) if $\lambda_X(t) = \frac{f_X(t)}{\overline{F}_X(t)}$ is increasing (decreasing).
2. A random variable X is said to be less than Y in dispersion ordering (denoted by $(X \overset{\text{disp}}{\leqslant} Y)$ if $F^{-1}(u) - F^{-1}(v) \leqslant G^{-1}(u) - G^{-1}(v)$, $\forall 0 \leqslant v \leqslant u \leqslant 1$.
3. A random variable X is said to be less than Y in likelihood ratio ordering (denoted by $X \overset{\text{lr}}{\leqslant} Y$) if $\frac{f_X(x)}{g_Y(x)}$ is non increasing in x.
4. A random variable X is said to be less than Y in the failure rate ordering (denoted by $X \overset{\text{fr}}{\leqslant} Y$) if $\lambda_F(x) \geqslant \lambda_G(x)$, for all $x \geqslant 0$, where $\lambda_F(x)$ and $\lambda_G(x)$ are the failure rates of X and Y, respectively.
5. A random variable X is said to be less than Y in the stochastic ordering (denoted by $X \overset{\text{st}}{\leqslant} Y$) if $\overline{F}(x) \leqslant \overline{G}(x)$ for all x, where $\overline{F}(x)$ and $\overline{G}(x)$ are the survival functions of X and Y respectively.
6. A random variable X is said to be smaller than Y in residual entropy ordering (denoted by $X \overset{\text{re}}{\leqslant} Y$) if $H(F;t) \leqslant H(G;t)$, for all $t > 0$.

It is well known that $X \overset{\text{lr}}{\leqslant} Y \Rightarrow X \overset{\text{fr}}{\leqslant} Y \Rightarrow X \overset{\text{st}}{\leqslant} Y$.

We want to compare the residual entropy of order statistics. For that we present the following results.

Theorem 3.1. *Let $X \overset{lr}{\leqslant} Y$ and $\lambda_F(x)$ or $\lambda_G(x)$ be non increasing in x. Then $X \overset{re}{\leqslant} Y$.*

Proof. Refer to Ebrahimi and Pellerey (1995), Theorem 2.3. □

The above result can be strengthened for failure rate ordering as follows.

Copyright: the authors

Theorem 3.2. *Let $X \overset{fr}{\leqslant} Y$ and $\lambda_F(x)$ or $\lambda_G(x)$ be non increasing in x. Then $X \overset{re}{\leqslant} Y$.*

Ebrahimi and Kirmani (1996) proved the following result for dispersive ordering.

Theorem 3.3. *Let $X \overset{disp}{\leqslant} Y$ and $\lambda_F(x)$ or $\lambda_G(x)$ be increasing in x. Then $X \overset{re}{\leqslant} Y$.*

Infact Bagai and Kochar (1986) proved the following.

Theorem 3.4. *Let $X \overset{disp}{\leqslant} Y$ and $\lambda_F(x)$ or $\lambda_G(x)$ be increasing in x. Then $X \overset{fr}{\leqslant} Y$.*

Let $X_1, X_2, \ldots, X_n$ be a random sample of size n from a distribution F and let $X_{1:n} < X_{2:n} < \cdots < X_{n:n}$ be the order statistics. It is known that $X_{1:n} \overset{\text{lr}}{<} X_{2:n} \overset{\text{lr}}{<} \cdots \overset{\text{lr}}{<} X_{n:n}$, see Chan *et al.* (1991).

Ma (1998), under some weaker conditions, extended the above result when $X_1, X_2, \ldots, X_n$ are independent, but not necessarily identically distributed.

Boland *et al.* (1994) showed that for independent but not necessarily identically distributed random variables $X_{k:n} \overset{\text{fr}}{\leqslant} X_{k+1:n}$, for $k = 1, 2, \ldots, n-1$.

Let us now compare the random variable X to $X_{i:n}$, $i = 1, 2, \ldots, n$, in the likelihood ratio. For that Raqab and Amin (1996) and Khaledi and Kochar (1999) proved that $X_{i:m} \overset{\text{lr}}{\leqslant} X_{j:n}$ whenever $i \leqslant j$ and $m - i \geqslant n - j$.

In particular $X_{1:n} \overset{\text{lr}}{\leqslant} X$ and $X \overset{\text{lr}}{\leqslant} X_{n:n}$. Using the above results we have the following theorem.

Theorem 3.5. *Suppose $X_{1:n} < X_{2:n} < \cdots < X_{n:n}$ be the order statistics based on a random sample of size n from a distribution $F(\cdot)$. Suppose X has a decreasing failure rate. Then $X \overset{re}{\leqslant} X_{n:n}$.*

Proof. As shown above $X \overset{\text{lr}}{\leqslant} X_{n:n}$. Since X has a decreasing failure rate, it follows from Theorem 3.1 that $X \overset{\text{re}}{\leqslant} X_{n:n}$. Note that if X has a decreasing failure rate, then $X_{n:n}$ has a decreasing failure rate, see Takahasi (1988). □

Now we compare $X_{i:n}$ and $X_{j:n}$, $i < j$. We have the following result.

Theorem 3.6. *Suppose $X_{1:n} < X_{2:n} < \cdots < X_{n:n}$ be the order statistics based on a random sample of size n from a distribution $F(\cdot)$. Suppose X has a decreasing failure rate. Then $X_{i:n} \overset{re}{\leqslant} X_{j:n}$, $i < j$.*

Proof. Using the result of Chan *et al.* (1991) we have $X_{i:n} \overset{\text{lr}}{\leqslant} X_{j:n}$. This implies that $X_{i:n} \overset{\text{fr}}{\leqslant} X_{j:n}$. Since X has a decreasing failure rate, $X_{i:n}$ has a decreasing failure rate, see Takahasi (1988). Using Theorem 3.2, we conclude that $X_{i:n} \overset{\text{re}}{\leqslant} X_{j:n}$. □

The following result deals with the likelihood ratio ordering of order statistics of different sample sizes.

Theorem 3.7. *Suppose $X_1, X_2, \ldots, X_n, X_{max(m,n)}$ are independent and identically distributed random variables where m and n are positive integers. Then $X_{j:m} \overset{lr}{\leqslant} X_{i:n}$ whenever $j \leqslant i$ and $m - j \geqslant n - i$.*

Proof. See Shaked and Shanthikumar (2007). □

Copyright: the authors

In particular $X_{n:n} \overset{\text{lr}}{\leqslant} X_{n+1:n+1}$ and $X_{1:n+1} \overset{\text{lr}}{\leqslant} X_{1:n}$. Using the above result, we have the following theorem.

Theorem 3.8. *Suppose $X_1, X_2, \ldots, X_{n+1}$ are independent and identically distributed random variables from a distribution function $F(\cdot)$. Suppose X has a decreasing failure rate. Then*

(i) $X_{n:n} \overset{re}{\leqslant} X_{n+1:n+1}$
(ii) $X_{1:n+1} \overset{re}{\leqslant} X_{1:n}$.

Proof. Using the above result, we have $X_{n:n} \overset{\text{lr}}{\leqslant} X_{n+1:n+1}$. Since X has decreasing failure rate, $X_{n:n}$ and $X_{n+1:n+1}$ have increasing failure rate. Using Theorem 3.1 we conclude that $X_{n:n} \overset{\text{re}}{\leqslant} X_{n+1:n+1}$. Similarly we can prove (ii). □

In the case of dispersive ordering, we have the following result.

Theorem 3.9. *Suppose $X_{1:n} < X_{2:n} < \cdots < X_{n:n}$ be the order statistics from a sample of size n from a distribution $F(\cdot)$. Suppose X has an increasing failure rate and $X_{i:n} \overset{disp}{<} X_{j:n}$, $i < j$. Then $X_{i:n} \overset{re}{<} X_{j:n}$.*

Proof. Since X has increasing failure rate, $X_{i:n}$ has increasing failure rate, see Takahasi (1988). Using Theorem 3.3 and the fact that $X_{i:n} \overset{\text{disp}}{<} X_{j:n}$, we can conclude that $X_{i:n} \overset{\text{re}}{<} X_{j:n}$. □

4. Some Characterization Results

In this section, we present some characterization results based on dynamic entropy of order statistics. Baratpour *et al.* (2007) have studied characterizations based on Shannon entropy of order statistics using Stone-Weistrass Theorem. We study characterizations with a different approach given below:

Consider a problem of finding sufficient condition for the uniqueness of the solution of the initial value problem (IVP)

$$\frac{dy}{dx} = f(x,y), \;\; y(x_0) = y_0, \tag{4.1}$$

where f is a given function of two variables whose domain is a region $D \subset \mathbb{R}^2$, (x_0, y_0) is a specified point in D, y is the unknown function. By the solution of the IVP on an interval $I \subset \mathbb{R}$, we mean a function $\phi(x)$ such that (i) ϕ is differentiable on I, (ii) the growth of ϕ lies in D, (iii) $\phi(x_0) = y_0$ and (iv) $\phi'(x) = f(x, \phi(x_0))$, for all $x \in I$. The following theorem together with other results will help in proving our characterization result.

Theorem 4.1. *Let the function f be defined and continuous in a domain $D \subset \mathbb{R}^2$, and let f satisfy a Lipschitz condition (with respect to y) in D, namely*

$$|f(x,y_1) - f(x,y_2)| \leqslant k\,|y_1 - y_2|, \quad k > 0, \tag{4.2}$$

for every point (x,y_1) and (x,y_2) in D. Then the function $y = \phi(x)$ satisfy the initial value problem $y' = f(x,y)$ and $\phi(x_0) = y_0$, $x \in I$, is unique.

Proof. See Gupta and Kirmani (2008). □

Copyright: the authors

For any function $f(x,y)$ of two variables defined in $D \subset \mathbb{R}^2$, we now present a sufficient condition which guarantees that the Lipschitz condition is satisfied in D.

Lemma 4.1. *Suppose that the function f is continuous in a convex region $D \subset \mathbb{R}^2$. Suppose further that $\frac{\partial f}{\partial y}$ exists and is continuous in D. Then the function f satisfies Lipschitz condition in D.*

Proof. See Gupta and Kirmani (1998). □

We now present our two characterization results.

Theorem 4.2. *Let X be a non-negative continuous random variable with distribution function $F(\cdot)$. Let the residual entropy of k^{th} order statistics based on a random sample of size n, be denoted by $H(F_{k:n};t) < \infty$, $t \geqslant 0$. Then $H(F_{k:n};t)$ characterizes the distribution.*

Proof. Suppose there exists two functions F_1 and F_2 such that

$$H(F_{1k:n};t) = H(F_{2k:n};t),$$

for all $t \geqslant 0$ and for all $k \leqslant n$. Then

$$H'(F_{ik:n};t) = \lambda_{F_{ik:n}}(t)[H(F_{ik:n};t) - 1 + \ln \lambda_{F_{ik}}(t)], \quad i = 1, 2. \tag{4.3}$$

where $\lambda_{F_{ik:n}}$ is the hazard rate of the k^{th} order statistics, for $i = 1, 2$. Differentiating the above equation with respect to t and simplifying, we get

$$\lambda'_{F_{ik:n}}(t) = \frac{\lambda_{F_{ik:n}}(t)}{\lambda_{F_{ik:n}}(t) + H'(F_{ik:n};t)}[H''(F_{ik:n}(t)) - \lambda_{F_{ik:n}}(t)H'_{F_{ik:n}}(t)] \tag{4.4}$$

Suppose now

$$H(F_{1k:n};t) = H(F_{2k:n};t) = g(t), \tag{4.5}$$

Then for all t,
$\lambda'_{F_{1k:n}}(t) = \psi(t, \lambda_{F_{1k:n}}(t))$ and $\lambda'_{F_{2k:n}}(t) = \psi(t, \lambda_{F_{2k:n}}(t))$, where

$$\psi(t,y) = \frac{y}{y + g'(t)}[g''(t) - y\, g'(t)].$$

It follows from Theorem 4.1 and Lemma 4.1 that $\lambda_{F_{1k:n}}(t) = \lambda_{F_{2k:n}}(t)$.
This proves our main characterization result. □

Theorem 4.3. *Let X be a non-negative continuous random variable with distribution function $F(\cdot)$. Let the past entropy of k^{th} order statistics based on random sample of size n, be denoted by $\overline{H}(F_{k:n};t) < \infty$, $t \geqslant 0$. Then $\overline{H}(F_{k:n};t) < \infty$ characterizes the distribution.*

Proof. Suppose that there are two functions F_1 and F_2 such that

$$\overline{H}(F_{1k:n};t) = \overline{H}(F_{2k:n};t)$$

for all $k \geqslant 0$ and for all $k \leqslant n$.

Then

$$\overline{H}'(F_{ik:n};t) = \tau_{F_{ik:n}}(t)[-\overline{H}(F_{ik:n};t) + 1 - \ln \tau_{F_{ik:n}}(t)], \quad i = 1, 2 \tag{4.6}$$

where $\tau_{F_{ik:n}}(t)$ is the reversed hazard rate of the k^{th} order statistics.

Copyright: the authors

Differentiating (4.7) with respect to t and simplifying, we get

$$\tau'_{F_{ik:n}}(t) = \frac{\tau_{F_{ik:n}}(t)}{\overline{H}'(F_{ik:n};t) - \tau_{F_{ik:n}}(t)}[\overline{H}''(F_{ik:n};t) + \tau_{F_{ik:n}}(t)\overline{H}'(F_{ik:n};t)], \quad i = 1, 2. \tag{4.7}$$

Suppose now

$$\overline{H}(F_{1k:n};t) = \overline{H}(F_{2k:n};t) = g(t), \text{ say.}$$

Then, for all $t \geqslant 0$,

$$\tau'_{F_{1k:n}}(t) = \psi(t, \tau_{F_{1k:n}}(t)), \quad \tau'_{F_{2k:n}}(t) = \psi(t, \tau_{F_{2k:n}}(t)),$$

where

$$\psi(t,y) = \frac{y}{g'(t) - y}[g''(t) + yg'(t)].$$

It follows from Theorem 4.1 and Lemma 4.1 that $\tau_{F_{1k:n}}(t) = \tau_{F_{2k:n}}(t)$. Since this result is true for all $t \geqslant 0$ and for all $k \leqslant n$, our characterization theorem is proved. □

Next we present a characterization result of the linear mean residual family of distributions based on Theorem 4.2. The linear mean residual life of a distribution is given by $\mu_F(t) = a + bt$, $a > 0$, $b > -1$. It can be verified that the corresponding failure rate is given by $\lambda_F(t) = \frac{1+b}{a+bt}$. This model has been studied among others by Hall and Wellner (1981), Oakes and Dasu (1990) and Gupta and Kirmani (1998). It includes the exponential distribution for $b = 0$ and the power distribution for $-1 < b < 0$.

Theorem 4.4. *Let X be a non negative absolutely continuous random variable with hazard rate $\lambda_F(t)$ and residual entropy $H(F;t)$. Then $H(X_{1:n};t) = 1 + \frac{b}{1+b} - \ln \lambda_{F_{1:n}}(t)$ if and only if $\mu_{F_{1:n}}(t) = a + bt$ and hazard rate $\lambda_{F_{1:n}}(t) = \frac{1+b}{a+bt}$.*

Proof. We have

$$\begin{aligned} H(X_{1:n};t) &= 1 - E[\ln \lambda_{F_{1:n}}(t) | X > t] \\ &= 1 - \ln(1+b) + \int_t^\infty \ln(a+bx)\frac{f(x)}{\overline{F}(t)}dx. \end{aligned}$$

To evaluate $\int_t^\infty \ln(a+bx)f(x)dx$, we proceed as follows.

Consider

$$\begin{aligned} E[(a+bX)^r | X > t] &= \int_t^\infty (a+bx)^r \frac{f(x)}{\overline{F}(t)}dx \\ &= \frac{(1+b)}{(b+1-br)}(a+bt)^r, \quad r < 1 + \frac{1}{b}. \end{aligned} \tag{4.8}$$

Taking the derivative of the above equation with respect to r and evaluating at $r = 0$, we get

$$E[\ln(a+bx) | X > t] = \frac{b}{1+b} + \ln(a+bt).$$

Copyright: the authors

Thus

$$\begin{aligned} H(X_{1:n};t) &= 1-\ln(1+b)+\frac{b}{1+b}+\ln(a+bt) \\ &= 1+\frac{b}{1+b}-\ln\left(\frac{1+b}{a+bt}\right) \\ &= 1+\frac{b}{1+b}-\ln\lambda_{F_{1:n}}(t). \end{aligned} \tag{4.9}$$

To prove the converse, equation (4.4) gives

$$\begin{aligned} H'(X_{1:n};t) &= \lambda_{F_{1:n}}(t)[H(F_{1:n};t)-1+\ln\lambda_{F_{1:n}}(t)] \\ &= \lambda_{F_{1:n}}(t)[1+b-\ln\lambda_{F_{1:n}}(t)-1+\ln\lambda_{F_{1:n}}(t)]. \end{aligned}$$

This gives

$$\lambda'_{F_{1:n}}(t)+\frac{b}{1+b}\lambda^2_{F_{1:n}}(t)=0,$$

whose solution is

$$\lambda_{F_{1:n}}(t)=\frac{1+b}{a+bt}.$$

□

5. Conclusions and comments

The concept of entropy as studied by Shannon (1948) in information theory plays a crucial role in many applications. For a system, which is observed at time t the residual and past entropies measure the uncertainty about the remaining and the past life of the distribution respectively. Entropy measures based on order statistics are crucial for measuring uncertainty in statistical modeling. The dynamic entropy measures based on order statistics characterize uniquely the underlying distribution and are also bounded above in terms of Shannon entropy of order statistics. The stochastic comparisons and the characterization results studied in this paper can be of wide interest and may find applications in statistical modeling.

References

[1] Arnold, B.C., Balakrishnan, N., Nagaraja, H.N., "A first Course in Order Statistics", *New York: John Wiley and Sons*, (1992).

[2] Bagai, I. and Kochar, S.C., "On tail ordering and comparison of failure rates", *Communications in Statistics: Theory and Methods*, **15**, 1377–1388, (1986).

[3] Baratpour, S., Ahmadi, J., Arghami, N.R., "Some characterizations based on entropy of order statistics and record values", *Communications in Statistics: Theory and Methods*, **36**, 47–57, (2007).

[4] Baratpour, S., Ahmadi, J., Arghami, N.R., "Characterizations based on Renyi entropy of order statistics and record values", *Journal of Statistical Planning and Inference*, **138**, 2544–2551, (2008).

[5] Belzunce, F., Navarro, J., Ruiz, J.M., Aguila, Y., "Some results on residual entropy function", *Metrika*, **59**, 147–161, (2004).

[6] Block, H.W. Savits, T.H. Singh, H., "The reversed hazard rate function", *Probability in the Engineering and Informational Sciences*, **12**, 69–90, (1998).

[7] Boland, P.J., El-Neweihi, E., and Proschan, F., "Applications of hazard rate ordering in reliability and order statistics", *Journal of Applied Probability*, **31**, 180–192, (1994).

Copyright: the authors

[8] Chan, W., Proschan, F. and Sethuraman, J., "Convex ordering among functions with applications to reliability and mathematical statistics", *In Block, H.W., Sampson, A.R., Savits, T.H. (eds.) Topics in Statistical Dependence. IMS Lecture Notes*, **16**, 121–134, (1991).
[9] David, H.A., Nagaraja, H.N. "Order Statistics", *New York: Wiley*, (2003).
[10] Di Crescenzo, A. and Longobardi, M., "Entropy-based measure of uncertainty in past lifetime distributions", *Journal of Applied Probability*, **39**, 434–440, (2002).
[11] Di Crescenzo, A. and Longobardi, M., "A measure of discrimination between past lifetime distributions", *Statistics Probability Letters*, **67**, 173–182, (2004).
[12] Ebrahimi, N., "How to measure uncertainty about residual lifetime", *Sankhya A*, **58**, 48–57, (1996).
[13] Ebrahimi, N., "Families of distributions characterized by entropy", *IEEE Tansactions on Information Theory*, **47**(5), 2042–2044, (2001).
[14] Ebrahimi, N. and Kirmani, S.N.U.A., "Some results on ordering of survival functions through uncertainty", *Statistics and Probability Letters*, **29**, 167–176, (1996).
[15] Ebrahimi, N. and Pellerey, F., "New partial ordering of survival functions based on the notion of uncertainty", *Journal of Applied Probability*, **32**, 202–211, (1995).
[16] Ebrahimi, N., Soofi, E.S., Zahedi, H., "Information properties of order statistics and spacings", *IEEE Transactions on Information Theory*, **50**, 177–183, (2004).
[17] Gupta, R.C., "Some characterization results based on residual entropy function", *Journal of Statistical Theory and Applications*, **8**(1), 45–59, (2009).
[18] Gupta, R.C. and Gupta, R.D., "Proportional reversed hazard rate model and its applications", *Journal of Statistical Planning and Inference*, **137**, 3525–3536, (2007).
[19] Gupta, R.C. and Kirmani, S.N.U.A., "Characterizations based on conditional mean function", *Journal of Statistical Planning and Inference*, **138**, 964–970, (2008).
[20] Hall, W.J. and Wellner, J.A., "Mean residual life", *Statistics and Related Topics, North-Holland, Amsterdam*, 169–184, (1981).
[21] Khaledi, B. and Kochar, S.C., "Stochastic orderings between distributions and their sample spaces II", *Statistics and Probability Letters*, **44**, 161–166, (1999).
[22] Ma, C., "Likelihood ratio ordering of order statistics", *Journal of Statistical Planning and Inference*, **70**, 255–261, (1998).
[23] Oakes, D. and Dasu, T., "A note on residual life", *Biometrika*, **77**, 409–410, (1990).
[24] Raqab, M.Z. and Amin, W.A., "Some ordering result on order statistics and record values", *IAPQR Transactions*, **21**, 1–8, (1996).
[25] Shaked, M. and Shanthikumar, J.G., "Stochastic Orders", *Springer Verlag*, (2007).
[26] Shannon, C.E., "A mathematical theory of communication", *Bell System Technical Journal*, 279–423 and 623–656, (1948).
[27] Takahasi, K., "A note on hazard rates of order statistics", *Communications in Statistics: Theory and Methods*, **17**(12), 4133–4136, (1988).

Copyright: the authors

Volume 1 (2014) 237-241 ISSN 2347 - 3258
International Journal of Advance Research and Innovation

Study of Aluminum Oxide Abrasive on Tempered Glass in Abrasive Jet Machining Using Taguchi Method

Punit Grover, Sanjay Kumar, Qasim Murtaza
Department of Mechanical Engineering, Delhi Technological University, Delhi, India

Article Info

Article history:
Received 1 January 2014
Received in revised form
20 February 2014
Accepted 28 February 2014
Available online 15 March 2014

Keywords

Abstract

The abrasive jet machining (AJM) is a non-conventional machining process in which a abrasive particles are made to impinge on the work material at a high velocity. The jet of abrasive particles is carried by carrier gas or air. The high velocity stream of abrasive is generated by converting the pressure energy of the carrier gas or air to its kinetic energy . The high velocity abrasive particles remove the material by micro-cutting action as well as brittle fracture of the work material . Abrasive jet machining is generally good for cutting hard or brittle materials and is usually performed to furnish machining or finishing operation such as cutting, deburring, etching, etc. This project deals with the fabrication of the Abrasive Jet Machine and machining on tempered glass, calculating the material removal varying various performance parameters like pressure, angle & abrasive grit size so on. Before performing the experiment ,fabrication done on AJM which are also discussed.. The different problem faced while machining on tempered glass are also discussed.Taguchi method and ANOVA is used for analysis of material removal rate .

1. Introduction

AJM unit with vortex type mixing chamber and it was restricted to abrasive jet drilling only [1]. Magnetic abrasive jet machining is a new concept in AJM used for in finishing processes for internal surfaces, in this method working fluid mixed with magnetic abrasives, which is jetted into the internal surface of the tube, with magnetic poles being provided on the external surface of the tube. In this study, the new-concept finishing process or the magnetic abrasive jet machining system was developed [2].For studied the Effect of work piece properties on mach inability in abrasive jet machining of ceramic materials. Abrasive jet machining (AJM), a specialized form of shot blasting using fine-grained abrasives was used; it is an attractive micro-machining method for ceramic materials. In this paper, the mach inability during the AJM process is compared to that given by the established models of in AJM is a technique in which a particle jet is directed towards a target for mechanical material solid particle erosion, in which the material removal is assumed to originate in the ideal crack formation system [3]. The specialized form of shot blasting in Abrasive jet machining (AJM) and is beneficial for hard, brittle materials such as structural ceramics [4]. For investigated Micro-grooving of glass by using micro-abrasive jet machining, Micro abrasive jet machining (AJM) is similar to sand blasting, and effectively removes hard and brittle materials [5].In the machining of small holes by the conventional micro abrasive jet machining, the colliding abrasives accumulate in the bottom of the hole, preventing the direct impact of successive abrasives onto the work piece. As a result, the machining efficiency decreases as the machining progresses. Hence introduces a new method of micro abrasive jet machining, called micro abrasive intermittent jet machining (MAIJM), in which there exists a period of time during which no abrasive is injected into the gas stream from the nozzle so that the continuous flow of gas without abrasives from the nozzle could blow away any abrasives that have accumulated in the hole. [6]. High Resolution Powder Blast Micromachining technique

Corresponding Author,
E-mail address: punitgrover112@gmail.com
All rights reserved: http://www.ijari.org

removal. It is a fast, cheap and accurate directional etch technique for brittle materials like glass, silicon and ceramics [13]. Some other methods in which the wax-coated abrasive particles are used and in this method polishing time reduces and achieves an improved surface finish.[14].

2. Experiment Procedure

Experiment was conducted to study the MRR (material removal rate) of tempered glass (toughened glass) at different parameters of AJM and these parameters are pressure, angle and abrasive mesh size. The parameters and levels were selected primarily based on the literature review of some of the studies.

Initially weight the glass work piece which is rectangle in shape (dimensions are 7*3 cm *5mm) with the help of digital balance and weight after machining is measured by using digital balance for calculating the MRR. Time of machining was 4 seconds. Thus MRR is calculated using the formula:

$$MRR = \frac{(\text{intial weight - final weight})}{\text{machining time}}$$

Nine experiments were conducted with different parameters. For this Taguchi L9 orthogonal array was used, which has nine rows corresponding to the number of tests, with three columns at three levels.

Table: 1. AJM Process Parameters

Parameter	code	Levels		
		1	**2**	**3**
Pressure (kg/cm^2)	A	4	6	8
Angle between the workpiece and nozzle jet (degree)	B	40^o	20^o	0^o
Abrasive(mesh size)	C	1000	500	320

Table: 2. MRR of Taguchi L9 Orthogonal Array

Expt. No.	A	B	C	MRR (g/sec.)
1	1	1	1	0.0034
2	1	2	2	0.0049
3	1	3	3	0.0084
4	2	1	2	0.0086
5	2	2	3	0.0102
6	2	3	1	0.0096
7	3	1	3	0.0126
8	3	2	1	0.0113
9	3	3	2	0.0148

The L_9 orthogonal arrays table with 9 rows (corresponding to the number of experiments).

3. Results and Analysis Of Experiments

3.1 Analysis of the S/N Ratio

Taguchi method stresses the importance of studying the response variation using the signal – to – noise (S/N) ratio, resulting in minimization of quality characteristic variation due to uncontrollable parameter. The metal removal rate was considered as the quality characteristic with the concept of "the larger-the-better" [27].

The S/N ratio values are calculated by using this equation.

S/N = -10*log (mean square deviation)

Where n is the number of measurements in a trial/row, in this case, n=1 and y is the measured value in a run/row. The S/N ratio values are calculated by taking into consideration above equation.

Table: 3. Taguchi Analysis Response Table for Signal to Noise Ratios Larger is better

Level	Pressure	Angle	Grit size
1	-45.69	-42.89	-42.89
2	-40.50	-41.65	-41.37
3	-37.84 [a]	-39.49 [a]	-39.78[a]
Delta	7.85	3.40	3.11
Rank	1	2	3

Optimum level (Level 3 is optimum level)

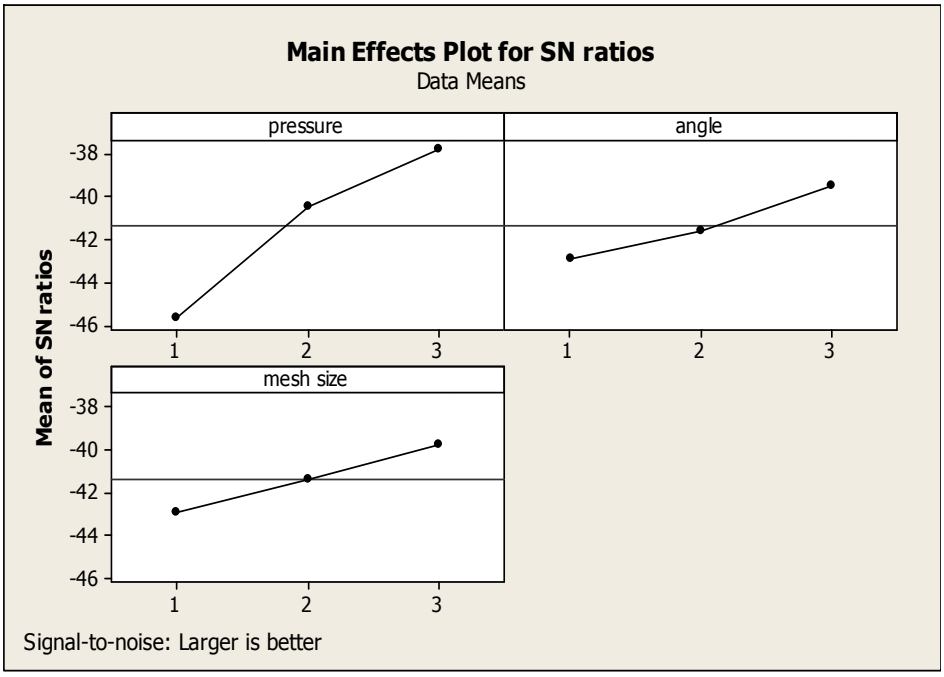


Fig: 1. Graph showing S-N Ratio, Larger is better

The MRR increases with increasing in Pressure and decreasing in angle and abrasive size in mesh of abrasive. MRR is proportional to the pressure. With the increase in pressure the kinetic energy of the abrasive particle also increases. The kinetic energy of the abrasive particle is responsible for material removal by erosion process. Hence increase in pressure enhancement the MRR. With the decrease in angle between the workpiece and nozzle jet and abrasive mesh size the MRR increase because the abrasive mixture impinge on the workpiece more directly without deflecting, with a larger force, thus results in greater removal rate. And as the abrasive meshsize decreases, abrasive particle size increases, thus smaller mesh abrasives removes more metal as compared to the particle of larger mesh.

4. Analysis of Variance (ANOVA)

ANOVA is a statistically based, objective decision making tool for detecting any differences in the average performance of groups of items tested. ANOVA helps in formally testing the significance of all main factors and their interactions by comparing the mean square against an estimate of the experimental errors at specific confidence levels. First, the total sum of squared deviations SST from the total mean S/N ratio nm can be calculated as [27]

$$SS_T = \sum_{i=1}^{n} (n_i - n_m)^2$$

Where n is the number of experiments in the orthogonal array and n_i is the mean S/N ratio for the i^{th} experiment.

Table: 4. ANOVA results for metal removal rate

Source of variation	Degrees of freedom (DOF)	Sum of squares (S)	Variance (V)	F-ratio (F)	P-value (P)	Percentage (%)
Model	6	1.012E-004	1.686E-005	96.65	0.0103	
A	2	8.078E-005	4.039E-005	231.52	0.0043	79.82%
B	2	1.238E-005	6.191E-006	35.49	0.0274	12.23%
C	2	8.002E-006	4.001E-006	22.94	0.0418	7.91%
Error	2	3.489E-007	1.744E-007			0.04%
Total	8	1.015E-004				

{*1.012E-004 means 1.012 times 10 to the -4th power (.0001). It should be 0.0001012}
The percentage contribution P can be calculated as.

$$P = \frac{SS_D}{SS_T}$$

Where SS_D is the sum of the squared deviations

Statistically, there is a tool called an F test, named after Fisher , to see which design parameters have a Statistically, there is a tool called an F test, named after Fisher , to see which design parameters have a significant effect on the quality characteristic. In the analysis, the F-ratio is a ratio of the mean square error to the residual error, and is traditionally used to determine the significance of a factor.

The P-value reports the significance level (suitable and unsuitable) in Table.4. If P-value < 0.05 level is significant and if P value> 0.05 level is insignificant. In Table.4 model P-value is 0.0103 which is less than 0.05 hence model is significant. Percent (%) is defined as the significance rate of the process parameters on the metal removal rate. The percent numbers depict that the pressure, angle and abrasive grit size have significant effects on the metal removal rate. It can observed from Table.4 that the pressure (A), angle (B) and abrasive (C) affect the metal removal rate by 79.82%, 12.23% and 7.91% in the abrasive jet machining(AJM) of tempered glass, respectively. A confirmation of the experimental design was necessary in order to verify the optimum cutting conditions.

5. Regression Analysis

The correlation between factors (Pressure, Angle and Abrasive mesh size) and metal removal rate on the Tempered (Toughened) glass were obtained by multiple linear regressions.

The standard commercial statistical software package MINITAB was used to derive the models of the form:

The regression equation is

MRR = - 0.00331 + 0.00366 pressure + 0.00120 mesh size + 0.00146 angle

R^2=0.981

In multiple linear regression analysis, R^2 is the regression coefficient (R^2 >0.90) for the models, which indicate that the fit of the experimental data is satisfactory.

$$R^2 = \frac{SS[Between]}{SS[Total]} = \frac{SSG}{SST}$$

6. Confirmation Test

The experimental confirmation test is the final step in verifying the results drawn based on Taguchi's design approach. The optimal conditions are set for the significant factors (the insignificant factors are set at economic levels) and a selected number of experiments are run under specified cutting conditions. The average of the results from the confirmation experiment is compared with the predicted average based on the parameters and levels tested. The confirmation experiment is a crucial step and is highly recommended by Taguchi to verify the experimental results . In this study, a confirmation experiment was conducted by utilizing the levels of the optimal process parameters (A3B3C3) for metal

removal rate value in the abrasive jet machining of tempered glass and obtained as 0.0158 g/min.

7. Conclusions

This study has discussed an application of the Taguchi method for investigating the effects of process parameters on the metal removal rate value in the abrasive jet machining (AJM) of tempered glass. In the AJM process, the parameters were selected taking into consideration of manufacturer and industrial requirements.

From the analysis of the results in the AJM process using the conceptual signal-to-noise (S/N) ratio approach, regression analysis, analysis of variance (ANOVA), and Taguchi's optimization method, the following can be concluded from the present study:

- Statistically designed experiments based on Taguchi methods were performed using L9 orthogonal arrays to analyze the metal removal rate as response variable. Conceptual S/N ratio and ANOVA approaches for data analysis drew similar conclusions.
- Statistical results (at a 95% confidence level) show that the pressure(A), angle (B), and abrasive grit size (C) affects the metal removal rate by 79.82%, 12.23% and 7.91% in the abrasive jet machining of tempered glass , respectively.
- The maximum metal removal rate is calculated as 0.00158 g/sec. by Taguchi's optimization method.
- In this study, the analysis of the confirmation experiment for metal removal rate has shown that Taguchi parameter design can successfully verify the optimum cutting parameters (A3B3C3), which are pressure=8 kg/cm^2 (A3) angle= 0^0 (B3) and abrasive = 320 mesh size (C3).
- Metal removal rate increases with increase in pressure and abrasive size (microns) in abrasive jet machining of tempered glass.
- Metal removal rate increases with the decrease in angle and abrasive mesh size in abrasive jet machining of tempered glass.

References

[1] P K Ray, Dr. A K Paul, Some studies on abrasive jet machining, Department of mechanical engineering regional engineering college Rourkela, 1987

[2] Jeong-Du Kim, Youn-Hee Kang, Young-Han Bae, Su-Won Lee , Developed finishing process using G rotating magnetic field, 1996

[3] M. Wakuda, Y. Yamauchi, S. Kanzaki, Effect of work piece properties on machinability in abrasive jet machining of ceramic materials, 2001

[4] Manabu Wakuda, Yukihiko Yamauchi, Shuzo Kanzaki, Material response to particle impact during abrasive jet machining of alumina ceramics, Industrial Scienceand Technology (AIST) , Japan November 2005

[5] Dong-Sam Park, Myeong-Woo Chob, Honghee Lee, Won-Seung Choca Micro-grooving of glass using micro-abrasive jet machining, 2003

[6] Lei Zhang, Tsunemoto Kuriyagawa, Yuya Yasutomi, Ji Zhao, Investigation into micro abrasive intermittent jet machining, 2004

[7] Henk Wensink, J. W. Berenschot, Henri V. Jansen, Miko C. Elwenspoek, High resolution powder blast micromachining, MESA' Research Institute, University of Twente, 2009

[8] Matthew W. Chastagner, Albert J. Shih, Abrasive jet machining for edge generation, Mechanical Engineering University of Michigan Ann Arbor, Michigan 2007

[9] Rao. S, Padmanabhan. G, Application of Taguchi methods and ANOVA in optimization of process parameters for metal removal rate in electrochemical machining of Al/5%SiC composites; International Journal of Engineering Research and Applications (IJERA), 2012

International Journal on Recent and Innovation Trends in Computing and Communication ISSN: 2321-8169
Volume: 2 Issue: 3 601 – 603

Study on Naive Bayesian Classifier and its relation to Information Gain

Anjana Kumari
Delhi Technological University
Delhi
anjana83.kumari@gmail.com

Abstract- Classification and clustering techniques in data mining are useful for a wide variety of real time applications dealing with large amount of data. Some of the application areas of data mining are text classification, medical diagnosis, intrusion detection systems etc. The Naive Bayes Classifier technique is based on the Bayesian theorem and is particularly suited when the dimensionality of the inputs is high. Despite its simplicity, Naive Bayes can often outperform more sophisticated classification methods. The approach is called "naïve" because it assumes the independence between the various attribute values. Naïve Bayes classification can be viewed as both a descriptive and a predictive type of algorithm. The probabilities are descriptive and are then used to predict the class membership for a untrained data.

Keywords: *Classification, Bayesian Formula, Information Gain, weighted naive Bayesian classifier, Kullback's Test, Conditional Probability, Marginal Independence*

*****

I. INTRODUCTION

Classification techniques analyze and categorize the data into known classes. Each data sample is labeled with a known class label. Clustering is a process of grouping objects resulting into set of clusters such that similar objects are members of the same cluster and dissimilar objects belongs to different clusters. In classification the classes are pre-defined. Training sample data are used to create a model, where each training sample is assigned a predefined label. Data mining involves the use of sophisticated data analysis tools to discover previously unknown, valid patterns and relationships in large data set. These tools can include statistical models, mathematical algorithm and machine learning methods. Other than collection and managing data, data mining also includes analysis and prediction. In this report we will try to understand the logic behind Bayesian classification. The Naive Bayes Classifier technique is based on the Bayesian theorem and is particularly suited when the dimensionality of the inputs is high. Despite its simplicity, Naive Bayes can often outperform more sophisticated classification methods.

II. DATA MINING

Data Mining is the technology utilising the data analysis tools to operate on large amount of data to extract or discover previously unknown hidden pattern and relationships [5]. The data mining techniques can be categorized into one of the three methods which are association rule mining, classification & prediction and clustering.

III. CLASSIFICATION

Classification is a supervised learning technique that classifies data item into pre-defined class label. [6]This technique builds model that predict future data trend. There are several algorithms for data classification such as Decision Tree, CART (Classification and Regression Tree) and Back Propagation neural network. Each technique employs a learning algorithm to identify a model that best fits the relationship between the attribute set and class label of the input data. The model generated by a learning algorithm should both fit the input data well and correctly predict the class labels of records it has never seen before.

IV. BAYESIAN CLASSIFICATION

Bayesian Classifiers are statistical classifiers. Bayesian Classification is based on Bayes Theorem which utilises the conditional probability to classify the data into pre-determined classes[2]. The approach is called "naïve" because it assumes the independence between the various attribute values. Naïve Bayes classification can be viewed as both a descriptive and a predictive type of algorithm. The probabilities are descriptive and are then used to predict the class membership for a untrained data. The naïve Bayes approach has several advantages:

- It is easy to use.
- Only one scan of the training data is required.
- Easily handle mining value by simply omitting that probability.

$$P(C_i \mid X) = \frac{P(X \mid C_i)P(C_i)}{P(X)}$$

- It requires a small amount of training data to estimate the parameters (means and variances of the variables) necessary for classification.
- In spite of their naive design and apparently over-simplified assumptions, naive bayes classifiers

have worked quite well in many complex real world situations.

A. CONDITIONAL PROBABILITY & BAYES' RULE

Bayes classification has been proposed that is based on Bayes rule of conditional probability. Conditional Probability can be defined as: What is the probability that something will happen, given that something else has already happened.

Bayes rule is a technique to estimate the likelihood of a property given the set of data as evidence or input[2]. Let X be an input data sample whose class label is not known. Let H be any hypothesis, such that X belongs to a specified class C. For classification we need to determine P(H|X), the probability that the hypothesis H holds given the input data sample is X. P(H) is the priori probability of H, is the probability that the class label is C regardless of input data sample. In the same way , P(X|H) is posterior probability of X conditioned on H. P(X) is the prior probability of X. Bayes rule or Bayes theorem provides a way of calculating the posterior probability P(H|X), given P(H), P(X) and P(X|H).Formula is given by:

$$P(H \mid X) = \frac{P(X \mid H)P(H)}{P(X)} \quad \text{Eq.1}$$

Bayes formula can be expressed informally in English by saying that

$$\text{Posterior} = \frac{\text{likelihood} \times \textit{prior}}{\textit{evidence}}$$

We know how frequently some particular evidence is observed, given a known outcome. We can use this known fact to compute the reverse, to compute the chance of that outcome happening, given the evidence.

B. ALGORITHM

The working of the Naive Bayes Classifier can be summarised as follows:[1]

1. Each of the input data item can be represented as an n-dimensional feature vector, such as
   X =(x_1,x_2,x_3,…….x_n).
2. Suppose that there are m classes, C_1,C_2,……..C_m. Given a data item X whose class label is not known, the classifier will predict that X belongs to the class having the highest posterior probability, conditioned on X. Therefore the Naïve Bayes Classifier assigns an unknown data item to the class C_i if and only if
   $P(C_i|X) > P(C_j|X)$ for $1 \le j \le m, j \ne i$.

By Bayes Theorem :

3. Only $P(X|C_i)$ $P(C_i)$ needs to be maximized as P(X) is constant for all classes. If the class prior probabilities are not known, then it is commonly assumed that the classes are equally likely, i.e., $P(C_1) = P(C_2) =$……..$= P(C_m)$ and we would therefore maximise $P(X|C_i)$. Class prior probability can be estimated by $P(C_i) = S_i/S$, where S_i is the number of training samples of class C_i, and S is the total number of training samples.
4. If the data item has many attributes, it would be extremely computationally expensive to compute $P(X|C_i)$. In order to reduce computation, Naïve Bayes assumes that the attributes are conditionally independent of one another.

Thus, $P(X|C_i) = \prod_{k=1}^{n} P(x_k \mid C_i)$.

The probabilities $P(x_1|C_i)$,$P(x_2|C_i)$,$P(x_3|C_i)$, ….,$P(x_n|C_i)$ can be estimated from the training samples, where

(a) If A_k is categorical, then $P(x_k|C_i)=S_{ik}/S_i$, where S_{ik} is the number of training samples of class C_i having value x_k and S_i is the number of training samples belonging to C_i .

(b) If A_k is continuous-valued, then the attribute is assumed to have a Gaussian distribution so that

$$P(x_k \mid C_i) = g(x_k, \mu c_i, \sigma c_i) = \frac{1}{\sqrt{2\pi\epsilon}\, c_i} e^{-\frac{(x_k - \mu c_i)^2}{2\sigma^2 c_i}}$$

Eq.2

Where $g(x_k, \mu c_i, \sigma c_i)$ is Guassian(normal) density function for attribute A_k , while μci and σci are the mean and standard deviation, respectively.

5. In order to classify an unknown data input X, $P(X|C_i)$ $P(C_i)$ is evaluated for each class C_i. X is then assigned to class C_i if $P(X|C_i)$ $P(C_i) > P(X|C_j)$ $P(C_j)$ for $1 \le j \le m, j \ne i$.

C. WEIGHTED NAIVE BAYESIAN

A new weighted Naive Bayesian Classifier model is proposed by DUAN Wei[8], which is based on information gain. According to which we can use information gain of an attribute to reduce attribute set, and assign relative weight to each classification attribute. In order to improve the classification efficiency propose a method of assign weight to attribute. The formula of weighted NBC as follow:

Argmax $P(h_j|x)$= argmax$\prod_{k=1}^{n} w_k P(x_k|h_j)$ P (h_j) ……. Eq.3

Where w_k represents the weight of attribute x_k .The larger the weight, the greater effect the attribute has on classification.

D. INFORMATION GAIN & ENTROPY

In information theory, entropy is a measure of the uncertainty in a random variable[9]. Entropy, H is a measure of impurity which is given by

$$H(S)=-\sum p_i \log_2 p_i \quad \ldots\ldots \text{Eq.4}$$

The measure of purity is called the information. It represents the expected amount of information that would be needed to specify whether a new instance should be classified as X or Y. Information gain is widely used method for calculating the importance for features in decision making.

Information_Gain = Entropy_before - Entropy_after

E. KULLBACK'S TEST FOR CONDITIONAL INDEPENDENCE

Information gain in terms of conditional probability[8] is given by I(X/Y) = H(X) - H(X|Y) where X,Y,Z are discrete random variables. Marginally Independent [8] term can be defined as Random variable X is marginally independent of random variable Y , knowledge of Y 's value doesn't affect your belief in the value of X for all xi ∈ dom(X), yj ∈ dom(Y) and yk ∈ dom(Y),

$$P(X = xi|Y = yj)$$

$$= P(X = xi|Y = yk)$$

$$= P(X = xi)$$

A test for marginal independence between X and Y can be set up in terms of information gain measures as follows:

H_0 : $I(X|Y) = 0, (X \perp Y)$

H_1 : $I(X|Y) > 0, (X \not\perp Y)$

A test for conditional independence of X and Y given Z, as proposed by Kullback, is based on the information gain on X given by Y once Z is known. The hypotheses to be tested are:

H_0 : $I(X|Z,Y) = 0, (X \perp Y, Z)$

H_1 : $I(X|Z,Y) > 0, (X \not\perp Y, Z)$

F. CONCLUSION

Applications of supervised learning are in almost any field or domain. The Naive Bayes algorithm affords fast, highly scalable model building and scoring. It scales linearly with the number of predictors and rows. The build process for Naive Bayes is parallelized. Naive Bayes can be used for both binary and multiclass classification problems. Naive Bayes handles missing values naturally as missing at random. The algorithm replaces sparse numerical data with zeros and sparse categorical data with zero vectors. Missing values in nested columns are interpreted as sparse. Missing values in columns with simple data types are interpreted as missing at random.

V. REFERENCES

[1] Jiawei Han,Micheline Kamber, "Data Mining: Concepts and Techniques", Morgan Kaufmann.

[2] Richard O. Duda,Peter E. Hart,David Stork, "Pattern Classification", Second Edition,Wiley.

[3] Duan Weil,Lu Xiang-yang, "Weighted Naïve Bayesian model based on information gain", 2010 International conference on Intelligent System Design and Engineering Application, IEEE computer Society

[4] Chang-Hwan Lee, Fernando Gutierrez Dejing Dou , "Calculating Feature Weights in Naive Bayes with Kullback-Leibler Measure" 11th IEEE International Conference on Data Mining 2011.

[5] Thair Nu Phyu, "Survey of Classification Techniques in Data Mining", Proceedings of the International MultiConference of Engineers and Computer Scientists 2009 Vol I IMECS 2009, March 18 - 20, 2009, Hong Kong.

[6] Jian Li, Jin-Mao Wei, Tian Yu and Hai-Wei Zhang ,"Feature Selection Based on Bayes Minimum Error Probability", 2012, 9th International Conference on Fuzzy Systems and Knowledge Discovery.

[7] http://en.wikipedia.org/wiki/Entropy_(information_theory)

[8] Manuel Martínez-Morales, Nicandro Cruz-Ramírez, José Luis Jiménez-Andrade, and Ramiro Garza-Domínguez, "Bayes-N: An Algorithm for Learning Bayesian Networks from Data Using Local Measures of Information Gain Applied to Classification Problems" MICAI 2004, LNAI 2972, pp. 527–535, 2004. Springer-Verlag Berlin Heidelberg

Volume 1 (2014) 40-49 ISSN 2347 - 3258
International Journal of Advance Research and Innovation

Thermodynamic Comparison of Linde and Claude Systems for Liquefaction of Gases

Devender Kumar *, R. S. Mishra
Department Of Mechanical Engineering, Delhi Technological University, Shahabad, Delhi, India

Article Info

Article history:
Received 2 January 2014
Received in revised form
29 January 2014
Accepted 20 February 2014
Available online 15 March 2014

Keywords

Energy and Exergy analysis,
First and Second law efficiency,
Cryogeinc Liquefaction mases

Abstract

The study deal with energy exergy comparative analysis of two cryogenics systems (i.e Linde Hampson and Claude) in terms of second law efficiency and the output (which in form of liquefaction mass) of gases,The numerical computation was carried out for above systems and it was conclude that by joining extra accessories in system make a system efficient in output result but in other hand making system large , its cost and as well as useful energy destruction of overall system are degraded which seen in from of low second law efficiency. Two system giving same atmospherics input condition and varying compressor pressure considered. Final results show the output of Claude system is more than the Linde system while seconde efficiency of of Linde system is 18 % more than the Claude system at 300 bar compressor pressure for all gases.

Nomenclature

W=work
Q=Heat input
η_I=First law efficiency
η_II=Second law efficiency
h=Enthalpy
s=Entropy
X=Dryness fraction
T=temperature
P=Pressure
m=mass
Ɛ =Effectiveness of heat exchanger (approx. 80%)
η comp=Efficiency of compressor (approx. 80%)
η expander=Efficiency of expander (approx. 80%)
C=Specific heat capacity fluid or gas
W_t=Work of reversible isothermal compression
W_comp=Shaft work supplied to compressor per unit mass

1. Introduction

Cryogenics is a field of acquiring very low temperature, the temperature which sufficient to liquefy most of gaes but generally the temperature below -150 ^{0}C is considered in range of cryogenics. In early centuries the throttling effect of cooling and various expansion device attract the scientist toward achieving low temperature but oxygen use in medical science and it storage factor turn 18 centuries scientist to attain low temperature which can liquefy air and in turn harness the oxygen from that liquefaction. In end of 18 centuries various research are done cryogenics field but first scientist which got success is Linde and after that lots of scientist liquefy various gas on their scale. Various system of cryogenics come in light in which Linde and Claude is widely used as system for liquefaction of air.

The system is made but how much they are efficient in industrial point of view is become matter of concern. Various method are employs to minimize the cost without affecting the production rate are investigated in various mathematical techniques and simulation technique is widely used. In all this a best method second law exergy analysis of system which is based on the second law of newton of energy destruction.

Exergy analysis is basically defined as the how much part of energy we can fully utilize in our work. Useful part of energy is called exergy while unused part is anergy. First law efficiency simply defined as the ratio of output to the input of energy while Second law efficiency deal with the exergy and defined as the ration of exergy output to the exergy input.

$$\eta_I = \frac{Output\ enegy(W)}{Input\ energy(Q)}$$

Corresponding Author,
E-mail address: devenderdahiya@in.com
All rights reserved: http://www.ijari.org

$$\eta_{II} = \frac{Exergy\ output}{Exergy\ Input}$$

Lots of research are done to optimize and to increase the second law efficiency of system. And for this lots of new techniques are experimentally studied. Yang et al. [1] performed a comparative study on the trans critical carbon dioxide refrigeration cycles with a throttling valve and with an expander, based on the first and second laws of thermodynamics. Ignacio L´opezPaniagua [2] find New Simple Method for Estimating Exergy Destruction in Heat Exchangers. Yongliang Li [3] study An optimal design methodology for large-scale gas liquefaction. Antungalovic [4] do detail Analysis of Exergy Destruction of an

Evaporator or/and a Condenser. The main cause of low Second law efficiency directly link to the irreversibility of system so for which is just a form of exergy losses in any system. Irreversibility is the reason why the exergy received by the cold fluid and that released by the hot fluid are not equal. In fact, the total exergy loss in an exchanger is another characteristic of its exergetic behavior commonly referred to in the literature [5,6].and only part of the exergy loss can be avoided in practice [7]

2. Thermal analysis of Linde system

Linde system is first system which is use for liquefaction of air. In Fig 1(a).This system consist a compressor, heat exchanger, throttle valve and a separator. The air or gas which is used to liquefy is circulate in this closed cycle with perfect insulation to avoid large losses to occur due to system and outer surrounding temperature difference.Fig 1(b)show the temperature entropy diagram for Linde system.

$$\eta_{comp} = \frac{W_t}{W_{comp}} \quad (1)$$

$$W_t = mRT ln \frac{P_2}{P_1} \quad (2)$$

$$W_{comp} = h_2 - h_1 - T_1 (s_2 - s_1) \quad (3)$$

$$W_{reversible} = W_{actual} - T_0 s_{gen} \quad (4)$$

$$W_{actual} = \frac{W_{comp}}{x} \quad (5)$$

$$W_{reversible} = h_5 - h_1 - T_0 (s_5 - s_1) \quad (6)$$

Heat Exchanger

$$m_2(h_2 - h_3) = m_6(h_1 - h_6) \quad (7)$$

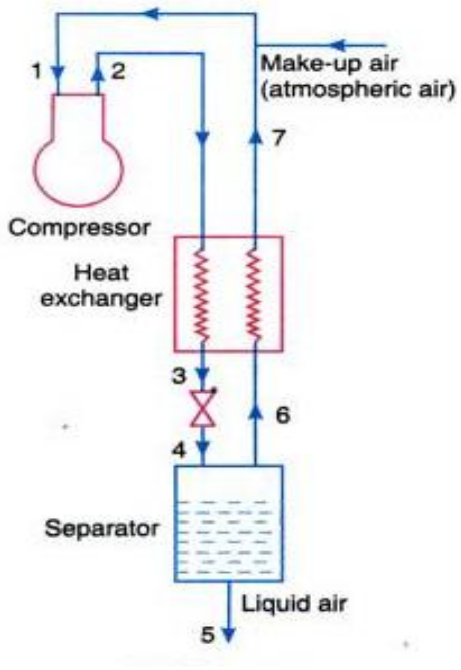


Fig: 1(a). Linde system for Liquefaction for gases

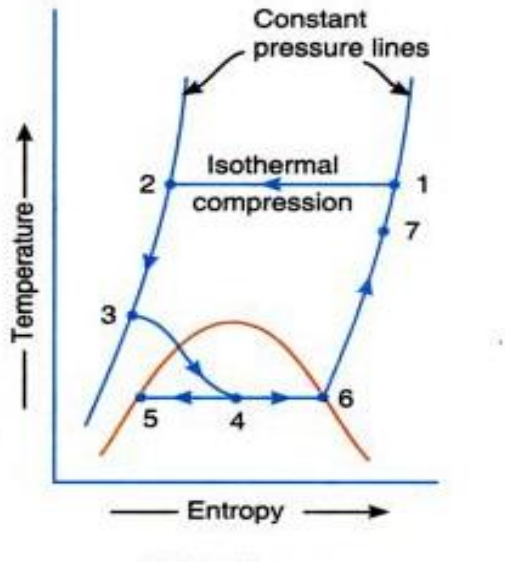


Fig: 1 (b). Tempertaure vs entropy of Linde system

$$m_2(h_2 - h_3) = (m_2 - m_5)(h_1 - h_6) \quad (8)$$

$$: m_6 = (m_2 - m_5) \quad (9)$$

$$\varepsilon = \frac{C_h (T_2 - T_3)}{C_{min} (T_2 - T_6)} \quad (10)$$

Throttling process:

$$h_3 = h_4 \quad (11)$$

Heat Balance of the separator

$$m_2 h_4 = m_5 h_5 + m_6 h_6 = m_5 h_5 + (m_2 - m_5)(h_6) \quad (12)$$

Second law analysis :

$$\eta_{II} = \frac{W_{rev}}{W_{actual}} \quad (13)$$

COP (coefficient of performance):

$$COP = \frac{h_2 - h_1}{h_2 - h_1 - T_1 (s_2 - s_1)} \quad (14)$$

2.2 Thermal analysis of Claude system

Claude system not only used for liquefaction of air but other gas also can be liquefy with this system also .Fig 2(a) show a block diagram of Claude system having two heat exchanger ,two separator and two throttle valve with an expander. Fig 2 (b) shows temperature entropy diagram.

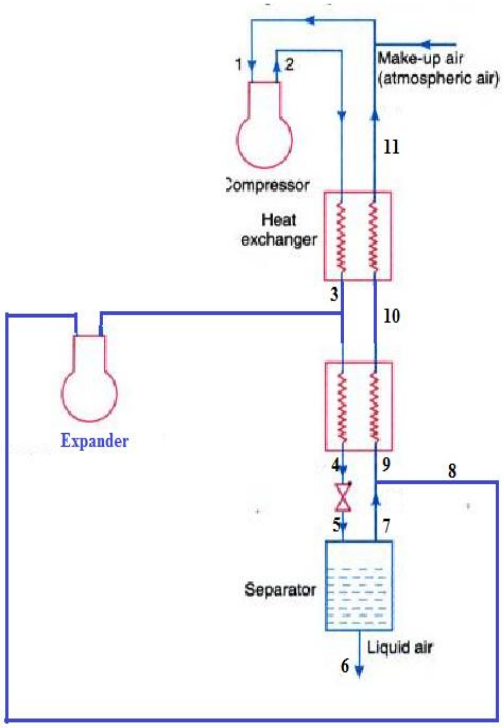


Fig: 2(a). Claude system for Liquefaction for gases

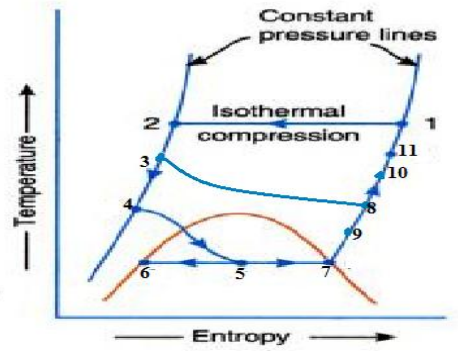


Fig: 2(b). Temperature vs entropy of Claude system

$$\eta_{comp} = \frac{W_t}{W_{comp}} \quad (15)$$

$$W_t = mRT \ln \frac{P_2}{P_1} \quad (16)$$

$$W_{comp} = h_2 - h_1 - T_1 (s_2 - s_1) \quad (17)$$

$$W_{reversible} = W_{actual} - T_0 S_{gen} \quad (18)$$

$$W_{Total} = W_{comp} + W_{Expander} \quad (19)$$

First heat exchanger:

$$m_2 (h_2 - h_3) = (m_2 - m_6)(h_1 - h_{10}) \quad (20)$$

Expander:

$$\frac{T_8}{T_9} = \left(\frac{P_8}{P_9}\right)^{\left(\frac{\gamma - 1}{\gamma}\right)} \eta_{expander} \quad (21)$$

$$W_{Expander} = h_8 - h_3 \quad (22)$$

$$(m_4 - m_6 + m_8) h_9 = m_8 h_8 + (m_4 - m_6)(h_7) \quad (23)$$

Second Heat exchanger:

$$m_4 (h_3 - h_4) = (m_2 - m_6)(h_{10} - h_9) \quad (24)$$

Throttle valve:

$$h_4 = h_5 \quad (25)$$

Heat Balance of the separator

$$m_4 h_5 = m_6 h_6 + (m_4 - m_6)(h_7) \quad (26)$$

Second law analysis:

$$\eta_{II}(\%) = m_6 \left(\frac{h_7 - h_6 - T_0 (s_7 - s_6)}{W_c}\right)_{*100} \quad (27)$$

COP (coefficient of performance):

$$COP = \frac{h_1 - h_7}{h_2 - h_1 - T_1 (s_2 - s_1)} \quad (28)$$

Table: 1. Performance perameters of Linde and Claude System for air

Linde System (Air)			
COP	η_2nd law(%)	m_Liq mass	P (Comp Pre)
0.5612	8.891	0.04751	100
0.487	12.64	0.0778	200
0.4501	13.58	0.09048	300
0.4253	12.92	0.0911	400
0.4063	11.43	0.08433	500

ClaudeSystem (Air)			
COP	η_2nd law(%)	m_Liq mass	P (Comp Pre)
0.4836	10.35	0.08203	200
0.4471	11.12	0.09533	300
0.4225	10.58	0.09603	400
0.4036	9.383	0.08913	500

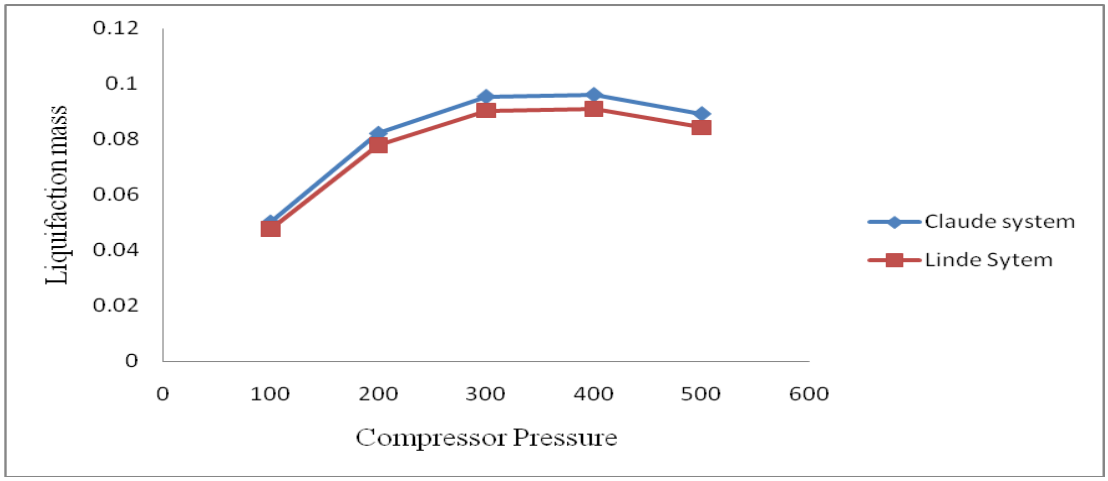


Fig: 3(a). Variation of Liquefaction mass with compressor pressure of air

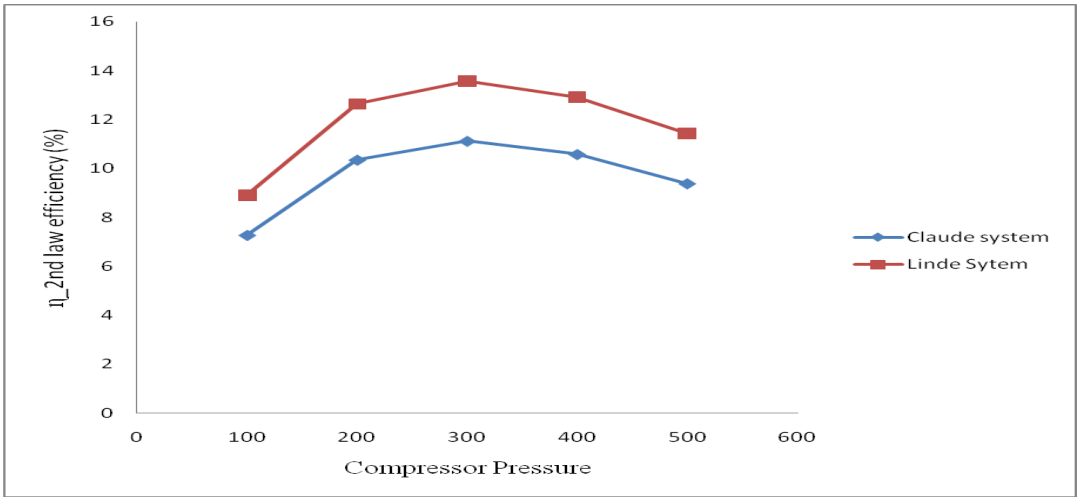


Fig: 3(b). Variation of Second law efficiency (%) with compressor pressure of air

Table: 2. Performance perameters of Linde and Claude System for Nitrogen

Claude System (N)			
COP	η_2nd law(%)	m_Liq mass	P (Comp Pre)
0.5679	6.818	0.04781	100
0.4921	9.851	0.07971	200
0.4543	10.87	0.09531	300
0.4287	10.67	0.09914	400
0.4091	9.795	0.09534	500

Linde System (N)			
COP	η_2nd law(%)	m_Liq mass	P (Comp Pre)
0.5721	8.521	0.04539	100
0.4954	12.3	0.07564	200
0.4571	13.57	0.09048	300
0.4314	13.32	0.09408	400
0.4116	12.2	0.0903	500

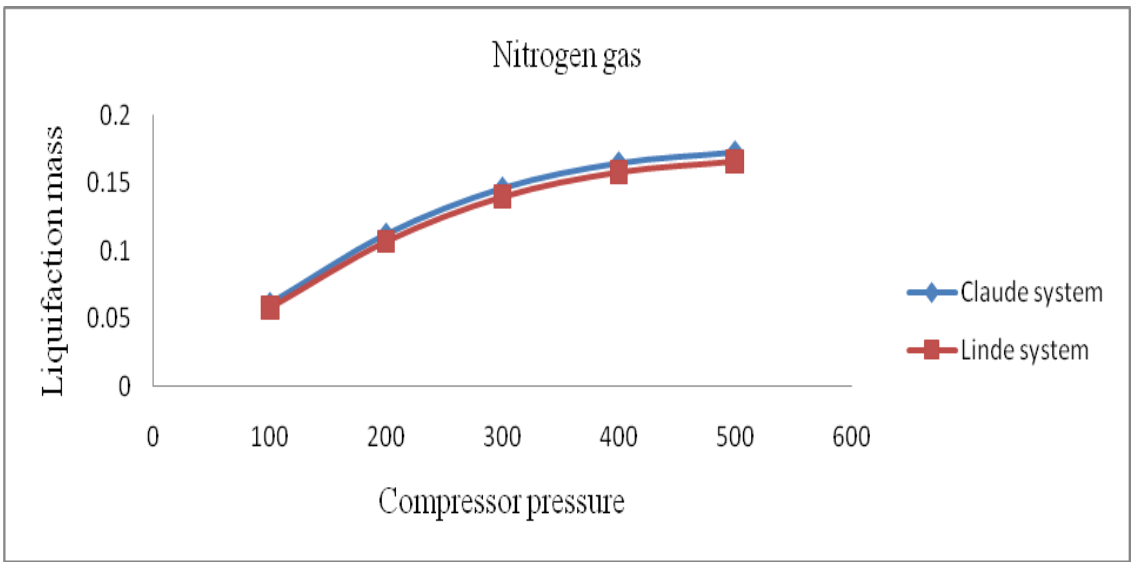


Fig: 3(c). Variation of Liquefaction mass with compressor pressure of nitrogen

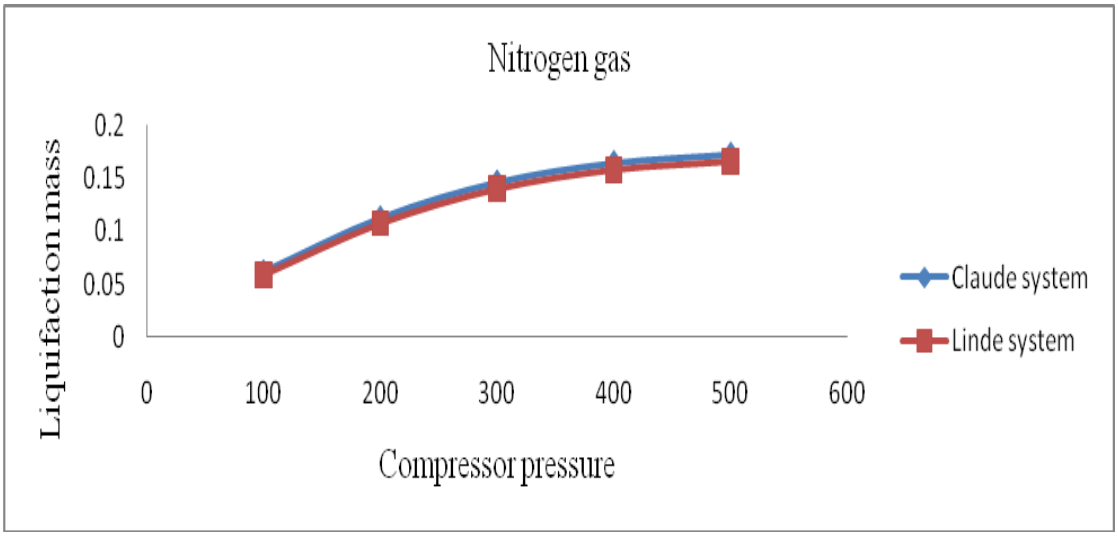


Fig: 3(d). Variation of Second law efficiency (%) with compressor pressure of nitrogen

Table: 3 Performance perameters of Linde and Claude System for Methane

ClaudeSystem (CH4)			
COP	η_2nd law(%)	m_Liq mass	P (Comp Pre)
0.5765	14.78	0.1164	100
0.5114	23.56	0.2091	200
0.4784	26.27	0.2492	300
0.4547	26.21	0.2615	400
0.4355	25.11	0.2617	500

LindeSystem (CH4)			
COP	η_2nd law(%)	m_Liq mass	P (Comp Pre)
0.5829	17.43	0.1105	100
0.5161	27.8	0.1991	200
0.4825	31.24	0.2392	300
0.4585	31.31	0.2523	400
0.4392	30.08	0.2531	500

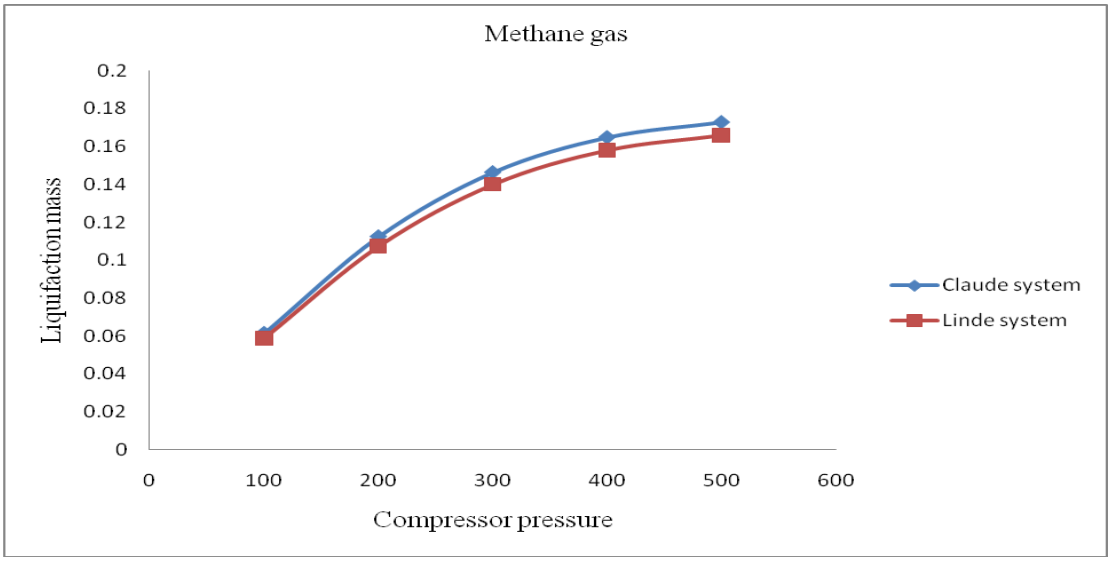


Fig: 3(e). Variation of Liquefaction mass with compressor pressure of methane

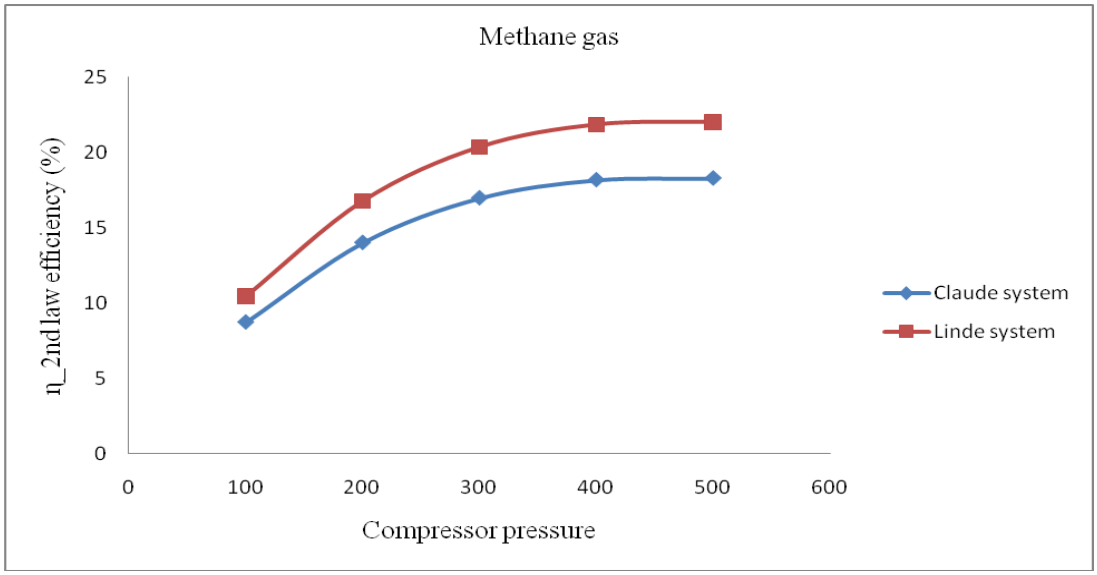


Fig: 3(f). Variation of Second law efficiency (%) with compressor pressure of methane

Table: 4. Performance perameters of Linde and Claude System for Flourine

ClaudeSystem (F)			
COP	η_2nd law(%)	m_Liq mass	P (Comp Pre)
0.5608	6.713	0.04466	100
0.489	10.57	0.08062	200
0.4541	13.01	0.1069	300
0.4311	14.22	0.123	400
0.4137	14.6	0.1316	500

LindeSystem (F)			
COP	η_2nd law(%)	m_Liq mass	P (Comp Pre)
0.5661	8.097	0.04266	100
0.4932	12.67	0.07665	200
0.4578	15.59	0.1016	300
0.4345	17.05	0.117	400
0.4169	17.52	0.1254	500

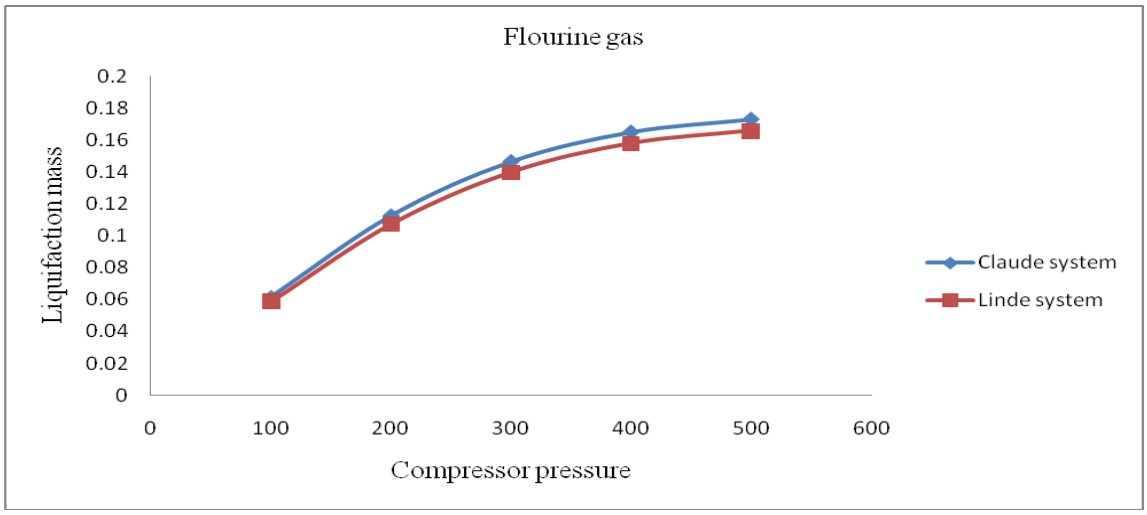


Fig: 3(g). Variation of Liquefaction mass with compressor pressure of Flourine

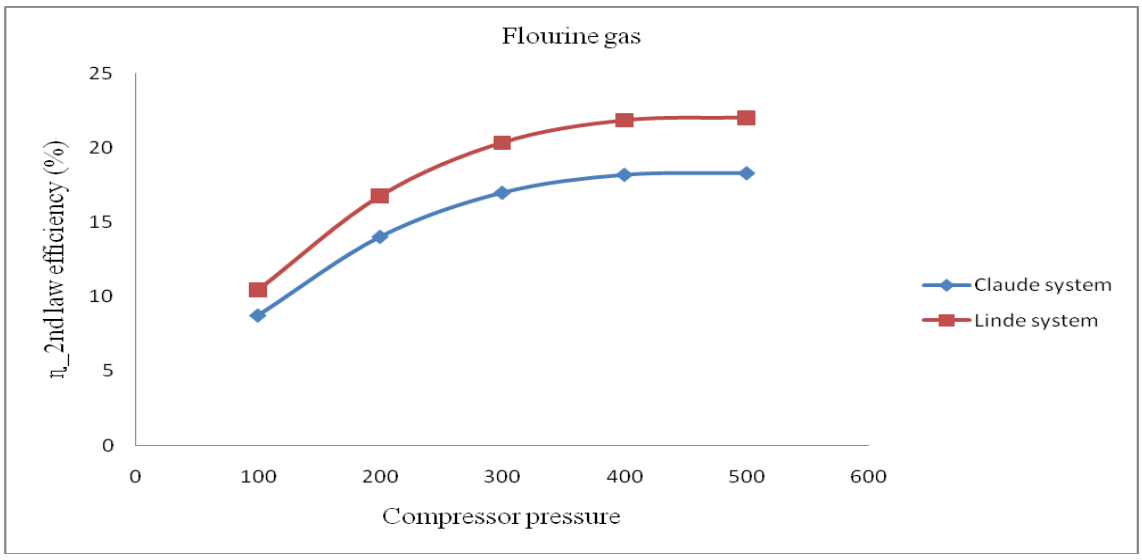


Fig: 3(h). Variation of Second law efficiency (%) with compressor pressure of Flourine

Table: 5. Performance perameters of Linde and Claude System for Argon

ClaudeSystem (Ar)			
COP	η_2nd law(%)	m_Liq mass	P (Comp Pre)
0.3923	9.83	0.06649	100
0.343	15.62	0.1209	200
0.3191	18.82	0.1565	300
0.3032	20.07	0.1757	400
0.291	20.12	0.1835	500

LindeSystem (Ar)			
COP	η_2nd law(%)	m_Liq mass	P (Comp Pre)
0.3955	11.1	0.06352	100
0.3454	17.61	0.1154	200
0.3212	21.24	0.1497	300
0.3051	22.7	0.1684	400
0.2928	22.79	0.1761	500

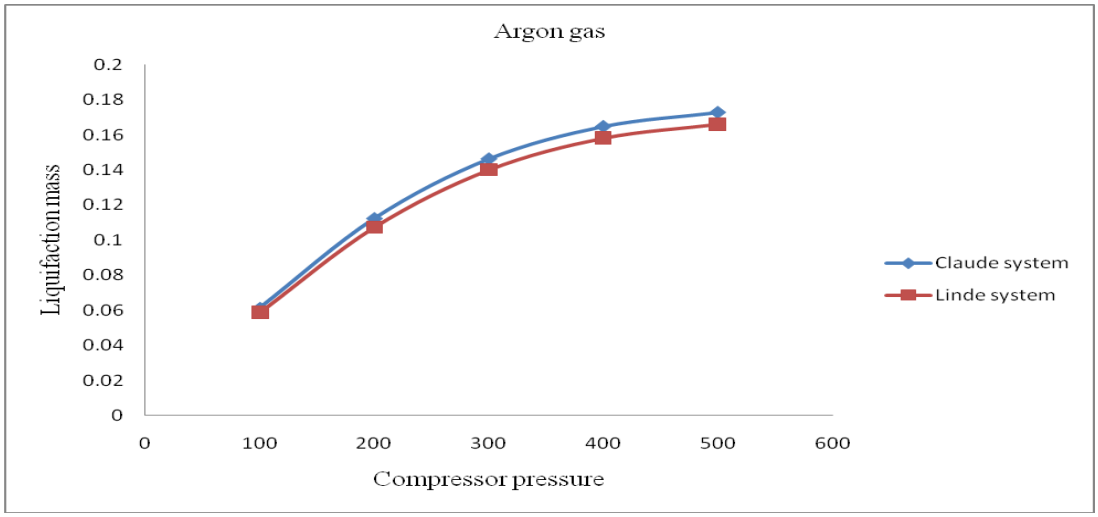


Fig: 3(i). Variation of Liquefaction mass with compressor pressure of Argon

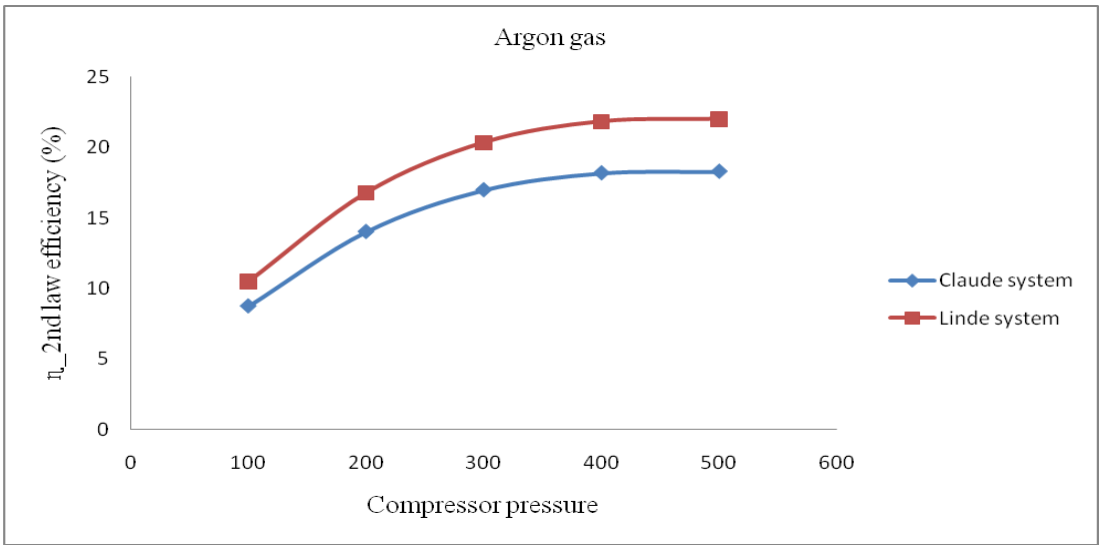


Fig: 3(j). Variation of Second law efficiency (%) with compressor pressure of Argon

Table: 6. Performance parameters of Linde and Claude System for Oxygen

ClaudeSystem (O2)			
COP	η_2nd law(%)	m_Liq mass	P (Comp Pre)
0.5395	8.732	0.06136	100
0.4719	14.01	0.1125	200
0.4392	16.97	0.1465	300
0.4174	18.17	0.165	400
0.4007	18.28	0.173	500

LindeSystem (O2)			
COP	η_2nd law(%)	m_Liq mass	P (Comp Pre)
0.5441	10.47	0.05851	100
0.4755	16.77	0.1072	200
0.4422	20.34	0.1399	300
0.4202	21.83	0.158	400
0.4033	22.01	0.1659	500

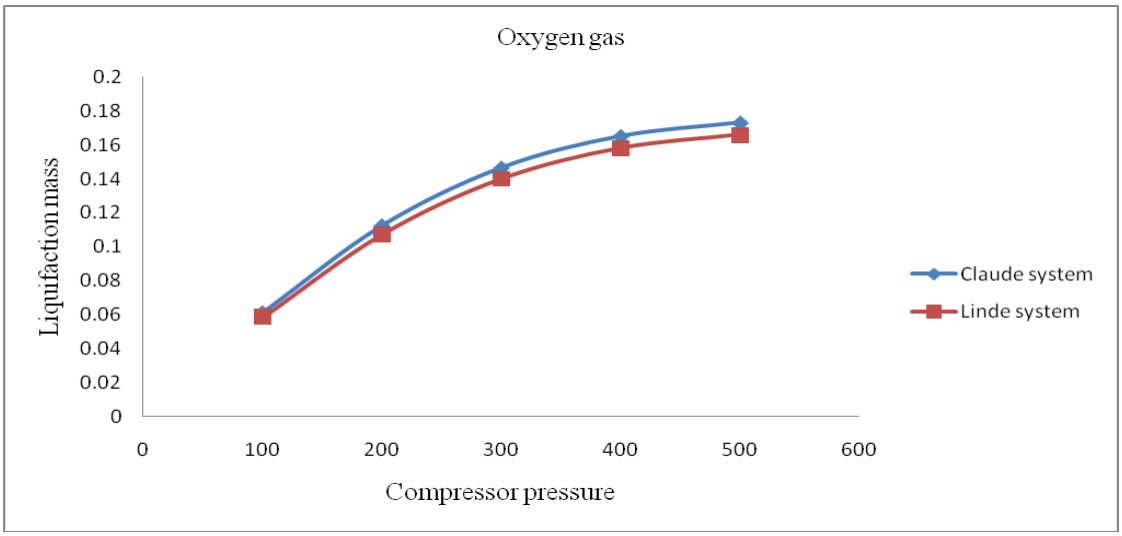


Fig: 3(k). Variation of Liquefaction mass with compressor pressure of Oxygen

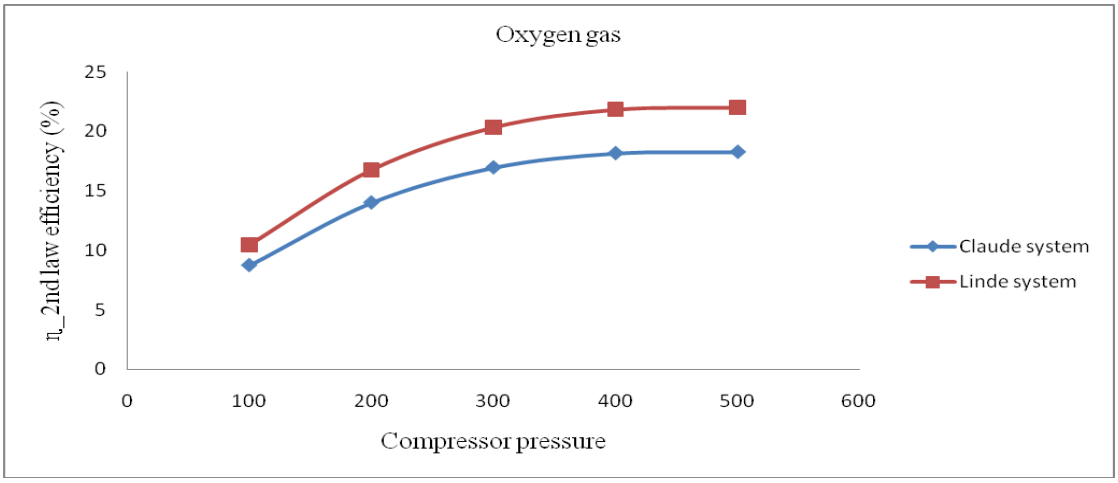


Fig: 3(l). Variation of Second law efficiency (%) with compressor pressure of Oxygen

3. Results and discussion

Using thermodynamic first and second law analysis, the comparison between Linde and Claude systems for liquefaction of gases have been made for constant inlet condition and performance parameters were evaluated are shown in table 1-6 respectively. Computational numerical technique is used for both system for varying compressor pressure and results are shown in Figs 3 respectively. It was observed that the liquefaction mass of gases is higher in Claude system as compared to Linde system ,so output of Claude system is more than the Linde system. The compressor pressure is not directly proportional to liquefaction mass ,liquefaction mass is higher in range of 300 to 400 bar compressor pressure ,further increase in pressure degrade the quantity of liquefaction mass in both system.

Using exergy analysis it was obsereved that that the second law efficiency of Linde system is more than the Claude system and compressor pressure in range of 300 to 330 bar show highest efficiency for all gaes

4. Conclusion

1. Linde system having less energy losses than Claude system showing higher second law efficiency than Claude system for all gases mention above.
2. Output wise the Claude system is better than Linde system for all gases mention above.
3. Compressor pressure range 300 to 350 show good result in both system at constant slandered atmospherics inlet conditions

References

[1] J. L. Yang, Y. T. Ma, M. X. Li, H. Q. Guan, "Exergy analysis of transcritical carbon dioxide refrigeration cycle with an expander", Energy 30 (2005) ISSN 1162-1175.

[2] Ignacio Lopez Paniagua, Javier Rodrıguez Mart´ın, Celina Gonzalez Fernandez, Angel Jimenez Alvaro, Rafael Nieto Carlier, "A new simple method for estimating exergy destruction in heat exchangers" , Entropy (2013), 15, 474-489; ISSN 1099-4300

[3] YongliangLi, Xiang Wang, Yulong Ding, "An optimal design methodology for large-scale gas liquefaction", Applied Energy 99 (2012) 484–490, ISSN 0306-2619

[4] Antungalovic, Marijazivicand Matokokanovic, "Analysis of exergy destruction of an evaporator or/and a condenser", Strojarstvo 51(1) 73-78 (2009), ISSN 0562-1887

[5] A. Franco, A. Russo, "Combined cycle plant efficiency increase based on the optimization of the heat recovery steam generator operating parameters", Int. J. Therm. Sci. 41 (2002), 843–859

[6] R. Saidur, J. Ahamed, Masjuki, H. Energy, "Exergy and economic analysis of industrial boilers", Energy Policy 38 (2010), ISSN 2188–219

[7] T. J. Kotas, "The Exergy Method of Thermal Plant Analysis", 1995 Ed.; Krieger Publishing Company: London, UK, 1985

International Journal of Advanced Information Science and Technology (IJAIST) ISSN: 2319:2682
Vol.15, No.15, July 2013

Two Zone Combustion Model for SI Engines to Study the Variations in Cylinder Pressures and Temperatures between Adiabatic Combustion and Eichelberg's Correlation

Vikram Singh
Undergraduate Student/Department of ME
Delhi Technological University, Delhi, India
vs.vikramsngh91@gmail.com

Rajkumar Singh
Associate Professor/Department of ME
Delhi Technological University, Delhi, India
rajkumarsingh@dce.ac.in

Sarthak Piplani
Undergraduate Student/Department of ME
Delhi Technological University, Delhi, India
sarthak.piplani@gmail.com

Aditya Tyagi
Undergraduate Student/Department of ME
Delhi Technological University, Delhi, India
tyagiaditya06@gmail.com

***Abstract* - Computer simulation of SI engines is a useful tool to predict engine performance due to changes in input variables and also study the effect of phenomena like heat transfer to the engine performance. The paper describes the building of a thermodynamic two zone combustion model for SI engines to observe the theoretical deviation in cylinder pressure and temperature between a case of adiabatic combustion and a case using Eichelberg's heat transfer correlation. The two zone model developed in MATLAB is a good platform to analyse such results as it can depict changes in peak burned gas temperature that single zone models can't and saves on the long computation time required in multi zone models. Existing two zone models do not study the effect of heat transfer on the engine's output. The work aims to find the deviation of engine cylinder pressure and temperature over a range of engine speeds and over the entire crank angle duration. The simulation shows that the pressure deviation was small compared to the temperature deviation, especially at higher engine speeds, where the peak pressure variations became negligible. The combustion model was verified using experimental data from referenced works.**

Keywords: ***Engine-Model-Combustion***

I. INTRODUCTION

Computer simulation of engines is an important tool in analyzing the effect of input variables like intake pressure, valve timings and spark advance. It helps in optimizing an engine design for particular applications. It also reduces the need for expensive engine tests and provides a cost effective method for engine study.

The simulation of combustion in SI engines can be done using zero dimensional or multi-dimensional combustion models. Zero dimensional models are purely thermodynamic models, they do not model the flow of the mixture inside the combustion chamber. Zero dimensional models can be further subdivided into single zone, two zone and multi zone models. Single zone models treat the entire combustion chamber as a single zone in which heat is added or subtracted. The zone has uniform properties throughout and has the same values of combustion pressure and temperature at all points. Ferguson's [2] original work had a FORTRAN code for a combustion model which was widely used. However the model was a single zone model and its accuracy was limited.

Two zone models divide the combustion chamber into burned gas mixtures and unburned gas mixtures with the flame front dividing the zones. The mixture which is further away from the spark plug is first compressed due to the increasing pressure generated by the advancing flame front and burning mixture and then burned, whereas the mixture closer to the spark plug is first burned and then compressed. This leads to a gradient of properties inside the combustion chamber. Multizone models hence, divide the combustion chamber into multiple zones, each with homogenous properties.

However with increasing complexity, the computation time required for the model also increases.

Heat transfer is a critical aspect in internal combustion engines. All thermodynamic processes within an IC engine are never truly adiabatic and heat is always rejected to the engine coolant through the combustion chamber walls to keep the engine temperatures in safe operating conditions. The two zone combustion chamber incorporates an Eichelberg heat transfer model to calculate the heat transfer coefficient to the walls of the combustion chamber.

Current simulations of Eichelberg's heat transfer correlation do not study the fundamental deviation of cylinder pressures and temperatures from adiabatic combustion due to it. This paper aims to study the behavior of Eichelberg's model and predicts the changes in engine output due to enabling heat transfer to the cylinder wall.

II. ASSUMPTIONS TAKEN

1. The model assumes that complete burning of the fuel takes place. That is, in cases of the fuel air equivalence ratio being less than 1, all fuel is converted to carbon dioxide and water vapor.
2. Unthrottled operation is assumed.
3. No valve overlap is allowed in the model.
4. The combustion chamber is assumed as disc shaped and the surface area of the burned zone with respect to the

flame front radius is taken according to this assumption.

5. Eichelberg's heat transfer model is taken for the computation of heat transfer coefficient.
6. The specific gas constant for each gas is taken as a constant and does not vary with temperature or pressure (dR = 0)
7. The flame front is assumed be perfectly spherical with the spark plug as the centre.
8. The motion of the charge or the gases inside the cylinder are not accounted for due to it being a zero dimensional model.

III. SIMULATION MODEL

The properties of each zone are calculated for each time step in the model based on the properties in the previous time step. Each time step corresponds to 0.1 degree of crank angle rotation. The model is sub divided into a number of sub-routines to simulate a particular process within the combustion chamber. The sub routines are intake, compression, combustion, expansion and exhaust.

A. Governing Equations For Combustion

The governing equations for the two zones can be written as –

$$dV_u + dV_b = dV \tag{1}$$

$$V_u dP + P dV_u - m_u R_u dT_u = R_u T_u dm_{ub} \tag{2}$$

$$P dV_u + m_u c_{v,u} dT_u = -dQ_u + (h_{ub} - u_u) dm_{ub} \tag{3}$$

$$V_b dP + P dV_b - m_b R_b dT_b = R_b T_b dm_{bu} \tag{4}$$

$$P dV_b + m_b c_{v,b} dT_b = -dQ_b + (h_{bu} - u_b) dm_{bu} \tag{5}$$

Where dV, dP and dT denote the changes in volume, pressure and temperature respectively for the zones. These values are calculated for each time step and are then added to the values at the previous iteration.

According to Nilsson [5], the gas is assumed to undergo combustion instantly as it leaves the unburned zone and enters the burned zone. This means that:

$$h_{ub} = h_{bu} = h_u \tag{6}$$

The value of dm is calculated using the cosine burn law for each 0.1 degree crank rotation. The fundamental formulation for the equations are taken from Nilsson[5].

The equations can be arranged in the form of

$$AX = B \tag{7}$$

Where

$$A = \begin{bmatrix} 0 & 1 & 0 & 1 & 0 \\ V_u & P & -m_u R_u & 0 & 0 \\ 0 & P & m_u c_{v,u} & 0 & 0 \\ V_b & 0 & 0 & P & -m_b R_b \\ 0 & 0 & 0 & P & m_b c_{v,b} \end{bmatrix} \tag{8}$$

$$X = \begin{bmatrix} dP \\ dV_u \\ dT_u \\ dV_b \\ dT_b \end{bmatrix} \tag{9}$$

$$B = \begin{bmatrix} dV \\ R_u T_u dm \\ -dQ_u + R_u T_u dm \\ R_b T_b dm \\ -dQb + (h_u - h_b + R_b T_b) dm \end{bmatrix} \tag{10}$$

This makes the solving easier as MATLAB can simply find the inverse of matrix A and multiply it to matrix B to get X. Adaptive scaling of the matrices is done to keep the condition number of the matrix within acceptable limits.

MATLAB provides a suitable platform for writing the code for such a simulation model, as pointed out by Buttsworth[8] in his work where he compares his code written in MATLAB to Ferguson's[2] code written in FORTRAN.

Properties of both unburned and burned gases were taken from Heywood[1]. These properties are approximations and reasonably conform to those according to JANAF[10] tables and Newhall's[9] work. The mass fraction burn rate was taken as a cosine function of the angle of combustion duration. The behavior of the mass burnt fraction with increasing crank angle was according to established norms.

An approach in which an empirical relation for flame front velocity would be used to calculate mass burnt fraction was also considered, similar to that done by Hosseini[7], this however did not give good agreement with combustion duration values for crank angle.

$$n = \frac{1}{2}\left[1 - \cos\left[\frac{\theta - \theta_i}{\Delta\theta_c}\,\pi\right]\right] \tag{11}$$

Where, n is the mass burned fraction, θ is the crank angle and θ_i is the crank angle at the start of combustion. $\Delta\theta_c$is the duration of the combustion process and is taken according to Taylor's[4] formulation as

$$\Delta\theta_c = 40 + 5\left(\frac{N}{600} - 1\right) + 166(\emptyset - 1.1)^2 \tag{12}$$

At each time step, the properties dV, dP and dT are calculated and the values are updated for the next time step.

B. Intake and Exhaust

The intake and exhaust simulation has been done similar to Ganesan's[3] single zone combustion model.

For simulating the flow across a restricted area, the intake and exhaust flow must be considered in two regimes – subsonic and supersonic. The ratio of upstream pressure to downstream pressure ($^{p}/_{p_0}$) must be under a critical value for subsonic flows. In supersonic flows the flow across the valve becomes choked, and the mass flow rate of the gas across the valve becomes constant, independent of the pressure ratio existing across the valve.

$$Critical\ Pressure\ Ratio = \left(\frac{\gamma+1}{2}\right)^{\frac{\gamma}{\gamma-1}} \quad (13)$$

Where γ = specific heat ratio of the gas or mixture

The mass flow rate across a restriction or the valve in case of subsonic flow is

$$\frac{dM}{dt} = Ap_0\sqrt{\frac{2\gamma}{RT(\gamma-1)}\left(\frac{p}{p_0}\right)^{\frac{\gamma-1}{\gamma}}\left[\left(\frac{p}{p_0}\right)^{\frac{\gamma-1}{\gamma}}-1\right]} \quad (14)$$

And in case of supersonic flow is

$$\frac{dM}{dt} = AP\sqrt{\frac{\gamma}{RT}\left(\frac{2}{\gamma+1}\right)^{\frac{\gamma+1}{\gamma-1}}} \quad (15)$$

C. Heat Transfer Model

Heat transfer within the internal combustion engine is an important aspect of the combustion process. It maintains the cylinder head, cylinder wall and the piston in safe operating conditions and keeps the temperatures lower than their melting point.

The equation for heat transfer to the cylinder walls is the standard equation for heat transfer due to convection.

$$Q = h_c A \Delta T \quad (16)$$

Where h_c is the heat transfer coefficient, A is the cylinder wall area and ΔT is the difference in temperature between the cylinder wall and the gas.

The problem however lies in determining the value of heat transfer coefficient of the gases to the cylinder walls. Various models and empirical formulae exist to calculate the value of the heat transfer coefficient. According to Luonici[6], Eichelberg's correlation has an acceptable accuracy, uses relatively low computation times and requires no tuning. The relation is given by

$$h_c = 2.1(C_m)^{1/3}(PT)^{1/2} \quad (17)$$

The area of the zones in contact with the cylinder walls was determinedby using the burned gas volume to determine the radius of the flame front from the spark plug. And the area was then determined from the enflamed region radius.

IV. RESULTS

The simulation was carried out under the following engine conditions. The data was taken similar to the engine specifications used by Ganesan[3].

Bore	79.4 mm
Stroke	111.2 mm
V_{disp}	550.8 cc
Connecting Rod Length	233.4 mm
Compression Ratio	7.4
Operation	Full Throttle
Intake manifold Pressure	1 atm
Intake Manifold Temperature	300 K
Air Fuel Equivalence Ratio	1.0
Speed	4000 RPM
Intake Valve Opening/ Intake Valve Closing	0 degree BTC/ 30 degrees ABC
Exhaust Valve Opening/ Exhaust Valve Closing	30 degree BBC/ 0 degree ATC

The simulation results can be seen in Figure 1 and Figure 2. Comparing the cylinder pressure data to Ganesan's[3] model, the simulation done has a peak pressure value closer to experimental pressure data than Ganesan's one zone model.

Figure 1 shows the drop in pressure due to activating Eichelberg's heat transfer correlation. The pressure drop is not significant during the earlier phase of combustion and the pressure difference is only slightly larger by the end of the expansion stroke, late in the expansion stroke. The reduction in peak pressure is only1.9% whereas the maiximum change in the pressure is 1.165 bar, which is 4.6%.

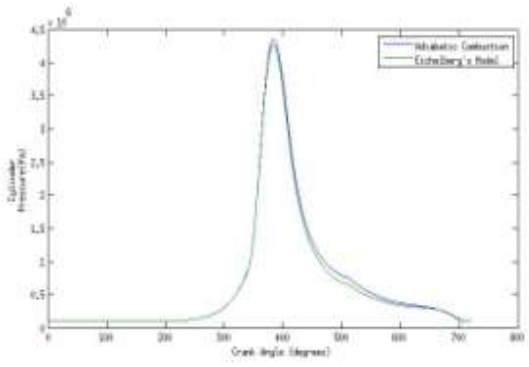


Figure 1: Pressure Comparison between Adiabatic combustion and Eichelberg's Heat Transfer Model

Figure 2 shows the variation of burned gas temperatures in the two zone model. The temperature difference in the zone is significant during the expansion stroke. The maximum drop in temperature in this case was 266.08 K which is a 13.37% change in cylinder temperature.

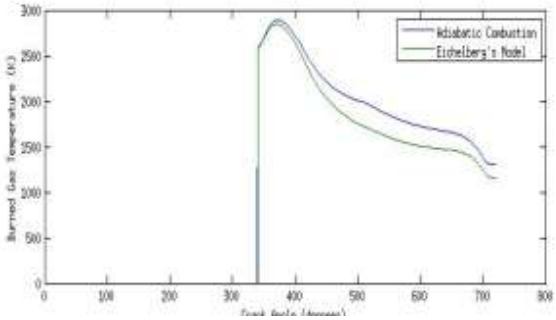


Figure 2: Burned gas temperature comparison between adiabatic combustion and Eichelberg's heat transfer model

Figure 3 shows the difference in peak cylinder pressures over a range of engine speeds. The difference in pressures is greater at lower speeds, than at higher speeds, due to longer times that the gas has to reside in the cylinder, hence convecting away more heat to the cylinder walls.

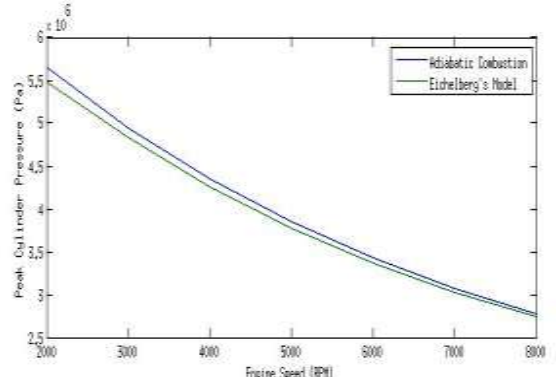


Figure 3: Peak cylinder pressure comparison between adiabatic combustion and Eichelberg's heat transfer model over a range of 2000 rpm - 8000 rpm

Figure 4 shows the variation in peak temperatures over the same engine speed range.

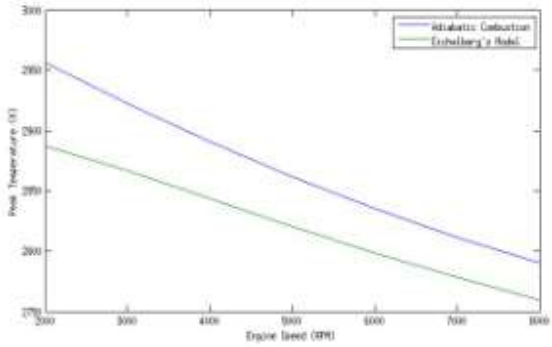


Figure 4:Peak temperature comparison between adiabatic combustion and Eichelberg's heat transfer model over a range of 2000rpm-8000rpm

V. CONCLUSION

The two zone model was successfully implemented and the integration of the Eichelberg's heat transfer model was done. The variations in cylinder pressure and burned gas temperatures can be seen in the simulation results.

The effect on temperature in the later stages of the expansion process and the exhaust stroke is significant and the burned gas temperature decreases by greater than 250 K. The deviation in cylinder pressure is not as significant during the engine cycle.

The variation in peak temperatures and pressures with changing engine speed showed a decreasing change in pressure. The peak pressure change was almost negligible at 8000 RPM. Peak cylinder temperatures still show a large variation even at higher engine speeds, though they show a decreasing trend.

VI. NOMENCLATURE

V - Volume (m^3)
P – Pressure (Pa)
R – Specific Gas Constant ($JK^{-1}g^{-1}$)
T – Temperature (K)
M – Mass (g)
c_v – Specific Heat Capacity at Constant Volume ($JK^{-1}g^{-1}$)
Q – Heat Transferred to the Cylinder Walls (J)
h – Specific Enthalpy (Jg^{-1})
u – Specific Internal Energy (Jg^{-1})
n – Mass Burnt Fraction
N – Engine Speed (RPM)
k – Ratio of specific heats ($^{c_p}/_{c_v}$)
C_m – Mean Piston Speed ($m\ s^{-1}$)
A – Valve Curtain Area (m^2)

Subscripts Used
u –unburntmixture property
b –burntmixture property
ub – property of mixture going from unburnt to burnt zone

bu – property of mixture going from burnt to unburnt zone

REFERENCES

[1] Heywood, J.B., 2011, *Internal Combustion Engine Fundamentals*, Tata McGraw Hill, New Delhi, 930 p.
[2] Ferguson, C.R., 1986, *Internal Combustion Engines: Applied Thermosciences*, John Wiley and Sons, New York, 384 p.
[3] Ganesan V., 1996, *Computer Simulation of Spark-ignition Engine Processes*, Universities Press (India) Limited, Hyderabad, 231 p.
[4] Taylor, C.F., 1985, *The Internal Combustion Engine in Theory and Practice*, MIT Press, Cambridge, 584 p.
[5] Nilsson, Y. and Eriksson L. (2001), A new formulation of multi-zone combustion engine models, *IFAC Workshop: Advances in Automotive Control*, March 28-30, 2001, Karlsruhe
[6] Lounici, M.S., Loubar, K., Balistrou, M. and Tazerout, M., 2011,Investigation on heat transfer evaluation for a more efficient two-zone combustion model in the case of natural gas SI engines, *Applied Thermal Engineering* v. 31, p. 319-328
[7] Hosseini, Seyedmohsen, Abdolah R., and Khani A., 2008,A developed quasi-dimensional combustion model in spark-ignition engines,*Proceedings of the World Congress on Engineering* Vol. 2. 2008.
[8] Buttsworth, D.,2009,Multizone Internal Combustion Engine Modelling: Initial Assessment of a Simulation Tool Developed in Matlab, *Proceedings of ICEE 2009 3rd International Conference on Energy and Environment*, December 7-8, 2009, Malacca
[9] Newhall, H.K. and Starkman, E.S., 1964, Thermodynamic Properties of Octane and Air for Engine Performance Calculations, *Digital Calculations of Engine Cycles, Progress in Technology*, v. TP-7, p. 38-48
[10] *JANAF Thermochemical Tables*, 2nded, NSRDS-NB537, U.S. National Bureau of Standards, June 1971